Review of Particle Physics at PSI

Editors: A.Signer, K.Kirch, C.M.Hoffman

Review of Particle Physics at PSI

Editors: A. Signer, K. Kirch and C. M. Hoffman

Contents

Particle Physics at PSI

A. Signer[1,2†], K. Kirch[1,3‡] and C. M. Hoffman[⋆]

1 Paul Scherrer Institute, Villigen PSI, Switzerland
2 University of Zurich, Physik-Institut, Zurich, Switzerland
3 ETH Zurich, Institute for Particle Physics and Astrophysics, Zurich, Switzerland

† adrian.signer@psi.ch, ‡ klaus.kirch@psi.ch
⋆ Retired from University of New Mexico, Albuquerque, USA
and Los Alamos National Laboratory, USA

Abstract

Particle physics results of constant value and significant impact have been obtained at PSI, and several efforts are presently ongoing and expected to deliver new findings in the near future. In this special SciPost volume we collect them together in a concise manner. Not yet included are ideas for future facility upgrades or completely new experimental efforts, but we are set to extend this volume in the years to come.

The intensity frontier of particle physics uses intense particle beams to perform precision tests of the Standard Model (SM) and to search for rare processes forbidden in the SM. This approach is complementary to the energy frontier. The proton accelerator facility at the Paul Scherrer Institute (PSI), with its ring cyclotron [3] generates high-intensity beams of pions, muons and ultracold neutrons. In this special SciPost volume, a collection of articles describes past, present and future experiments using these beams at the intensity frontier, as well as a description of the facility. Ideas for future facility upgrades or completely new experimental efforts are not included here, but we are ready to extend this volume in the years to come.

PSI is the largest federal research institute in Switzerland. It belongs to the ETH domain and serves as a national laboratory to provide large-scale research infrastructure, such as accelerators, that are beyond the means of a single university. PSI was formed in 1988 by the merger of two predecessor institutions: EIR (Eidgenössisches Institut fur Reaktorforschung) and SIN (Schweizer Institut für Nuklearforschung). SIN was founded to host Switzerland's "pion factory", a high-intensity proton accelerator complex with target stations and secondary beam lines. We use the term "PSI" to include facilities and activities at both SIN and PSI.

The proton accelerator facility at PSI produced its first pions shortly after it went into operation in 1974. The design of the high-intensity ring cyclotron was novel and innovative, aiming at a proton current of $100\,\mu A$ at a kinetic energy of $590\,MeV$. The accelerator has been continuously improved and upgraded and has far outperformed these design goals. It is currently

among the world's most powerful proton accelerators, producing an average beam power of up to 1.4 MW, with a beam current of over 2 mA. Several low-momentum beams of pions and muons are produced with the highest intensities available [4]. In the last 10 years, a dedicated neutron spallation target has been added, which serves as a high-intensity source of ultracold neutrons [5]. As new experiments need even higher intensities to reach their ambitious goals, plans to further upgrade the facility are under discussion.

Many of the particle physics experiments performed at PSI use the high beam fluxes to precisely measure the parameters of the SM, or to search for the possible existence of physics beyond the SM with improved sensitivity. While the results from these studies have been published in many articles and journals over the years, there has been no review to date collecting all of these in one volume. This SciPost Volume aims to fill that void.

Peter Truöl[1] published a monograph in 2007 [2] entitled *Myonen und Pionen in Teilchenphysik und Anwendungen – 30 Jahre experimentelle Forschung an der Schweizer Mesonenfabrik in Villigen*. This was, unfortunately, only available in German, and was meant for a different audience than this volume. Peter Truöl, together with one of the editors of this volume (KK), wanted to update and extend this nice booklet into a major review article aimed at an international audience of interested particle physicists. While that project was never realized, the present editors teamed up to assemble this special volume. We distributed much of the work to the many colleagues who are actually much better able to write individual parts of this review, reporting on their own work. We are grateful to all of the authors who accepted our request, and contributed their articles.

When we started this project some time ago, we asked two very dear colleagues, Claude Petijean and Manfred Daum, to serve as guinea pigs. They wrote several example contributions, which were discussed and used to help fix the instructions and templates for the other authors. Claude and Manfred also wrote several final contributions and served as critical reviewers for many other papers. In addition, many other authors and colleagues served as anonymous referees for the contributions to this special volume. We give a huge "thank you" to all those who helped!

We hope that this volume will remain as a reference for the achievements in particle physics at PSI, and expect that many future contributions will extend this collection.

Klaus Kirch, Adrian Signer, Cy Hoffman

References

[1] P. A. Zyla et al., *Review of particle physics*, Progr. Theor. Exp. Phys. 083C01 (2020), doi:10.1093/ptep/ptaa104.

[2] P. Truöl, *Myonen und Pionen in Teilchenphysik und Anwendungen – 30 Jahre experimentelle Forschung an der Schweizer Mesonenfabrik in Villigen*, Naturforschende Gesellschaft in Zürich (2007), ISSN 0379-1327.

[3] J. Grillenberger, C. Baumgarten and M. Seidel, *The high intensity proton accelerator facility*, SciPost Phys. Proc. **5**, 002 (2021), doi:10.21468/SciPostPhysProc.5.002.

[4] D. Kiselev, P. A. Duperrex, S. Jollet, S. Joray, D. Laube, D. Reggiani, R. Sobbia and V. Talanov, *The Meson Production Targets in the high energy beamline of HIPA at PSI*, SciPost Phys. Proc. **5**, 003 (2021), doi:10.21468/SciPostPhysProc.5.003.

---

[1]Peter Truöl (1939-2020) was professor of experimental particle physics at the University of Zurich and chairman of the particle physics advisory committee at PSI for ten years, 1993-2002, after which one of the volume editors (CMH) took over this duty for another long period, 2002-2014.

[5] B. Lauss and B. Blau, *UCN, the ultracold neutron source – neutrons for particle physics*, SciPost Phys. Proc. **5**, 004 (2021), doi:10.21468/SciPostPhysProc.5.004.

The High Intensity Proton Accelerator Facility

J. Grillenberger⋆, C. Baumgarten and M. Seidel

Paul Scherrer Institut, 5232 Villigen PSI, Switzerland

⋆ joachim.grillenberger@psi.ch

Abstract

The High Intensity Proton Accelerator Facility at PSI routinely produces a proton beam with up to $1.4\,$MW **power at a kinetic energy of** $590\,$MeV. **The beam is used to generate neutrons in spallation targets, and pions in meson production targets. The pions decay into muons and neutrinos. Pions and muons are used for condensed matter and particle physics research at the intensity frontier. This section presents the main physics and technology concepts utilized in the facility. It includes beam dynamics and the control of beam losses and activation, power conversion, efficiency aspects, and performance figures, including the availability of the facility.**

2.1 Introduction

The original proposal for the accelerator facility that is now known as the PSI high intensity proton accelerator (HIPA)[1], was completed 1963 [2]. The objective was to produce a proton beam of several tens of microampere with an extraction rate higher than 50 % and an energy above 450 MeV, with the main goal to produce π-mesons and muons[2]. The final beam energy was later raised to $\geq$ 580 MeV and the specified beam current raised to 100 μA [3]. The main accelerator is the Ring cyclotron, an isochronous proton machine with eight separate magnet sectors and four main accelerating cavities operating at 50.6 MHz. The Ring cyclotron is designed to accelerate an injected 72 MeV proton beam to 590 MeV. The first pre-accelerator, called the Injector I cyclotron, was designed and constructed by Philips (Eindhoven). Injector I was a multi-purpose machine, that accelerated protons up to 72 MeV with a maximal extracted current of $I_{\max} \leq 180\,\mu$A, and also light ions for nuclear physics research. After one year of operation, in 1975, the highest beam current on target was 25 μA. The performance of the Ring cyclotron was steadily improved, especially the extraction efficiency. In December 1976 an extraction efficiency of 99.9 % (Ring) and of 85 % (Injector I) was achieved. The peak

---

[1]Formerly named the *Isochronous Cyclotron Meson Factory of ETH Zurich* [1], then the Schweizerische Institut für Nuklearforschung (S.I.N.) Ring Cyclotron.

[2]The term *meson* production targets was established for historical reasons - even though muons are leptons.
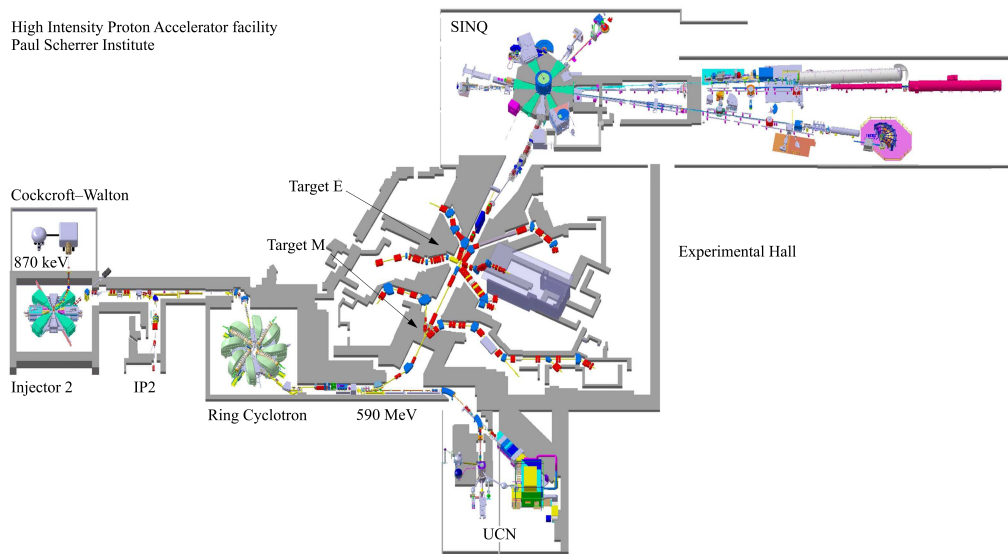
Figure 2.1: Layout of the High Intensity Proton Accelerator facility at the Paul Scherrer Institute.

intensity was raised within two years from $12\,\mu$A to $112\,\mu$A [4]. The beam current was limited by the 9 % beam losses at the extraction of Injector I and the resulting activation of components. Injector I was also used for low-energy experiments. During these experiments, Injector I was not available as a proton driver for the Ring cyclotron. Injector I was not able to deliver beam currents higher than about $180\,\mu$A (originally $100\,\mu$A specified), while the performance of the Ring cyclotron indicated the capability for much higher currents with low losses. Therefore, studies for an upgrade of the Ring cyclotron with a flattop cavity and a new injector cyclotron with a Cockcroft-Walton type pre-accelerator for beam currents of up to 1 mA were in progress while the commissioning was still ongoing [5]. At this stage, it was estimated that the Ring cyclotron had the potential to accelerate currents of up to $2-4$ mA [6]. The proposal to use two pre-accelerators, a 860 keV Cockcroft-Walton type accelerator followed by the new Injector II cyclotron, was approved in 1978.

Since 2010 the protons are produced by a compact small electron cyclotron resonance source with a 60 kV extraction system [7]. Two solenoids are used to focus the extracted protons onto a collimator. Hydrogen ions (H_2^+ and H_3^+), which are extracted as well, are only weakly focused due to their lower charge-to-mass ratio, and are stopped. The protons are accelerated in three stages. A Cockcroft-Walton DC linear accelerator, shown left in Figure 2.1, is used to pre-accelerate the DC proton beam to 0.87 MeV as required for the injection into the first turn of the Injector II cyclotron. The beamline is equipped with a bunching system a few meter upstream of the axial injection line, to match the beam phase space to the acceptance of Injector II. Injector II accelerates the pre-bunched beam with two high-voltage double-gap resonators[3] to an energy of 72 MeV within 80 turns. The extracted beam is then sent to an electrostatic beam splitter, where up to $100\,\mu$A can be split off for the production of radio-isotopes. The main part of the beam is injected into the Ring cyclotron with an electrostatic inflection channel. Eight normal-conducting magnets keep the particles' on their spiral path in the cyclotron. Four 50.6 MHz cavities accelerate the beam to its final kinetic energy of 590 MeV. After about 180 turns in the cyclotron, the beam is extracted with an electrostatic element (see Figure 2.2) and sent to the meson production targets [8]. These targets are

---

[3]A double-gap resonator is equivalent to a conventional Dee with two accelerating areas (gaps). In contrast the PSI Ring cyclotron uses hollow "single-gap" cavities.

Figure 2.2: Pictures of the electrostatic extraction channel EEC without (left) and with attached aluminium shroud (right). The red arrow denotes the beam passing through the channel. The dashed part of the arrow denotes the parts where the beam passes through in between the grounded tungsten stripes and the aluminium cathode. The electric field of $8-10$ MV/m deflects the beam by 8 mrad on 920 mm effective length so it can be extracted from the cyclotron by a subsequent septum magnet.

made of graphite and limited in thickness so that the beam loses only a small fraction of its energy. After passing through a collimation system, needed due to multiple scattering in the meson production targets, roughly 60 (70) % of the beam current is left for a target thickness of 60(40) mm, and is then sent to the neutron spallation source SINQ [9–14]. If SINQ is not ready for beam, the beam is sent to the 590 MeV beam dump. Due to cooling issues, the beam current is then limited to 1.7(2.0) mA on a 40(60) mm thick meson production target. The Ultracold Neutron Source (UCN) is in operation since 2011 [15–19]. A fast kicker magnet just upstream of the meson production targets deflects the beam for a short time between 2 and 8 s to the UCN facility [20]. The duty cycle is restricted to a maximum of 3%.

The intention of this article is to present performance figures for the accelerator together with the main physics and technology concepts utilized in the facility. This includes beam dynamics and space charge effects in the cyclotrons, the control of beam losses and activation, power conversion, and efficiencies. While some of these topics are relevant only for cyclotrons, many themes are discussed that are important for any type of high intensity proton accelerator. In the following sections, the basic physics and main parameters of the three accelerators are described.

2.2 Injector II

The Injector II cyclotron was designed for high current operation, 1 mA and above, with minimal extraction losses. High extraction efficiency in a cyclotron demands a large turn separation. This can be achieved by the combination of high accelerating voltage, large radius, large gap magnets and low energy spread. To counter the strong defocusing space charge forces, a high vertical ("axial") betatron-tune[4] is required. Hence Injector II was designed as a low-field separate sector machine using four wedge sectors. The sector magnets leave space for two high-voltage double-gap resonators operating at the 10th harmonic of the orbital frequency and two single-gap flat-top resonators to minimize the energy spread. Since the injection energy of 870 keV is well below the Coulomb threshold, the first few turns can be used to collimate the beam and clean up halo [21].

---

[4]The "tune" is the number of vertical or horizontal oscillations of a particle per turn and characterizes the strength of vertical/horizontal focusing. Isochronous cyclotrons have, in contrast to synchrotons, no intrinsic longitudinal focusing.

M.M. Gordon was the first to recognize that space charge in isochronous cyclotrons can lead to (as he called it) "vortex motion" [22]. Later Chabert, Luong and Promé as well as Chasman and Baltz backed this up theoretically [23, 24]. Numerical simulations, performed by Adam, Koscielniak, Adelmann and others, confirmed this effect [25–28]. The vortex effect can lead to increased halo formation and bunch "breakup". This has been experimentally investigated by Pozdeyev *et al* in the *small isochronous ring* (SIR) experiment [29]. The beam breaks up only if it is long initially and the breakup typically generates a number of self-sustaining round sub-bunches [29]. In case of a single initially short and compact bunch, the vortex effect stabilizes the bunch: the space charge induces a coupling between the longitudinal and horizontal motion that generates a weak (but non-zero) longitudinal focusing, an effect that can be understood with an analysis of the linear coupling terms of an isochronous cyclotron [30], although this is somewhat counter-intuitive. The usefulness of the self-focusing was discovered by the PSI operation crew, who achieved a high extracted current with low losses while the flat-tops were switched off by accident. Since the flat-top system was –with an appropriate setup– no longer required to achieve a low energy spread, the phase was reversed so as to operate in an accelerating mode. This enabled a further increase in the energy gain per turn and hence to reduce the turn number N. A maximum beam current of 2.7 mA has been extracted from Injector II on beam dump and 2.4 mA in combination with the Ring cyclotron.

The flat-top resonators will be replaced, in an ongoing upgrade program, by two 50 MHz high-voltage resonators. This should further reduce extraction losses and allow for even higher beam currents. However, the vortex effect generates bunches in a meta-stable state and is sensitive to various possible distortions [31, 32]. Making use of the vortex effect in Injector II may be possible due to the very conservative layout of the cyclotron, including a strict isochronism, [30] with a central region equipped with various movable collimators to optimize the bunch formation and to eliminate the halo [21]. Injector II is the only production cyclotron world-wide that is known to take advantage of the vortex effect.

2.3 The Ring Cyclotron

In 1975, after one year of operation, the highest beam current on target was 25 μA. The performance of the Ring cyclotron was steadily improved, especially the extraction efficiency. In the beginning, only a well-centered beam was able to pass the Walkinshaw-resonance without substantial beam loss, as the beam had to pass the resonance four times before extraction [5, 33]. A modification of the tune diagram by an improved setting of trim coils reduced this to two fast passages through the resonance and allowed relaxation of the requirement of beam centering [34, 35]. This enabled a considerable increase in the turn separation at extraction by means of precessionally-enhanced turn separation. In December 1976 an extraction efficiency of 99.9 % was achieved with a peak intensity of 112 μA [4]. Ten years later, after the first commissioning of the new pre-accelerators, a beam current of 1 mA was achieved with Injector II alone, and 310 μA in combination with the Ring cyclotron.

In 1981, Werner Joho presented an analysis of high intensity problems in cyclotrons [36], known as Joho's N^3-Law, which states that the loss dominated current limit I_{max} scales with the inverse third power of the number of turns N, $I_{max} \propto N^{-3}$. This formula predicted the performance of the PSI Ring cyclotron of the following two decades with high accuracy [37, 38].

An upgrade of the RF system of the Ring was required and initiated for another substantial intensity increase [39]. In parallel, a bunching system was built and commissioned in the 870 keV injection line to better match the DC beam to the phase acceptance of Injector II [40, 41]. The upgrade of the RF system allowed a significant reduction of the number of turns in the Ring cyclotron and an increase of the production current to 2.2 mA (test-wise in dedicated shifts up to 2.4 mA) and the beam power to 1.3 MW (1.4 MW), in good agreement with Joho's
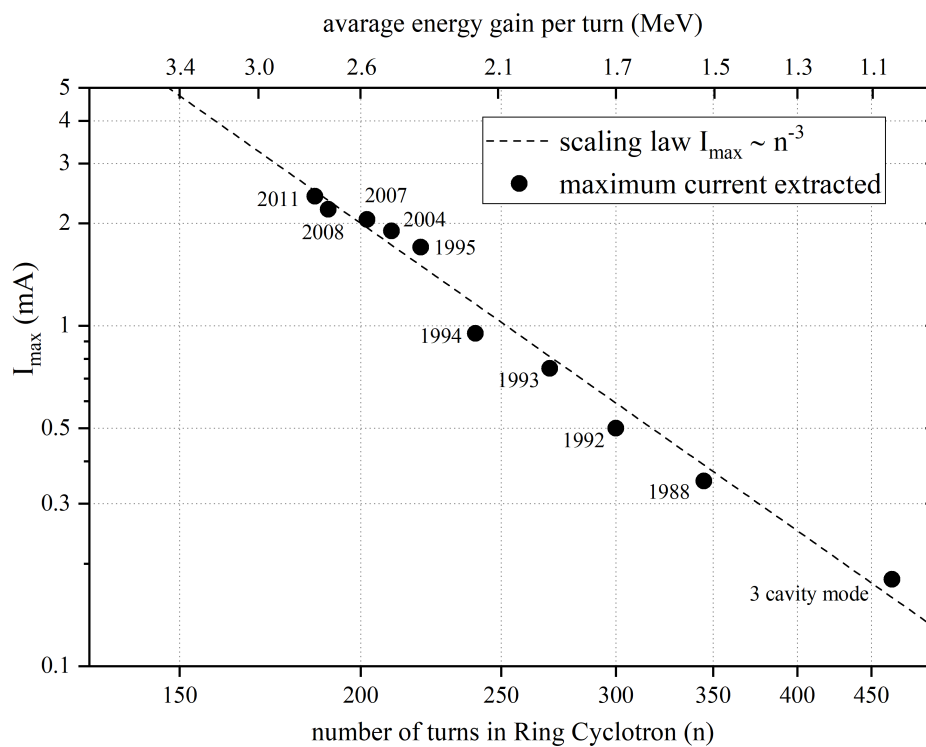
Figure 2.3: Joho's empirical law.

N^3-Law (see Figure 2.3). On full completion of the upgrade programs, which includes the replacement of the old 150 MHz flattop cavity, a beam current of 3 mA with a power of 1.8 MW should be within reach of both, Injector II [21] and the Ring cyclotron [42, 43].

2.4 Facility Performance

Every year, PSI has 1500-2000 user visits at the neutron source (SINQ), the muon source (SμS), and the facilities for particle physics (CHRISP) including the UCN Source. During more than 3000 instrument-days, over 800 experiments are performed each year. These user facilities are all part of the HIPA facility which operates at a beam power of up to 1.42 MW. In the following sections we describe the basic operation scheme of the facility and present the main details of the experimental stations. The performance of the accelerator, i.e., the achievable beam power, the availability, and its energy efficiency are also addressed.

2.4.1 Operation Scheme

A typical year of operation starts in the beginning of May after the shutdown and ends on Christmas with the next shutdown. The start of user operation may vary depending on the duration of the necessary maintenance and planned upgrade. The beam time schedule is compiled by the facility management in close collaboration with the user office of PSI. During regular user operation, the accelerators are operated nonstop for 24 hours the day. With the user operation starting in the beginning of May and ending at Christmas, the accelerator facility typically provides 200 days of primary beam for experiments. After three weeks of user operation, a maintenance period of two days is scheduled. In addition, two shifts of beam development before and after each maintenance are carried out to reduce beam losses and to improve the performance of the facility.

2.4.2 Pion and Muon Production

The production of pions and muons is possible with beam sent either to the spallation neutron target or to the beam dump. In the latter case, the maximum beam current extracted from the Ring cyclotron is limited to 1.7 mA due to the cooling limitations of the beam dump. Nevertheless, meson production is possible even though the spallation source may not be operational. The meson targets provide secondary particles for the experimental facilities. The performance of the meson facilities, i.e., the particle fluxes are given in Table 2.1.

Table 2.1: Particle types available at the meson experimental facilities. The rate is given in particles per second and per *mA* beam current and may vary with the selected momentum.

Target (thickness)	User facility	Particle type	Momentum range (MeV/c)	max. rate ($s^{-1}mA^{-1}$)
M (5mm)	πM1	e/π/μ/p	$10-450$	$2 \cdot 10^8$
	πM3.1-3	μ	$10-40$	$3 \cdot 10^6$
E (4 or 6cm)	πE1	π/μ/p	$10-450$	$1 \cdot 10^9$
	πE3	μ	$10-40$	$3 \cdot 10^7$
	πE5	π/μ	$10-120$	$5 \cdot 10^8$
	μE1	μ	$60-120$	$6 \cdot 10^7$
	μE4	μ	$10-40$	$4 \cdot 10^8$

2.4.3 Neutron production

The main beam passes through the two graphite targets before striking the spallation neutron target of SINQ so it has to be collimated due to a five-fold increase in beam emittance. For an E-target thickness of 4(6) cm, about 70 %(60 %) of the beam current remains. The proton kinetic energy is degraded to 570 MeV (565 MeV). The remaining beam is first bent downwards and then sent back up vertically onto the spallation target. The thermal neutron flux scales with the beam current and is approximately $1.5 \cdot 10^{14}$ cm^{-2}s^{-1} near the target.

The UCN facility was commissioned in 2010 and a measurement of the neutron electric dipole moment, nEDM, began in 2011. For this experiment, the full 590 MeV beam is switched periodically from the meson production targets to the UCN target with a fast-switching magnet. Typically, the beam is switched every 12 minutes for 8 seconds. Both the pulse duration and frequency can vary depending on the requirements of the experiments. This corresponds to a duty cycle of approximately 1 %. The pulse sequence is controlled by a software routine that decreases the beam intensity by 20 % roughly 2 s before the kick. After switching on the kicker magnet, the maximum intensity is then re-set to the nominal value during another 2 s. The reverse routine applies after the kick.

When the beam is switched back to the meson production and SINQ targets, the beam current is lowered below 1 mA and then raised back to the maximum within 20 s. This is done to avoid high thermal stress to the targets, particularly the SINQ-target.

2.4.4 Isotope Production

The Injector II cyclotron can produce 72 MeV protons for the production of radioactive isotopes. Two operating modes are possible: An electrostatic beam splitter can split off up to 100 μA of the main beam, which is directed to the isotope production target along a dedicated beamline. In this case, both the isotope production beam and main beam onto meson and

neutron production targets can operate simultaneously. Alternatively, the full beam, limited to $100\,\mu$A, can be sent to the isotope production target.

2.4.5 Accelerator Performance and Beam Intensity

The facility, originally designed for a maximum beam current of $100\,\mu$A, has continuously been improved to reach a maximum beam power of 1.42 MW, at present. The following section describes the performance characteristics of the accelerator facility, in particular the beam power and availability.

The maximum beam power is limited by the tolerable amount of proton losses during acceleration to meet legal obligations and to avoid activation and damaging of accelerator components. Currently, PSI is authorized to extract a maximum beam current of 2.4 mA from the Ring cyclotron, which has been achieved in the years 2011, 2012, 2015, and 2016. Furthermore, PSI may increase the beam current to a maximum of 2.6 mA during dedicated beam development shifts for eight hours every four weeks. Major steps in the increase of the beam power were achieved by replacing the Injector I cyclotron with the Cockcroft-Walton and Injector II pre-accelerators in 1985, and by continuous upgrades of the RF systems starting in 1990. Newly designed meson production targets have been used since 1991 to tolerate the thermal stress imposed by the higher beam power. After the commissioning of the spallation neutron target SINQ in 1996, the beam power was increased from 826 to 885 kW.

Following the installation of the fourth and last new copper cavity in the Ring cyclotron, the beam losses in the cyclotron were further reduced by increasing the peak voltage of each accelerating cavity from 790 MV to 850 MV. A maximum beam current of 2.4 mA was extracted on 20 June 2011 for the first time. The corresponding beam power of 1.42 MW was the highest ever achieved with any accelerator at that time. In Figure 2.4, the increase of the beam power for the years from 1974 to 2020 is shown.

The charge delivered on the meson and the neutron production targets scales with the average beam current extracted from the Ring cyclotron and is shown in Figure 2.5.

The beam intensity in HIPA is limited by beam losses. As practical experience has shown, the highest acceptable losses for hands-on maintenance are of the order of 100 W (10^{-4} for 1 MW of beam power) per location. A major contribution is scattering of halo particles in the high voltage electrode of the extraction septum. Such losses are then distributed over several meters of beamline elements and lead to activation with maximum dose rates of the order of a few millisievers per hour. Such dose rates are acceptable for service work and handling components. For any further increase of the beam current, the relative losses in the cyclotron and the beam line would have to be reduced inversely proportional to the intensity to keep the activation at an acceptable level. The extremely high extraction efficiency of the PSI Ring cyclotron is a property that was optimized to allow the operation with high intensities. There are two key elements for low loss beam extraction: The generation of beam tails must be suppressed as best as possible, and the turn separation at the extraction septum must be maximized. In this way the density of halo particles at the position of the extraction septum is minimized. For an isochronous cyclotron the radial increment of the orbit radius per turn can be computed as

$$\frac{\mathrm{d}R}{\mathrm{d}n_{\mathrm{t}}} = \frac{U_{\mathrm{t}}}{m_0\,c^2}\frac{\gamma R}{(\gamma^2-1)\,\nu_r^2}. \tag{2.1}$$

$$= \frac{U_{\mathrm{t}}}{m_0 c^2}\frac{R}{(\gamma^2-1)\gamma}. \tag{2.2}$$

Here γ is the relativistic energy factor, ν_r the radial tune, U_t the energy gain per turn and m_0 the rest mass of the proton. Clearly a high acceleration voltage helps, but one finds a very strong
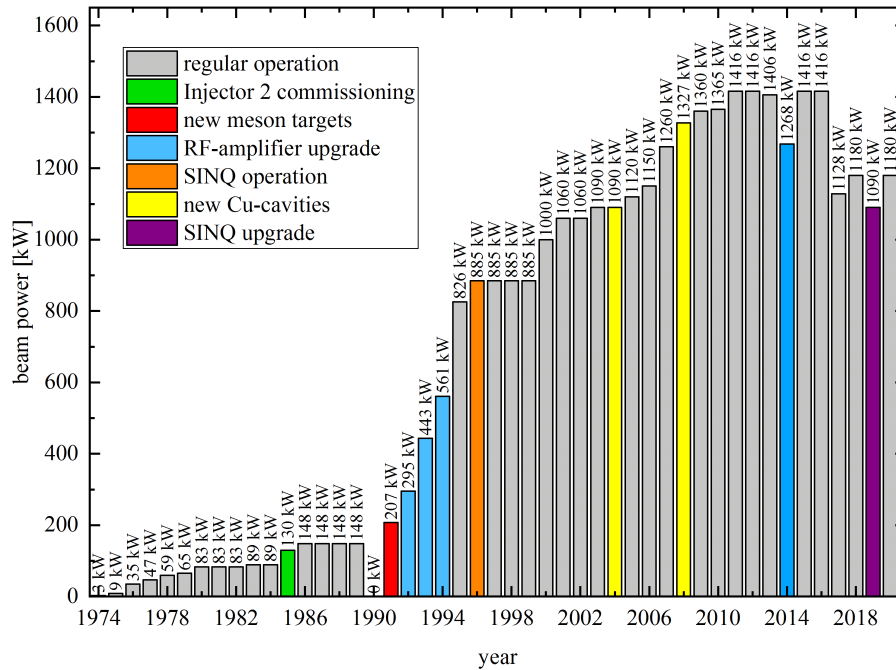
Figure 2.4: The maximum beam power achieved in the accelerator facility. In 1990 the facility was off line for the installation of new RF-amplifiers for the Ring cyclotron and the new meson production target station E including the beamline up to the beamdump.
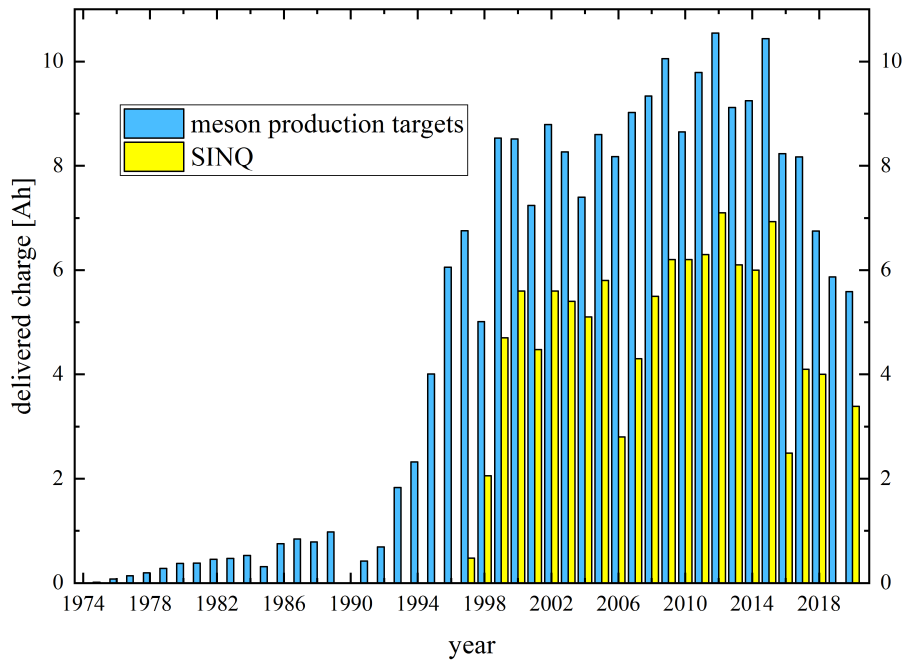

Figure 2.5: History of the charge delivered per year to the meson production targets and the neutron spallation target SINQ.

reduction with γ for higher energies. Equation (2.1) illustrates the possibility to influence the turn separation by weaker focusing over the outer turns of the cyclotron. This violates the isochronous condition and is therefore only possible over a small number of turns. The second line (2.2) is the more general relation, for which $\nu_r \approx \gamma$. We also note the scaling with the extraction radius R, i.e. the size of the cyclotron. With an extraction radius of 4.5 m, the PSI Ring cyclotron is one of the largest cyclotrons in the world. An effective way to increase the turn separation at the extraction element is the introduction of orbit oscillations by deliberately injecting the beam slightly off centre. When the phase and amplitude of the orbit oscillation are chosen appropriately, and the behaviour of the radial tune is controlled in a suitable way, the beam separation can be increased by a factor of three. This gain is equivalent to a cyclotron three times larger and is thus significant. Figure 2.6 illustrates how this scheme is used in the PSI Ring cyclotron. In [44], the beam profile in the outer turns was computed numerically for realistic conditions, and the results are in good agreement with measurements.

In Figure 2.7 the frequency of beam losses at a certain current is depicted for the user operation at 2 mA in 2010 and at 2.2 mA in 2015.

2.5 Operating Statistics

High beam power is important for precise measurements of short duration. However, the availability of a large research facility is often of even greater importance to users. In this section, we describe beam time statistics and outage characteristics.

The availability of the HIPA facility requires a beam current of at least 1 mA extracted from the Ring cyclotron during scheduled user operation. According to this definition, the accelerator availability is 100 % if the beam current measured at the meson production target is equal or greater 1 mA. The lower limit of 1 mA is used to meet the needs of the experimental facilities, which require at least this current for performing meaningful measurements. A beam current of least 700 μA onto the spallation target is required for neutron experiments. This corresponds to 1 mA of beam current extracted from the Ring cyclotron. The lowest beam current considered as useful for the user community has been raised from 150 μA to 1000 μA in 2001. An outage of the spallation neutron target SINQ does not affect the availability of the accelerator since the collimated beam after the graphite targets can be sent onto the beam dump. Figure 2.8 shows the availability from 1974 to 2020.

A short interruption refers to outages lasting less than five minutes. The average number of short interruptions per year is roughly 15000, but it varies by more than a factor of seven as shown in Figure 2.9.

After the replacement of the first aluminium cavity with a copper cavity in the Ring cyclotron in 2005, major problems were experienced with the electrostatic elements in the cyclotron. Stable operation was not possible during the first month after the yearly shutdown. Frequent discharges, especially of the electrostatic injection device, made it impossible to tune the accelerator to sufficiently high beam currents. The injection device had to be replaced several times due to damage to the insulators supporting the cathode, caused the discharges. RF-power decoupled from the new copper cavity was causing the problems. Two different effects were determined to induce the discharges. On the one hand, RF-power decoupled from the cavity is absorbed by the electrodes of the electrostatic element which leads to the accumulation of charge on the electrodes, creation of halos, and secondary electron emission. In 2014 on the other hand, the high amount of short interruptions was mainly caused by plasma phenomena in the Ring cyclotron. The decoupled RF-power from the flattop cavity resonantly excites secondary electron emission in between the magnet poles of the neighbouring sector magnet. These electrons in turn hit the surface of the trim coils of the magnet and produce ions that stray in the vacuum chamber and are attracted by the electric field of the electrostatic elements. This leads to vapor deposition of conductive material on the insulators that support
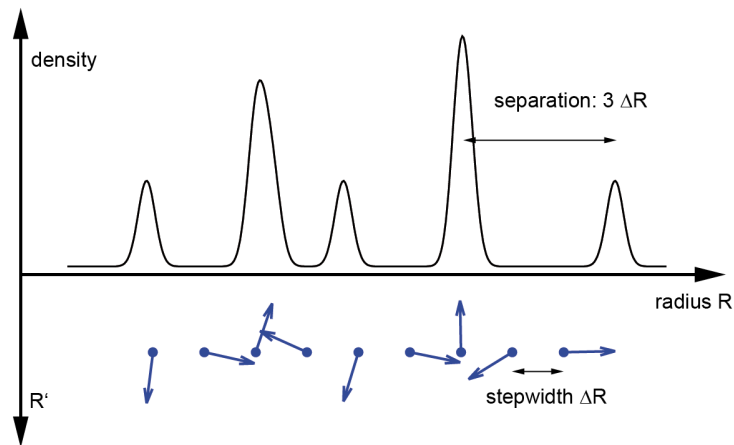
Figure 2.6: Principle scheme of maximizing the beam separation at extraction by utilizing betatron oscillations of the beam center. Important is only the relation between turn-separation and beam width. The 'stepwidth' ΔR is the distance between turns for betatron amplitude zero. The upper plot shows the beam density along the radius, which is a superposition of Gaussian profiles. In the lower half, the clockwise-rotating phase space vector of the centroid of the beam is shown for each turn. The reduction of the radial tune to ≈ 1.5 on the last turns is essential for the intended operation of this scheme.
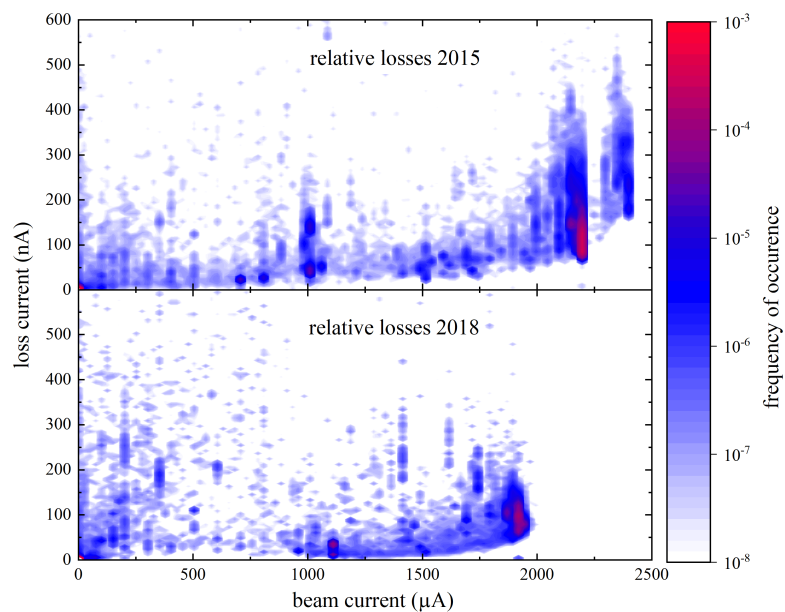
Figure 2.7: Relative losses in the Ring cyclotron during two different operation scenarios. The upper graph depicts the relative losses during the operation in 2015 with a beam current of 2.2 mA for standard operation and 2.4 mA for beam development shifts, respectively. The average loss current at 2.4 mA is approx. 230(44) nA and thus two times higher than at 2.2 mA. Due to the Injector II upgrade, the beam current was limited to 2.0 mA in 2018. The average losses at this current are approx. 82(25) nA
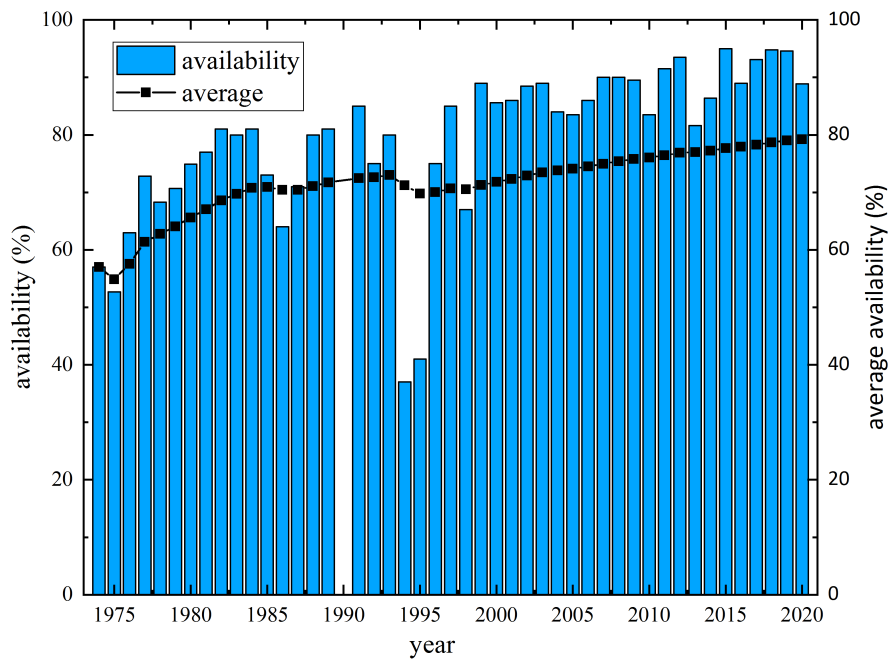
Figure 2.8: Availability of the high intensity proton accelerator facility for the years from 1974 to 2020. The black curve represents the average availability.

Figure 2.9: Total number of short interruptions for the years 2004 to 2020 (hatched). The solid bars denote the relative number of short interruptions normalized to the number of scheduled days of user operation, i.e., average number of short interruptions (< 5 min.) per day.

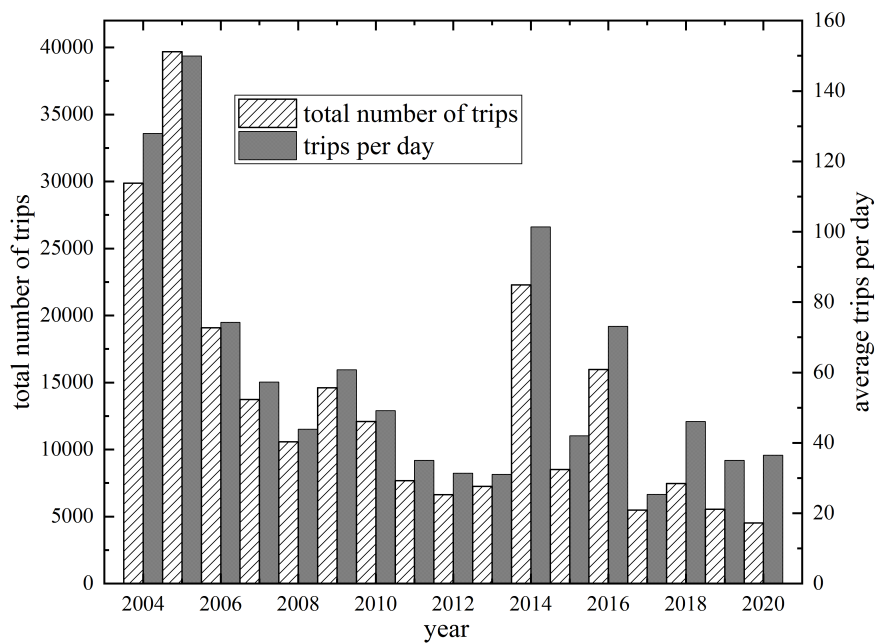the cathode and thus discharges of the electrostatic elements. To mitigate this effect, an aluminium shroud was attached to the electrostatic devices to shield the RF-power and screen it from straying ions.

Though recovery from a discharge of the electrostatic elements may occur in much shorter time, the automatic ramping up of the accelerators lasts between 20 to 30 seconds. Therefore, short interruptions may have a non-negligible impact on the yearly availability. Assuming an average of 15000 short interruptions per year the aggregate downtime constitutes approximately 80 hours. Given 5000 hours of user operation, this results in a loss of availability of 1.6 %

In Figure 2.10, the accumulated outage characteristics for 2004 through 2020 are shown. The most prominent events causing outages are site cooling (15 %), radio frequency systems (13 %), and targets (12 %). Although this does not reflect the characteristics related to each year of operation, it is a guideline for risk management and stock-keeping of spares.
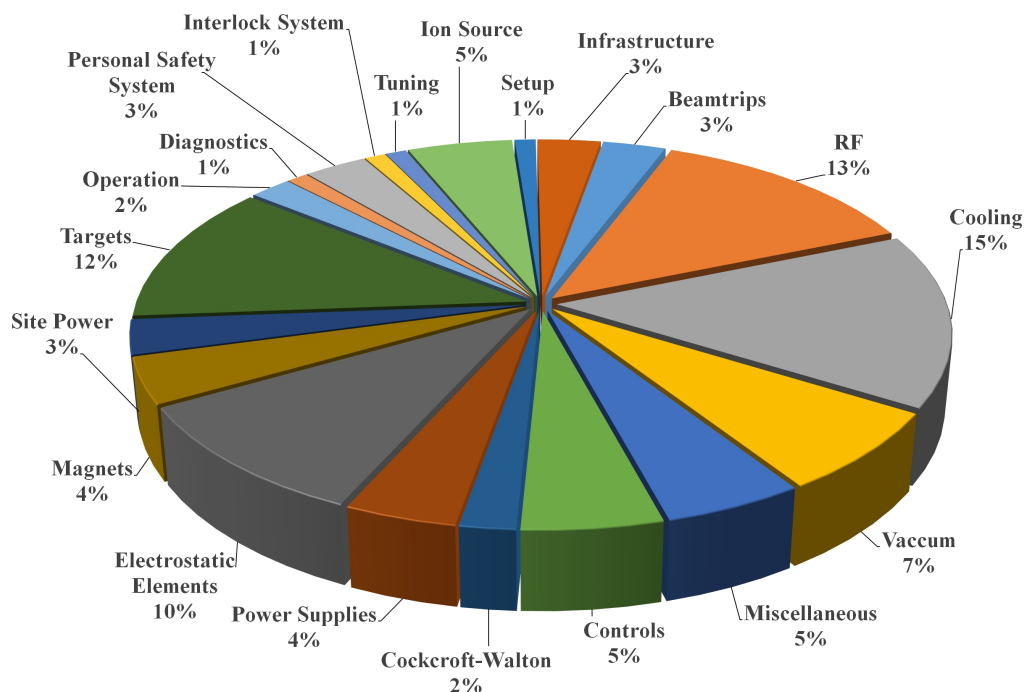
Figure 2.10: Accumulated outage characteristics for the High Intensity Proton Accelerator facility for the years 2004 to 2020.

2.6 Grid Power Consumption and Energy Efficiency

The experiments at HIPA require highest intensity particle beams for precise measurements. Producing a megawatt proton beam requires the consumption of several megawatts of electrical power. The goal of further upgrades will be to achieve higher particle flux, rates, and brightness, which will require even greater power. Concurrently, the growing global energy consumption challenges the energy efficiency of any technology including accelerator-driven research facilities. Inevitably, a discussion on improving the energy efficiency of the existing facility presents itself. In this section, the energy efficiency of HIPA will be discussed in detail. Furthermore, it will be shown that by increasing the beam power an even higher energy efficiency may be achieved.

Figure 2.11 shows the power consumption break down of the proton facility. The overall power consumption of the facility in routine operation at 2.2 mA beam current is approxi-

mately 12.5 MW. The 5.4 MW of the RF-to-beam power conversion dominates the power consumption. This value scales roughly linearly with beam power (see Figure 2.12): the power consumption of the magnets and auxiliary systems, e.g., cooling, conventional systems, and instruments is virtually independent of the beam power.

With a beam power of up to 1.3 MW and a total power consumption of 12.5 MW, the energy efficiency of the facility is 11 %. This does not reflect the energy efficiency of the bare accelerator, as all experimental facilities (IP2, UCN, SINQ, and all secondary beamline experiments) that require electrical power contribute to the total power consumption. In a detailed study [45], the power consumption of each subsystem (RF-System, magnets, and infrastructure) required only for beam production, was analyzed. According to this study, a minimum of 7.12 MW of power from the power grid is required for a beam current of 2.2 mA. Thus, the energy efficiency of the bare accelerator is 18 %. One might expect the energy efficiency of the facility to increase linearly with beam power, corresponding to the linear behavior of the RF- to beam power conversion denoted in Figure 2.12. However, the power consumption P_{RF} of the RF-System was measured as a function of the beam current keeping the voltage of the accelerating cavities constant (850 kV per cavity). According to the empirical law of Joho [36] the number of turns in a cyclotron has to be reduced to achieve higher beam currents for constant beam losses. This, in turn, is only possible by increasing the peak voltage V_{acc} of the accelerating cavities. Since the wall losses P_{loss} in a cavity scale with $V_{acc}^2/2R$ (where R is the shunt impedance of the cavities), correspondingly more electrical power is needed to increase the beam current. Since $P_{RF} = P_{loss} + k \cdot P_{beam}$ where k characterizes the efficiency of the RF-amplifier chain, this results in a non-linear behavior of the RF- to beam power conversion. The considerations in the following section will proof that increasing the beam current by reducing the number of turns in the cyclotron will nevertheless increase the energy efficiency of the accelerator facility.

The efficiency η_{acc} of the bare accelerator is defined as the ratio of the beam power P_{beam} and the total power P_{tot} needed to operate the accelerator. In a simplified model, P_{tot} is $P_{loss} + k \cdot P_{beam} + P_{aux}$. The power consumption P_{aux} of the magnets and auxiliary system, e.g., cooling, conventional systems, and instruments is virtually independent of the beam power. Therefore, the efficiency of the accelerator is

$$\eta_{acc} = \frac{P_{beam}}{P_{loss} + P_{aux} + k \cdot P_{beam}} . \tag{2.3}$$

As the maximum current I_{max} extracted from a cyclotron is proportional to $1/N^3$ [36], the number of turns N is

$$N = \frac{E_{kin}}{q \cdot V_{acc} \cdot N_c} , \tag{2.4}$$

where N_c is the number of cavities and E_{kin} is the gain in energy of the particles and q their charge. Thus

$$I_{max} \propto \frac{q^3 \cdot V_{acc}^3 \cdot N_c^3}{E_{kin}^3} \text{ and } V_{acc} = \epsilon \cdot \frac{E_{kin}}{q \, N_c} \cdot I_{max}^{1/3}, \tag{2.5}$$

where ϵ is a constant factor. The efficiency of the accelerator as a function of the beam current can then be deduced to be

$$\eta_{acc} \approx \frac{E_{kin} \cdot I}{\frac{\epsilon^2 \cdot E_{kin}^2}{2 \cdot N_c \cdot Z \cdot q} \cdot I_{max}^{\frac{2}{3}} + k \cdot E_{kin} \cdot I + q \cdot P_{aux}} . \tag{2.6}$$

As the denominator contains the beam current with an exponent of ≤ 1 the efficiency will increase with the beam current. With the actual setup of the Ring cyclotron, i.e., cavity voltages

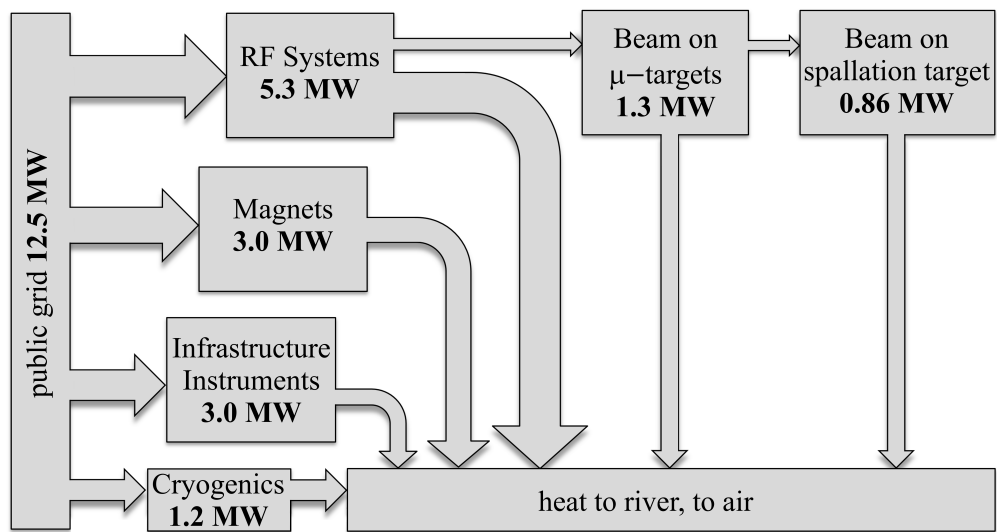Figure 2.11: Breakdown of the power flow in the Proton Accelerator facility for a beam current of 2.2 mA.
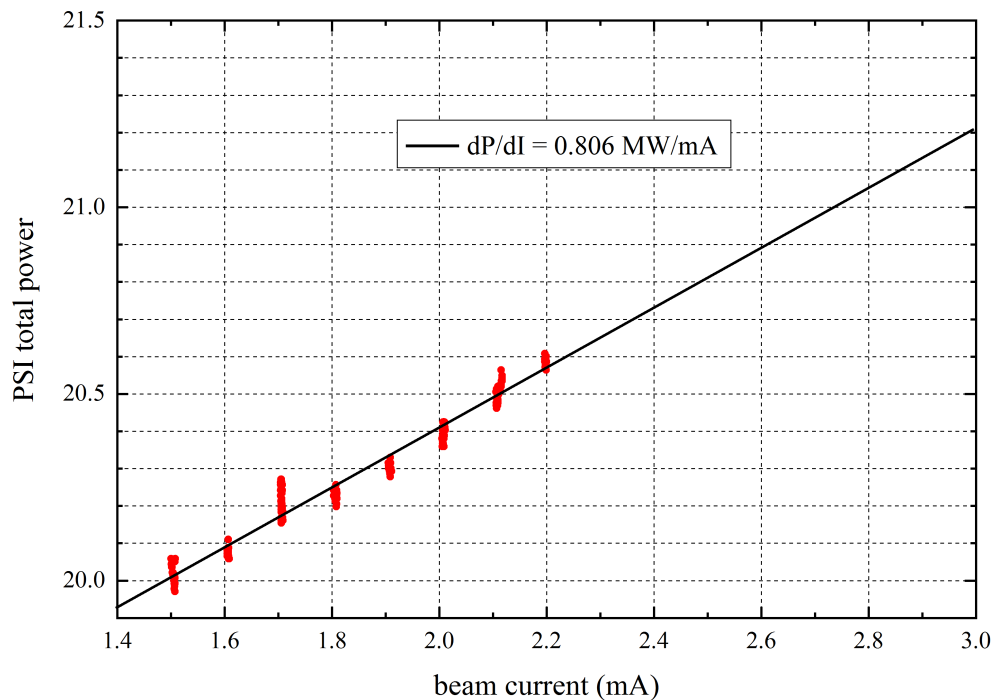

Figure 2.12: Grid to beam power conversion as a function of the beam current. The measurements (red) where recorded with a fixed cavity voltage of each 850 kV. The black line denotes a linear regression of the data. Extrapolated to 3 mA of beam current, a power of 21.2 MW from the grid would be needed.

of $V_{\text{acc}} = 850\,\text{kV}$ and a beam current of $2.4\,\text{mA}$, the efficiency is 0.18, which is the highest for any high power accelerator existing to date [46]. By increasing the beam current to the ultimate goal of $3.0\,\text{mA}$ at a cavity voltage of $1\,\text{MV}$ an efficiency 0.21 could be achieved. This is feasible at PSI, since the RF-system is designed for a peak voltage of up to $1.2\,\text{MV}$. The limitation of $850\,\text{kV}$ and thus the maximum beam current is given by the flattop cavity system. Currently, the maximum flattop voltage is $550\,\text{kV}$ corresponding to the necessary $11\,\%$ of the main cavity voltage. For an operation at higher voltages the flattop system, including the cavity and the amplifiers, would have to be replaced. It is important to note, that these values are valid for the specific setup of the Ring cyclotron, i.e., four accelerating cavities with a given shunt impedance R. If the acceleration voltage or the energy gain per turn respectively were distributed among 8 cavities, the wall losses per cavity would be lower. If calculated for eight cavities, the efficiency would be 0.2 at $2.4\,\text{mA}$. It is obvious that the shunt impedance R is one of the main parameters to optimize the efficiency at a given gap voltage. In fact, the shunt impedance only depends on the geometry and choice of material of the cavity and is, therefore, the parameter to optimize. This is an important consideration for future cyclotron based accelerator driven systems.

References

[1] J. P. Blaser and H. A. Willax, *Progress report on the 500 MeV isochronous cyclotron meson factory of ETH Zurich*, In F. Howard, ed., 4th International Conference on Isochronous Cyclotrons (Cyclotrons '66), vol. 13, pp. 194–213. IEEE, ISBN 978-3-95450-098-7 (1966).

[2] H. A. Willax, *Proposal for a 500 MeV isochronous cyclotron with ring magnet*, In F. Howard and N. Vogt-Nilsen, eds., CERN Report 63-19, pp. 386–397, ISBN 978-3-95450-086-4 (1963).

[3] H. A. Willax, *Status report on S.I.N.*, In McIlroy [47], pp. 58–72 (1969).

[4] W. Joho, M. Olivo, T. Stammbach and H. Willax, *The SIN accelerators, operational experience and improvement programs*, In Proceedings, 1977 Particle Accelerator Conference: Accelerator Engineering and Technology, **24**, 1618, IEEE, New York (1977).

[5] W. Joho, *The S.I.N. Ring cyclotron after one year of operation*, In F. E. Mills, ed., Proceedings, 1975 Particle Accelerator Conference, Accelerator Engineering and Technology, **22**, 1397, IEEE, New York (1975).

[6] W. Joho, *Recent and future developments at S.I.N.*, In Proceedings, 1979 Particle Accelerator Conference: Accelerator Engineering and Technology, **26**, 1949, IEEE, New York (1979).

[7] C. Baumgarten, A. Barchetti, H. Einenkel, D. Goetz and P. A. Schmelzbach, *A compact electron cyclotron resonance proton source for the Paul Scherrer Institute's proton accelerator facility*, Rev. Sci. Instrum. **82**, 053304 (2011), doi:10.1063/1.3590777.

[8] D. Kiselev, P. Duperrex, S. Jollet, D. Laube, D. Reggiani, R. Sobbia and V. Talanov, *The Meson Production Targets in the high energy beamline of HIPA at PSI*, SciPost. Phys. Proc. **5**, 003 (2021), doi:10.21468/SciPostPhysProc.5.003.

[9] Y. Dai and G. S. Bauer, *Status of the first SINQ irradiation experiment, stip-i*, J. Nucl. Mat. **296**, 43 (2001), doi:10.1016/S0022-3115(01)00544-X.

[10] W. Wagner, J. Mesot, P. Allenspach, G. Kuehne and H. M. Ronnow, *The swiss spallation neutron source SINQ developments and upgrades for optimized user service*, Physica B **385-386**, 968 (2006), doi:10.1016/j.physb.2006.05.285.

[11] G. S. Bauer, *Operation and development of the new spallation neutron source SINQ at the Paul Scherrer Institut*, Nucl. Instrum. Meth. Phys. Research B **139**, 65 (1998), doi:10.1016/S0168-583X(97)00956-7.

[12] W. Wagner, Y. Dai, H. Glasbrenner, M. Grosse and E. Lehmann, *Status of SINQ, the only MW spallation neutron source—highlighting target development and industrial applications*, Nucl. Instr. Meth. A **562**, 541 (2006), doi:10.1016/j.nima.2006.02.026.

[13] B. Blau et al., *The swiss spallation neutron source SINQ at Paul Scherrer Institut*, Neutron News **20**, 5 (2009), doi:10.1080/10448630903120387.

[14] R. M. Bergmann, U. Filges, D. Kiselev, T. Reiss, V. Talanov and M. Wohlmuther, *Upgrades to the SINQ cold neutron source*, J. Phys.: Conf. Series **746**, 012035 (2015), doi:10.1088/1742-6596/746/1/012035.

[15] A. Anghel et al., *The psi ultra-cold neutron source*, Nucl. Instrum. Meth. Phys. Research A **611**, 272 (2009), doi:https://doi.org/10.1016/j.nima.2009.07.077.

[16] G. Bison, B. Blau, M. Daum, L. Göltl, R. Henneck, K. Kirch, B. Lauss, D. Ries, P. Schmidt-Wellenburg and G. Zsigmond, *Neutron optics of the PSI ultracold-neutron source: characterization and simulation*, Europ. Phys. J. A **56**, 33 (2020), doi:10.1140/epja/s10050-020-00027-w.

[17] B. Lauss and the PSI UCN Project Team, *Commissioning of the new high-intensity ultracold neutron source at the Paul Scherrer institut*, J, Phys.: Conf. Series **312**, 052005 (2011), doi:10.1088/1742-6596/312/5/052005.

[18] B. Lauss, *Startup of the high-intensity ultracold neutron source at the Paul Scherrer Institute*, In P. Bühler, O. Hartmann, K. Suzuki, E. Widmann and J. Zmeskal, eds., Proceedings of EXA 2011, pp. 297–301, Springer, Dordrecht, Netherlands, ISBN 978-94-007-4890-3 (2012).

[19] B. Lauss, *Ultracold neutron production at the second spallation target of the Paul Scherrer Institute*, Physics Procedia **51**, 98 (2014), doi:10.1016/j.phpro.2013.12.022.

[20] D. Anicic et al., *A fast kicker magnet for the PSI 600MeV proton beam to the PSI ultra-cold neutron source*, Nucl. Instrum. Meth. Phys. Research A **541**, 598 (2005), doi:10.1016/j.nima.2004.12.032.

[21] A. Kolano, A. Adelmann, R. Barlow and C. Baumgarten, *Intensity limits of the PSI Injector II cyclotron*, Nucl. Instrum. Meth. in Phys. Res. A **885**, 54 (2018), doi:10.1016/j.nima.2017.12.045.

[22] M. M. Gordon, *The longitudinal space charge effect and energy resolution*, In McIlroy [47], pp. 305–317 (1969).

[23] A. Chabert, T. Luong and M. Promé, *Separate sector cyclotrons beam dynamics*, In W. Joho, ed., Proceedings of the 7th International Conference on Cyclotron and their Applications, pp. 245–247, Birkhäuser, Basel CH, ISBN 978-3-95450-159-5 (1975).

[24] C. Chasman and A. J. Baltz, *Space charge effects in a heavy ion cyclotron*, Nucl. Instr. Meth. A **219**, 279 (1984), doi:10.1016/0167-5087(84)90333-8.

[25] S. Adam, *Calculation of space charge effects in isochronous cyclotrons*, In A. Strathdee, ed., Proceedings of the 1985 Particle Accelerator Conference (PAC1985), **32**, 2507 (1985), IEEE, Piscataway, NJ, doi:10.1109/TNS.1985.4333654.

[26] R. Koscielniak and S. Adam, *Simulation of space-charge dominated beam dynamics in an isochronous AVF cyclotron*, In S. T. Corneliussen and L. Carlton, eds., Proceedings of the 1993 Particle Accelerator Conference (PAC 93), pp. 3639–3641, IEEE, Piscataway, NJ, ISBN 9780780312036 (1993).

[27] S. Adam, *Space charge effect in cyclotrons - from simulations to insights*, In Comell [49], pp. 446–448 (1995).

[28] J. J. Yang, A. Adelmann, M. Humbel, M. Seidel and T. J. Zhang, *Beam dynamics in high intensity cyclotrons including neighboring bunch effects: Model, implementation, and application*, Phys. Rev. ST Accel. Beams **13**, 064201 (2010), doi:10.1103/PhysRevSTAB.13.064201.

[29] E. Pozdeyev, J. A. Rodriguez, F. Marti and R. C. York, *Longitudinal beam dynamics studies with space charge in small isochronous ring*, Phys. Rev. ST Accel. Beams **12**, 054202 (2009), doi:10.1103/PhysRevSTAB.12.054202.

[30] C. Baumgarten, *Transverse-longitudinal coupling by space charge in cyclotrons*, Phys. Rev. ST Accel. Beams **14**, 114201 (2011), doi:10.1103/PhysRevSTAB.14.114201.

[31] C. Baumgarten, *Transverse-longitudinal coupling by space-charge in cyclotrons*, In J. Thomson and V. Schaa, eds., Proceedings of the 20th International Conference on Cyclotrons and their Applications, pp. 315–319, JaCoW, ISBN 978-3-95450-128-1 (2013).

[32] C. Baumgarten, *Factors influencing the vortex effect in high-intensity cyclotrons*, In L. Conradie, J. G. De Villiers and V. R. W. Schaa, eds., Proceedings of the 22nd International Conference on Cyclotrons and their Applications, pp. 270–274, JACoW, Geneva, Switzerland, ISBN 978-3-95450-205-9 (2019).

[33] *SIN annual report*, Swiss Institute for Nuclear Research (S.I.N.), Villigen, Switzerland. (1974).

[34] *SIN annual report*, Swiss Institute for Nuclear Research (S.I.N.), Villigen, Switzerland. (1975).

[35] Y. Bi, A. Adelmann, R. Dölling, M. Humbel, W. Joho, M. Seidel and T. Zhang, *Challenges in simulating MW beams in cyclotrons*, In A. Adelmann, J. Chrin, M. Marx, V. R. W. Schaa and M. Seidel, eds., Proceedings of the 46th ICFA Advanced Beam Dynamics Workshop on High-Intensity and High-Brightness Hadron Beams (HB2010), pp. 295–299, PSI, Villigen, Switzerland (2011).

[36] W. Joho, *High intensity problems in cyclotrons*, In G. Gendreau, ed., Proceedings of the 9th International Conference on Cyclotron and their Applications, pp. 337–47, Les Editions de Physique, BP 112, 91402 Orsay, France (1981), ISBN 978-3-95450-160-1.

[37] T. Stammbach, S. Adam, H. R. Fitze, W. Joho and U. Schryber, *Potential of cyclotron based accelerators for energy production and transmutation*, AIP Conf. Proc. **346**, 229 (1995), doi:10.1063/1.49093.

[38] U. Schryber et al., *High power operation of the PSI accelerators*, In Comell [49], pp. 32–35 (1995).

[39] W. Joho, *High intensity beam acceleration with the SIN cyclotron facility*, In M. Sekiguchi, Y. Yano and K. Hatanaka, eds., Proceedings of the 11th International Conference on Cyclotron and their Applications, pp. 31–37, Ionics Publ., Tokyo (1987), ISBN 978-3-95450-166-3.

[40] J. Stetson, S. Adam, M. Humbel, W. Joho and T. Stammbach, *The commissioning of PSI Injector 2 for high intensity, high quality beams*, In G. Dutto and M. Craddock, eds., Proceedings of the 13th International Conference on Cyclotrons and their Applications, pp. 36–39. World Scientific (1993).

[41] J. Grillenberger, M. Humbel, J. Y. Raguin and P. A. Schmelzbach, *Commissioning of the new buncher system in the 870 keV injection beamline*, In Refuggiato [48], pp. 464–466 (2007).

[42] M. Seidel and P. Schmelzbach, *Upgrade of the PSI cyclotron facility to 1.8 MW*, In Refuggiato [48], pp. 157–162 (2007).

[43] M. Seidel, J. Grillenberger and A. Mezger, *High intensity operation and control of beam losses in a cyclotron based accelerator*, In N. Zhao, J. Chrin, V. R. W. Schaa, C. Petit-Jean-Genaz, D. Ji and H. Yan, eds., Proceedings of the 52nd ICFA Advanced Beam Dynamics Workshop on High-Intensity and High-Brightness Hadron Beams (HB2012), JACoW conferences, pp. 555–559, JACoW, Geneva, Switzerland (2013).

[44] Y. J. Bi, A. Adelmann, R. Dölling, M. Humbel, W. Joho, M. Seidel and T. J. Zhang, *Towards quantitative simulations of high power proton cyclotrons*, Phys. Rev. ST Accel. Beams **14**, 054402 (2011), doi:10.1103/PhysRevSTAB.14.054402.

[45] A. Kovach, A. Parfenova, J. Grillenberger and M. Seidel, *Energy efficiency and saving potential analysis of the high intensity proton accelerator HIPA at PSI*, J. Phys.: Conf. Series **874**, 012058 (2017), doi:10.1088/1742-6596/874/1/012058.

[46] J. Grillenberger, S.-H. Kim, M. Yoshii, M. Seidel and V. Yakolev, *The energy efficiency of high intensity proton driver concepts*, In V. R. W. Schaa, G. Arduini, M. Lindroos and J. Pranke, eds., Part 2, Proceedings of the 8th International Particle accelerator Conference (IPAC 2017), vol. 874, pp. 4842–4847, JACoW, Geneva, Switzerland (2017).

[47] R. McIlroy, ed., *Proceedings of the 5th International Conference on Cyclotrons and their Applications*, Butterworth London (1971), ISBN 978-3-95450-102-1.

[48] D. Refuggiato, ed., *18th International Conference on Cyclotrons and their Applications*, INFN - LNS Catania, Italy (2008), ISBN 978-3-95450-041-3.

[49] J. Comell, ed., *14th International Conference on Cyclotrons and their Applications*. World Scientific (1995).

The Meson Production Targets in the
high energy beamline of HIPA at PSI

Daniela Kiselev⋆, Pierre-André Duperrex, Sven Jollet, Stefan Joray,
Daniel Laube, Davide Reggiani, Raffaello Sobbia and Vadim Talanov

Paul Scherrer Institut, 5232 Villigen PSI, Switzerland

⋆ Daniela.Kiselev@psi.ch

Abstract

Two target stations in the 590 MeV proton beamline of the High Intensity Proton Accelerator (HIPA) at the Paul Scherrer Institut (PSI) produce pions and muons for seven secondary beamlines, leading to several experimental stations. The two target stations are 18 m apart. Target M is a graphite target with an effective thickness of 5 mm, Target E is a graphite wheel with a thickness of 40 mm or 60 mm. Due to the spreading of the beam in the thick target, a high power collimator system is needed to shape the beam for further transport. The beam is then transported to either the SINQ target, a neutron spallation source, or stopped in the beam dump, where about 450 kW beam power is dissipated. Targets, collimators and beam dumps are described.

3.1 Introduction

The High Intensity Proton Accelerator (HIPA) at PSI [1] delivers a 590 MeV continuous proton beam of up to 2.4 mA, which is accelerated in three stages and described in [2] (of this proceedings). After the Ring cyclotron, the proton beam is sent to the two meson production target stations, M and E [1] [3]. As the Meson Production Target stations have to provide good transmission to the SINQ spallation target, losses due to multiple scattering and nuclear reactions in the targets have to be kept low while keeping the pion/muon yield high. A low Z material is the best target choice according to [4]. In the 1980's, beryllium was used, which failed after a short time at above 120 μA due to bending stresses on the location of a crack [5]. Another reason for abandon this material was the poisonous and radioactive Be contamination of the surrounding vacuum chamber walls. Since the 1990's graphite has been used for both targets. They last for several years or up to about 40 Ah of proton beam. With a 40-mm (60-mm)-thick target E, the beam transmission is about 70%, (60%). About 10% of the

---

[1]The naming for the two targets, M and E, is derived from the French for thin (mince) and thick (épaisse).

beam is scattered out of the target. For further transport the beam is shaped by a collimator system, where a large fraction of the beam is stopped. Targets, collimators, beam dumps and their environment have to be cooled to dissipate the heat produced. Due to nuclear reactions this area is highly radioactive and needs to be well shielded. Therefore special measures for maintenance have to be considered and provided.

3.2 Meson Production Target Stations

Pions are produced by nuclear reactions of the 590 MeV protons with the nucleons in the target above a threshold of about 280 MeV in the center-of-mass frame. Muons are produced by pion decay. When a pion is stopped within 1 mm from the surface of the target, positive muons can escape. These are called surface muons and are used for particle as well as solid-state physics experiments, e.g. the examination of the magnetic properties of materials. Surface muons have energies below 4.1 MeV (corresponding to 29.8 MeV/c) and are almost 100% polarized. Pions exiting the target can produce muons by decay in flight with much higher energies. These are called cloud muons and can have positive or negative charge, although the negative charge is suppressed by a factor 3-4.

Target M feeds two beamlines in the forward direction called PiM1 and PiM3. Target E provides secondary particles for five beamlines, two in forward direction, PiE1 and MuE1, two perpendicular to the proton beamline, MuE4 and PiE3, and one (PiE5) at a backward angle. Muon and pion rates are given in Section 2 [2]. Each target is a 40-cm-diameter graphite wheel that rotates at 1 Hz to distribute the heat spot from the pencil beam. Standard pyrolytic graphite failed due to thermal stress as the expansion coefficients differ strongly in the axial and lateral directions. Radiation induced swelling might have also played a role. Thus polycrystalline graphite from SGL Carbon company is used. It consists of small single crystallites of 10 to 20 μm, which are irregularly arranged in space. Therefore, the physical properties are almost isotropic, as small grain sizes further improve the isotropy.

3.2.1 Target station E

20 (30) kW/mA of power is deposited by the beam in the 40 mm (60 mm) thick target E. At an operating temperature of about 1700 K at 2 mA, the target is cooled primarily by radiation due to the large emissivity of graphite. Water-cooled copper shields are mounted on the rear of the target within the vacuum chamber to dissipate the heat. As the target is mainly surface cooled, the maximum temperature is approximately independent of the target thickness. However, since the beam losses are higher with the 60 mm target, the maximum beam current for a 60-mm thick target is limited to 2 mA due to cooling issues.

The target with its shielding plug (Figure 3.1 right) is inserted vertically into the beamline. As a consequence, the horizontal rotating shaft has to be small and so the two bearings must be close to the target. For this reason, heat transfer to the bearings has to be reduced by proper target design. For this, the graphite and the hub with the bearings are connected by only six hollow spokes, which maintain the target shape but can also follow dimensional changes due to thermal expansion. After 2002, the graphite rim has been separated into 12 segments by slits of 1 mm to reduce deformation of the rim (Figure 3.2 left). Before, the radial deformation of the graphite wheel was observed to increase with rising beam current. This could cause the proton beam to partly miss the target as its width is just 6 mm. The small width favours surface muons from the produced pion distribution, which roughly follows the beam shape. It also keeps the temperature gradient between the center and the surface of the target small, which reduces thermal stress. However, it requires that the proton beam is always well centered. This is accomplished by a beam centering system relying on the beam position monitors in front of the target stations. Further, the transmission of the beam is controlled constantly and

a deviation leads to a beam interlock as a pencil like beam missing the target could damage the SINQ target.

Figure 3.1: Left: Exchange flask (yellow) for the Target E insert. In the background in orange is the exchange flask of Target M. Right: Target E insert with the old graphite wheel design.

Recently, the sensitivity to deviations of the beam from the center of the target was significantly improved with a modified version of the graphite wheel. For this, small grooves on both sides of the graphite target were applied (see Figure 3.2 right). In this way, the beam transmitted through the target is modulated, when it deviates more than 0.5 mm from the target centre. From there on, the amplitude of the modulation depends strongly on the position of the beam. Since different spacings are used between the grooves inside and outside, a deviation left and right from the center can be identified. More details, including information about the Fast Fourier Transformation used for the signal analysis, can be found in [6].

As the bearings degrade from heat and radiation, they have to be replaced after a few months of operation. First, several meters of concrete have to be removed from beamline. Then the target insert with the shielding plug is pulled into the exchange flask by remote control. The 42-t exchange flask (Figure 3.1 left) is well shielded by up to 40 cm steel for the up to 3 Sv/h graphite wheel [7]. The same shielding flask is used for removing collimators and beam dumps out of the beamline. The exchange flask is transported with the 60 t crane to a door lock above the service cell (ATEC) at PSI. The door lock is remotely opened by the control unit of the exchange flask. Then the target insert is lowered into the service cell,

Figure 3.2: Different Target E types from 2002 on. Left: Graphite wheel with 12 segments. Middle: Slanted target type. Right: Target E with grooves.

which is equipped with manipulators for remote handling. The hub with the two bearings are exchanged using these manipulators. During scheduled user beam time, the second target insert, which is fully equipped and has been stored in a vacuum chamber, is put back into the beamline to reduce the downtime.

A new type of target wheel was successfully tested at the end of 2019. Unlike the standard wheel, the beam here passes with a small angle through the graphite, keeping the effective target thickness (40 mm) the same (see Figure 3.2 middle). This configuration, called slanted target, results in a larger active surface and has two locations, the entrance and exit of the beam, where the beam is close to the surface. Both effects lead to an increase of surface muons. A first analysis [8] indicates an increase of 40 - 50%.

3.2.2 Target station M

As the Target M has a much smaller thickness, and the bearings are far from the beam and placed in the shielding, the demands are much less challenging than for Target E. The rim of the target is about 2-cm wide with a thickness of 2 mm. As the beam passes through the rim at an angle of 30°, its effective thickness is 5.2 mm (see Figure 3.3 left). This leads to a beam loss of only about 1.6% in the target and the following collimator system. The power deposition is about 2.4 kW/mA and the target operates at around 1100 K, mainly cooled by thermal conduction.

The original design dates back to 1985. The 85-cm steel shielding plug is placed upstream of the target and is not accessible during beam operation. The target insert is mounted horizontally, which has the advantage that the rotating shaft is long and the two bearings are well shielded. This results in bearing lifetimes of several years. In 2012/13 a new target insert was designed and installed in the beamline (see Figure 3.3 right). The bearing lifetime is improved due to better cooling of the front of the shielding plug close to target and beam. Here an additional copper plate cooled by water, is attached. The rotating shaft is made of low conducting material, titanium-vanadium, to reduce the heat flux from the target to the bearings. In this design the bearings can be exchanged without changing the target by pulling the shaft through the shielding plug. Further improvements in the maintenance and handling of the vacuum seal at the rear of the target insert were implemented in the new design.

In the near future, precision particle physics experiments will require higher rates, particularly for surface muons, to stay at the forefront of muon intensity. HIMB, High Intensity Muon Beam, aims to increase the surface muon rate with a 20-mm thick slanted target design and beamlines transporting a large fraction of the secondary particles produced. An increase of two orders of magnitude in the rates for surface muons is envisaged.
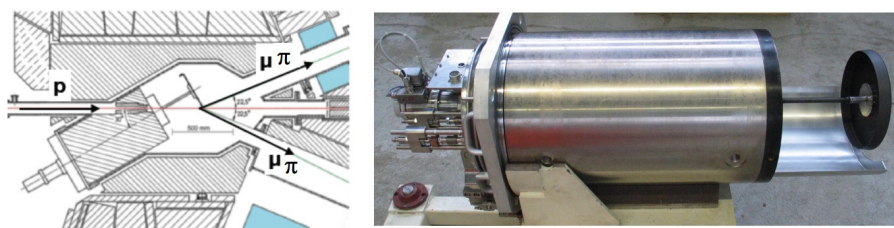

Figure 3.3: Left: Schematic view of the Target M insert at the beamline. Right: The Target M insert, new design.

3.3   High Energy Collimators and Beam dump

As the collimators and beam dumps have to stand high power from the proton beam, both devices are similar in their design. Like Target E, they are inserted vertically and contain steel shielding above the component. Collimators and beam dumps are both made from oxygen-free, high purity copper for three reasons: to have good thermal conductivity, to avoid hydrogen embrittlement and for brazing of the steel tubes onto the copper body. Hydrogen embrittlement occurs at high temperatures and can lead to cracks. The hydrogen is not an impurity in the copper but produced by spallation reactions of the protons with copper. Hydrogen bonds to the oxygen present in copper as impurity to form water, which then causes cracks at elevated temperatures. Brazing requires an oxygen-free surface. However, during brazing at temperatures around 800°C oxygen diffuses out of the copper and passivates the surface leading to a bad junction and thermal contact.

Cooling is quite important to avoid not only melting but temperatures above the homologous temperature (half of the melting temperature in Kelvin), where the structure of the material starts to change significantly. Therefore, temperatures above 400°C in copper must be avoided. Since direct contact of the water with the proton beam is not recommended due to the production of aggressive ions that lead to corrosion, the water pipes are wound outside of the cylindrical body. With a water flux of about 8 m/s the tubes cannot be made from copper, since they would suffer from abrasion, which leads to erosion corrosion. Therefore steel tubes are brazed to the copper body, which requires a good thermal contact in between. Before a new device is put into the beamline, the thermal contact is tested by heat exchange experiments.
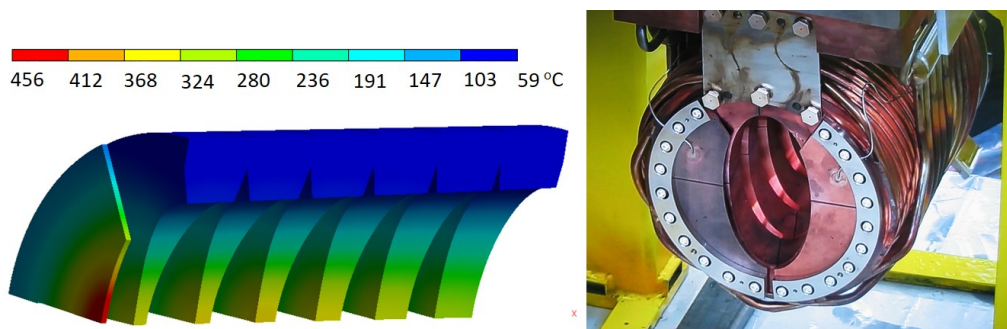

Figure 3.4:   Left: Temperature distribution of the KHE2 with 2 mA beam. Right: Collimator KHE2 with sample plate from the backside.

The cylindrical copper body is composed of five or six slices, which are later brazed together. This shape cannot be manufactured from one block, since some of the slices are tailored on both sides to reduce the energy deposit of the proton beam by reducing the amount of material. Slits between the slices also help to reduce the thermal stress. Each slice also contains four radial slits for thermal expansion. The optimal shape of the collimator has to be found by computational fluid dynamics (CFD) or equivalent simulations, which take into account the actual distribution of the proton beam or import the energy deposition region-wise from particle transport Monte Carlo simulations. The temperature distribution inside the collimator KHE2 along the beam direction is shown in Figure 3.4 left. More than one device is often necessary to absorb the beam under the constraint that the maximum temperature is kept below the homologous temperature and that the device still fits in the exchange flask. In fact, the collimator system after Target E and the beam dump each consist of four parts. The maximum length of each part is 400 mm. The collimator system after Target E is distributed along 4 m, whereas the beam dump sections are separated from each other by about 100 mm.

An aperture, separated in four sectors, is mounted in front of most devices. It consists of 100 μm Nickel foil, where free electrons from ionization due to protons are collected. This signal is proportional to the fraction of the beam in a section, and serves as an indication of the beam position as well as the beam size. The aperture is used to protect the device behind with a machine interlock, if the beam properties deviate from normal.

The KHE2, the third collimator after Target E, absorbs between 100 kW and 140 kW of the beam depending on the beam tuning and the thickness of Target E. This means that a large fraction of the beam hits the collimator and might cause radiation damage. An early estimate using the particle transport Monte Carlo package MCNPX2.5.0 [9] predicted an average DPA (Displacements Per Atom) of around 20. Regions close to the beam have an up to four times higher DPA value. Therefore, visible signs of radiation damage were expected and the collimator was inspected in the hot and service cell ATEC of PSI. The inside of the collimator was examined by an inspection tool to avoid high doses to the camera [10], which was well shielded without direct view to the collimator. This was necessary due to a dose rate of 310 Sv/h, 10 cm from the entrance of the collimator. No cracks or serious damage were observed except for some pieces peeling off the collimator. These pieces were identified as graphite (by the grey color) as well as due to the presence of ^{7}Be, a typical radioisotope from carbon activation. The graphite likely sublimated from Target E. A sample was taken and later a measurement with a HPGe (High Purity Germanium) detector was performed. In addition, traces from the brazing material, such as silver isotopes, were found. In 2013 the KHE2 was replaced by a new collimator of identical design, but with more thermocouples and additional sample plates from copper and Glidcop, a copper matrix with 0.3 wt % aluminum oxide, for later material studies after irradiation (See Figure 3.4 right). Glidcop is a promising candidate with similar properties as copper but keeping a large fraction of the thermal conductivity under irradiation.

In the meantime a new collimator system KHE2 and KHE3 with a different inner shape was manufactured, which will stand up to 3 mA beam current. The maximum current for the present KHE2 is 2.15 mA according to CFD simulations, which use the physical and mechanical properties for unirradiated copper. The main difference in the design is that the inner cone of the present collimator KHE2 has a diameter that widens in beam direction, whereas in the new design it decreases as in the beam dumps. Therefore, on the slices in front of the new designed KHE2 much less beam power is absorbed as the cone opening at this position is much wider. A side effect is that the slices are only slightly tailored. With the new design beam transport with a 3% larger transmission is possible up to the SINQ target.

In 2016 a sudden increase of the vacuum pressure inside the beam tube in the vicinity of the beam dump indicated a malfunctioning component. However, it was not clear which component was causing the problem. A mass spectrometer connected to the beam tube indicated the presence of water, which restricted the leak to a component cooled by water. However, there are many components, such as slits, vacuum chambers and beam dumps, connected to the cooling water cycle. The leak appeared at a beam current above 1.4 mA measured in front of the 40-mm Target E. However, it was very difficult to locate the leak, since it could not be detected without beam, and also did not show up when the device was heated with 150°C pressurized water. Since the full beam dump consists of four parts, the malfuntioning part had to be identified before a replacement could be manufactured. The leak was identified with beam studies, and finally confirmed when the leak disappeared in 2018 with a new identical BHE1 in place. During the time the first beam dump section was removed from the beamline and transferred to ATEC for inspection and replacement, a periscope using mirrors was inserted into the beamline at the position of BHE1. A camera at its end took pictures from the second part of the beam dump as well as the entry of the vacuum chamber. A view on the BHE2 from this camera is shown in Figure 3.5 left. On the right of the figure, BHE2 is shown

before irradiation. As can be seen from the pictures BHE1 is intact despite withstanding 150 kW with beam.

Figure 3.5: Left: Beam dump BHE2 with aperture in the beamline as seen from the periscope. Right: BHE2 without aperture before irradiation in 1990.

3.4 Summary

The two meson production stations M and E use rotating polycrystalline graphite targets. They have been working well since the 1990's, serving seven beamlines with pions and muons. A special target design with grooves was recently tested and allows a very precise detection of the beam position on the target. For HIMB aiming to increase the surface muon rate by up to a factor of 100, beamline simulation and design studies for an upgrade of the target M station with the new type of slanted target design are ongoing. In the Target E station the slanted target type already demonstrated a 40-50% increase of the surface muon rate.

The collimator system as well as the beam dump have to stand more then 100 kW per component. Except for a water leak in the first beam dump element, which is likely due to thermal cyclic stress, no visible signs of radiation damage are observed. The design of a segmented copper body cooled by water in steel tubes, which are brazed to the copper, has proven its reliability.

References

[1] D. Kiselev et al., *Status and future frojects of the PSI High Intensity Proton Accelerator*, JPS Conf. Proc. **33**, 011004 (2021), doi:10.7566/JPSCP.33.011004.

[2] J. Grillenberger et al., *The high intensity proton accelerator at PSI*, SciPost Phys. Proc. **5**, 002 (2021), doi:10.21468/SciPostPhysProc.5.002.

[3] D. Kiselev et al., *Progress and challenges of the PSI meson targets and relevant systems*, JPS Conf. Proc. **33**, 011102 (2021), doi:10.7566/JPSCP.33.011102.

[4] F. Berg et al., *Target studies for surface muon production*, Phys. Rev. Accel. Beams **19**, 024701 (2016), doi:10.1103/PhysRevAccelBeams.19.024701.

[5] G. Heidenreich, *Carbon and beryllium targets at PSI*, AIP Conf. Proc. **642**, 122 (2002), doi:10.1063/1.1522602.

[6] P.-A. Duperrex, P. Baumann, S. Joray, D. Kiselev, D. Laube and D. Reggiani, *New centering beam monitor for high power proton beam rotating target*, in Proc. Cyclotrons'19, Joint Accelerator Conf. Web. 189 (2020), doi:10.18429/JACoW-Cyclotrons2019-TUP016.

[7] D. Kiselev, R. Bergmann, D. Schumann, V. Talanov and M. Wohlmuther, *Proton induced activity in graphite - comparison between measurement and simulation*, J. Phys.: Conf. Ser. **1046**, 012003 (2018), doi:10.1088/1742-6596/1046/1/012003.

[8] P.-R. Kettle, Private communication (2020).

[9] D. B. Pelowitz, editor, *CNPX user's manual, version 2.5.0*, LA-CP-05-0369 (2005).

[10] Å. Strinning, P. Baumann, M. Gandel, D. Kiselev, Y. Lee and S. Adam, *Visual inspection of a copper collimator irradiated by 590 MeV protons at PSI*, in Proc. HB2010 245 (2010).

UCN, the ultracold neutron source - neutrons for particle physics

Bernhard Lauss[⋆] and Bertrand Blau

Paul Scherrer Institut, CH-5232 Villigen PSI, Switzerland

⋆ bernhard.lauss@psi.ch

Abstract

Ultracold neutrons provide a unique tool for the study of neutron properties. An overview is given of the ultracold neutron (UCN) source at PSI, which produces the highest UCN intensities to fundamental physics experiments by exploiting the high intensity proton beam in combination with the high UCN yield in solid deuterium at a temperature of 5 K. We briefly list important fundamental physics results based on measurements with neutrons at PSI.

4.1 Introduction

Ultracold neutrons (UCNs) are at the lowest end of the neutron energy spectrum, with kinetic energies below about 300 neV, corresponding to velocities below 8 m/s, and to temperatures below 4 mK. Hence they are called "ultracold". This energy is the same as the neutron optical potential of certain materials. Thus material bottles can be used to store UCNs. This energy also corresponds to the potential difference of a neutron raised by 3 meters in the Earth's gravitational field, and also to the potential difference of a 5 Tesla magnetic field gradient acting on the neutron magnetic moment. Thus, UCNs can be relatively easily confined and manipulated. Therefore, they are a unique tool to study the properties of the neutron itself. The highest UCN intensities are needed to reach the highest sensitivity range in fundamental physics experiments; the most prominent such experiment is the search for a permanent electric dipole moment of the neutron (nEDM) [1,2].

The idea to build an intense UCN source at PSI was formulated in the late 1990's. The UCN project was initiated and realized under the leadership of Manfred Daum. The technical design presented in 2000 [3,4] was based on earlier studies in Russia [5–7] and a successful operation of a solid-deuterium based UCN source at the Los Alamos National Laboratory [8]. The main scientific goal was to push the sensitivity of the nEDM search to a new level. Several pioneering experiments by the PSI UCN group determining e.g. UCN production in solid deuterium [9,10] and UCN loss cross-sections [11,12], paved the way for the final design. The UCN source was then installed as the second spallation neutron source at the PSI high intensity proton facility

(HIPA). After a short test beam period at the end of 2010, the UCN source started regular operation in 2011 [13–15] providing UCNs to experiments at three beam ports.
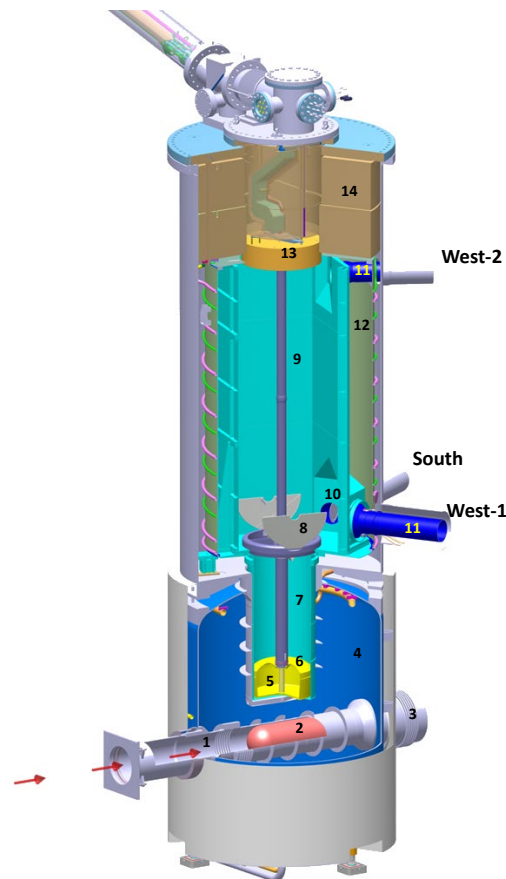
4.2 UCN Source Setup

Figure 4.1: CAD image of the UCN tank with indicated parts relevant to UCN production and transport. 1 - proton beam tube, 2 - lead spallation target, 3 - target shielding, 4 - heavy water moderator tank, 5 - D_2 moderator vessel, 6 - lid, 7 - vertical guide, 8 - flapper valve, 9 - storage vessel, 10 - UCN guide shutter, 11 - UCN guide section, 12 - thermal shield, 13 - cryo-pump, at 5 K, 14 - iron shielding.

The PSI UCN source operates in the following way: The 590 MeV, 2.4 mA proton beam is deflected by a kicker magnet [16] for up to 8 s onto the lead spallation target (label 2) in Figure 4.1) [17]. In a spallation reaction between a lead nucleus and a 590 MeV proton, an average of 8 free neutrons is produced [18]. The neutrons are thermalized in the surrounding heavy water (label 4). The central moderator vessel (label 5) contains solid deuterium (sD$_2$) at a temperature of 5 K, which serves as both a cold moderator and as the UCN production medium. The cryogenics system needed for the manipulation, cooling and freezing of the deuterium [19] is shown in Figure 4.2. UCNs exit the moderator vessel through a thin aluminum lid (label 6 of Figure 4.1) into a vertical guide where the energy boost from the sD$_2$ surface [20] is lost by gravity. The flapper valve (label 8) of the 1.6 m^3 large storage vessel is closed at the end of the proton pulse. UCNs trapped in the storage vessel are delivered via about 8 m long neutron guides (label 11) to three beam ports, named West-1, South and West-2, with the latter extracting UCN from the top of the storage vessel. Great attention was spent

on quality checks of all elements, and extensive tests were performed before installation, e.g. the cryo-performance of several parts, most importantly the flapper valves (label 8) and UCN guide shutters (label 11). The UCN transport performance of all UCN guides [21] was confirmed prior to their installation. The overall neutron optics performance was later analyzed and understood in terms of a detailed simulation of the entire UCN source [22].
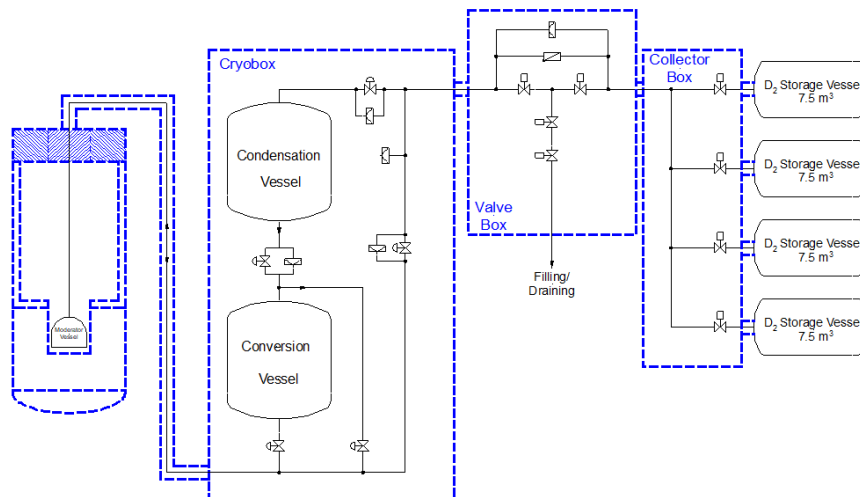

Figure 4.2: Schematic view of the subsystems needed for the preparation of the solid ortho-deuterium (see text).

The core of the UCN source is the solid deuterium moderator, which also serves as a UCN converter at a temperature of 5 K. The 30 liters of solid D_2 require very careful preparation in order to achieve optimal UCN output. A schematic view of the involved subsystem is shown in Figure 4.2. Preparation starts from the $30\,m^3$ ultra clean and isotopically pure D_2 gas, stored in large tanks at ambient temperature, which is slowly transferred by freezing into the 40 liter copper-made 'condensation' vessel. The D_2 is then slowly liquefied and transferred by gravity into the 'conversion' vessel at about 20 K where an ortho-D2 concentration of about 97% is achieved within 24 h by means of a spin-flip process on Oxisorb, a chromium-oxide-based catalyzer material. Raman spectroscopy is used to check the ortho-D_2 concentration [23, 24], which rises up to above 99% during longer operation periods. Once the required ortho concentration is reached in the conversion vessel, the liquid D_2 is transferred by gravity through a 10 m-long cold transfer line into the moderator vessel. Here it is slowly solidified over several days to achieve a good ice quality and, consequently, a high UCN output. The moderator vessel, shown in Figure 4.3a, is entirely made from AlMg3 with special coolant channels for the supercritical He cooling fluid at 4.7 K. These channels enter in the center of the vessel and direct the He stream to the outside wall, up and back in 8 separated sections, as schematically depicted in Fig. 4.3b.

The delivered UCN intensity reflects the quality of the achieved solid deuterium, likely a mosaic crystal with many defects and cracks, as was shown in the pioneering UCN experiments [9–12]. Slow freezing is crucial in the preparation process of the source. Figure 4.4 shows the typical UCN intensity behavior (green line) during such a slow freezing process. The vapor pressure (blue line) which is a direct measure of the D_2 (surface) temperature decreases from above 400 mbar (liquid D_2) to the triple point at about 171 mbar, where the liquid D_2 solidifies. After solidification the vapor pressure rapidly decreases below 10^{-2} mbar. The UCN output shows the opposite behavior. UCN loss processes dominate at higher temperatures, especially in the liquid D_2 and the high-density vapor located above the D_2. Once 5 K are
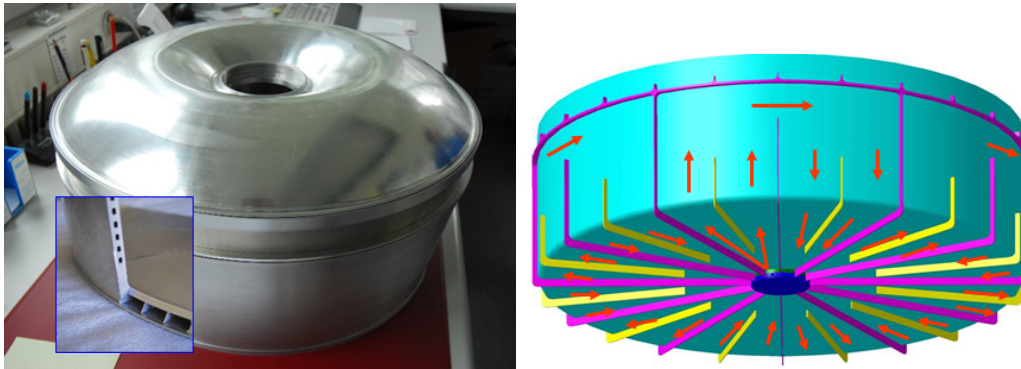
Figure 4.3: a) View of the moderator vessel with a cut insert view from a test vessel wall. b) Schematic view of the He coolant flow in the vessel demonstrating the sectional cooling.

reached, thermal losses are minimized and the UCN output is at its maximum.

4.3 UCN Source Performance

An important performance parameter is the number of UCNs delivered at a beam port in a given time interval as this determines the number of UCNs available in an experiment. The typical time structure of UCNs for a proton beam pulse is shown in Figure 4.5. The flaps of the storage vessel open before the proton beam hits the spallation target and their closing time is optimized with respect to the end of the proton pulse to provide the maximum number of UCNs to the experiments. The measured exponential decay of the UCN count rate at the West-1 beam port, Figure 4.5a), has a time constant of about 30 s, reflecting the emptying time of the central storage vessel through the West-1 guide into the UCN detector. The UCN rate at the South beam port behaves identically. If all shutters to the UCN guides remain closed on the storage vessel, the storage time constant for UCNs trapped inside the vessel is about 90 s. At the end of the filling/extraction period, which is typically 300 s long, the flaps are re-opened to be ready for the next proton beam pulse.

Figure 4.5b shows the UCN rate observed at the West-2 beam port located 230 cm above the bottom of the storage vessel [22]. The faster exponential decay demonstrates that the UCNs with energies high enough to reach up to 230 cm, are quickly drained through that port. The total number of UCNs delivered at the West-1 or South beam port was has been up to 45 million at the best operating conditions. The total number of delivered UCNs depends on the status of the solid deuterium, and was increased over the years with improvements in the operating conditions.

Several studies to understand all aspects of the UCN source have been conducted since its inauguration. The proton beam current and position is constantly monitored online with beam monitors. Neutron production and thermalization were checked using neutron activation measurements on gold. The observed activation was well reproduced in detailed neutron transport simulations using MCNP [18]. Neutron moderation was studied using tritium production in the solid D_2 moderator [24]. The high ortho D_2 concentration and the high isotopic purity of 0.09% H atoms (bound in HD molecules) of the D_2 was confirmed [24].

UCN transport from production in the solid deuterium to a beam port has been carefully studied as is detailed in the thesis works [25, 26]. Many geometry details were put into a full simulation model and the simulation results then matched well with observations [22].

The measured integral UCN intensity per beam pulse also shows a time dependence on
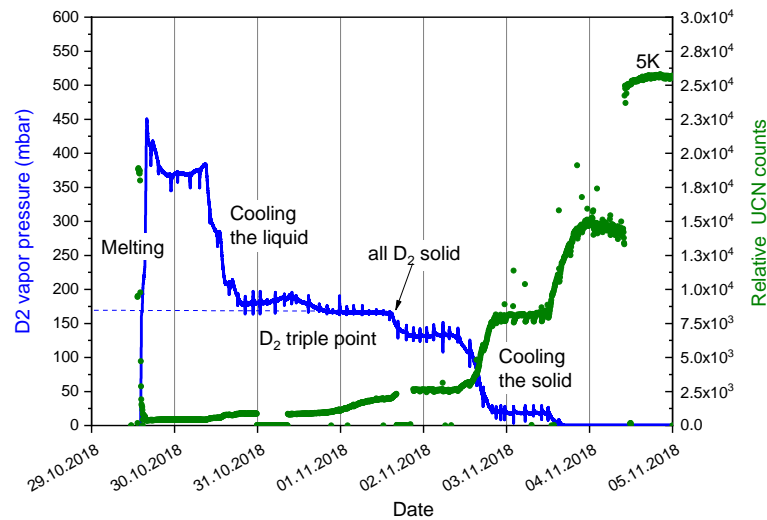
Figure 4.4: The observed behavior during the slow freezing of the deuterium. The vapor pressure of the D_2 (blue line) indicates the D_2 temperature. The D_2 was fully melted. When it reaches about 400 mbar vapor pressure, cooling starts and the D_2 slowly approaches the triple point at 171 mbar (horizontal dashed line). Here the D_2 solidifies. When the solid D_2 is further cooled down to 5 K the vapor pressure drops well below 10^{-2} mbar. The large increase in UCN output shown by the green bullets demonstrates the strong reduction in UCN losses within the D_2.

the scale of several hours to days, which considerably decreases the average UCN output. After several studies, a temperature-cycling procedure, called "conditioning", was developed that gets rid of the accumulated losses and regains maximum UCN intensity. This UCN count rate behavior is shown in Figure 4.6a, where the times when the conditioning procedure was applied are labeled by the vertical arrows. Figure 4.6b shows the measured deuterium vapor pressure in the moderator vessel during a 2-hour conditioning process. The rise in vapor pressure during a proton beam pulse, noted with the blue arrow, is minuscule. The rise during temperature cycling is up to about 50 Pa, depending on the total operation time since the previous conditioning. This is far below the triple-point pressure of 171 mbar and is due to sublimation, movement and resublimation of surface molecules during conditioning. Interesting enough, full rate recovery occurs.

One of the key characteristics of a UCN source is the UCN density that can be achieved in a given storage vessel. A stainless steel 'standard UCN storage vessel' with a volume of 20 liters [27] was built. This bottle was used to characterize the height-dependent UCN density at the West-1 beam port [26]. The UCN density peaks around 50 cm above the beam port as shown in Figure 4.7. This standard bottle was then used to characterize UCN densities of other sources in a comparable way [26, 28, 29]. As a result it has been shown that the PSI source provides world-leading performance to UCN storage experiments.

The PSI UCN source has been operating since 2011 on a regular schedule, mainly providing UCNs to the nEDM experiment. The yearly operation can be characterized by the integral of the proton beam current onto the UCN spallation target and the number of proton beam pulses, shown in Figure 4.8. The peak in 2016 was driven by the main data taking period of the nEDM experiment. The lower numbers in the subsequent years are due to longer periods of solid deuterium studies for UCN source improvements, which needed longer times with fewer
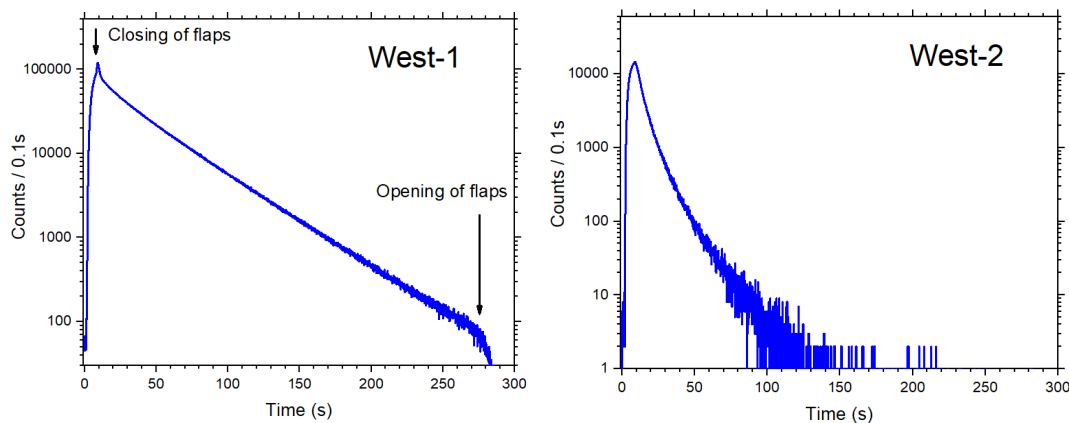
Figure 4.5: a) UCN counts after one proton beam pulse at the West-1 beam port. Closing and opening of the flaps refers to the central flapper valves. b) Same as a) but at the West-2 beam port.

proton beam pulses for performance checks.

4.4 Physics results at the UCN source

The construction of the UCN source at PSI was driven by the experiment to search for a neutron electric dipole moment. The resulting new nEDM limit was published in 2020 [2]. Significant physics results were also obtained on neutron properties and effects:

- a precision measurement of the mercury-to-neutron magnetic moment ratio [30];

- spin-echo spectroscopy with ultracold neutrons [31]

- measurement of gravitational depolarization of ultracold neutrons [32]

and on physics beyond the Standard Model:

- a limit for spin-dependent forces mediated by axion-like particles [33];

- the first laboratory limit for oscillating electric dipole moments [34];

- new limits for mirror-neutron oscillations in mirror magnetic fields [35].

Some of these results are treated in Section 18 [36] and Section 19 [37] of this volume.

4.5 Particle physics at the SINQ

The UCN source was conceived and built for research in fundamental neutron physics. However, the first spallation neutron source built at PSI was the SINQ facility [38]. While mainly dedicated to neutron scattering instruments, it has also been used as a polarized cold-neutron beam line for fundamental neutron physics. The 'FUNSPIN' beam line [39] (now called 'BOA') provided 6×10^8 neutrons $cm^{-2}s^{-1}mA^{-1}$ with 95% polarization [40].

The main physics results came from a series of measurements by the nTRV collaboration of neutron decay parameters. A precise determination of electron-neutron correlation coefficients R and N provided a precise test of the Standard Model and a search for exotic scalar and tensor interactions in neutron decay [41–44].

Another experiment produced a new measurement of the spin-dependent doublet neutron-deuteron scattering length [45, 46]. A Ramsey-type experiment resulted in an upper limit
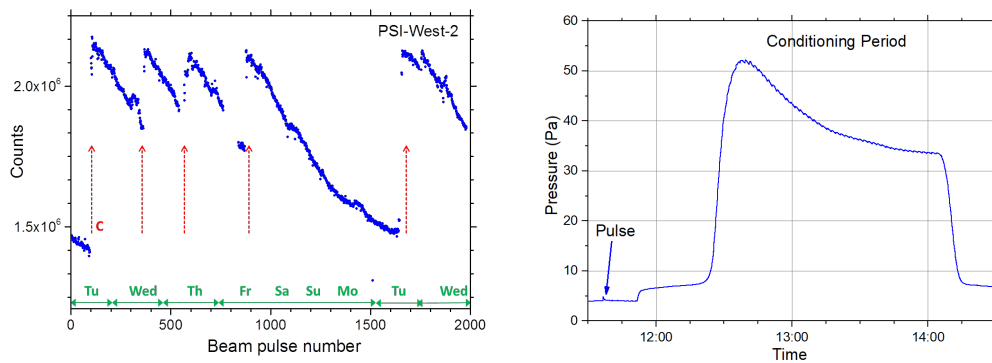
Figure 4.6: a) The UCN count rate behavior as observed over a 9-day operating period. The drop is interpreted as a frost effect. The count rate increases to the original level when the conditioning procedure is applied at the times depicted by the dashed arrows. Figure from [22] with kind permission of The European Physical Journal (EPJ). b) Vapor pressure of the solid deuterium surface in the moderator vessel during a full conditioning cycle.
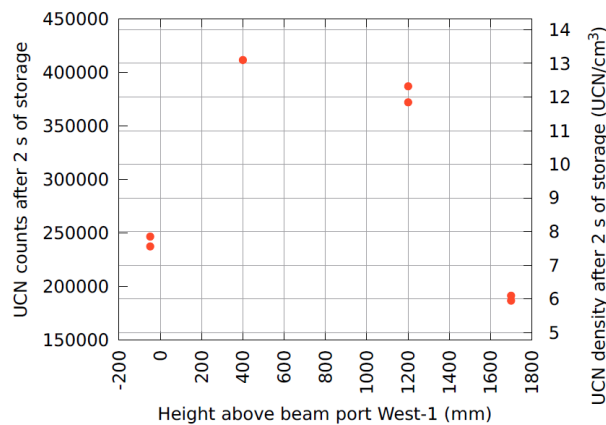

Figure 4.7: The UCN density measured at different heights with respect to the West-1 beam port. Picture from [26].

on the strength of an axial coupling constant for a new light spin 1 boson in the millimeter range [47].

Finally, we note the importance of the FUNSPIN beamline for many measurements conducted in preparation of the UCN source where many parameters of UCN production and loss were determined [9–12, 48–50].

4.6 Summary

A high-intensity source for ultracold neutrons, designed and built at PSI, has been operating since 2011. The layout, operation and performance are described. Some observations on the solid deuterium converter and its surface conditions are presented. Finally, a list of physics results in fundamental neutron physics results achieved with the UCN source and SINQ is given.
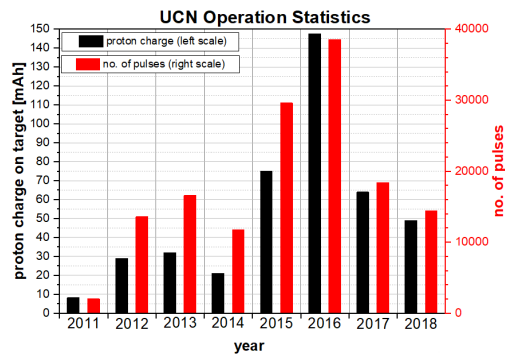
Figure 4.8: Annual statistics of the first operating years of the UCN source showing total accumulated beam current on target (black bars) and number of beam pulses (red bars) on the UCN spallation target.

References

[1] J. M. Pendlebury et al., *Revised experimental upper limit on the electric dipole moment of the neutron*, Phys. Rev. D **92**, 092003 (2015), doi:10.1103/PhysRevD.92.092003.

[2] C. Abel et al., *Measurement of the permanent electric dipole moment of the neutron*, Phys. Rev. Lett. **124**, 081803 (2020), doi:10.1103/PhysRevLett.124.081803.

[3] M. Daum et al., *Proposal for an ultracold neutron facility at PSI*, PSI Proposal, R-00-03, Nov. (1999).

[4] A. Fomin et al., *An ultracold neutron facility at PSI - spallation ultracold neutron source (SUNS) for the neutron edm experiment*, Technical Review, November 2000.

[5] Y. Pokotilovski, *Production and storage of ultracold neutrons at pulsed neutron sources with low repetition rates*, Nucl. Instrum. Methods A **356**, 412 (1995), doi:10.1016/0168-9002(94)01325-X.

[6] A. P. Serebrov, V. A. Mityukhlyaev, A. A. Zakharov, T. Bowles, G. Greene and J. Sromicki, *Solid deuterium source of ultracold neutrons based on a pulsed spallation source*, JETP Lett. **66**, 802 (1997).

[7] A. Serebrov et al., *Studies of a solid-deuterium source for ultra-cold neutrons*, Nucl. Instrum. Methods A **440**, 658 (2000), doi:10.1016/S0168-9002(99)01058-X.

[8] R. Hill et al., *Performance of the prototype LANL solid deuterium ultra-cold neutron source*, Nucl. Instrum. Methods A **440**, 674 (2000), doi:10.1016/S0168-9002(99)01060-8.

[9] F. Atchison et al., *Production of ultracold neutrons from a cold neutron beam on a $^2H_2$ target*, Phys. Rev. C **71**, 054601 (2005), doi:10.1103/PhysRevC.71.054601.

[10] F. Atchison et al., *Investigation of solid D_2, O_2 and CD_4 for ultracold neutron production*, Nucl. Instrum. Methods A **611**, 252 (2009), doi:10.1016/j.nima.2009.07.072.

[11] F. Atchison et al., *Measured total cross sections of slow neutrons scattered by gaseous and liquid $^2H_2$*, Phys. Rev. Lett. **94**, 212502 (2005), doi:10.1103/PhysRevLett.94.212502.

[12] F. Atchison et al., *Measured total cross sections of slow neutrons scattered by solid deuterium and implications for ultracold neutron sources*, Phys. Rev. Lett. **95**, 182502 (2005), doi:10.1103/PhysRevLett.95.182502.

[13] B. Lauss, *A new facility for fundamental particle physics: The high-intensity ultracold neutron source at the Paul Scherrer Institute*, AIP Conf. Proc. **1441**, 576 (2012), doi:10.1063/1.3700622.

[14] B. Lauss, *Startup of the high-intensity ultracold neutron source at the Paul Scherrer Institute*, Hyperf. Int. **211**, 21 (2012), doi:10.1007/s10751-012-0578-7.

[15] B. Lauss, *Ultracold neutron production at the second spallation target of the Paul Scherrer Institute*, Phys. Proc. **51**, 98 (2014), doi:10.1016/j.phpro.2013.12.022.

[16] D. Anicic et al., *A fast kicker magnet for the PSI 600MeV proton beam to the PSI ultra-cold neutron source*, Nucl. Instrum. Method. A **541**, 598 (2005), doi:10.1016/j.nima.2004.12.032.

[17] M. Wohlmuther and G. Heidenreich, *The spallation target of the ultra-cold neutron source UCN at PSI*, Nucl. Instrum. Methods A **564**, 51 (2006), doi:10.1016/j.nima.2006.03.040.

[18] H. Becker et al., *Neutron production and thermal moderation at the PSI UCN source*, Nucl. Instrum. Methods A **777**, 20 (2015), doi:10.1016/j.nima.2014.12.091.

[19] A. Anghel, B. Blau, M. Daum, K. Kirch and S. Grigoriev, *Cryogenic system of the Swiss ultra-cold neutron source*, In Proc. of the 10th IIR International Conference Cryogenics, 04/21-04/25, 2008, Prague, Czech Republic (2008).

[20] I. Altarev et al., *Neutron velocity distribution from a superthermal solid 2H2 ultracold neutron source*, Eur. Phys. J. A **37**, 9 (2008), doi:10.1140/epja/i2008-10604-8.

[21] B. Blau, M. Daum, M. Fertl, P. Geltenbort, L. Goeltl, R. Henneck, K. Kirch, A. Knecht, B. Lauss, P. Schmidt-Wellenburg and G. Zsigmond, *A prestorage method to measure neutron transmission of ultracold neutron guides*, Nucl. Instrum. Methods A **807**, 30 (2016), doi:10.1016/j.nima.2015.10.075.

[22] G. Bison, B. Blau, M. Daum, L. Göltl, R. Henneck, K. Kirch, B. Lauss, D. Ries, P. Schmidt-Wellenburg and G. Zsigmond, *Neutron optics of the PSI ultracold-neutron source: characterization and simulation*, Europ. Phys. J. A **56**, 33 (2020), doi:10.1140/epja/s10050-020-00027-w.

[23] K. Bodek et al., *An apparatus for the investigation of solid D_2 with respect to ultra-cold neutron sources*, Nucl. Instrum. Methods A **533**, 491 (2004), doi:10.1016/j.nima.2004.06.157.

[24] N. Hild, *Studies of the Deuterium used in the PSI UCN Source*, Ph.D. thesis, ETH Zürich (2019).

[25] L. Göltl, *Characterization of the PSI ultra-cold neutron source*, Ph.D. thesis, ETH Zürich, No.20350 (2012).

[26] D. Ries, *Characterisation and Optimisation of the Source for Ultracold Neutrons at the Paul Scherrer Institute*, Ph.D. thesis, ETH Zürich, No.23671 (2016).

[27] G. Bison, F. Burri, M. Daum, K. Kirch, J. Krempel, B. Lauss, M. Meiter, D. Ries, P. Schmidt-Wellenburg and G. Zsigmond, *An ultracold neutron storage bottle for UCN density measurements*, Nucl. Instrum. Methods A **830**, 449 (2016), doi:10.1016/j.nima.2016.06.025.

[28] G. Bison et al., *Comparison of ultracold neutron sources for fundamental physics measurements*, Phys. Rev. C **95**, 045503 (2017), doi:10.1103/PhysRevC.95.045503.

[29] J. Kahlenberg et al., *Upgrade of the ultracold neutron source at the pulsed reactor TRIGA Mainz*, Europ. Phys. J. A **53**, 226 (2017), doi:10.1140/epja/i2017-12428-9.

[30] S. Afach et al., *A measurement of the neutron to ^{199}Hg magnetic moment ratio*, Phys. Lett. B **739**, 128 (2014), doi:10.1016/j.physletb.2014.10.046.

[31] S. Afach et al., *Observation of gravitationally induced vertical striation of polarized ultracold neutrons by spin-echo spectroscopy*, Phys. Rev. Lett. **115**, 162502 (2015), doi:10.1103/PhysRevLett.115.162502.

[32] S. Afach et al., *Gravitational depolarization of ultracold neutrons: Comparison with data*, Phys. Rev. D **92**, 052008 (2015), doi:10.1103/PhysRevD.92.052008.

[33] S. Afach et al., *Constraining interactions mediated by axion-like particles with ultracold neutrons*, Phys. Lett. B **745**, 58 (2015), doi:10.1016/j.physletb.2015.04.024.

[34] C. Abel et al., *Search for axionlike dark matter through nuclear spin precession in electric and magnetic fields*, Phys. Rev. X **7**, 041034 (2017), doi:10.1103/PhysRevX.7.041034.

[35] C. Abel et al., *A search for neutron to mirror-neutron oscillations*, Phys. Lett. B **812**, 135993 (2021), doi:10.1016/j.physletb.2020.135993.

[36] G. Pignol and P. Schmidt-Wellenburg, *The search for the neutron electric dipole moment at PSI*, SciPost Phys. Proc. **5**, 027 (2021), doi:10.21468/SciPostPhysProc.5.027.

[37] S. Roccia and G. Zsigmond, *Indirect searches for dark matter with the nEDM spectrometer*, SciPost Phys. Proc. **5**, 028 (2021), doi:10.21468/SciPostPhysProc.5.028.

[38] W. Wagner, M. Wohlmuther, U. Stuhr, V. Davydov, J. Repper, S. Van Petegem, U. Filges, B. Blau, B. Lauss, L. Goeltl, M. Hildebrandt, K. Thomsen, B. Hammer, J. Neuhausen, D. Schumann, *SINQ and UCN - two high-power spallation sources operating at PSI*, In Proceedings of ICANS XX 20th Meeting of the International Collaboration on Advanced Neutron Sources, Bariloche, Argentina March 4 - 9, 2012, Open Access (2012).

[39] K. Bodek et al., *Physics with polarized cold neutrons at the spallation source SINQ*, AIP Conf. Proc. **549**, 983 (2000), doi:10.1063/1.1345413.

[40] J. Zejma et al., *FUNSPIN polarized cold-neutron beam at PSI*, Nucl. Instrum. Methods A **539**, 622 (2005), doi:10.1016/j.nima.2004.11.004.

[41] G. Ban et al., *Search for exotic couplings in neutron decay: A measurement of the transverse polarization of electrons*, Nucl. Phys. A **827**, 422c (2009), doi:10.1016/j.nuclphysa.2009.05.090.

[42] A. Kozela et al., *Measurement of the transverse polarization of electrons emitted in free-neutron decay*, Phys. Rev. Lett. **102**, 172301 (2009), doi:10.1103/PhysRevLett.102.172301.

[43] K. Bodek, G. Ban, A. Bialek, P. Gorel, K. Kirch, S. Kistryn, A. Kozela, M. Kuzniak, O. Naviliat-Cuncic, N. Severijns, E. Stephan and J. Zejma, *R- and N-correlation coefficients in neutron decay: Search for scalar and tensor couplings in weak interactions*, Phys. Proc. **17**, 30 (2011), doi:10.1016/j.phpro.2011.06.014.

[44] A. Kozela, G. Ban, A. Bialek, K. Bodek, P. Gorel, K. Kirch, S. Kistryn, O. Naviliat-Cuncic, N. Severijns, E. Stephan and J. Zejma, *Measurement of the transverse polarization of electrons emitted in free neutron decay*, Phys. Rev. C **85**, 045501 (2012), doi:10.1103/PhysRevC.85.045501.

[45] B. van den Brandt, H. Glättli, H. Grießhammer, P. Hautle, J. Kohlbrecher, J. A. Konter, F. M. Piegsa, J. P. Urrego-Blanco, B. S. Schlimme and O. Zimmer, *A high-accuracy measurement of the spin-dependent neutron scattering length of the deuteron*, AIP Conf. Proc. **842**, 814 (2007), doi:10.1063/1.2220391.

[46] B. van den Brandt, H. Glättli, P. Hautle, J. A. Konter, F. M. Piegsa and O. Zimmer, *The measurement of the incoherent neutron scattering length of the deuteron*, Nucl. Instrum. Methods A **611**, 231 (2009), doi:10.1016/j.nima.2009.07.053.

[47] F. M. Piegsa and G. Pignol, *Limits on the axial coupling constant of new light bosons*, Phys. Rev. Lett, **108**, 181801 (2012), doi:10.1103/PhysRevLett.108.181801.

[48] F. Atchison et al., *Cold neutron energy dependent production of ultracold neutrons in solid deuterium*, Phys. Rev. Lett. **99**, 262502 (2007), doi:10.1103/PhysRevLett.99.262502.

[49] F. Atchison et al., *Loss and spinflip probabilities for ultracold neutrons interacting with diamondlike carbon and beryllium surfaces*, Phys. Rev. C **76**, 044001 (2007), doi:10.1103/PhysRevC.76.044001.

[50] F. Atchison et al., *Production of ultracold neutrons from cryogenic $2H_2$, O_2, and C_2H_4 converters*, Eur. Phys. Lett **95**, 12001 (2011), doi:10.1209/0295-5075/95/12001.

A theory vade mecum for PSI experiments

G. Colangelo[1], F. Hagelstein[2], A. Signer[2,3*] and P. Stoffer[4]

1 Albert Einstein Center for Fundamental Physics, Institute for Theoretical Physics,
University of Bern, Switzerland
2 Paul Scherrer Institut, 5232 Villigen PSI, Switzerland
3 University of Zurich, Physik-Institut, 8057 Zurich, Switzerland
4 University of Vienna, Faculty of Physics, Boltzmanngasse 5, 1090 Vienna, Austria

* adrian.signer@psi.ch

Abstract

This article gives a compact introduction and overview of the theory underlying the experiments described in the rest of this review.

5.1 Introduction

The purpose of this article is to give a broad overview of the theory background to the experiments that have been and are carried out at the Paul Scherrer Institute. Space limitations make it impossible to go into depth or provide a self-contained theoretical summary. Much more modestly, we aim to put the experiments into context and provide key references for further reading. The experiments we refer to are listed in Table 5.1 and they will be described in greater detail in separate sections/articles of the Review of Particle Physics at PSI [1–23]. These experiments either lead to precise determinations of physical parameters required as input for other experiments (e.g., muon life time, pion mass), or search for physics beyond the Standard Model (BSM). The BSM searches proceed along different frontiers. One way to search for new physics is to consider physical observables whose Standard Model (SM) contributions either vanish or are too small to be experimentally accessible. In other words, they are identical to zero for practical purposes. Examples are charged lepton-flavor violating (cLFV) muon decays or a permanent neutron electric dipole moment (EDM). To put constraints on the branching ratios of BSM decays, one has to observe a large number of decays. This is, thus, called a search at the intensity frontier. Another way to search for new physics is to consider precision observables and search for deviations from the SM expectations. Prominent examples are the precision QED tests with muonium, as well as the precision laser spectroscopy experiments with muonic atoms. These are, thus, called searches at the precision frontier.

The low-energy experiments at PSI are complementary to the experiments at LHC, which sit at the energy frontier.

After a general overview of the theoretical methods applied to describe the processes and bound states in Table 5.1, we will, in turn, consider the muon, the proton, nucleons and nuclei, the free neutron, and the pions.

5.2 Overview

The experiments we are primarily concerned with involve low-energy interactions of electrons, muons, protons, neutrons, and pions. In Section 5.2.1 we first describe these interactions in the SM before we discuss the generalization to BSM scenarios in Section 5.2.2. While the theoretical methods for these cases are dominated by perturbative expansions in the couplings, Section 5.2.3 is devoted to hadronic effects that often play an important part in low-energy experiments.

5.2.1 Standard Model at low energies

In the SM the dynamics of the particles listed above is described by the gauge theory of strong and electroweak interactions. In view of the large masses of the Higgs and weak gauge bosons, the weak part of the SM Lagrangian is essentially frozen at low energies (it will later be considered as a small correction). In this regime, the SM reduces to the standard QED and QCD Lagrangian

$$\mathcal{L}_{\text{QED+QCD}} = \sum_f \bar{f} \left(i\slashed{D} - m_f \right) f - \frac{1}{4} F_{\alpha\beta} F^{\alpha\beta} - \frac{1}{4} G_{\alpha\beta} G^{\alpha\beta} \,, \tag{5.1}$$

where the electromagnetic and gluonic field-strength tensors are expressed in terms of the photon and gluon fields, A^α and G^α, as $F^{\alpha\beta} = \partial^\alpha A^\beta - \partial^\beta A^\alpha$, $G^{\alpha\beta} = \partial^\alpha G^\beta - \partial^\beta G^\alpha - i g_s [G^\alpha, G^\beta]$, and where for clarity we have omitted gauge-fixing and ghost terms. The sum runs over all fermions of mass m_f, electric charge $e Q_f$, and color charge $g_s t_f^a$, and the covariant derivative acts on the fermion fields as $D_\alpha f = (\partial_\alpha - i e Q_f A_\alpha - i g_s t_f^a G_\alpha^a) f$. For $f = \ell \in \{e, \mu, \tau\}$ we have $Q_\ell = -1$ and $t_\ell^a = 0$, whereas for quarks $Q_u = 2/3$, $Q_d = -1/3$, and $t_{u,d}^a = \lambda^a/2$ with Gell-Mann matrices λ^a. In several experiments of interest here the photon acts as a probe: it is coupled to the electromagnetic current J_{em}^α as

$$\mathcal{L}_{\text{QED}}^{\text{int}} = e A_\alpha J_{\text{em}}^\alpha \equiv e A_\alpha \sum_f Q_f \bar{f} \gamma^\alpha f \,. \tag{5.2}$$

If we use (5.1) to compute the matrix element of J_{em}^α between two states of pointlike leptons ℓ with momenta p_1 and $p_2 = p_1 + q$, we find

$$\langle \ell(p_2) | J_{\text{em}}^\alpha | \ell(p_1) \rangle = \bar{u}(p_2, m_\ell) \left(F_1^{(\ell)}(q^2) \gamma^\alpha + F_2^{(\ell)}(q^2) \frac{i \sigma^{\alpha\beta} q_\beta}{2 m_\ell} \right) u(p_1, m_\ell), \tag{5.3}$$

where u and $\bar{u}$ are the usual spinors. The decomposition (5.3) directly follows from the Lorentz and $U(1)_{\text{em}}$ gauge symmetries of the theory and is valid beyond perturbation theory. While $F_1^{(\ell)}$ is related to the electric charge, $F_2^{(\ell)}$ is related to the anomalous magnetic moment (AMM) of ℓ as

$$F_2^{(\ell)}(0) = a_\ell = \frac{(g-2)_\ell}{2} \,. \tag{5.4}$$

Table 5.1: Processes and particles (bound states) that are investigated at PSI, where the driving interaction to be studied is indicated by the color as follows: BSM, weak, weak and try to learn about strong, EM, EM and try to learn about strong, strong. In addition the mass or charge radius of particles are measured. The section number refers to the Review of Particle Physics at PSI.

	experiment	section	process / particles / (bound states)
[1]	muon decay	6	$\mu^+ \to e^+ \nu_e \bar{\nu}_\mu$
[2]	MuLan	16	$\mu^+ \to e^+ \nu_e \bar{\nu}_\mu$
[3]	SINDRUM	7	$\mu^+ \to e^+ ee$, $\mu^+ \to e^+ \nu_e \bar{\nu}_\mu ee$, $\pi^+ \to e^+ \nu_e ee$, $\pi^0 \to ee$
[4]	SINDRUM II	8	$\mu^- {}^A_Z N \to e^- {}^A_Z N$ for Au, Pb, Ti
[5]	MEG	19	$\mu^+ \to e^+ \gamma$, $\mu^+ \to e^+ \nu_e \bar{\nu}_\mu \gamma$, $\mu^+ \to e^+ X \to e^+ \gamma\gamma$
[6]	Mu3e	20	$\mu^+ \to e^+ ee$, $\mu^+ \to e^+ \nu_e \bar{\nu}_\mu ee$
[7]	Mspec, Mu-Mass	29	$M = (\mu^+ e^-)$, μ^+
[8]	MACS	9	$M = (\mu^+ e^-) \leftrightarrow \bar{M} = (\mu^- e^+)$
[9]	CREMA	21	$(\mu^- p)$, $(\mu^- d)$, $(\mu^- \text{He})$, p, d, He
[10]	muX	22	$(\mu^- {}^A_Z N)$, ${}^{248}_{96}\text{Cm}$, ${}^{226}_{88}\text{Ra}$
[11]	MUSE	23	$e^\pm p \to e^\pm p$, $\mu^\pm p \to \mu^\pm p$
[12]	MuCap	17	$\mu^- p \to \nu_\mu n$
[13]	MuSun	18	$\mu^- d \to \nu_\mu n n$
[14]	pionic hydrogen	14	$(\pi^- p)$, $(\pi^- d)$
[15]	pionic helium	26	$(\pi^- e^- {}^4\text{He}^{++})$, π^-
[16]	nTRV	15	$n \to p e^- \bar{\nu}_e$
[17]	nEDM	27	n, n
[18]	indirect nEDM	28	n / dark matter / exotic
[19]	negative pions	10	$(\pi^- p)$, π^-
[20]	positive pions	11	$\pi^+ \to \mu^+ \nu_\mu$, π^+, ν_μ
[21]	neutral pions	12	$\pi^- p \to \pi^0 n$, π^0
[22]	PiBeta	24	$\pi^+ \to \pi^0 e^+ \nu_e$, $\pi^+ \to e^+ \nu_e (+\gamma)$, $\mu^+ \to e^+ \nu_e \bar{\nu}_\mu \gamma$
[23]	PEN	25	$\pi^+ \to e^+ \nu_e (+\gamma)$, $\mu^+ \to e^+ \nu_e \bar{\nu}_\mu \gamma$

In contrast to the leptons, quarks do not appear as free particles in nature, but are confined inside hadrons by the strong interaction. The general principles on which the decomposition (5.3) is based, also hold for non-pointlike particles, such as the nucleons $N \in \{p, n\}$

$$\langle N(p_2)|J_{\text{em}}^{\alpha}|N(p_1)\rangle = \bar{u}(p_2, m_N)\left(F_1^{(N)}(Q^2)\gamma^{\alpha} + F_2^{(N)}(Q^2)\frac{i\,\sigma^{\alpha\beta}q_{\beta}}{2\,m_N}\right)u(p_1, m_N), \qquad (5.5)$$

where we have introduced the common definition $Q^2 \equiv -q^2$. A relation between the AMM and $F_2^{(N)}$ analogous to (5.4) still holds. However, this quantity depends on strong dynamics, which at low energies cannot be computed in perturbation theory.

In the case of the nucleons, often the electric and magnetic form factors

$$G_E^{(N)}(Q^2) \equiv F_1^{(N)}(Q^2) - \frac{Q^2}{4m_N^2}F_2^{(N)}(Q^2), \qquad G_M^{(N)}(Q^2) \equiv F_1^{(N)}(Q^2) + F_2^{(N)}(Q^2), \qquad (5.6)$$

are used. In the limit of small Q^2 all form factors $F_i(Q^2)$ can be understood as the Fourier transform of an extended classical 'charge' distribution $\rho_i(r)$ in the Breit frame where $q^{\mu} = (0, \vec{q})$. Upon expansion in small Q^2 we get

$$F_i(Q^2) = \int d^3\vec{r}\, e^{-i\vec{q}\cdot\vec{r}}\,\rho_i(r) = \int d^3\vec{r}\,\rho_i(r) - \frac{1}{6}Q^2\int d^3\vec{r}\, r^2\,\rho_i(r) + \dots \qquad (5.7)$$

This leads to a general expression for the second moment of the charge distribution ρ_i

$$r_i^2 \equiv \frac{1}{N}\int d^3\vec{r}\, r^2\,\rho_i(r) = -6\frac{1}{N}\frac{dF_i(Q^2)}{dQ^2}\bigg|_{Q^2=0}, \qquad N = \begin{cases} 1 & \text{if } F_i(0) = 0, \\ F_i(0) & \text{else.} \end{cases} \qquad (5.8)$$

The relation above is used for example to determine the root-mean-square, $R_i = \sqrt{r_i^2}$, charge and magnetic radii of the proton as well as the axial radius of the nucleon.

If we now consider the weak interactions, we must arrange fermions into left-handed doublets and right-handed singlets. An important role for low-energy processes is played by the charged weak current

$$J_{\text{cc}}^{\alpha} = \sum_{\ell}\bar{\nu}_{\ell}\gamma^{\alpha}P_L\ell + \sum_{ij}V_{ij}\bar{u}_i\gamma^{\alpha}P_L d_j, \qquad (5.9)$$

which couples only to left-handed fermions, $P_L \equiv (1 - \gamma_5)/2$. In the sum over the quark-field terms, the CKM matrix V_{ij} describes the flavor-changing effects of the weak interactions. Including for completeness also the neutral weak current J_{nc}^{α}, the interactions of (5.2) are modified to

$$\mathcal{L}_{\text{EW}}^{\text{int}} = eA_{\alpha}J_{\text{em}}^{\alpha} + \frac{g}{\sqrt{2}}\left(W_{\alpha}^+ J_{\text{cc}}^{\alpha} + \text{h.c.}\right) + g_Z Z_{\alpha}J_{\text{nc}}^{\alpha}, \qquad (5.10)$$

where $g = e/\sin\theta_W$, $g_Z = g/\cos\theta_W$ are the weak $SU(2)_L$ couplings that can be expressed in terms of e and the electroweak mixing (Weinberg) angle θ_W. At the typical energy of processes considered here, much smaller than m_W and m_Z, the W and Z boson masses, we can integrate out the W and Z bosons and adopt an effective field theory (EFT) approach. This results in the Fermi theory of current-current interactions

$$\mathcal{L}_{4F} = -\frac{4G_F}{\sqrt{2}}\left(J_{\text{cc}}^{\alpha}(J_{\text{cc}})_{\alpha}^{\dagger} + J_{\text{nc}}^{\alpha}(J_{\text{nc}})_{\alpha}\right), \qquad (5.11)$$

where $4G_F/\sqrt{2} = g^2/(2m_W^2)$ is the matching (Wilson) coefficient at tree level. Using (5.9) (and the corresponding expression for J_{nc}^{α}) to express $\mathcal{L}_{4F}$ in terms of fermion fields we end

up with vector contact interactions. They correspond to dimension-6 four-fermion vector operators of the generic form

$$\left[O^{V,XY}_{\{\ell/q\}}\right]_{ijkl} = \left(\bar{\psi}_i \gamma^\alpha P_X \psi_j\right)\left(\bar{\psi}_k \gamma_\alpha P_Y \psi_l\right), \tag{5.12}$$

where $X, Y \in \{L, R\}$ and $\{i, j, k, l\}$ are generation indices. The notion 'vector' refers to the Lorentz structure of the bilinears, which in turn is closely related to the nature of the exchange particle that is integrated out. Since the fermion fields ψ_i can be quarks or leptons of any generation, there are in principle quite a lot of different operators. However, only a subset of those are generated by integrating out the W and Z fields. In particular, there are no charged cLFV operators due to an accidental symmetry of the SM.

Because the masses of the top quark and the Higgs boson are of the same order as m_W, these fields can also be integrated out. Operators beyond the four-fermion vector operators appear in the SM with an additional suppression, such as scalar dimension-6 four-fermion operators

$$\left[O^{S,XY}_{\{\ell/q\}}\right]_{ijkl} = \left(\bar{\psi}_i P_X \psi_j\right)\left(\bar{\psi}_k P_Y \psi_l\right), \quad X, Y \in \{L, R\}, \tag{5.13}$$

which are parametrically suppressed by Yukawa couplings [24], or dimension-5 dipole operators (and their Hermitian conjugate)

$$\left[O^{D}_{\{\ell/q\}\gamma}\right]_{ij} = \left(\bar{\psi}_i \sigma_{\alpha\beta} P_R \psi_j\right) F^{\alpha\beta}, \quad \left[O^{D}_{qG}\right]_{ij} = \left(\bar{\psi}_i \sigma_{\alpha\beta} G^{\alpha\beta} P_R \psi_j\right), \tag{5.14}$$

which appear at the loop level. Thus, we arrive at an EFT that consistently describes low-energy processes. It only contains fields with masses much lower than m_W. In particular, the photon and the gluons are the only gauge bosons present. The gauge symmetry of the SM, $SU(3)_c \times SU(2)_L \times U(1)_Y$, is reduced to the gauge symmetry of QCD and QED, $SU(3)_c \times U(1)_{\text{em}}$. The effect of the heavy degrees of freedom of the SM is encoded in the Wilson coefficients that multiply the operators, with G_F in (5.11) being one such example.

5.2.2 Low-energy physics beyond the Standard Model

Many of the experiments listed in Table 5.1 are motivated by the search for new physics. One can think of a plethora of BSM scenarios. They rely on different interaction mechanisms, and can be roughly classified based on the masses of the BSM particles and their coupling strengths.

Light BSM particles should only have a small coupling to SM particles, which would explain their small contribution to physical observables. The most prominent examples are dark photons, axions, or axion-like particles (ALPs). The axion has been proposed as a dynamical solution to the strong CP problem [25–28], i.e., the "naturalness" problem of the small QCD θ parameter. It is introduced as the Nambu-Goldstone boson associated with a spontaneously broken additional global $U(1)_{\text{PQ}}$ symmetry of the SM Lagrangian. The modified SM Lagrangian reads

$$\mathcal{L}^{\text{eff.}}_{\text{SM}} = \mathcal{L}_{\text{SM}} + \mathcal{L}_{\text{int}}[\partial^\mu a_{\text{phys.}}/f_a; \psi] \tag{5.15}$$
$$- \frac{1}{2} \partial^\mu a_{\text{phys.}} \partial_\mu a_{\text{phys.}} - \frac{m_a^2}{2} a^2_{\text{phys.}} + \frac{a_{\text{phys.}}}{f_a} \zeta \frac{g_s^2}{32\pi^2} \tilde{G}_{\alpha\beta} G^{\alpha\beta},$$

where $a_{\text{phys.}} = a - \langle a \rangle$ is the physical axion field with mass m_a, and f_a is the $U(1)_{\text{PQ}}$ symmetry breaking scale. The axion is a pseudoscalar that couples derivatively to any field ψ. In addition, because of the chiral anomaly of the $U(1)_{\text{PQ}}$ current, it directly couples to the gluon density, where ζ is a model-dependent parameter. The minimum of the effective potential occurs at the axion vacuum expectation value $\langle a \rangle = -\theta f_a/\zeta$, which leads to a cancellation

of the CP violating QCD θ term and dynamically solves the strong CP problem. The defining characteristic of the axion, distinguishing it from an ALP, is $m_a f_a \sim m_\pi f_\pi$. This follows from mixing of the axion with the light π and η mesons.

In the following, we will be mainly concerned with heavy BSM particles. In Section 5.2.1, we described how the W and Z bosons can be integrated out in an EFT approach. Similarly, whatever BSM physics there is, as long as it respects QED and QCD gauge symmetry and involves degrees of freedom with a 'large' mass scale Λ, it can be integrated out and its effects will be encoded in Wilson coefficients of gauge-invariant higher-dimensional operators. Operators that were absent in the SM case might now be generated. Thus, we are led to write down the most general relativistic Lagrangian that respects electromagnetic $U(1)_{\mathrm{em}}$ and strong $SU(3)_c$ gauge invariance and obtain a general low-energy effective field theory (LEFT)

$$\mathcal{L}_{\mathrm{LEFT}} = \mathcal{L}_{\mathrm{QED+QCD}} + \frac{1}{\Lambda} \sum_i C_i^{(5)} O_i^{(5)} + \frac{1}{\Lambda^2} \sum_j C_j^{(6)} O_j^{(6)} + \dots \qquad (5.16)$$

Here Λ is the scale of physics that is not dynamically described by the degrees of freedom present in $\mathcal{L}_{\mathrm{LEFT}}$. If we include all charged leptons and all quarks apart from the top in $\mathcal{L}_{\mathrm{LEFT}}$, the scale Λ is assumed to be larger than the mass of the b quark but not larger than the electroweak scale m_W. The sums i and j run over all possible operators of dimension 5 and 6, respectively. Typically, operators of dimension larger than 6 are neglected. $O^{(5)}$ and $O^{(6)}$ denote the operators, $C^{(5)}$ and $C^{(6)}$ are the corresponding Wilson coefficients. Operators that are related through Fierz identities or those that can be eliminated through equations of motion are not included. Naturally, the choice of the operator basis is not unique, but a complete basis up to dimension 6 can be found in [24].

The Lagrangian (5.16) provides a consistent quantum-field theoretical framework to relate low-energy measurements to the determination of parameters of the SM and constraints on BSM physics. Many different routes have been taken to generically parametrize low-energy observables and measuring or constraining the associated parameters. The prime example is the Michel decay, where an analysis with initially a single parameter [29] was generalized and written in terms of parameters related to scalar, vector and tensor contact interactions[1] [30]. A similar effort has been made for cLFV decays $\mu \to e\gamma$ and $\mu \to eee$ considering lepton-flavor-violating contact interactions [31].

At first sight this is very similar to constraining the Wilson coefficients of (5.16). Indeed, the bulk of the operators of (5.16) are also scalar, vector and tensor interactions. However, the Wilson coefficients are well-defined couplings of a quantum field theory. In particular, typically they run and mix under renormalization-group evolution (RGE). If a low-energy observable is expressed in terms of Wilson coefficients, they are understood to be evaluated at the low scale, $C_i^{(n)}(m_\mu)$. On the other hand, to relate the Wilson coefficients of the EFT to a BSM model, the heavy degrees of freedom of the latter have to be integrated out. This yields the Wilson coefficients at the high scale, $C_i^{(n)}(\Lambda)$. Including RGE of $C_i^{(n)}(\Lambda)$ to $C_i^{(n)}(m_\mu)$ is not in the first instance about increasing precision, but to include qualitatively new effects through mixing. This has a profound impact on using low-energy measurements to constrain BSM models.

Of course, it is also possible that BSM physics appears only at a scale much larger than m_W. If this is the case, in a first step another effective theory has to be used, the SM effective field theory (SMEFT). This is a theory similar to (5.16), but with all fields and symmetries of the SM. It contains all operators $\mathcal{O}_i^{(n)}$ expressed in terms of the SM gauge fields, the Higgs doublet, as well as left-handed doublet and right-handed singlet fermion fields that respect

---

[1] Section 6: Muon decay [1].

the SM gauge symmetry $SU(3)_c \times SU(2)_L \times U(1)_Y$,

$$\mathcal{L}_{\text{SMEFT}} = \mathcal{L}_{\text{SM}} + \frac{1}{\Lambda}\big(\mathcal{C}^{(5)}\mathcal{O}^{(5)} + \text{h.c.}\big) + \frac{1}{\Lambda^2}\sum_j \mathcal{C}_j^{(6)}\mathcal{O}_j^{(6)} + \dots \tag{5.17}$$

SMEFT has only one dimension-5 operator $\mathcal{O}^{(5)}$ (and its Hermitian conjugate). This is the Weinberg operator [32] that is associated with neutrino masses. At dimension 6 there are numerous operators, some of which violate baryon number. As for $\mathcal{L}_{\text{LEFT}}$ different bases are possible, but the so-called Warsaw basis [33] is used frequently.

In the case $\Lambda \gg m_W$ the input of the BSM model is given through Wilson coefficients $\mathcal{C}_i^{(n)}(\Lambda)$. Then, the RGE is used to obtain $\mathcal{C}_i^{(n)}(m_W)$. In a next step, SMEFT is matched to LEFT at the electroweak scale. This means that $C_i^{(n)}(m_W)$ are expressed in terms of $\mathcal{C}_i^{(n)}(m_W)$. Finally, the Wilson coefficients of LEFT, $C_i^{(n)}(m_W)$, are run with the RGE of LEFT from the scale m_W to the low scale m_μ, and we are ready to express physical low-energy observables. The complete dimension-6 RGEs of SMEFT and LEFT, and the matching equations between the two EFTs are known at one loop [34–38], whereas beyond only partial results are known.

Now that we have a framework that incorporates the effects of the full SM and potential BSM physics on low-energy observables, we can return to our starting point, the matrix elements of the electromagnetic currents. Moving from (5.1) to (5.16) leads to a generalization of (5.2), (5.3), and (5.5). In particular, the current itself is modified and includes additional terms from the dimension-5 dipole operators. The most general expression for a vector current depending on p_1 and p_2 can be written as combination of six possible structures: γ^α, $\gamma^\alpha\gamma_5$, q^α, $q^\alpha\gamma_5$, $q_\beta\sigma^{\alpha\beta}$ and $q_\beta\sigma^{\alpha\beta}\gamma_5$. Replacing $q = p_2 - p_1$ by $p_2 + p_1$ does not lead to new independent structures, as can be shown by using the Dirac equation. Since the electromagnetic current is conserved $\partial_\alpha J_{\text{em}}^\alpha = 0$ only four terms remain and we get

$$\langle f(p_2)|J_{\text{em}}^\alpha|f(p_1)\rangle = \bar{u}(p_2,m_f)\Big(F_1^{(f)}(q^2)\gamma^\alpha + \big(F_2^{(f)}(q^2) - i\gamma_5 F_3^{(f)}(q^2)\big)\frac{i\,\sigma^{\alpha\beta}q_\beta}{2\,m_f} \tag{5.18}$$

$$+ F_4^{(f)}(q^2)\frac{1}{m_f^2}\big(q^2\gamma^\alpha - 2m_f q^\alpha\big)\gamma_5\Big)u(p_1,m_f).$$

The CP-violating form factor F_3 is associated with the EDM of the lepton d_f through

$$d_f = \frac{eF_3^{(f)}(0)}{2m_f}. \tag{5.19}$$

In the SM, d_f starts to receive contributions at three loops for quarks [39] and at four loops for leptons [40], induced by the CP violation in the CKM matrix. For protons and neutrons there is an additional source for an EDM [41] through the CP-violating θ term in QCD

$$\mathcal{L}_{\text{QCD}} \supset \frac{g_s^2\theta}{32\pi^2}\tilde{G}_{\alpha\beta}G^{\alpha\beta}, \tag{5.20}$$

which we have neglected in (5.1). This term has to be included as it respects $SU(3)_c$ gauge invariance. Even though it can be written as a total derivative and, so does not affect the classical equations of motion, the θ term does have effects at the quantum level. Thus strong interactions seem to violate CP. However, due to experimental constraints on the neutron EDM, we know that the θ parameter is extremely small, see Section 5.6. The lack of an explanation for this smallness is referred to as the strong CP problem. In generic BSM models, one usually expects much larger CP-violating effects [42,43]. The parity-violating anapole form factor F_4 is

also induced due to weak interactions of the SM, or potentially through BSM effects. However, it is not an observable by itself [44].

As mentioned above, matrix elements of the weak charged current J_{cc}^{α} also play an important role. It gives rise to non-vanishing matrix elements between different particles of left-handed $SU(2)$ doublets, such as (ν_{ℓ}, ℓ) or (p, n). The former leads to muon decay, whereas the latter for example to beta decay, or quasi-elastic scattering $\ell\, p \to \nu_{\ell}\, n$. In this case, all six structures appear and setting $m_p = m_n \equiv m_N$ we have

$$\langle p(p_2)|J_{\text{cc}}^{\alpha}|n(p_1)\rangle = \bar{u}(p_2, m_N)\left(F_1^{(pn)}(q^2)\gamma^{\alpha} + F_2^{(pn)}(q^2)\frac{i\,\sigma^{\alpha\beta}q_{\beta}}{2\,m_N} + F_A^{(pn)}(q^2)\gamma^{\alpha}\gamma_5 \right. \tag{5.21}$$

$$\left. + F_P^{(pn)}(q^2)\frac{q^{\alpha}\gamma_5}{2\,m_N} + F_S^{(pn)}(q^2)\frac{q^{\alpha}}{m_N} + F_T^{(pn)}(q^2)\frac{i\,\sigma^{\alpha\beta}q_{\beta}\gamma_5}{2\,m_N} \right) u(p_1, m_N)\,.$$

The scalar and tensor form factors F_S and F_T are referred to as second-class currents and often are omitted. However, we will return to them in Section 5.6 in connection with the nucleon β^- decay, see (5.48), which can be related to $F_{S,T}^{(pn)}$ and $F_{S,T}^{(\nu_e e^-)}$. The axial-vector and the pseudoscalar form factors, $F_A^{(pn)}$, and $F_P^{(pn)}$ are related to often used couplings as

$$g_A \equiv F_A^{(pn)}(0), \qquad \bar{g}_A \equiv F_A^{(pn)}(q_0^2), \qquad \bar{g}_P \equiv \frac{m_{\mu}}{m_N}F_P^{(pn)}(q_0^2), \tag{5.22}$$

where $q_0^2 = -0.88\, m_{\mu}^2$ is the momentum transfer of μ^- capture on the proton, neglecting binding energies.

5.2.3 Hadronic effects

Not only the Wilson coefficients of the EFTs are subject to RGEs and thus scale dependent, but also the gauge couplings $\alpha = e^2/(4\pi)$ and $\alpha_s = g_s^2/(4\pi)$ in (5.1). Both depend on the energy of the phenomenon they are used to describe, but while $\alpha(Q^2)$ decreases towards $\alpha(0) \sim 1/137$, the strong coupling $\alpha_s(Q^2)$ increases as we go to lower energies. For energy scales below a couple of GeV, a perturbative expansion in α_s no longer works — the relevant degrees of freedom related to the strong interactions at low energies are not quarks and gluons, but light hadrons. Once more, EFTs come to the rescue, in this case chiral perturbation theory (χPT) [45–47]. As for all EFTs, the first step is to identify the relevant degrees of freedom in the energy range of interest. The second is to write down the most general Lagrangian for these degrees of freedom that is compatible with the symmetries of the underlying theory. For the strong interactions the answer to the first question is related to the phenomenon of spontaneous chiral symmetry breaking, which generates Goldstone bosons, the only massless particles of strong interactions. Actually in the spectrum of QCD there are no massless particles, but a triplet of very light pseudoscalars, the pions $\vec{\pi} = (\pi^+, \pi^0, \pi^-)$. The fact that they are not exactly massless is well understood and due to the presence of an explicit, but small, chiral symmetry breaking term in the QCD Lagrangian: the quark mass term. In the limit of zero up and down quark masses, i.e., $m_d = m_u = 0$, the three pions become massless, and since there are no other mechanisms to generate massless particles in QCD in the chiral limit, these are the only relevant degrees of freedom at low energy.

The rules to write down an effective Lagrangian for Goldstone bosons are well known. Goldstone bosons transform nonlinearly under the symmetry of the underlying theory, which leads to a non-renormalizable Lagrangian containing only derivative couplings. Symmetry constrains their interaction to become weaker as one lowers the energy. How to include an explicit symmetry breaking is also well known. The symmetry breaking parameters are promoted to spurions, fields with given transformation laws, and the effective Lagrangian must

include these fields too and still satisfy the requirement of being invariant under symmetry transformations. In the case of QCD, in addition to derivative couplings, it is also possible to have couplings proportional to the quark masses $m_{u,d}$. Clearly, there are infinitely many such terms and the Lagrangian only becomes useful with an organizing principle. Since this is a low-energy EFT, we count powers of energy or momenta as small, and since it is relativistic, they come in even powers. The smallest possible number is two, then four, six and so on. Quark masses (or explicit symmetry breaking in general) also count as small, but there is no unique choice concerning the relative importance of powers of quark masses and derivatives. The standard one is $m \sim p^2$. According to this choice the lowest-order Lagrangian contains all possible terms with two powers of derivatives or one power of quark masses and it turns out that there are only two:

$$\mathcal{L}_{\chi\text{PT}} = \mathcal{L}_2 + \mathcal{L}_4 + \mathcal{L}_6 + \dots, \quad \mathcal{L}_2 = \frac{F^2}{4} \langle u_\mu u^\mu + \chi_+ \rangle, \tag{5.23}$$

where $u_\mu = iu^\dagger \partial_\mu U u^\dagger$, $\chi_+ = u^\dagger \chi u^\dagger + u \chi^\dagger u$, and

$$U = uu = \exp(i\phi/F), \quad \phi = \pi^a \tau_a, \quad \chi = 2B \operatorname{diag}(m_u, m_d), \tag{5.24}$$

with π^a the triplet of pion fields and τ_a the Pauli matrices. The low-energy constant (LEC) F is related to the pion decay constant

$$\langle 0|(J_A^a)_\mu(0)|\pi^b(p)\rangle = i\delta^{ab} F_\pi p_\mu, \quad F_\pi = F\left(1 + \mathcal{O}(m_q)\right), \tag{5.25}$$

with $(J_A^a)_\mu$ the isospin-triplet axial current. The second LEC B is defined through the quark condensate in the chiral limit,

$$B = -\frac{\langle 0|\bar{u}u|0\rangle}{F^2} = -\frac{\langle 0|\bar{d}d|0\rangle}{F^2}, \tag{5.26}$$

and also relates the pion mass to the quark mass according to the Gell-Mann–Oakes–Renner relation [48]

$$m_\pi^2 = 2B\hat{m}\left(1 + \mathcal{O}(m_q)\right), \tag{5.27}$$

with $\hat{m} = (m_u + m_d)/2$. Calculating tree-level diagrams with $\mathcal{L}_2$ gives a leading-order (LO) result. Going to next-to-leading order (NLO) requires calculating one-loop diagrams with vertices only from $\mathcal{L}_2$ and tree-level diagrams with one vertex from $\mathcal{L}_4$ [32,46]. At next-to-next-to leading order (NNLO) two-loop diagrams with vertices only from $\mathcal{L}_2$, one-loop diagrams with one vertex from $\mathcal{L}_4$ and tree-level diagrams with two vertices from $\mathcal{L}_4$ or one from $\mathcal{L}_6$ contribute [49–51], and so on.

The limit of validity of this EFT is given by the scale of chiral symmetry breaking. In the expansion in powers of momenta and quark masses that is generated by the effective Lagrangian above, the relevant scale is represented by $\Lambda_\chi = 4\pi F_\pi \sim 1.2$ GeV. Physically it represents the scale at which degrees of freedom other than Goldstone bosons get excited, such as the ρ, whose mass $m_\rho \sim 0.77$ GeV is indeed close to Λ_χ.

The same approach also works for other particles beyond the pions. In the limit $m_s \to 0$ also the kaons and the eta become Goldstone bosons and can be included in the formalism above [52]. The field ϕ becomes a 3×3 matrix containing the octet of Goldstone bosons $\phi = \phi^a \lambda_a$, and χ has to be trivially extended to a diagonal 3×3 quark-mass matrix.

A less trivial extension concerns the baryon sector [53–56]. At first sight this would seem impossible, since the mass of the nucleons is close to Λ_χ. But the baryon number n_B is conserved in strong interactions and one can split the spectrum in separated sectors, labeled by

n_B. Quantities like the nucleon masses, their form factors, or their scattering amplitude with a pion (or any other Goldstone boson(s)) all belong to the sector $n_B = 1$ and can also be studied with the help of the chiral expansion. In this case this represents an expansion in powers of momenta and quark masses around the ground-state energy, which in this sector is equal to the mass of the nucleon m_N, rather than zero.

From the point of view of their transformation properties, nucleons are spin-1/2 as well as isospin-1/2 particles, and transform linearly under chiral transformations. In particular the fact that they are spin-1/2 particles has an important consequence as the expansion of the Lagrangian in powers of momenta (derivatives) contains both even and odd powers

$$\mathcal{L}_N = \mathcal{L}_1 + \mathcal{L}_2 + \mathcal{L}_3 + \dots \tag{5.28}$$

The leading-order Lagrangian looks as follows

$$\mathcal{L}_1 = \bar{N}(i\slashed{D} - m)N + \frac{1}{2}g_A \bar{N}\slashed{u}\gamma_5 N, \tag{5.29}$$

with the covariant derivative defined as

$$D_\mu = \partial_\mu + \Gamma_\mu, \quad \Gamma_\mu = \frac{1}{2}[u^\dagger, \partial_\mu u], \tag{5.30}$$

and $\bar{N} = (\bar{p}, \bar{n})$ the isospin doublet containing the Dirac spinors of the proton and neutron. The parameters m and g_A represent the mass and the axial coupling of the nucleon in the chiral limit, respectively. Note that the chiral symmetry imposes the presence of the pion field both in the covariant derivative as well as in the coupling to the nucleon axial current. From this follows the famous Golberger-Treiman relation [57]

$$g_{\pi N} = \frac{g_A m_N}{F_\pi}, \tag{5.31}$$

between the pion-nucleon coupling constant $g_{\pi N}$ (whose square is the residue of the nucleon pole in the πN scattering amplitude), the physical nucleon mass, and the axial coupling.

The low-energy description of the strong-interaction effects in terms of χPT cannot only be formulated for pure QCD as the underlying theory. While QED effects can be included in terms of explicit low-energy degrees of freedom, the chiral realization of higher-dimensional operators again is based on the external-field and spurion technique. Traditionally, this has been done to include weak-interaction effects and it can be generalized to include BSM effects encoded in the LEFT Lagrangian (5.16).

5.3 The muon

The muon is a fundamental lepton similar to the electron, however with a much larger mass, $m_\mu \simeq 105.66\,\text{MeV}$. It is unstable and predominantly decays through the Michel process

$$\mu \to e\,\nu\,\bar{\nu}, \tag{5.32}$$

which leads[2] to a lifetime of about $\tau_\mu \simeq 2.2\,\mu\text{s}$. As discussed in the context of (5.21) the decay is mediated by the charged current J_{cc}^α, leading to a non-vanishing current-current interaction $\langle \nu_\mu | J_{cc}^\alpha | \mu \rangle \langle e | (J_{cc})_\alpha^\dagger | \nu_e \rangle$. From an EFT point of view this corresponds to a four-fermion operator $(\bar{\nu}_\mu \gamma^\alpha P_L \mu)(\bar{e}\gamma_\alpha P_L \nu_e)$ and its Hermitian conjugate. For computational reasons it is more

---

[2] Section 16: MuLan [2].

convenient to work with the Fierz transform of this operator. This results in the Fermi theory, an EFT defined through the Lagrangian

$$\mathcal{L}_{\text{Fermi}} = -\frac{4\,G_F}{\sqrt{2}}\left(\bar{\nu}_\mu\gamma_\alpha P_L\,\nu_e\right)\left(\bar{e}\gamma^\alpha P_L\mu\right) + \text{h.c.} + \mathcal{L}_{\text{QED+QCD}}\,, \tag{5.33}$$

where it is implicitly assumed that only light quarks are included in $\mathcal{L}_{\text{QCD}}$. The first term on the r.h.s. of (5.33) corresponds to the operator $[O^{V,LL}_{\nu\ell}]_{2112}$ as introduced in (5.12). Its Wilson coefficient, $4\,G_F/\sqrt{2}$, has the special property that it does not get renormalized [58]. Thus, the Lagrangian (5.33) can be used to consistently compute at leading order in G_F but to all orders in the electromagnetic coupling α. Only the usual QED renormalization procedure has to be applied. As an example, the lifetime of the muon can be expressed as

$$\frac{1}{\tau_\mu} \equiv \Gamma_\mu = \Gamma_0\big(1 + \Delta q\big) = \frac{G_F^2 m_\mu^5}{192\,\pi^3}\big(1 + \Delta q\big), \tag{5.34}$$

where Δq contains all corrections to Γ_0 (the tree-level result for massless electrons) that are induced by (5.33). This includes electron-mass effects, higher-order QED corrections, as well as hadronic corrections. While the former two can be computed in perturbation theory, the latter are more delicate. As mentioned above, QCD is non-perturbative at scales typical for muonic processes, $q^2 \sim m_\mu^2$. Thus, the hadronic contributions have to be determined by other means. This is often the leading theoretical uncertainty. The fact that such corrections for muonic processes enter only at NNLO makes the muon a rather clean laboratory for precision physics. Typically, $\mathcal{L}_{\text{QED}}$ contains muon and electron fields, but the inclusion of τ leptons is straightforward, as is the inclusion of heavy quarks in $\mathcal{L}_{\text{QCD}}$.

The corrections Δq are known at NNLO with full electron mass dependence [59–62]. Thus, with a precision measurement of the muon lifetime, the Wilson coefficient in (5.33), or equivalently G_F, can be determined extremely precisely. This, in turn, is an important input for electroweak precision tests. In fact, G_F can be related to m_W and m_Z through

$$\frac{4\,G_F}{\sqrt{2}} = \frac{g^2}{2m_W^2}\big(1 + \Delta r\big) = \frac{2\pi\,\alpha}{\sin^2\theta_W\,m_W^2}\big(1 + \Delta r\big), \tag{5.35}$$

where (in the on-shell scheme) $\sin^2\theta_W = 1 - m_W^2/m_Z^2$. The SM corrections Δr contain (partially hadronic) fermion loop contributions to the charge renormalization. Additional contributions depend also on the top and Higgs mass. This makes G_F a decisive input for SM consistency checks. As mentioned in [2] only the availability of the NNLO result [59] allowed for a full exploitation of the experimental results.

While SM corrections are crucial for the electroweak precision tests the tree-level matching of the SM to the Fermi theory yields the matching condition (5.35) with $\Delta r \to 0$ that is used in (5.33). Furthermore, terms of order q^2/m_W^2 relative to the four-fermion interaction are also neglected in (5.33) and typically in (5.16). In the literature (5.34) is often written with an additional factor $(1 + 3/5\,(m_\mu/m_W)^2)$ which results in a 10^{-6} correction. Within the EFT, such corrections are reproduced by dimension-8 operators, which are missing in (5.33). There are also numerous dimension-6 operators generated by the SM that are not included in (5.33). The corresponding Wilson coefficients are related to the general parametrization of muon decay parameters.[1]

Apart from the Michel decay, two further SM decay processes are of interest; the radiative and rare decays

$$\mu \to e\,\nu\bar{\nu}\gamma\,, \qquad\qquad \mu \to e\,\nu\bar{\nu}e^+e^-\,. \tag{5.36}$$

In order to be well defined and to avoid infrared singularities, the branching ratio for the radiative decay must be defined requiring a minimal energy of the photon. For $E_\gamma > 10$ MeV we have $B(\mu \to e\nu\bar{\nu}\gamma) \sim 1.3 \times 10^{-2}$. For the rare decay the branching ratio is $B(\mu \to e\nu\bar{\nu}ee) \sim 3.6 \times 10^{-5}$. A fully differential NLO description of these processes in the Fermi theory (5.33) is available [63–66]. Depending on the cuts that are applied, the NLO QED corrections can be sizeable. Experimental information on the branching ratio of the radiative decay has been obtained by MEG [67] and PiBeta [68].

A particularly attractive feature of particle physics with muons is the study of cLFV decays. There are three "golden" channels

$$\mu \to e\gamma\,, \qquad\qquad \mu \to eee\,, \qquad\qquad \mu^- {}^A_Z N \to e^- {}^A_Z N\,. \qquad (5.37)$$

PSI has a long tradition in corresponding experimental searches.[3,4,5,6] For the first two processes typically μ^+ are used, whereas μ^- must be used for muon conversion in the field of a nucleus ${}^A_Z N$ with atomic number Z and mass number A. In the SM (with non-vanishing neutrino masses) the branching ratios for these processes are smaller than 10^{-50}, but not zero [69]. Hence, from a theory point of view there is nothing sacred about lepton flavor. As we know that it is not conserved, it is very natural to expect much larger cLFV branching ratios in BSM than in the SM. In fact, generic extensions of the SM do typically lead to large cLFV rates and suppressing them requires additional tuning or model-building efforts.

To extract constraints on BSM physics from limits on the branching ratios of the processes (5.37), they are computed in $\mathcal{L}_{\text{LEFT}}$, typically at tree level. For $\mu \to e\gamma$ the dipole operator $[O^D_{\ell\gamma}]_{21}$ (5.14) enters. Thus we get a limit on the corresponding Wilson coefficient at the low scale $[C^D_{\ell\gamma}]_{21}(m_\mu)$. In a next step, the RGE is used to convert this to limits for the Wilson coefficients at the high scale, $C_i(\Lambda)$. Some scalar four-fermion interactions mix at NLO whereas vector four-fermion interactions enter at NNLO. Nevertheless, this results in very stringent limits on contact interactions induced by BSM physics. They have to be combined with limits from $\mu \to eee$ and muon conversion, where contact interactions already appear at leading order. Using as many operators as possible in connection with RGE maximizes the information that can be obtained from low-energy observables.

These computations can be made [70] for $\mu \to e\gamma$ and $\mu \to eee$ using standard perturbative methods with the Lagrangian (5.16), although for some contributions, non-perturbative effects play a role [71]. However, additional input is required for muon conversion. First, the nuclear matrix elements $\langle {}^A_Z N | J | {}^A_Z N \rangle$ for vector and scalar currents/operators are required. The former can be obtained trivially through current conversion, but the latter need input from lattice QCD or χPT. Second, the overlap integrals of the lepton wave function with the nucleus are required [72]. In principle different target nuclei provide different limits on the various coefficients, but in practice the model discriminating power is limited [73]. A further complication is due to background from the decay in orbit (DIO). This is the Michel decay of the μ^- bound in the nucleus

$$\mu^- {}^A_Z N \to e^- \nu_\mu \bar{\nu}_e {}^A_Z N\,. \qquad (5.38)$$

Due to nuclear recoil effects the energy spectrum of the electron has a tail up to m_μ, the energy of the signal for the electron from muon conversion. Thus DIO has to be studied as a background process [74].

So far the nucleus has acted only as a spectator. The only nuclear physics that was required is the nuclear matrix element. For completeness we mention here two processes relevant to

---

[3] Section 7: SINDRUM [3].
[4] Section 8: SINDRUM II [4].
[5] Section 19: MEG [5].
[6] Section 20: Mu3e [6].

muon conversion, where the nuclear physics is much more involved. When the μ^- is bound to the nucleus, it quickly cascades to the $1S$ ground state. Then it might undergo muon capture

$$\mu^- {}^A_Z N \to \nu_\mu {}^A_{Z-1} N \tag{5.39}$$

before it decays. The corresponding nuclear matrix element $\langle {}^A_{Z-1} N | (J^\alpha_{cc})^\dagger | {}^A_Z N \rangle$ is an extended version of (5.21). It depends on the details of ${}^A_Z N$ and is not easily accessible with theoretical methods. We will return to muon capture in Section 5.4.

The muon can not only form bound states with a nucleus, but also with an electron. Muonium, $M = (\mu^+ e^-)$, is a bound state like hydrogen, but with the proton replaced by a positive muon. As the latter is a pointlike fermion, muonium is an excellent laboratory for QED tests, and for a precise determination of the muon mass.[7] As the muonium mass is dominated by antimatter, M is also an interesting option to study experimentally gravity of antimatter [75]. In addition, muonium-antimuonium oscillations

$$M = (\mu^+ e^-) \leftrightarrow \bar{M} = (\mu^- e^+), \tag{5.40}$$

which are forbidden in the SM, are another channel to scrutinize BSM physics.[8] A bound state of two muons, true muonium $(\mu^+ \mu^-)$, is unfortunately, not experimentally accessible in the foreseeable future.

Two further properties of the muon that are of utmost importance are the AMM (5.4) and EDM (5.19). The motivation to study them in detail is again driven by the desire to test the SM. For the AMM very precise measurements are confronted with similarly precise theoretical predictions [76]. At the time of writing, there is an intriguing tension between SM theory and experiment. For the EDM, the situation is similar to cLFV searches in that the SM value is zero for practical experimental purposes. Hence, experimental verification of a non-vanishing muon EDM is a clear indication of BSM. So far, these quantities have not been measured by PSI experiments. However, future involvement, in particular for the EDM, is being considered [77].

5.4 The proton

Like the electron and muon, the proton is a charged spin $1/2$ fermion. However, because the proton is a bound state, the form factors (5.5) cannot be computed perturbatively simply using $\mathcal{L}_{QED+QCD}$. Most information is obtained from experiment, with additional input from lattice QCD and χPT [78]. From the charge and measurements of the AMM we know $F_1^{(p)}(0) = 1$ and $F_2^{(p)}(0) = \kappa_p \simeq 1.79$.

A quantity that has received a lot of attention in the past years is the proton charge radius $r_E^{(p)}$. As discussed in the context of (5.8), the radius can be extracted as the slope of $G_E^{(p)}(q^2)$ at $q^2 \to 0$. This can be determined by low-q^2 lepton-proton scattering with a careful $q^2 \to 0$ extrapolation. An alternative approach is to use spectroscopy of normal hydrogen or better muonic hydrogen. The overlap of the lepton wave function with the proton charge distribution impacts on the energy levels. Thus, a precise measurement of different transition energies allows the extraction of information on the proton radius. As the Bohr radius is proportional to $1/m_\ell$, the effect in muonic atoms is considerably larger. This has resulted in a very precise new determination of the proton radius[9] and a new world average of $r_E^{(p)} \simeq 0.84$ fm. The disagreement with earlier determinations of $r_E^{(p)}$ was referred to as proton radius puzzle [79, 80], but the puzzle is fading away [81].

---

[7] Section 29: MSpec, Mu-Mass [7].
[8] Section 9: MACS [8].
[9] Section 21: CREMA [9].

The CREMA collaboration[9] has measured two transition frequencies for muonic hydrogen; the triplet $E\left(2P_{3/2}^{F=2}\right) - E\left(2S_{1/2}^{F=1}\right)$ and singlet $E\left(2P_{3/2}^{F=1}\right) - E\left(2S_{1/2}^{F=0}\right)$. From these two values and theoretical input for the fine structure, it is possible to extract the Lamb shift $E_L = E\left(2P_{1/2}\right) - E\left(2S_{1/2}\right)$ and the hyperfine splitting $E_{HFS} = E\left(2S_{1/2}^{F=1}\right) - E\left(2S_{1/2}^{F=0}\right)$. The discrepancy of the proton radius determination from muonic hydrogen with earlier values initiated a flurry of activities to revisit the theoretical calculations of the energy levels, as summarized in [82]. This involves radiative corrections and recoil effects, which can in principle be computed in perturbation theory.

In addition there are proton-structure effects, which are divided into two categories: a) finite-size effects, which depend on the charge ρ_E and magnetic moment distribution ρ_M of the proton, i.e., the charges related to the form factors $G_E^{(p)}$ and $G_M^{(p)}$, introduced in (5.6); b) polarizability effects.

The leading finite-size effect for E_L is in fact proportional to $\left(r_E^{(p)}\right)^2$ and it is precisely this effect that allows an accurate determination of $r_E^{(p)}$ from muonic hydrogen spectroscopy to be made. There are also higher-order effects which have to be included, most notably a contribution from the so-called third Zemach moment

$$\left(r_F^{(p)}\right)^3 \equiv \frac{48}{\pi} \int_0^\infty \frac{dQ}{Q^4}\left(\left[G_E^{(p)}(Q^2)\right]^2 - 1 + \frac{1}{3}\left[r_E^{(p)}\right]^2 Q^2\right), \tag{5.41}$$

where $r_F^{(p)}$ is referred to as Friar radius. This contribution is related to the elastic two-photon exchange (TPE), where elastic refers to the fact that the intermediate hadronic state is still a proton. The inelastic TPE, i.e., TPE where the intermediate hadronic state is more complicated, is often referred to as polarizability correction.

A similar distinction between perturbative and finite-size contributions can be made for the hyperfine splitting E_{HFS}. In this case, the leading finite-size effect is proportional to the Zemach radius $r_Z^{(p)} \simeq 1.0$ fm, a convolution of the charge distribution with the magnetic moment distribution

$$r_Z^{(p)} \equiv \int d^3\vec{r}_1 \int d^3\vec{r}_2\; \rho_E^{(p)}(\vec{r}_1)\rho_M^{(p)}(\vec{r}_2)|\vec{r}_1 - \vec{r}_2|. \tag{5.42}$$

While the determination of the magnetic radius of the proton $r_M^{(p)} \simeq 0.8$ fm was discussed less controversially, there is also quite a spread in the values obtained from different extractions [83]. This spread is typically attributed to different treatment of TPE contributions.

The CREMA collaboration also investigated muonic deuterium and helium[9] and determined the corresponding charge radii. Measuring the charge radii of higher Z nuclei[10] provides crucial input for potential atomic parity violation experiments.

Returning to the proton, as mentioned above, studying lepton-proton scattering at low q^2 is an important source to obtain information on the proton form factors and, hence, the proton radius. At tree level, which implies the one-photon approximation, this process is described by the famous Rosenbluth formula

$$\frac{d\sigma}{d\Omega} = \frac{\alpha^2}{4E_1^2 \sin^4\theta_2}\frac{E_3}{E_1}\left(\frac{\left[G_E^{(p)}(q^2)\right]^2 + \tau\left[G_M^{(p)}(q^2)\right]^2}{1+\tau}\cos^2\theta_2 + 2\tau\left[G_M^{(p)}(q^2)\right]^2 \sin^2\theta_2\right), \tag{5.43}$$

---

[10] Section 22: muX [10].

in terms of $\tau = -q^2/(4m_p^2)$, the scattering angle $\theta = 2\theta_2$, and the energies of the incoming and outgoing leptons, E_1 and E_3, respectively. Using the standard dipole form $G_D(q^2)$ for the form factors gives a good fit to the experimental data:

$$G_E^{(p)}(q^2) \simeq \frac{G_M^{(p)}(q^2)}{1+\kappa_p} \simeq G_D(q^2) = \frac{1}{(1-q^2/\Lambda^2)^2} \qquad \text{with} \quad \Lambda^2 = 0.71\,\text{GeV}^2. \qquad (5.44)$$

For very small q^2 the form factors deviate from (5.44) and — coming back to the proton radius issue — it is a delicate problem to extract the slope of the form factors in the limit $q^2 \to 0$ from scattering data.

Given the importance of lepton-proton scattering, there is a vast literature on the computation of higher-order corrections to (5.43). These corrections can be split into gauge independent and finite subsets by separately considering radiative corrections from the lepton line, radiation from the proton line, and multi-photon exchange between the proton and electron.

A full NLO calculation, superseding earlier ones where various approximations had been used, has been presented in [84] and there are several Monte Carlo generators with these corrections implemented [85, 86]. Corrections at NNLO due to radiation from the electron line have also been computed [87, 88]. Due to the small mass of the lepton, these are the dominant corrections, particularly for electron-proton scattering. As for spectroscopy, from a theoretical point of view, multi-photon exchange contributions between the lepton and proton are the most difficult ones to handle. Accordingly, TPE contributions have received a lot of attention, also including the inelastic parts, see e.g. [89–92].

Traditionally, these experiments have been carried out with electrons. The MUSE collaboration[11] proposes to measure $\ell\,p \to \ell\,p$ with $\ell \in \{e^\pm, \mu^\pm\}$. This offers the opportunity to compare $e\,p$ and $\mu\,p$ scattering within the same experimental setup. In addition, experimental information on TPE can be obtained by measuring the difference between $\ell^+ p$ and $\ell^- p$ scattering.

To the best of our knowledge, the proton is a stable particle and in all processes discussed so far, has been left intact. A low-energy process that affects the proton much more dramatically is muon capture, $\mu^- p \to n\nu_\mu$. This process can be described by the transition matrix element (5.21) as a current-current interaction $\langle \nu_\mu | J_{cc}^\alpha | \mu \rangle \langle n | (J_{cc})_\alpha^\dagger | p \rangle$. In fact, muon capture on the proton as measured by MuCap[12] gives valuable information on the corresponding form factors, in particular $\bar{g}_P$ (5.22) [93]. The inverse process would be related to neutrino-nucleon scattering. Muon capture on the deuterium has been investigated by MuSun.[13]

5.5 Nucleons and nuclei

The proton and neutron together form an isospin doublet. They differ by their isospin projection, $I_3 = +1/2$ and $I_3 = -1/2$, and quark content, uud and udd, respectively. The neutron's Dirac and Pauli form factors are normalized as $F_1^{(n)}(0) = 0$ and $F_2^{(n)}(0) = \kappa_n \simeq -1.91$. The former differs from the proton form factor at zero momentum transfer, $F_1^{(p)}(0) = 1$, due to the vanishing charge of the neutron. Therefore, the electric Sachs form factor of the neutron cannot be approximated with a dipole form factor (5.44). Instead, the Galster form factor could be used as a simple parametrization [94]:

$$G_E^{(n)}(q^2) = \frac{q^2 \kappa_n}{4m_n^2 - \eta q^2} G_D(q^2), \qquad (5.45)$$

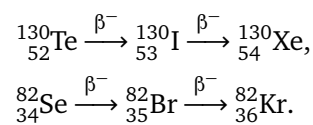[11] Section 23: MUSE [11].
[12] Section 17: MuCap [12].
[13] Section 18: MuSun [13].

with $\eta = 5.6$. Since there are no free neutron targets, one has to rely on scattering off light nuclei (e.g., ^{2}H or ^{3}He) to extract the neutron form factors and polarizabilities. Thereby, few-nucleon EFTs are needed to separate the neutron from proton and nuclear effects.

As highlighted in the previous section, muonic atoms are sensitive to the nuclear structure. The measurement of the muonic-hydrogen Lamb shift by the CREMA collaboration[9] allowed the extraction of the proton root-mean-square charge radius with unprecedented precision. From the measured the Lamb shifts in μD, μ^3He$^+$ and μ^4He$^+$ the deuteron, helion and α-particle charge radii can be extracted. In the future, the ground-state hyperfine splitting of μ^3He$^+$ shall be measured to extract the helion Zemach radius. To extract the different nuclear radii, precise theory predictions for the energy levels in muonic atoms are needed, see theory summaries in [95–97]. Among other contributions, one needs the finite-size effects, through which the different radii enter, and the polarizability effects. For the light muonic atoms, not only the proton polarizability enters, but also the polarizabilities of the neutron and the nucleus as a whole. Similar complications arise when going from pionic hydrogen to pionic deuterium[14] or helium.[15] The nuclear polarizabilities are typically several orders of magnitude larger than the nucleon polarizabilities, and thus, more important. Take for instance the electric dipole polarizability, $\alpha_{E1}^{(n)} = 11.8(1.1) \times 10^{-4}$ fm^3 [98] and $\alpha_{E1}^{(d)} = 0.6314(19)$ fm^3 [99], which describes the deformation of a composite particle in an external electric field and gives a dominant contribution to the two-photon exchange. The nuclear polarizability effects can be calculated in a dispersion relations framework [100, 101] or based on nuclear potentials. For the latter, one distinguishes calculations with phenomenological models [102] fit to nucleon-nucleon scattering data, such as the AV18 potential [103], or with nucleon-nucleon interactions derived from chiral EFT [104–107]. The nucleon-structure contributions are often deduced by rescaling the proton-structure contributions to μH. Take, for example, the nucleon-polarizability contribution

$$\delta_{\mathrm{pol}}^{\mathrm{N}}(\mu\mathrm{A}) = (\mathrm{N} + \mathrm{Z})\left[\mathrm{Z}m_r(\mu\mathrm{A})/m_r(\mu\mathrm{H})\right]^3 \delta_{\mathrm{pol}}^{\mathrm{N}}(\mu\mathrm{H}), \tag{5.46}$$

where m_r is the reduced mass of the muonic atom and Z, N, A are the numbers of protons, neutrons and nucleons in the nucleus.

Also in the field of muonic atoms, the muX project[10] determines nuclear charge radii of radioactive elements and rare isotopes, e.g, ^{248}Cm and ^{226}Ra, through muonic X-ray measurements. These are needed as input for atomic parity violation experiments. In addition, muX probes nuclei that are at the end of a double β decay chain. These are interesting in view of possible neutrinoless double β decay that could occur if neutrinos were Majorana particles. Two examples are the following $\beta^-\beta^-$ decays:

$$^{130}_{52}\mathrm{Te} \xrightarrow{\beta^-} {}^{130}_{53}\mathrm{I} \xrightarrow{\beta^-} {}^{130}_{54}\mathrm{Xe},$$

$$^{82}_{34}\mathrm{Se} \xrightarrow{\beta^-} {}^{82}_{35}\mathrm{Br} \xrightarrow{\beta^-} {}^{82}_{36}\mathrm{Kr}.$$

Here one uses muon capture to study excited states of ^{130}Xe and ^{82}Kr. In the future, direct searches for BSM interactions between muons and nuclei might be possible with the muX setup.

To further advance the precision of the few nucleon EFTs mentioned in this section, the MuSun experiment[13] is studying muon-capture on deuterium: $\mu^-d \to nn\nu_\mu$. The aim is to determine the LEC of the axial-vector four-nucleon interaction d [108]

$$\mathcal{L}_{NN} = -2d(N^\dagger S \cdot uN)N^\dagger N, \tag{5.47}$$

---

[14] Section 14: Pionic hydrogen and deuterium [14].
[15] Section 26: Pionic helium [15].

where S^μ is the nucleon covariant spin operator, $N(x)$ is the nucleon field, and u_μ is given below (5.23). Presently, this LEC has only been extracted from $A = 3$ nuclei. The MuSun experiment has the potential for an improved extraction at the 20 % level.

5.6 The free neutron

In the previous section, we discussed nuclei and bound neutrons. In the following, we discuss free neutrons provided by the Swiss Spallation Neutron Source (SINQ) and the PSI Ultra Cold Neutron (UCN) source [109]. As we will see, the neutron experiments at PSI are dedicated to BSM searches, and in particular, to the search for CP violation in the light quark sector.

The neutron is unstable with a lifetime of about 880 s. The long-standing tension between measurements with in-flight and stored neutrons has led to speculations that there could be 'dark' BSM decay channels [110, 111]. Within the SM, the neutron decays into the proton, where the dominant decay channel is the classical β^- decay $n \to pe^-\bar{\nu}_e$, described by the current-current interaction from the Fermi theory, (5.11). Besides the dominant $V-A$ structure of the weak interaction, there could be small admixtures of scalar and tensor couplings. Using the general formulation of Lee and Yang, which is an older version of the parametrization in (5.21), the β^- decay reads [112]

$$\langle pe^-\bar{\nu}_e|n\rangle = \frac{G_F V_{ud}}{\sqrt{2}}\Bigg[\langle p|n\rangle\langle e^-|C_S - C'_S\gamma_5|\nu_e\rangle + \langle p|\gamma_\mu|n\rangle\langle e^-|\gamma^\mu\big(C_V - C'_V\gamma_5\big)|\nu_e\rangle$$
$$+ \tfrac{1}{2}\langle p|\sigma_{\lambda\mu}|n\rangle\langle e^-|\sigma^{\lambda\mu}\big(C_T - C'_T\gamma_5\big)|\nu_e\rangle - \langle p|\gamma_\mu\gamma_5|n\rangle\langle e^-|\gamma^\mu\gamma_5\big(C_A - C'_A\gamma_5\big)|\nu_e\rangle$$
$$+ \langle p|\gamma_5|n\rangle\langle e^-|\gamma_5\big(C_P - C'_P\gamma_5\big)|\nu_e\rangle + \text{h.c.}\Bigg], \tag{5.48}$$

where $C_i^{(\prime)}$ are 10 complex coupling constants. For the SM with conserved vector current, $g_V = 1$, the only non-vanishing couplings are $C_V = C'_V = 1$ and $C_A = C'_A = -g_A$. Parity violation is assured if $C_i \neq 0$ and $C'_i \neq 0$. Time reversal violation (TRV), or CP violation, is found if $\text{Im}(C_i/C_j) \neq 0$ or $\text{Im}(C'_i/C_j) \neq 0$, i.e., if at least one coupling has an imaginary phase relative to the others. The nTRV experiment[16] accessed the scalar and tensor couplings through the measurement of the transverse polarization of electrons from the decay of polarized free neutrons. At the present level of precision, the results are in agreement with the SM, thus, setting constraints on BSM physics. For a review on electroweak SM tests with nuclear β decays see [113].

The observation of a nonzero permanent EDM of the neutron could be interpreted as a signal of CP violating BSM interactions or a measurement of the QCD θ parameter, see (5.20). The current best limit $|d_n| < 1.8 \times 10^{-26}\,e\,\text{cm}$ is from the nEDM experiment[17] at PSI. This limit is still compatible with the CKM-induced SM contributions to d_n, which are negligible as explained below (5.19). The n2EDM experiment will improve the sensitivity to d_n by an order of magnitude and probe BSM physics at the multi-TeV scale [43]. The electric field of these experiments is of the order of $10^6\,\text{V/m}$. This is well below the critical electric field strength, $E_{\text{crit.}} \sim 10^{23}\,\text{V/m}$, that would be able to induce an EDM proportional to the neutron electric dipole polarizability $d_{\text{ind.}} = 4\pi\alpha_{E1}\vec{E}$ [114]. The nEDM spectrometer has also been used in indirect searches for Dark Matter (DM) candidates, e.g., mirror matter or axions and axion-like particles (ALPs).[18]

---

[16] Section 15: nTRV [16].
[17] Section 27: nEDM [17].
[18] Section 28: nEDMX [18].

5.7 The pion

Low-energy pion physics provides access to a large variety of phenomena, ranging from strong non-perturbative dynamics over electroweak precision tests to probes of BSM physics. The pions are stable in pure QCD and as asymptotic QCD states they play a special role in many hadronic processes, where they appear as hadronic final states. Pion interactions can be understood beyond the chiral expansion by employing unitarity and analyticity of transition amplitudes, which provide a means to resum pion-rescattering effects. Most notably, $\pi\pi$ scattering has been accurately described in terms of the Roy equations [115–117], and the resulting precise determination of the scattering phase shifts provides a central input in the analysis of a host of other hadronic processes at low energies.

An important probe of QCD at low energies is provided by the interaction of pions with nucleons. Pionic atoms provide access to S-wave πN scattering lengths [118], because the strong interaction changes the spectrum compared to pure QED, resulting in shifts of the energy levels and in finite widths of the bound state. The most precise measurements of pionic hydrogen and deuterium have been performed at PSI.[14] The S-wave scattering lengths enter as important constraints in a dispersive Roy–Steiner analysis of the πN scattering amplitude [119].

Compared to pure strong dynamics in the isospin limit, both electromagnetic effects and the mass difference between up and down quarks generate small isospin-breaking corrections. The mass difference of charged and neutral pions is understood to arise almost exclusively from electromagnetic effects [46, 120, 121]. This mass difference $m_{\pi^-} - m_{\pi^0}$ has been determined with high precision at PSI[19] starting from $(\pi^- p)$ bound states with subsequent charge-exchange reaction $\pi^- p \to \pi^0 n$. m_{π^-} has also been determined at PSI by measuring the energy spectrum of pionic hydrogen $(\pi^- p)$.[20]

In the presence of electromagnetism, the neutral pion is not a stable particle, and decays predominantly into two photons. The decay results from the anomalous non-conservation of the axial current that couples to the pion. Quark-mass and electromagnetic corrections to the leading Adler–Bell–Jackiw anomaly have been worked out [122, 123]. Further decay modes, such as $\pi^0 \to e^+ e^- \gamma$, $\pi^0 \to 4e$, and $\pi^0 \to e^+ e^-$ involve the transition $\pi^0 \to \gamma^* \gamma^{(*)}$ with one or two virtual photons. The transition form factor for this process has received considerable interest in connection with hadronic contributions to the muon anomalous magnetic moment [76, 124–126].

Charged pions only decay due to the weak interaction. The hadronic part of the decay rate for $\pi^+ \to \ell^+ \nu_\ell$ is governed by the pion decay constant F_π of (5.25), whereas the leptonic part results in a helicity suppression by a factor m_ℓ^2. Hence, the muonic decay mode dominates over the electronic mode and has been used to measure[21] the mass of π^+. Several other decay modes have been measured at PSI by the SINDRUM,[3] PiBeta,[22] and PEN[23] experiments, including the radiative decays $\pi^+ \to \ell^+ \nu_\ell \gamma$ and $\pi^+ \to e^+ \nu_e e^+ e^-$ and pion beta decay[22] $\pi^+ \to \pi^0 e^+ \nu_e$. The theoretical description of the radiative decay $\pi^+ \to \ell^+ \nu_\ell \gamma$ is split into two parts, the so-called inner bremsstrahlung contributions (IB) and the structure-dependent terms (SD). The IB consist of the normal pion decay with additional emission of a photon from the charged external legs. This part depends on F_π. The SD terms require a more involved parametrization of the QCD effects in terms of two form factors. Apart from an axial form factor F_A also a vector form factor F_V contributes [127].

The charged-pion decays probe the weak interaction in the low-energy regime, where an excellent description is provided by Fermi's effective theory of current-current interaction, or

---

[19] Section 12: neutral pions [21].
[20] Section 10: negative pions [19].
[21] Section 11: positive pions [20].
[22] Section 24: PiBeta [22].
[23] Section 25: PEN [23].

more generally the LEFT framework explained in Section 5.2. The relevant operator is

$$\mathcal{L}_{\text{LEFT}} \supset \sum_{i,j,k,l} C^{V,LL}_{\substack{vedu \\ ijkl}} (\bar{\nu}_i \gamma^\alpha P_L \ell_j)(\bar{d}_k \gamma_\alpha P_L u_l) + \text{h.c.}, \tag{5.49}$$

with flavor indices i, j, k, l and the SM tree-level matching at the weak scale given by $C^{V,LL}_{\substack{vedu \\ ijkl}} = -\frac{4G_F}{\sqrt{2}} \delta_{ij} V^\dagger_{kl}$. Therefore, the pion decays probe the CKM matrix element V_{ud}, with a value of $|V_{ud}| = 0.9739(27)$ resulting from the PiBeta measurement of pion beta decay. Although precise, this value is not competitive with determinations from superallowed nuclear beta decays [98], which currently are in some tension with first-row CKM unitarity. With the absence of nuclear structure aspects and with radiative corrections under good theoretical control [128], pion beta decays are theoretically clean but remain experimentally challenging due to the tiny branching ratio $\sim 10^{-8}$.

Additional semileptonic operators in the LEFT Lagrangian with different Dirac structures parametrize deviations from the SM and can be probed by several pion decay modes [129]. E.g., strong constraints on the first-generation tensor-operator coefficient $\text{Re}(C^{T,RR}_{vedu})$ arise from the $\pi^+ \to e^+ \nu_e \gamma$ Dalitz-plot study of the PiBeta experiment.

5.8 Conclusions

Low-energy, high-precision experiments provide essential input to improve our understanding of the fundamental interactions. They complement and extend information obtained from the energy frontier. EFTs are the theoretical tool of choice to describe and interpret their results and indeed they are well suited to describe both the SM and potential deviations therefrom in a model-independent way. In particular it is possible, and crucial, to analyze if potential deviations from the SM in different observables are linked and have a common explanation. There are numerous examples where low-energy constraints rule out apparently attractive new physics scenarios. A broad and vigorous world-wide low-energy experimental program is indispensable to make further progress in testing the SM and searching for physics beyond. Past and future experiments at PSI will continue to play their part in this challenge.

References

[1] W. Fetscher, *Muon decay*, SciPost Phys. Proc. **5**, 006 (2021), doi:10.21468/SciPostPhysProc.5.006.

[2] R. Carey, T. Gorringe and D. Hertzog, *Mulan: a part-per-million measurement of the muon lifetime and determination of the Fermi constant*, SciPost Phys. Proc. **5**, 016 (2021), doi:10.21468/SciPostPhysProc.5.016.

[3] R. Eichler and C. Grab, *The SINDRUM-I experiment*, SciPost Phys. Proc. **5**, 007 (2021), doi:10.21468/SciPostPhysProc.5.007.

[4] A. van der Schaaf, *Sindrum II* , SciPost Phys. Proc. **5**, 008 (2021), doi:10.21468/SciPostPhysProc.5.008.

[5] A. Baldini and T. Mori, *MEG: Muon to electron and gamma*, SciPost Phys. Proc. **5**, 019 (2021), doi:10.21468/SciPostPhysProc.5.019.

[6] F. Wauters, *The Mu3e experiment*, SciPost Phys. Proc. **5**, 020 (2021), doi:10.21468/SciPostPhysProc.5.020.

[7] B. Ohayon, Z. Burkley and P. Crivelli, *Mspec: Muonium spectroscopy*, SciPost Phys. Proc. **5**, 029 (2021), doi:10.21468/SciPostPhysProc.5.029.

[8] L. Willmann and K. Jungmann, *Muonium-antimuonium conversion*, SciPost Phys. Proc. **5**, 009 (2021), doi:10.21468/SciPostPhysProc.5.009.

[9] A. Antognini, F. Kottmann and R. Pohl, *Laser spectroscopy of light muonic atoms and the nuclear charge radii*, SciPost Phys. Proc. **5**, 021 (2021), doi:10.21468/SciPostPhysProc.5.021.

[10] F. Wauters and A. Knecht, *The muX project*, SciPost Phys. Proc. **5**, 020 (2021), doi:10.21468/SciPostPhysProc.5.020.

[11] E. Cline, J. Bernauer, E.J. Downie and R. Gilman, *MUSE: The MUon Scattering Experiment*, SciPost Phys. Proc. **5**, 023 (2021), doi:10.21468/SciPostPhysProc.5.023.

[12] M. Hildebrandt and C. Petitjean, *MuCap: Muon capture on the proton*, SciPost Phys. Proc. **5**, 017 (2021), doi:10.21468/SciPostPhysProc.5.017.

[13] P. Kammel, *MuSun - Muon capture on the deuteron*, SciPost Phys. Proc. **5**, 018 (2021), doi:10.21468/SciPostPhysProc.5.018.

[14] D. Gotta and L. Simons, *Pionic hydrogen and deuterium*, SciPost Phys. Proc. **5**, 014 (2021), doi:10.21468/SciPostPhysProc.5.014.

[15] M. Hori, H. Aghai-Khozani, A. Sótér, A. Dax and D. Barna, *Recent results of laser spectroscopy experiments of pionic helium atoms at PSI*, SciPost Phys. Proc. **5**, 026 (2021), doi:10.21468/SciPostPhysProc.5.026.

[16] K. Bodek and A. Kozela, *Measurement of the transverse polarization of electrons emitted in neutron decay – nTRV experiment*, SciPost Phys. Proc. **5**, 015 (2021), doi:10.21468/SciPostPhysProc.5.015.

[17] G. Pignol and P. Schmidt-Wellenburg, *The search for the neutron electric dipole moment at PSI*, SciPost Phys. Proc. **5**, 027 (2021), doi:10.21468/SciPostPhysProc.5.027.

[18] S. Roccia and G. Zsigmond, *Indirect searches for dark matter with the nEDM spectrometer*, SciPost Phys. Proc. **5**, 028 (2021), doi:10.21468/SciPostPhysProc.5.028.

[19] M. Daum and D. Gotta, *The mass of the π^-*, SciPost Phys. Proc. **5**, 010 (2021), doi:10.21468/SciPostPhysProc.5.010.

[20] M. Daum and P.-R. Kettle, *The mass of the π^+*, SciPost Phys. Proc. **5**, 011 (2021), doi:10.21468/SciPostPhysProc.5.011.

[21] M. Daum and P.-R. Kettle, *The π^0 mass and the first experimental verification of Coulomb de-excitation in pinoic hydrogen*, SciPost Phys. Proc. **5**, 012 (2021), doi:10.21468/SciPostPhysProc.5.012.

[22] D. Počanić, *The pion beta and radiative electronic decays*, SciPost Phys. Proc. **5**, 024 (2021), doi:10.21468/SciPostPhysProc.5.024.

[23] D. Počanić, *Pion electronic decay and lepton universality*, SciPost Phys. Proc. **5**, 025 (2021), doi:10.21468/SciPostPhysProc.5.025.

[24] E. E. Jenkins, A. V. Manohar and P. Stoffer, *Low-energy effective field theory below the electroweak scale: operators and matching*, J. High Energy Phys. **03**, 016 (2018), doi:10.1007/JHEP03(2018)016.

[25] R. D. Peccei and H. R. Quinn, *CP Conservation in the presence of pseudoparticles*, Phys. Rev. Lett. **38**, 1440 (1977), doi:10.1103/PhysRevLett.38.1440.

[26] R. D. Peccei and H. R. Quinn, *Constraints imposed by CP conservation in the presence of pseudoparticles*, Phys. Rev. D **16**, 1791 (1977), doi:10.1103/PhysRevD.16.1791.

[27] F. Wilczek and A. Zee, *Instantons and spin forces between massive quarks*, Phys. Rev. Lett. **40**, 83 (1978), doi:10.1103/PhysRevLett.40.83.

[28] S. Weinberg, *A new light boson?*, Phys. Rev. Lett. **40**, 223 (1978), doi:10.1103/PhysRevLett.40.223.

[29] L. Michel, *Interaction between four half-spin particles and the decay of the μ-meson*, Proc. Phys. Soc. A **63**, 514 (1950), doi:10.1088/0370-1298/63/5/311.

[30] W. Fetscher, H.-J. Gerber and K. F. Johnson, *Muon decay: complete determination of the interaction and comparison with the standard model*, Phys. Lett. B **173**, 102 (1986), doi:10.1016/0370-2693(86)91239-6.

[31] Y. Kuno and Y. Okada, *Muon decay and physics beyond the standard model*, Rev. Mod. Phys. **73**, 151 (2001), doi:10.1103/RevModPhys.73.151.

[32] S. Weinberg, *Baryon- and lepton-nonconserving processes*, Phys. Rev. Lett. **43**, 1566 (1979), doi:10.1103/PhysRevLett.43.1566.

[33] B. Grzadkowski, M. Iskrzyński, M. Misiak and J. Rosiek, *Dimension-six terms in the Standard Model Lagrangian*, J. High Energy Phys. **10**, 085 (2010), doi:10.1007/JHEP10(2010)085.

[34] E. E. Jenkins, A. V. Manohar and M. Trott, *Renormalization group evolution of the standard model dimension six operators. I: formalism and λ dependence*, J. High Energy Phys. **10**, 087 (2013), doi:10.1007/JHEP10(2013)087.

[35] E. E. Jenkins, A. V. Manohar and M. Trott, *Renormalization group evolution of the Standard Model dimension six operators II: Yukawa dependence*, J. High Energy Phys. **01**, 035 (2014), doi:10.1007/JHEP01(2014)035.

[36] R. Alonso, E. E. Jenkins, A. V. Manohar and M. Trott, *Renormalization group evolution of the Standard Model dimension six operators III: gauge coupling dependence and phenomenology*, J. High Energy Phys. **04**, 159 (2014), doi:10.1007/JHEP04(2014)159.

[37] E. E. Jenkins, A. V. Manohar and P. Stoffer, *Low-energy effective field theory below the electroweak scale: anomalous dimensions*, J. High Energy Phys. **01**, 084 (2018), doi:10.1007/JHEP01(2018)084.

[38] W. Dekens and P. Stoffer, *Low-energy effective field theory below the electroweak scale: matching at one loop*, J. High Energy Phys. **10**, 197 (2019), doi:10.1007/JHEP10(2019)197.

[39] A. Czarnecki and B. Krause, *Neutron electric dipole moment in the Standard Model: Complete three-loop calculation of the valence quark contributions*, Phys. Rev. Lett. **78**, 4339 (1997), doi:10.1103/PhysRevLett.78.4339.

[40] M. E. Pospelov and I. B. Khriplovich, *Electric dipole moment of the W boson and the electron in the Kobayashi-Maskawa model*, Sov. J. Nucl. Phys. **53**, 638 (1991).

[41] M. Pospelov and A. Ritz, *Theta-induced electric dipole moment of the neutron via QCD sum rules*, Phys. Rev. Lett. **83**, 2526 (1999), doi:10.1103/PhysRevLett.83.2526.

[42] M. Pospelov and A. Ritz, *Electric dipole moments as probes of new physics*, Ann. Phys. **318**, 119 (2005), doi:10.1016/j.aop.2005.04.002.

[43] J. Engel, M. J. Ramsey-Musolf and U. van Kolck, *Electric dipole moments of nucleons, nuclei, and atoms: The Standard Model and beyond*, Prog. Part. Nucl. Phys. **71**, 21 (2013), doi:10.1016/j.ppnp.2013.03.003.

[44] M. J. Musolf and B. R. Holstein, *Observability of the anapole moment and neutrino charge radius*, Phys. Rev. D **43**, 2956 (1991), doi:10.1103/PhysRevD.43.2956.

[45] S. Weinberg, *Phenomenological Lagrangians*, Phys. A: Stat. Mech. Appl. **96**, 327 (1979), doi:10.1016/0378-4371(79)90223-1.

[46] J. Gasser and H. Leutwyler, *Chiral perturbation theory to one loop*, Ann. Phys. **158**, 142 (1984), doi:10.1016/0003-4916(84)90242-2.

[47] H. Leutwyler, *On the foundations of chiral perturbation theory*, Ann. Phys. **235**, 165 (1994), doi:10.1006/aphy.1994.1094.

[48] M. Gell-Mann, R. J. Oakes and B. Renner, *Behavior of current divergences under $SU_3 \times SU_3$*, Phys. Rev. **175**, 2195 (1968), doi:10.1103/PhysRev.175.2195.

[49] H. W. Fearing and S. Scherer, *Extension of the chiral perturbation theory meson Lagrangian to order p^6*, Phys. Rev. D **53**, 315 (1996), doi:10.1103/PhysRevD.53.315.

[50] J. Bijnens, G. Colangelo and G. Ecker, *Renormalization of chiral perturbation theory to order p^6*, Ann. Phys. **280**, 100 (2000), doi:10.1006/aphy.1999.5982.

[51] J. Bijnens, G. Colangelo and G. Ecker, *The mesonic chiral lagrangean of order p^6*, J. High Energy Phys. **02**, 020 (1999), doi:10.1088/1126-6708/1999/02/020.

[52] J. Gasser and H. Leutwyler, *Chiral perturbation theory: Expansions in the mass of the strange quark*, Nucl. Phys. B **250**, 465 (1985), doi:10.1016/0550-3213(85)90492-4.

[53] J. Gasser, M. E. Sainio and A. Švarc, *Nucleons with chiral loops*, Nucl. Phys. B **307**, 779 (1988), doi:10.1016/0550-3213(88)90108-3.

[54] E. Jenkins and A. V. Manohar, *Baryon chiral perturbation theory using a heavy fermion lagrangian*, Phys. Lett. B **255**, 558 (1991), doi:10.1016/0370-2693(91)90266-S.

[55] V. Bernard, N. Kaiser, J. Kambor and U.-G. Meißner, *Chiral structure of the nucleon*, Nucl. Phys. B **388**, 315 (1992), doi:10.1016/0550-3213(92)90615-I.

[56] T. Becher and H. Leutwyler, *Baryon chiral perturbation theory in manifestly Lorentz invariant form*, Eur. Phys. J. C **9**, 643 (1999), doi:10.1007/PL00021673.

[57] M. L. Goldberger and S. B. Treiman, *Conserved currents in the theory of Fermi interactions*, Phys. Rev. **110**, 1478 (1958), doi:10.1103/PhysRev.110.1478.

[58] S. M. Berman and A. Sirlin, *Some considerations on the radiative corrections to muon and neutron decay*, Ann. Phys. **20**, 20 (1962), doi:10.1016/0003-4916(62)90114-8.

[59] T. van Ritbergen and R. G. Stuart, *Complete 2-loop quantum electrodynamic contributions to the muon lifetime in the Fermi model*, Phys. Rev. Lett. **82**, 488 (1999), doi:10.1103/PhysRevLett.82.488.

[60] C. Anastasiou, K. Melnikov and F. Petriello, *The electron energy spectrum in muon decay through* $\mathcal{O}(\alpha^2)$, J. High Energy Phys. **09**, 014 (2007), doi:10.1088/1126-6708/2007/09/014.

[61] A. Pak and A. Czarnecki, *Mass effects in muon and semileptonic* $b \to c$ *decays*, Phys. Rev. Lett. **100**, 241807 (2008), doi:10.1103/PhysRevLett.100.241807.

[62] T. Engel, A. Signer and Y. Ulrich, *A subtraction scheme for massive QED*, J. High Energy Phys. **01**, 085 (2020), doi:10.1007/JHEP01(2020)085.

[63] M. Fael, L. Mercolli and M. Passera, *Radiative* μ *and* τ *leptonic decays at NLO*, J. High Energy Phys. **07**, 153 (2015), doi:10.1007/JHEP07(2015)153.

[64] G. M. Pruna, A. Signer and Y. Ulrich, *Fully differential NLO predictions for the radiative decay of muons and taus*, Phys. Lett. B **772**, 452 (2017), doi:10.1016/j.physletb.2017.07.008.

[65] G. M. Pruna, A. Signer and Y. Ulrich, *Fully differential NLO predictions for the rare muon decay*, Phys. Lett. B **765**, 280 (2017), doi:10.1016/j.physletb.2016.12.039.

[66] M. Fael and C. Greub, *Next-to-leading order prediction for the decay* $\mu \to e(e^+e^-)\nu\bar{\nu}$, J. High Energy Phys. **01**, 084 (2017), doi:10.1007/JHEP01(2017)084.

[67] A. M. Baldini *et al.*, *Measurement of the radiative decay of polarized muons in the MEG experiment*, Eur. Phys. J. C **76**, 108 (2016), doi:10.1140/epjc/s10052-016-3947-6.

[68] D. Počanić *et al.*, *New results in rare allowed muon and pion decays*, Int. J. Mod. Phys. Conf. Ser. **35**, 1460437 (2014), doi:10.1142/S2010194514604372.

[69] S. T. Petcov, *The Processes* $\mu \to e + \gamma, \mu \to e + \bar{e}, \nu' \to \nu + \gamma$ *in the Weinberg-Salam model with neutrino mixing*, Sov. J. Nucl. Phys. **25**, 340 (1977), [Erratum: Sov. J. Nucl. Phys. **25**, 698 (1977), Erratum: Yad. Fiz. **25**, 1336 (1977)].

[70] A. Crivellin, S. Davidson, G. M. Pruna and A. Signer, *Renormalisation-group improved analysis of* $\mu \to e$ *processes in a systematic effective-field-theory approach*, J. High Energy Phys. **05**, 117 (2017), doi:10.1007/JHEP05(2017)117.

[71] W. Dekens, E. E. Jenkins, A. V. Manohar and P. Stoffer, *Non-perturbative effects in* $\mu \to e\gamma$, J. High Energy Phys. **01**, 088 (2019), doi:10.1007/JHEP01(2019)088.

[72] R. Kitano, M. Koike and Y. Okada, *Detailed calculation of lepton flavor violating muon-electron conversion rate for various nuclei*, Phys. Rev. D **66**, 096002 (2002), doi:10.1103/PhysRevD.76.059902, [Erratum: Phys. Rev. D **76**, 059902 (2007), doi:10.1103/PhysRevD.66.096002].

[73] V. Cirigliano, R. Kitano, Y. Okada and P. Tuzon, *Model discriminating power of* $\mu \to e$ *conversion in nuclei*, Phys. Rev. D **80**, 013002 (2009), doi:10.1103/PhysRevD.80.013002.

[74] A. Czarnecki, M. Dowling, X. Garcia i Tormo, W. J. Marciano and R. Szafron, *Michel decay spectrum for a muon bound to a nucleus*, Phys. Rev. D **90**, 093002 (2014), doi:10.1103/PhysRevD.90.093002.

[75] A. Antognini *et al.*, *Studying antimatter gravity with muonium*, Atoms **6**, 17 (2018), doi:10.3390/atoms6020017.

[76] T. Aoyama *et al.*, *The anomalous magnetic moment of the muon in the Standard Model*, Phys. Rep. **887**, 1 (2020), doi:10.1016/j.physrep.2020.07.006.

[77] K. Kirch and P. Schmidt-Wellenburg, *Search for electric dipole moments*, EPJ Web Conf. **234**, 01007 (2020), doi:10.1051/epjconf/202023401007.

[78] C. F. Perdrisat, V. Punjabi and M. Vanderhaeghen, *Nucleon electromagnetic form factors*, Prog. Part. Nucl. Phys. **59**, 694 (2007), doi:10.1016/j.ppnp.2007.05.001.

[79] R. Pohl, R. Gilman, G. A. Miller and K. Pachucki, *Muonic hydrogen and the proton radius puzzle*, Annu. Rev. Nucl. Part. Sci. **63**, 175 (2013), doi:10.1146/annurev-nucl-102212-170627.

[80] C. E. Carlson, *The proton radius puzzle*, Prog. Part. Nucl. Phys. **82**, 59 (2015), doi:10.1016/j.ppnp.2015.01.002.

[81] H.-W. Hammer and U.-G. Meißner, *The proton radius: from a puzzle to precision*, Sci. Bull. **65**, 257 (2020), doi:10.1016/j.scib.2019.12.012.

[82] A. Antognini, F. Kottmann, F. Biraben, P. Indelicato, F. Nez and R. Pohl, *Theory of the 2S–2P Lamb shift and 2S hyperfine splitting in muonic hydrogen*, Ann. Phys. **331**, 127 (2013), doi:10.1016/j.aop.2012.12.003.

[83] J. M. Alarcón, D. W. Higinbotham and C. Weiss, *Precise determination of the proton magnetic radius from electron scattering data*, Phys. Rev. C **102**, 035203 (2020), doi:10.1103/PhysRevC.102.035203.

[84] L. C. Maximon and J. A. Tjon, *Radiative corrections to electron-proton scattering*, Phys. Rev. C **62**, 054320 (2000), doi:10.1103/physrevc.62.054320.

[85] A. V. Gramolin, V. S. Fadin, A. L. Feldman, R. E. Gerasimov, D. M. Nikolenko, I. A. Rachek and D. K. Toporkov, *A new event generator for the elastic scattering of charged leptons on protons*, J. Phys. G: Nucl. Part. Phys. **41**, 115001 (2014), doi:10.1088/0954-3899/41/11/115001.

[86] I. Akushevich, H. Gao, A. Ilyichev and M. Meziane, *Radiative corrections beyond the ultra relativistic limit in unpolarized ep elastic and Møller scatterings for the PRad Experiment at Jefferson Laboratory*, Eur. Phys. J. A **51**, 1 (2015), doi:10.1140/epja/i2015-15001-8.

[87] R.-D. Bucoveanu and H. Spiesberger, *Second-order leptonic radiative corrections for lepton-proton scattering*, Eur. Phys. J. A **55**, 57 (2019), doi:10.1140/epja/i2019-12727-1.

[88] P. Banerjee, T. Engel, A. Signer and Y. Ulrich, *QED at NNLO with McMule*, SciPost Phys. **9**, 027 (2020), doi:10.21468/SciPostPhys.9.2.027.

[89] C. E. Carlson and M. Vanderhaeghen, *Two-photon physics in hadronic processes*, Annu. Rev. Nucl. Part. Sci. **57**, 171 (2007), doi:10.1146/annurev.nucl.57.090506.123116.

[90] J. Arrington, P. G. Blunden and W. Melnitchouk, *Review of two-photon exchange in electron scattering*, Prog. Part. Nucl. Phys. **66**, 782 (2011), doi:10.1016/j.ppnp.2011.07.003.

[91] A. Afanasev, P. G. Blunden, D. Hasell and B. A. Raue, *Two-photon exchange in elastic electron–proton scattering*, Prog. Part. Nucl. Phys. **95**, 245 (2017), doi:10.1016/j.ppnp.2017.03.004.

[92] O. Tomalak, B. Pasquini and M. Vanderhaeghen, *Two-photon exchange contribution to elastic e^--proton scattering: Full dispersive treatment of πN states and comparison with data*, Phys. Rev. D **96**, 096001 (2017), doi:10.1103/PhysRevD.96.096001.

[93] R. J. Hill, P. Kammel, W. J. Marciano and A. Sirlin, *Nucleon axial radius and muonic hydrogen — a new analysis and review*, Rep. Prog. Phys. **81**, 096301 (2018), doi:10.1088/1361-6633/aac190.

[94] S. Galster, H. Klein, J. Moritz, K. H. Schmidt, D. Wegener and J. Bleckwenn, *Elastic electron-deuteron scattering and the electric neutron form factor at four-momentum transfers $5fm^{-2} < q^2 < 14fm^{-2}$*, Nucl. Phys. B **32**, 221 (1971), doi:10.1016/0550-3213(71)90068-X.

[95] J. J. Krauth, M. Diepold, B. Franke, A. Antognini, F. Kottmann and R. Pohl, *Theory of the n=2 levels in muonic deuterium*, Ann. Phys. **366**, 168 (2016), doi:10.1016/j.aop.2015.12.006.

[96] B. Franke, J. J. Krauth, A. Antognini, M. Diepold, F. Kottmann and R. Pohl, *Theory of the n = 2 levels in muonic helium-3 ions*, Eur. Phys. J. D **71**, 341 (2017), doi:10.1140/epjd/e2017-80296-1.

[97] M. Diepold, B. Franke, J. J. Krauth, A. Antognini, F. Kottmann and R. Pohl, *Theory of the Lamb Shift and fine structure in muonic ^{4}He ions and the muonic ^{3}He–^{4}He Isotope Shift*, Ann. Phys. **396**, 220 (2018), doi:10.1016/j.aop.2018.07.015.

[98] P. A. Zyla *et al.*, *Review of particle physics*, Prog. Theor. Exp. Phys., 083C01 (2020), doi:10.1093/ptep/ptaa104.

[99] D. R. Phillips, G. Rupak and M. J. Savage, *Improving the convergence of NN effective field theory*, Phys. Lett. B **473**, 209 (2000), doi:10.1016/S0370-2693(99)01496-3.

[100] C. E. Carlson, M. Gorchtein and M. Vanderhaeghen, *Nuclear-structure contribution to the Lamb shift in muonic deuterium*, Phys. Rev. A **89**, 022504 (2014), doi:10.1103/PhysRevA.89.022504.

[101] C. E. Carlson, M. Gorchtein and M. Vanderhaeghen, *Two-photon exchange correction to $2S - 2P$ splitting in muonic ^{3}He ions*, Phys. Rev. A **95**, 012506 (2017), doi:10.1103/PhysRevA.95.012506.

[102] K. Pachucki and A. Wienczek, *Nuclear structure effects in light muonic atoms*, Phys. Rev. A **91**, 040503 (2015), doi:10.1103/PhysRevA.91.040503.

[103] R. B. Wiringa, V. G. J. Stoks and R. Schiavilla, *Accurate nucleon-nucleon potential with charge-independence breaking*, Phys. Rev. C **51**, 38 (1995), doi:10.1103/PhysRevC.51.38.

[104] C. Ji, N. Nevo Dinur, S. Bacca and N. Barnea, *Nuclear polarization corrections to the μ^4He^+ Lamb Shift*, Phys. Rev. Lett. **111**, 143402 (2013), doi:10.1103/PhysRevLett.111.143402.

[105] O. J. Hernandez, C. Ji, S. Bacca, N. Nevo Dinur and N. Barnea, *Improved estimates of the nuclear structure corrections in μD*, Phys. Lett. B **736**, 344 (2014), doi:10.1016/j.physletb.2014.07.039.

[106] N. Nevo Dinur, C. Ji, S. Bacca and N. Barnea, *Nuclear structure corrections to the Lamb shift in μ^3He^+ and μ^3H*, Phys. Lett. B **755**, 380 (2016), doi:10.1016/j.physletb.2016.02.023.

[107] C. Ji, S. Bacca, N. Barnea, O. J. Hernandez and N. Nevo Dinur, *Ab initio calculation of nuclear-structure corrections in muonic atoms*, J. Phys. G: Nucl. Part. Phys. **45**, 093002 (2018), doi:10.1088/1361-6471/aad3eb.

[108] S. Pastore, F. Myhrer and K. Kubodera, *An update of muon capture on hydrogen*, Int. J. Mod. Phys. E **23**, 1430010 (2014), doi:10.1142/S0218301314300100.

[109] B. Lauss and B. Blau, *UCN, the ultracold neutron source – neutrons for particle physics*, SciPost Phys. Proc. **5**, 004 (2021), doi:10.21468/SciPostPhysProc.5.004.

[110] B. Fornal and B. Grinstein, *Dark matter interpretation of the neutron decay anomaly*, Phys. Rev. Lett. **120**, 191801 (2018), doi:10.1103/PhysRevLett.120.191801.

[111] A. Czarnecki, W. J. Marciano and A. Sirlin, *Neutron lifetime and axial coupling connection*, Phys. Rev. Lett. **120**, 202002 (2018), doi:10.1103/PhysRevLett.120.202002.

[112] T. D. Lee and C. N. Yang, *Question of parity conservation in weak interactions*, Phys. Rev. **104**, 254 (1956), doi:10.1103/PhysRev.104.254.

[113] N. Severijns, M. Beck and O. Naviliat-Cuncic, *Tests of the standard electroweak model in nuclear beta decay*, Rev. Mod. Phys. **78**, 991 (2006), doi:10.1103/RevModPhys.78.991.

[114] F. Hagelstein, R. Miskimen and V. Pascalutsa, *Nucleon polarizabilities: From Compton scattering to hydrogen atom*, Prog. Part. Nucl. Phys. **88**, 29 (2016), doi:10.1016/j.ppnp.2015.12.001.

[115] B. Ananthanarayan, G. Colangelo, J. Gasser and H. Leutwyler, *Roy equation analysis of $\pi\pi$ scattering*, Phys. Rep. **353**, 207 (2001), doi:10.1016/S0370-1573(01)00009-6.

[116] I. Caprini, G. Colangelo and H. Leutwyler, *Regge analysis of the $\pi\pi$ scattering amplitude*, Eur. Phys. J. C **72**, 1860 (2012), doi:10.1140/epjc/s10052-012-1860-1.

[117] R. García-Martín, R. Kamiński, J. R. Peláez, J. Ruiz de Elvira and F. J. Ynduráin, *Pion-pion scattering amplitude. IV. Improved analysis with once subtracted Roy-like equations up to 1100 MeV*, Phys. Rev. D **83**, 074004 (2011), doi:10.1103/PhysRevD.83.074004.

[118] J. Gasser, V. E. Lyubovitskij and A. Rusetsky, *Hadronic atoms in QCD+QED*, Phys. Rep. **456**, 167 (2008), doi:10.1016/j.physrep.2007.09.006.

[119] M. Hoferichter, J. Ruiz de Elvira, B. Kubis and U.-G. Meißner, *Roy–Steiner-equation analysis of pion–nucleon scattering*, Phys. Rep. **625**, 1 (2016), doi:10.1016/j.physrep.2016.02.002.

[120] T. Das, G. S. Guralnik, V. S. Mathur, F. E. Low and J. E. Young, *Electromagnetic mass difference of pions*, Phys. Rev. Lett. **18**, 759 (1967), doi:10.1103/PhysRevLett.18.759.

[121] J. F. Donoghue and A. F. Pérez, *Electromagnetic mass differences of pions and kaons*, Phys. Rev. D **55**, 7075 (1997), doi:10.1103/PhysRevD.55.7075.

[122] B. Ananthanarayan and B. Moussallam, *Electromagnetic corrections in the anomaly sector*, J. High Energy Phys. **05**, 052 (2002), doi:10.1088/1126-6708/2002/05/052.

[123] K. Kampf and B. Moussallam, *Chiral expansions of the π^0 lifetime*, Phys. Rev. D **79**, 076005 (2009), doi:10.1103/PhysRevD.79.076005.

[124] P. Masjuan and P. Sanchez-Puertas, *Pseudoscalar-pole contribution to the $(g_\mu - 2)$: A rational approach*, Phys. Rev. D **95**, 054026 (2017), doi:10.1103/PhysRevD.95.054026.

[125] M. Hoferichter, B.-L. Hoid, B. Kubis, S. Leupold and S. P. Schneider, *Dispersion relation for hadronic light-by-light scattering: pion pole*, J. High Energy Phys. **10**, 141 (2018), doi:10.1007/JHEP10(2018)141.

[126] A. Gérardin, H. B. Meyer and A. Nyffeler, *Lattice calculation of the pion transition form factor with $N_f = 2 + 1$ Wilson quarks*, Phys. Rev. D **100**, 034520 (2019), doi:10.1103/PhysRevD.100.034520.

[127] D. A. Bryman, P. Depommier and C. Leroy, $\pi \to e\,\nu$, $\pi \to e\,\nu\gamma$ *decays and related processes*, Phys. Rep. **88**, 151 (1982), doi:10.1016/0370-1573(82)90162-4.

[128] V. Cirigliano, M. Knecht, H. Neufeld and H. Pichl, *The pionic beta decay in chiral perturbation theory*, Eur. Phys. J. C **27**, 255 (2003), doi:10.1140/epjc/s2002-01093-2.

[129] V. Cirigliano, S. Gardner and B. R. Holstein, *Beta decays and non-standard interactions in the LHC era*, Prog. Part. Nucl. Phys. **71**, 93 (2013), doi:10.1016/j.ppnp.2013.03.005.

Muon decay

W. Fetscher[★]

Institute for Physics and Astrophysics, ETH Zürich

★ fetscher@phys.ethz.ch

Abstract

The decay of the muon has been studied at PSI with several precision measurements: The longitudinal polarization $P_\mathrm{L}(E)$ with the muon decay parameters ξ', ξ'', the Time-Reversal Invariance (TRI) conserving transverse polarization $P_{\mathrm{T}_1}(E)$ with the muon decay parameters η, η'', the TRI violating transverse polarization $P_{\mathrm{T}_2}(E)$, with α'/A, β'/A and the muon decay asymmetry with $P_\mu\xi$. The detailed theoretical analysis of all measurements of normal and inverse muon decay has led for the first time to a lower limit $|g_{LL}^V| > 0.960$ ("$V-A$") and upper limits for nine other possible complex couplings, especially the scalar coupling $|g_{LL}^S| < 0.550$ which had not been excluded before.

6.1 Introduction

Muon decay, $\mu^+ \to \overline{\nu}_\mu e^+ \nu_e$, as a purely leptonic process, provides a precise source of information on the charged current weak interaction. Before the advent of the meson factories LAMPF, TRIUMF and SIN, experimental results were scarce and theoretical descriptions inappropriate to uniquely deduce the interaction. In a combined effort, the ETH-SIN group has performed decisive precision measurements and, simultaneously, developed the theoretical description in a way that allowed the determination of the interaction from experimental results, taken exclusively from normal and inverse muon decay ($\nu_\mu + e^- \to \mu^- + \nu_e$).

6.2 General Matrix Element

The three leptonic decays $\mu^+ \to \bar{\nu}_\mu e^+ \nu_e$, $\tau^+ \to \bar{\nu}_\tau \mu^+ \nu_\mu$ and $\tau^+ \to \bar{\nu}_\tau e^+ \nu_e$, as well as their charge conjugate decays, can be described by the most general, local, derivative-free and lepton-number conserving four-fermion contact interaction Hamiltonian. The contact interaction allows the use of equivalent Hamiltonians, which differ in the way the fermions are grouped together [1, 2]. The older literature preferred a "charge retention" form with parity-odd and parity-even terms in which e^+ and μ^+, as the usually detected particles, were grouped

together [3, 4]. This had the advantage that limits to some coupling constants could be obtained from then existing results. The disadvantage was that this Hamiltonian represents interactions proceeding via the exchange of a neutral boson X that would carry the lepton numbers both of muon and electron, and so would not be universal. The use of a "charge-changing" form, where the charged leptons are grouped with their neutrinos and which is adapted to charged boson exchange, results in absolute values of differences of coupling constants. Both of these forms are complicated by the fact that a fully parity-violating interaction, such as e.g. the $V-A$- interaction, is represented by *four* coupling constants C_V, C'_V, C_A and C'_A.

In the following, we will use a charge-changing Hamiltonian characterized by fields of definite chirality [5, 6]. We use the notation of Fetscher *et. al.* [7], which in turn uses the sign conventions and definitions of Scheck [8]. The general matrix element can then be written as

$$M = 4\frac{G_F}{\sqrt{2}} \sum_{\substack{\gamma=S,V,T \\ \varepsilon,\mu=R,L}} g^\gamma_{\varepsilon\mu} \langle \bar{e}_\varepsilon | \Gamma^\gamma | (\nu_e)_n \rangle \langle (\bar{\nu}_\mu)_m | \Gamma_\gamma | \mu_\mu \rangle. \tag{6.1}$$

Here, G_F is the Fermi coupling constant, while $\gamma = S, V, T$ indicates a 4-scalar, 4-vector, or 4-tensor interaction; the corresponding Γ^γ could be either Dirac γ matrices or, when using the Weyl spinors of Eqs. (6.2) to (6.4), Pauli matrices. The indices $\varepsilon, \mu = R, L$ indicate the chirality (right- or left-handed) of the spinors of the electron or muon. The chiralities n and m of the ν_e and $\bar{\nu}_\mu$ are then determined by the values of γ, ε, and μ. In this picture, the coupling constants $g^\gamma_{\varepsilon\mu}$ have a simple physical interpretation: $n_\gamma |g^\gamma_{\varepsilon\mu}|^2$ is equal to the (relative) probability for a μ-handed muon to decay into an ε-handed electron by the interaction Γ^γ; the factors $n_S = 1/4$, $n_V = 1$ and $n_T = 3$ take care of the proper normalisation. The standard model thus corresponds to $g^V_{LL} = 1$, with all other couplings being zero.

We emphasise that here right- and left-handed definitely means chirality and not helicity. The left-handed spinor $\overset{\circ}{\chi}$ of a fermion in its rest system transforms under a Lorentz-boost as

$$\chi_L(\boldsymbol{p}) = \frac{(E+m)\sigma^0 - \boldsymbol{p}\cdot\boldsymbol{\sigma}}{\sqrt{2m(E+m)}} \overset{\circ}{\chi}, \tag{6.2}$$

where σ^0 and $\boldsymbol{\sigma}$ are the four Pauli matrices. By a parity operation, $\chi_L(\boldsymbol{p})$ becomes the right-handed spinor $\chi_R(\boldsymbol{p})$. Left- and right-handed spinors are contained in separate $\mathbb{C}2$-spaces. The right-handed spinor transforms under a Lorentz-boost as

$$\chi_R(\boldsymbol{p}) = \frac{(E+m)\sigma^0 + \boldsymbol{p}\cdot\boldsymbol{\sigma}}{\sqrt{2m(E+m)}} \overset{\circ}{\chi}. \tag{6.3}$$

The spinor of the antiparticle is given by

$$\varphi_L(\boldsymbol{p}) = +i\sigma^2 \chi_R^*(\boldsymbol{p}) \quad \text{and} \quad \varphi_R(\boldsymbol{p}) = -i\sigma^2 \chi_L^*(\boldsymbol{p}). \tag{6.4}$$

6.3 Observables

The differential decay probability to obtain an $e^\pm$ with (reduced) energy between x and $x+dx$, emitted in the direction $\hat{\boldsymbol{x}}_3$ at an angle between ϑ and $\vartheta+d\vartheta$ with respect to the muon polarization vector $\boldsymbol{P}_\mu$, and with its spin parallel to the arbitrary direction $\hat{\boldsymbol{\zeta}}$, neglecting radiative corrections, is given by

$$\frac{d^2\Gamma}{dx\,d\cos\vartheta} = \frac{m_\mu}{4\pi^3} W^4_{e\mu} G^2_F \sqrt{x^2-x^2_0} \cdot \left\{ F_{IS}(x) \pm P_\mu \cos\vartheta F_{AS}(x) \right\} \cdot \left\{ 1 + \hat{\boldsymbol{\zeta}} \cdot \boldsymbol{P}_e(x,\vartheta) \right\}. \tag{6.5}$$
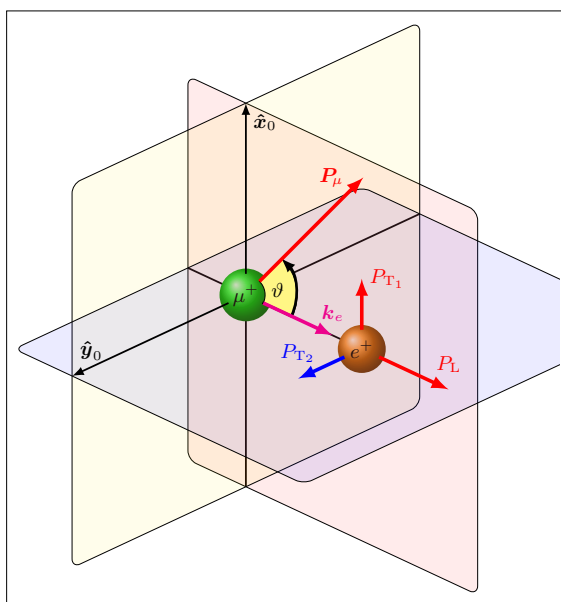
Figure 6.1: Definition of the observables in polarized muon decay: muon polarization $\boldsymbol{P}_\mu$, positron momentum $\boldsymbol{k}_e$, longitudinal positron polarization P_{L}, transverse positron polarization $(P_{\mathrm{T}_1}, P_{\mathrm{T}_2})$ and angle of emission ϑ (relative to $\boldsymbol{P}_\mu$). Time reversal invariance is violated if $P_{\mathrm{T}_2} \neq 0$. From [11].

Here, $W_{e\mu} = \max(E_e) = (m_\mu^2 + m_e^2)/(2m_\mu)$ is the maximum $e^\pm$ energy, $x = E_e/W_{e\mu}$ is the reduced energy, $x_0 = m_e/W_{e\mu} = 9.67 \times 10^{-3}$, and $P_\mu = |\boldsymbol{P}_\mu|$ is the degree of muon polarization. $\hat{\boldsymbol{\zeta}}$ is the direction in which a perfect polarization-sensitive electron detector is most sensitive. The isotropic part of the spectrum, $F_{\mathrm{IS}}(x)$, the anisotropic part $F_{\mathrm{AS}}(x)$, and the electron polarization, $\boldsymbol{P}_e(x, \vartheta)$, may be parameterized by the Michel parameter ρ [1], by η [9], by ξ and δ [3, 10], etc. These are bilinear combinations of the coupling constants $g_{\varepsilon\mu}^\gamma$, which occur in the matrix element (given below).

If the masses of the neutrinos as well as x_0 are neglected, the energy and angular distribution of the electron in the rest frame of a muon ($\mu^\pm$) measured by a polarization insensitive detector is given by

$$\frac{\mathrm{d}^2\Gamma}{\mathrm{d}x\,\mathrm{d}\cos\vartheta} \sim x^2 \cdot \left\{ 3(1-x) + \frac{2\rho}{3}(4x-3) + 3\eta x_0(1-x)/x \right.$$
$$\left. \pm P_\mu \cdot \xi \cdot \cos\vartheta \left[1 - x + \frac{2\delta}{3}(4x-3) \right] \right\}. \tag{6.6}$$

Here, ϑ is the angle between the electron momentum and the muon spin, and $x \equiv 2E_e/m_\mu$. Within the Standard Model, we obtain $\rho = \xi\delta = 3/4$, $\xi = 1$, $\eta = 0$ and the differential decay rate is

$$\frac{\mathrm{d}^2\Gamma}{\mathrm{d}x\,\mathrm{d}\cos\vartheta} = \frac{G_F^2 m_\mu^5}{192\pi^3} \left[3 - 2x \pm P_\mu \cos\vartheta(2x-1) \right] x^2. \tag{6.7}$$

The coefficient in front of the square bracket is the total decay rate.

The observables in the decay of polarized muons are shown in Figure 6.1. We have defined a right-handed coordinate system with

$$\hat{\boldsymbol{z}}_0 = \frac{\boldsymbol{k}_e}{|\boldsymbol{k}_e|}, \quad \hat{\boldsymbol{y}}_0 = \frac{\boldsymbol{k}_e \times \boldsymbol{P}_\mu}{|\boldsymbol{k}_e \times \boldsymbol{P}_\mu|}, \quad \hat{\boldsymbol{x}}_0 = \hat{\boldsymbol{y}}_0 \times \hat{\boldsymbol{z}}_0. \tag{6.8}$$

Here, $\mathbf{k}_e$ is the momentum vector of the electron, while P_{L} designates the longitudinal polarization, P_{T_1} the transverse component of $\mathbf{P}_e$ lying in the plane defined by $\mathbf{k}_e$ and $\mathbf{P}_\mu$, and P_{T_2} is the component perpendicular to that plane. $P_{\mathrm{T}_2} \neq 0$ signals violation of time-reversal symmetry. These polarization components are

$$P_{\mathrm{T}_1}(x,\vartheta) = \frac{P_\mu \sin\vartheta \cdot F_{\mathrm{T}_1}(x)}{F_{\mathrm{IS}}(x) \pm P_\mu \cos\vartheta \cdot F_{\mathrm{AS}}(x)}, \tag{6.9}$$

$$P_{\mathrm{T}_2}(x,\vartheta) = \frac{P_\mu \sin\vartheta \cdot F_{\mathrm{T}_2}(x)}{F_{\mathrm{IS}}(x) \pm P_\mu \cos\vartheta \cdot F_{\mathrm{AS}}(x)}, \tag{6.10}$$

$$P_{\mathrm{L}}(x,\vartheta) = \frac{\pm F_{\mathrm{IP}}(x) + P_\mu \cos\vartheta \cdot F_{\mathrm{AP}}(x)}{F_{\mathrm{IS}}(x) \pm P_\mu \cos\vartheta \cdot F_{\mathrm{AS}}(x)}. \tag{6.11}$$

If only the neutrino masses are neglected, and if the $e^\pm$ polarization is detected, then the functions in (6.5) can be decomposed as [12]

$$F_\nu(x) = F_\nu^{V-A}(x) + G_\nu(x), \tag{6.12}$$

where $G_\nu(x) \equiv 0$ for $g_{LL}^V = 1$ ("$V-A$"). Physics beyond the Standard Model would thus be contained *exclusively* in the $G_\nu(x)$. The index ν stands for IS (isotropic part of the spectrum), AS (anisotropic part of the spectrum), T_1 (transverse polarization P_{T_1}), T_2 (transverse polarization P_{T_2}), IP (isotropic part of the longitudinal polarization) and AP (anisotropic part of the longitudinal polarization). The $F_\nu^{V-A}(x)$ do not depend on specific decay parameters:

$$F_{\mathrm{IS}}^{V-A}(x) = \tfrac{1}{6}\left\{-2x^2 + 3x - x_0^2\right\}, \tag{6.13a}$$

$$F_{\mathrm{AS}}^{V-A}(x) = \tfrac{1}{6}\left(x^2 - x_0^2\right)^{1/2}\left\{2x - 2 + \left(1 - x_0^2\right)^{1/2}\right\}, \tag{6.13b}$$

$$F_{\mathrm{T}_1}^{V-A}(x) = -\tfrac{1}{6}(1-x)x_0, \tag{6.13c}$$

$$F_{\mathrm{T}_2}^{V-A}(x) = 0, \tag{6.13d}$$

$$F_{\mathrm{IP}}^{V-A}(x) = \tfrac{1}{6}\left(x^2 - x_0^2\right)^{1/2}\left\{-2x + 2 + \left(1 - x_0^2\right)^{1/2}\right\}, \tag{6.13e}$$

$$F_{\mathrm{AP}}^{V-A}(x) = \tfrac{1}{6}\left\{2x^2 - x - x_0^2\right\}. \tag{6.13f}$$

The functions $G_\nu(x)$ depend on the decay parameters $\rho, \xi'', \xi', \xi, \delta, \eta, \eta'', \alpha'/A, \beta'/A$, where $\eta = (\alpha - 2\beta)/A$ and $\eta'' = (3\alpha + 2\beta)/A$:

$$G_{\mathrm{IS}}(x) = \tfrac{1}{9}\left\{2\left(\rho - \tfrac{3}{4}\right)\left(4x^2 - 3x - x_0^2\right) + 9\eta(1-x)x_0\right\}, \tag{6.14a}$$

$$\begin{aligned}G_{\mathrm{AS}}(x) = \tfrac{1}{9}\left(x^2 - x_0^2\right)^{1/2}&\left\{3(\xi-1)(1-x),\right.\\&\left.+2\left(\xi\delta - \tfrac{3}{4}\right)\left(4x - 4 + \left(1 - x_0^2\right)^{1/2}\right)\right\},\end{aligned} \tag{6.14b}$$

$$\begin{aligned}G_{\mathrm{T}_1}(x) = \tfrac{1}{12}&\left\{-2\left[(\xi''-1) + 12\left(\rho - \tfrac{3}{4}\right)\right](1-x)x_0\right.\\&\left.-3\eta\left(x^2 - x_0^2\right) + \eta''\left(-3x^2 + 4x - x_0^2\right)\right\},\end{aligned} \tag{6.14c}$$

$$G_{\mathrm{T}_2}(x) = \tfrac{1}{3}\left(x^2 - x_0^2\right)^{1/2}\left\{3\frac{\alpha'}{A}(1-x) + 2\frac{\beta'}{A}\left(1 - x_0^2\right)^{1/2}\right\}, \tag{6.14d}$$

$$\begin{aligned}G_{\mathrm{IP}}(x) = \tfrac{1}{54}\left(x^2 - x_0^2\right)^{1/2}&\left\{9(\xi'-1)\left[-2x + 2 + \left(1 - x_0^2\right)^{1/2}\right]\right.\\&\left.+4\xi\left(\delta - \tfrac{3}{4}\right)\left[4x - 4 + \left(1 - x_0^2\right)^{1/2}\right]\right\},\end{aligned} \tag{6.14e}$$

$$\begin{aligned}G_{\mathrm{AP}}(x) = \tfrac{1}{6}&\left\{(\xi''-1)\left(2a^2 - x - x_0^2\right) + 4\left(\rho - \tfrac{3}{4}\right)\left(4x^2 - 3x - x_0^2\right)\right.\\&\left.+2\eta''(1-x)x_0\right\}.\end{aligned} \tag{6.14f}$$

Several of the decay parameters $\{\rho, \xi, \xi', \xi'', \delta, \eta, \eta'', \alpha/A, \beta/A, \alpha'/A, \beta'/A\}$, which are not all independent, have been measured in the past. Past experiments have also been analyzed using the parameters a, b, c, a', b', c', α/A, β/A, α'/A, β'/A (and $\eta = (\alpha - 2\beta)/2A$), as defined by Kinoshita and Sirlin [3, 10]. They serve as a model-independent summary of all possible measurements on the decay electron (see Listings below). The relations between the two sets of parameters are

$$\rho - \tfrac{3}{4} = \tfrac{3}{4}(-a + 2c)/A, \tag{6.15}$$

$$\eta = (\alpha - 2\beta)/A, \tag{6.16}$$

$$\eta'' = (3\alpha + 2\beta)/A, \tag{6.17}$$

$$\delta - \tfrac{3}{4} = \tfrac{9}{4} \frac{\left(a' - 2c'\right)/A}{1 - \left[a + 3a' + 4(b + b') + 6c - 14c'\right]/A}, \tag{6.18}$$

$$1 - \xi \frac{\delta}{\rho} = 4 \frac{\left[(b + b') + 2\left(c - c'\right)\right]/A}{1 - (a - 2c)/A}, \tag{6.19}$$

$$1 - \xi' = \left[(a + a') + 4(b + b') + 6(c + c')\right]/A, \tag{6.20}$$

$$1 - \xi'' = (-2a + 20c)/A, \tag{6.21}$$

where

$$A = a + 4b + 6c. \tag{6.22}$$

The ten complex amplitudes $g^{\gamma}_{\varepsilon\mu}$ (g^T_{RR} and g^T_{LL} are identically zero) and G_F constitute 20 independent (real) parameters to be determined by experiment. The Standard Model interaction corresponds to one single amplitude g^V_{LL} being unity and all the others being zero.

6.4 Lorentz Structure

The nine parameters $\{\rho, \xi, \xi', \xi'', \delta, \eta, \eta'', \alpha'/A, \beta'/A\}$ describing the electron spectrum, decay asymmetry and polarization vector can be represented [3] by the intermediate quantities $\{a, a', \alpha, \alpha', b, b', \beta, \beta', c, c'\}$, whose values are known from experiment [13]. They are all real, bilinear combinations of the coupling constants:

$$a = 16\left(|g^V_{RL}|^2 + |g^V_{LR}|^2\right) + |g^S_{RL} + 6g^T_{RL}|^2 + |g^S_{LR} + 6g^T_{LR}|^2, \tag{6.23a}$$

$$a' = 16\left(|g^V_{RL}|^2 - |g^V_{LR}|^2\right) + |g^S_{RL} + 6g^T_{RL}|^2 - |g^S_{LR} + 6g^T_{LR}|^2, \tag{6.23b}$$

$$\alpha = 8Re\left\{g^V_{LR}(g^{S*}_{RL} + 6g^{T*}_{RL}) + g^V_{RL}(g^{S*}_{LR} + 6g^{T*}_{LR})\right\}, \tag{6.23c}$$

$$\alpha' = 8Im\left\{g^V_{LR}(g^{S*}_{RL} + 6g^{T*}_{RL}) - g^V_{RL}(g^{S*}_{LR} + 6g^{T*}_{LR})\right\}, \tag{6.23d}$$

$$b = 4\left(|g^V_{RR}|^2 + |g^V_{LL}|^2\right) + |g^S_{RR}|^2 + |g^S_{LL}|^2, \tag{6.23e}$$

$$b' = 4\left(|g^V_{RR}|^2 - |g^V_{LL}|^2\right) + |g^S_{RR}|^2 - |g^S_{LL}|^2, \tag{6.23f}$$

$$\beta = -4Re\{g^V_{RR}g^{S*}_{LL} + g^V_{LL}g^{S*}_{RR}\}, \tag{6.23g}$$

$$\beta' = 4Im\{g^V_{RR}g^{S*}_{LL} - g^V_{LL}g^{S*}_{RR}\}, \tag{6.23h}$$

$$c = \tfrac{1}{2}\{|g^S_{RL} - 2g^T_{RL}|^2 + |g^S_{LR} - 2g^T_{LR}|^2\}, \tag{6.23i}$$

$$c' = \tfrac{1}{2}\{|g^S_{RL} - 2g^T_{RL}|^2 - |g^S_{LR} - 2g^T_{LR}|^2\}. \tag{6.23j}$$

From (6.23a) to (6.23j) it can be seen that these quantities are not completely independent. The transformation from the 20-dimensional space of the complex $g^{\gamma}_{\varepsilon\mu}$ to the 10-dimensional

space of the $\{a,\ldots,c'\}$ leads to the following constraints [14]:

$$a \geq 0 \qquad\qquad a^2 \geq a'^2 + \alpha^2 + \alpha'^2 , \qquad\qquad (6.24)$$

$$b \geq 0 \qquad\qquad b^2 \geq b'^2 + \beta^2 + \beta'^2 , \qquad\qquad (6.25)$$

$$c \geq 0 \qquad\qquad c^2 \geq c'^2 . \qquad\qquad (6.26)$$

These constraints are very important for any general analysis of muon decay, as they strongly influence the final errors of the quantities they relate.

The precise measurement of individual decay parameters alone generally does not give conclusive information about the kind of interaction due to the many different couplings and the interference terms between them. A good example for this is the famous Michel parameter ϱ. A precise measurement yielding the value $3/4$ as predicted by $V-A$ by no means establishes the $V-A$ interaction. In fact any interaction consisting of an arbitrary combination of g_{LL}^S, g_{LR}^S, g_{RL}^S, g_{RR}^S, g_{RR}^V and g_{LL}^V will yield exactly $\varrho = \frac{3}{4}$. This can be seen if we write ϱ in the form [15]

$$\varrho - \tfrac{3}{4} = -\tfrac{3}{4}\{|g_{LR}^V|^2 + |g_{RL}^V|^2 + 2(|g_{LR}^T|^2 + |g_{RL}^T|^2) - Re(g_{LR}^S g_{LR}^{T*} + g_{RL}^S g_{RL}^{T*})\} . \qquad (6.27)$$

For $\varrho = 3/4$ and $g_{LR}^T = g_{RL}^T = 0$ (no tensor interaction) we find $g_{LR}^V = g_{RL}^V = 0$, with all the remaining six couplings being arbitrary!

The magnitude of the interaction is contained in the Fermi coupling constant G_F. Thus the $g_{\mu\nu}^\gamma$ may be normalized, dimensionless coupling constants, resulting in

$$A \equiv a + 4b + 6c = 16 . \qquad\qquad (6.28)$$

This is equivalent to

$$Q_{RR} + Q_{LR} + Q_{RL} + Q_{LL} = 1 , \qquad\qquad (6.29)$$

where

$$Q_{RR} = \tfrac{1}{4}|g_{RR}^S|^2 + |g_{RR}^V|^2 , \qquad\qquad (6.30)$$

$$Q_{RL} = \tfrac{1}{4}|g_{RL}^S|^2 + |g_{RL}^V|^2 + 3|g_{RL}^T|^2 , \qquad\qquad (6.31)$$

$$Q_{LR} = \tfrac{1}{4}|g_{LR}^S|^2 + |g_{LR}^V|^2 + 3|g_{LR}^T|^2 , \qquad\qquad (6.32)$$

$$Q_{LL} = \tfrac{1}{4}|g_{LL}^S|^2 + |g_{LL}^V|^2 . \qquad\qquad (6.33)$$

We note that $0 \leq Q_{\varepsilon\mu} \leq 1$ and $\sum_{\varepsilon\mu} Q_{\varepsilon\mu} = 1$. $Q_{\varepsilon\mu}$ is then the probability for the decay of a muon of handedness μ into an electron of handedness ε. The main point is now that the $Q_{\varepsilon\mu}$ can be expressed by the known quantities $\{a,\ldots,c'\}$ [7]:

$$Q_{RR} = 2(b + b')/A , \qquad\qquad (6.34)$$

$$Q_{RL} = [(a - a') + 6(c - c')]/(2A) , \qquad\qquad (6.35)$$

$$Q_{LR} = [(a + a') + 6(c + c')]/(2A) , \qquad\qquad (6.36)$$

$$Q_{LL} = 2(b - b')/A . \qquad\qquad (6.37)$$

In the Standard Model, $Q_{LL} = 1$ while the others are zero. The existing measurements show that the three probabilities Q_{RR}, Q_{LR} and Q_{LL} are zero, within errors. This gives upper limits to the absolute values of eight of the ten complex coupling constants. Furthermore, we find that Q_{LL} is bounded by a lower limit which shows that both muon and electron are left-handed. It can be seen from (6.33), however, that the data from the measurements of the muon and the electron observables do not allow one to distinguish a vector (g_{LL}^V) from a scalar (g_{LL}^S)

interaction. This type of ambiguity has been noted before in the context of a different Hamiltonian [16, 17] and electron-neutrino correlation measurements (not performed up to date) have been proposed. The total rate S, normalized to the rate predicted by $V - A$ for the reaction $\nu_\mu + e^- \to \mu^- + \nu_e$ with ν_μ of negative helicity, has been found to be close to 1 [17, 18]. S effectively depends only on those five coupling constants g_{LL}^V, g_{RL}^V, g_{LR}^S, g_{LR}^T and g_{RR}^S that describe interactions with a left-handed ν_μ. The four latter coupling constants are found to be small. One thus obtains [7]

$$S = |g_{LL}^V|^2\,, \tag{6.38}$$

which yields a *lower* limit for $|g_{LL}^V|$, and through the normalisation requirement (6.29) an upper limit for the remaining $|g_{LL}^S|$:

$$|g_{LL}^S| < 2\sqrt{1 - S}\,. \tag{6.39}$$

Thus the weak interaction has been completely determined for muon decay using only data from this purely leptonic interaction.

6.5 Experiments

6.5.1 Longitudinal Positron Polarization

The measurement of the longitudinal polarization $P_{\rm L}$ of the electrons from the decay of polarized or unpolarized muons allows the determination of the parameters ξ' and ξ'', as can be seen from Eqs. (6.11), (6.12), (6.14e) and (6.14f). The parameter ξ' is of special interest. In terms of the coupling constants $g_{\varepsilon\mu}^\gamma$ we have

$$\begin{aligned}
1 - \xi' &= \tfrac{1}{2} \left\{ 4 \cdot \left(|g_{RR}^V|^2 + |g_{RL}^V|^2 \right) + \left(|g_{RR}^S|^2 + |g_{RL}^S|^2 \right) + 12 \cdot |g_{RL}^T|^2 \right\} \\
&= 2(Q_{RR} + Q_{RL}) \equiv 2Q_R^e\,,
\end{aligned} \tag{6.40}$$

where Q_R^e is the probability of the decay of a muon with chirality μ into an electron with chirality ε. Note that (6.40) is a sum of absolute squares where only coupling constants with $\varepsilon = R$ appear. A deviation of ξ' from 1 would require the existence of a coupling with the right-handed components of the electron, i.e. at least one $g_{R\mu}^\gamma \neq 0$. Conversely, a measurement with the result $\xi' = 1$ would prove that the coupling acts exclusively on the left-handed component of the electron.

To determine ξ', the longitudinal polarization $P_{\rm L}$ of the electrons from unpolarized muons has been measured. For the purpose of illustration, we neglect the electron mass m_e and use the experimentally well confirmed values $\varrho = \delta = \tfrac{3}{4}$ and obtain from (6.11)

$$\xi' = P_{\rm L}\,. \tag{6.41}$$

The measurement of the electron's longitudinal polarization $P_{\rm L}$ consists of a comparison with the spin polarization of the electrons contained in a piece of saturated ferromagnetic material [19–21]. The comparison is done by scattering the decay electrons from the electrons of a ferromagnet, using the fact that relativistic electron-electron scattering most often occurs when the two spins have opposite directions.

The experiment was performed at the πE1 beam line at SIN. A schematic view of the apparatus is shown in Figure 6.2. The 150-MeV/c π^+ beam was stopped in an oak target, where the π^+ decay resulted in an unpolarized sample of μ^+ within the oak target. Positrons from muon decay crossed a magnetised iron foil, where they could annihilate in flight with polarized electrons (ANN), $e^+ e^- \to \gamma\gamma$, or scatter elastically: Bhabha-scattering BHA), $e^+ e^- \to e^+ e^-$. Both
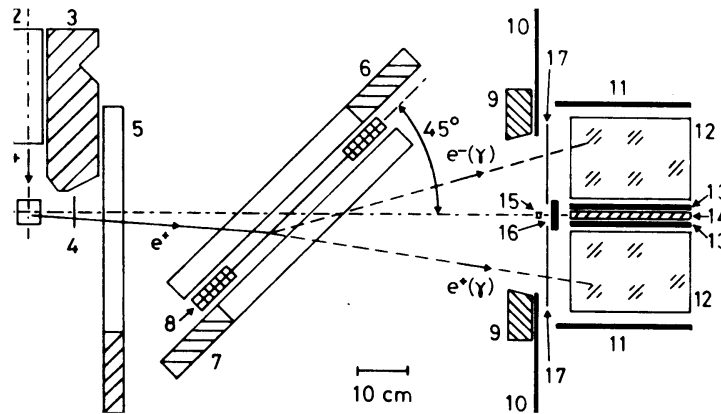
Figure 6.2: Schematic top view of the apparatus used for the measurement of P_L. A typical event is shown for either ANN or BHA. The experimental arrangement: (1) oak stopping target; (2) Be-CH$_2$ moderator; (3) shielding; (4) timing counter; (5), (6), and (7) multiwire proportional chambers labeled in the text WC$_1$, WC$_2$, and WC$_3$, respectively); and (8) magnet with iron foil. The total-absorption spectrometer is symmetric to the central axis. It consists of (12) four NaI detectors (only the upper pair is shown); (9) square Pb collimator; (10) square-aperture anticoincidence counter; (15) Am-Be calibration source; (17) four electron-identification counters; (16) vertical anticoincidence counter and monitor; (11) and (13) vertical anticoincidence counters; 14) vertical Fe-Pb photon converters. Not shown are the horizontal counterparts of (11), (13), (14) and (16).

reactions have high analysing powers up to 90 %. The electron polarization in the iron foil was $(54.44 \pm 0.56) \times 10^{-3}$. The final result of this experiment is [14]

$$\langle |P_L| \rangle = 0.998 \pm 0.042 \,. \tag{6.42}$$

From the resulting error of ξ', which is dominated by the error of $\langle |P_L| \rangle$, upper limits for all couplings of right-handed electrons to muons (of any handedness) $g^\gamma_{R\mu}, \mu = R, L$, follow, in principle, from (6.40). Improved values of these limits are obtained for $|g^V_{RL}|$ and $|g^S_{RL} + 6g^T_{RL}|$ by also considering

$$B_{RL} = \tfrac{1}{16}|g^S_{RL} + 6g^T_{RL}|^2 + |g^V_{RL}|^2 = \tfrac{1}{2A}(a + a') \,. \tag{6.43}$$

The parameter ξ'' in μ^+ decay has been determined from a measurement of $P_L(x, \vartheta)$ as a function of the reduced energy x and the angle ϑ between the muon spin and the positron momentum [14]. The precision of the measured combination $(\xi'' - \xi\xi')/\xi = -0.35 \pm 0.33$ does, however, not lead to better constraints of the couplings. With a new dedicated setup this value was considerably improved to [22]

$$\xi'' = 0.981 \pm 0.045_{\text{stat.}} \pm 0.003_{\text{syst.}} \,. \tag{6.44}$$

6.5.2 Transverse Positron Polarization

The transverse electron polarization $\boldsymbol{P}_T = (P_{T_1}, P_{T_2})$ is defined in Figure 6.1 and Eqs. (6.9) and (6.10). Independent of any assumption about the mechanism of muon decay or even
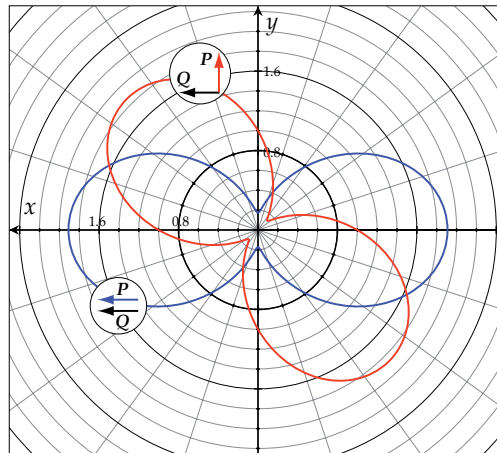
Figure 6.3: Intensity distributions of the annihilation photons at $E_3 = E_4 = 50\,m_e$ for parallel spins (e^- : $\boldsymbol{Q} = 1$, e^+ : $\boldsymbol{P}_{\mathrm{T}} = 1$) and for perpendicular spins. The maximum of the intensity lies on the bisector of the angle ωt between the two spins. Thus the "figure of eight" moves with angular frequency $\omega/2$. For a fixed detector pair at azimuthal angle ψ the time dependence is still given by the angular frequency ω due to the two symmetric lobes of the "figure of eight". From [11, 23].

the nature of the two unobserved neutral particles, time reversal invariance (disregarding the negligible final state interactions) requires $P_{\mathrm{T}_2} = 0$.

The measurement of $\boldsymbol{P}_{\mathrm{T}}$ as a function of energy yields a determination of the parameters η, η'', α'/A and β'/A (see Eqs. (6.16), (6.17), (6.23d) and (6.23h)). η is of special interest. η, together with the Michel parameter ϱ, determines the shape of the (isotropic) positron energy spectrum. However, it is difficult to deduce its value from a spectrum measurement, as its influence is suppressed by a factor $x_0 \approx 10^{-2}$. On the other hand, a precise value is needed for a precise determination of ϱ, as η and ϱ are statistically highly correlated. In (6.14c) for P_{T_1}, η arises without a suppression factor. It is interesting to note that P_{T_1} does not vanish in the Standard Model interaction, as can be seen from (6.9), and it may take sizeable values ($|P_{\mathrm{T}_1}| \leq 1/3$) for positron energies of a few MeV.

The experiment was performed with basically the same setup used for measuring the longitudinal polarization. It also uses a comparison with the spin polarized electrons in a ferromagnetic foil from annihilation in flight $e^+ e^- \to \gamma\gamma$. It is based on the fact that the photons from the annihilation of a relativistic, transversely polarized positron electron pair are preferentially emitted in the plane defined by the particle line-of-flight $\boldsymbol{k}_{e^+}$ and the bisector $\boldsymbol{b}$ between the (transverse) polarization directions $\boldsymbol{p}_{\mathrm{T}}$ and $\boldsymbol{p}_{e^-}$ (see Figure 6.3).

The results of a general, unrestricted analysis of the data are an improved value for $\eta = (11 \pm 85) \times 10^{-3}$ and the first results for $\eta'' = (48 \pm 125) \times 10^{-3}$ and the T-violating parameters $\alpha'/A = (-47 \pm 52) \times 10^{-3}$ and $\beta'/A = (17 \pm 18) \times 10^{-3}$ [13].

An improved experiment, where all the major parts of the previous experiment have been replaced by newly designed equipment to increase the event rate and reduce the systematic errors, has been described in detail elsewhere [24]. The four NaI detectors were replaced by an array of 127 BGO detectors (see Figure 6.4). A longitudinally polarized μ^+ beam ($P_\mu^b = 91\,\%$) enters a beryllium stop target with bunches every 19.75 ns. The polarization $P_\mu(t)$ of the stopped muons precesses in a homogeneous magnetic field ($B = 373.6 \pm 0.4$ mT) with the same angular frequency ω as the accelerator radio frequency. This ensures that $P_\mu(t) \parallel P_\mu^b$ for
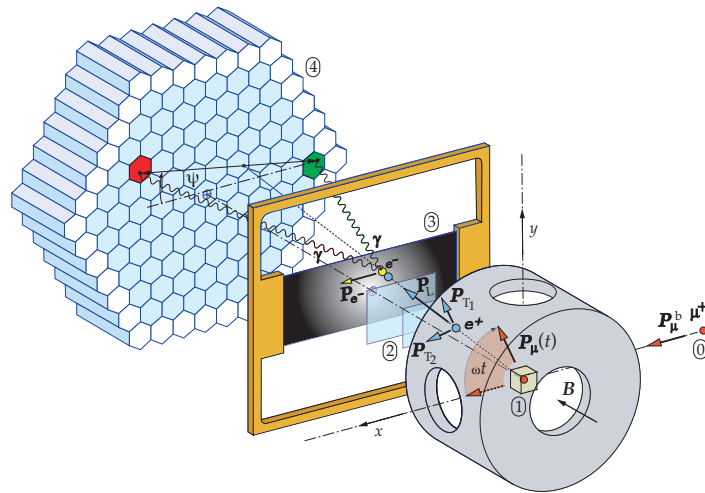
Figure 6.4: Schematic view of the experimental setup for the measurement of P_T. **0:** Burst of polarized muons (angular frequency ω, polarization P_μ^b). **1:** Be stop target and precession field B. **2:** Two plastic scintillation counters selecting decay positrons **3:** Magnetized Vacoflux 50^{TM} foil serving as a polarization analyzer. **4:** Array of 127 BGO scintillators to detect the two γ's from e^+ annihilation-in-flight. From [25].

each newly arriving μ^+ bunch. Because of the burst width of 3.9 ns (FWHM) the polarization $P_\mu(0)$ of the stopped μ^+ is reduced to $(82 \pm 2)\%$. A system of drift chambers (not shown) and two thin plastic scintillator counters T_0 and T_1 select decay e^+'s emitted in the direction of B. A 1-mm-thick magnetized Vacoflux 50^{TM} foil (49 % Fe, 49 % Co, 2 %V) in the central region with its polarized e^- ($P_{e^-} = 7.2$ %) serves as polarization analyzer. The two γ's from e^+ annihilation-in-flight with the polarized e^- are selected by an array of 91 interior $Bi_4Ge_3O_{12}$ (BGO) crystals with plastic veto counters in front of them to reject charged particles. The outer layer of 36 BGOs assists in an efficient collection of the deposited energy. Valid events are selected by using the correlation between the γ energies and their opening angle. The intensity distribution of the two γ's has roughly the shape of the figure eight with a maximum in the direction of the bisector of $P_T(t)$ and the e^- polarization P_{e^-} [11,23] (see Figure 6.3). The precession of $P_\mu(t)$ implies a precession of $P_T(t)$, while P_{e^-} remains constant in time. Thus the intensity distribution of the γ's also precesses with frequency ω. For any given pair ij of BGO detectors we ideally expect a signal for the normalized annihilation rate $N_{ij}(t)$ in the form

$$N_{ij}(t) = 1 + a_{ij}\cos(\omega t + \delta_0) + b_{ij}\sin(\omega t + \delta_0), \tag{6.45}$$

where t denotes the time the e^+ traverses counter T_0 and δ_0 an instrumental phase common to all time spectra. The events are contained in a time window of 39.5 ns total width, corresponding to two periods of the accelerator RF. The Fourier coefficients a_{ij} and b_{ij} contain the complete information of the transverse positron polarization. The analyzing power for annihilation in flight is large in most of the kinematic regions of the experiment. Figure 6.5 shows, as an example, the contour lines for the transverse analyzing power A_x (in %) as a function of the sum $u = (E_3 + E_4)/m_e$ and the difference $v = (E_3 - E_4)/m_e$ of the normalized photon energies E_3 and E_4.

Due to the finite acceptance solid angle for events, the rate of ANN events also varies with the frequency ω because of a small muon spin rotation (μSR) decay asymmetry modulated by the precessing $P_\mu(t)$. By adding or subtracting the Fourier coefficients of appropriate pairs
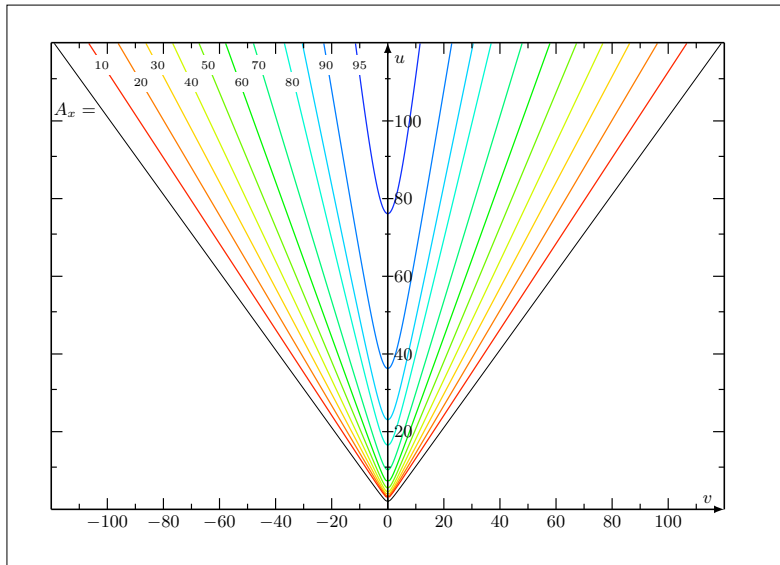
Figure 6.5: Contour lines for the transverse analyzing power A_x (in %) as a function of the sum $u = (E_3 + E_4)/m_e$ and the difference $v = (E_3 - E_4)/m_e$ of the normalized photon energies E_3 and E_4. The outermost line is the kinematic boundary. From [11].

ij and $i'j'$, it was possible to derive either the μSR - or the P_T signal, respectively. The μSR signal is essential for the experiment, as it allows the decomposition of the vector $\boldsymbol{P}_T$ into its components (P_{T_1}, P_{T_2}), since $\boldsymbol{P}_{T_1}$ lies in the plane of $\boldsymbol{k}_{e^+}$ and $\boldsymbol{P}_\mu(t)$ and $\boldsymbol{P}_{T_2}$ perpendicular to that plane (see Figure 6.1).

Table 6.1 shows the results of the general and of a restricted analysis [25]. The average polarization components $\langle P_{T_1} \rangle$ and $\langle P_{T_2} \rangle$ have been calculated from the values of η, η'', and α'/A, β'/A, respectively. Based on the most general 4-fermion contact interaction ("general analysis") the parameter η is given by [12]

$$\eta = \frac{1}{2} Re \left\{ g_{LL}^V g_{RR}^{S*} + g_{RR}^V g_{LL}^{S*} + g_{LR}^V \left(g_{RL}^{S*} + 6 g_{RL}^{T*} \right) + g_{RL}^V \left(g_{LR}^{S*} + 6 g_{LR}^{T*} \right) \right\}. \qquad (6.46)$$

With $g_{LL}^V \approx 1$, and all other $g_{\varepsilon\mu}^\gamma \approx 0$ [7], one can simplify (6.46) considerably by neglecting all terms quadratic in non-standard couplings. This amounts to assuming one additional coupling beyond $V - A$. Then only two independent parameters remain ("restricted analysis"):

$$\eta = \tfrac{1}{2} Re\{g_{RR}^S\}, \quad \beta'/A = -\tfrac{1}{4} Im\{g_{RR}^S\}. \qquad (6.47)$$

Here, g_{RR}^S is a scalar coupling with right-handed μ and e.

The Fermi coupling constant G_F is generally derived assuming an exclusive $V - A$ interaction, which amounts to setting $\eta = 0$. However, G_F depends on η [2, 12]:

$$G_F \approx G_F^{V-A} \cdot \left(1 - 2\eta \frac{m_e}{m_\mu} \right), \qquad (6.48)$$

where m_e/m_μ is the mass ratio of electron and muon. Taking η into account increases the relative error $\Delta G_F/G_F$ from 9×10^{-6} to 360×10^{-6} (general analysis) resp. to 68×10^{-6} (restricted analysis).

Note that the results on α'/A, β'/A (and deduced from these, $\langle P_{T_2} \rangle$ and Im $\{g_{RR}^S\}$) are the only experimental data sensitive to the violation of time reversal invariance (TRI) for a purely

Table 6.1: $V - A$ values and experimental results. All values, except χ^2/d.o.f., in units of 10^{-3}. The correlation coefficients ρ_{ij} are all compatible with zero except the two coefficients listed. The errors are statistical and systematic.

	$V - A$	General analysis	Restricted analysis
η	0	$71 \pm 37 \quad \pm 5$	$-2.1 \pm 7.0 \pm 1.0$
η''	0	$105 \pm 52 \quad \pm 6$	$\equiv -\eta$
α'/A	0	$-3.4 \pm 21.3 \pm 4.9$	$\equiv 0$
β'/A	0	$-0.5 \pm 7.8 \quad \pm 1.8$	$-1.3 \pm 3.5 \pm 0.6$
$\rho_{\eta\eta''}$		946	—
$\rho_{\alpha'\beta'}$		-893	—
χ^2/d.o.f.		46.2/33	50.3/35
Re $\{g^S_{RR}\}$	0	—	$-4.2 \pm 14.0 \pm 2.0$
Im $\{g^S_{RR}\}$	0	—	$5.2 \pm 14.0 \pm 2.4$
$\langle P_{T_1} \rangle$	-3	$6.3 \pm 7.7 \quad \pm 3.4$	
$\langle P_{T_2} \rangle$	0	$-3.7 \pm 7.7 \quad \pm 3.4$	

leptonic *reaction*. In contrast to the violation of TRI in the neutral kaon system [26], a T-odd observable in muon decay would be due to an interference between two couplings with different phase angles and thus be an unambiguous signal of new physics beyond the Standard Model.

6.5.3 Electron Decay Asymmetry

The measurement of the electron decay asymmetry, $\mathcal{A}(x)$, from polarized muons [27], determines how strongly the chiral components (L, R) of the muon take part in the interaction. This has been used to search for right-handed currents and other muon decay modes outside the Standard Model.

If the combination

$$\tfrac{1}{18}(9 + 3\xi - 16 \cdot \xi \cdot \delta) = \tfrac{1}{4}|g^S_{RR}|^2 + \tfrac{1}{4}|g^S_{LR}|^2 + |g^V_{RR}|^2 + |g^V_{LR}|^2 + 3|g^T_{LR}|^2$$
$$\equiv Q_{RR} + Q_{LR} \equiv Q^\mu_R \tag{6.49}$$

has a value different from zero, then a coupling to the right-handed component of the muon has to exist, i.e. at least one $g^\gamma_{\varepsilon R} \neq 0$. Conversely, if $Q^\mu_R = 0$, then the coupling acts exclusively on the left-handed muon.

The distribution of the flight direction of the positrons (electrons) is given by (6.5) with $P_e = 0$ as

$$\frac{\mathrm{d}^2\Gamma}{\mathrm{d}x\,\mathrm{d}\cos\vartheta} \equiv w(x, \vartheta) \sim \left\{ F_{\mathrm{IS}}(x) \pm P_\mu \cos\vartheta F_{\mathrm{AS}}(x) \right\}. \tag{6.50}$$

This depends on the reduced energy, x, the angle ϑ between the muon polarization and the positron momentum as chosen by the detector, and on the degree of polarization $P_\mu > 0$. The asymmetry

$$\mathcal{A}(x) \equiv \frac{w(x, 0) - w(x, \pi)}{w(x, 0) + w(x, \pi)} = P_\mu \cdot \frac{F_{\mathrm{IS}}(x)}{F_{\mathrm{AS}}(x)} \tag{6.51}$$
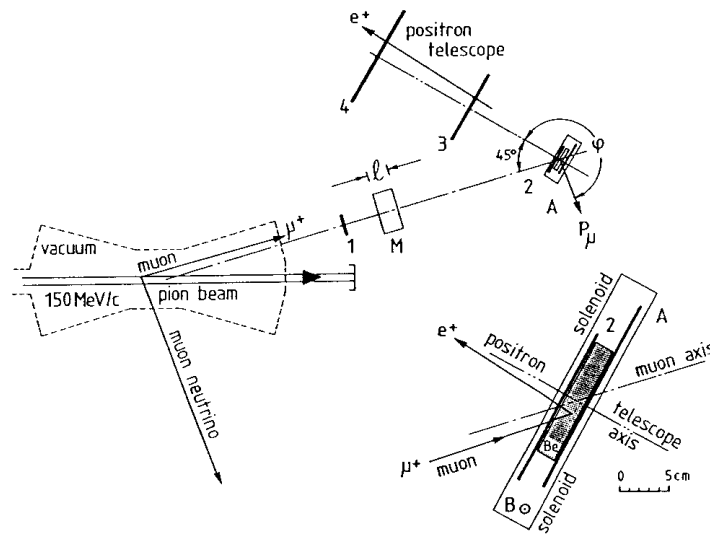
Figure 6.6: Muon Spin Rotation apparatus used to measure the integral asymmetry of the e^+ direction distribution following the decay of highly polarized muons. A parallel beam of monoenergetic ($150\,\mathrm{MeV}/c$) pions decays in flight in vacuum. Muons with energies within a well-determined interval are selected to stop in a beryllium plate, Be, employing a moderator of length ℓ. The original orientation of the muon polarization vector P_μ is thus defined. A rectangular solenoid produces a vertical magnetic field $B = 3\,\mathrm{mT}$ causing the polarization of the stopped muons to precess in the horizontal plane. This gives rise to a sinusoidal modulation of the exponential decrease of the positron rate. The amplitude of the modulation ($\approx 1/3$) is proportional to the quantity desired, $P_\mu\xi$. From [27].

depends on the parameters ϱ, η, ξ and $\xi\delta$ (see Eqs. (6.13a), (6.13b), (6.14a) and (6.14b)).

The distributions of the flight directions of the positrons (electrons) as seen by an apparatus that is equally sensitive to positrons of all energies is given by

$$\frac{\mathrm{d}\Gamma}{\mathrm{d}\cos\vartheta} \sim \int_{x_0}^{1} \mathrm{d}x \cdot \sqrt{x^2 - x_0^2} \cdot F_{\mathrm{IS}}(x) \pm P_\mu \cos\vartheta \cdot \int_{x_0}^{1} \mathrm{d}x \cdot \sqrt{x^2 - x_0^2} \cdot F_{\mathrm{AS}}(x)$$

$$\sim (1 \pm \mathcal{A}' \cdot \cos\vartheta). \tag{6.52}$$

The integral asymmetry, $\mathcal{A}'$, is proportional to $P_\mu \cdot \xi$ and depends on η in first order and on δ in second order of x_0. Neglecting x_0 ($x_0 = 0$) one obtains

$$\mathcal{A}' = \tfrac{1}{3} \cdot P_\mu \cdot \xi. \tag{6.53}$$

This allows the determination of ξ from an experiment using muons of known polarization. In the analysis, the knowledge of the values of other muon decay parameters is unimportant.

Muon beams produced from pions decaying in flight in vacuum avoid Coulomb multiple scattering. The muon spin lies in the plane of the laboratory line of flight of the original pion, $\boldsymbol{k}_\pi$, and and its decay muon, $\boldsymbol{k}_\mu$. It points inwards (towards $\boldsymbol{k}_\pi$) for μ^+ and outwards for μ^- (see Figure 6.6). The transverse and longitudinal muon spin components, ζ_T and ζ_L with

respect to the muon's laboratory line-of-flight are simply given by

$$\zeta_T = \frac{\sin\vartheta_\mu}{\sin\Theta_\mu}, \qquad\qquad \zeta_L = \mp\sqrt{1-\zeta_T^2}, \qquad\qquad (6.54)$$

where the upper (lower) sign applies for the muon emitted with smaller (larger) momentum for the given angle of emission ϑ_μ, and where

$$\vartheta_\mu = \text{laboratory angle between } \boldsymbol{k}_\pi \text{ and } \boldsymbol{k}_\mu\,,$$
$$\Theta_\mu = \text{maximum laboratory angle by kinematics (Jacobian peak angle)}\,,$$
$$\sin\Theta_\mu = \left(m_\pi^2 + m_\mu^2\right)/(2m_\pi k_\pi)\,,$$
$$k_\pi = \text{pion beam momentum}.$$

The selection of a small slice of muon energy in the laboratory in the vicinity of the Jacobian peak corresponds to a choice of a small range of neutrino directions and thus of a degree of polarization $P_\mu = G \cdot P_{\nu_\mu}$. The geometrical factor G, which also has been studied experimentally [28], is close to one (> 0.99), and it is known with an uncertainty of $< 10^{-3}$ [27].

To measure the decay asymmetry, the muons are stopped in a metal (Be, Al) immersed in a transverse magnetic field where the spins precess. Detectors track the muon and the decay positron momenta. The positron intensity has a time modulation corresponding to the decay asymmetry. It is fortunate that there are substances (Al, Cu, Ag, Au, bromoform) that barely influence the spin direction of muons inside them. The disappearance of muon polarization during slowing down [21, 29] and thermalisation [30], i.e. at earlier times compared to the muon precession time, mimics a smaller $\mathcal{A}_{\text{exp}}$. Depolarization at later times is seen in the data [31,32]. It can be accounted for by extrapolating the precession signal amplitude to time zero. The determination of the extrapolating-function parameters in the same experiment generally considerably reduces the statistical significance of the data due to their strong correlation with the signal. The relaxation time in pure metals at room temperature is often conveniently large compared to the muon lifetime.

Positron detectors with low energy thresholds are used for the measurement of $P_\mu\xi$. The result obtained from this experiment is [27]

$$P_\mu^\pi\xi = (1002.7 \pm 7.9_{\text{stat.}} \pm 3.0_{\text{syst.}}) \times 10^{-3}\,. \qquad\qquad (6.55)$$

As ξ is not limited close to the measured value of $P_\mu\xi$, we cannot draw any specific conclusion on P_μ and ξ separately. In fact, $-3 \le \xi \le +3$. To isolate ξ from $P_\mu\xi$, one has to deduce P_μ from the measurement of $P_\mu\xi\delta/\varrho$ of [32].

6.6 Results for τ-lepton and neutrino physics

For muon decay, we have shown that a hamiltonian with parity-odd and -even terms is not well suited for the description of a fully parity-violating interaction. Thus we have extended the concept of the *chiral* hamiltonian to leptonic τ decays [33]. Assuming universality for leptonic τ decays sensitivities for the different τ decay constants can be derived.

For the complete determination of the interaction in muon decay, it was essential to have experimental proof that the helicity of left-handed ν_μ is equal to -1. Previous measurements had yielded $h_{\bar\nu_\mu} = (+990 \pm 160) \times 10^{-3}$ [34] and $h_{\nu_\mu} = (-1060 \pm 110) \times 10^{-3}$ [35]. It was then realized that the measurement of $P_\mu\xi\delta/\varrho$ in muon decay by Carr et al. [36] not only yields a new lower limit for a possible right-handed W_R boson, but is also suited to derive a vastly improved limit for the helicity of the ν_μ [37]:
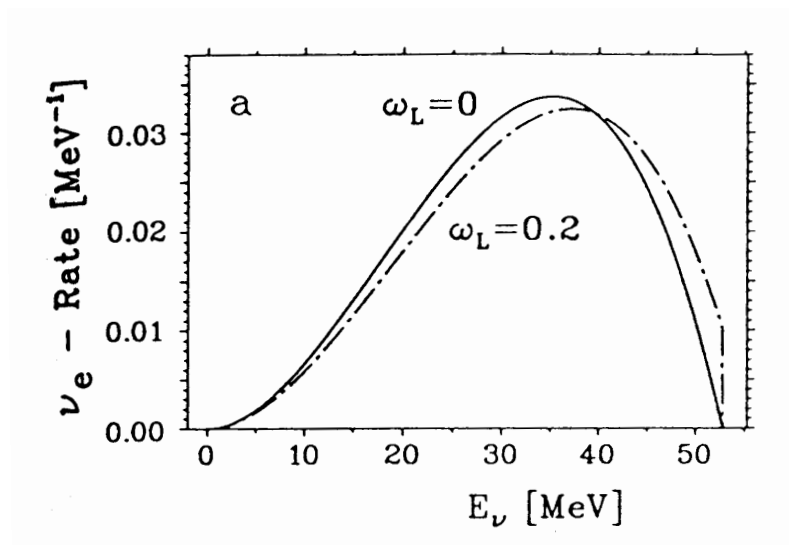
Figure 6.7: Normalized energy distributions of left-handed ν_e from the decay of unpolarized μ^+. The spectrum shape parameter ω_L is the analog of the Michel parameter ϱ of the e^+. For a pure $V - A$ interaction ω_L is equal to zero. From [38].

The normalized positron rate $\mathrm{d}^2\Gamma/\mathrm{d}x\,\mathrm{d}\cos\vartheta$ at the spectrum end point can be written as

$$\frac{\mathrm{d}^2\Gamma}{\mathrm{d}x\,\mathrm{d}\cos\vartheta} = (1 + P_\mu \cdot (\xi\delta/\varrho) \cdot \cos\vartheta). \tag{6.56}$$

It is obvious that the factor $|P_\mu \xi\delta/\varrho| \le 1$, since the rate cannot be negative. P_μ is the polarization of the muon from the decay $\pi^+ \to \mu^+ \nu_\mu$ and independent of the muon decay constant. Therefore we find

$$|P_\mu| \le 1 \quad \text{and} \quad |\xi\delta/\varrho| \le 1. \tag{6.57}$$

On the other hand, from the measurement one gets a lower limit for the product [36]

$$P_\mu \xi\delta/\varrho > 995.9 \times 10^{-3} \quad (90\,\%\mathrm{CL}). \tag{6.58}$$

Since $P_\mu = -h_{\nu_\mu}$ we derive a lower limit for $|h_{\nu_\mu}|$ [37]:

$$|P_\mu| = |h_{\nu_\mu}| > 995.9 \times 10^{-3} \quad (90\,\%\mathrm{CL}). \tag{6.59}$$

It has also been realized that experiments that detect the ν_e from the decay of unpolarized μ^+ by the reaction $^{12}\mathrm{C}(\nu_e, e^-)^{12}\mathrm{N}(\mathrm{g.s.})$ not only determine the neutrino absorption cross section but also measure the ν_e energy spectrum [38]. The energy spectrum can be described by the spectrum shape parameters ω_L and η_L for left-handed and ω_R and η_R for right-handed ν_e. In contrast to the energy spectrum of the electrons it allows a new null-test of the standard model [38]. The right-handed ν_e cannot be detected as they are sterile in matter. For the energy spectrum of the left-handed ν_e one obtains

$$\frac{\mathrm{d}\Gamma_L}{\mathrm{d}y} = \frac{m_\mu^5 G_F^2}{16\pi^3} \cdot Q_L^{\nu_e} \cdot \{F_1(y) + \omega_L \cdot F_2(y) + \eta_L x_0 F_3(y)\}. \tag{6.60}$$

Here, $\mathrm{d}\Gamma/\mathrm{d}y$ is the probability of a left-handed ν_e to be emitted with the reduced energy $y = 2E_\nu/m_\mu$. The functions $F_1(y)$, $F_2(y)$ and $F_3(y)$ are given in [38]. The probability $Q_L^{\nu_e}$ of

the ν_e to be left-handed, the spectral shape parameter ω_L and the low energy parameter η_L are

$$Q_L^{\nu_e} = \tfrac{1}{4}|g_{RL}^S|^2 + \tfrac{1}{4}|g_{RR}^S|^2 + |g_{LL}^V|^2 + |g_{LR}^V|^2 + 3|g_{RL}^T|^2 = \tfrac{1}{2}\left(1 - P_{\nu_e}\right), \quad (6.61)$$

$$\omega_L = \tfrac{3}{4} \frac{\left\{|g_{RR}^S|^2 + 4|g_{LR}^V|^2 + |g_{RL}^S + 2g_{RL}^T|^2\right\}}{\left\{|g_{RL}^S|^2 + |g_{RR}^S|^2 + 4|g_{LL}^V|^2 + 4|g_{LR}^V|^2 + 12|g_{RL}^T|^2\right\}}, \quad (6.62)$$

$$\eta_L = 2 \frac{Re\left\{g_{LL}^V g_{RR}^{S*} + g_{LR}^V\left(g_{RL}^{S*} + 6g_{RL}^{T*}\right)\right\}}{\left\{|g_{RL}^S|^2 + |g_{RR}^S|^2 + 4|g_{LL}^V|^2 + 4|g_{LR}^V|^2 + 12|g_{RL}^T|^2\right\}}, \quad (6.63)$$

where P_{ν_e} denotes the longitudinal polarization of the ν_e. Figure 6.7 , as an example, shows the normalized energy distributions for the $V-A$ prediction $\omega_L^{V-A} = 0$ and for $\omega_L = 0.2$. A value $\omega_L > 0$ results in events at the spectrum end where none are expected for the $V-A$ interaction.

References

[1] L. Michel, *Interaction between four half spin particles and the decay of the µ meson*, Proc. Phys. Soc. A **63**, 514 (1950), doi:10.1088/0370-1298/63/5/311.

[2] F. Scheck, *Muon physics*, Phys. Rep. **44**, 187 (1978), doi:10.1016/0370-1573(78)90014-5.

[3] T. Kinoshita and A. Sirlin, *Polarization of electrons in muon decay with general parity nonconserving interactions*, Phys. Rev. **108**, 844 (1957), doi:10.1103/PhysRev.108.844.

[4] M. Fierz, *Zur FERMIschen Theorie des β-Zerfalls*, Z. Physik **101**, 553 (1937), doi:10.1007/BF01330070.

[5] F. Scheck, *Leptons, hadrons and nuclei*, North-Holland, Amsterdam (1983).

[6] K. Mursula and F. Scheck, *Analysis of leptonic charged weak interactions*, Nucl. Phys. B **253**, 189 (1985), doi:10.1016/0550-3213(85)90526-7.

[7] W. Fetscher, H. J. Gerber and K. F. Johnson, *Muon decay: Complete determination of the interaction and comparison with the standard model*, Phys. Lett. B **173**, 102 (1986), doi:10.1016/0370-2693(86)91239-6.

[8] F. Scheck, *Electroweak and strong interactions: An introduction to theoretical particle physics*, Springer, Berlin (1996).

[9] C. Bouchiat and L. Michel, *Theory of µ-meson decay with the hypothesis of nonconserving of parity*, Phys. Rev. **106**, 170 (1957), doi:10.1103/PhysRev.106.170.

[10] T. Kinoshita and A. Sirlin, *Muon decay with parity nonconserving interactions and radiative corrections in the two-component theory*, Phys. Rev. **107**, 593 (1957), doi:10.1103/PhysRev.107.593.

[11] W. Fetscher, *Annihilation-in-flight of polarised positrons with polarised electrons as an analyser of the positron polarisation from muon decay*, Eur. Phys. J. C **52**, 1 (2007), doi:10.1140/epjc/s10052-007-0384-6.

[12] W. Fetscher and H. J. Gerber, in *Precision Tests of the Standard Electroweak Model*, chap. *Precision Tests in Muon and Tau Decays*, pp. 657, ed. P. Langacker, World Scientific, Singapore (1995).

[13] H. Burkard et al., *Muon decay: Measurement of the transverse positron polarization and general analysis*, Phys. Lett. B **160**, 343 (1985), doi:10.1016/0370-2693(85)91340-1.

[14] H. Burkard et al., *Muon decay: Measurement of the positron polarization and implications for the spectrum shape parameter eta, v-a and t invariance*, Phys. Lett. B **150**, 242 (1985), doi:10.1016/0370-2693(85)90178-9.

[15] H.-J. Gerber, *Lepton properties*, International Europhysics Conference on High Energy Physics (1987).

[16] C. Jarlskog, *Determination of the coupling constants in muon decay from experiments*, Nucl. Phys. **75**, 659 (1966), doi:10.1016/0029-5582(66)90986-2.

[17] S. Mishra *et al.*, *Inverse muon decay, $\nu_\mu e \to \mu^- \nu_e$, at the Fermilab Tevatron*, Phys. Lett. B **252**, 170 (1990), doi:10.1016/0370-2693(90)91099-W.

[18] D. Geiregat *et al.*, *A New measurement of the cross-section of the inverse muon decay reaction muon-neutrino e- → mu- electron-neutrino*, Phys. Lett. B **247**, 131 (1990), doi:10.1016/0370-2693(90)91061-F.

[19] H. Toelhoek, *Electron polarization, theory and experiment* Rev. Mod. Phys. **28**, 277 (1956), doi:10.1103/RevModPhys.28.277.

[20] J. DeRaad, Lester L. and Y. J. Ng, *Electron electron scattering. 3. Helicity cross-sections for electron electron scattering*, Phys. Rev. D **11**, 1586 (1975), doi:10.1103/PhysRevD.11.1586.

[21] G. Ford and C. Mullin, *Scattering of polarized Dirac particles on electrons*, Phys. Rev. **108**, 477 (1957), doi:10.1103/PhysRev.108.477.

[22] R. Prieels et al., *Measurement of the parameter ξ'' in polarized muon decay and implications on exotic couplings of the leptonic weak interaction*, Phys. Rev. D **90**, 112003 (2014), doi:10.1103/PhysRevD.90.112003.

[23] F. Corriveau et al., *Does the positron from muon decay have transverse polarization?*, Phys. Lett. B **129**, 260 (1983), doi:10.1016/0370-2693(83)90857-2.

[24] I. C. Barnett et al., *An apparatus for the measurement of the transverse polarization of positrons from the decay of polarized muons*, Nucl. Instrum. Meth. A **455**, 329 (2000), doi:10.1016/S0168-9002(00)00525-8.

[25] N. Danneberg et al., *Muon decay: Measurement of the transverse polarization of the decay positrons and its implications for the Fermi coupling constant and time reversal invariance*, Phys. Rev. Lett. **94**, 021802 (2005), doi:10.1103/PhysRevLett.94.021802.

[26] A. Angelopoulos et al., *First direct observation of time-reversal non-invariance in the neutral kaon system*, Phys. Lett. B **444**, 43 (1998), doi:10.1016/S0370-2693(98)01356-2.

[27] I. Beltrami, H. Burkard, R. Von Dincklage, W. Fetscher, H. Gerber, K. Johnson, E. Pedroni, M. Salzmann and F. Scheck, *Muon decay: Measurement of the integral asymmetry parameter*, Phys. Lett. B **194**, 326 (1987), doi:10.1016/0370-2693(87)90552-1.

[28] I. Beltrami et al., *Measurement of the integral asymmetry in mu decay and implication for the wino mass*, Helv. Phys. Acta **60**, 611 (1987).

[29] J. Heintze, *Nachweis der Polarisation der β-Teilchen von $Sr^{90}+Y^{90}$* Z. Physik **148**, 560 (1957), doi:10.1007/BF01328707.

[30] F. G. J.H. Brewer, K.M. Crowe and A. Schenck, *Muon physics*, vol. III, Academic, New York (1975).

[31] D. Stoker *et al.*, *Search for right-handed currents using muon spin rotation*, Phys. Rev. Lett. **54**, 1887 (1985), doi:10.1103/PhysRevLett.54.1887.

[32] A. Jodidio *et al.*, *Search for right-handed currents in muon decay*, Phys. Rev. D **34**, 1967 (1986), doi:10.1103/PhysRevD.34.1967, [Erratum: Phys. Rev. D **37**, 237 (1988), doi:10.1103/PhysRevD.37.237].

[33] W. Fetscher, *Leptonic tau decays: How to determine the Lorentz structure of the charged leptonic weak interaction by experiment*, Phys. Rev. D **42**, 1544 (1990), doi:10.1103/PhysRevD.42.1544.

[34] R. Abela, G. Backenstoss, W. Kunold, L. Simons and R. Metzner, *Measurements of the polarization of the 2P and 1S states in muonic atoms and the helicity of the muon in pion decay*, Nucl. Phys. A **395**, 413 (1983), doi:10.1016/0375-9474(83)90051-9.

[35] L. Roesch, V. Telegdi, P. Truttmann, A. Zehnder, L. Grenacs and L. Palffy, *Measurement of the average and longitudinal recoil polarizations in the reaction C-12 (mu-, neutrino) B-12 (G.S.): pseudoscalar coupling and neutrino helicity*, Helv. Phys. Acta **55**, 74 (1982).

[36] J. Carr *et al.*, *Search for right-handed currents in muon decay*, Phys. Rev. Lett. **51**, 627 (1983), doi:10.1103/PhysRevLett.51.627, [Erratum: Phys. Rev. Lett. **51**, 1222 (1983), doi:10.1103/PhysRevLett.51.1222].

[37] W. Fetscher, *Helicity of the muon-neutrino in pi+ decay: a comment on the measurement of P (MU) XI DELTA / RHO in muon decay*, Phys. Lett. B **140**, 117 (1984), doi:10.1016/0370-2693(84)91059-1.

[38] W. Fetscher, *Muon decay: Measurement of the energy spectrum of the electron-neutrino as a novel precision test for the Standard Model*, Phys. Rev. Lett. **69**, 2758 (1992), doi:10.1103/PhysRevLett.69.2758, [Erratum: Phys. Rev. Lett. 71, 2511 (1993), doi:10.1103/PhysRevLett.71.2511].

The SINDRUM-I experiment

Ralph Eichler and Christoph Grab⋆

Department of Physics, ETH Zürich, 8093 Zürich, Switzerland

⋆ grab@ethz.ch

Abstract

SINDRUM-I was the first nearly 4π spectrometer at SIN. It was initially designed to search for the forbidden decay $\mu^+ \rightarrow e^+e^-e^+$, but also successfully studied various other processes with high precision. The upper limit obtained for the branching ratio of $B_{\mu \rightarrow 3e} = \Gamma(\mu^+ \rightarrow e^+e^-e^+)/\Gamma(\mu^+ \rightarrow e^+ \nu_e \bar{\nu}_\mu) < 1.0 \times 10^{-12}(90\%\ \text{CL})$ from 1988 is still the best. The first statistically significant observation of the rare decay $\mu^+ \rightarrow e^+e^-e^+ \nu_e \bar{\nu}_\mu$, achieved in 1985, yielded a branching ratio of $B_{\mu \rightarrow 3e2\nu} = (3.4 \pm 0.2 \pm 0.2) \times 10^{-5}$. Several other measurements of rare processes were undertaken. The first observation of the π-decay $\pi^+ \rightarrow e^+ \nu_e e^- e^+$ resulted in the value $\Gamma(\pi^+ \rightarrow e^+ \nu_e e^- e^+)/\Gamma(\pi^+ \rightarrow \mu^+ \nu_\mu) = (3.2 \pm 0.5 \pm 0.2) \times 10^{-9}$, also still the best measurement. The determination of the ratio of the weak axial- to vector-form factor $F_A/F_V = (0.7 \pm 0.5)$ resolved a long-standing ambiguity. In addition, upper limits for $\mu^+ \rightarrow e^+ \phi$ and $\pi^+ \rightarrow e^+ \nu_e \phi$ with subsequent decay $\phi \rightarrow e^+e^-$ (search for "massless" Goldstone bosons ϕ) and $\pi^0 \rightarrow e^+e^- < 1.3 \times 10^{-7}$ were obtained.

7.1 History - how it all began

In the fall of 1976 rumors spread about an experiment performed at SIN for the search of the decay $\mu \rightarrow e\gamma$. A debate was going on, whether or not the decay had been observed. The rumors traveled from SIN via email to R. Eichler at Stanford and from him to a graduate student in the lecture-class of James Bjorken. The next week, J. Bjorken in turn gave the students an exercise to compute the decay rate and also confronted his colleague Steven Weinberg with the rumor. It took a few weeks after Weinberg's talk at the APS meeting to reach the New York Times. There it read on February 8th 1977: *Experimenters in Switzerland have reportedly observed an "impossible" transmutation of atomic particles. This has thrown the world community of theoretical physicists into a frenzy of speculations, calculations and publications (S. Weinberg).* This inspired R. Hofstadter of Stanford to initiate an experiment at LAMPF for $\mu^+ \rightarrow e^+ \gamma$ to try to resolve the dispute around the SIN experiment.

The results from the SIN experiment were finally published as an upper limit for the muon decay $\mu \to e\gamma$. However, all these speculations triggered a wider range of searches of muon flavour violating decays at LAMPF and SIN, and these activities continue presently at PSI, Fermilab and J-PARC.

7.2 The lepton flavour violating process $\mu^+ \to e^+ e^- e^+$

In the Standard Model (SM), charged lepton flavour violating reactions (LFV) are forbidden at tree level and can only be induced by lepton mixing through higher-order diagrams. One of the dominant contributions, the mixing through loop diagrams with massive neutrinos, see Figure 7.1a, is strongly suppressed in the SM with a predicted branching ratio B below the level of 10^{-50} [1] . Thus, the decay $\mu^+ \to e^+ e^- e^+$ potentially provides very high sensitivity to LFV reactions in various models of physics Beyond the Standard Model, in which the couplings are mediated by completely new particles.

At the time of the SINDRUM-I experiment, lepton flavour violation in the neutral lepton sector (neutrino oscillations) were not yet established, and theories were focused on extensions of the SM by introducing different new heavy particles that can mediate charged LFV either in virtual loops (Figure 7.1b), at tree level (see Figure 7.1c), or in box diagrams. These new models included right-handed bosons, additional Higgs doublets, neutral scalar singlets, familons, extended technicolor gauge bosons, doubly charged so-called "heptons", various "horizontal" models, and notably supersymmetric (SUSY) models with scalar leptons. An example is Figure 7.1b, in which a γ/Z-penguin diagram is shown with new SUSY particles running in a loop. These loop contributions are important for all models where new particle couplings to electrons and muons are introduced.

Not all of these models have survived with equal popularity today. However, modern models also include new particles such as Higgs particles or doubly charged Higgs particles, R-parity-violating scalar neutrinos, supersymmetric particles and new heavy vector bosons.

(a) massive neutrinos   (b) SUSY   (c) tree level
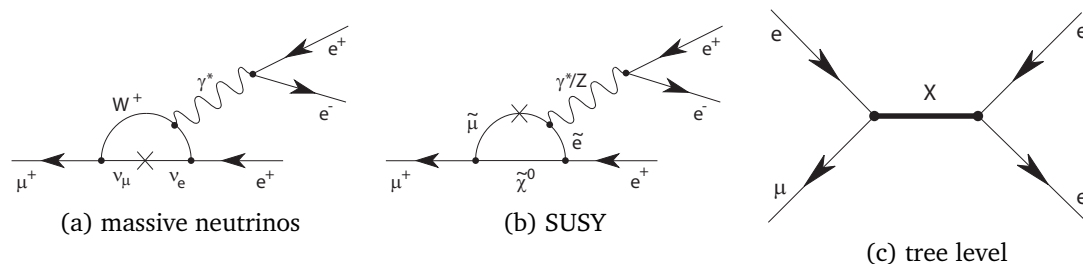
Figure 7.1: Feynman diagrams for lepton flavour violation in $\mu^+ \to e^+ e^- e^+$. (a) by massive neutrino mixing; (b) by heavy mediating particles, such as in SUSY models; (c) tree level mediating particles.

7.3 What physics did we learn from the SINDRUM-I experiment ?

7.3.1 Search for the decay $\mu^+ \to e^+ e^- e^+$

The main focus of the SINDRUM I experiment was the search for the decay $\mu^+ \to e^+ e^- e^+$ [2–4], with the aim to improve the sensitivity substantially beyond the then existing limits of $B_{\mu\to 3e} < 1.9 \times 10^{-9}$ at 90% C.L. [5].

The unique kinematic topology of the 3-body decay was exploited in the analysis, namely three identical-mass electrons (and positrons) with all tracks originating from one common vertex, coincident in time, with vanishing total momentum and a total energy equal to the

muon mass. The dominant background stems from accidental combinations of tracks (e.g. in combination with Bhabha scattering) and from the irreducible, allowed but strongly suppressed internal radiative decay $\mu^+ \to e^+ e^- e^+ \nu_e \bar{\nu}_\mu$. The data reduction was achieved with a multiple stage trigger, taking advantage of track and charge preselectors, requiring at least one negatively and two positively charged tracks within a time window of 7 ns. This was complemented by a track correlator which limited the total transverse momentum of the $e^+ e^- e^+$-triplet to below 17 MeV/c. A full three-dimensional event reconstruction was performed offline. As an example, a reconstructed $\mu^+ \to e^+ e^- e^+$ event candidate is shown in Figure 7.2b. The acceptances and efficiencies were determined by Monte Carlo simulations. Prompt events were distinguished from accidentals by time difference constraints between the mean time of the $e^+ e^-$-pair and the time of the second e^+. The final number of potentially observed $\mu^+ \to e^+ e^- e^+$ candidate decays was determined from the 2-dimensional distribution of ($\sum E_i$ vs $\hat{p}^2$) for both the prompt and the accidental events. Energy conservation requires $\sum E_i = m_\mu$ within errors for true $\mu^+ \to e^+ e^- e^+$ events, and $\hat{p}^2 = (p_\parallel/\sigma_{p_\parallel})^2 + (p_\perp/\sigma_{p_\perp})^2$ to be centered at zero. The distribution is shown in Figure 7.2a for the measured prompt events. No events were observed within the indicated 95% C.L. contour for $\mu^+ \to e^+ e^- e^+$ decays. Based on zero observed events an upper limit on the decay branching ratio $B_{\mu^+ \to e^+ e^- e^+}$ was determined by normalising to the number of observed $\mu^+ \to e^+ e^- e^+ \nu_e \bar{\nu}_\mu$ events. Already during construction of SINDRUM-I with four out of five tracking chambers an order of magnitude better limit [2] compared to [5] was published. Combining then the data from all running periods, the final branching ratio obtained [4] was

$$B_{\mu \to 3e} < 1.0 \times 10^{-12} \quad \text{at 90\% C.L..} \tag{7.1}$$
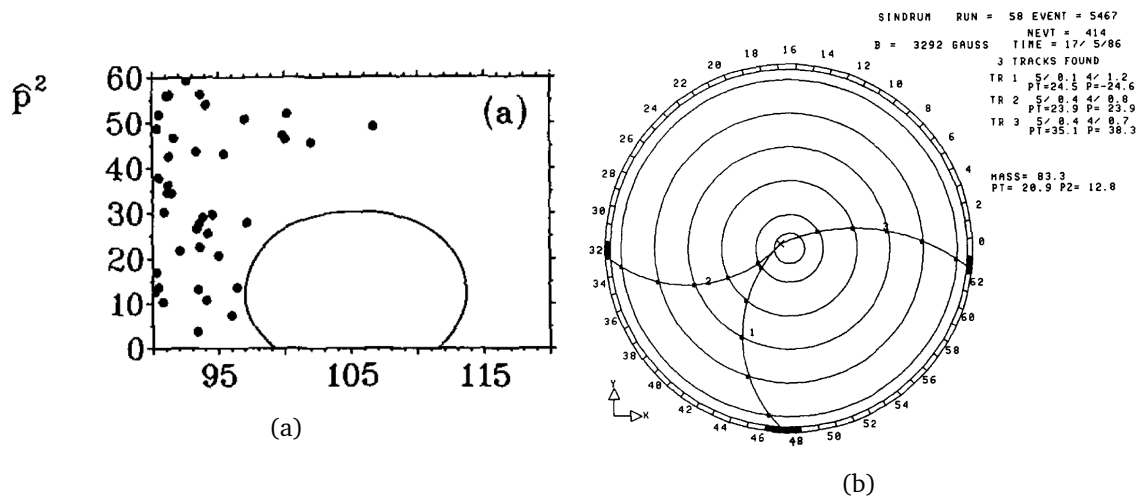
Figure 7.2: (a) Distribution of the (ΣE_i vs $\hat{p}^2$) for prompt events; the contour defines the 95% C.L. region for $\mu^+ \to e^+ e^- e^+$ decays. (b) Example of a reconstructed $\mu^+ \to e^+ e^- e^+$ candidate event, shown in the $r - \phi$ plane.

7.3.2 Measurement of the internal radiative decay $\mu^+ \to e^+ e^- e^+ \nu_e \bar{\nu}_\mu$

The internal radiative decay $\mu^+ \to e^+ e^- e^+ \nu_e \bar{\nu}_\mu$ constitutes the main irreducible background contribution for the $\mu^+ \to e^+ e^- e^+$ search. This rare decay is also of interest itself as it can be calculated to a precision below the per mille level. Hence, this decay was also analysed in parallel to $\mu^+ \to e^+ e^- e^+$, using the same time and vertex constraints. During the first data taking runs with the complete SINDRUM-I detector, a total of $N = (7.3 \pm 0.5) \cdot 10^{12}$

muons were stopped in the target and were used for the analyses of both $\mu^+ \to e^+ e^- e^+$ and $\mu^+ \to e^+ e^- e^+ \nu_e \bar{\nu}_\mu$. Based on the observation of 7443 $\mu^+ \to e^+ e^- e^+ \nu_e \bar{\nu}_\mu$ events and an efficiency of 3×10^{-5}, a decay branching ratio of $B_{\mu \to 3e2\nu} = (3.4 \pm 0.2 \pm 0.2) \times 10^{-5}$ was measured [3], consistent with the SM prediction, and is still the most accurate as of this writing. Previous experiments had only been able to observe a handful of events (≤ 7 events). Thus, this was the first statistically significant observation of the $\mu^+ \to e^+ e^- e^+ \nu_e \bar{\nu}_\mu$ decay.

7.3.3 Measurement of $\pi^+ \to e^+ \nu_e e^- e^+$

In the decays $\pi^+ \to e^+ \nu_e \gamma$ and $\pi^+ \to e^+ \nu_e e^- e^+$, both the vector- and axial-vector weak hadronic currents contribute to the decay amplitudes and are parameterized by the vector and axial vector form factors F_V and F_A, respectively. There is a firm prediction for the value of F_V. The conserved vector current rule connects F_V with the π^0 lifetime so that $|F_V| = 0.0255$, but the sign is undetermined. Contrary to the case of $\pi^+ \to e^+ \nu_e \gamma$, the ratio of F_A/F_V is unambiguously measurable in the decay $\pi^+ \to e^+ \nu_e e^- e^+$ and the result of [6] excludes a possible negative value of F_A/F_V from the $\pi^+ \to e^+ \nu_e \gamma$ experiments. In the high statistics run of SINDRUM-I [7] the first determination of

$$B_{\pi^+ \to e^+ \nu_e e^- e^+} = \Gamma(\pi^+ \to e^+ \nu_e e^- e^+)/\Gamma(\pi^+ \to \mu^+ \nu_\mu) = (3.2 \pm 0.5 \pm 0.2) \times 10^{-9} \qquad (7.2)$$

was achieved, where the first error is the statistical uncertainty and the second error is due to the uncertainty of the form factors. This $B_{\pi^+ \to e^+ \nu_e e^- e^+}$ still holds as of this writing. By fixing the value $F_V = 0.0255$ the form factor $F_A = 0.019 \pm 0.008$ was determined.

7.3.4 Search for light particles produced in muon- or pion decays

Many theories beyond the Standard Model predict "massless" Nambu-Goldstone bosons arising from the breaking of an underlying symmetry. Examples are the "familon" for a broken family hierarchy, the "axion" for a broken axial baryon number proposed to solve the strong CP problem, the majoron, and neutral scalar bosons.

In the search for a light Higgs h in the decay $\pi^+ \to e^+ \nu_e h$, where the Higgs decays in $h \to e^+ e^-$, the same selection criteria as for the analysis of the pion form factors were applied [7]. Higgs particles with a decay length less than the vertex resolution of the SINDRUM detector should be visible in the decay $\pi^+ \to e^+ \nu_e e^- e^+$ as a peak in the $e^+ e^-$ -invariant mass distribution. No such signal was observed for Higgs masses $2m_e < m_h < 110$ MeV/c^2.

A similar search was made for an axion-like neutral particle produced in both μ or π decays, $\mu^+ \to e^+ \phi$ and $\pi^+ \to e^+ \nu \phi$, with a subsequent decay $\phi \to e^+ e^-$. No candidates were found, and therefore upper limits for the branching ratios were determined as a function of the ϕ masses and lifetimes. For ϕ lifetimes below 10^{-10} s limits on B down to 2×10^{-12} were obtained [8].

Furthermore, a search for weakly interacting neutral bosons (X) produced in $\pi^- p$ interactions at rest and decaying into $e^+ e^-$ pairs was performed with the SINDRUM detector. The data sample searched contained 98400 $\pi^0 \to e^+ e^- \gamma$ decays and 27200 $\pi^- p \to n e^+ e^-$ events, each with an $e^+ e^-$ invariant mass between 25 and 139 MeV/c. Upper limits for the branching ratios $\Gamma(\pi^0 \to X\gamma, X \to e^+ e^-)/\Gamma(\pi^0 \to all)$ and $\Gamma(\pi^- p \to Xn, X \to e^+ e^-)/\Gamma(\pi^- \to all)$ for X lifetimes between 10^{-23}s and 10^{-11}s were obtained. Upper limits at 90% C.L. range from 10^{-3} at an invariant $e^+ e^-$ mass of 25 MeV/c^2 to 10^{-5} at 100 MeV/c^2 [9].

7.3.5 Measurement of the decay $\pi^0 \to e^+ e^-$ and $\pi^0 \to e^+ e^- \gamma$

The large helicity suppression of the electromagnetic amplitude of the decay $\pi^0 \to e^+ e^-$ has led to speculations that additional contributions might be important. Anomalous quark-lepton

couplings could lead to significant enhancements of the value for this branching ratio. A branching ratio above the unitarity value would be a sign of CP violating neutral currents. The reaction $\pi^- p \to \pi^0 n$ at rest was used as a source of tagged mono - energetic π^0 in a search for the decay $\pi^0 \to e^+ e^-$ with the SINDRUM I spectrometer. The measurement resulted in [10]

$$B_{\pi^0 \to e^+ e^-} = \Gamma(\pi^0 \to e^+ e^-)/\Gamma(\pi^0 \to \gamma\gamma) < 1.3 \times 10^{-7} \text{ at } 90\% \text{ C.L.,} \tag{7.3}$$

consistent with the QED prediction $B_{\pi^0 \to e^+ e^-} = (6.5 \pm 0.5) \times 10^{-8}$. The combined result of two previous measurements, $B_{\pi^0 \to e^+ e^-} = (1.8 \pm 0.7) \times 10^{-7}$, had suggested sizeable additional contributions to the decay amplitude. This possibility seemed most likely ruled out by the SINDRUM result.

In the decay $\pi^0 \to e^+ e^- \gamma$, the hadronic structure of the pion is parameterized by a form factor $F = 1/(1 - ax)$ with $x = m_{e^+ e^-}/m_{\pi^0}$. The SINDRUM-I analysis of the Dalitz plot distribution measured the value as $a = 0.02 \pm 0.02 \pm 0.04$ [11] with the uncertainties being statistical and systematic, respectively. This value is consistent with the prediction of vector meson dominance of $a \approx 0.03$.

7.4 General description of the SINDRUM-I Apparatus

A schematic view of the SINDRUM spectrometer is given in Figure 7.3, with the coordinate system shown. With the help of the evacuated solenoid S, a surface muon beam with momentum 25 MeV/c and intensity 7×10^6 s^{-1} (produced by a 120 μA proton current extracted from the cyclotron) was refocussed from the entrance collimator to the target T, where it stopped. The target was a hollow double-cone shaped body of 58 mm diameter and 220 mm length made of Rohacell[1] with a thickness of 1 mm (11 mg/cm^2). The cylindrical magnet with a normal conducting coil M produced a homogeneous ($\Delta B/B < 1\%$) magnetic field of up to 0.6 T parallel to the symmetry axis (z-axis) in a volume of 110 cm length × 75 cm diameter. Tracks of decay particles were measured with five concentric self-supporting cylindrical multiwire proportional chambers C of low mass density. Three of them were equipped with cathode strips in order to obtain z-coordinates for three-dimensional reconstruction of tracks. For a field of $B = 0.334$ T, as used in the experiment, the momentum resolution is $\Delta p/p = (12.0 \pm 0.5)\%$ and $(8.5 \pm 0.5)\%$ (FWHM) for p = 50 MeV/c and 20 MeV/c, respectively. The angular resolution at the target is $\Delta \theta = (65 \pm 3)$ mrad (FWHM) for tracks of 20 MeV/c momentum. Fast timing signals were obtained from the cylindrical scintillator hodoscope H placed between the coil M and the chambers C. The 64 hodoscope elements were viewed at both ends by photomultipliers P. A time resolution of $\Delta t = 0.57$ ns (FWHM) between two hodoscope counters was obtained after correcting for walk and time of flight. The solid angle covered by the spectrometer was 0.73 of 4π.

7.5 The low mass multiwire proportional chamber (MWPC)

A main issue of concern for the design of SINDRUM was multiple scattering of the low-energy electrons. A very low mass for the target and the tracking chambers was a real challenge. The spectrometer was equipped with five very thin cylindrical MWPCs, three of which had cathode strip readouts. Each chamber consisted of two concentric Kapton/Rohacell sandwich cylinders, which were assembled on steel mandrels. Glass-fiber epoxy rings were glued to the ends of the cylinders supporting printed circuit rings onto which the 20μm anode wires, resistors, condensors, and multipin connectors were soldered. The cathodes of chambers 1, 3, and 5 consisted of strips of aluminum evaporated on Kapton having an angle of ±45° for the outer and inner cathodes, respectively. The strips were connected to end printed circuit boards

---

[1]Rohacell manufactured by Röhm Gmbh, Darmstadt, Germany
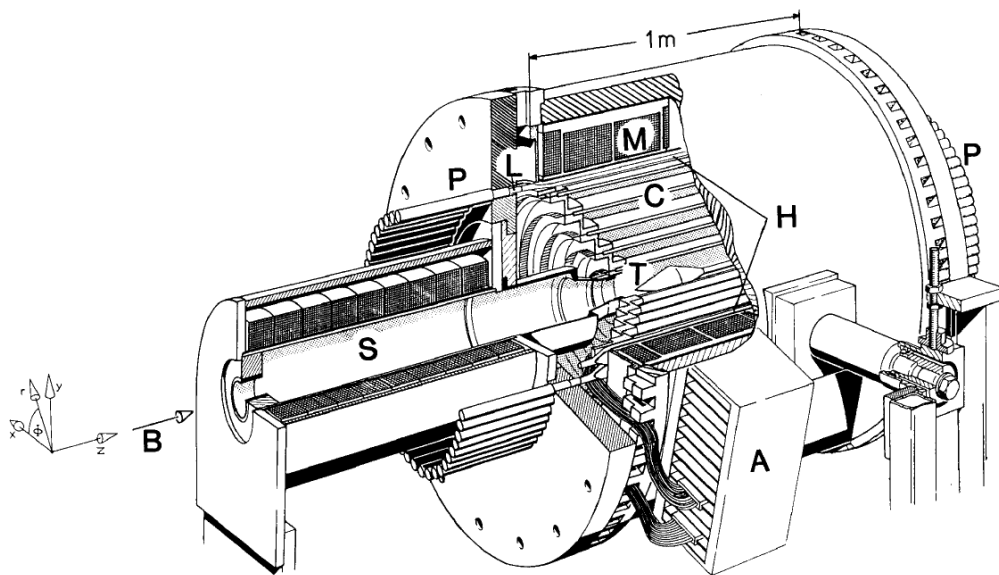
Figure 7.3: The SINDRUM I detector in the horizontal operating orientation.

with conductive paint. The strips of chamber 1 were divided in the middle and read out at both ends of the chamber to reduce the rate per strip. The chambers were operated with a gas mixture of 49.9% Ar, 49.9% C_2H_6 and 0.2% freon at a gas gain of $\sim 5 \times 10^4$. The chamber electrodes were connected through 1 m long 75Ω coaxial cables to the amplifiers mounted around the circumference of the magnet. The spatial resolution of the φ-measurement was limited by the wire spacing of 2 mm ($\sigma \simeq 0.6$ mm) and the z-resolution was determined with cosmic rays to be $\sigma \simeq 0.3$ mm. The chambers were successfully operated throughout the lifetime of the SINDRUM-I experiment. Their conception not only served as an important rôle model for part of the H1-detector construction at the HERA ring in Hamburg, but also laid ground for a very fruitful cooperation between ETH Zurich, Univ. of Zurich and SIN (PSI today).

7.6 Summary

The highlight of the SINDRUM-I experiment is clearly the improvement of the sensitivity on the rare decay $\mu^+ \to e^+e^-e^+$ by three order of magnitudes, reaching an upper limit $BR < 1.0 \times 10^{-12}$ at 90% C.L. The experiment was statistically limited and was not suffering from backgrounds. However, to gain another order of magnitude in precision, a much higher intensity of the muon beam would have been required. Thus, the successor experiment, SINDRUM-II, concentrated on the complementary muon-electron conversion process. As the SINDRUM-I detector resolution was not sufficient for competitive $\mu - e$-conversion measurements, a major upgrade of the detector was done, followed by measurements achieving best upper limits for $\mu - e$-conversion [12, 13].

Figure 7.4: The assembly of the SINDRUM I detector in the vertical orientation. The MWPC are being lowered into the setup by (clockwise from top left) Erwin Hermes (technician UZH), Norbert Kraus (PhD student UZH), Nik Lordong (Technician PSI), and within the setup Michael Doser (Master student ETHZ).

References

[1] Y. Kuno and Y. Okada, *Muon decay and physics beyond the standard model*, Rev. Mod. Phys. **73**, 151 (2001), doi:10.1103/RevModPhys.73.151.

[2] W. H. Bertl et al., *A new upper limit for the decay* $\mu^+ \to e^+e^+e^-$, Phys. Lett. B **140**, 299 (1984), doi:10.1016/0370-2693(84)90757-3.

[3] W. H. Bertl et al., *Search for the decay* $\mu^+ \to e^+e^+e^-$, Nucl. Phys. B **260**, 1 (1985), doi:10.1016/0550-3213(85)90308-6.

[4] U. Bellgardt et al., *Search for the decay* $\mu^+ \to e^+e^+e^-$, Nucl. Phys. B **299**, 1 (1988), doi:10.1016/0550-3213(88)90462-2.

[5] S. M. Korenchenko, B. F. Kostin, G. Mitselmakher, K. G. Nekrasov and V. S. Smirnov, *Search for* $\mu^+ \to e^+e^+e^-$ *decay*, Sov. Phys. JETP **43**, 1 (1976).

[6] S. Egli et al., *First observation of the decay* $\pi^+ \to e^+\nu_e e^+e^-$ *and a determination of the form-factors* F_A, F_V, R, Phys. Lett. B **175**, 97 (1986), doi:10.1016/0370-2693(86)90338-2.

[7] S. Egli et al., *Measurement of the decay $\pi^+ \rightarrow e^+ \nu_e e^+ e^-$ and search for a light Higgs boson*, Phys. Lett. B **222**, 533 (1989), doi:10.1016/0370-2693(89)90358-4.

[8] R. Eichler et al., *Limits for short-lived neutral particles emitted in μ^+ or π^+ decay*, Phys. Lett. B **175**, 101 (1986), doi:10.1016/0370-2693(86)90339-4.

[9] R. Meijer Drees et al., *Search for weakly interacting neutral bosons produced in $\pi^- - p$ interactions at rest and decaying into e^+e^- pairs.*, Phys. Rev. Lett. **68**, 3845 (1992), doi:10.1103/PhysRevLett.68.3845.

[10] C. Niebuhr et al., *Search for the decay $\pi^0 \rightarrow e^+ e^-$*, Phys. Rev. D **40**, 2796 (1989), doi:10.1103/PhysRevD.40.2796.

[11] R. Meijer Drees et al., *Measurement of the π^0 electromagnetic transition form factor*, AIP Conf. Proc. **243**, 657 (1992), doi:10.1063/1.41578.

[12] W. H. Bertl et al., *A Search for $\mu - e$ conversion in muonic gold*, Eur. Phys. J. C **47**, 337 (2006), doi:10.1140/epjc/s2006-02582-x.

[13] C. Dohmen et al., *Test of lepton flavor conservation in $\mu \rightarrow e$ conversion on titanium*, Phys. Lett. B **317**, 631 (1993), doi:10.1016/0370-2693(93)91383-X.

SINDRUM II

Andries van der Schaaf*

Physik-Institut der Universität Zürich, CH-8057 Zürich, Switzerland

* andries@physik.uzh.ch

Abstract

In 1987 a collaboration including ETHZ - UZH - PSI - RWTH Aachen - Univ. Tbilisi proposed a new search for μe conversion in muonic atoms. The SINDRUM II spectrometer came into operation in the μE1 area in 1989, but a dedicated beam line was delayed until 1998 by technical setbacks.

Check for
updates

8.1 Introduction

μe-Conversion in muonic atoms would result in the emission of an electron with energy

$$E_{\mu e} = m_\mu c^2 - B_\mu - R_N,\qquad(8.1)$$

with B_μ and R_N being the muon binding energy and nuclear recoil energy, respectively. $E_{\mu e}$ is the endpoint energy of muon decay in orbit (MIO) where the energies of the two outgoing neutrinos vanish. For gold $E_{\mu e} = 95.55$ MeV [1]. Around the time of the SINDRUM II proposal, the best limit obtained for a heavy target was B($\mu^- Pb\rightarrow e^- $Pb) $< 4.9 \times 10^{-8}$ (90% C.L.)) [2].

8.2 SINDRUM II

To distinguish conversion electrons from MIO background at the planned sensitivity level, the spectrometer was designed with an energy resolution around 1% FWHM. SINDRUM II used a superconducting solenoid [3], formerly operated at the CERN ISR (see Figure 8.1). Two plastic scintillator hodoscopes (D) and a lucite Cerenkov hodoscope (E) are used for timing and triggering. The electron momentum is determined from the tracks recorded in the inner radial drift chamber (F), filled with CO_2/iC_4H_{10} (70/30), a slow drift gas that results in a 6° Lorentz deflection. The geometric acceptance for conversion electrons, when requiring the particle to completely cross drift chamber F before reaching an endcap detector, is 44% of 4π sr. The axial sense wires are located close to the outer cathode foil which is subdivided into
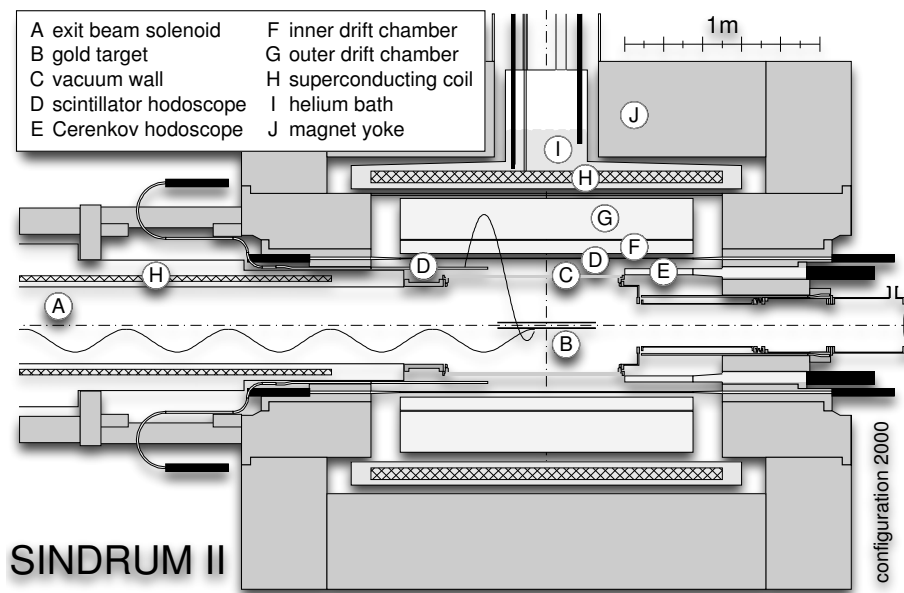
Figure 8.1: The SINDRUM II spectrometer as configured in the year 2000.

4.4 mm wide strips oriented 72° relative to the wires. Correlated signals from wires and strips allow a 3d track reconstruction. The outer radial drift chamber (G) used a He/iC4H10 (88/12) gas mixture, that has a large radiation length to reduce multiple scattering. Figure 8.2 shows the online display of a multi-turn event recorded in 1989 with beam on. Note the energy loss along the spiralling path through the spectrometer. As can be seen in Figure 8.3, consecutive turns are always well separated so later tracks do not interfere with the first, main turn. The left side of the peak allows sensitive checks of the material budget and the momentum resolution.
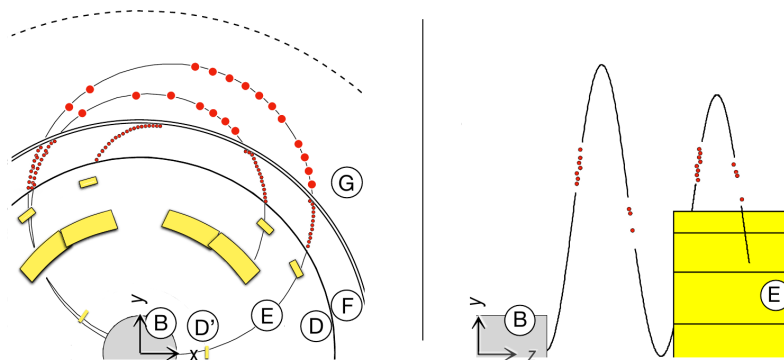
Figure 8.2: Traces of a 100 MeV/c e^- in *xy* and *zy* views. The particle shown made 2 1/2 turns before leaving the tracker. Labeling is as in Figure 8.1.

8.3 The beam line

A beam pion stopping in the target produces isotropic background through radiative pion capture, followed by asymmetric internal and external e^+e^- pair production, with a probability around 10^{-5} (see Section 8.5). Thus, no more than 10^4 pions may reach the target during the entire data-taking period. Muons penetrate twice as deep into matter as pions of the
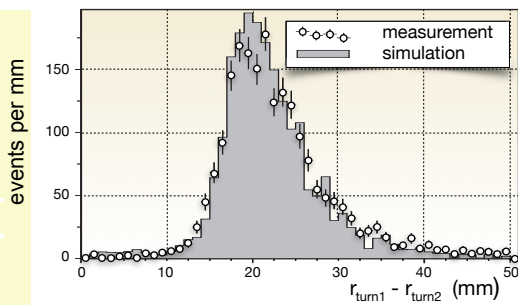
Figure 8.3: Change in radius of the first two turns of a multi-turn path caused by energy loss in the plastic hodoscope in particular. Thanks to this loss, the turns don't overlap, which otherwise might have confused the reconstruction.
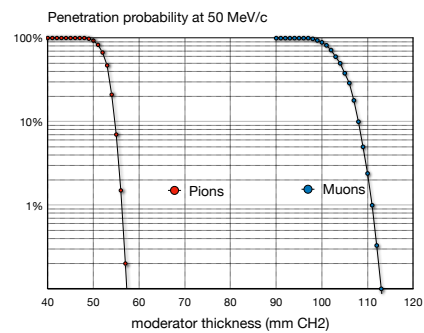
Figure 8.4: Simulated penetration probabilities of pions and muons in CH_2 at 50 MeV/c.

same momentum (see Figure 8.4). This was utilized to eliminate beam pions: the fraction eliminated is limited by the high-momentum tail of the beam. The pion contamination was reduced in three steps (see Figure 8.5). First a momentum-selected beam was focused on a wedge-shaped degrader inside a final bending magnet. The few pions that penetrate do so with a wide momentum spread and have little chance to reach a second degrader in a collimator at the entrance of the transport solenoid. The beam was studied in great detail with dedicated diagnostic tools to tune the settings of the magnets and the slits. In this process the high-momentum tail of the beam was reduced by two orders of magnitude. Muons crossed the degraders but only very few pions emerged to enter the solenoid. These pions are slow and 99.99% decayed before reaching the target.
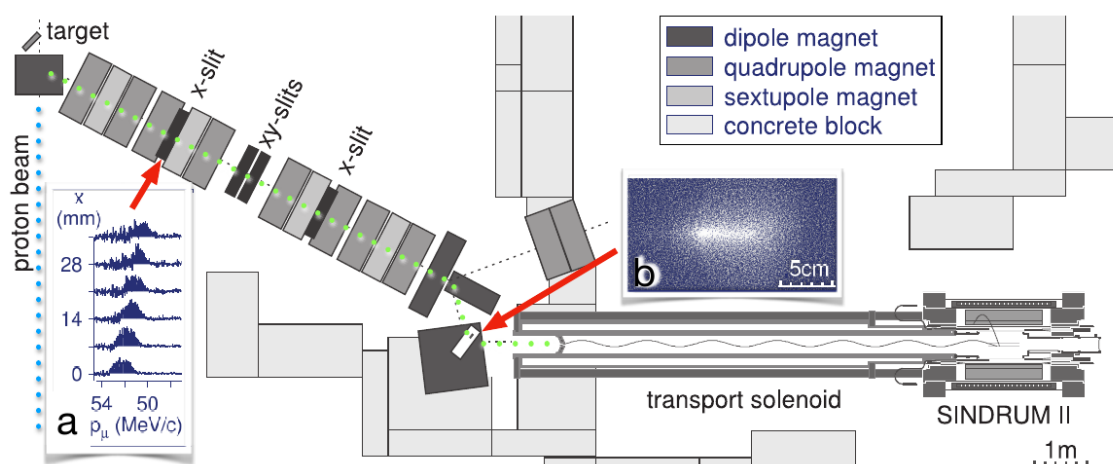
Figure 8.5: Plan view of the experiment at the $\pi E5$ secondary beam line during the final measuring period in the year 2000. A quadrupole channel extracted a beam with a similar amount of π's and μ's in the backward direction from the production target. Inset **a** shows the impact of the momentum slit in the first dispersive focus. The momentum was determined by time of flight, based on the 50 MHz cyclotron rf signal. Inset **b** shows a CCD image of the beam spot. From here muons were guided to the target by a 9 m long transport solenoid.
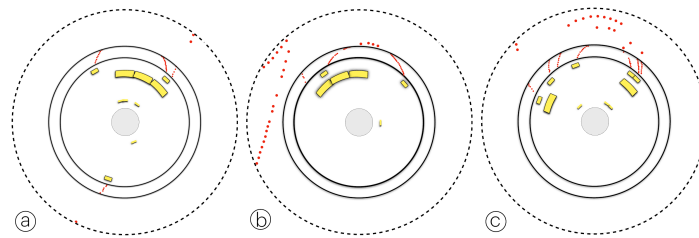
Figure 8.6: Three cosmic-ray events in the $r\phi$ projection. Signals recorded in the drift chambers (red), the plastic hodoscopes and Čerenkov counters (yellow) are indicated: a) a high momentum muon knocking an e^- out of a Čerenkov counter, b) a high momentum muon creating an e^+e^- pair in the magnet coil and c) an e^+ (most likely from the decay of a distant cosmic muon) spiraling in from outside.

Data was acquired even with the beam off as there are no beam counters in the final configuration. When requiring a circular track crossing drift chamber F, the trigger rate without beam was typically one per second. Figure 8.6 shows three examples.

8.4 Background

Cosmic-ray background was collected for more than a year with beam off: it can be recognized by the presence of additional signals in various detectors or by requiring the trajectory to originate in the target. What remains is associated with photons in cosmic-ray showers that enter through the cryogenic supply tower (see Figure 8.1). This background component was removed by an angular cut at the cost of a 5% loss in acceptance.

Another potential source of electrons with momenta around 100 MeV/c is radiative pion capture, mostly through intermediate photons producing asymmetric e^+e^- pairs, in the target. Pion capture is much more likely in the moderator inside the collimator at the entrance of the transport solenoid (see Figure 8.5) and the resulting electrons and positrons may easily reach the target where they may scatter into the detector solid angle. This background can be recognized as it is strongly peaked in the forward direction and it has a characteristic time correlation with the cyclotron rf signal.
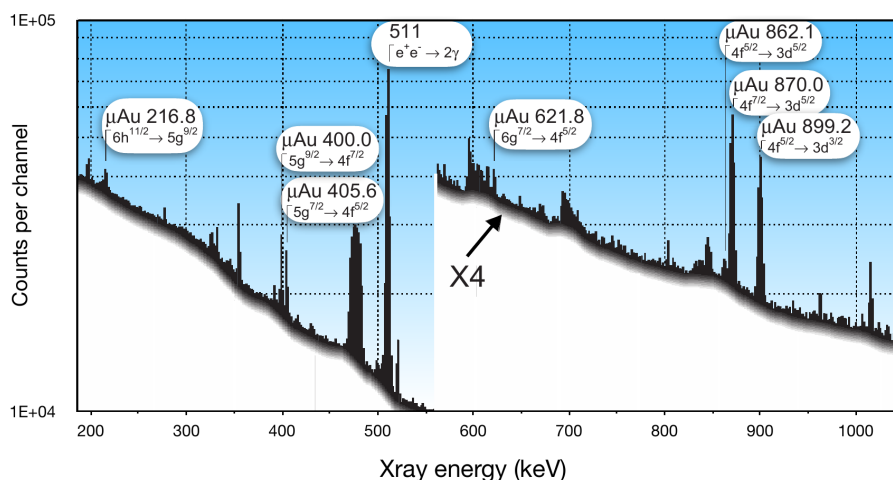
Figure 8.7: X ray spectrum recorded with a Ge(Li) detector during data taking to monitor the number of muons stopping in the gold target.

8.5 The 2000 data set

In the final 81-day period of data-taking in 2000 with a gold target,

$$N_{\mu stop} = (4.30 \pm 0.3_{stat} \pm 0.3_{sys}) \times 10^{13} \tag{8.2}$$

muons stopped in the target, as deduced from the muonic X-rays escaping the setup (see Figure 8.7). The monitor was calibrated with radioactive sources.

The analysis is based primarily on the momentum spectrum of electrons originating in the target. A cut is made on the position coordinates at the point of closest approach of the track to the central axis and is illustrated in Figure 8.8 for events surviving the cosmic-ray background checks.
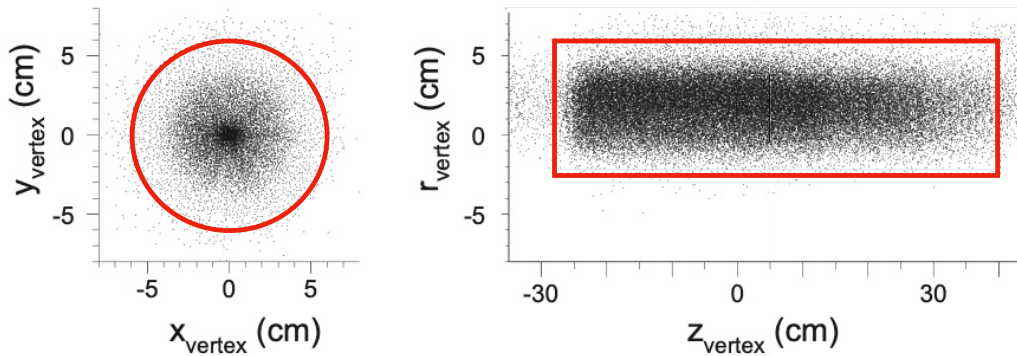
Figure 8.8:   Reconstructed point of closest approach to the z axis in the *xy* and *zr* projections. The contours indicate the selected target region.

The vast majority of the selected events are muon decays in orbit (MIO). Following Shanker, the MIO spectrum used as input for the GEANT simulation has been approximated by [4]

$$N(E)dE \propto \left(\frac{E}{m_\mu c^2} \right)^2 \left(\frac{E_{\mu e} - E}{m_\mu c^2} \right)^5 dE + h.c. \tag{8.3}$$

The rate is proportional to E^2 at the low energy end, as is known from the Michel spectrum. At the high energy end, the rate falls proportional to the missing (neutrinos) energy to the fifth power. As shown in Figure 8.9 there is fair agreement between measurement and MIO simulation.
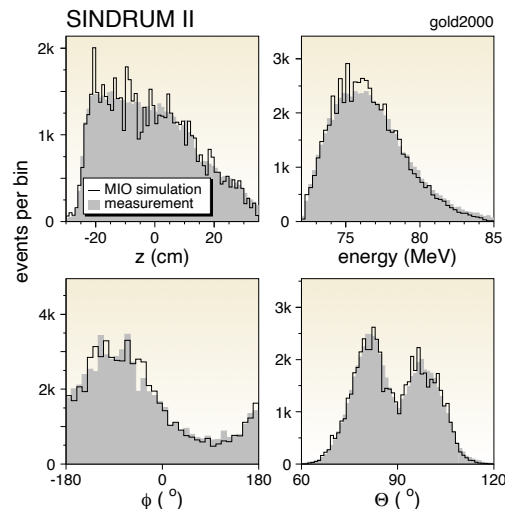
Figure 8.9:

Comparison of measurement and MIO simulation for four kinematic quantities.

The following comments may be helpful to explain some features:

- Muons come from $z<0$ and follow helical trajectories. Thus the stopping distribution falls from upstream to downstream.

- The fall of the rate at the low side of the energy distribution reflects the requirement that the electron crosses the inner drift chamber. This results in a transverse momentum threshold of around 70 MeV/c.

- There is a large ϕ anisotropy that is, however, antisymmetric about 0^0, as expected for the up-down symmetry of the beam line (horizontal bending plane).

- The dip at $\theta = 90^o$ results from e^-'s that need too many turns to reach an endcap.

The θ and ϕ distortions are threshold effects that disappear towards $E_{\mu e}$.

The upper end of the electron momentum distribution, measured with a 53 MeV/c stopped μ^- beam, is compared with distributions from simulations of bound muon decay and coherent μe conversion in Figure 8.10. The rate falls steeply towards $E_{\mu e}$ in agreement with the simulation, both in shape and in the number of events. Also shown are the results with 63 MeV/c stopped π^- showing the enormous background reaching up to the pion mass, and the familiar Michel spectrum taken with 48 MeV/c μ^+ beam. The μ^+ data were taken at reduced spectrometer field for increased acceptance at the lower momenta and give an independent check of the momentum calibration and resolution.
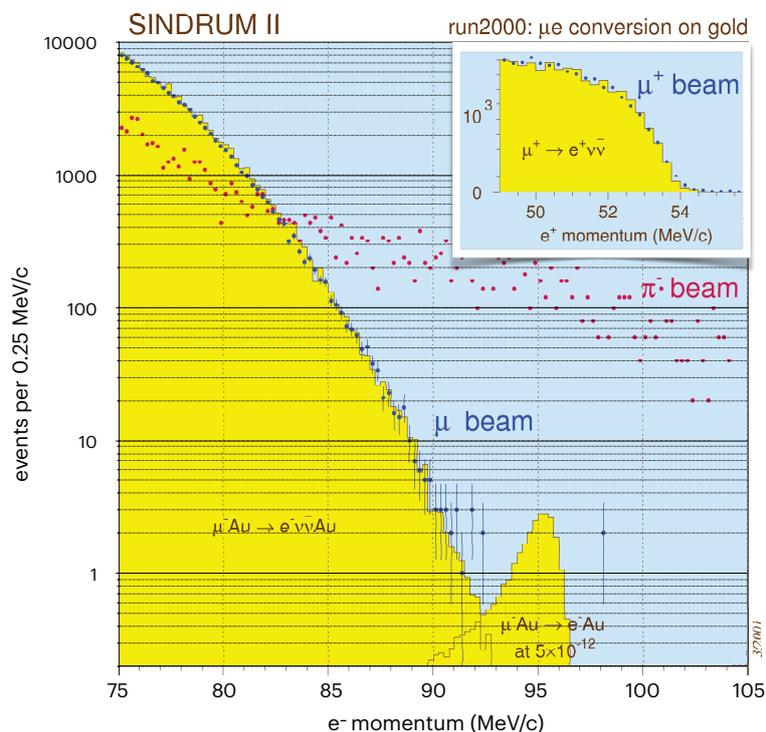
Figure 8.10: Momentum distributions for three different beam momenta and polarities: (i) 53 MeV/c negative muons, optimized for μ^- stops, (ii) 63 MeV/c negative pions, optimized for π^- stops, and (iii) 48 MeV/c positive muons, optimized for μ^+ stops. The 63 MeV/c data were normalized to the same measuring time. The measurement with the stopped μ^- beam is compared with GEANT simulations of decay in orbit and μe conversion.

No convincing signal events are observed in the main e^- momentum spectrum shown in Figure 8.10 and a maximum likelihood analysis of that spectrum results in a lowering of our own 90% C.L. upper limit by one and a half orders of magnitude. This result is included in Table 8.1 with all upper limits on $\mu^- e^-$ and $\mu^- e^+$ conversion obtained by SINDRUM II.

Table 8.1: SINDRUM II results over the years.

beam line	year meas.	process	beam MeV/c	days	stops	upper limit 90 % C.L.	Ref.
	1989	$\mu^- \text{Ti} \rightarrow e^- \text{Ti}$	100	25	$4.28(32) \times 10^{12}$	4.2×10^{-12}	[5]
$\mu E1$	1992	$\mu^- \text{Pb} \rightarrow e^- \text{Pb}$	86	10	$1.72(34) \times 10^{12}$	4.6×10^{-11}	[6]
	1993	$\mu^- \text{Ti} \rightarrow e^+ \text{Ca}$	86	60	$2.76(21) \times 10^{13}$	7.3×10^{-13}	[7]
$\pi E5$	1997	$\mu^- \text{Au} \rightarrow e^- \text{Au}$	20	24	7.6×10^{11}	1.91×10^{-11}	[8]
	2000	$\mu^- \text{Au} \rightarrow e^- \text{Au}$	53	81	$4.37(32) \times 10^{13}$	7×10^{-13}	[9]

8.6   Conclusions and outlook

After a decade long campaign, SINDRUM II took its final data in 2000. The resulting upper limits on μe conversion were pushed below 10^{-12}. The effort took longer and brought us not quite as far as was promised in the proposal but now, almost twenty years later, the SINDRUM limits still stand. The new more ambitious experiments are simply getting bigger, more complex, more expensive, require more manpower and often rely on new detector concepts and thus time consuming R&D.

There are two new efforts planning to continue where SINDRUM II ended: COMET (J-PARC, Japan) [10] and MU2E (Fermilab, U.S.A) [11]. Both use a pulsed beam and a delayed time window to fight prompt (pion) background which excludes heavy targets such as gold, with their correspondingly short decay times. Both use a staged approach, so with a bit of luck, new territory may be reached before the end of the decade.

The "search for nothing" keeps moving on!

References

[1] R. Watanabe et al., *Asymmetry and energy spectrum of electrons in bound-muon decay*, Atomic Data and Nuclear Data Tables **54**, 165 (1993), doi:10.1006/adnd.1993.1012.

[2] S. Ahmad et al., *Search for muon-electron and muon-positron conversion*, Phys. Rev. D **38**, 2102 (1988), doi:10.1103/PhysRevD.38.2102.

[3] M. Morpurgo, *Design and construction of a superconducting aluminium stabilized solenoid*, Cryogenics **17**, 89 (1977), doi:10.1016/0011-2275(77)90103-5.

[4] O. Shanker, *High-energy electrons from bound-muon decay*, Phys. Rev. D **25**, 1847 (1982), doi:10.1103/PhysRevD.25.1847.

[5] C. Dohmen et al., *Test of lepton-flavour conservation in $\mu \rightarrow e$ conversion on titanium*, Phys. Rev. Lett. **317**, 631 (1993), doi:10.1016/0370-2693(93)91383-X.

[6] W. Honecker et al., *Improved limit on the branching ratio of $\mu \rightarrow e$ conversion on lead*, Phys. Rev. Lett. **76**, 200 (1996), doi:10.1103/PhysRevLett.76.200.

[7] J. Kaulard et al., *Improved limit on the branching ratio of $\mu^- \to e^+$ conversion on titanium*, Phys. Lett. B **422**, 334 (1998), doi:10.1016/S0370-2693(97)01423-8.

[8] F. Riepenhausen, *Suche nach der Myon-Elektron-Konversion in Gold, $\mu^- Au \to e^- Au$*, Ph.D. thesis, Physik Institut, Zurich (1999).

[9] W. H. Bertl et al., *A Search for muon to electron conversion in muonic gold*, Eur. Phys. J. C **47**, 337 (2006), doi:10.1140/epjc/s2006-02582-x.

[10] R. Abramishvili et al., *Comet phase-i technical design report*, Prog. Theor. Exper. Phys. 033C01 (2020), doi:10.1093/ptep/ptz125.

[11] L. Bartoszek et al., *Mu2e technical design report* (2015), arXiv:1501.05241.

Muonium-antimuonium conversion

Lorenz Willmann* and Klaus Jungmann

Van Swinderen Institute, University of Groningen, 9747 AA, Groningen, The Netherlands

* L.Willmann@rug.nl

Abstract

The MACS experiment performed at PSI in the 1990s provided an yet unchallenged upper bound on the probability for a spontaneous conversion of the muonium atom, $M = (\mu^+ e^-)$, into its antiatom, antimuonium $\overline{M} = (\mu^- e^+)$. It comprises the culmination of a series of measurements at various accelerator laboratories worldwide. The experimental limits on the process have provided input and steering for the further development of a variety of theoretical models beyond the standard theory, in particular for models which address lepton number violating processes and matter-antimatter oscillations. Several models beyond the standard theory could be strongly disfavored. There is interest in a new measurement and improved sensitivity could be reached by exploiting the time evolution of the conversion process, e.g., at intense pulsed muonium sources.

9.1 Introduction

The bound state of a positive muon (μ^+) and an electron (e^-) is an exotic atom which has been named muonium (M) by V. Telegdi. This exotic atom was first produced and observed by V.W. Hughes and collaborators in 1960 [1]. It is well suited for precision experiments as it consists of two point-like leptons of different masses that belong to two different particle generations. The constituents of the M atom experience a rather long interaction time, which ultimately is limited by the muon lifetime $\tau_\mu = 2.2\ \mu s$ [2]. The M atom has been employed for series of precision measurements. The results can be used to make precise tests of theory, in particular Quantum Electrodynamics. Due to the absence of direct strong interactions between the two constituents, the properties of M can be calculated within the Standard Model (SM) to very high accuracy. Precise experiments yield accurate values of different fundamental constants such as the muon mass m_μ and the electromagnetic fine structure constant α. Further, tests of fundamental symmetries, among which are lepton universality and the equality of the muon and electron electric charges, q_e/q_μ, can be conducted, and scrutiny of lepton family number conservation is enabled [3].
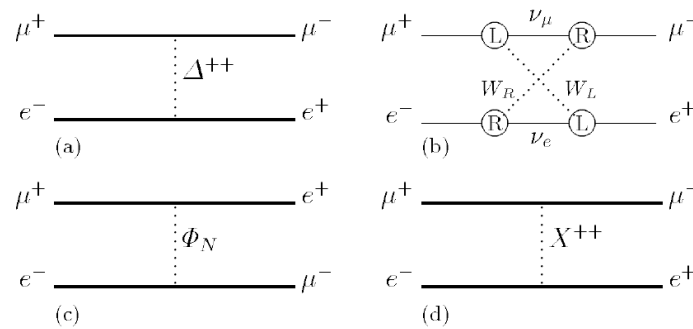
Figure 9.1: M-$\overline{\text{M}}$ conversion for various scenarios beyond the Standard Model. (a) Doubly charged Higgs bosons Δ^{++}, (b) heavy Majorana neutrinos, (c) neutral scalars Φ_N, , or(d) a bileptonic gauge boson X^{++} could mediate the process (from [4]).

Spontaneous conversion of muonium M into antimuonium $\overline{\text{M}}$ would violate additive lepton family (generation) number conservation by two units. Like other processes such as $\mu \to e\gamma$, $\mu \to eee$, $\mu + Z \to e + Z$ and the decay mode $\mu^+ \to e^+ + \nu_\mu + \overline{\nu_e}$ [2], M-$\overline{\text{M}}$ conversion is not allowed in the Standard Model. Charged leptons appear to observe lepton family number. There is no guidance from theory as to which of these various rare decay modes beyond the SM would be more favored by nature. Therefore searches for all of them are well motivated. A series of experiments searching for M-$\overline{\text{M}}$ conversion with ever increasing sensitivity was started in the mid 1960s. They yielded various strong limits on speculative theories [4], such as left-right symmetry, supersymmetry, 3-1-1 models and others (Figure 9.1). Numerous theoretical models have been proposed over the past decades [5–8], where lepton family number violation is a natural feature and where M-$\overline{\text{M}}$ conversion is an essential part.
Oscillations in the lepton sector between neutrinos of different flavors have been observed and are the subject of ongoing precision experiments [9] in a very active field. K^0-$\overline{K^0}$ and B^0-$\overline{B^0}$ oscillations are well established in the quark sector [2]. The K^0 particle consists of two quarks from the 1st and the 2nd quark generations, i.e., it is the quark analogue of M, which consists of charged leptons from the 1st and 2nd lepton generations. Non-observation of spontaneous conversion of M into $\overline{\text{M}}$ (or even oscillations between particle and antiparticle) makes it an intriguing puzzle waiting for explanation.
Historically the M-$\overline{\text{M}}$ conversion process has been described via effective four fermion interaction with a coupling constant $G_{M\overline{M}}$, which can be compared to the Fermi coupling constant G_F in weak interactions [10]. For a system starting as an M atom at time $t = 0$, we have at a later time t the probability

$$P_{M\overline{M}}(t) = \left(\frac{\delta t}{2\hbar}\right)^2 \cdot \exp\left(-\frac{t}{\tau_\mu}\right) \tag{9.1}$$

to observe it as $\overline{\text{M}}$, where

$$\delta = \frac{8G_F}{\sqrt{2}n^2\pi a_0^3} \frac{G_{M\overline{M}}}{G_F}, \tag{9.2}$$

with a_0 the M Bohr radius and n the atomic state principal quantum number. Integrating (9.1) over all times yields

$$P_{M\overline{M}} = 2.56 \cdot 10^{-5} \frac{G_{M\overline{M}}}{G_F}. \tag{9.3}$$

In external magnetic fields the degeneracy of energy levels in M and $\overline{M}$ is lifted and hence the conversion probability $P_{M\overline{M}}$ is reduced [11,12]. At a magnetic field strength of 1 kG the probability is reduced to $\approx 35\%$ its value at 0 kG.

Collisions of M atoms in gases or condensed matter lead to further substantial suppression of $P_{M\overline{M}}$, which can be orders of magnitude depending on the material density. The first search for M-$\overline{M}$ conversion at the NEVIS cyclotron was performed in 1 atm Ar gas, where M can be produced efficiently. Thus the experiment established a rather high limit of $G_{M\overline{M}} < 5800\,G_F$ [13]. Substantial progress was made after the discovery that M produced inside SiO_2 powder grains can emerge into a surrounding vacuum [14]. This discovery started a number of new and successful experiments (for more details see e.g. [15]).

9.2 The PSI M-$\overline{M}$ Experiment

The latest and most precise experiment was conducted with MACS, the Muonium Antimuonium Conversion Spectrometer at PSI. Data were taken at the PSI beamlines $\pi E3$ and $\pi E5$ [4]. In the course of 1730 h data taking M atoms were produced in a SiO_2 powder target from which they emerged with an efficiency of several per cent of the stopped muons into vacuum. A μ^+ beam momentum of order 21 MeV/c and a very narrow momentum bite of order 1 %, was essential for this rather high yield so that the μ^+ could be efficiently stopped near the surface of a fluffy SiO_2 powder target. In total the decay of $5.6(2) \cdot 10^{10}$ M atoms *in vacuo* were monitored. This permitted the establishment of a limit on the probability for M-$\overline{M}$ conversion of $P_{M\overline{M}} \leq 8.3(3) \cdot 10^{-11}$ (90% C.L.). This is a substantial improvement over previous other projects [2].

The MACS (Figure 9.2) design manifests the strong symmetry in the detection signatures for M and $\overline{M}$. The signature used for constant monitoring of M production rates provided for crucial calibration information of all parts of the detector with good accuracy. Monitoring the M yield every ≈ 5 h for ≈ 15 min proved indispensable as the SiO_2 targets deteriorated within a week. Targets were replaced once the yield had dropped by 50%. MACS has an acceptance of 0.71 sr for the detection of the Michel e^+/e^- and 4π extraction of the atomic shell e^-/e^+. The high energy decay e^-/e^+ are detected in the cylindrical magnetic spectrometer (SINDRUM I) operated at B = 1kG magnetic field. The magnetic spectrometer consisted of 5 proportional wire chambers equipped with cathode strip readout and a plastic scintillator hodoscope for timing purposes. SINDRUM I had been refurbished with a new electronic hardware pipeline system for the wire chambers which had 100 MHz clock rate and 256 cycle pipeline depth. The e^+/e^- from μ^+/μ^--decays have a continuous energy (Michel) spectrum with energies up to $E = 1/2 \cdot m_\mu \cdot c^2 = 53$ MeV. The momentum resolution for positrons at the highest energy has been determined to be 54(2)% in the spectrometer. This value was dominated by the 2 mm spacing between wires in the cylindrical wire chambers.

M ($\overline{M}$) atom decays were identified through a coincidence signature between high energy e^+ (e^-) from muon decay in the magnetic spectrometer, and the low energy atomic shell e^- (e^+) which was transported and detected at the MCP/CsI detector. The low energy particles had average kinetic energies equaling the M ($\overline{M}$) atomic binding energy $E_b = 13.6 eV$. The intrinsic 16(2)% efficiency of the MCP for 10 keV e^- (e^+) was enhanced 4-fold by a MgO coated C foil a few mm in front of it [16]. The pipeline readout system enabled an efficient readout after a trigger from the full coincidence. This resulted in a readout rate in $\overline{M}$ search mode of order a few s^{-1} for muon beam intensities of order $10^7\ s^{-1}$. The clean coincidence signature resulted in the suppression of the accidental combinatoric background to about 1 for the total collected statistics. The main limitation for further data collection arises from allowed physical processes. These are presented in Figure 9.3 which display sample time-of-flight (TOF) spectra of possible background as it arises from Bhabha scattering and the low energy tail of the decay $\mu \to 3e2\nu$.
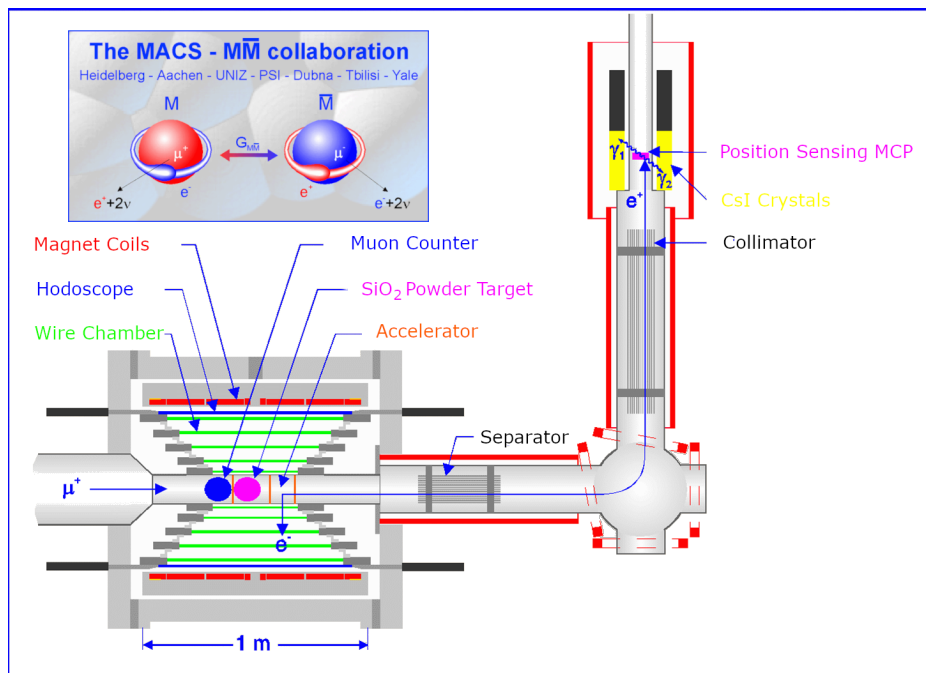
Figure 9.2: The MACS setup consists of the refurbished SINDRUM I magnetic spectrometer for detection of Michel e^+/e^- from μ^+/μ^--decay combined with a transport and imaging system for atomic shell e^-/e^+. The detector comprises maximum symmetry for the detection of M and $\overline{M}$. Switching between M-mode for monitoring M-production and $\overline{M}$-search-mode was achieved by reversing the magnetic field directions and changing the 10 keV extraction voltage polarity for the atomic shell particle remaining after $M/\overline{M}$-decay. The spectrometer consists of five cylindrical wire chambers and a hodoscope for timing. The axial magnetic field in the transport system provided for axial confinement and retracing of the position information from a microchannel plate (MCP) detector to obtain the decay vertex with 8.0(4)mm resolution. Further background suppression in $\overline{M}$-mode is provided by an electrostatic separator and a collimator in the transport system as well as e^+ identification via annihilation γ s in CsI crystals near the MCP.

The M-$\overline{M}$ experiment collected data in three stages. Between these stages several substantial upgrades were implemented. In particular using a cathode strip readout of the wire chambers proved essential since it improved the 3D reconstruction of the vertex between the Michel particle and the low energy atomic shell particle detected on the position sensitive MCP detector. Data were recorded for a total of 1730h in the overall experiment. One candidate event survived the analysis with stringent cuts on the reconstructed vertex, TOF and required 511 keV γ-detection for positron identification (Figure 9.4). The resulting limit on $P_{M\overline{M}}$ corresponds to an upper limit on the coupling constant in an effective 4 fermion coupling of $G_{M\overline{M}} < 3.0 \cdot 10^{-3}$ G_F. The experiment was limited in its sensitivity by physical background in the acceptance of the detector.

9.3 Conclusions

M-$\overline{M}$ conversion is of great interest and new experiments with improved apparatus exploiting the time dependence of the conversion process could reach substantially more stringent bounds [15]. In the recent years the upper limit established in the MACS experiment has been
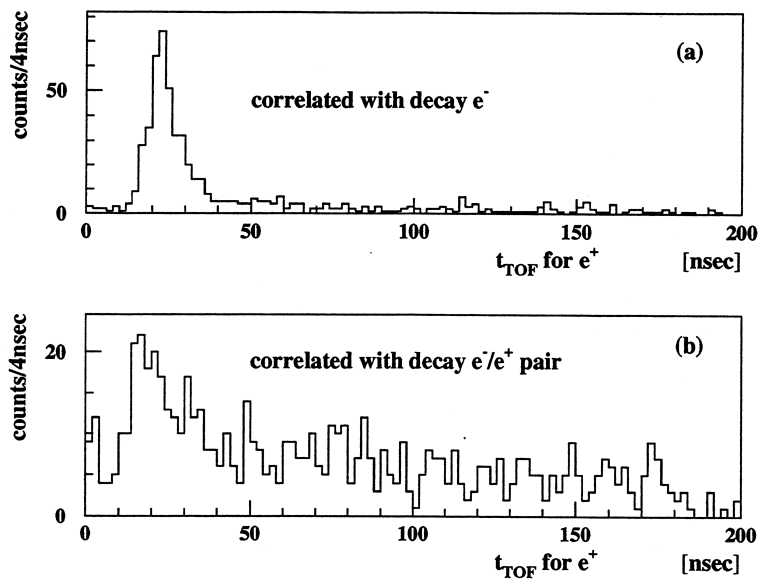
Figure 9.3: Dominant physical background observed in 440 h of running when relaxing the stringent coincidence requirements. (a) Bhabha scattering of Michel e$^+$ electrons in the support structure. (b) A small fraction of phase space for allowed $\mu \rightarrow 3e2\nu$ decay results in e$^+$/e$^-$ pairs detected by the magnetic spectrometer coincident with a low energy e$^+$ within the acceptance of the detector. The expected arrival time for a e$^+$ from $\overline{\text{M}}$-decay is 78.1(1)ns.

exploited to disfavor single flavor-violating axion-like particle (ALP) based explanations for anomalies observed in electron and muon g-2 measurements [6]. Improved future M-$\overline{\text{M}}$ experiments can probe a similar parameter space as experiments at a future lepton collider which are searching for charged lepton flavor violation via, e.g., on-shell production of bileptons [7]. In view of this a new M-$\overline{\text{M}}$ would be very well motivated.

Since the MACS experiment reached its possible sensitivity limit, an improved concept and a refined setup are required to establish tighter bounds. At a pulsed muon source one can benefit from exploiting the time evolution of the conversion process [15]. All muon decay related background decreases on a time scale given by the μ^+ lifetime. For an n-fold coincidence signature this background drops significantly with $\exp(-\text{n} \cdot \frac{t}{\tau_\mu})$. The probability of finding $\overline{\text{M}}$ grows in time to a maximum at $2\tau_\mu$ (see Figure 9.5). Thus the ratio of M to $\overline{\text{M}}$ decays grows with t^2. In case of a multiple coincidence, as in MACS, this implies that the potential $\overline{\text{M}}$ signal/background increased. Therefore a new experiment should be considered, e.g., in connection with the muon source of a muon collider, provided high muon beam quality, i.e. a narrow μ^+ momentum band at subsurface μ^+ momentum. We note that for such an improved experiment beam repetition rates of up to several 10 kHz with μ^+ bunches of up to $\approx \mu s$ length would be ideal.

With a new experiment, from the viewpoint of signal to background ratio, an improved value for $\text{G}_{\text{M}\overline{\text{M}}}$ by at least 2 orders of magnitude should be possible, i.e., 4 orders of magnitude in the conversion probability. At such sensitivity there would be strong constraints for the development of models beyond standard theory [5–8].
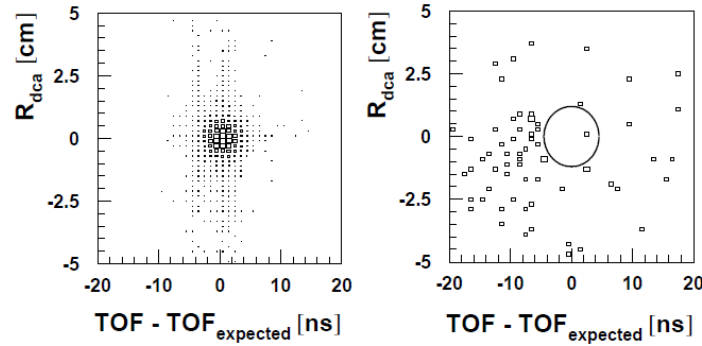
Figure 9.4: The distribution of the distance of closest approach R_{dcad} between a trace from a particle registered in the magnetic spectrometer and the back-projected position on the MCP as a function of the TOF for the atomic shell particle as measured for M atoms (left). The data recorded in the final data-taking period of 1290h searching for $\overline{M}$ (right).
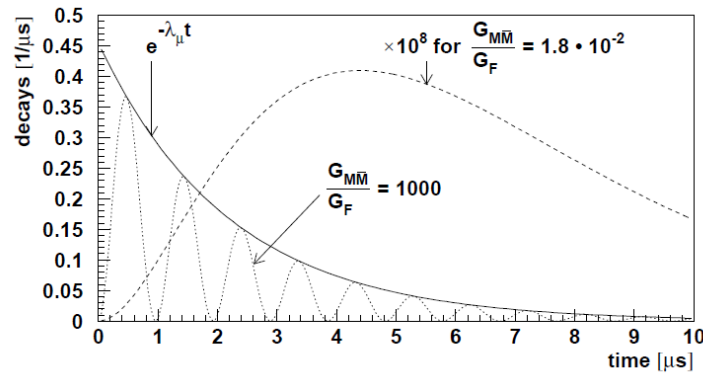
Figure 9.5: The probability for observing an $\overline{M}$ decay increases with time and reaches a maximum at about $2\tau_{\mu}$. In particular he ratio of $\overline{M}$ to μ^+-decays increases further with time. Therefore an enhanced signal to background ratio could be expected from experiments in which the time from M formation and the subsequent M- or $\overline{M}$-decay can recorded [15]. This would favor future experiments at intense future pulsed muon sources [17].

Acknowledgments

References

[1] M. E. Zeller, ed., *A Festschrift in honor of Vernon W. Hughes*, Proceedings, Symposium, New Haven, USA (1992).

[2] M. Tanabashi et al., *Review of particle physics*, Phys. Rev. D **98**, 030001 (2018), doi:10.1103/PhysRevD.98.030001.

[3] K. P. Jungmann, *Precision muonium spectroscopy*, J. Phys. Soc. Jpn. **85**, 091004 (2016), doi:10.7566/JPSJ.85.091004.

[4] L. Willmann et al., *New bounds from a search for muonium to antimuonium conversion*, Phys. Rev. Lett. **82**, 49 (1999), doi:10.1103/PhysRevLett.82.49.

[5] A. Ilakovac, *Lepton flavor violation in the standard model extended by heavy singlet dirac neutrinos*, Phys. Rev. D **62**, 036010 (2000), doi:10.1103/PhysRevD.62.036010.

[6] M. Endo, S. Iguro and T. Kitahara, *Probing eμ flavor-violating ALP at Belle II*, J. High Energy Phys. **06**, 040 (2020), doi:10.1007/JHEP06(2020)040.

[7] T. Li and M. A. Schmidt, *Sensitivity of future lepton colliders and low-energy experiments to charged lepton flavor violation from bileptons*, Phys. Rev. D **100**, 115007 (2019), doi:10.1103/PhysRevD.100.115007.

[8] P. Bhupal Dev and Y. Zhang, *Displaced vertex signatures of doubly charged scalars in the type-II seesaw and its left-right extensions*, J. High Energy Phys. **10**, 199 (2018), doi:10.1007/JHEP10(2018)199.

[9] J. Bernabeu, *Symmetries and their breaking in the fundamental laws of physics*, Symmetry-Basel **12**, 1316 (2020), doi:10.3390/sym12081316.

[10] G. Feinberg and S. Weinberg, *Conversion of muonium into antimuonium*, Phys. Rev. **123**, 1439 (1961), doi:10.1103/PhysRev.123.1439.

[11] K. Horikawa and K. Sasaki, *Muonium-antimuonium conversion in models with dilepton gauge bosons*, Phys. Rev. D **53**, 560 (1996), doi:10.1103/PhysRevD.53.560.

[12] W.-S. Hou and G.-G. Wong, *Muonium-antimuonium transitions via neutral scalar bosons*, Phys. Rev. D **53**, 1537 (1996), doi:10.1103/PhysRevD.53.1537.

[13] J. Amato, P. Crane, V. Hughes, J. Rothberg and P. Thompson, *Search for muonium-antimuonium conversion*, Phys. Rev. Lett. **21**, 1709 (1968), doi:10.1103/PhysRevLett.21.1709.

[14] G. Marshall, J. Warren, D. Garner, G. Clark, J. Brewer and D. Fleming, *Production of thermal muonium in vacuum between grains of fine silica powders*, Phys. Lett. A **65**, 351 (1978), doi:10.1016/0375-9601(78)90727-2.

[15] L. Willmann and K. Jungmann, *The muonium atom as a probe of physics beyond the standard model*, Lect. Notes Phys. **499**, 43 (1997), doi:10.1007/BFb0104314.

[16] P. Schmidt et al., *An efficient position sensitive detector for 3 to 30 kev positrons and electrons*, Nucl. Instr. Meth. Phys. Res. Sec. A **376**, 139 (1996), doi:https://doi.org/10.1016/0168-9002(96)00267-7.

[17] J. Äystö et al., *Physics with low-energy muons at a neutrino factory complex* (2001), arXiv:hep-ph/0109217.

The mass of the π^-

M. Daum[1] and D. Gotta[2]⋆

1 Paul Scherrer Institut, 5232 Villigen PSI, Switzerland
2 Institut für Kernphysik, Forschungszentrum Jülich, 52425 Jülich, Germany

⋆ d.gotta@fz-juelich.de

Abstract

The most precise values of the mass of the negatively charged pion have been determined from several measurements of X-ray wavelengths for transitions in pionic atoms at PSI. The Particle Data Group gives the average $m_{\pi^-} = (139.570\,61 \pm 0.000\,24)$ MeV/c^2.

10.1 Introduction

The most accurate determination of the mass of the negatively charged pion, m_{π^-}, is obtained from measurements of X-ray transition energies in pionic atoms. X-rays stem from a de-excitation cascade after capture into high-lying atomic states of a nucleus N_Z^A with mass number A and charge Z.

The atomic binding energies E_{nl} are directly related to the reduced mass μ of the πN_Z^A system. The relativistic description of E_{nl} is given for spin 0 particles by [1]

$$E_{nl} = \frac{-\mu c^2}{2}\left(\frac{Z\alpha}{n}\right)^2\left[1+\left(\frac{Z\alpha}{n}\right)^2\left(\frac{n}{l+1/2}-\frac{3}{4}\right)\right]+\mathcal{O}\left[(Z\alpha)^6\right]. \qquad (10.1)$$

Here, n and l are the principal and angular momentum quantum numbers of the atomic level, respectively, and α is the fine structure constant. The leading term of $\mathcal{O}\left[(Z\alpha)^2\right]$ coincides with the well-known Bohr formula. (10.1) holds for $Z \lesssim 1/(2\alpha) = 68$.

For high-precision experiments, further contributions to E_{nl}, not included in (10.1), must be considered. Most important are QED effects, i.e. vacuum polarization, relativistic recoil ($\mathcal{O}\left[(Z\alpha)^4\right]$), as well as hyperfine and strong-interaction shifts. Recent QED calculations achieve an accuracy of $\leq \pm 1$ meV for pure electromagnetic transition energies [2].

10.2 Measurements at PSI

New measurements began following discussions of muon neutrino mass limits, aiming at a precision of about 1 ppm for the mass of the π^-. The three most recent and precise determinations of m_{π^-} [3] were performed at PSI, using the high pion fluxes available there. The X-ray transition energies E_X are obtained via the measurement of the angle of diffraction, the Bragg angle Θ_B, with crystal spectrometers by using Bragg's law $n\lambda = 2d \cdot \sin\Theta_B$, where n is the order of reflection, $\lambda = h/E_X$ the X-ray's wave length, h Planck's constant, and d the lattice constant of the corresponding crystal planes.
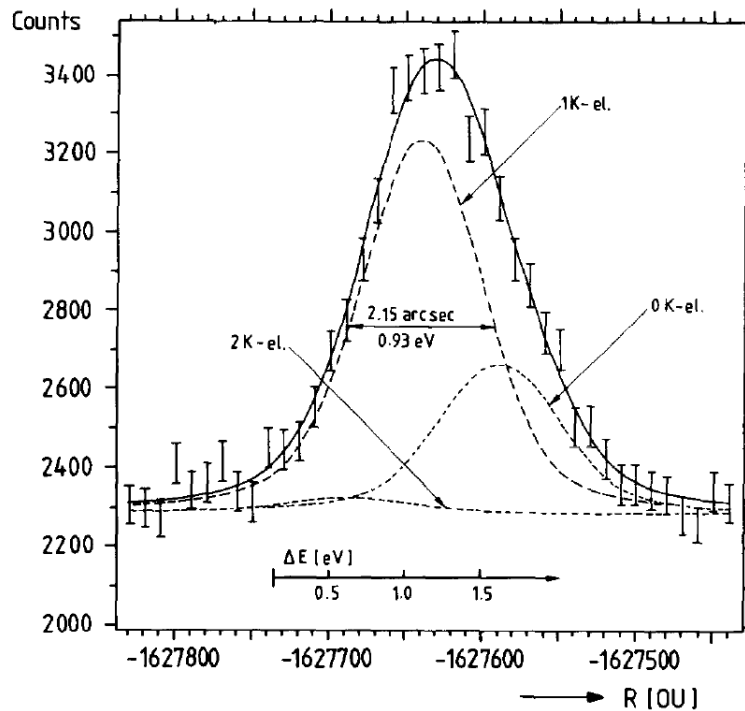
Figure 10.1: Bragg reflection of the $(4f - 3d)$ transition in pionic ^{24}Mg measured with a (110) quartz crystal in third order of diffraction; x-axis: R is the interferometer read-out in optical units (OU). The fit function is marked by the solid line; it is the sum of three individual peaks corresponding to the cases of having two, one or zero K-electrons present during the pionic transition. The line shapes of the different peaks are obtained by folding the instrumental response function with the natural line width of the transition (from [4,5]).

In the first of these experiments, a DuMond crystal spectrometer was used to measure the πMg$(4f - 3d)$ transition at 26.9 keV in a solid magnesium target [4,5]. Energy calibration and experimental resolution were provided by the 25.7 keV γ line from ^{161}Tb decay. The observed line width, however, was larger than the instrumental resolution of 0.93 eV (Figure 10.1). This was attributed to the occurrence of different populations of the electronic K shell and, consequently, different screenings of the nuclear charge. Based on a measurement of the intensity balance of the sum of the $(nf - 3d)$ transitions to the $(3d - 2p)$ line, which yielded a K electron shell population of (0.44 ± 0.30), it was originally assumed that the strongest component in the spectrum corresponds to one K-shell electron. The corresponding result for the pion mass (solution A) is given in Table 10.1 - entry 1986.

Later, this result came into strong disagreement with the continuously improved precision measurements of the muon momentum p_{μ^+} from pion decay at rest $\pi^+ \to \mu^+ \nu_\mu$ [9–11]. The

Table 10.1: Recent results for the mass of the negatively charged pion. The PDG derived an average from the entries 1994, 1998, and 2016. The uncertainty includes a scale factor of 1.6. Earlier measurements have been omitted as they may have incorrect K-shell screening corrections [3].

year	method	m_{π^-} / MeV/c^2	reference
1986	πMg$(4f-3d)/^{161}$Tbγ (A)	$139.568\,71 \pm 0.000\,53$	[4,5]
1994	πMg$(4f-3d)/^{161}$Tbγ (B)	$139.569\,95 \pm 0.000\,37$	[6]
1998	πN$(5g-4f)/$Cu Kα	$139.570\,71 \pm 0.000\,53$	[7]
2016	πN$(5g-4f)/\mu$O$(5g-4f)$	$139.570\,77 \pm 0.000\,18$	[8]
2018	π^- PDG average	$139.570\,61 \pm 0.000\,23$	[3]

lower limit thus derived for m_{π^+} was 3.5 standard deviations higher than the world average for m_{π^-} as obtained from pionic magnesium. In addition, the squared muon neutrino mass determined from p_{μ^+} and m_{π^-} then became negative by 6 standard deviations [10,11].

A re-assessment of the π^-Mg$(4f-3d)$ line shape experiment led to the conclusion that when interpreting the strongest component in Figure 10.1 as the two K-electron contribution [6], the above-mentioned discrepancy in the m_{π^+} results is removed. The alternative value for m_{π^-} (solution B) is given in Table 10.1 - entry 1994. This is in line with the discussion on the ionization state during the de-excitation cascade, which assumes a continuous refilling of electrons for metals [12].

In view of the importance of the questions involved, a new measurement of the π^- mass was undertaken [7]. The increased pion flux resulting from the larger proton current in the PSI cyclotron allowed the use of the cyclotron trap [13,14], gas targets of about 1 bar pressure (NTP), and a Johann-type crystal spectrometer. The big advantage of gaseous targets is that K-electron contamination is expected to be small [12].

The $(5g-4f)$ transition in pionic nitrogen is an ideal candidate. With an energy of 4.055 keV, the reflectivity of silicon Bragg crystals in second order and the efficiency of X-ray detectors are close to optimum. The copper Kα_1 fluorescence line of 8.048 keV provides the energy calibration at practically the same Bragg angle when measured in fourth order [7]. As in the πMg case, different electron screening contributions would be apparent as distortions of the line shape. The energy shift due to one (two) K electron(s) is $-456\,(-814)$ meV, while the spectrometer resolution is about 450 meV. The natural line width of 8 meV is negligibly small, and strong-interaction effects in the $4f$ level can be estimated sufficiently accurate. The mass value derived from the πN$(5g-4f)$ transition (Figure 10.2) is in agreement both with solution B of the πMg experiment [6] and the results deduced from π^+-decay [10,11] (Table 10.1 - entry 1998).

In a second experiment, the two shortcomings of the Cu calibration were avoided: (i) Spectra of fluorescence X-rays always include satellite lines from multiple ionization depending on details of the excitation conditions. Therefore, measured energies may slightly deviate from published reference values. (ii) Measuring in different orders of reflection requires substantial corrections to the Bragg angle resulting in additional uncertainties [7].

A comparison of X-ray transition energies shows a near coincidence for μO and πN. The muonic line provides an accurate calibration due to the precise knowledge of the muon mass to 23 ppb [3,15,16]. Choosing again the $(5g-4f)$ lines for both atoms and using a O$_2$/N$_2$ gas mixture allows a simultaneous measurement in the same order of reflection without any manipulation of the set-up [8] (Figure 10.3). The result of this measurement agrees well with the previous πN measurement [7] (Table 10.1 - entry 2016).
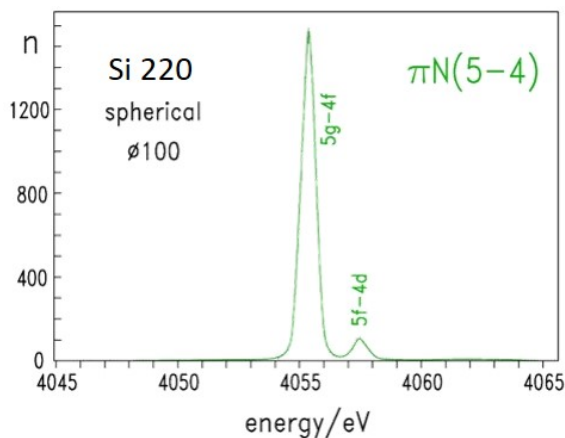
Figure 10.2: πN(5 − 4) complex measured with a spherically bent Si(110) crystal in 2nd order. The pion mass is determined from the energy of the πN(5g − 4f) transition (adapted from [7]).

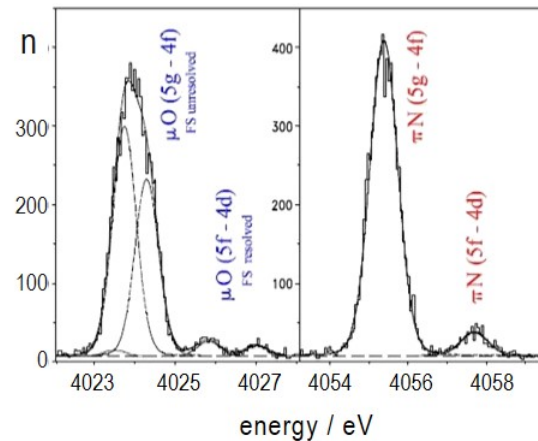Figure 10.3: πN and μO (5g − 4f) transitions from the simultaneous measurement with an O$_2$/N$_2$ (10%/90%) gas mixture at 1.4 bar pressure (adapted from [8]).

The measured πN and μO line widths are $\approx$ 800 meV, much larger than the spectrometer resolution. The increase of the widths is due to Doppler broadening from Coulomb explosion, a recoil effect appearing in molecules [17], and, in contrast to πMg, not to any electron screening. The analysis of the πN(5g − 4f) line shape provides an upper limit for the K-electron contamination of 10^{-6}, which is much less than the 10% predicted by cascade calculations [18], but corroborates the results from experiments measuring the density dependence of X-ray yields [19]. Measuring the fine-structure splitting generated by the angular momentum dependence in pionic atoms, gives the best available test of the Klein-Gordon equation, (10.1). The recent πN(5−4) measurement (Figure 10.3) achieves an accuracy of 0.4% for the fine-structure splitting [7], which improves earlier tests [20, 21] by one order of magnitude.

In conclusion, the present study demonstrates the potential of crystal spectroscopy with bent crystals in the field of exotic atoms. As an application, X-rays of hydrogen-like pionic atoms can be used to provide calibration standards in the few keV range, where suitable radioactive sources are not available [22]. The accuracy of such standards is given by the present uncertainty of the pion mass [2].

Facing the fact that pion beams at PSI provide a flux of about 10^9/s, the use of double-flat crystal spectrometers may be considered allowing for absolute angle calibrations choosing specific narrow hydrogen-like pionic transitions not affected by Coulomb explosion, e. g. from pionic neon. A precision for the pion mass determination of the order of 0.5 ppm would be feasible. A method based on laser spectroscopy of metastable pionic helium, if successfully applied, could further improve significantly on the accuracy for the π^- mass [23–25].

References

[1] T. Ericson and W. Weise, *Pions and Nuclei*, Clarendon Press, New York (1988).

[2] M. Trassinelli and P. Indelicato, *Relativistic calculations of pionic and kaonic atoms hyperfine structure*, Phys. Rev. A **76**, 012510 (2007), doi:10.1103/PhysRevA.76.012510.

[3] M. Tanabashi et al., *Review of particle physics*, Phys. Rev. D **98**, 030001 (2018), doi:10.1103/PhysRevD.98.030001.

[4] B. Jeckelmann et al., *New precision determination of the π^- mass from pionic X-rays*, Phys. Rev. Lett. **56**, 1444 (1986), doi:10.1103/PhysRevLett.56.1444.

[5] B. Jeckelmann et al., *New precision determination of the π^- mass from pionic X-rays*, Nucl. Phys. A **457**, 709 (1986), doi:10.1016/0375-9474(86)90476-8.

[6] B. Jeckelmann, P. F. A. Goudsmit and H. J. Leisi, *The mass of the negative pion*, Phys. Lett. B **335**, 326 (1994), doi:10.1016/0370-2693(94)90358-1.

[7] S. Lenz et al., *A new determination of the mass of the charged pion*, Phys. Lett. B **416**, 50 (1998), doi:10.1016/S0370-2693(97)01337-3.

[8] M. Trassinelli et al., *Measurement of the charged pion mass using X-ray spectroscopy of exotic atoms*, Phys. Lett. B **759**, 583 (2016), doi:10.1016/j.physletb.2016.06.025, 1605.03300.

[9] M. Daum, R. Frosch, D. Herter, M. Janousch and P. R. Kettle, *New precision measurement of the muon momentum in pion decay at rest*, Phys. Lett. B **265**, 425 (1991), doi:10.1016/0370-2693(91)90078-5.

[10] K. Assamagan et al., *Measurement of the muon momentum in pion decay at rest using a surface muon beam*, Phys. Lett. B **335**, 231 (1994), doi:10.1016/0370-2693(94)91419-2.

[11] K. Assamagan et al., *Upper limit of the muon-neutrino mass and charged pion mass from momentum analysis of a surface muon beam*, Phys. Rev. D **53**, 6065 (1996), doi:10.1103/PhysRevD.53.6065.

[12] R. Bacher, D. Gotta, L. M. Simons, J. H. Missimer and N. C. Mukhopadhyay, *On Muonic Atoms With Vacant Electron Shells*, Phys. Rev. Lett. **54**, 2087 (1985), doi:10.1103/PhysRevLett.54.2087.

[13] L. M. Simons, *Recent results on anti-protonic atoms using a cyclotron trap at LEAR*, Phys. Scripta 90 (1988), doi:10.1088/0031-8949/1988/T22/013.

[14] L. M. Simons, *The cyclotron trap for antiprotons*, Hyperfine Interact. **81**, 253 (1993), doi:10.1007/BF00567270.

[15] W. Liu et al., *High precision measurements of the ground state hyperfine structure interval of muonium and of the muon magnetic moment*, Phys. Rev. Lett. **82**, 711 (1999), doi:10.1103/PhysRevLett.82.711.

[16] P. J. Mohr, D. B. Newell and B. N. Taylor, *CODATA recommended values of the fundamental physical constants: 2014*, Rev. Mod. Phys. **88**, 035009 (2016), doi:10.1103/RevModPhys.88.035009, 1507.07956.

[17] T. Siems, D. F. Anagnostopoulos, G. Borchert, D. Gotta, P. Hauser, K. Kirch, L. M. Simons, P. El-Khoury, P. Indelicato, M. Augsburger, D. Chatellard and J.-P. Egger, *First direct observation of Coulomb explosion during the formation of exotic atoms*, Phys. Rev. Lett. **84**, 4573 (2000), doi:10.1103/PhysRevLett.84.4573.

[18] V. R. Akylas and P. Vogel, *Muonic atom cascade program*, Comput. Phys. Commun. **15**, 291 (1978), doi:10.1016/0010-4655(78)90099-1.

[19] K. Kirch, D. Abbott, B. Bach, P. Hauser, P. Indelicato, F. Kottmann, J. Missimer, P. Patte, R. T. Siegel, L. M. Simons and D. Viel, *Muonic cascades in isolated low-Z atoms and molecules*, Phys. Rev. A **59**, 3375 (1999), doi:10.1103/PhysRevA.59.3375.

[20] K. C. Wang, F. Boehm, A. A. Hahn, H. E. Henrikson, J. P. Miller, R. J. Powers, P. Vogel, J. L. Vuilleumier and R. Kunselman, *Experimental determination of the relativistic fine structure splitting in a pionic atom*, Phys. Lett. B **79**, 170 (1978), doi:10.1016/0370-2693(78)90461-6.

[21] L. Delker, G. Dugan, C. S. Wu, D. C. Lu, A. J. Caffrey, Y. T. Cheng and Y. K. Lee, *Experimental verification of the relativistic fine-structure term of the Klein-Gordon equation in pionic titanium atoms*, Phys. Rev. Lett. **42**, 89 (1979), doi:10.1103/PhysRevLett.42.89.

[22] D. F. Anagnostopoulos, D. Gotta, P. Indelicato and L. M. Simons, *Low-energy X-ray standards from hydrogenlike pionic atoms*, Phys. Rev. Lett. **91**, 240801 (2003), doi:10.1103/PhysRevLett.91.240801.

[23] M. Hori, V. I. Korobov and A. Sótér, *Proposed method for laser spectroscopy of pionic helium atoms to determine the charged-pion mass*, Phys. Rev. **A 89**, 042515 (2014), doi:10.1103/PhysRevA.89.042515.

[24] M. Hori, H. Aghai-Khozani, A. Sótér, A. Dax and D. Barna, *Laser spectroscopy of pionic helium atoms*, Nature **581**, 37 (2020), doi:10.1038/s41586-020-2240-x.

[25] M. Hori, H. Aghai-Khozani, A. Sótér, A. Dax and D. Barna, *Recent results of laser spectroscopy experiments of pionic helium atoms at PSI*, SciPost Phys. Proc. **5**, 026 (2021), doi:10.21468/SciPostPhysProc.5.026.

The mass of the π^+

M. Daum and P.-R. Kettle

Paul Scherrer Institut, 5232 Villigen PSI, Switzerland

Abstract

The most precise value for the pion mass was determined from a precision measurement at PSI of the muon momentum in pion decay at rest, $\pi^+ \to \mu^+ + \nu_\mu$. The result is $m_{\pi^+} = 139.57021(14)$ MeV/c^2. This value is more precise, however, in agreement with the recent compilation of the Particle Data Group for m_{π^-}. The agreement of m_{π^+} with the recent measurement. This yields a new quantitative measure of CPT invariance in the pion sector: $(m_{\pi^+} - m_{\pi^-})/m_\pi(\text{av}) = (-2.9 \pm 2.0) \cdot 10^{-6}$, an improvement by two orders of magnitude.

11.1 Introduction

There has been a long-term effort at PSI to measure the momentum $p = |\vec{p}\,|$ of the muon from pion decay at rest [1–7],

$$\pi^+ \to \mu^+ + \nu_\mu. \tag{11.1}$$

Using energy and momentum conservation for the case of a pion at rest, its mass can be obtained as

$$m_{\pi^+} = \sqrt{m_{\mu^+}^2 + p^2} + \sqrt{m_{\nu_\mu}^2 + p^2}. \tag{11.2}$$

Assuming the validity of the CPT theorem, $m_{\pi^+} = m_{\pi^-}$, so this can also be written as

$$m_{\nu_\mu}^2 = m_{\pi^-}^2 + m_{\mu^+}^2 - 2m_{\pi^-}\sqrt{m_{\mu^+}^2 + p^2}. \tag{11.3}$$

The measurements of p were originally intended to determine the mass of the muon neutrino, m_{ν_μ}, or its upper limit through (11.3). With stringent upper bounds on the neutrino mass from recent experiments of the neutrino sector, it is also possible to use (11.2) to obtain precise values for m_{π^+} [8].
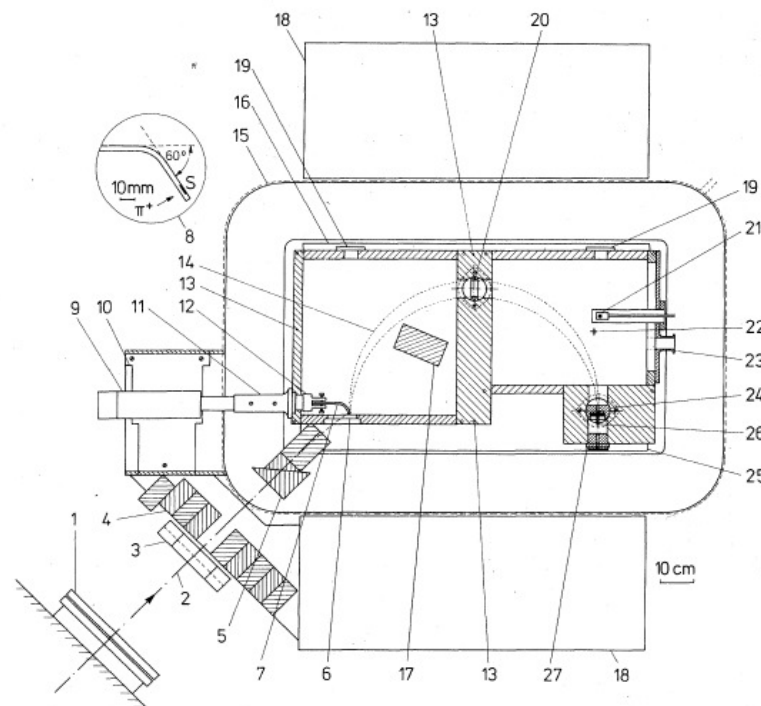
Figure 11.1: Experimental arrangement for the muon momentum measurement for Mark I-III: (1) exit vacuum window of the pion channel, (2) central trajectory of the pion beam, (3) multiwire proportional chamber for beam profile measurements, (4) lead collimator, (5) remotely controlled pion degrader, (6) window of the spectrometer vacuum chamber, (7) light guide of the pion-stop scintillation counter S, (8) enlarged view of the counter S, (9) photomultiplier of the counter S, (10) adjustable support of the photomultiplier, (11) vacuum feed through of the light guide, (12) positioning mechanism for the scintillator S, (13) vacuum chamber of the spectrometer, (14) region of accepted muon trajectories, (15) correction coils for magnetic field stabilization, (16) magnet pole, (17) beam stopper, (18) magnet yoke, (19) ports of the glass windows used for optical measurements of scintillator and collimator positions, (20) copper collimator, (21) NMR probe for magnetic field stabilization, (22) ^{241}Am α source for the calibration of the silicon detector, (23) port for vacuum pump, (24) copper collimator, (25) magnet coils, (26) silicon surface barrier detector (Si) for muon detection, (27) coaxial vacuum feed-through for the counter Si.

11.2 Measurements at PSI

The measurement of the muon momentum in pion decay at rest was performed during five experimental periods (Mark I - V). A single focusing semicircular spectrometer with a homogeneous magnetic field was used. The experimental setup for Mark I-III is shown in Figure 11.1.

Positive pions of momentum 220 MeV/c enter the spectrometer and are slowed down in a degrader. A fraction of the pions stop in a small scintillator. The pions of interest are those that come to rest close to the downstream surface of the scintillator. Their decay muons can leave the scintillator with little or no energy loss. A muon created at the scintillator surface that starts along the central trajectory of the spectrometer, travels along this trajectory if the magnetic field is about 2760 Gauss. It is identified at the end of the trajectory by a silicon surface barrier detector. At higher magnetic fields the detected muon rate decreases to zero. At lower magnetic fields, detected muons come from a finite depth of the scintillator and
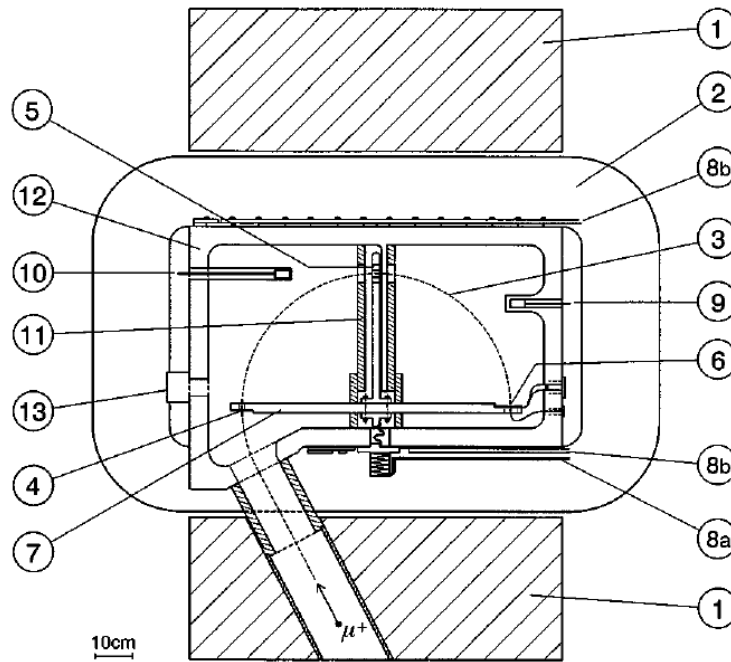
Figure 11.2: Experimental arrangement for the muon momentum measurement for Mark IV and V: (1) magnet yoke, (2) magnet coils, (3) central muon trajectory, (4)-(6) copper collimators, (7) titanium support (8a) and (8b) cooling water pipes, (9) and (10) NMR probes, (11) lead shielding, (12) vacuum chamber, (13) port for vacuum pumping.

therefore lose some of their energy before leaving the scintillator. Details of the apparatus and the analysis are described in [3].

The experimental setup for the Mark IV and V experiments is shown in Figure 11.2. In these experiments, a surface muon beam is used. The muons enter the spectrometer through a hole in the iron yoke of the spectrometer magnet. The angle between the axis of the hole and the outer surface of the yoke was 27°, chosen so that muons entering the hole on the axis have the appropriate flight direction at the entry collimator (item 4, Figure 11.2). These muons travel through the trajectory region and are detected in a position sensitive silicon microstrip detector behind a collimator (item 6, Figure 11.2). The 4.12 MeV muons lose about 0.9 MeV in passing through this detector and are then stopped in a 1 mm thick depletion layer of a single silicon surface barrier detector. The corresponding large signals from this latter detector were used as an event trigger for the data taking electronics. Details of the experiment and the analysis are described in [7].

The results from the five different experimental periods (Mark I to V) are given in Table 11.1. Initially, these results were used with (11.3) to obtain an upper limit on m_{ν_μ}. Using the known values for m_{μ^+} and m_{π^-} at the time gives $m_{\nu_\mu}^2 = (-0.016 \pm 0.023) \, (\mathrm{MeV}/c^2)^2$, which leads to an upper limit, $m_{\nu_\mu} \leq 170 \, \mathrm{keV}/c^2$ with 90 % confidence [7]. Later, the accuracy of the π^- and μ^+ masses were improved [9–13]. These new mass values gives:

$$m_{\nu_\mu}^2 = (0.024 \pm 0.017) \, (\mathrm{MeV}/c^2)^2 \tag{11.4}$$

which results in an upper limit with 90 % confidence,

$$m_{\nu_\mu} \leq 230 \, \mathrm{keV}/c^2. \tag{11.5}$$

Table 11.1: Results for the muon momentum from pion decay at rest. *This value includes the Mark I result [1–3]. **This value includes the Mark II result [4]. ***This value includes the Mark IV result [6].

Mark	Year	p [MeV/c]	Reference
I	1979	29.7885 ± 0.0019	[3,4]
II*)	1984	29.79139 ± 0.00083	[4]
III**)	1991	29.79206 ± 0.00068	[5]
IV	1994	29.79207 ± 0.00012	[6]
V***)	1996	29.79200 ± 0.00011	[7]
weighted mean	2019	29.79200 ± 0.00011	[8]

An upper limit for the electron neutrino mass m_{ν_e} has been measured at the level of $m_{\nu_e} \leq 2$ eV/c^2 [11, 14, 15], and has recently been improved further [16]. This mass value represents the "effective" electron neutrino mass, which is the weighted sum of the mass eigenstates,

$$m_{\nu_e}^2 = \sum_{i=1}^{3} |U_{ei}|^2 m_{\nu_i}^2. \tag{11.6}$$

Here U is the Pontecorvo–Maki–Nakagawa–Sakata matrix that relates the mass eigenstates ν_i, $i = (1, 2, 3)$ to the flavor eigenstates m_{ν_e}, m_{ν_μ} and m_{ν_τ}. The mass differences Δm_{21} and Δm_{32} are experimentally found to be in the meV range [11, 17–20]. Consequently, the muon and tau neutrino masses must be equal to or less than ~ 2 eV/c^2. Thus, the measurements of the muon momentum from pion decay at rest can be re-interpreted as a precise direct determination of the mass of the positively charged pion, m_{π^+}.

According to (11.2), the uncertainty Δm_{π^+} is limited by the uncertainties of p, m_{μ^+}, and m_{ν_μ}. Taking the values $m_\mu = (105.6583745 \pm 0.0000024)$ MeV/c^2 [11–13] and (conservatively) $m_{\nu_\mu} = (2.0 \pm 2.0) \cdot 10^{-6}$ MeV/c^2, the total uncertainty is dominated by p. With the value as given in Table 11.1, the result for the mass of the positively charged pion is [8]

$$m_{\pi^+} = (139.57021 \pm 0.00014) \text{ MeV/c}^2. \tag{11.7}$$

While (11.7) is nearly the same value as published earlier [7], it is not affected by the limited knowledge of neutrino masses. In fact, the value of [7] was at the time interpreted as a lower limit on m_{π^+}, whereas now (11.7) is simply the most precise value for the charged pion mass with a precision of 1 ppm.

11.3 Summary of m_π measurements at PSI

The measured values of m_{π^-} from pionic atoms (see Section 10 [23]) and m_{π^+} from our measurements are shown in Figure 11.3. The result (11.7) is more precise than and within 1.45 σ of the recent compilation of the Particle Data Group (PDG) for $m_{\pi^\pm}$ [11]

$$m_{\pi^\pm} = (139.57061 \pm 0.00024) \text{ MeV/c}^2, \tag{11.8}$$

which uses the three most recent pionic atom experiments [9, 10, 22].[1] The agreement with the most precise single measurement of m_{π^-} [10],

$$m_{\pi^-} = (139.57077 \pm 0.00018) \text{ MeV/c}^2 \tag{11.9}$$

---

[1]In fact, the Particle Data Group uses for their average only [9, 10] and solution B of [22].
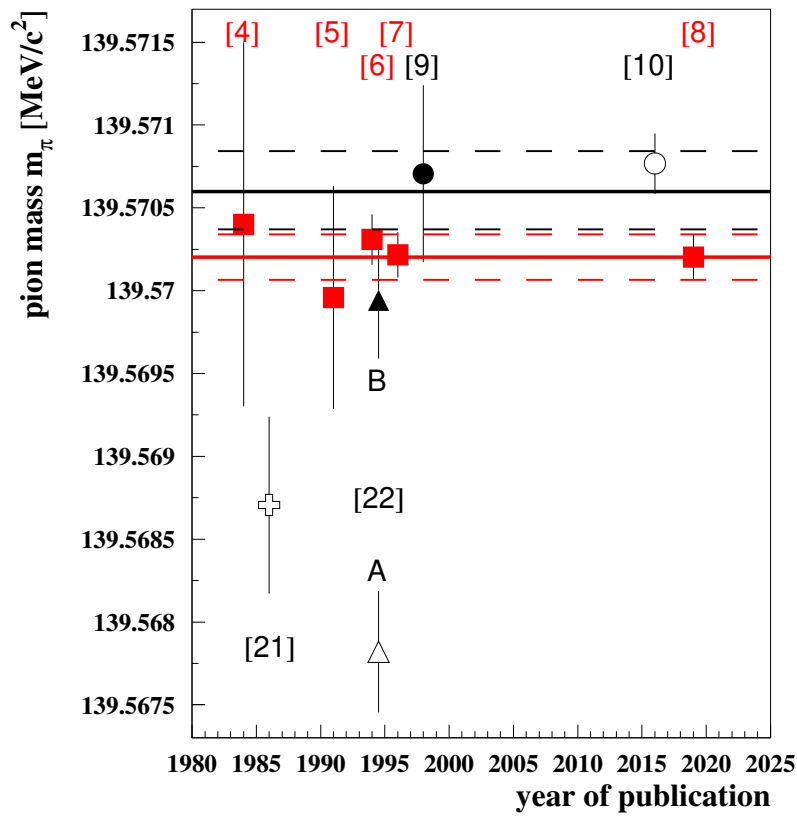
Figure 11.3: Plot of the evolution of the measured charged pion mass. Black symbols and lines: results for m_{π^-} from pionic atoms. Red symbols and lines: results for m_{π^+} from muon momentum in pion decay at rest. The π^- measurements of [21] were re-analyzed after the π^+ results of [6] were published in view of the large discrepancy. The re-analysis resulted in two solutions in [22] A and B. The continuous and dashed black lines show the PDG average and 1 σ band for the charged pion mass which comprises of purely pionic atom measurements: [22] solution B and [9,10], as earlier measurements and [22] solution A may have incorrect K-shell corrections [11]. The continuous and dashed red lines represent the final result, the weighted mean of our 1991 and 1996 values of m_{π^+} together with the 1 σ uncertainty band.

is only fair (2.4 σ)

$$m_{\pi^-} - m_{\pi^+} = (0.000\,56 \pm 0.000\,23) \text{ MeV/c}^2. \tag{11.10}$$

Furthermore, by considering the masses of the positive and negative pion separately and comparing the PDG value, (11.8) which is based solely on π^- measurements, with our π^+-value one has a quantitative measure of the CPT invariance in the pion sector. Using the PDG nomenclature one obtains

$$\frac{m_{\pi^+} - m_{\pi^-}}{m_{\text{av}}} = (-2.9 \pm 2.0) \cdot 10^{-6}. \tag{11.11}$$

This is two orders of magnitude more precise than the best value so far, $(2 \pm 5) \cdot 10^{-4}$ [24]. Our result is consistent within 1.45 σ with the CPT theorem.

References

[1] M. Daum, L. Dubal, G. H. Eaton, R. Frosch, J. Mcculloch, R. C. Minehart, E. Steiner, C. Amsler and R. Hausammann, *New determination of the upper limit for the muon neutrino mass*, Phys. Lett. B **60**, 380 (1976), doi:10.1016/0370-2693(76)90755-3.

[2] M. Daum, G. H. Eaton, R. Frosch, H. Hirschmann, J. McCulloch, R. C. Minehart and E. Steiner, *Precision measurement of the muon momentum in pion decay at rest*, Phys. Lett. B **74**, 126 (1978), doi:10.1016/0370-2693(78)90077-1.

[3] M. Daum, G. H. Eaton, R. Frosch, H. Hirschmann, J. McCulloch, R. C. Minehart and E. Steiner, *Precision measurement of the muon momentum in pion decay at rest*, Phys. Rev. D **20**, 2692 (1979), doi:10.1103/PhysRevD.20.2692.

[4] R. Abela, M. Daum, G. H. Eaton, R. Frosch, B. Jost, P. R. Kettle and E. Steiner, *Precision measurement of the muon momentum in pion decay at rest*, Phys. Lett. B **146**, 431 (1984), doi:10.1016/0370-2693(84)90155-2.

[5] M. Daum, R. Frosch, D. Herter, M. Janousch and P. R. Kettle, *New precision measurement of the muon momentum in pion decay at rest*, Phys. Lett. B **265**, 425 (1991), doi:10.1016/0370-2693(91)90078-5.

[6] K. Assamagan et al., *Measurement of the muon momentum in pion decay at rest using a surface muon beam*, Phys. Lett. B **335**, 231 (1994), doi:10.1016/0370-2693(94)91419-2.

[7] K. Assamagan et al., *Upper limit of the muon-neutrino mass and charged pion mass from momentum analysis of a surface muon beam*, Phys. Rev. D **53**, 6065 (1996), doi:10.1103/PhysRevD.53.6065.

[8] M. Daum, R. Frosch and P. R. Kettle, *The charged and neutral pion masses revisited*, Phys. Lett. B **796**, 11 (2019), doi:10.1016/j.physletb.2019.07.027.

[9] S. Lenz et al., *A New determination of the mass of the charged pion*, Phys. Lett. B **416**, 50 (1998), doi:10.1016/S0370-2693(97)01337-3.

[10] M. Trassinelli et al., *Measurement of the charged pion mass using X-ray spectroscopy of exotic atoms*, Phys. Lett. B **759**, 583 (2016), doi:10.1016/j.physletb.2016.06.025.

[11] M. Tanabashi et al., *Review of particle physics*, Phys. Rev. D **98**, 030001 (2018), doi:10.1103/PhysRevD.98.030001.

[12] W. Liu et al., *High precision measurements of the ground state hyperfine structure interval of muonium and of the muon magnetic moment*, Phys. Rev. Lett. **82**, 711 (1999), doi:10.1103/PhysRevLett.82.711.

[13] P. J. Mohr, D. B. Newell and B. N. Taylor, *CODATA recommended values of the fundamental physical constants: 2014*, Rev. Mod. Phys. **88**, 035009 (2016), doi:10.1103/RevModPhys.88.035009.

[14] C. Kraus et al., *Final results from phase II of the Mainz neutrino mass search in tritium beta decay*, Eur. Phys. J. C **40**, 447 (2005), doi:10.1140/epjc/s2005-02139-7.

[15] V. N. Aseev et al., *An upper limit on electron antineutrino mass from Troitsk experiment*, Phys. Rev. D **84**, 112003 (2011), doi:10.1103/PhysRevD.84.112003.

[16] M. Aker et al., *Improved upper limit on the neutrino mass from a direct kinematic method by KATRIN*, Phys. Rev. Lett. **123**, 221802 (2019), doi:10.1103/PhysRevLett.123.221802.

[17] A. Gando et al., *Reactor on-off antineutrino measurement with KamLAND*, Phys. Rev. D **88**, 033001 (2013), doi:10.1103/PhysRevD.88.033001.

[18] K. Abe et al., *Observation of electron neutrino appearance in a muon neutrino beam*, Phys. Rev. Lett. **112**, 061802 (2014), doi:10.1103/PhysRevLett.112.061802.

[19] P. Adamson et al., *Combined analysis of ν_μ disappearance and $\nu_\mu \rightarrow \nu_e$ appearance in MINOS using accelerator and atmospheric neutrinos*, Phys. Rev. Lett. **112**, 191801 (2014), doi:10.1103/PhysRevLett.112.191801.

[20] F. P. An et al., *Spectral measurement of electron antineutrino oscillation amplitude and frequency at Daya Bay*, Phys. Rev. Lett. **112**, 061801 (2014), doi:10.1103/PhysRevLett.112.061801.

[21] B. Jeckelmann et al., *New precision determination of the π^- mass from pionic X-rays*, Nucl. Phys. A **457**, 709 (1986), doi:10.1016/0375-9474(86)90476-8.

[22] B. Jeckelmann, P. F. A. Goudsmit and H. J. Leisi, *The Mass of the negative pion*, Phys. Lett. B **335**, 326 (1994), doi:10.1016/0370-2693(94)90358-1.

[23] M. Daum and D. Gotta, *The mass of the π^-*, SciPost Phys. Proc. **5**, 010 (2021), doi:10.21468/SciPostPhysProc.5.010.

[24] D. S. Ayers, A. M. Cormack, A. J. Greenberg, R. W. Kenney, D. O. Caldwell, V. B. Elings, W. P. Hesse and R. J. Morrison, *Measurements of the lifetimes of positive and negative pions*, Phys. Rev. D **3**, 1051 (1971), doi:10.1103/PhysRevD.3.1051.

The π^0 mass and the first experimental verification of Coulomb de-excitation in pionic hydrogen

Manfred Daum[⋆] and P.-R. Kettle

Paul Scherrer Institut, 5232 Villigen PSI, Switzerland

⋆ manfred.daum@psi.ch

Abstract

The most precise value for the π^0 mass was obtained from the measurement of the mass difference $m_{\pi^-} - m_{\pi^0} = 4.593\,64(48)\,\text{MeV/c}^2$ in the charge exchange reaction $\pi^- p \to \pi^0 n$ at PSI. With the most precise charged pion mass value, $m_{\pi^+} = 139.570\,21(14)\,\text{MeV/c}^2$ and the validity of the CPT theorem ($m_{\pi^-} = m_{\pi^+}$), a value $m_{\pi^0} = 134.976\,57(50)\,\text{MeV/c}^2$ is obtained. The measurements also revealed, for the first time, evidence of an unexpectedly large contribution from Coulomb de-excitation states during the pionic atom cascade.

12.1 The mass of the π^0

One of the main motivations in 1984 for a precision measurement of m_{π^0} was that it allowed for a far more precise comparison between experiment and theory of the rare pion β decay rate $\Gamma_{\pi\beta}(\pi^+ \to \pi^0 e^+ \nu)$, for which the phase space depends on the fifth-power of $D_\pi = m_{\pi^-} - m_{\pi^0}$. This required a precision on D_π to better than $\Delta D_\pi / D_\pi < 0.001$, a condition that was not met by the world average at the time [1–3].

In this measurement of D_π, negative pions are stopped in a liquid-hydrogen target to form pionic hydrogen atoms. A fraction $R \approx R_P/(R_P + 1) \approx 0.6$ of these $\pi^- p$ atoms, where R_P is the Panofsky ratio [4], undergo the charge-exchange reaction (CEX)

$$\pi^- p \to \pi^0 n, \tag{12.1}$$

whereas the remaining 40 % of the $\pi^- p$ atoms undergo radiative capture

$$\pi^- p \to \gamma n. \tag{12.2}$$

The mass difference D_π is derived from time-of-flight (TOF) distributions of neutrons from reaction (12.1), measured at flight distances of 3.2, 7.9, and 18.1 m. Since the $\pi^- p$ atoms are

almost at rest, these neutrons generate a TOF peak corresponding to their velocity of about 0.894 cm/ns.

If the $\pi^- p$ atom is at rest before reaction (12.1) , energy and momentum conservation lead to the following equation for the mass difference D_π:

$$D_\pi = m_{\pi^-} - [(m_{\pi^-} - D_N - E_B)^2 - 2(\gamma_{nr} - 1)(m_p + D_N)(m_{\pi^-} + m_p - E_B)]^{1/2}. \qquad (12.3)$$

Here, $D_N \equiv m_n - m_p$ is the nucleon mass difference and E_B is the binding energy of the $\pi^- p$ atom just prior to reaction (12.1). The rest mass of the $\pi^- p$ atom is $m_{\pi p} = m_{\pi^-} + m_p - E_B$; $\gamma_{nr} \equiv (1 + \beta_{nr}^2)^{-1/2}$ is the usual function of the neutron velocity $v_{nr} = c\beta_{nr}$ for $\pi^- p$ atoms at rest; we set $c = 1$, except where the units are given explicitly.

From (12.3) it follows that the experimental uncertainty of D_π contains five contributions, $\beta_{nr}, m_{\pi^-}, m_p, D_N$, and E_B, see [5–7], resulting in a relative uncertainty of D_π of the same order as that of β_{nr}:

$$(\Delta D_\pi)_{\beta_{nr}}/D_\pi = 1.46\Delta\beta_{nr}/\beta_{nr}. \qquad (12.4)$$

The remaining four contributions can be neglected, see [7]. Thus, the experiment consists of determining the velocity of the neutron from the charge-exchange reaction (12.1).
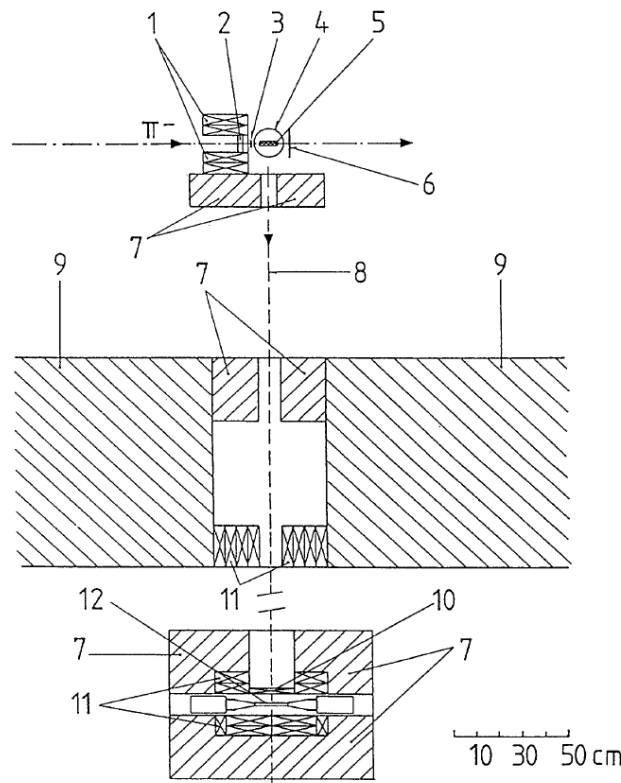
Figure 12.1: Experimental setup: (1) lead collimator; (2) CH_2 degrader; (3) Scintillator S_1; (4) vacuum chamber of the liquid hydrogen target; (5) liquid hydrogen target; (6) scintillator S_2; (7) CH_2 shielding; (8) central neutron trajectory; (9) concrete shielding; (10) lead converter; (11) lead collimator; (12) Scintillator S_3.

The measurements were made at the 590 MeV proton accelerator at PSI. The experimental layout is shown in Figure 12.1. Negative pions with a momentum of 120 MeV/c were transported by the secondary beam line πE1 to a liquid hydrogen target assembly. At that

momentum, the substantial electron contamination in the beam was suppressed using time-of-flight (TOF), by requiring a coincidence between the scintillator S_1 and the radio frequency signal of the accelerator.

The pions passed through a CH_2 degrader, optimized to maximize the pion stopping rate in the liquid hydrogen. The hydrogen was contained in a cylindrical stainless steel cell with a length of 1.6 cm and a radius of 4.5 cm, oriented so that the cylinder axis coincided with the neutron flight direction, see Figure 12.1.

The incoming pions were detected by a plastic scintillator S_1 in anti-coincidence with the scintillator S_2. The coincidence $(S_1 \cdot \text{rf}) \cdot \overline{(S_2 \cdot \text{rf})}$ indicated a stopping pion. Neutrons and photons from the liquid hydrogen target were observed after a flight path of variable length (3-18 m) defined by a series of CH_2 and Pb collimators.

The neutrons and photons from reactions (12.1) and (12.2) were detected by a NE102A organic scintillator S_3 of thickness 1.6 cm viewed from opposite sides through lucite light guides by two photomultipliers. The neutron detector was shielded by CH_2 and lead as shown in Figure 12.1. The neutron detector assembly was mounted on a steel cart equipped with optical targets for surveying.

Data were taken with the neutron detector at three distances from the nominal hydrogen target location: (i) 3.1966 m, (ii) 7.9283 m, and (iii) 18.1005 m. The distance between positions (i) and (ii) was determined to ±0.1 mm and that between positions (i) and (iii) to ±0.4 mm. For more information see [7].

The method of determining the neutron velocity is similar to that of [1]. However, the older method depended on the measurement of signal velocities in the coaxial delay cables, whereas in our case this time standard is replaced by the precisely known radio frequency structure of the pion beam. The neutron velocity v_{nr} from the charge exchange reaction (12.1) is derived from the position of the neutron peak in the TOF spectra (Figure 12.2) relative to the pattern of the accidental photon peaks. These peaks appear at regular intervals of $\tau_{rf} = (19.750\,034 \pm 0.000\,002)$ ns.

The raw time distribution of the events, as recorded by a time-to-digital converter (TDC) at a flight path of 7.9 m, is shown in Figure 12.2. The data are shown in Figure 12.3 after background subtraction, for all three distances.

Neglecting the fact that the $\pi^- p$ atoms have a finite kinetic energy $T_{\pi p}$ and are in different atomic states at the time of reaction (12.1), all neutrons from that reaction would have the same velocity, v_{nr}, which is related to the particle masses by energy and momentum conservation ($c = 1$)

$$m_{\pi p} = E_n + E_{\pi^0} = \sqrt{m_n^2 + p_n^2} + \sqrt{m_{\pi^0}^2 + p_{\pi^0}^2}. \tag{12.5}$$

Here, E_n and E_{π^0} are the total neutron and π^0 energies, respectively, and $p_n = m_n \beta_{nr} \gamma_{nr}$ is the neutron momentum.

Without the assumption of the initial $\pi^- p$ atoms being at rest, the predicted neutron TOF distribution $F(\tau)$ for a given neutron flight path l_n has a finite width. It can be shown [7] that, for an isotropic distribution of the $\pi^- p$ atom velocities, the mean of the neutron TOF distribution is equal to the TOF for $\pi^- p$ atoms at rest. The standard deviation of the function $F(\tau)$ is [7]

$$\sigma_\tau = (2\overline{T_{\pi p}}/3m_{\pi p})^{1/2} l_n/v_{nr}^2, \tag{12.6}$$

where $\overline{T_{\pi p}}$ is the mean kinetic energy of the $\pi^- p$ atom. It is seen from (12.6) that the standard deviation of the TOF distribution function $F(\tau)$ increases linearly with the neutron flight path l_n.

The broadening of the TOF peaks with increasing flight path is indeed observed in the spectra of Figure 12.3. The tails to the right of the neutron peaks, i.e., to longer times-of-flight, are due not only to the finite kinetic energy of the $\pi^- p$ atoms but also to neutrons which have
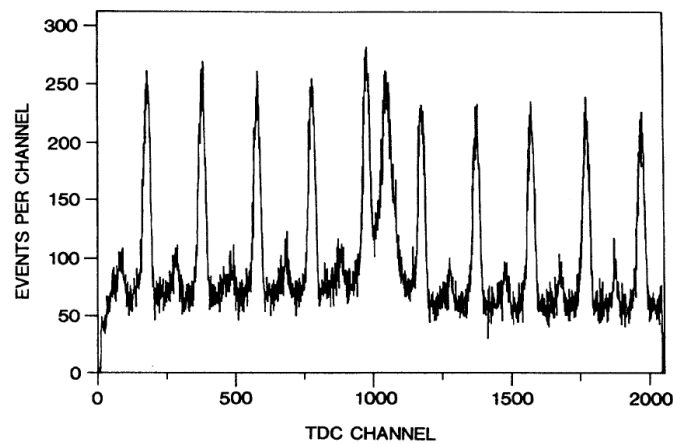
Figure 12.2: Uncorrected time spectrum recorded at a flight path of $l = 7.9$ m. Abscissa: TDC channel number for S_3; channel $\approx$0.1 ns. Ordinate: number of events per channel. This distribution contains three classes of events: (a) The peak at channel 1040 of Figure 12.2 is due to neutrons from the charge exchange reaction (12.1). (b) The narrow peaks at channels 180, 380, 580, ..., are due to photons from the π^0 decay following reaction (12.1) and photons from reaction (12.2). (c) The small peaks about halfway between the photon peaks, i.e., at channels 80, 280, 480, ..., originate from accidental events in which the TDC was started by a neutron detector signal due to beam electrons scattered in the liquid hydrogen target assembly.

reached the detector after scattering in the materials in and around the flight channel. In contrast, the tails to the left are not contaminated by neutron scattering. The tail visible at 3.2 m, extends to about 10 ns (20 ns) before the peak at 7.9 m (18.1 m), corresponding to an energy distribution $f(T_{\pi p})$ extending to about 70 eV.

The curves in Figure 12.3 were obtained by fitting nine free parameters simultaneously to all three experimental spectra, for details see [7]. An energy distribution found to fit the data is shown in Figure 12.4 together with the corresponding neutron TOF distribution $F(\tau)$ for a fixed flight path of 18.1 m. The χ^2 of the fit shown in Figure 12.3 is 1265 for 1191 degrees of freedom.

The resulting neutron velocity from the charge exchange reaction (12.1) and for the $\pi^- p$ atom at rest is

$$v_{nr} = (0.894\,266 \pm 0.000\,063) \text{ cm/ns.} \tag{12.7}$$

The corresponding mass difference is

$$D_\pi = m_{\pi^-} - m_{\pi^0} = (4.593\,64 \pm 0.000\,48) \text{ MeV/c}^2. \tag{12.8}$$

This result agrees with our previous measurement [5]. The deviation from the former world average [3], ($D_\pi = 4.604\,3\pm0.003\,7$) MeV/c^2, which was dominated by the values of [1,2] is thus confirmed at a level of 2.9 σ. Assuming the validity of the CPT theorem ($m_{\pi^+} = m_{\pi^-}$), subtracting the mass difference (12.8) from the charged pion mass [8], $m_{\pi^+} = 139.570\,21(14)$ MeV/c^2 gives the new π^0 mass value,

$$m_{\pi^0} = (134.976\,57 \pm 0.000\,50) \text{ MeV/c}^2. \tag{12.9}$$

A similar analysis based on the fast neutron TOF spectra from the simultaneously measured radiative capture reaction (12.2) results in a value for the negative pion mass, consistent with
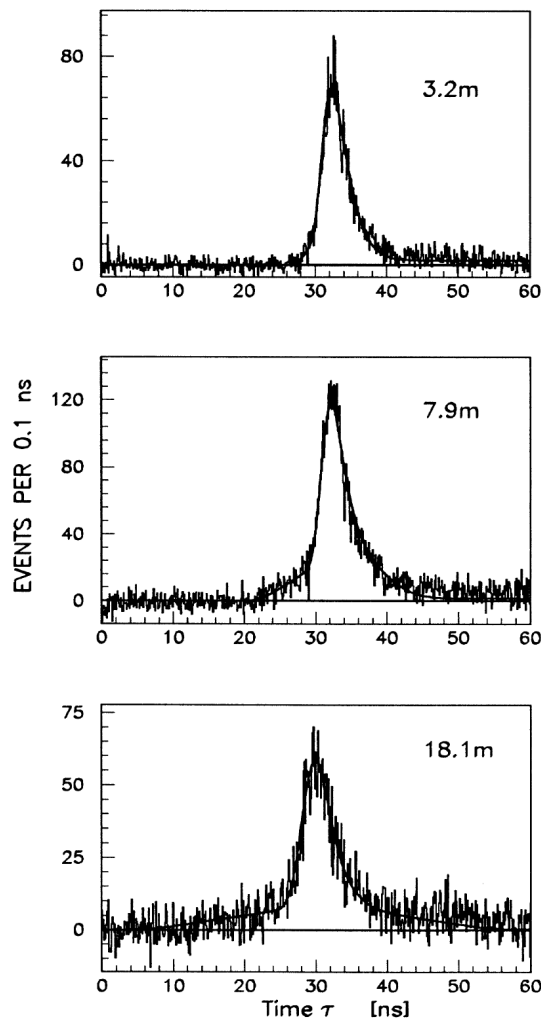
Figure 12.3: Experimental TOF spectra of neutrons from the charge exchange reaction $\pi^- p \to \pi^0 n$, after background subtraction, for flight paths of 3.2 m, 7.9 m, and 18.1 m. The time shown is from an accidental photon peak about 30 ns before the neutron peak. Curves: theoretical distributions fitted to the data, c.f. [7].

the world average value, albeit with reduced precision. As the dominant uncertainty is from the neutron velocity, this provides evidence of the validity of the velocity analysis method used.

The fit also allows the extraction of the corresponding mean kinetic energy of the $\pi^- p$ atom

$$\overline{T_{\pi p}} = (16.2 \pm 1.3) \text{ eV} \tag{12.10}$$

confirming the strong deviation from the velocity spread quoted in [1] which corresponded to $\overline{T_{\pi p}} = (115 \pm 43)$ eV.

12.2 First experimental verification of Coulomb de-excitation in pionic hydrogen

The TOF-data for the D_π measurement show a Doppler broadening of the neutron peaks with increasing flight distance, attributed to 'high-energy' pionic atoms at the time of the CEX-reaction. Further evidence for this was reported later by an experiment in gaseous hydrogen [9].
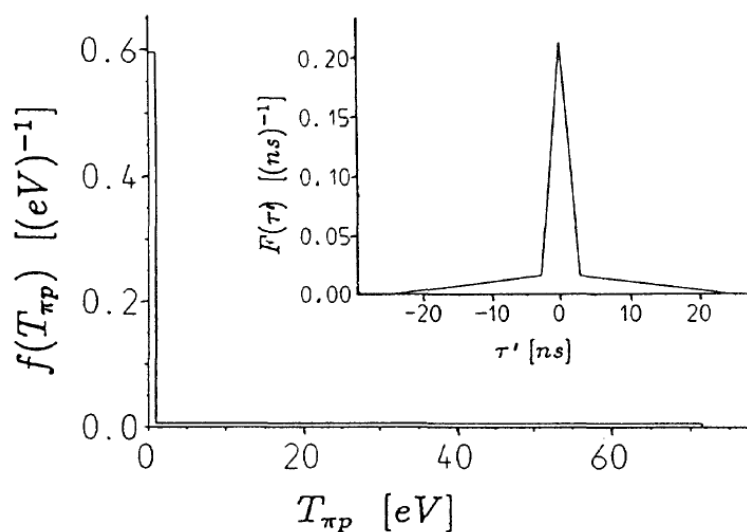
Figure 12.4: Model distribution function $f(T_{\pi p})$ found to fit the neutron TOF spectra of Figure 12.3; $T_{\pi p}$ is the kinetic energy of the $\pi^- p$ atom just prior to the charge exchange reaction (12.1); $F(\tau')$ is the corresponding neutron TOF distribution for a flight path of 18.1 m.

The kinetic energy distribution $f(T_{\pi p})$ and the corresponding TOF-distribution $F(\tau)$ for this simple model for the D_π-data was further refined in a new experiment, undertaken to prove the existence of the Coulomb de-excitation process [10, 11] in liquid and gaseous hydrogen, and to determine if it is responsible for the broadening. A further aim was to verify that the multi-component structure of the kinetic energy distribution is associated with this process.

The motivation for this experiment was to test the cross-section predictions for various cascade processes for exotic hydrogen atoms, which are important for experiments such as pionic X-ray transition measurements to determine the ground state strong interaction width [12–14] and the effect of the Doppler broadening of pionic X-ray lines in the determination of the pion-nucleon scattering lengths. The most likely process capable of producing such a broadening effect is Coulomb de-excitation [10, 11]. Here, $(\pi^- p)_n + p \rightarrow (\pi^- p)_{n'} + p$ where the smaller neutral pionic atom collides with a proton of a hydrogen atom causing a transition of the pionic atom, whereby the de-excitation energy is shared between the collision partners. Other possible processes either reduce $T_{\pi p}$ or leave it almost unchanged. Coulomb de-excitation predictions calculated by several authors [11, 15–17] vary by more than an order-of-magnitude so that precise data are necessary to test the predictions.

Here we outline the new experiment, concentrating on the liquid hydrogen results [18]. Several experimental improvements [5–7] were implemented:

1. Background reduction and increased statistics by use of (i) an extra neutron collimator system close to the target, (ii) an array of neutron counters with specially selected low-noise photomultipliers, and (iii) a 64-counter array of NaI photon counters for tagging the neutrons from reactions (12.1) and (12.2).

2. Improved time-resolution, by reducing both the thickness of the neutron detectors and the liquid hydrogen cell [18, 19].

In this experiment, negative pions of 117 MeV/c were slowed down in a carbon degrader and stopped in a liquid hydrogen target. Neutrons from reaction (12.1) were detected for

various flight-path lengths between 3 and 11 m. Time-of-flight and pulse-height data were recorded by time-to-digital (TDC) and analogue-to-digital (ADC) convertors.
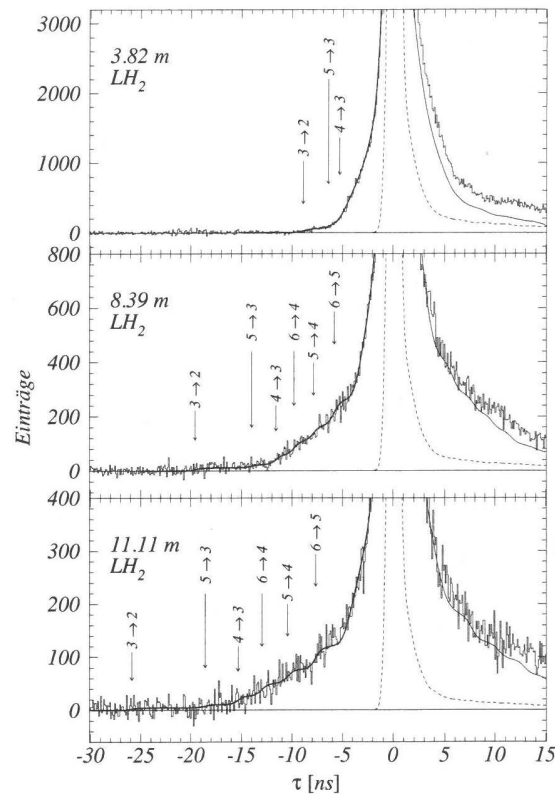
Figure 12.5: Neutron time-of-flight spectra from the charge exchange reaction $\pi^- p \to \pi^0 n$ in a liquid hydrogen target (LH$_2$). The time is measured from the centre of the neutron peak corresponding to the reaction at rest. Solid curves: fit to the data including Coulomb de-excitation processes. The numbers $n \to n'$ indicate the expected positions of the steps in the TOF distribution of neutrons emitted after the corresponding Coulomb de-excitation. Dashed line: unbroadened neutron TOF distribution from Monte Carlo program.

Figure 12.5 shows the neutron TOF-spectra taken at 3.82 m, 8.39 m and 11.11 m, after background subtraction and pulse-height cuts to remove noise and accidental photon events from π^0-decay and radiative capture, as well as bremsstrahlung events from beam electrons. Further energy cuts (between 60 and 110 MeV) on the photon detected in the NaI array eliminated both bremsstrahlung and radiative capture events. Figure 12.5 shows a clear distance-dependent broadening of the neutron line shape, when compared to the Mont-Carlo generated intrinsic line shape.

The data of Figure 12.5 were analyzed by applying three fitting procedures; two based on the full model of Coulomb de-excitation shown in Figure 12.6 - one including both $\Delta n = 1$ and $\Delta n = 2$ pionic atom transitions in the fitted $F(\tau)$ distributions and one including only the $\Delta n = 1$ transitions. The third procedure used the simplified model of Figure 12.4 for comparison.

Clear step-like structures in the data at 3.8 m and 8.4 m can be seen reaching to -9 ns and -20 ns, respectively, corresponding to the $\Delta n = 1$ transition $3 \to 2$ having a kinetic energy of 209 eV. A second component visible at all three distances corresponding to -6 ns, -12 ns and -15 ns, signals the $\Delta n = 1$ transition $4 \to 3$ in the pionic atom with a kinetic energy of about
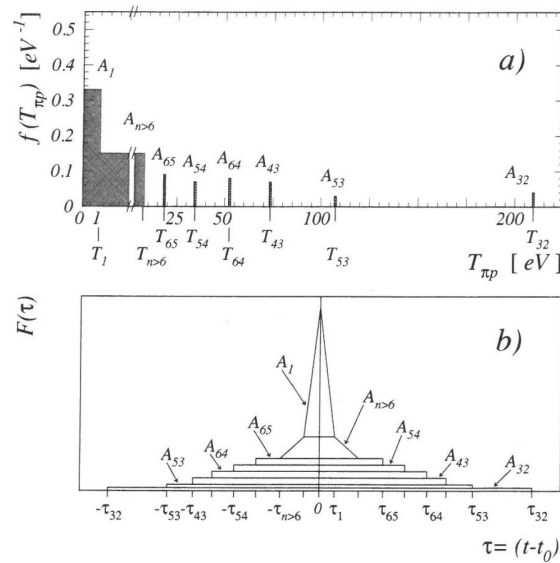
Figure 12.6: (a) Idealized distribution function $f(T_{\pi p})$ of the kinetic energy $T_{\pi p}$ of pionic hydrogen atoms at the instant of nuclear capture. For clarity, T_1 and the widths of the four δ-like peaks at $T_{nn'}$ are drawn to be 1 eV. The energy distribution $f(T_{n>6})$ is about 7 eV wide and describes all transitions $n \to n'$ with $n > 6$. The integrals of these distributions and peaks correspond to the relative yields A_1, $A_{nn'}$ and $A_{n>6}$, respectively. (b) Neutron TOF-distribution $F(\tau)$ corresponding to the kinetic energy distribution of Fig. 1(a).

70 eV.

The final results from the experiment for the kinetic energy distribution for pionic hydrogen, based on Coulomb de-excitation transitions, are shown in Table 12.1, for both liquid and gaseous hydrogen and are based on the three independent fits [18]. Although visually, the significance of the steps in the TOF-spectra is only fair, their true significance can be seen from the fit results in the table, when the theoretical model of Figure 12.6 is fitted simultaneously to all three TOF spectra. Here, a 16-parameter fit of the model-based TOF spectra are fitted to the measured distributions and involve: (i) four yields from $\Delta n = 1$ transition $6 \to 5$, $5 \to 4$, $4 \to 3$ and $3 \to 2$; (ii) two yields for $\Delta n = 2$ transitions $6 \to 4$ and $5 \to 3$; (iii) one yield and one upper energy bound for $n > 6$ transitions; (iv) the energy parameter T1 for the low-energy component; (v) a distance independent Gaussian electronic time-jitter [7]; (vi) three normalization factors for the ordinates; (vii) three time shifts (0.3 ± 0.1) channels, as free parameters.

The fits incorporating the $\Delta n = 1$ and $\Delta n = 2$ transitions gave a χ^2/DOF of 0.96 with 740 degrees of freedom (DOF); this corresponds to a confidence level of 77.7 %. The data were also fitted with the parameterization of [7] (two uniform kinetic-energy distributions of the $\pi^- p$-atom, cf. Figure 12.4). In this case, the resulting χ^2 was 2.43/DOF (cf. also [19]). The poor fit due to this parameterization originates from the lack of discrete components, e.g. the 3→2 transition.

For comparison, fits were also made excluding the Coulomb de-excitation components with $\Delta n = 2$. These fits gave a χ^2/DOF of 1.06 with 742 DOF which corresponds to a confidence level of 13.1 %. The differences in the χ^2/DOF between the fits with and without $\Delta n = 2$ transitions are not very significant; however, there is strong evidence for components with $\Delta n = 2$ from the two other model-independent methods used in the analysis to extract the

Table 12.1: Fitted yields $A_{nn'}$ of Coulomb de-excitation peaks in the kinetic energy distribution $f(T_{\pi p})$ for the transitions $n \rightarrow n'$ in liquid and gaseous hydrogen. Fit results including $\Delta n = 2$ (left) and $\Delta n = 1$ only (right).

transition	energy	$A_{nn'}$ [%]			
$n \rightarrow n'$	$T_{nn'}$ [eV]	LH$_2$	H$_2$ gas	LH$_2$	H$_2$ gas
n > 6	< 18.4	27 ± 2	19 ± 5	26 ± 2	21 ± 5
$6 \rightarrow 5$	18.4	9 ± 1	9 ± 3	7 ± 1	6 ± 3
$5 \rightarrow 4$	33.9	7 ± 1	7 ± 4	12 ± 1	14 ± 3
$4 \rightarrow 3$	73.2	7 ± 1	5 ± 3	14 ± 1	10 ± 2
$3 \rightarrow 2$	209.1	3 ± 1	5 ± 1	4 ± 1	4 ± 1
$6 \rightarrow 4$	52.3	8 ± 1	9 ± 4	/	/
$5 \rightarrow 3$	107.1	3 ± 1	0^{+2}_{-0}	/	/
χ^2/DOF		0.96	0.96	1.06	0.96
T$_1$ [eV]		1.0±0.1	1.6±0.2	1.0±0.1	1.5±0.3
A$_1$ [%]		36 ± 2	46 ± 6	36 ± 2	45 ± 6
T$_{n>6}$ [eV]		7.6±0.3	6.7±2.2	7.9±0.4	6.8±2.3

kinetic energy distribution $f(T_{\pi p})$ from the data, see [18]. In addition, the difference between the predicted and the observed transition energies $T_{nn'}$ reported in [19] can be accounted for and made to vanish in our present analysis if we include the $\Delta n = 2$ Coulomb de-excitation transitions. Then, the resultant energies $T_{nn'}$ for $n \leq 6$ perfectly match the theoretical values derived from the Coulomb de-excitation model and do not have to be taken as free parameters. This is considered as a strong indication of the existence of the $\Delta n = 2$ Coulomb de-excitation transitions.

In conclusion, the first estimates of the Coulomb de-excitation were made by Bracci and Fiorentini [11]. They were criticized by Ponomarev and Solov'ev [17] who obtained significantly smaller Coulomb de-excitation rates which, however, disagreed with the experimental results [18, 19] and this paper. Significant progress came with the more advanced theoretical calculations by Popov and Pomerantsev [20]. The cascade calculations using these cross sections predict a substantial high-energy component. Finally, Hirtl et al. [21] state that the theoretical prediction for the kinetic energy distributions and the experimental results do not show any drastic inconsistencies.

References

[1] J. B. Czirr, *Determination of π-meson masses by neutron time of flight*, Phys. Rev. **130**, 341 (1963), doi:10.1103/PhysRev.130.341.

[2] I. M. Vasilevsky, V. V. Vishnyakov and A. F. Dunaitsev, *Mass difference of the negative and neutral pions*, Phys. Lett. **23**, 281 (1966), doi:10.1016/0031-9163(66)90184-3.

[3] M. Aguilar-Benitez et al., *Review of particle properties. Particle Data Group*, Phys. Lett. B **170**, 1 (1986).

[4] W. K. H. Panofsky, R. L. Aamodt and J. Hadley, *The gamma-ray spectrum resulting from capture of negative π-mesons in hydrogen and deuterium*, Phys. Rev. **81**, 565 (1951), doi:10.1103/PhysRev.81.565.

[5] J. F. Crawford, M. Daum, R. Frosch, B. Jost, P. R. Kettle, R. M. Marshall and K. O. H. Ziock, *Precision measurement of the mass difference m_{π^-} - m_{π^0}*, Phys. Rev. Lett. **56**, 1043 (1986), doi:10.1103/PhysRevLett.56.1043.

[6] J. F. Crawford, M. Daum, R. Frosch, B. Jost, P. R. Kettle, R. M. Marshall, B. K. Wright and K. O. H. Ziock, *Precision measurement of the mass difference m_{π^-} - m_{π^0}*, Phys. Lett. B **213**, 391 (1988), doi:10.1016/0370-2693(88)91782-0.

[7] J. F. Crawford, M. Daum, R. Frosch, B. Jost, P. R. Kettle, R. M. Marshall, B. K. Wright and K. O. H. Ziock, *Precision measurement of the pion mass difference m_{π^-} - m_{π^0}*, Phys. Rev. D **43**, 46 (1991), doi:10.1103/PhysRevD.43.46.

[8] M. Daum, R. Frosch and P. R. Kettle, *The charged and neutral pion masses revisited*, Phys. Lett. B **796**, 11 (2019), doi:10.1016/j.physletb.2019.07.027.

[9] E. C. Aschenauer *et al.*, *Cascade processes and the kinetic-energy distribution of pionic hydrogen atoms*, Phys. Rev. A **51**, 1965 (1995), doi:10.1103/PhysRevA.51.1965.

[10] M. Leon and H. A. Bethe, *Negative meson absorption in liquid hydrogen*, Phys. Rev. **127**, 636 (1962), doi:10.1103/PhysRev.127.636.

[11] L. Bracci and G. Fiorentini, *Coulomb deexcitation of mesic hydrogen*, Nuovo Cim. A **43**, 9 (1978), doi:10.1007/BF02729003.

[12] W. Beer *et al.*, *Determination of the strong interaction shift in pionic hydrogen with a high resolution crystal spectrometer system*, Phys. Lett. B **261**, 16 (1991), doi:10.1016/0370-2693(91)91317-O.

[13] D. Sigg *et al.*, *The Strong interaction shift and width of the 1S level in pionic hydrogen*, Phys. Rev. Lett. **75**, 3245 (1995), doi:10.1103/PhysRevLett.75.3245.

[14] D. Sigg *et al.*, *The strong interaction shift and width of the ground state of pionic hydrogen*, Nucl. Phys. A **609**, 269 (1996), doi:10.1016/S0375-9474(96)00280-1, [Erratum: Nucl. Phys. A **617**, 526 (1997)].

[15] L. Men'shikov, *Mesic atom acceleration mechanisms in cascade transitions*, Muon Catalyzed Fusion **2**, 173 (1988).

[16] W. Czaplinski, A. Gula, A. Kravtsov, A. Mikhailov and N. Popov, *Kinetics of excited muonic hydrogen*, Phys. Rev. A **50**, 525 (1994), doi:10.1103/PhysRevA.50.525.

[17] L. I. Ponomarev and E. A. Solov'ev, *Cascade acceleration of $p\pi$ atoms in the Coulomb deexcitation process*, J. Exp. Theor. Phys. Lett. **64**, 135 (1996), doi:10.1134/1.567164.

[18] A. Badertscher, P. F. A. Goudsmit, M. Janousch, Z. G. Zhao, M. Daum, P. R. Kettle, V. E. Markushin, J. Schottmueller and J. Koglin, *Experimental verification of Coulomb deexcitation in pionic hydrogen*, Europhys. Lett. **54**, 313 (2001), doi:10.1209/epl/i2001-00243-1.

[19] A. Badertscher, M. Daum, R. Frosch, P. F. A. Goudsmit, W. Hajdas, M. Janousch, P. R. Kettle, V. Markushin, J. Schottmuller and Z. G. Zhao, *Experimental determination of the kinetic energy distribution of $\pi^- p$ atoms in liquid hydrogen*, Phys. Lett. B **392**, 278 (1997), doi:10.1016/S0370-2693(96)01545-6.

[20] V. P. Popov and V. N. Pomerantsev, *Kinetic energy distributions of muonic and pionic hydrogen atoms*, Hyperfine Interact. **209**, 75 (2012), doi:10.1007/s10751-011-0514-2.

[21] A. Hirtl *et al.*, *Redetermination of the strong-interaction width in pionic hydrogen*, Eur. Phys. J. A **57**, 70 (2021), doi:10.1140/epja/s10050-021-00387-x.

Cyclotron trap

D. Gotta[1][*] and L. M. Simons[2]

1 Institut für Kernphysik, Forschungszentrum Jülich, D-52425 Jülich, Germany
2 Paul Scherrer Institut, CH-5232 Villigen, Switzerland

[*] d.gotta@fz-juelich.de

Abstract

The cyclotron trap was developed at SIN/PSI to increase the stopping density of negatively charged particle beams for the formation of exotic atoms in low pressure gases. A weak focusing magnetic field, produced by superconducting solenoids, is used. Particles are injected radially through the fringe field to a moderator, which decelerates them into orbits bound by the field. Further deceleration by moderators and/or low-pressure gases leads the particles to the centre of the device, where they can be stopped or eventually extracted. Experiments became feasible with this technique, such as those dealing with pionic hydrogen/deuterium at SIN/PSI. Muonic hydrogen laser experiments also became possible with the extraction of muons from the cyclotron trap. The formation of antiprotonic hydrogen in low pressure targets led to successful experiments at LEAR/CERN.

13.1 Introduction

The advent of meson factories in the 70's and of the antiproton factory LEAR in the 80's, resulted in a revival of interest in the physics of exotic atoms. Before then, the main focus of research was the investigation of nuclear charge parameters with muonic atoms, and the determination of the strong interaction shift and broadening in hadronic atoms [1]. Experiments had been almost exclusively performed in medium- to high-Z solid or high-pressure targets. Exotic atoms were produced by decelerating the beam particles with a linear array of low-Z moderators, such as Be, CH_2, or C to minimize straggling.

This technique was sufficient for the purposes at that time, but was not adequate for experiments of more fundamental interest. Such experiments have in common the need of low-pressure gas targets. As an example, neutral exotic hydrogen/deuterium atoms can penetrate deeply into the field of neighbouring atoms. At higher pressures they are destroyed by the Stark effect before they can emit the X-rays one wants to measure [2].

A second example is given by exotic atoms of higher Z gases. Here, a completely ionized electron shell can keep the exotic atom free from interactions with neighbouring atoms, thus

approaching the state of an ideal exotic atom. The X-rays in question, with energies in the keV region, suffer self-absorption in high Z gases. In addition, thin windows must be used. Both reasons argue against high-pressure gas targets.

Experiments planned at LEAR/CERN to measure X-rays from antiprotonic hydrogen and deuterium, motivated a new technique to stop particles at the lowest pressures. The cyclotron trap (CT I), developed and built by a group from the University of Karlsruhe working at SIN and at LEAR, met this requirement. CT I was used both at LEAR with antiprotons, and at SIN/PSI with pions and muons. A second instrument (CT II) was developed later, specially tailored to the pion and muon beams at PSI.

13.2 The basic principle

In the following, cylindrical coordinates are used, with r, θ, and z for radius, azimuthal angle, and axial direction, respectively.

The working principle of the cyclotron trap is to wind up the range path of particles inside a rotationally symmetric weak-focusing magnetic field B characterized by $0 \leq n \leq 1$, where n is the field index given by

$$n = -(\delta B/\delta r) \cdot (r/B) . \tag{13.1}$$

Particles with momenta p_{beam} are injected radially through the fringe field to a radius r_{in} in a direction opposite to that for ejection from a cyclotron accelerator. At this radius they are decelerated by a moderator to momenta p_θ

$$p_\theta = -\frac{e}{c} B_z \cdot r_{in} , \tag{13.2}$$

which ideally leads to circular orbits at a given field B_z. A deviation from this ideal picture is caused by the injection method itself. Betatron oscillations are deliberately excited at injection for radii with $0.5 \leq n \leq 0.8$ to prevent the particles from hitting the moderator in one of the subsequent revolutions. More important is the radial spread Δr_p caused by the momentum spread Δp from deceleration in the injection moderator. This depends strongly on the injection scheme chosen for the different particle beams and is given by

$$\Delta r_p = r \cdot \frac{\Delta p}{p} \cdot \frac{1}{1-n} . \tag{13.3}$$

This leads to spreads of a few millimeters for antiproton beams at LEAR, and to a few centimeters for pion injection at SIN/PSI as the worst case. Assuming a smooth energy loss beyond this point, the particles can then be guided by the weak focusing cyclotron field and be led to the centre of the device.

A first comparison with a linear arrangement for stopping particles with range length R is given here. For a linear arrangement, the stopping process leads to a longitudinal range straggling, δR, and Coulomb scattering leads to a lateral widening of the order of $2 \cdot \delta R$. The stopping volume then is of the order of $4 \cdot (\delta R)^3$ [3]. With the cyclotron trap, the range is wound up into a spiral with its end at the centre of the cyclotron trap, yielding, in first approximation, a radial spread of $\Delta r_{stop} = r_{in} \cdot \delta R/R$. The uncertainty in range leads only to an azimuthal uncertainty and multiple scattering leads to a broadening in the z direction. If the deceleration is slow enough, the orbits would adiabatically follow the shrinking radius corresponding to the decreasing momentum p. The stopping distribution in the cyclotron trap scales with the value for the injection radius, so that a stopping volume is:

$$V_{stop}^{cyc} \propto \left(r_{in} \cdot \frac{\delta R}{R} \right)^3 . \tag{13.4}$$

A gain of the order of $(\frac{R}{r_{in}})^3$, compared with a linear degrader arrangement, can, in principle, be reached. In practice, the gain factor is smaller. This is caused mainly for pions by the short lifetime requiring the use of additional moderators. For pion and muon beams, losses occur during the injection through the fringe field because of the quality of the beam. In addition, range straggling in the moderator and deliberate detuning in the beginning of the deceleration process must be taken into account for all types of particles. These factors result in an additional increase of the stopping distribution.

For antiprotons, a gain factor of 10^4 was measured. For pions and muons, gain factors of the order of 10 to 30 proved to be realistic.

13.3 The principle in more detail

An instructive way to visualize the principle of the cyclotron trap is given by the quasipotential picture [4, 5]. The quasipotential $U(r, z)$ is given by

$$U(r,z) = \frac{1}{2m} \cdot \left(\frac{P}{r} - \frac{e}{cr} \cdot \int_0^r B_z(r',z)r'dr' \right)^2 \tag{13.5}$$

with P being the so-called generalized angular momentum

$$P = rp_\theta + \frac{e}{c} \int_0^r B_z(r',z)r'dr' = \text{const.} \tag{13.6}$$

Values for the quasipotential are depicted in Figure 13.1 and in Figure 13.2 for the field of CT I. Bound orbits require minima of the quasipotential curves both in radial and axial direction. This leads to the requirement $0 < n < 1$. For the minima in $U(r, z = 0)$ the radius of an orbiting particle is given by equation (13.2).

As seen from Figure 13.1, values of P higher than about 6 MeV/c·m cannot lead to bound orbits as minima develop only for smaller values. The injection, e.g. of antiprotons with a momentum of 200 MeV/c, requires a momentum loss of 70 MeV/c in a moderator of suitable thickness placed at a radius of about 140 mm. In this way they are captured in a shallow potential well with P slightly lower than 6 MeV/c·m. Without any further energy loss, the particles would be stopped in one of the next orbits by this moderator. If there is an additional energy loss, they eventually follow the developing potential minima. If the energy loss is sufficiently small, the particles oscillate around the newly established equilibrium radii and will be guided adiabatically to the centre of the trap. If the energy loss is too large, the centre of the device will not be included in the orbit of the particles. A negative generalized momentum would develop and the particles would even be expelled from the centre [5].

In the axial direction the focusing is very strong in the beginning of the deceleration process, and decreases when the particles orbit to the centre of the cyclotron trap. They will be stopped at short axial distances from the centre because of their low energy. In addition the magnetic mirror effect will contain them axially. Applying an axial electric field provides the opportunity to extract them to form a particle beam. This approach was used to provide a low-energy muon beam for an experiment to determine the proton radius mentioned in Section 13.6.2.

13.4 Phase space considerations

The phase space development in the case of energy loss is described by the extended Liouville theorem [6]. For the deceleration of particles in matter the dissipative force given by the energy loss (Bethe-Bloch formula) can be approximated as a function of the momentum p by

$$Q \propto p^{\alpha(p)} . \tag{13.7}$$
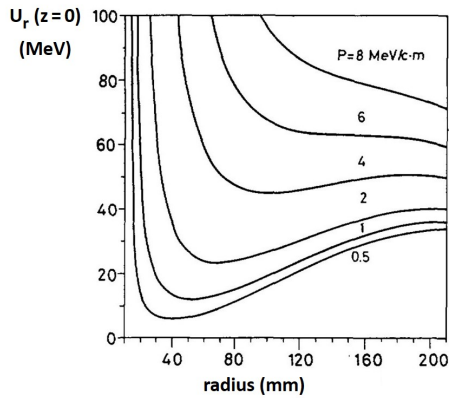
Figure 13.1: Radial distribution of the quasipotential in the median plane for different positive values of the generalized momentum P.
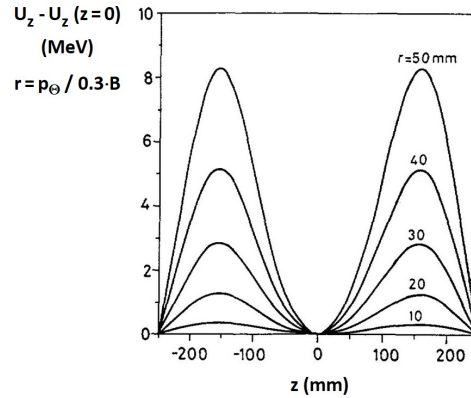

Figure 13.2: The difference of the axial distribution of the quasipotential to its value at $z = 0$ is shown for different values of the equilibrium radii r_0.

The value of α varies between -1.4 and -1.7 for materials with low ionization potentials. Assuming α is piecewise constant, and partitioning the deceleration path into constant time intervals, the ratio of the momentum spread at the beginning (i) and the end (f) of an interval is given by

$$\frac{\Delta p_f}{\Delta p_i} = \left(\frac{p_f}{p_i}\right)^\alpha. \tag{13.8}$$

This relation does not hold if the emittance changes during deceleration, as is the case for the deceleration by an electric field. Energy loss, however, applies equally in any spatial direction resulting in a constant emittance. Going from linear to circular motion, we arrive at an expression that is central for understanding the working principle of the cyclotron trap

$$\frac{\Delta p_f}{\Delta p_i} = \left(\frac{p_f}{p_i}\right)^\alpha \cdot \frac{\omega_i}{\omega_f} \tag{13.9}$$

with ω, the circular frequency of motion, being proportional to the magnetic field strength. The increase of Δp, caused by the momentum decrease, is partially counteracted by the increase of the cyclotron frequency at smaller radii. The interesting quantity for the formation of exotic atoms, however, is the radial spread Δr_p. It is connected to the momentum spread via equation (13.3). For the orbits with small radii and n approaching a value of 0, a decrease of Δr_p can be expected.

Extensive calculations of the dynamics of the injected and decelerated particles with real beam parameters and the geometry of the finally-built cyclotron traps confirmed these expectations. The radial extension of the stopping distribution corresponds to the radial spread of the beam at the beginning of the deceleration process. The axial extension of the stopping distribution, however, is almost a factor of 2 bigger than the axial extension at the beginning.

13.5 Technical realisation

The weak focusing field is produced by two superconducting ring coils. Because of the high field strength, the dimensions of the device can be kept small. The field direction is horizontal so that the particle orbits are in the vertical plane. Access to the stopping region is provided by a borehole in the cryostat housing of the coils. We describe here the set-up of CT II shown in Figure 13.3 and Figure 13.4.
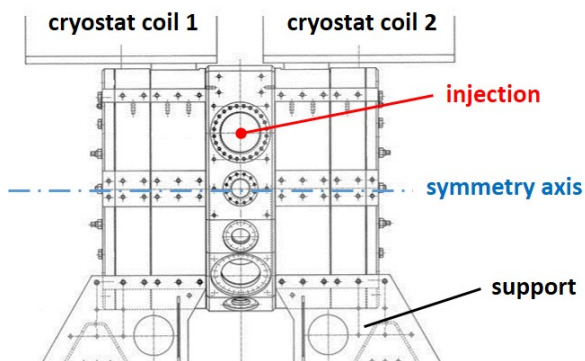
Figure 13.3: The set-up of CT II. The magnetic field is horizontal with the injection point in the vertical symmetry plane, about 200 mm from the symmetry axis. The supporting table and the two separated cryostats are indicated.
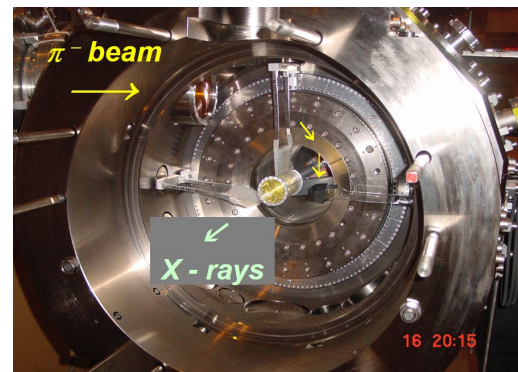
Figure 13.4: The interior part of CT II with one of the two halves removed. The beam enters from the left and is guided to a gas target on the symmetry axis with the help of additional moderators.

The two superconducting coils are located in separated cryostats. They are surrounded by a soft iron return yoke that also serves as magnetic shielding to reduce the fringe field. Additional soft iron pieces are mounted at the inner cryostat walls to optimize the field. Iron rings are mounted to balance magnetic forces. Beams are injected through a hole in the shielding as shown in Figure 13.4. The two halves can be separated to access the interior, thus providing a high versatility.

13.6 Particle physics experiments

As most of the experiments performed with the two cyclotron traps were discussed in a review paper by D. Gotta [7] including extensive references, the following discussion can be brief.

13.6.1 Antiprotonic atoms

The possibility of experiments with antiprotonic atoms at LEAR/CERN motivated the construction of the cyclotron trap CT I. The 105 MeV/c antiproton beams were ideal for the deceleration with the cyclotron trap. Of the incoming beam, 86% can be stopped in a 30 mbar hydrogen gas target with a diameter of 20 mm (FWHM). This resulted in an increase of stopping densities of more than 4 orders of magnitude, and led to successful measurements of the ground state shift and width in antiprotonic hydrogen isotopes. A measurement of these quantities for the 2p-state in these atoms with a crystal spectrometer was also made [8].

13.6.2 Muonic and pionic atoms

The muon and pion beams at SIN/PSI presented considerable difficulties for the use of the cyclotron trap. The emittance of the beams and the lifetimes of the particles, deviated from the ideal situation encountered with antiprotons. Nonetheless, experiments with the first cyclotron trap (CT I) proved to be successful. In a first experiment, the pion mass was determined from pionic atoms formed in nitrogen gas with an almost depleted electron shell [9]. Earlier experiments suffered from the lack of knowledge of the state of the electron shell, as a solid Mg target was used. The determination of the pion mass was later improved by using CT II, allowing for energy calibration with muonic oxygen [10] (Section 10 [11]). Coulomb explosion was directly observed for the first time; this occurs in the formation of exotic atoms from molecules

such as N_2 [12]. A first round of crystal spectrometer measurements of X-rays in pionic hydrogen isotopes was also performed. The work with muonic atoms led to the observation of the two-photon transition in muonic boron [13].

The second cyclotron trap (CT II) was developed to adapt its acceptance to the emittance of the pion and muon beams at PSI. For pions, about 1% of the initial beam could be stopped in a hydrogen target at STP. For muon beams, this number is about one order of magnitude higher. This led to a successful series of measurements in muonic hydrogen and in both pionic hydrogen and deuterium, reducing typical measuring times to a month (Section 14 [14]). The line shape of the muonic hydrogen $K\beta$ transition was determined with high precision as a prerequisite for later experiments in pionic hydrogen [15]. A method was developed to extract muons from the centre of the trap to form a low-energy muon beam. This opened a path for important experiments to determine the proton radius via the Lamb shift in muonic hydrogen [16] (Section 21 [17]).

13.7 Atomic physics experiments

13.7.1 Ionized exotic atoms

It became clear at an early stage that the possibility of forming exotic atoms in low pressure gases can lead to a complete ionization of the electron shell [18]. After formation, the electromagnetic cascade depletes the electron shell up to $Z = 36$ for antiprotons, and up to $Z = 18$ for muons or pions. As the natural linewidth of the corresponding transitions is negligibly small, these X-rays can be used for calibration of some atomic and particle physics experiments [10, 19]. The atomic physics aspect of these experiments proved to be interesting by itself [20, 21].

13.7.2 ECR-source: a by-product

The crystal spectrometer experiment in pionic hydrogen and deuterium required a precise knowledge of the response function of the device. To achieve this, the geometry of CT II was changed to that of an ECR source providing a high-intensity X-ray source. Here the distance of the solenoids had to be changed and a hexapole was inserted on the axis of CT II [22]. Then, the crystal spectrometer could be calibrated in a set-up equivalent to the pionic and muonic experiments [23].

References

[1] J. Hüfner, F. Scheck and C. S. Wu, *Muon physics I*, Academic Press, New York (1977).

[2] E. Borie and M. Leon, *X-ray yields in protonium and mesic hydrogen*, Phys. Rev. A **21**, 1460 (1980), doi:10.1103/PhysRevA.21.1460.

[3] L. M. Simons et al., *Exotic atoms and their electron shell*, Nucl. Instr. and Meth. B **87**, 293 (1994), doi:10.1016/0168-583X(94)95275-2.

[4] A. A. Kolomensky and A. N. Lebedev, *Theory of cyclic accelerators*, North-Holland Publishing Company, Amsterdam (1966).

[5] L. M. Simons, *Recent results on antiprotonic atoms using a cyclotron trap at LEAR*, Physica Scripta T22 (1988), doi:10.1088/0031-8949/1988/T22/013.

[6] A. J. Lichtenberg, *Phase space dynamics of particles*, J. Wileys, New York (1969).

[7] D. Gotta, *Precision spectroscopy of light exotic atoms*, Progr. Part. Nucl. Phys. **52**, 133 (2004), doi:10.1016/j.ppnp.2003.09.003.

[8] D. Gotta et al., *Balmer α transitions in antiprotonic hydrogen and deuterium*, Nucl. Phys. A **660**, 283 (1999), doi:10.1016/S0375-9474(99)00385-1.

[9] S. Lenz et al., *A new determination of the mass of the charged pion*, Phys. Lett. B **416**, 50 (1998), doi:10.1016/S0370-2693(97)01337-3.

[10] M. Trassinelli et al., *Measurement of the charged pion mass using X-ray spectroscopy of exotic atoms*, Phys. Lett. B **759**, 583 (2016), doi:10.1016/j.physletb.2016.06.025.

[11] M. Daum and D. Gotta, *The mass of the π^-*, SciPost Phys. Proc. **5**, 010 (2021), doi:10.21468/SciPostPhysProc.5.010.

[12] T. Siems et al., *First direct observation of Coulomb explosion during the formation of exotic atoms*, Phys. Rev. Lett. **84**, 4573 (2000), doi:10.1103/PhysRevLett.84.4573.

[13] K. Kirch et al., *Metastability of the muonic boron 2S state*, Phys. Rev. Lett **78**, 4363 (1997), doi:10.1103/PhysRevLett.78.4363.

[14] D. Gotta and L. M. Simons, *Pionic hydrogen and deuterium*, SciPost Phys. Proc. **5**, 014 (2021), doi:10.21468/SciPostPhysProc.5.014.

[15] D. S. Covita et al., *Line shape analysis of the Kβ transition in muonic hydrogen*, Eur. Phys. J. D **72**, 72 (2018), doi:10.1140/epjd/e2018-80593-1.

[16] A. Antognini et al., *Proton structure from the measurement of the $2s − 2p$ transition frequencies of muonic hydrogen*, Science **339**, 417 (2013), doi:10.1126/science.1230016.

[17] A. Antognini, F. Kottmann and R. Pohl, *Laser spectroscopy of light muonic atoms and the nuclear charge radii*, SciPost Phys. Proc. **5**, 021 (2021), doi:10.21468/SciPostPhysProc.5.021.

[18] R. Bacher et al., *Muonic atoms with vacant electron shells*, Phys. Rev. Lett. **54**, 2087 (1985), doi:10.1103/PhysRevLett.54.2087.

[19] D. F. Anagnostopoulos et al., *Low-energy X-ray standards from hydrogenlike pionic atoms*, Phys. Rev. Lett. **91**, 240801 (2003), doi:10.1103/PhysRevLett.91.240801.

[20] K. Kirch et al., *Muonic cascades in isolated low-Z atoms and molecules*, Phys. Rev. A **59**, 3375 (1999), doi:10.1103/PhysRevA.59.3375.

[21] D. Gotta et al., *X-ray transitions from antiprotonic noble gases*, Eur. Phys. J. D **47**, 11 (2008), doi:10.1140/epjd/e2008-00025-3.

[22] S. Biri et al., *Electron cyclotron resonance ion trap: A hybrid magnetic system with very high mirror ratio for highly charged ion production and trapping*, Rev. Sci. Instr. **71**, 1116 (2000), doi:10.1063/1.1150401.

[23] D. F. Anagnostopoulos et al., *On the characterisation of a Bragg spectrometer with X–rays from an ECR source*, Nucl. Instr. and Meth. A **545**, 217 (2005), doi:10.1016/j.nima.2005.01.311.

Pionic hydrogen and deuterium

D. Gotta[1*] and L. M. Simons[2]

1 Institut für Kernphysik, Forschungszentrum Jülich GmbH, D-52425 Jülich, Germany
2 Paul Scherrer Institut, CH-5232 Villigen, Switzerland

* d.gotta@fz-juelich.de

Abstract

The measurement of strong-interaction shift and broadening in pionic hydrogen and deuterium yields pion-nucleon scattering lengths as well as the threshold pion-production strength on isoscalar NN pairs. Results from recent high-resolution experiments at PSI using crystal spectrometers allow important comparisons with the outcome of the modern low-energy description of QCD within the framework of effective field theories.

14.1 Introduction

The last decades have seen a successful theoretical description of strong-interaction phenomena at threshold within effective field-theory (EFT) approaches: the chiral symmetry of the QCD Lagrangian allows the derivation of so-called low-energy theorems. In reality, the chiral symmetry is explicitly broken because of the finite masses of the light quarks u, d, and s. This leads, *e. g.* to a finite pion mass which is, however, still small compared to the hadronic scale given by the nucleon mass. The deviations from low-energy theorems reveal the amount of symmetry breaking.

Chiral Perturbation Theory (χPT) offers a systematic way of quantifying these symmetry-breaking effects. A chiral expansion, ordered by the powers of (small) momenta, the quark-mass differences, and the fine structure constant α, includes strong isospin-breaking effects resulting from the quark-mass differences and those of electromagnetic origin on the same footing. The unknown structure of QCD at short distances is parametrized by so-called low-energy constants (LECs), which must be taken from experiment as long as results from lattice-QCD calculations are not available.

Pions, being composite particles of the lightest quarks u and d, and their interactions, play a prominent role. Hence, $\pi N \rightarrow \pi N$ reactions and the corresponding scattering lengths are of fundamental interest for the understanding of low-energy QCD phenomena. In the limit of isospin conservation, all $\pi N \rightarrow \pi N$ reactions are completely determined by only two independent real numbers, the scattering lengths corresponding to the isospin combinations

$I = 1/2$ and $3/2$ of the πN system. Therefore, quantitative tests of isospin-breaking effects, predicted to be of the order of a few per cent by advanced χPT calculations, are of great importance.

The corresponding precision for the experimental approach is achieved by means of high-resolution X-ray spectroscopy of pionic hydrogen and deuterium. Considering the energy regime of such atomic systems, the measurement of the strong-interaction effects constitutes a scattering experiment at threshold.

Concepts and recent theoretical efforts on low-energy πN scattering and pionic hydrogen are reviewed in [1, 2]. Properties of exotic atoms and experimental methods are outlined in [3].

14.2 Strong-interaction effects

Exotic atoms provide an ideal laboratory for the extraction of scattering lengths from experiment, because problems due to normalization and extrapolation to threshold inherent to scattering experiments are absent. Such atoms are formed when negatively charged particles, such as pions, are captured in high-lying atomic levels of the Coulomb potential of a nucleus: a de-excitation cascade subsequently starts. The strong interaction gives rise to a change of the total energy of the particle-nucleus system ΔE and to its lifetime observed as an energy shift ϵ and a broadening Γ of lower-lying atomic levels, where the overlap of the atomic bound-state wave function with the nucleus of mass number A becomes significant. For atomic states with principle quantum number n and angular momentum $\ell = 0$, ns, the complex energy shift is directly related to the complex scattering length $a_{\pi A}$ [4]

$$\Delta E_{ns}^{\pi A} - i\,\frac{\Gamma_{ns}^{\pi A}}{2} = -\frac{2\alpha^3 \mu_A^2 c^4}{\hbar c} \cdot \frac{1}{n^3} \cdot a_{\pi A} + ... \,, \tag{14.1}$$

where α is the fine structure constant and μ_A is the reduced mass of the particle-nucleus system. The ellipses stand for higher order corrections [1, 2]. In this paper, the sign convention for atomic level shifts ϵ is the change of the X-ray transition energy, *i. e.* $\epsilon \equiv -\Delta E$.

In the case of pionic hydrogen, only the ground-state effects are detectable by high-resolution X-ray spectroscopy. The two independent scattering lengths may be described by isoscalar and isovector scattering lengths a^+ and a^- for the elastic channels:

$$a^{\pm} \equiv (a_{\pi^- p \to \pi^- p} \pm a_{\pi^+ p \to \pi^+ p})\,. \tag{14.2}$$

In terms of the isospin combinations $I = 1/2$ and $I = 3/2$, a^+ and a^- are given by:

$$a^+ = \frac{1}{3}(a_{1/2} + 2a_{3/2}) \;\; \text{and} \tag{14.3}$$

$$a^- = \frac{1}{3}(a_{1/2} - a_{3/2})\,. \tag{14.4}$$

In leading order, pionic hydrogen and deuterium give access to the scattering lengths of the elastic reactions $\pi^- p \to \pi^- p$ and $\pi^- n \to \pi^- n$ and to the charge exchange channel $\pi^- p \to \pi^0 n$ after correcting for the radiative capture contribution $\pi^- p \to \gamma n$. As seen from (14.5) – (14.7), three experimental quantities are available for the two independent scattering lengths: the 1s-level strong-interaction shifts in pionic hydrogen and deuterium $\epsilon_{1s}^{\pi H}$ and $\epsilon_{1s}^{\pi D}$ and broadening in pionic hydrogen, $\Gamma_{1s}^{\pi H}$. Hence, such measurements constitute a decisive constraint both on the experimental and theoretical approaches.

$$\epsilon_{1s}^{\pi H} \;\propto\; \mathrm{Re}\, a_{\pi^- p} \;\propto\; a_{\pi^- p \to \pi^- p} \qquad\qquad = a^+ + a^- + ... \tag{14.5}$$

$$\Gamma_{1s}^{\pi H} \;\propto\; \mathfrak{I}\, a_{\pi^- p} \;\propto\; (a_{\pi^- p \to \pi^0 n})^2 \qquad\qquad = (a^-)^2 + ... \tag{14.6}$$

$$\epsilon_{1s}^{\pi D} \;\propto\; \mathrm{Re}\, a_{\pi^- d} \;\propto\; a_{\pi^- p \to \pi^- p} + a_{\pi^- n \to \pi^- n} \quad = 2 \cdot a^+ + ... \;. \tag{14.7}$$

The ellipses indicate the corrections needed to derive the QCD quantities a^+ and a^- from the measurable quantities $a_{\pi N \to \pi N}$. These corrections are given by recent χPT calculations [1,2]. For the pionic deuterium case, in addition substantial multi-body corrections are necessary which, however, are well under control [5]. The check of consistency of these results is an essential outcome of the experimental and theoretical efforts of the last decades.

The imaginary part $\operatorname{Im} a_{\pi D}$, which gives the leading contribution to the hadronic broadening $\Gamma_{1s}^{\pi D}$ in pionic deuterium, measures the transition strength α of s-wave pions on an isoscalar nucleon-nucleon pair $\pi NN \leftrightarrow NN$ and is an independent quantity not related to the scattering lengths a^+ and a^- [6,7].

$$\Gamma_{1s}^{\pi D} \; \propto \; \Im \, a_{\pi^- d} \; \propto \; \sigma_{\pi^+ d \to pp}^{threshold} \; \propto \; \alpha \,. \tag{14.8}$$

14.3 Experimental approach

The possibility of performing high-statistics experiments of exotic hydrogen even in dilute targets with high-resolution devices like crystal spectrometers became possible by using the cyclotron trap (Section 13 [8]). Figure 14.1 shows the set-up of cyclotron trap and crystal spectrometer for the studies described here [7,9–11]. With a massive specially tailored concrete shielding an improvement in the beam-induced background of up to a factor of 50 is achieved compared to previous experiments.
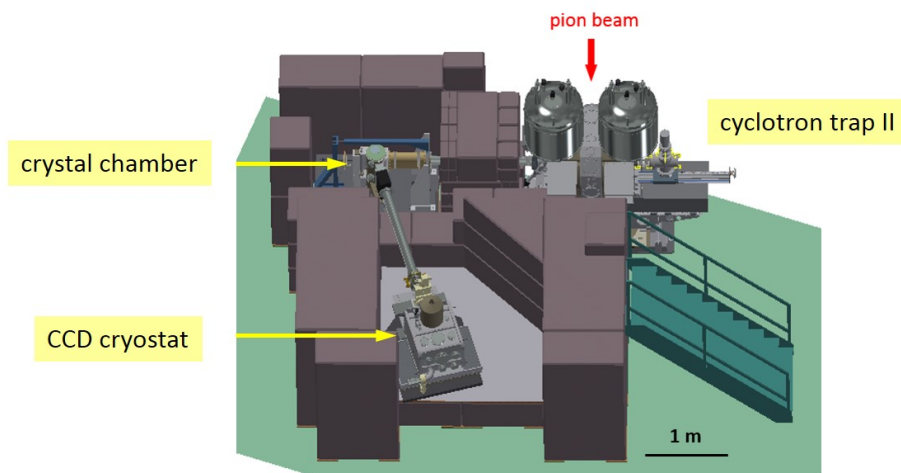
Figure 14.1: Set-up in the πE5 area at PSI. The Bragg crystal is mounted inside a vacuum chamber and connected to the cyclotron trap and the CCD X-ray detector by a vacuum system to minimize absorption losses. The roof of the concrete cave is not shown.

The crystal spectrometer was set up in Johann configuration which allows the measurement of an energy interval corresponding to the extension of the X-ray source in the direction of dispersion [12]. Thin polished slabs of silicon and quartz were used as Bragg crystals. They are spherically bent with radii of about $R_c = 3\,\mathrm{m}$ when attached to glass lenses of optical quality by adhesive forces only (Figure 14.2). Resolutions of $270 - 460\,\mathrm{meV}$ were achieved for the X-rays in the energy range of $2.2 - 3.1\,\mathrm{keV}$ which is very close to the theoretical limit achievable for the particular crystal and reflection.

The detector extension in the direction of dispersion has to be matched to the source size to utilize the capabilities of the Johann set-up. The detector is realized as a 2 x 3 array of Charge-Coupled Devices (CCDs) of total area of 48 x 72 mm^2 (Figure 14.2) and located at the

distance $R_c \cdot \sin \Theta_B$ given by the focussing condition where Θ_B is the Bragg angle. The diffracted X-rays create a cone-like hit pattern in the detection plane which, after curvature correction and projection to the direction of dispersion, directly yields an energy spectrum (Figure 14.3). The necessary two-dimensional position resolution is provided by the $40\,\mu m \times 40\,\mu m$ pixel structure of the CCDs.

Figure 14.2: Left: quartz disk attached adhesively to a concave glass lens, middle: crystal mounting in an adjustable support frame with an aperture to limit the so-called Johann defocussing, right: focal-plane X-ray detector removed from the cryostat [13].

Energy determination in Johann-type set-ups requires a calibration line ideally at the same Bragg angle as the X-ray line of interest. In this experiment, the energy of the pionic oxygen line $(6-5)$ is very close to the one of pionic hydrogen $(3-1)$. The precise knowledge of the charged pion mass then allows the calibration of pionic-atom transitions among themselves [14] (Section 10 [15]).

The understanding of collisional processes during the lifetime of pionic hydrogen plays a key role for a precision determination of the strong-interaction effects. For the πH system, X-ray transition energies are of the order of 3 keV while hadronic shifts are of the order of a few eV and the broadening around 1 eV. Therefore, a thorough study of possible collision-induced energy shifts and broadening has been performed. Such a study essentially means the measurement of various transitions at various target densities as well as a comparison with muonic hydrogen. The hydrogen density was adjusted in the cryogenic target by temperature variation in order to allow the use of thin windows.

Energy shifts, which would spoil the result for ϵ_{1s}, may appear if after molecular formation $\pi H + H_2 \to [(pp\pi)p]ee$ X-ray emission from molecular states occurs. As the formation rate scales with collision probability, a density-dependent X-ray energy would demonstrate its appearance. No such effect was observed for either hydrogen and deuterium [7, 9, 10].

The main obstacle to a precision determination of the hadronic broadening Γ_{1s} is Doppler broadening due to Coulomb de-excitation [16–18]. During these non-radiative transitions, the energy of the de-excitation step $(n-n')$ is transferred into kinetic energy of the collision partners. The competition of acceleration by Coulomb de-excitation and deceleration by elastic and inelastic collisions leads to a complex kinetic energy distribution at the time of X-ray emission. Hence, the measured line shape is a convolution of spectrometer response, Doppler broadening, and the Lorentzian representing the hadronic broadening. For that reason, a measurement of the twin system muonic hydrogen was performed, where the absence of the strong interaction allows the possibility of directly studying the effect of Doppler broadening.

Consequently, the ultimate knowledge of the spectrometer response is of great importance. Here, the cyclotron trap offers another unique possibility when extended to operate as ECR

source (Section 13 [8]). The ECR source yields narrow X-rays at high rates from helium-like low Z elements like sulphur, chlorine, and argon which almost coincide in energy with the pionic hydrogen and deuterium X-ray transitions.

14.4 Results

Spectra of the $(3p - 1s)$ transitions are shown in Figure 14.3. Above the oxygen freeze-out temperature the simultaneous measurement of the πO calibration line and πH line is feasible by means of a small O_2 admixture to the H_2 gas. For lower temperature, hydrogen and oxygen measurements were performed alternately.
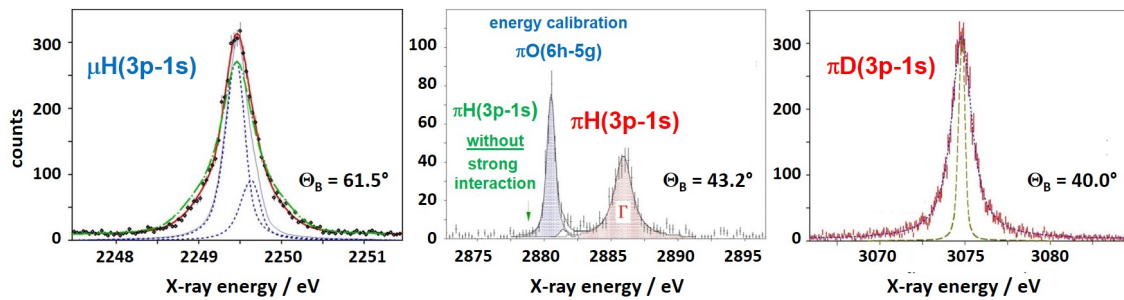
Figure 14.3: Spectra of the $(3p - 1s)$ transitions in muonic [9] and pionic hydrogen [10] and pionic deuterium [7]. The narrow structures displayed inside the μH and πD lines demonstrate the resolution of the spectrometer equipped with a Si 111 crystal as measured by using an ECR source [19].

The muonic hydrogen spectrum shows the importance of the Doppler-induced broadening (Figure 14.3). A satisfactory description requires that about 2/3 of the μH atoms have kinetic energies below a few eV contributing only to a negligible amount to the broadening. The remaining 1/3 can be attributed to energies around 24 and 56 eV, which corresponds to the Coulomb de-excitation transitions $(5 - 4)$ and $(4 - 3)$. Within the uncertainties of such an analysis, there is good agreement with cascade theory [9].

In pionic hydrogen, again a large fraction, about 60-80%, of the πH atoms have kinetic energies below a few eV. The appearance of higher energies is needed to describe the line shape. However, because of the hadronic broadening an assignment to particular Coulomb de-excitation transitions is impossible [11].

It is worth mentioning that no Doppler contribution could be identified in pionic deuterium within the experimental uncertainties [7]. A theoretical explanation for such behavior is provided by cascade theory [20].

The strong-interaction effects, summarized in Table 14.1, represent the weighted average over the various transitions measured and target densities.

Table 14.1: Measured strong-interaction effects in pionic hydrogen and deuterium (in meV).

$\epsilon_{1s}^{\pi H}$	$\Gamma_{1s}^{\pi H}$	$\epsilon_{1s}^{\pi D}$	$\Gamma_{1s}^{\pi D}$
7085.8 ± 9.6 [10]	856 ± 27 [11]	-2356 ± 31 [7]	1171_{-49}^{+23} [7]

14.5 Summary

The three constraints on the two independent isoscalar and isovector πN scattering lengths are shown in Figure 14.4. Because of the poor knowledge of LECs, the use of a modified isoscalar scattering length $\tilde{a}^+$ is more convenient in the constraint analyses. The most recent χPT calculation gives $\tilde{a}^+ - a^+ = (-6.1 \pm 2.5) \cdot 10^{-3} \, m_\pi^{-1}$ [2]. It is important to note that good overlap is achieved, although substantial chiral corrections have to be applied [2].

The precise result for the pion-production strength α demonstrates the advantage of exotic atoms, namely that the strong-interaction effects are determined without normalisation and extrapolation. In Figure 14.5, the pionic-deuterium results are marked as the shaded area, which is compared with pion-production experiments that typically specify statistical errors only. The only theoretical approach yielding a reliable uncertainty is due to a χPT calculations which, however, suffers at present from the scarce precision of some LECs [6].

Table 14.2: Isoscalar and isovector scattering length $\tilde{a}^+$ and a^- and threshold pion-production strength as derived from the strong-interaction effects in pionic hydrogen and deuterium.

$\tilde{a}^+$	a^-	α
$(1.7 \pm 0.8) \cdot 10^{-3} \, m_\pi^{-1}$ [11]	$(86.6 \pm 1.0) \cdot 10^{-3} \, m_\pi^{-1}$ [11]	$(251 \, {}^{+5}_{-11}) \, \text{mb}$ [7]
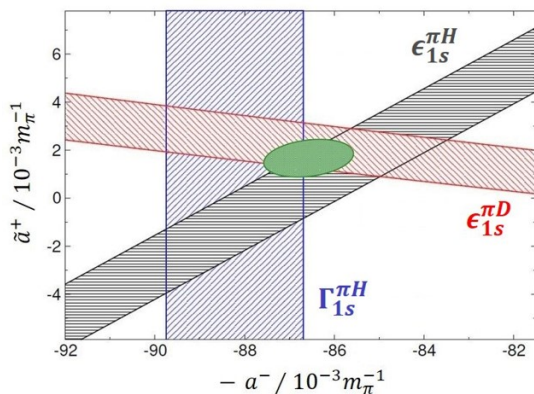
Figure 14.4: Constraints (bands) and combined result (ellipse) for the isoscalar and isovector πN scattering lengths $\tilde{a}^+$ and a^- as derived from $\epsilon_{1s}^{\pi H}$, $\epsilon_{1s}^{\pi D}$, and $\Gamma_{1s}^{\pi H}$ [11].
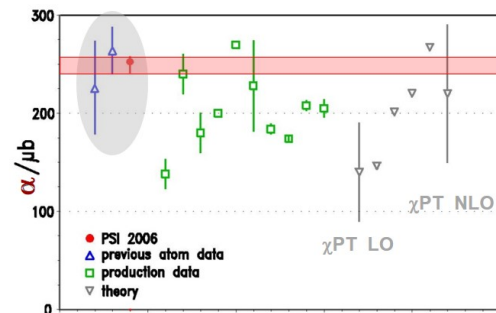
Figure 14.5: Comparison of results for pion-production strength α at threshold on isoscalar NN pairs. The horizontal band represents the precision of the most recent result for $\Gamma_{1s}^{\pi D}$ [7].

Exotic-atom data yield values for the reaction scattering lengths $a_{\pi^- p \to \pi^- p}$ and $a_{\pi^- p \to \pi^0 n}$ [10, 11]. Applying the corrections provided by χPT calculations, as well $a_{\pi^+ p \to \pi^+ p}$ as the isospin-separated scattering lengths $a_{1/2}$ and $a_{3/2}$ are attainable [2, 11]. The results are in very good agreement with recent analyses of low-energy πN scattering data [21].

In summary, recent πH, πD, and low-energy πN scattering data are quantitatively very consistent when analysed within the framework of χPT.

References

[1] J. Gasser, V. E. Lyubovitzkij and A. Rusetski, *Hadronic atoms in QCD+QED*, Phys. Rep. **456**, 167 (2008), doi:10.1016/j.physrep.2007.09.006.

[2] M. Hoferichter, J. Ruiz de Elvira, B. Kubis and U.-G. Meißner, *Roy–Steiner-equation analysis of pion–nucleon scattering*, Phys. Rep. **625**, 1 (2016), doi:10.1016/j.physrep.2016.02.002.

[3] D. Gotta, *Precision spectroscopy of light exotic atoms*, Prog. Part. Nucl. Phys. **52**, 133 (2004), doi:10.1016/j.ppnp.2003.09.003.

[4] S. Deser, M. L. Goldberger, K. Baumann and W. Thirring, *Energy level displacements in pi-mesonic atoms*, Phys. Rev. **96**, 774 (1954), doi:10.1103/PhysRev.96.774.

[5] V. Baru, C. Hanhart, M. Hoferichter, B. Kubis, A. Nogga and D. R. Phillips, *Precision calculation of threshold $\pi^- d$ scattering, πN scattering lengths, and the GMO sum rule*, Nucl. Phys. A **872**, 69 (2011), doi:10.1016/j.nuclphysa.2011.09.015.

[6] V. Lensky, V. Baru, J. Haidenbauer, C. Hanhart, A. E. Kudryavtsev and U.-G. Meißner, *Towards a field theoretic understanding of $NN \to NN\pi$*, Eur. Phys. J. A **27**, 37 (2006), doi:10.1140/epja/i2006-10002-4.

[7] Th. Strauch et al., *Pionic deuterium*, Eur. Phys. J. A **47**, 88 (2011), doi:10.1140/epja/i2011-11088-1.

[8] D. Gotta and L. M. Simons, *Cyclotron trap*, SciPost Phys. Proc. **5**, 013 (2021), doi:10.21468/SciPostPhysProc.5.013.

[9] D. S. Covita et al., *Line shape analysis of the Kβ transition in muonic hydrogen*, Eur. Phys. J. D **72**, 72 (2018), doi:10.1140/epjd/e2018-80593-1.

[10] M. Hennebach et al., *Hadronic shift in pionic hydrogen*, Eur. Phys. J. A **50**, 190 (2014), doi:10.1140/epja/i2014-14190-x.

[11] A. Hirtl et al., *Redetermination of the strong-interaction width in pionic hydrogen*, Eur. Phys. J. A **57**, 70 (2021), doi:10.1140/epja/s10050-021-00387-x.

[12] D. E. Gotta and L. M. Simons, *Remarks on a Johann spectrometer for exotic-atom research and more*, Spectrochim. Acta B **120**, 9 (2016), doi:10.1016/j.sab.2016.03.006.

[13] N. Nelms et al., *A large area CCD X-ray detector for exotic atom spectroscopy*, Nucl. Instr. Meth. A **484**, 419 (2002), doi:10.1016/S0168-9002(01)02051-4.

[14] M. Trassinelli et al., *Measurement of the charged pion mass using X-ray spectroscopy of exotic atoms*, Phys. Lett. B **759**, 583 (2016), doi:10.1016/j.physletb.2016.06.025.

[15] M. Daum and D. Gotta, *The mass of the π^-*, SciPost Phys. Proc. **5**, 010 (2021), doi:10.21468/SciPostPhysProc.5.010.

[16] L. Bracci and G. Fiorentini, *Coulomb de-excitation of mesic hydrogen*, Nuov. Cim. A **43**, 9 (1978), doi:10.1007/BF02729003.

[17] T. S. Jensen and V. E. Markushin, *Atomic cascade and precision physics with light muonic and hadronic atoms*, in Lecture Notes in Physics, Springer Berlin Heidelberg, ISBN 9783540404897 (2003), doi:10.1007/978-3-540-45059-7_3.

[18] V. N. Pomerantsev and V. P. Popov, *Coulomb deexcitation of pionic hydrogen within the close-coupling method*, Phys. Rev. A **73**, 040501 (2006), doi:10.1103/PhysRevA.73.040501.

[19] D. F. Anagnostopoulos et al., *On the characterisation of a Bragg spectrometer with X-rays from an ECR source*, Nucl. Instr. Meth. A **545**, 217 (2005), doi:10.1016/j.nima.2005.01.311.

[20] V. P. Popov and V. N. Pomerantsev, *Isotopic effects in scattering and kinetics of the atomic cascade of excited $\mu^- p$ and $\mu^- d$ atoms*, Phys. Rev. A **95**, 022506 (2017), doi:10.1103/PhysRevA.95.022506.

[21] J. Ruiz de Elvira, M. Hoferichter, B. Kubis and U.-G. Meißner, *Extracting the σ-term from low-energy pion-nucleon scattering*, J. Phys. G: Nucl. Part. Phys. **45**, 024001 (2017), doi:10.1088/1361-6471/aa9422.

Measurement of the transverse polarization of electrons emitted in neutron decay – nTRV experiment

Kazimierz Bodek[1][*] and Adam Kozela[2]

1 M. Smoluchowski Institute of Physics, Jagiellonian University, Cracow, Poland
2 H. Niewodniczański Institute of Nuclear Physics,
Polish Academy of Sciences, Cracow, Poland

[*] kazimierz.bodek@uj.edu.pl

Abstract

This paper recalls the main achievements of the nTRV experiment which measured two components of the transverse polarization (σ_{T_1}, σ_{T_2}) of electrons emitted in the β-decay of polarized, free neutrons and deduced two correlation coefficients, R and N, that are sensitive to physics beyond the Standard Model. The value of time-reversal odd coefficient R, 0.004±0.012±0.005, significantly improved limits on the relative strength of imaginary scalar coupling constant in the weak interaction. The value obtained for the time-reversal even correlation coefficient N, 0.067±0.011±0.004, agrees with the Standard Model expectation, providing an important sensitivity test of the electron polarimeter. One of the conclusions of this pioneering experiment was that the transverse electron polarization in the neutron β-decay is worth more systematic exploring by measurements of yet experimentally not attempted correlation coefficients such as H, L, S, U and V. This article presents a brief outlook on that questions.

15.1 Introduction

Beta decay theory was firmly established about six decades ago and became a part of the Standard Model (SM). It describes the semi-leptonic and strangeness-conserving processes in the 1-st particle generation mediated by charged W-boson exchange. Among the empirical foundations of the electroweak sector of the SM, the assumptions of maximal parity violation, the vector and axial-vector character, and massless neutrinos are directly linked to nuclear and neutron beta decay experiments. In this way, nuclear and neutron beta decay have played a central role in the development of the weak interaction theory. Beta decay experiments with increasing precision still confirm the first two assumptions – only the neutrino masses have been shown to be finite. However, many open questions remain such as the origin of parity

violation, the hierarchy of fermion masses, the number of particle generations, the mechanism of CP violation, and the unexplained large number of parameters of the theory. The CKM matrix induced mechanism of CP violation reported for heavier systems in [1, 2] is far too weak to explain the matter-antimatter asymmetry of universe so that new CP- or T-violation sources are subject of intensive searches. In particular, interesting are processes in the systems built of light quarks with vanishingly small contributions of the CKM matrix mechanism such as nuclear beta decay. Experiments with free neutrons play a particularly important role since their interpretation is not biased with nuclear and atomic structure uncertainties. In addition, the effects of electromagnetic interaction of charged decay products in the final state (proton, electron), which can mimic T-violation, are small and can be reliably calculated [3–5].

The nTRV project at PSI, was the first experimental search for the real and imaginary parts of the scalar and tensor couplings using the measurement of the transverse polarization of electrons emitted in the free neutron decay. There are very few measurements of this observable in general [6,7], and only two in nuclear beta decays. One of them, for the ^{8}Li system [8], provides the most stringent limit on the tensor coupling constants of the weak interaction.

According to [9], the decay rate distribution from polarized neutrons as a function of electron energy (E) and momentum (**p**) is proportional to:

$$\omega(\mathbf{J}, \hat{\boldsymbol{\sigma}}, E, \mathbf{p}) \propto 1 + \frac{\langle \mathbf{J} \rangle}{J} \cdot \left(A\frac{\mathbf{p}}{E} + N\hat{\boldsymbol{\sigma}} + R\frac{\mathbf{p} \times \hat{\boldsymbol{\sigma}}}{E} \right) + \dots, \tag{15.1}$$

where $\frac{\langle \mathbf{J} \rangle}{J}$ ($J = |\mathbf{J}|$) is the neutron polarization, $\hat{\boldsymbol{\sigma}}$ is the unit vector onto which the electron spin is projected, and A is the beta decay asymmetry parameter. N and R are correlation coefficients which, for neutron decay with usual SM assumptions: $C_V = C_V' = 1$, $C_A = C_A' = \lambda = -1.276$ [10] and allowing for a small admixture of scalar and tensor couplings C_S, C_T, C_S', C_T', can be expressed as:

$$N = -0.218 \cdot \mathrm{Re}(\mathfrak{S}) + 0.335 \cdot \mathrm{Re}(\mathfrak{T}) - \frac{m}{E} \cdot A, \tag{15.2}$$

$$R = -0.218 \cdot \mathrm{Im}(\mathfrak{S}) + 0.335 \cdot \mathrm{Im}(\mathfrak{T}) - \frac{m}{137\,p} \cdot A, \tag{15.3}$$

where $\mathfrak{S} \equiv (C_S + C_S')/C_V$, $\mathfrak{T} \equiv (C_T + C_T')/C_A$ and m is the electron mass. The SM value of N is finite, $N \approx -\frac{m}{E} \cdot A \approx 0.068$, and well within reach of this experiment. Its determination provides an important test of the experimental sensitivity. The R correlation coefficient vanishes in the lowest order SM calculations. It becomes finite if final state interactions are included, $R_{FSI} \approx -\frac{m}{137p} \cdot A \approx 0.0006$, two orders of magnitude below the sensitivity of this experiment. A larger value of R would provide evidence for the existence of exotic couplings, and a new source of time reversal violation (TRV). Using Mott polarimetry, both transverse components of the electron polarization can be measured simultaneously: σ_{T_1} contained in the decay plane defined by the neutron spin and electron momentum associated with N, and σ_{T_1} perpendicular to the decay plane and associated with R.

15.2 Experiment

The experiment was carried out at the high intensity cold neutron beam line [11] at the neutron source SINQ of the Paul Scherrer Institute, Villigen, Switzerland. The final result is based on the analysis of two data sets collected in 2006 and 2007. It profits additionally from the experience gained during another two test runs performed in 2003 and 2004. Each of those measurements featured slightly different basic conditions such as beam polarization, Mott foil thickness, spin holding magnetic field and collected statistics.

Applied detector setup was left-right symmetric. Two identical systems of detectors were arranged in planar configuration on each side of the decay volume (Figure 15.1). Each of
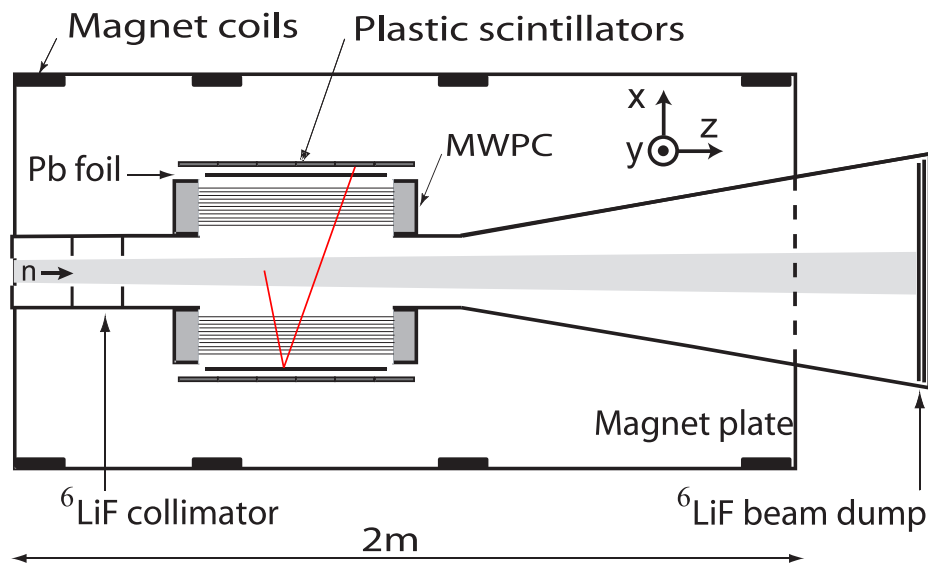
Figure 15.1: Schematic top view of the experimental setup. An electron V-track event seen by both MWPCs and scintillator on one side is indicated in red [12].

them consisted of a multi-wire proportional chamber (MWPC) for tracking of the electron trajectories and a scintillator hodoscope for electron energy measurement. Between these detectors a removable, remotely controlled, Mott scatterer (1-2 μm Pb layer evaporated on a 2.5 μm thick Mylar foil) was installed. The whole structure was mounted inside a large-volume dipole magnet providing a homogeneous vertical spin-holding field of 0.5 mT within the beam fiducial volume. A system of two RF-spin flippers (not shown in Figure 15.1) was used to control the orientation of the neutron beam polarization, reversing it at a regular time intervals, typically every 16 s.

Scintillator hodoscopes, formed by six 10-mm-thick and 60-cm-long plastic scintillator slabs were used for the electron energy reconstruction with the resolution of 33 keV at 500 keV. As the light signal produced in each segment was read out from its both ends, the up-down asymmetry has been used to determine the vertical hit position with a resolution of about 6 cm. The width of each segment (10 cm) of this hodoscope provided an approximate estimate of the position in horizontal direction (z-coordinate). Matching the position information from the MWPC and that from the scintillator hodoscope considerably helped to reduce background and random coincidences.

A 1.3-m-long multi-slit ^{6}Li-based collimator defined the beam cross section to 4×16 cm^2 at the entrance of the Mott polarimeter. The beam was transported in pure helium at atmospheric pressure and the whole surface of the decay chamber was lined with ^{6}Li loaded polymer. The total flux of the collimated beam was typically about 10^{10} neutrons/sec.

Dedicated measurement was performed to study the beam polarization as a function of neutron wavelength and position [11]. It showed a substantial dependence of polarization on the position in the beam fiducial volume. As a consequence the average beam polarization, necessary for the evaluation of the N- and R-correlation coefficients, was extracted from the observed decay asymmetry using the beta decay asymmetry parameter $A = -0.1196 \pm 0.0002$ [10] measured accurately in other experiments. This approach automatically accounts for the position-dependent beam density and polarization as well as for the detector acceptance. For this analysis, a large sample of single track events corresponding to electrons from neutrons decay (with only one reconstructed track segment on the triggering scintillator side) was
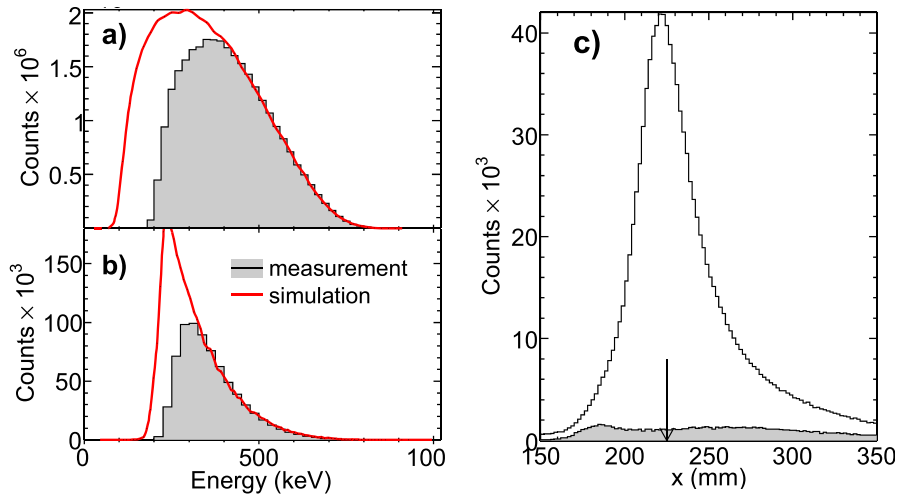
Figure 15.2: Background-corrected experimental energy distributions (shaded areas) of (a) the single-track and (b) V-track events compared with simulations. (c) Background contribution (shaded) to vertex x-coordinate distribution of V-track events. The arrow indicates the Mott foil position [12].

recorded, using a dedicated prescaled trigger. The main event trigger was used to identify and record all V-track candidates: events with two reconstructed segments on one side (indicating at Mott scattering from lead) and one segment accompanied by a scintillator hit on the opposite side, (see Figure 15.1). For more details on experimental setup, beam quality and performance of the detectors see [13].

The following asymmetries were analyzed to extract the beam polarization, P:

$$\mathcal{E}(\beta, \gamma) = \frac{N^+(\beta, \gamma) - N^-(\beta, \gamma)}{N^+(\beta, \gamma) + N^-(\beta, \gamma)} = P \beta A cos(\gamma), \tag{15.4}$$

where $N^\pm$ are experimental, background-corrected counts of single tracks sorted in 4 bins of the electron velocity β, and 15 bins of the electron emission angle γ with respect to the neutron polarization direction. The sign in the superscripts reflects the beam polarization direction.

A comparison between the measured and MC simulated energy spectra for direct and Mott-scattered electrons is shown in Figure 15.2 a and b, respectively. Electronic thresholds are not included in the simulation – this is why the measured and simulated distributions do not match at the low energy side.

Another set of asymmetries was used to extract the N and R correlation coefficients :

$$\mathcal{A}(\alpha) = \frac{n^+(\alpha) - n^-(\alpha)}{n^+(\alpha) + n^-(\alpha)}, \tag{15.5}$$

where $n^\pm$ represent background-corrected experimental numbers of counts of V-track events, sorted in 12 bins of α, the angle between electron scattering and neutron decay planes. In the case of V-track events, beside the background discussed previously, events for which the scattering took place in the surrounding of the Mott-target provide an additional source of background. Figure 15.2 c shows the distribution of the reconstructed vertex positions in the x-direction for data collected with and without the Mott foil. The distribution clearly peaks at the foil position. This relatively broad distribution is a result of extrapolation of two electron track segments crossing at relatively small angle ($20^o - 60^o$). Additionally, the
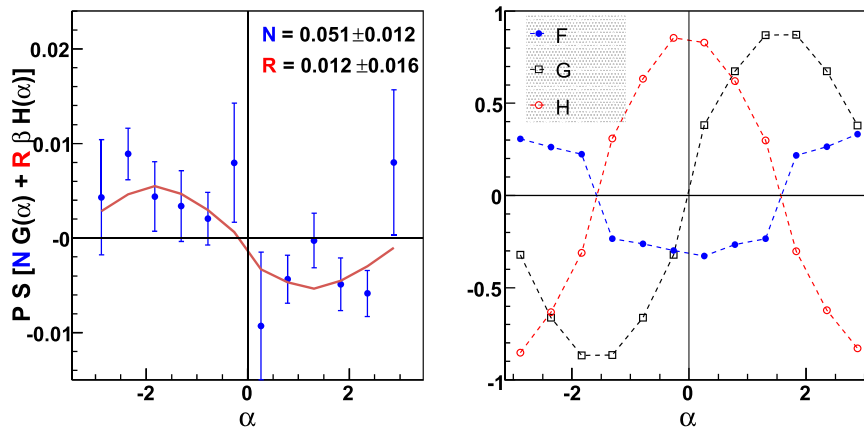
Figure 15.3: Left panel: experimental asymmetries $\mathcal{A}$ corrected for the $P\bar{\beta}A\bar{\mathcal{F}}$ term for the 2007 data set as a function of α (defined in text). The solid line illustrates a two-parameter (N, R) least-square fit to the data. The indicated errors are statistical. Right panel: geometrical factors $\bar{\mathcal{F}}(\alpha)$, $\bar{\mathcal{G}}(\alpha)$ and $\bar{\mathcal{H}}(\alpha)$ for the same data set [12].

electron straggling effects contribute to this broadening. The "foil-out" distribution has been scaled appropriately by a factor deduced from the accumulated neutron beam.

It can be shown [13] that

$$\mathcal{A}(\alpha) - P\bar{\beta}A\bar{\mathcal{F}}(\alpha) = P\bar{S}(\alpha)\left[N\bar{\mathcal{G}}(\alpha) + R\bar{\beta}\bar{\mathcal{H}}(\alpha)\right], \tag{15.6}$$

where the kinematical factors $\bar{\mathcal{F}}(\alpha)$, $\bar{\mathcal{G}}(\alpha)$, and $\bar{\mathcal{H}}(\alpha)$ represent the average values of the quantities $\hat{\mathbf{J}}\cdot\hat{\mathbf{p}}$, $\hat{\mathbf{J}}\cdot\hat{\boldsymbol{\sigma}}$ and $\hat{\mathbf{J}}\cdot\hat{\mathbf{p}}\times\hat{\boldsymbol{\sigma}}$, respectively, $\bar{S}$ is the effective analyzing power of the electron Mott scattering, known in the literature as "Sherman function", and the bar over a letter indicates event-by-event averaging. The term $P\bar{\beta}A\bar{\mathcal{F}}$ accounts for the β-decay-asymmetry-induced nonuniform illumination of the Mott foil. Since the $\bar{\beta}$ and $\bar{\mathcal{F}}$ are known precisely from event-by-event averaging, the uncertainty of this term is dominated by the error of the average beam polarization P.

Mean values of the effective analyzing powers as a function of electron energy, scattering and incidence angles were calculated using the Geant 4 simulation framework [14], following guidelines presented in [15, 16]. This approach accounts properly for the atomic structure, nuclear size effects as well as the effects introduced by multiple scattering in thick foils.

The systematic uncertainty is dominated by the effects introduced by the background subtraction procedure, connected with the choice of the geometrical cuts defining event classes "from-beam" and "off-beam". To estimate this effect, the cuts were varied in a range limited solely by the geometry of the apparatus. Because the radio–frequency of the spin flippers was a small source of noise in the readout electronics, tiny spin-flipper-correlated dead time variations were observed. The result was corrected for this effect.

The asymmetries as defined in (15.4) and (15.5) have been calculated for events with energies above the neutron β-decay end-point energy and for events originating outside of the beam fiducial volume: they were found to be consistent with zero within the statistical accuracy, which proves that the data analysis was not biased e.g. with a spin-flipper-related false asymmetry.

A fit of the experimental asymmetries $\mathcal{A}$, corrected for the $P\bar{\beta}A\bar{\mathcal{F}}$ term for the experimental data set of 2007 is shown in Figure 15.3.

From the approximate symmetry of the detector with respect to the transformation $\alpha \to -\alpha$, it follows that $\bar{\beta}, \bar{S}$ and the factors $\bar{\mathcal{F}}, \bar{\mathcal{H}}$ are all symmetric, while $\bar{\mathcal{G}}$ is an antisymmetric function of α (see Figure 15.3). This allows the extraction of the N coefficient from the expression [13]:

$$N \approx \frac{(r-1)}{(r+1)} \cdot \frac{1 - \frac{1}{2}(P\bar{\beta}A\bar{F})^2}{P\bar{S}\bar{\mathcal{G}}}, \quad r = \sqrt{\frac{n^+(\alpha)\,n^-(-\alpha)}{n^-(\alpha)\,n^+(-\alpha)}}. \tag{15.7}$$

The advantage of this method is that the impact of uncertainty of the term $P\bar{\beta}A\bar{F}$ is suppressed by a factor of about 60 compared to (15.6). The good agreement between the N values obtained in both ways enhances confidence in the extracted N and R coefficient values.

The systematic uncertainties in the evaluation of the R and N coefficients are dominated by effects introduced by the background subtraction procedure and the choice of specific values of the cuts that determine whether an individual event is attributed to "signal" or to "background". The impact of these effects was systematically studied for all data sets. Another systematics is related to the Mott-target mass distribution as it can influence the electron depolarization leading to increased uncertainty of the effective Sherman function. Additional calibration measurements were performed to determine the Mott-target thickness distribution using the photon induced X-ray emission method [17]. A detailed description of the data analysis process can be found in [12,18] together with the final result comprising all available experimental data.

$$N \;=\; 0.067 \pm 0.022_\text{stat} \pm 0.004_\text{syst}, \tag{15.8}$$
$$R \;=\; 0.004 \pm 0.012_\text{stat} \pm 0.005_\text{syst}. \tag{15.9}$$

This was the first determination of the N correlation coefficient in β-decay.

In Figure 15.4 the new results are included in exclusion plots containing all experimental information available from nuclear and neutron beta decays as surveyed in [19]. The upper plots contain the normalized scalar and tensor coupling constants $\mathfrak{S}$ and $\mathfrak{T}$, while the lower plots correspond to the helicity projection amplitudes in the leptoquark exchange model, as defined in [20]. Although the achieved accuracy does not improve the already strong constraints on the real part of the couplings (left panels), the result is consistent with the existing data and increases confidence in the validity of the extraction of R. For the imaginary part (right panels), the new experimental value of the R coefficient significantly constrains scalar couplings beyond the limits from all previous measurements. The result is consistent with the SM.

15.3 Outlook – the BRAND project

The successful determination of two transverse components of the polarization of electrons emitted in neutron decay in a pioneering and nearly optimal experiment led to the following conclusions: (i) it seems quite possible to decrease the systematic uncertainty by an order of magnitude using existing techniques, (ii) the transverse electron polarization can be studied in a more systematic way by correlating it with the electron momentum, the neutron spin, and also with the recoil proton momentum by constructing larger and higher acceptance detecting systems like e.g. proposed by [21] and operating with the highest intensity polarized cold neutron beam available. In this way, one can study seven correlation coefficients: $H, L, N, R,$
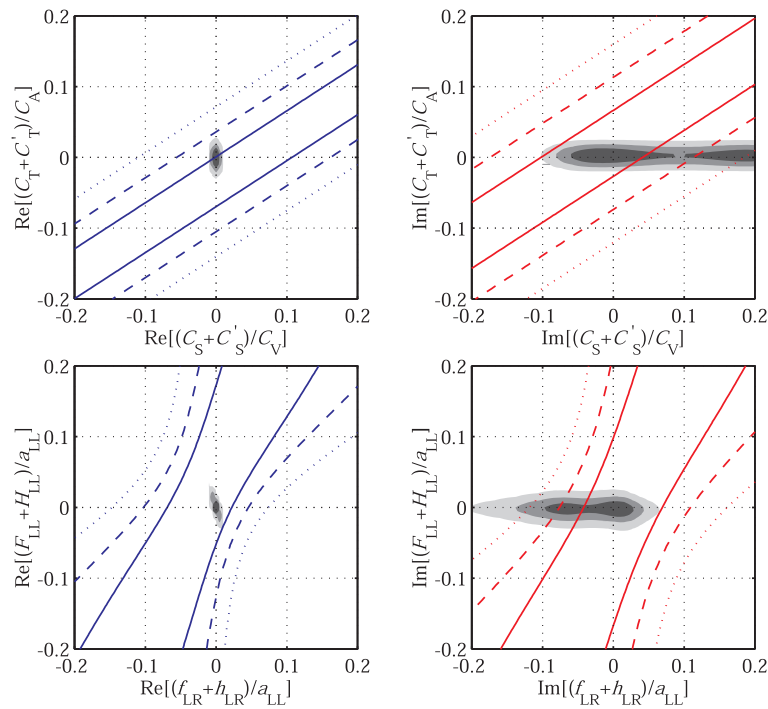
Figure 15.4: Experimental bounds on the scalar vs. tensor normalized couplings (upper) and leptoquark exchange helicity projection amplitudes (lower panels) published in [12]. The gray areas represent the available to date empirical information as listed in [19], while the lines represent the limits resulting from the present experiment. Solid, dashed and dotted lines correspond to 1-, 2- and 3- sigma confidence levels, respectively, in analogy to decreasing intensity of the grey areas.

S, U and V where five of them (H, L, S, U, V) have never been experimentally studied:

$$
\begin{aligned}
\omega(E_e, \Omega_e, \Omega_{\bar{\nu}}) \propto\ & 1 + \\
& a\,\frac{\mathbf{p}_e \cdot \mathbf{p}_{\bar{\nu}}}{E_e E_{\bar{\nu}}} + b\,\frac{m_e}{E_e} + \frac{\langle \mathbf{J} \rangle}{J} \cdot \left[A\,\frac{\mathbf{p}_e}{E_e} + B\,\frac{\mathbf{p}_{\bar{\nu}}}{E_{\bar{\nu}}} + D\,\frac{\mathbf{p}_e \times \mathbf{p}_{\bar{\nu}}}{E_e E_{\bar{\nu}}} \right] + \\
& \boldsymbol{\sigma}_{\perp} \cdot \left[H\,\frac{\mathbf{p}_{\bar{\nu}}}{E_{\bar{\nu}}} + L\,\frac{\mathbf{p}_e \times \mathbf{p}_{\bar{\nu}}}{E_e E_{\bar{\nu}}} + N\,\frac{\langle \mathbf{J} \rangle}{J} + R\,\frac{\langle \mathbf{J} \rangle \times \mathbf{p}_e}{J\,E_e} + \right. \\
& \left. S\,\frac{\langle \mathbf{J} \rangle}{J}\frac{\mathbf{p}_e \cdot \mathbf{p}_{\bar{\nu}}}{E_e E_{\bar{\nu}}} + U\,\mathbf{p}_{\bar{\nu}}\frac{\langle \mathbf{J} \rangle \cdot \mathbf{p}_e}{J\,E_e E_{\bar{\nu}}} + V\,\frac{\mathbf{p}_{\bar{\nu}} \times \langle \mathbf{J} \rangle}{J\,E_{\bar{\nu}}} \right],
\end{aligned}
\tag{15.10}
$$

where $\boldsymbol{\sigma}_{\perp}$ represents a unit vector perpendicular to the electron momentum $\mathbf{p}_e$ and $J = |\mathbf{J}|$. $\mathbf{p}_{\bar{\nu}}$ and $E_{\bar{\nu}}$ are the antineutrino momentum and energy, respectively.

The coefficients relating the transverse electron polarization to $\mathbf{p}_e$, $\mathbf{p}_{\bar{\nu}}$ and $\mathbf{J}$ have several interesting features. They vanish for the SM weak interaction, and reveal the variable size of the electromagnetic contributions. For H and N, the electromagnetic contributions are of the order of 0.06, which can be used for an internal sensitivity check of the Mott polarimeter. Finally, the dependence on the real and imaginary parts of the scalar and tensor couplings alternates exclusively from one correlation coefficient to another with varying sensitivity. This feature allows a complete set of constraints to be determined from the neutron decay alone.

The idea of implementing such a complex measurement was proposed in [22]. An updated version of the measurement can be found in [23]. Presently, the first test run devoted to the verification of the applied detectors and techniques has been completed on the PF1B cold neutron beam at the Laue Langevin Institute in Grenoble, France (ILL).
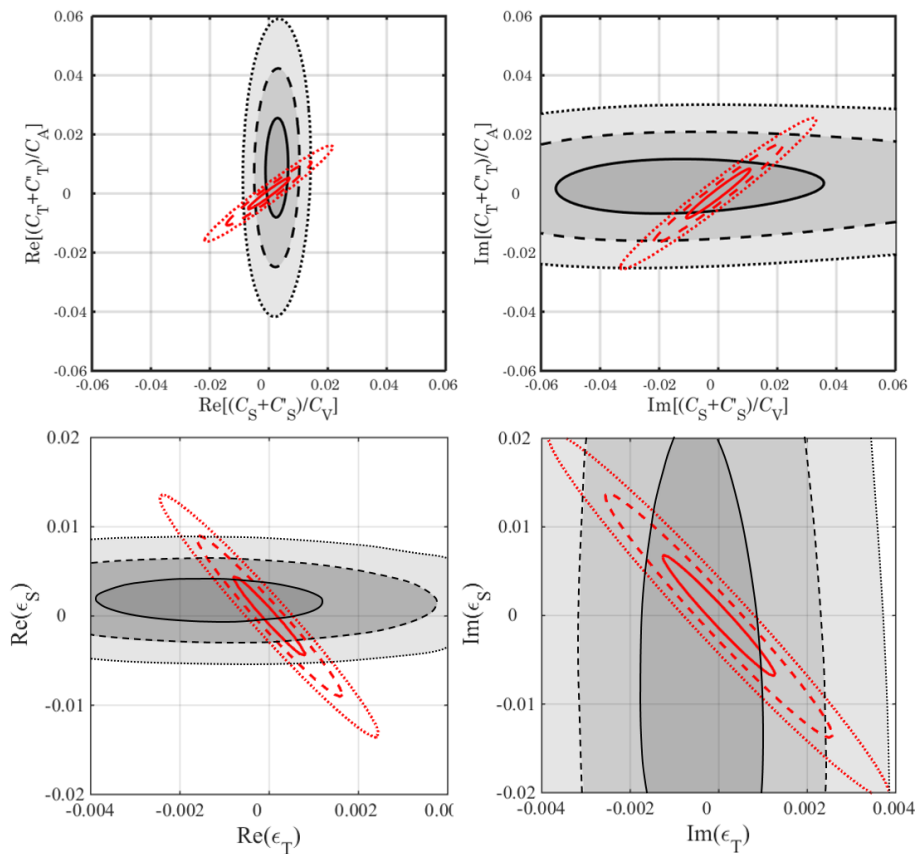
Figure 15.5: Experimental bounds on the scalar vs. tensor couplings $\mathfrak{S}$, $\mathfrak{T}$ from (15.2) (upper panels) and translated to EFT parameters ϵ_S, ϵ_T (lower panels) published in [23]. The gray areas represent the information deduced from available experiments as listed in [24], while the red lines represent the limits resulting from the correlation coefficients H, L, N, R, S, U and V measured with the anticipated accuracy of 5×10^{-4}. Solid, dashed and dotted lines correspond to 1-, 2- and 3-σ confidence levels, respectively, in analogy to decreasing intensity of the grey areas.

15.4   EFT parameterization

In order to permit for sensitivity comparison of low-energy charged-current observables with measurements carried out at high-energy colliders, the model-independent effective field theory (EFT) framework is employed. This approach bridges the classical β-decay formalism with high-energy physics. The effective nucleon-level couplings C_i, C_i' ($i \in [V, A, S, T]$) can be generally expressed as combinations of the quark-level parameters ϵ_i, $\tilde{\epsilon}_i$ ($i \in [L, R, S, T]$) [25]. The real parts of the scalar and tensor couplings parameterize CP-conserving and imaginary parts – CP-violating contributions. The high energy BSM physics quantity that can be compared with β-decay observables is the cross section for electrons and missing transverse energy (MET) in $pp \rightarrow e\bar{\nu} + MET + \ldots$ channel. Both have the same underlying partonic process: $\bar{u}d \rightarrow e\bar{\nu}$. Anticipating the experimental accuracy of about 5×10^{-4} for the transverse electron polarization related correlation coefficients in the BRAND experiment one would obtain significantly tighter bounds on the real and imaginary parts of scalar and tensor coupling constants and, consequently, on ϵ_S and ϵ_T as shown in Figure 15.5. It should be noted that such limits would be competitive to those extracted from the analysis of 20 fb^{-1} CMS collaboration data collected at 8 TeV [26, 27] and even to the planned measurements at 14 TeV.

Acknowledgments

References

[1] J. H. Christenson et al., *Evidence for the 2π decay of the K_2^0 meson*, Phys. Rev. Lett. **13**, 138 (1964), doi:10.1103/PhysRevLett.13.138.

[2] K. Abe et al., *Improved measurement of mixing-induced CP violation in the neutral B meson system*, Phys. Rev. D **66**, 071102 (2002), doi:10.1103/PhysRevD.66.071102.

[3] P. Vogel and B. Werner, *Final-state interactions and time-reversal tests in nuclear β-decay*, Nucl. Phys. A **404**, 345 (1983), doi:10.1016/0375-9474(83)90553-5.

[4] A. N. Ivanov et al., *Test of the standard model in neutron beta decay with polarized electron and unpolarized neutron and proton*, Phys. Rev. D **99**, 053004 (2019), doi:10.1103/PhysRevD.99.053004.

[5] A. N. Ivanov et al., *Corrections of order $O(E_e^2/m_N^2)$, caused by weak magnetism and proton recoil, to the neutron lifetime and correlation coefficients of the neutron beta decay*, Results Phys. **21**, 103806 (2021), doi:10.1016/j.rinp.2020.103806.

[6] N. Danneberg et al., *Muon decay: Measurement of the transverse polarization of the decay positrons and its implications for the Fermi coupling constant and time reversal invariance*, Phys. Rev. Lett. **94**, 021802 (2005), doi:10.1103/PhysRevLett.94.021802.

[7] M. Abe et al., *New limit on the T-violating transverse muon polarization in $K^+ \rightarrow \pi^0 \mu^+ \nu$ decays*, Phys. Rev. Lett. **93**, 131601 (2004), doi:10.1103/PhysRevLett.93.131601.

[8] R. Huber et al., *Search for time-reversal violation in the β decay of polarized ^8Li nuclei*, Phys. Rev. Lett. **90**, 202301 (2003), doi:10.1103/PhysRevLett.90.202301.

[9] J. D. Jackson et al., *Possible tests of time reversal invariance in beta decay*, Phys. Rev. **106**, 517 (1957), doi:10.1103/PhysRev.106.517.

[10] P. A. Zyla et al., *Review of particle physics*, Prog. Theor. Exp. Phys. 083C01 (2020), doi:10.1093/ptep/ptaa104.

[11] J. Zejma et al., *FUNSPIN polarized cold-neutron beam at PSI*, Nucl. Instr. Meth. Phys. Res., Sect. A **539**, 622 (2005), doi:10.1016/j.nima.2004.11.004.

[12] A. Kozela et al., *Measurement of the transverse polarization of electrons emitted in free-neutron decay*, Phys. Rev. Lett. **102**, 172301 (2009), doi:10.1103/PhysRevLett.102.172301.

[13] G. Ban et al., *A Mott polarimeter for the search of time reversal violation in the decay of free neutrons*, Nucl. Instr. Meth. Phys. Res., Sect. A **565**, 711 (2006), doi:10.1016/j.nima.2006.05.166.

[14] S. Agostinelli et al., *Geant4 – a simulation toolkit*, Nucl. Instr. Meth. Phys. Res. Sect. A **506**, 250 (2003), doi:10.1016/S0168-9002(03)01368-8.

[15] F. Salvat et al., *ELSEPA – Dirac partial-wave calculation of elastic scattering of electrons and positrons by atoms, positive ions and molecules*, Comp. Phys. Comm. **165**, 157 (2005), doi:10.1016/j.cpc.2004.09.006.

[16] M. A. Khakoo et al., *Monte Carlo studies of Mott scattering asymmetries from gold foils*, Phys. Rev. D **64**, 052713 (2001), doi:10.1103/PhysRevA.64.052713.

[17] A. Kozela et al., *Thickness scan of metallic layer by photon induced X-ray emission*, Nucl. Instr. Meth. in Phys. Res., Sect. B **269**, 1767 (2010), doi:10.1016/j.nimb.2011.04.114.

[18] A. Kozela et al., *Measurement of the transverse polarization of electrons emitted in free neutron decay*, Phys. Rev. C. **85**, 045501 (2012), doi:10.1103/PhysRevC.85.045501.

[19] N. Severijns et al., *Tests of the standard electroweak model in beta decay*, Rev. Mod. Phys., Sect. A **78**, 991 (2006), doi:10.1103/RevModPhys.78.991.

[20] P. Herczeg, *Beta decay beyond the standard model*, Prog. Part. Nucl. Phys. **46**, 413 (2001), doi:10.1016/S0146-6410(01)00149-1.

[21] J. Sromicki, *T violation in the weak scalar and tensor interaction: neutron and nuclei*, Nucl. Instr. Meth. in Phys. Res., Sect. A **440**, 609 (2000), doi:10.1016/S0168-9002(99)01050-5.

[22] K. Bodek, *R- and N-correlation cofficients in neutron decay: Search for scalar and tensor couplings in weak interactions*, Phys. Proc. **17**, 30 (2011), doi:10.1016/j.phpro.2011.06.014.

[23] K. Bodek et al., *BRAND: Search for BSM physics at TeV scale by exploring transverse polarization of electrons emitted in neutron decay*, EPJ Web Conf. **219**, 04001 (2018), doi:10.1051/epjconf/201921904001.

[24] M. Gonzalez-Alonso et al., *New physics searches in nuclear and neutron β decay*, Prog. Part. Nucl. Phys **104**, 165 (2019), doi:10.1016/j.ppnp.2018.08.002.

[25] O. Naviliat-Cuncic et al., *Prospects for precision measurements in nuclear β decay in the LHC era*, Ann. Phys. **525**, 600 (2013), doi:10.1002/andp.201300072.

[26] S. Chatrchyan et al. [CMS Collaboration], *Search for new physics in events with same-sign dileptons and b-tagged jets in pp collisions at $\sqrt{s}$ =7 TeV*, J. High Energy Phys. **08**, 110 (2012), doi:10.1007/JHEP08(2012)110.

[27] V. Khachatryan et al. [CMS Collaboration], *Search for physics beyond the standard model in final states with a lepton and missing transverse energy in proton-proton collisions at $\sqrt{s} = 8$ TeV*, Phys. Rev. D **91**, 092005 (2015), doi:10.1103/PhyRevD.91.092005.

Mulan: a part-per-million measurement of the muon lifetime and determination of the Fermi constant

Robert Carey[1], Tim Gorringe[2*] and David W. Hertzog[3]

1 Dept. of Physics, Boston University, Boston, MA 02215, USA
2 Dept. of Physics and Astronomy, University of Kentucky, Lexington, KY 40506, USA
3 Dept. of Physics, University of Washington, Seattle, WA 98195, USA

⋆ tim.gorringe@uky.edu

Abstract

The part-per-million measurement of the positive muon lifetime and determination of the Fermi constant by the MuLan experiment at the Paul Scherrer Institute is reviewed. The experiment used an innovative, time-structured, surface muon beam and a near-4π, finely-segmented, plastic scintillator positron detector. Two in-vacuum muon stopping targets were used: a ferromagnetic foil with a large internal magnetic field, and a quartz crystal in a moderate external magnetic field. The experiment acquired a dataset of 1.6×10^{12} positive muon decays and obtained a muon lifetime $\tau_\mu = 2\,196\,980.3(2.2)$ ps (1.0 ppm) and Fermi constant $G_F = 1.166\,378\,7(6) \times 10^{-5}$ GeV^{-2} (0.5 ppm). The thirty-fold improvement in τ_μ has proven valuable for precision measurements in nuclear muon capture and the commensurate improvement in G_F has proven valuable for precision tests of the standard model.

16.1 Introduction

The electromagnetic (α_e), strong (α_s), gravitational (G) and weak (G_F) couplings are the "calibration constants" of nature [1]. Their magnitudes haven't been determined by theory but rather are obtained from measurement. Collectively, they determine the dynamics and bindings of microscopic and macroscopic matter and the character of the universe.

The fine-structure constant α_e governs the scale of atomic energy levels and the rates of all electromagnetic processes. It is known to the astonishing precision of 0.15 parts per billion.

The energy-scale-dependent effective coupling α_s governs the binding of protons and neutrons to form nuclei and the production of chemical elements in stars. It also controls the emergence of the two faces of the strong interaction: quark confinement at large distances and asymptotic freedom at short distances.

Despite the omnipresence of the gravitational force and its implications for the structure of the universe, the precision determination of the gravitational constant G has been deceptively difficult. Since its original measurement by Cavendish, the surprising inconsistences between modern methods have meant little overall improvement in our knowledge of this constant [2].

Finally, the weak interaction governs the thermonuclear reactions in the sun that are ultimately responsible for light, energy and life. The understanding of weak interactions enables the computation of phenomena from cosmology and astrophysics to nuclear and particle physics, including exacting tests of electroweak theory. Fermi described the weak processes by a simple four-fermion contact interaction with the coupling strength that became known as G_F. This constant and the current-current weak interaction description have survived many decades as a very convenient, low-energy, effective theory. Of course, our modern understanding of weak interactions has evolved to incorporate such features as parity violating $V - A$ currents and heavy W, Z gauge bosons, in a unified electroweak theory described by two gauge couplings and the Higgs energy density. The Fermi constant G_F, together with measurements of α_e and M_Z, provide by far the best determinations of the gauge couplings and Higgs energy density.

Since its discovery in 1933, the muon, a heavy sibling of ordinary electrons, has played a significant role in subatomic physics. Muons are undoubtedly the best tool for the precise determination of the Fermi constant and, uniquely from the considerations above, provide by far the most precise measure of the weak coupling. From the theoretical perspective, the purely-leptonic muon decay is well suited to precision calculations within the Fermi theory, and from the experimental perspective, its microsecond-scale lifetime is well suited to modern techniques for time measurements. Because the best method to determine G_F is from the muon lifetime, it is appropriate to recognize that what is measured is G_μ, the muon constant in weak decay. The assumption of lepton universality allows the relation $G_F \equiv G_\mu$, which we assume here, but can and should be challenged by other weak interaction processes.

An important breakthrough for determining G_F was work by van Ritbergen and Stuart [3] and Pak and Czarnecki [4]. Using Fermi theory with 2-loop QED corrections, these authors reduced the theoretical uncertainty in the relation between the muon lifetime and the Fermi constant from 15 parts-per-million to 150 parts-per-billion. Their work thus opened the door for the MuLan experiment at PSI [5,6], a part-per-million measurement of the muon lifetime τ_μ and determination of the Fermi constant G_F – a thirty-fold improvement over earlier measurements.

16.2 Experimental setup

The principle of the MuLan measurement of the muon lifetime is straightforward.

First, prepare a small "source" of positive muons. Next, measure the times of decay positrons. Finally, construct the exponential decay curve and extract the positive muon lifetime. In practice we repeated the sequence of source preparation and positron measurement at approximately 30 KHz over a period of roughly 20 weeks in two running periods.

The experiment used longitudinally polarized, 29 MeV/c, positive muons from the πE3 secondary beamline at the PSI proton cyclotron. Incoming muons were stopped in solid targets and outgoing positrons were detected in a near-4π, finely segmented, fast-timing, plastic scintillator positron detector. The analog signals from individual scintillators were recorded by 450 MSPS (mega samples per second) waveform digitizers and accumulated by a high-speed data acquisition system.

One innovative feature of the system was the imposition of time structure in the πE3 beamline. The experiment operated in repeating cycles of beam-on accumulation periods, in which surface muons were accumulated in the stopping target, and beam-off measurement periods, in which decay positrons were detected in the MuLan detector. The time structure

avoided the need to associate the decay positrons with parent muons – a limiting factor of earlier experiments using continuous beams.

The specific time structure comprised a 5 μs-long beam-on accumulation period (T_A), and a 22 μs-long beam-off measurement period (T_M). The time structure was imposed on the πE3 beam using a custom-built, fast-switching, 25 kV electrostatic kicker. When the kicker was de-energized, the muons were transported to the Target; when the kicker was energized, the muons were deflected into a collimator. A sample time distribution of incoming muons and outgoing positrons that illustrates the accumulation and measurement periods is shown in Figure 16.1.
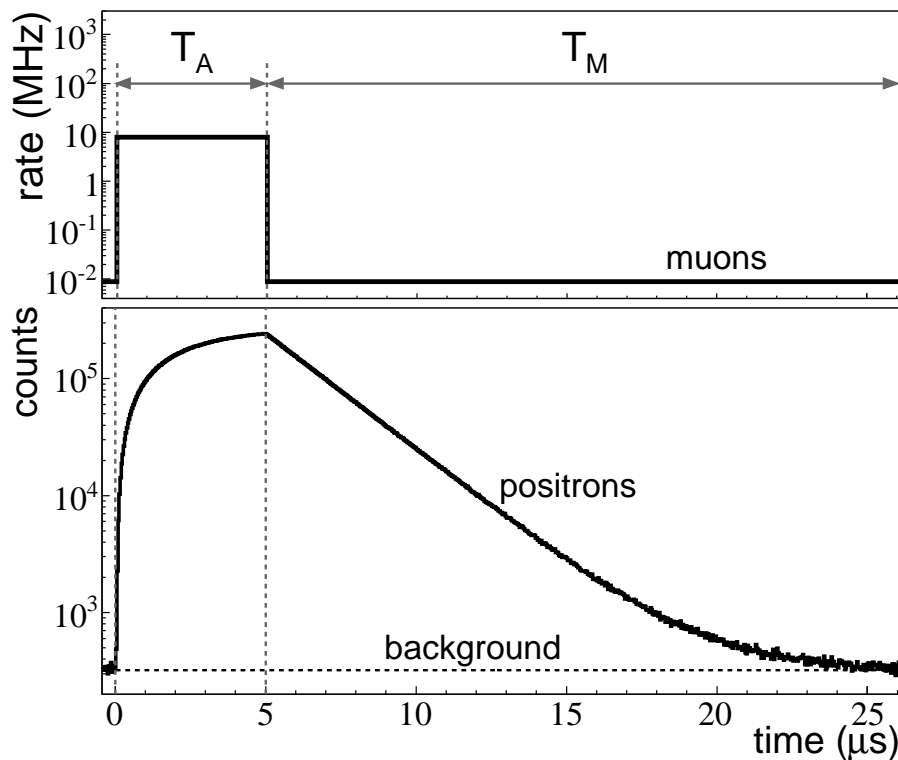
Figure 16.1: Plot of the time dependence of the muon arrival rate (upper panel) and decay positron counts (lower panel) that was imposed by the electrostatic kicker. The durations of the beam-on accumulation period and beam-off measurement period were $T_A = 5$ μs and $T_M = 22$ μs, respectively. Figure courtesy of the MuLan collaboration.

Other innovative features of the experiment were the use of in-vacuum stopping targets and near-4π positron detection. A consequence of parity violation in weak interactions is that the emitted positrons in muon decay are asymmetrically distributed about the muon spin direction. This poses a problem as spin precession and spin relaxation of stopped muons could distort the pure exponential time distribution of the decay positrons and bias the extraction of τ_μ.

A fully 4π, perfectly isotropic, positron detector would negate this issue of precession and relaxation by detecting positrons with identical probability in all directions. The Mulan combination of an in-vacuum, detector-centered target for incoming muons and near-4π, near-isotropic, detector for outgoing positrons, was an important part of the experimental strategy for minimizing such spin precession and relaxation effects.

In addition, the experiment deployed two different combinations of stopping target materi-
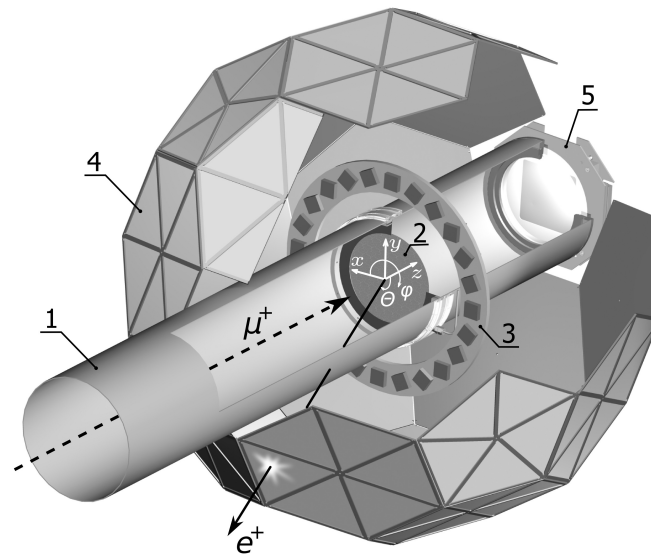
Figure 16.2: A cutaway view of the Mulan experimental setup showing the (1) vacuum beamline, (2) in-vacuum stopping target, (3) Halbach arrangement permanent magnet, (4) soccer ball geometry scintillator array, and (5) beam monitor. We used the Halbach magnet for the external magnetic field in the quartz target data-taking. Figure courtesy of the MuLan collaboration.

als and transverse magnetic fields in order to further reduce the spin precession and relaxation effects. One setup involved a magnetized Fe-Cr-Co foil (Arnokrome-III) with a ∼4 kG internal B-field. Another setup involved a quartz crystal disk (SiO_2) in a 130 G external B-field. In the ferromagnetic target, where muons reside as diamagnetic ions, the μ^+ precession frequency was about 50 MHz. In the quartz target the primary muonium (μ^+e^-) population has a 180 MHz precession frequency and the secondary muon (μ^+) population has a 1.8 MHz precession frequency. In both strategies, spin dephasing during muon accumulation yielded a roughly 1000-fold reduction in the ensemble-averaged μ^+ polarization at the beginning of the measurement period.

The positron detector was constructed of 170 triangle-shaped, plastic scintillator pairs arranged in a soccer ball geometry (Figure 16.2). Each pair comprised an inner and outer scintillator tile. The pairs were grouped into ten pentagonal enclosures containing five tile-pairs and twenty hexagonal enclosures containing six tile-pairs, which together formed the soccer ball geometry. The segmentation was important in reducing positron pile-up in individual detector elements. The symmetric arrangement of detector elements was important in reducing the effects of muon spin rotation / relaxation.

16.3 Data analysis

A total of 1.1×10^{12} decays from positive muon stops in Arnokrome-III and 5.4×10^{11} decays from positive muon stops in quartz were collected. Other datasets with different orientations of the magnetic field and different centering of the muon stopping distribution were collected in order to study the systematic errors associated with spin precession and relaxation.

The time and amplitude of individual pulses were determined from least square fits to digitized waveform templates. The procedure fit a higher-resolution template waveform (0.22 ns sampling-interval) to the lower-resolution individual waveforms (2.2 ns sampling-interval). The higher-resolution templates were constructed by combining a large sample of 2.2 ns

sampling-interval, single positron, digitized waveforms. The fitting procedure would add / remove pulses to obtain the best χ^2.

Positrons were defined as inner-outer tile-pair coincidences. In identifying the coincidences, cuts were applied to define an unambiguous amplitude threshold A_{thr} for detector hits and to define an unambiguous artificial deadtime (ADT) between detector pulses. Hits that survived these cuts were sorted into time distributions of inner singles, outer singles and inner-outer coincidences. The construction of coincidence histograms with different thresholds and deadtimes was important for studying the distortions that arise from pulse pileup and gain changes. The typical rates were 40 stopped muons per accumulation period and 15 detected positrons per measurement period. The nominal 13.3 ns ADT yielded a pileup distortion of roughly 10^{-3} at the start of the measurement period and roughly 10^{-7} at the end of the measurement period.

A hit is lost if it occurs in the artificial deadtime of an earlier hit. Our procedure for correcting for pileup took advantage of the time structure of the incident beam. The pileup losses were statistically recovered by replacing the lost hits in each measurement period with measured hits at equivalent times in neighboring measurement periods. For example, to correct for leading-order pileup, if a hit is observed at time t_i in fill j (the "trigger" hit), a hit is searched for within the interval $t_i \to t_i + \text{ADT}$ in fill $j+1$ (the "shadow" hit). Adding the resulting histogram of shadow hit times to the original histogram of trigger hit times thus statistically recovers the lost hits (similar shadow methods were employed for handling the higher-order pileup).

As mentioned, only hits with amplitudes exceeding the threshold A_{thr} were used. Consequently, if the detector gain changes over the measurement period, then the time histogram will be distorted by either additional hits climbing above A_{thr} or additional hits falling below A_{thr} cut. We corrected for gain changes versus measurement time by monitoring changes in the positron minimally ionizing particle (MIP) peak amplitude over the measurement period.

A simple procedure was used to extract the lifetime τ_μ from the Arnokrome-III target. The summed tile-pair time histogram of coincidence hits was fit to $Ne^{-t/\tau_\mu}+C$. The approach relied on sufficient cancellation of Arnokrome-III precession and relaxation effects by combination of the spin dephasing and the opposite-pair detector geometry.

A more complicated procedure was needed to extract the lifetime τ_μ from the quartz target. First, 170 geometry-dependent effective lifetimes were extracted for each tile-pair from fits to

$$N(t) = Ne^{-t/\tau_{\text{eff}}}[1+f(t)]+C, \tag{16.1}$$

where $f(t)$ accounts for time-dependent effects of transverse-field (TF) spin precession and relaxation. Then, the true positive muon lifetime τ_μ was extracted by fitting the effective lifetimes, τ_{eff}, to

$$\tau_{\text{eff}}(\theta_B, \phi_B) = \tau_\mu[1+\delta(\theta_B, \phi_B)], \tag{16.2}$$

where $\delta(\theta_B, \phi_B)$ accounts for geometry-dependent effects of longitudinal-field (LF) spin relaxation. Together the two steps were sufficient to handle the effects of precession and relaxation in quartz.

16.4 Results

The individual results from the Arnokrome-III dataset and the quartz dataset, and the weighted average are given in Table 16.1.

The weighted average corresponds to an overall uncertainty in the positive muon lifetime of 2.2 ps, or 1.0 ppm. The largest contributions to the systematic uncertainties are associated with the aforementioned pulse pileup, gain changes, and muon precession and relaxation effects, as well as the knowledge of the time independence of the beam extinction during the

Table 16.1: Muon lifetime results from the Arnokrome-III dataset, quartz dataset, and their weighted average.

Target material	Positive muon lifetime (ps)
Arnokrome-III	$2\,196\,979.9 \pm 2.5(stat) \pm 0.9(syst)$
Quartz	$2\,196\,981.2 \pm 3.7(stat) \pm 0.9(syst)$
Weighted average	$2\,196\,980.3 \pm 2.1(stat) \pm 0.7(syst)$

measurement period. The final result for τ_μ is in agreement with the earlier work of Giovanetti *et al.* [7], Balandin *et al.* [8] and Bardin *et al.* [9].

We note the precision determination of τ_μ is important to work on nuclear muon capture. The MuCap experiment [10] at PSI determined the μp singlet capture rate from the small difference between the positive muon lifetime and the muonic hydrogen atom lifetime. Similarly, the MuSun experiment [11] at PSI will determine the μd doublet capture rate from the small difference between the positive muon lifetime and the muonic deuterium atom lifetime. These two experiments are described in Section 17 [12] and Section 18 [13], respectively.

The Fermi constant G_F was extracted using the relation obtained by van Ritbergen and Stuart (vRS) [3] and yields $G_F(\text{MuLan}) = 1.166\,378\,7(6) \times 10^{-5}\text{GeV}^{-2}(0.5 \text{ ppm})$ – a thirty-fold improvement over the earlier 1998 Particle Data Group [14] value that pre-dated the vRS theoretical work and MuLan experimental work. The 0.5 ppm error is dominated by the 1.0 ppm uncertainty of the lifetime measurement, with contributions of 0.08 ppm from the muon mass measurement and 0.15 ppm from the theoretical corrections.

Together, the fine structure constant α, Fermi coupling constant G_F, and Z boson mass M_Z, fix the electroweak parameters of the standard model. The thirty-fold improvement in the determination of the Fermi constant G_F, together with other improvements in determinations of α and M_Z, have allowed for improved tests of the standard model and improved searches for new phenomena.

References

[1] P. Zyla et al., *Review of particle physics*, Prog. Theor. Exper. Phys. 083C01 (2020), doi:10.1093/ptep/ptaa104.

[2] C. Rothleitner and S. Schlamminger, *Measurements of the newtonian constant of gravitation*, Rev. Sci. Instrum. **88**, 111101 (2017), doi:10.1063/1.4994619.

[3] T. van Ritbergen and R. G. Stuart, *On the precise determination of the Fermi coupling constant from the muon lifetime*, Nucl.Phys. B **564**, 343 (2000), doi:10.1016/S0550-3213(99)00572-6.

[4] A. Pak and A. Czarnecki, *Mass effects in muon and semileptonic $b \rightarrow c$ decays*, Phys. Rev. Lett. **100**, 241807 (2008), doi:10.1103/PhysRevLett.100.241807.

[5] D. Webber et al., *Measurement of the positive muon lifetime and determination of the Fermi constant to part-per-million precision*, Phys. Rev. Lett. **106**, 041803 (2011), doi:10.1103/PhysRevLett.106.041803.

[6] V. Tishchenko et al., *Detailed report of the MuLan measurement of the positive muon lifetime and determination of the Fermi constant*, Phys. Rev. D **87**, 052003 (2013), doi:10.1103/PhysRevD.87.052003.

[7] K. Giovanetti et al., *Mean life of the positive muon*, Phys. Rev. D **29**, 343 (1984), doi:10.1103/PhysRevD.29.343.

[8] M. Balandin, V. Grebenyuk, V. Zinov, A. Konin and A. Ponomarev, *Measurement of the lifetime of the positive muon*, Sov. Phys. JETP **40**, 811 (1975), Available at http://ivanik3.narod.ru/TimeLifeMezon/e_040_05_0811Balandin.pdf.

[9] G. Bardin, J. Duclos, A. Magnon, J. Martino, E. Zavattini, A. Bertin, M. Capponi, M. Piccinini and A. Vitale, *A new measurement of the positive muon lifetime*, Phys. Lett. B **137**, 135 (1984), doi:10.1016/0370-2693(84)91121-3.

[10] V. Andreev et al., *Measurement of the rate of muon capture in hydrogen gas and determination of the proton's pseudoscalar coupling g_P*, Phys. Rev. Lett. **99**, 032002 (2007), doi:10.1103/PhysRevLett.99.032002.

[11] P. Kammel, *Precision muon capture at PSI*, Proc. Sci. **172**, 016 (2013), doi:10.22323/1.172.0016.

[12] M. Hildebrandt and C. Petitjean, *MuCap: Muon capture on the proton*, SciPost Phys. Proc. **5**, 017 (2021), doi:10.21468/SciPostPhysProc.5.017.

[13] P. Kammel, *MuSun - Muon capture on the deuteron*, SciPost Phys. Proc. **5**, 018 (2021), doi:10.21468/SciPostPhysProc.5.018.

[14] C. Caso et al., *Review of particle physics. Particle data group*, Eur. Phys. J. C **3**, 1 (1998), doi:10.1007/s10052-998-0104-x.

MuCap: Muon Capture on the Proton

Malte Hildebrandt and Claude Petitjean*

Paul Scherrer Institut, 5232 Villigen PSI, Switzerland

$\star$ claude.petitjean@psi.ch

Abstract

The singlet muon capture rate Λ_S on the proton $\mu^- p \to \nu_\mu n$ is determined in a high precision lifetime measurement. The main apparatus consists of a new hydrogen time projection chamber as muon detector, developed by PSI, surrounded by cylindrical wire chambers and a plastic scintillator hodoscope as electron detectors. The parameter Λ_S is evaluated as the difference between the inverse μp lifetime and that of the free μ^+. The result $\Lambda_S^{\text{MuCap}} = (715.6 \pm 5.4^{\text{stat}} \pm 5.1^{\text{sys}}) \, \text{s}^{-1}$ is in excellent agreement with the prediction of chiral perturbation theory $\Lambda_S^{\chi\text{PT}} = (715.4 \pm 6.9) \, \text{s}^{-1}$. From Λ_S^{MuCap} a recent analysis derives for the induced pseudoscalar coupling $g_p^{\text{MuCap}} = 8.23 \pm 0.83$ whereas $\bar{g}_p^{\chi\text{PT}} = 8.25 \pm 0.25$.

0.1 Introduction

Muon capture on the proton

$$\mu^- p \to \nu_\mu n \tag{0.1}$$

is a very important elementary process in weak interactions [1]. A measurement of the singlet capture rate Λ_S is directly related to fundamental electroweak coupling constants g_A and g_P. While g_A is accurately known from measurements of the neutron lifetime, the induced pseudoscalar coupling g_P, can only be precisely determined from the muon capture rate. In low-energy chiral perturbation theory (χPT), g_P can be expressed as[1]

$$g_P^{\chi\text{PT}}(q^2) = \frac{2m_\mu g_{\pi NN} f_\pi}{m_\pi^2 - q^2} - \frac{1}{3} g_A(0) m_\mu m_N r_A^2. \tag{0.2}$$

This leads to a theoretical prediction [3,4] of

$$\bar{g}_P^{\chi\text{PT}} \equiv g_P^{\chi\text{PT}}(q_0^2) = 8.26 \pm 0.23, \tag{0.3}$$

---

[1]The function $g_P(q^2) \equiv m_\mu/m_N \, F_P^{cc}(q^2)$ and $\bar{g}_P$ are defined in Section 5 [2].

where $q_0^2 = -0.88 m_\mu^2$. A precise measurement of Λ_S represents therefore an important test of low-energy χPT.

Historically, many experimental attempts to determine Λ_S were already made in the 1960's at the leading accelerator labs to determine the μp capture rate. These experiments resulted however only in a precision of $\sim$15%, suffering mainly from two major challenges:

1) The output channel $\nu_\mu n$ consists only of neutral particles, where the ν_μ escapes detection and the neutron is very difficult to be determined with high absolute precision. Modern experiments avoid this problem by using the lifetime method: instead of measuring absolute neutron rates, the disappearance rate of the muon, λ_μ, is measured, i.e.

$$\frac{dN_\mu}{dt} = N_\mu e^{-\lambda_\mu t}, \qquad\qquad \lambda_\mu = \lambda_0 + \Lambda_S. \qquad (0.4)$$

Here, $\lambda_0 = 0.455 \times 10^6\,\mathrm{s}^{-1}$ is the decay constant[2] of the free muon and $\Lambda_S \simeq 700\,\mathrm{s}^{-1}$ is just a small (1.5×10^{-3}) additional component of λ_μ. Lifetime measurements therefore require high precision, i.e. large statistics. A first successful lifetime experiment was performed 1981 in Saclay [5] in a target with liquid hydrogen.

2) Negative muons in hydrogen quickly combine to neutral (μp) atoms which behave like neutrons; they diffuse around and scatter with the surrounding nuclei. In collisions they can get easily transferred to heavier nuclei (d,N,O) contained in the hydrogen. Moreover they can form the mesic molecule $(p\mu p)$

$$(\mu p)\,p \to (p\mu p) \qquad (0.5)$$

with a rate of about $\lambda_{pp\mu} \simeq 2 \times 10^6\,\mathrm{s}^{-1}$. Two species of $(p\mu p)$ molecules exist, ortho-$(p\mu p)$ and para-$(p\mu p)$. In the formation process, predominantly ortho-molecules are created, which eventually convert to the energetically lower para-molecule with rate λ_{op}. Unfortunately, λ_{op} is not well known (theoretical value $\lambda_{\mathrm{op}}^{\mathrm{Th}} = (7.1 \pm 1.2) \times 10^4\,\mathrm{s}^{-1}$ [6]). The capture rates differ strongly for the two states (for ortho-$(p\mu p) \sim 545\,\mathrm{s}^{-1}$, for para-$(p\mu p) \sim 215\,\mathrm{s}^{-1}$). This makes the interpretation of capture measurements in $(p\mu p)$ molecules difficult. This problem can be strongly reduced in hydrogen at low density, where the $(p\mu p)$ formation rate is small.

In addition to these two major issues, isotope and chemical purities play an important role in the experiment. Natural hydrogen contains $\sim$150 ppm deuterium nuclei. Muons in such a medium get quickly transferred to the heavier isotope

$$(\mu p)\,d \to (\mu d)\,p. \qquad (0.6)$$

The (μd) atoms are created at initial kinetic energy of $\sim$45 eV, and have a very large diffusion rate due to a (μd)-p scattering minimum around 10 eV (Ramsauer-Townsend effect). In collisions with deuterium nuclei they can form $(p\mu d)$ molecules leading to the muon catalyzed fusion

$$(\mu p)\,d \to (p\mu d), (p\mu d) \to \mathrm{He}^3 + \mu + 5.5\,\mathrm{MeV}. \qquad (0.7)$$
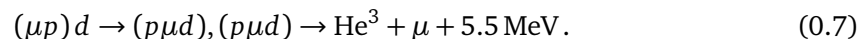
These processes would strongly interfere in a μp capture measurement. Therefore, hydrogen depleted from deuterium (so called protium) has to be used. Furthermore, the protium must be kept at highest purity to avoid transfers to higher-Z nuclei.

---

[2]denoted by Γ_μ in Section 5 [2]
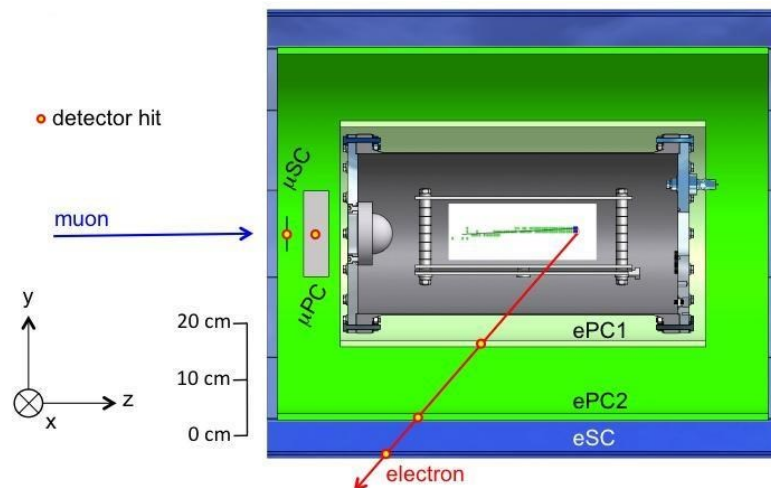
Figure 0.1: Cross section of the full MuCap apparatus with illustration of a typical event. Every muon was tracked individually to its stopping point. The electrons were tracked back to the muon stop location. Thanks to fiducial cuts, background from accidental electrons was suppressed to the 10^{-4} level.

0.2 The MuCap experiment

The MuCap experiment was proposed in 1997 with the goal to measure the singlet μp capture rate Λ_S to 1% precision which would then determine $g_P(q_0^2)$ to ~6%. This goal can be reached by a high precision measurement of the muon lifetime to the level 10^{-5} which requires a statistics of $\sim 10^{10}$ muon decay events.

Figure 0.1 shows a cross section of the MuCap experiment. The muon detector in the center consists of three components, a thin scintillator μSC providing the fast timing signal of the incoming muon, a wire chamber μPC and a time projection chamber TPC [7, 8] tracking the muon to the stopping point. The TPC is mounted inside an aluminium pressure vessel filled with 10 bar of ultra-pure protium gas. It acts simultaneously as muon stopping target and detector. The density of the protium gas is ~1% of liquid hydrogen, thus avoiding the problems involved with meso-molecular processes. A special isotope separation column was constructed for MuCap [9] which removed deuterium to a negligible level. A special gas circulation system [10] was constructed using thermo-dynamical cycles and cryo-absorption by Zeolite filters for continuous cleaning of the protium gas. The system reduced impurity levels to values below 20 ppb.

The TPC was operated with a 2 kV/cm vertical electrical field. The electrons from the ionizing muon tracks – after drifting downwards to a multi-wire proportional chamber at the bottom – were collected in x and z coordinates. Combined with the drift time information (y coordinate) every muon track was reconstructed in three dimensions. After suitable fiducial cuts false muon stops were suppressed below the 10^{-5} level, necessary to keep the slope of the muon decay curve free from distortions. The electron detector consists of two cylindrical wire chambers ePC1, ePC2, and a plastic scintillation hodoscope eSC. The wire chambers – originally developed by PSI for the SINDRUM rare decay experiments, Section 7 [11] – provide directional information for each electron track, while the scintillators yield the fast timing signal of the muon decay.

The anticipated precision was reached by collection of more than 10^{10} single good muon decay events. A significant boost of the statistics was achieved with help of the muon kicker [12] from the MuLan experiment [13] ('muons on request' method). The system transmitted single
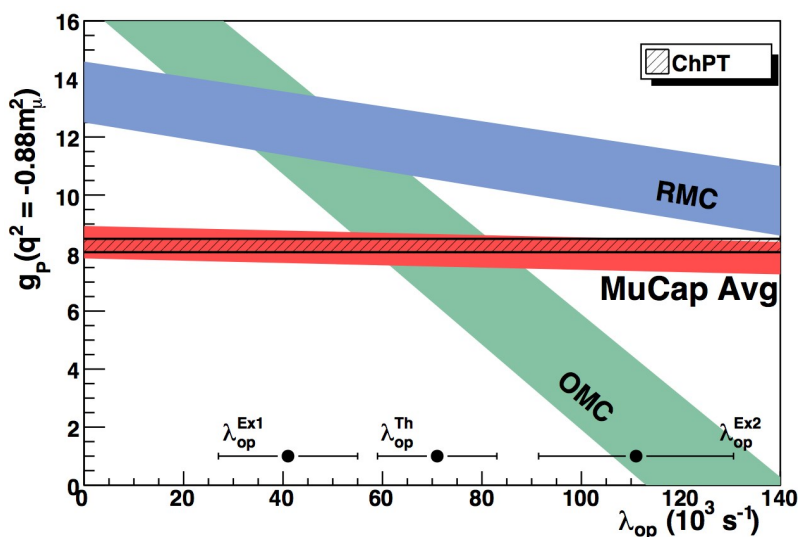
Figure 0.2: Extracted values for g_P as a function of the poorly known molecular transition rate λ_{op}. OMC = Saclay experiment [5], RMC = TRIUMF experiment [17]. Also shown are results of two inconsistent λ_{op} measurements ($\lambda_{\mathrm{op}}^{\mathrm{Ex1}}$ from Saclay [18], $\lambda_{\mathrm{op}}^{\mathrm{Ex2}}$ from TRIUMF [19]), and the theoretical calculation $\lambda_{\mathrm{op}}^{\mathrm{Th}}$ [6].

muons into the TPC without pile-up from second particles. This method increased the data collection rate by a factor 2 to 3.

0.3 Results

During three independent production runs [14, 15] 1.2×10^{10} fully reconstructed μ^- decays plus 0.6×10^{10} μ^+ decays for systematic controls were collected. The systematic corrections include distortion effects due to impurities, removal of μp scatter events, μp and μd diffusion, uncertainties of fiducial volume cuts, inefficiencies and electron track definitions. Averaging these data and using the μ^+ decay constant measured by the MuLan experiment [13], $\lambda_{\mu^+} = (455'170.05 \pm 0.46)\,\mathrm{s}^{-1}$, the final result of the singlet muon capture rate on the proton is obtained as [15]

$$\Lambda_S^{\mathrm{MuCap}} = \left(714.9 \pm 5.4^{\mathrm{stat}} \pm 5.1^{\mathrm{sys}}\right)\mathrm{s}^{-1} \tag{0.8}$$

in excellent agreement with χPT theory $\Lambda_S^{\chi\mathrm{PT}} = (715.4 \pm 6.9)\,\mathrm{s}^{-1}$ [16]. From this result

$$g_P^{\mathrm{MuCap}}(q_0^2) = 8.06 \pm 0.48^{\mathrm{exp}} \pm 0.28^{\mathrm{th}} \tag{0.9}$$

is deduced [15]. This value is in agreement with χPT (0.3).

Figure 0.2 shows $\bar{g}_P$ from recent experiments as function of the poorly known transition rate λ_{op}. In contrast to previous experiments which were mostly carried out in liquid hydrogen, the MuCap experiment is virtually not sensitive to λ_{op} and, thus, avoided this longstanding problem.

In a refined analysis [20] a new value for $\lambda_{pp\mu}$ was derived from the MuCap data and this led to an updated value of

$$\Lambda_S^{\mathrm{MuCap}} = \left(715.6 \pm 5.4^{\mathrm{stat}} \pm 5.1^{\mathrm{sys}}\right)\mathrm{s}^{-1} \tag{0.10}$$

and a change of -0.045 in $g_P^{\mathrm{MuCap}}(q_0^2)$. The change of the latter by only 8% of its uncertainty has no (visible) influence on Figure 0.2.

0.4 Outlook

The determination of $\bar{g}_p$ from both theory and experiment requires the input of the axial vector charge radius squared r_a^2. In a recent review [16] discussing the values and uncertainties of r_a^2 obtained by different methods, the MuCap result was re-analysed. Based on the value $r_a^2 = (0.46 \pm 0.22)$ fm^2 evaluated from neutrino-nucleon scattering data the updated MuCap result changes to $g_p^{\text{MuCap}}(q_0^2) = 8.23 \pm 0.83$. This is in very good agreement with the updated value $\bar{g}_p^{\chi\text{PT}} = 8.25 \pm 0.25$ which is still very close to the value of the Meissner group [3, 4].

Following this path the value of r_a^2 is now considered to contain the largest theoretical uncertainty. Fixing $\bar{g}_p$ to the χPT value, the MuCap result can be interpreted as an independent measurement of r_a^2: it results in the same value $r_a^2(\mu\text{H}) = (0.46 \pm 0.24)$ fm^2 as from neutrino scattering.

Consequently, a new MuCap experiment with greatly increased statistics would allow a testing of the nucleon axial radius at the correspondingly increased sensitivity. Such an effort would require a newly constructed apparatus using improved detector techniques and muon beam handling.

References

[1] P. Kammel and K. Kubodera, *Precision muon capture*, Ann. Rev. Nucl. Part. Sci. **60**, 327 (2010), doi:10.1146/annurev-nucl-100809-131946.

[2] G. Colangelo and A. Signer, *A theory guide for PSI experiments*, SciPost Phys. Proc. **5**, 005 (2021), doi:10.21468/SciPostPhysProc.5.005.

[3] V. Bernard, N. Kaiser and U. G. Meissner, *QCD accurately predicts the induced pseudoscalar coupling constant*, Phys. Rev. D **50**, 6899 (1994), doi:10.1103/PhysRevD.50.6899, arXiv:hep-ph/9403351.

[4] V. Bernard, L. Elouadrhiri and U.-G. Meissner, *Axial structure of the nucleon: Topical Review*, J. Phys. G **28**, R1 (2002), doi:10.1088/0954-3899/28/1/201, arXiv:hep-ph/0107088.

[5] G. Bardin, J. Duclos, A. Magnon, J. Martino, A. Richter, E. Zavattini, A. Bertin, M. Piccinini, A. Vitale and D. F. Measday, *A novel measurement of the muon capture rate in liquid hydrogen by the lifetime technique*, Nucl. Phys. A **352**, 365 (1981), doi:10.1016/0375-9474(81)90416-4.

[6] D. D. Bakalov, M. P. Faifman, L. I. Ponomarev and S. I. Vinitsky, *μ capture and ortho - para transitions in mesic molecule ppμ*, Nucl. Phys. A **384**, 302 (1982), doi:10.1016/0375-9474(82)90337-2.

[7] J. Egger, M. Hildebrandt and C. Petitjean, *The 10 bar hydrogen time projection chamber of the MuCap experiment*, Nucl. Instrum. Meth. A **628**, 199 (2011), doi:10.1016/j.nima.2010.06.316.

[8] J. Egger et al., *A high-pressure hydrogen time projection chamber for the MuCap experiment*, Eur. Phys. J. A **50**, 163 (2014), doi:10.1140/epja/i2014-14163-1, arXiv:1405.2853.

[9] I. Alekseev et al., *Cryogenic distillation facility for isotopic purification of protium and deuterium*, Rev. Sci. Instr. **86**, 125102 (2015), doi:10.1063/1.4936413.

[10] V. A. Ganzha et al., *A Circulating hydrogen ultra-high purification system for the MuCap experiment*, Nucl. Instrum. Meth. A **578**, 485 (2007), doi:10.1016/j.nima.2007.06.010, arXiv:0705.1473.

[11] R. Eichler and C. Grab, *The SINDRUM-I Experiment*, SciPost Phys. Proc. **5**, 007 (2021), doi:10.21468/SciPostPhysProc.5.007.

[12] M. J. Barnes and G. D. Wait, *A 25-kV 75-kHz Kicker for measurement of muon lifetime*, IEEE Trans. Plasma Sci. **32**, 1932 (2004), doi:10.1109/TPS.2004.835455.

[13] D. M. Webber et al., *Measurement of the positive muon lifetime and determination of the Fermi constant to part-per-million precision*, Phys. Rev. Lett. **106**, 041803 (2011), doi:10.1103/PhysRevLett.106.041803, arXiv:1010.0991.

[14] V. A. Andreev et al., *Measurement of the rate of muon capture in hydrogen gas and determination of the proton's pseudoscalar coupling g(P)*, Phys. Rev. Lett. **99**, 032002 (2007), doi:10.1103/PhysRevLett.99.032002, arXiv:00704.2072.

[15] V. A. Andreev *et al.*, *Measurement of muon capture on the proton to 1% precision and determination of the pseudoscalar coupling g_P*, Phys. Rev. Lett. **110**, 012504 (2013), doi:10.1103/PhysRevLett.110.012504, arXiv:1210.6545.

[16] R. J. Hill, P. Kammel, W. J. Marciano and A. Sirlin, *Nucleon axial radius and muonic hydrogen — A new analysis and review*, Rept. Prog. Phys. **81**, 096301 (2018), doi:10.1088/1361-6633/aac190, arXiv:1708.08462.

[17] D. H. Wright *et al.*, *Measurement of the induced pseudoscalar coupling using radiative muon capture on hydrogen*, Phys. Rev. C **57**, 373 (1998), doi:10.1103/PhysRevC.57.373.

[18] G. Bardin, J. Duclos, A. Magnon, J. Martino, A. Richter, E. Zavattini, A. Bertin, M. Piccinini and A. Vitale, *Measurement of the ortho - para transition rate in the pμp molecule and deduction of the pseudoscalar coupling constant*, Phys. Lett. B **104**, 320 (1981), doi:10.1016/0370-2693(81)90134-9.

[19] J. H. D. Clark, D. S. Armstrong, T. P. Gorringe, M. D. Hasinoff, P. M. King, T. J. Stocki, S. Tripathi, D. H. Wright and P. A. Zolnierczuk, *Ortho-para transition rate in mu-molecular hydrogen and the proton's induced pseudoscalar coupling g(p)*, Phys. Rev. Lett. **96**, 073401 (2006), doi:10.1103/PhysRevLett.96.073401, arXiv:nucl-ex/0509025.

[20] V. A. Andreev *et al.*, *Measurement of the formation rate of muonic hydrogen molecules*, Phys. Rev. C **91**, 055502 (2015), doi:10.1103/PhysRevC.91.055502, arXiv:1502.00913.

MuSun - Muon Capture on the Deuteron

P. Kammel[1][⋆] on behalf of the MuSun collaboration[1]

1 Center for Experimental Nuclear Physics and Astrophysics, and Department of Physics, University of Washington, Seattle, WA 98195, USA

⋆ pkammel@uw.edu

Abstract

The MuSun experiment is a precision measurement of the rate for nuclear muon capture on the deuteron, designed to resolve a long-standing disagreement between experiment and theory, and to determine an important low-energy constant relevant for a variety of weak and strong dynamics. The experiment is based on a novel active target method employing a pure deuterium cryogenic time-projection chamber. The data taking was completed in two main campaigns and the analysis is well advanced. The unique challenges and corresponding strategy of the experiment as well as the status of the analysis are presented.

18.1 Introduction

Muon capture is a powerful tool to study the properties and structure of the nucleon and few nucleon systems as predicted by effective theories (EFT) founded on Quantum Chromodynamics. Our program focuses on capture from the simplest of all muonic atoms, namely on the proton in the theoretically-pristine muonic hydrogen (MuCap experiment) [1–3] as well as on the simplest nucleus in muonic deuterium (MuSun experiment [4]), which is presented here. Our collaboration has pioneered a novel active-target method based upon the development of high-pressure time-projection chambers (TPC) filled with hydrogen/deuterium gas, and in an earlier experiment ³He [5].

One of the most interesting topics for muon capture in the few-body sector is the family of two-nucleon weak-interaction processes. As shown in Figure 18.1 this family contains muon capture on the deuteron,

$$\mu + d \rightarrow n + n + \nu \tag{18.1}$$

---

[1]Petersburg Nuclear Physics Inst. - Univ. of Washington - Paul Scherrer Inst. - Univ. of Kentucky - Boston Univ. - Univ. Cath. Louvain - Regis Univ. - Univ. of South Carolina
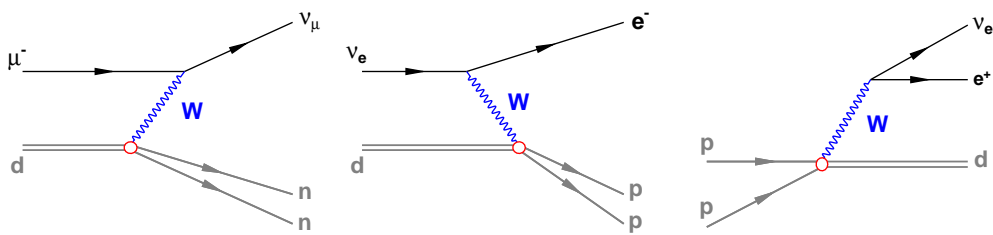
Figure 18.1: The hadronic vertex (red circle) in the three weak processes muon capture, neutrino deuteron scattering and pp fusion is characterized by a common parameter.

together with two astrophysics reactions of fundamental interest, in particular, *pp* fusion, which is the primary energy source in the sun and the main sequence stars, and the *νd* reactions, which provides the evidence for solar neutrino oscillations by measuring the flavor-separated neutrino flux at the Sudbury Neutrino Observatory. The extremely small rates of these processes do not allow their cross sections to be measured under terrestrial conditions; they can only be calculated by theory [6–9], with information derived from the more-complex three-nucleon system.

These interactions all involve the same axial-vector coupling at a four-nucleon vertex [10, 11], the two-nucleon analog to g_A for the nucleon. The strength of this coupling is characterized by a single, poorly known low energy constant (LEC) in the EFT description up to the required order. Moreover, this LEC is an essential ingredient in the construction of chiral three-nucleon forces [12, 13] and in other weak and strong processes [14, 15].

MuSun plans to determine the rate Λ_d of muon capture on the deuteron to 1.5%, where Λ_d denotes the capture rate from the doublet hyperfine state in a muonic deuterium atom. Current experiments are at the 6-10% level, and the most precise one [16] disagrees with the latest theory calculation of $\Lambda_d = 399 \pm 3\,\mathrm{s}^{-1}$ [8, 9], see also [17], by more than 3-sigma. The LEC will be determined at the 20% level, i.e. 5 times better than what is presently known from the two-nucleon system.

18.2 MuSun Experiment

The MuSun experiment uses the so-called "lifetime method" consisting of a precision measurement of the muon disappearance rate in deuterium. The time distribution of electrons from muon decay in deuterium follows[2]

$$\frac{dN_e}{dt}(t) \propto e^{-(\lambda_{\mu^+} + \Lambda_d)t} \tag{18.2}$$

i.e. the disappearance rate $\lambda_{d\mu}$ measured by MuSun is the sum of the free muon decay rate λ_{μ^+} [18], and the capture rate Λ_d. Λ_d is determined by subtracting the precisely known λ_{μ^+} from $\lambda_{d\mu}$. The basic experimental technique is similar to the MuCap experiment described in Section 17 [3]. Muons pass through the entrance detectors and a beryllium window to stop in a cryogenic time-projecton-chamber (cryo-TPC) filled with ultra-pure deuterium gas (Figure 18.2). Decay electrons are detected in two cylindrical wire chambers and a 16-fold segmented scintillator barrel. The lifetime is determined from the measured time difference between the fast muon entrance detector and the decay electron scintillator array. After a muon hits the entrance counter, a fast kicker [19] turns off the beam for the measurement interval to reduce pileup.

---

[2]approximate expression after muons have reached the doublet hyperfine state.
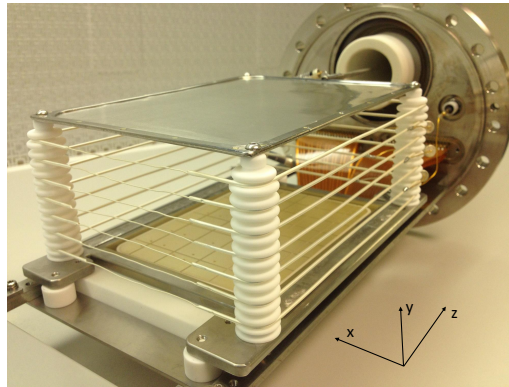
Figure 18.2: Cryogenic TPC with a sensitive volume of 9.6×7.1×12.5 cm^3 segmented into 6×8 pads. Muon beam enters from the front. The grid and field cage wires are made of gold and silver plated tungsten, respectively, and the HV anode consists of a silver foil. The grid frame has a composite construction to withstand thermal cycling.

The experiment must simultaneously meet several stringent requirements. i) The target conditions (T=31 K and density 6.5% of liquid-hydrogen density) are optimized for an unambiguous extraction of Λ_d, and the suppression of muonic atomic-physics complications that arise when muons stop in deuterium, such as muon-catalyzed fusion [20]. ii) Muons are stopped in an active target, the unique high-density cyro-TPC, specifically developed for MuSun. Three-dimensional tracking in the TPC eliminates most muon-stops in wall material. High-Z material is used for most TPC materials, so that remaining muons stopping there are quickly captured. iii) Muon transfer to impurity elements, where capture occurs with a much higher rate than in deuterium, is suppressed by keeping the gas contamination at the 10^{-9} level with a continuous circulation and filter system [21]. The purity is monitored *in situ* in the TPC by gas chromatography [22]. Isotopically pure deuterium was produced in an on-site cryogenic distillation system [23].

The high gas density in the cryo-TPC requires a drift voltage of 80 kV to achieve a drift velocity of 5 mm/μs and prohibits signal amplification in the gas. Thus the TPC was operated as an ionization chamber. A challenging aspect of the design was the Frisch grid, which was strung with gold-plated tungsten wires of 50 μm diameter with 400 μm pitch. It features a composite frame, where the side bars along the wires direction were also made of tungsten to match the thermal expansion while the cross bars were made of stainless steel to allow soldering the wires. This construction withstood numerous cryogenic temperature cycles over several years without damage. Excellent energy resolution of ≈17 keV rms was realized with custom built cyro-preamplifiers [24] which operated inside the insulation vacuum in close vicinity to the TPC at a stabilized temperature of 140 K.

After several technical developments and upgrades, MuSun collected its full statistics of 1.4×10^{10} events in two main production runs R2014 and R2015 at the PSI πE1 beamline, followed, in 2016, by a shorter run focused on systematic effects.

18.3 Status of the Analysis

As the capture rate Λ_d amounts to less than one per mill of the muon decay rate λ_{μ^+}, the muon disappearance rate $\lambda_{d\mu}$ has to be measured to 13 ppm to determine Λ_d to 1.5% or ± 6 s^{-1}. Such a precision requires careful attention to systematics from physical as well as instrumental effects. In particular early to late effects within the fit range of 1-24 μs must be tightly controlled.

The analysis starts with the muon stop definition. This is a critical step as subsequent
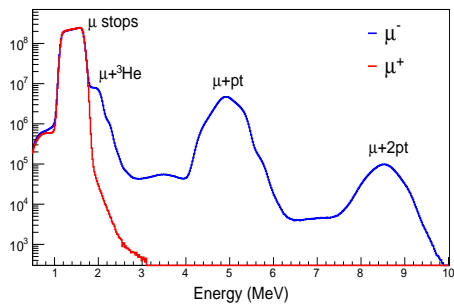
Figure 18.3: Energy deposition in TPC around muon stop location. Pileup with fusion recoils from ^{3}He and pt leads to distinct structures at higher energies in the μ^- spectrum. The μ^+ spectrum with lower statistics was scaled up.
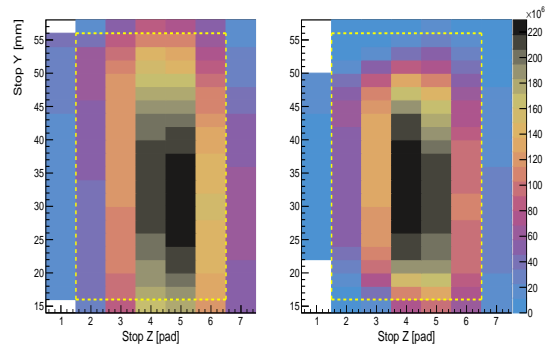
Figure 18.4: Muon stopping distribution in y-z projection with fiducial boundaries (yellow lines). The full stopping distribution (left panel) can be shaped by cuts on the first TPC pad row to reduce the muon population close to the boundaries (right panel).

muon-catalyzed-fusion products can overlap the muon track, see Figure 18.3, leading to mis-reconstruction of the muon stopping point. Most tracks are muon stops with energy deposition up to 1.8 MeV. However, $d\mu$ atoms can combine to muonic $dd\mu$ molecules, from which spontaneous fusion proceeds in two branches ^{3}He (0.8 MeV)+n (2.4 MeV) and p (3.0 MeV)+t (1.0 MeV). The higher energy structures in the μ^- spectrum are indicative for fusion recoils not separated from the muon tracks. While the time distribution of all decays is well described by (18.2), the time distributions for decay electrons with or without fusion reactions differ. Thus both event types have to be reconstructed with the same acceptance at sub percent accuracy to avoid biasing the lifetime measurement. The dominant mechanism for acceptance differences are misreconstruction of muon stops at the TPC fiducial boundaries caused by the overlap with the 3 MeV protons from p+t reactions which have a range of 13 mm. The approach to study these corrections is indicated in Figure 18.4. By imposing x, y and dE/dx cuts on the first pad
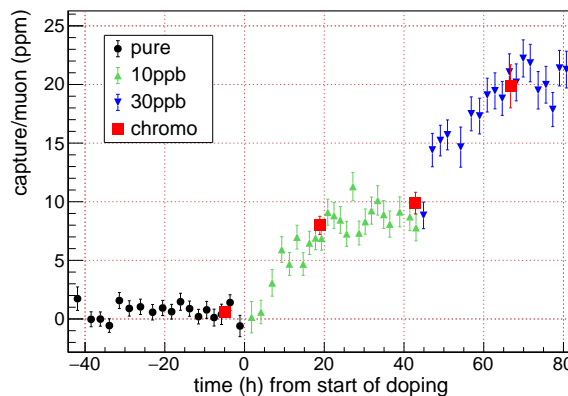
Figure 18.5: Calibration of capture yield from N$_2$ impurities. After an initial high purity run, the circulating flow was doped with 10 ppb and 30 ppb admixtures, respectively. The concentrations build up over hours in the TPC as monitored by the increasing yield of capture recoils. The chromatography measurements (red squares) track the capture yield and are used to calibrate it.

row of the TPC the stopping distribution can be shaped in all dimensions, reducing or enhancing the muon population at the fiducial volume boundaries and quantifying the associated acceptance losses. Currently the uncertainty of this method is estimated as $\approx 6\,s^{-1}$.

At the operating temperature T=31 K of MuSun, most impurities have frozen out, but the partial pressure of potential nitrogen trace admixtures would be too high. As the rate for muon transfer from deuterium to nitrogen at cryogenic conditions was unknown, MuSun determined the sensitivity to the nitrogen concentration c_N in a dedicated experiment as $\partial \lambda_{d\mu}/\partial c_N \approx 4\,s^{-1}$ per ppb. During R2015 the MuSun chromatography was able to limit c_N to about 1 ppb [22]. A more direct method applied to all runs is the detection of the capture recoil from $\mu + N \rightarrow C^* + \nu$ in the TPC, c.f. Figure 18.5. Identifying those rare low energy signals of about 150 keV is challenging against the background of Michel electrons and ^{3}He recoils, but was achieved due to the excellent energy resolution of the cryo-TPC. This analysis is in progress, as the observed capture yield still requires a correction for scattering of $\mu + d$ capture neutrons inside the TPC.
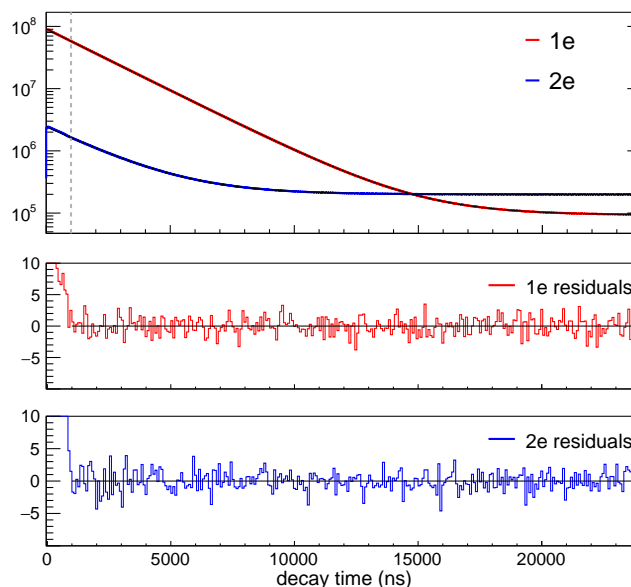
Figure 18.6: Muon decay spectra from scintillators observed in R2014 requiring one (1e) or two (2e) electrons in the region of interest of 0-24000 ns. The fit range is 1-24 μs with a bin width of 40 ns. The fit model is a single exponential and an accidental component with a small linear term. The fit curves and the data are not discernible by eye. The normalized residual plots demonstrate consistency once early kicker induced background has subsided.

The muon decay spectra, see Figure 18.6, are built by histogramming the electron scintillator barrel hits against the entrance scintillator time for muons that were tracked to stop inside the fiducial volume of the TPC. For decay electrons the signals in the scintillator are used or, alternatively, this information is combined with tracking in the electron wire chambers. This provides some complementarity, as the scintillators are fast and simple, while the chambers are slower and more sensitive to noise pickup but define an electron track vector. The time spectra shown in the figure are sorted depending whether only one (1e), or two (2e) electrons were detected in the region of interest (ROI) 0-24 μs after muons stop. In the 1e spectrum accidentals are suppressed as their detection probability is decreased by $(1 - \epsilon_e)$, where $\epsilon_e = 0.7$ is the detection efficiency for Michel electrons. On the other hand, in the 2e spectrum muon decay electrons are suppressed by the small probability of $\approx 3\%$ of an accidental hit within the ROI. Thus the 1e time spectrum is favorable to obtain clean decay information, while the 2e spectrum is useful to study the properties of the background. In fact, a slight time-dependent

decrease of the background is observed, which is probably related to the fast kicker, and is accounted for in a simultaneous fit of both spectra. The linear correction term leads to a few Hz shift in the fitted disappearance rate $\lambda_{\mu d}$ with an uncertainty currently estimated as $\approx 3\,\text{s}^{-1}$.

A fraction of the data has been taken with a μ^+ beam to study systematic effects free of the aforementioned μ^- physics processes, albeit with the additional complication of muon spin rotation affecting positive muons. This data has been unblinded and found in agreement with the MuLan muon lifetime [18] (see also Section 16 [25]), well within the statistical uncertainty of 21 s^{-1} of the MuSun μ^+ dataset. This is an important consistency check to limit instrumental systematic effects that apply to μ^- as well to μ^+.

18.4 Summary and Outlook

The strategy and analysis of the MuSun experiment has been described. In particular, the main sources of uncertainty have been discussed, while deferring several others to a more detailed publication. The presence of muon-catalyzed-fusion in deuterium, absent in MuCap, required intricate studies of the cryo-TPC response derived from high statistics datasets. The analysis is advanced with final work and cross checks still under way. The collaboration plans to unblind the first μ^- dataset R2014 within the next few months, which has sufficient statistics to clarify the long-standing discrepancy between experiment and theory on nuclear muon capture on the deuteron. The final analysis will include a larger second dataset R2015 to obtain a capture rate with 1-2% uncertainty, commensurate with the current precision of theoretical calculations. The comparison of experiment and theory will test whether there are still surprises in the description of the weak coupling of the two-nucleon system and will establish a low-energy constant relevant for a variety of weak and strong dynamics.

Acknowledgment

References

[1] V. A. Andreev et al., *Measurement of muon capture on the proton to 1% precision and determination of the pseudoscalar coupling g_P*, Phys. Rev. Lett. **110**, 012504 (2013), doi:10.1103/PhysRevLett.110.012504.

[2] V. A. Andreev et al., *Measurement of the formation rate of muonic hydrogen molecules*, Phys. Rev. C **91**, 055502 (2015), doi:10.1103/PhysRevC.91.055502.

[3] M. Hildebrandt and C. Petitjean, *MuCap: Muon Capture on the Proton*, SciPost Phys. Proc. **5**, 017 (2021), doi:10.21468/SciPostPhysProc.5.017.

[4] V. A. Andreev *et al.*, *Muon Capture on the Deuteron – The MuSun Experiment* (2010), arXiv:1004.1754.

[5] P. Ackerbauer et al., *A precision measurement of nuclear muon capture on ^3He*, Phys. Lett. B **417**, 224 (1998), doi:10.1016/S0370-2693(97)01382-8, arXiv:hep-ph/9708487.

[6] E. G. Adelberger et al., *Solar fusion cross sections. II. the pp chain and CNO cycles*, Rev. Mod. Phys. **83**, 195 (2011), doi:10.1103/RevModPhys.83.195.

[7] B. Acharya, B. Carlsson, A. Ekström, C. Forssén and L. Platter, *Uncertainty quantification for proton–proton fusion in chiral effective field theory*, Phys. Lett. B **760**, 584 (2016), doi:10.1016/j.physletb.2016.07.032.

[8] L. Marcucci, A. Kievsky, S. Rosati, R. Schiavilla and M. Viviani, *Chiral effective field theory predictions for muon capture on deuteron and* ^3He, Phys. Rev. Lett. **108**, 052502 (2012), doi:10.1103/PhysRevLett.108.052502, arXiv:1109.5563.

[9] L. E. Marcucci, A. Kievsky, S. Rosati, R. Schiavilla and M. Viviani, *Erratum: Chiral effective field theory predictions for muon capture on deuteron and* ^{3}He, Phys. Rev. Lett. **108**, 052502 (2012), doi:10.1103/PhysRevLett.108.052502, [Phys. Rev. Lett. **121**, 049901 (2018), doi:10.1103/PhysRevLett.121.049901].

[10] J.-W. Chen, K. M. Heeger and R. G. H. Robertson, *Constraining the leading weak axial two-body current by recent solar neutrino flux data*, Phys. Rev. C **67**, 025801 (2003), doi:10.1103/PhysRevC.67.025801, arXiv:nucl-th/0210073.

[11] S. Pastore, F. Myhrer and K. Kubodera, *An update of muon capture on hydrogen*, Int. J. Mod. Phys. E **23**, 1430010 (2014), doi:10.1142/S0218301314300100, arXiv:1405.1358.

[12] D. Gazit, S. Quaglioni and P. Navrátil, *Three-nucleon low-energy constants from the consistency of interactions and currents in chiral effective field theory*, Phys. Rev. Lett. **103**, 102502 (2009), doi:10.1103/PhysRevLett.103.102502.

[13] D. Gazit, S. Quaglioni and P. Navrátil, *Erratum: Three-nucleon low-energy constants from the consistency of interactions and currents in chiral effective field theory*, Phys. Rev. Lett. **103** , 102502 (2009), doi:10.1103/PhysRevLett.103.102502, [Phys. Rev. Lett. **122**, 029901 (2019), doi:10.1103/PhysRevLett.122.029901].

[14] G. B. King, L. Andreoli, S. Pastore, M. Piarulli, R. Schiavilla, R. B. Wiringa, J. Carlson and S. Gandolfi, *Chiral effective field theory calculations of weak transitions in light nuclei*, Phys. Rev. C **102**, 025501 (2020), doi:10.1103/PhysRevC.102.025501.

[15] T. Hüther, K. Vobig, K. Hebeler, R. Machleidt and R. Roth, *Family of chiral two- plus three-nucleon interactions for accurate nuclear structure studies*, Phys. Lett. B **808**, 135651 (2020), doi:10.1016/j.physletb.2020.135651.

[16] G. Bardin, J. Duclos, J. Martino, A. Bertin, M. Capponi, M. Piccinini and A. Vitale, *A measurement of the muon capture rate in liquid deuterium by the lifetime technique*, Nucl. Phys. A **453**, 591 (1986), doi:10.1016/0375-9474(86)90253-8.

[17] B. Acharya, A. Ekström and L. Platter, *Effective-field-theory predictions of the muon-deuteron capture rate*, Phys. Rev. C **98**, 065506 (2018), doi:10.1103/PhysRevC.98.065506.

[18] V. Tishchenko et al., *Detailed report of the MuLan measurement of the positive muon lifetime and determination of the Fermi constant*, Phys. Rev. D **87**, 052003 (2013), doi:10.1103/PhysRevD.87.052003.

[19] M. J. Barnes and G. D. Wait, *A 25-kv 75-khz kicker for measurement of muon lifetime*, IEEE Trans. Plasma Sci. **32**, 1932 (2004), doi:10.1109/TPS.2004.835455.

[20] P. Kammel and K. Kubodera, *Precision muon capture*, Ann. Rev. Nucl. Part. Sci. **60**, 327 (2010), doi:10.1146/annurev-nucl-100809-131946.

[21] V. Ganzha et al., *A circulating hydrogen ultra-high purification system for the MuCap experiment*, Nucl. Inst. Meth. Phys. Res. A **578**, 485 (2007), doi:10.1016/j.nima.2007.06.010.

[22] V. Ganzha, K. Ivshin, P. Kammel, P. Kravchenko, P. Kravtsov, C. Petitjean, V. Trofimov, A. Vasilyev, A. Vorobyov, M. Vznuzdaev and F. Wauters, *Measurement of trace impurities in ultra pure hydrogen and deuterium at the parts-per-billion level using gas chromatography*, Nucl. Inst. Meth. Phys. Res. A **880**, 181 (2018), doi:10.1016/j.nima.2017.10.096.

[23] I. Alekseev et al., *Cryogenic distillation facility for isotopic purification of protium and deuterium*, Rev. Sci. Inst. **86**, 125102 (2015), doi:10.1063/1.4936413.

[24] R. A. Ryan et al., *Design and operation of a cryogenic charge-integrating preamplifier for the MuSun experiment*, J. Instr. **9**, P07029 (2014), doi:10.1088/1748-0221/9/07/p07029.

[25] R. Carey, T. Gorringe and D. Hertzog, *MuLan: a part-per-million measurement of the muon lifetime and determination of the Fermi constant*, SciPost Phys. Proc. **5**, 016 (2021), doi:10.21468/SciPostPhysProc.5.016.

The Mu3e experiment

F. Wauters[⋆] on behalf of the Mu3e collaboration

PRISMA+ Cluster of Excellence and Institute of Nuclear Physics,
Johannes Gutenberg Universität Mainz, Germany

⋆ fwauters@uni-mainz.de

Abstract

The *Mu3e* experiment aims for a single event sensitivity of $2 \cdot 10^{-15}$ on the charged lepton flavour violating $\mu^+ \to e^+ e^+ e^-$ decay. The experimental apparatus, a light-weight tracker based on custom High-Voltage Monolithic Active Pixel Sensors placed in a 1 T magnetic field is currently under construction at the Paul Scherrer Institute, where it will fully use the intense 10^8 μ^+/s beam available. A final sensitivity of $1 \cdot 10^{-16}$ is envisioned for a phase II experiment, driving the development of a new high-intensity continuous muon source which will deliver $>10^9$ μ^+/s to the experiment.

20.1 Introduction

Searches for Charged Lepton Flavour Violation (CLFV) in muon decays are a remarkably sensitive method to search for new physics processes [1]. These decays are free from Standard Model backgrounds, and leave a relatively simple and clear signature in the experimental apparatus. In addition, intense muon beams are available at several facilities, where the relatively long-lived muons get transported from a production target to an experimental area.

The Paul Scherrer Institute (PSI) has been at the forefront of CLFV searches, with the current best limit on the $\mu^+ \to e^+ \gamma$ decay channel of $4.2 \cdot 10^{-13}$ (90% CL) from the *MEG* experiment [2]. The *SINDRUM* experiment [3] set the best limit on the $\mu^+ \to e^+ e^+ e^-$ decay channel, and the *SINDRUM II* experiment [4] on muon conversion $\mu^- \to e^-$ on gold. A new generation of experiments pursuing these three *golden* channels, which probe for new physics in a complementary manner [5], is currently under construction: the *Mu2e* experiment at Fermilab, the *COMET* experiment at J-PARC, and the *MEGII* experiment at PSI. The *Mu3e* experiment aims for a 10^{-16} single-event sensitivity for the $\mu^+ \to e^+ e^+ e^-$ CLFV decay channel, an improvement by four orders of magnitude compared to the limit set by the SINDRUM experiment [3]. Such a leap in sensitivity is enabled by the availibility of high-intensity muon beams, the use of silicon pixel detectors instead of multi-wire proportional chambers to track the decay products, and a modern data-aqcuisition system able to handle the vast amount of

data producted by the detector at high beam rates. A first phase of the experiment is currently under construction at the πE5 beamline at PSI, where the intense DC surface muon beam of 10^8 μ^+/s will be exploited to achieve a single event sensitivity of $2 \cdot 10^{-15}$ in 300 days of data taking [6].

The *Mu3e* detector is optimized for the $\mu^+ \rightarrow e^+ e^+ e^-$ decay. It is designed to track the two positrons and one electron from muons decaying at rest with a light-weight tracker placed inside a 1 T magnetic field, thereby reconstructing the decay vertex and invariant mass. The momentum balance of the three reconstructed particles should be consistent with a muon decaying at rest. Several background processes can potentially meet the same criteria as the reconstructed signal events. The dominating accidental background originates from the overlay of two ordinary muon decays where one of the positrons produces an additional electron track through Bhabha scattering in the target material. This process is sufficiently suppressed by means of a good vertex resolution of better than 300 μm, a timing resolution of a few 100 ps, the requirement of an invariant mass equal to the muon mass, and a balanced momentum budget. Additional background from $\mu^+ \rightarrow e^+ e^+ e^- \nu_e \bar{\nu}_\mu$ internal conversion decays can only be suppressed by means of an excellent momentum resolution of $\sigma_p < 1$ MeV , as shown in Figure 20.1.

All *Mu3e* detector sub-systems, as described in Section 20.2, are currently under construction. With the solenoid magnet (Figure 20.2) installed at PSI, the first engineering runs are planned for spring 2021.
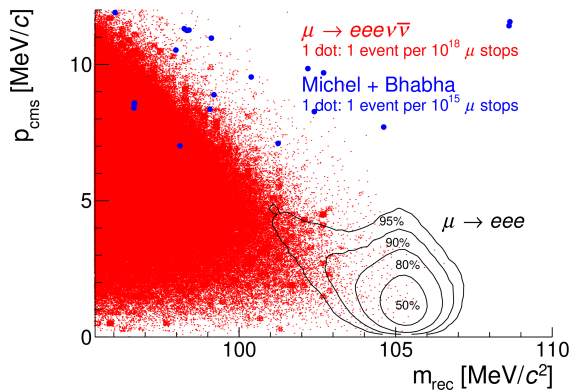
Figure 20.1: The simulated reconstructed mass versus the momentum balance of two positrons and one electron from a common vertex [6]. The accidental background is shown in blue, the dominating background from internal conversion is shown in red.

Figure 20.2: The 30 ton *Mu3e* magnet arriving at PSI. The magnet is curently installed and commissioned in the πE5 experimental area, providing a magnetic field of up to 2.6 Tesla with a $\frac{\Delta B}{B}$ uniformity and stability of $\mathcal{O}(10^{-4})$.

20.2 The Mu3e detector

The *Mu3e* detector is located at the Compact Muon Beam Line at the πE5 channel. After the positron contamination is removed from the beam by a Wien filter, the surface μ^+ beam of up to 10^8 μ^+/s is transported to the center of the *Mu3e* solenoid magnet, and stopped on a hollow double-cone target, which spreads out the decay vertices in z and minimises the amount of target material traversed by the decay particles. The target is surrounded by the cylindrical central tracker, consisting of the inner silicon pixel detector, a scintillating fibre tracker for time measurements, and the outer silicon pixel detector. A momentum resolution of better than 1 MeV/c is achieved by letting the positrons(electrons) recurl in the magnetic field,
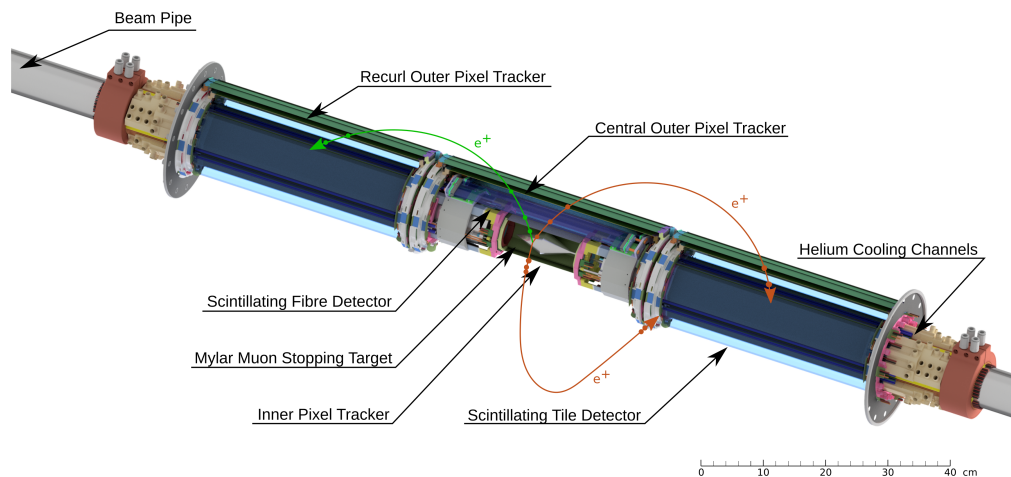
Figure 20.3: The active part of the *Mu3e* detector, with a central tracker surrounding the target, and upstream and downstream outer pixel tracking stations. The large lever arm created by the recurling tracks enables the high momentum resolution required.

either crossing the central tracker again, or hitting the outer tracking stations surrounding the upstream and downstream beam pipe. These stations consist of a silicon pixel tracker, and a scintillating tile detector mounted on the inside of the pixel tracker. The 5 mm thick tiles enable a time resolution for the tracks reaching these outer stations of better than 100 ps. The active part of the *Mu3e* detector is depicted in Figure 20.3.

As multiple Coulomb scattering is the dominating factor affecting the momentum resolution, it is crucial to minimize the material budget in the tracking detectors. For this purpose, the collaboration has developed a custom High-Voltage Monolithic Active Pixel Sensor [7] (HV-MAPS) based on a commercial 180 nm HV-CMOS process. After a series of prototypes, the sensor showed good efficiency (>99%) and time resolution ($\mathcal{O}(10$ ns)) [8] [9]. The *Mu3e MuPix* HV-MAPS is a 2x2 cm^2 sensor with 80x80 μm^2 active pixels, thinned to 50 μm (Figure 20.4). The digital periphery provides up to three 1.25 Gbit/s Low-Voltage Differential Signaling (LVDS) continuous data connections to the front-end electronics. The sensors are bonded to a thin aluminum/polyimide flex print carrying all electrical signals. Together with a polyimide support structure, the entire silicon tracking module has a thickness of ca. 0.0012 radiation lengths. The pixel sensors generate about 250 mW/cm^2 of heat. To remove this heat whilst keeping the material budget of the tracker sufficiently low, a gaseous He cooling system [10] is deployed providing well controlled He flows at atmospheric pressure between and outside the pixel layers.

A time resolution of about 10 ns is insufficient to determine the direction and thus the charge of the decay particles. A scintillating fibre detector is therefore placed between the inner and outer layer of the central silicon-pixel tracker, consisting of a dozen 30 cm long ribbons made from three staggered layers of 250 μm diameter multiclad round fibers, read out by Silicon Photomultipliers (SiPM) arrays on both sides [11]. Located at the very end of the recurling particle trajectories hitting the upstream or downstream tracker, where the constraints on the material budget are less stringent, the tile detector provides the needed precise timing information of the particle tracks, in conjunction with the fibre detector significantly reducing the accidental background associated with the intense rate of 10^8 μ^+/s. Each of the 5824 individually wrapped tiles is read out by a single SiPM. Both the fibre and tile SIPM signals are processed by a custom Application-Specific Integrated Circuit (ASIC), the 32 channel *MuTrig*

chip [12], which applies 2 thresholds to the analogue signal for time and energy information. The *MuTrig* chip has a 1.25 Gbit/s LVDS data connection, similar to the *MuPix* chip readout. For tile and fibre detector a respective time resolution of <50 ps and <400 ps is achieved.

The entire *Mu3e* detector is mounted in the bore of a superconducting magnet. Figure 20.2 shows the 3 m long solenoid magnet with the iron return yoke. It has a 1 m wide bore housing the active detector, in addition to the support structures and services such as the front-end readout electronics and DC-DC power converters for the detector ASICs. The two flanges below and above the beam pipe provide access for the water and gaseous helium cooling pipes, the power cables, and the optical data connections.
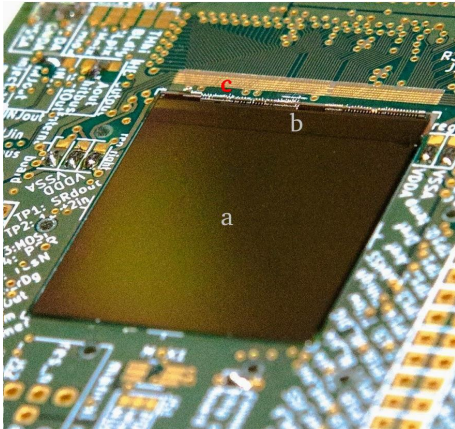
Figure 20.4: The full sized MuPix sensor, with a) a 2x2 cm^2 sized active area, and b) a periphery with the pixel hit digitization and readout state machine. This chip is c) wire bonded to a PCB for testing purposes.
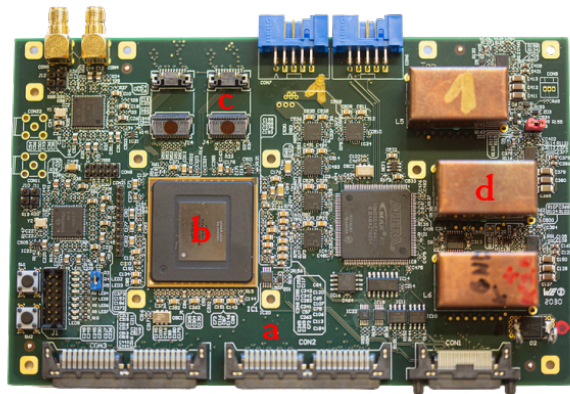
Figure 20.5: The front-end readout board, combining and time sorting the a) data from up to 36 detector ASICs on b) an Arria V FPGA, before sending the data via the c) optical Samtec FireFly tranceivers. d) Custom DC-DC converters with air coils regulate the power on the board.

20.3   Readout and online event selection

With three lepton tracks going in different (opposite) directions, the topology of a $\mu^+ \to e^+ e^+ e^-$ event is such, that a global picture of the detector is needed before candidate events can be selected. This leads to a trigger-less readout scheme as shown in Figure 20.6, where all pixel, fibre and tile hits are continuously being digitized and merged into a data stream of up to 100 Gbit/s. A series of PC's housing powerful Graphics Processing Units (GPU) perform an online event-selection, reducing the data rate to a manageable 50-100 MByte/s which is stored for further offline processing.

Each detector ASIC, a *MuTrig* or *MuPix* chip, assigns a timestamp and address to each hit, and sends the serialized data through a series of flex-prints and twisted pair cables to a front-end board (Figure 20.5). Each of these readout boards is located inside the magnet bore and accepts up to 45 electric LVDS links. The data streams are merged and time-sorted on an Arria V Field-Programmable Gate Array (FPGA). Two optical transceivers provide eight 6 GBit/s links to the outside, sending off the merged and sorted hit information combined with the slow-control data. In addition, the front-end FPGA also configures the detector ASICs, including tuning the very large number of individual *MuPix* pixels, and distributes the clock and reset signals.

All incoming and outgoing data connections to and from the detector volume travel via optical fibres to the counting house. The data links from the 112 front-end boards are con-

nected to the *Switching boards*, where the data from different detector modules are merged into 64 ns time slices containing the full detector hit information. This custom *PCIe40* board housing a large Arria 10 FPGA and 48 fast optical receivers and 48 fast optical transmitters was developed for the LHCb and ALICE upgrades [13].

The online event selection must decide which of these 64 ns *snapshots* of the detector to store for later (offline) processing, in the process keeping less than 1% of the data. A simple time coincidence between 3 tracks is insufficient to achieve this. Instead an online filter farm reconstructs all tracks in software, and performs the selection by requiring 3 tracks having a common vertex and the kinematics of a possible $\mu^+ \to e^+e^+e^-$ event. The filter farm consists of 12 PC's housing a FPGA board receiving the data and a powerful commercial GPU performing the event selection. With simple geometric cuts, candidate tracks are first selected on the FPGA from hits in the central pixel tracker. The track fitting [14] is performed on the GPU, where $1 \cdot 10^9$ fits per second have been achieved on a NVIDIA GTX 980 GPU, sufficient to be able to process the expected 10^8 muon decays/s. A newer more powerful GPU will be selected when equipping the farm PCs.

The MIDAS[1]-based data-acquisition system sends the filtered data to on-site and off-site storage for later processing. This integrated DAQ also takes care of the configuration, monitoring, and logging of all parameters of the detector and its services such as the water and helium cooling system and power distribution.
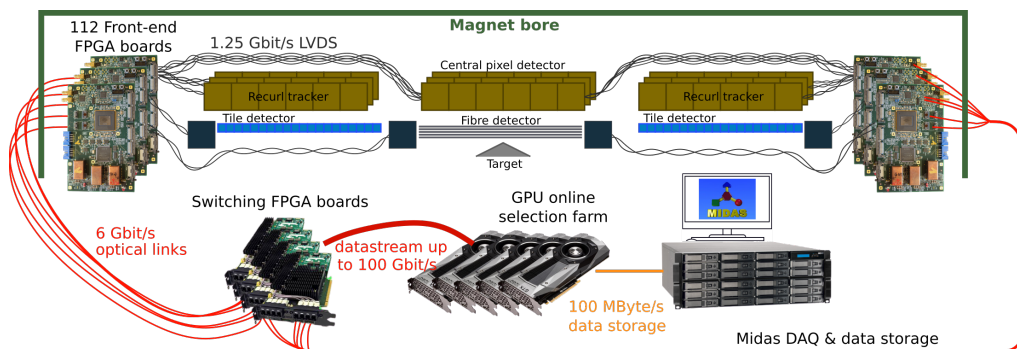
Figure 20.6: A sketch of the *Mu3e* triggerless readout scheme [15], where all detector hits are piped to the online filter farm. A selection algorithm based on massive parallelised track fitting sends off a subset of the data for further offline processing.

20.4 Conclusions and outlook

With the magnet installed at the Paul Scherrer Institute, the Mu3e experiment is entering its construction phase. All sub-detector demonstrators have met the required specification, and are currently being integrated to a single lightweight electron/positron tracker. This also includes a novel read-out system of the apparatus, which pipes the full detector information to an online filter farm. Aside from being a necessary requirement set by the CLFV decay event topology, this readout scheme where the full and global detector information is available for online analysis, also allows other new-physics searches such as CLFV two-body decays and Dark Photon searches [16].

The *Mu3e* phase II experiment envisions a branching ratio sensitivity of $1 \cdot 10^{-16}$. Many detector sub-systems are already designed with this goal in mind, but significant research and development on the detector side still has to be done. An order of magnitude increase in

---

[1]https://midas.triumf.ca

sensitivity also requires a more intense, and currently unavailable muon flux of μ^+/s of $\mathcal{O}(10^9)$. For this purpose, a new High-Intensity Muon Beamline [17] to be installed at the target M is currently under development at the Paul Scherrer Institute, replacing the conventional muon extraction beamline elements with solenoids. The timeline of this project coincides with the envisioned start of the *Mu3e* Phase II construction at the end of this decade.

References

[1] Y. Kuno and Y. Okada, *Muon decay and physics beyond the standard model*, Rev. Mod. Phys. **73**, 151 (2001), doi:10.1103/RevModPhys.73.151.

[2] A. M. Baldini et al., *Search for the lepton flavour violating decay $\mu^+ \rightarrow e^+\gamma$ with the full dataset of the MEG experiment*, Eur. Phys. J. C **76**, 434 (2016), doi:10.1140/epjc/s10052-016-4271-x.

[3] U. Bellgardt et al., *Search for the decay $\mu^+ \rightarrow e^+e^+e^-$*, Nucl. Phys. B **299**, 1 (1988), doi:10.1016/0550-3213(88)90462-2.

[4] W. H. Bertl et al., *A search for μ-e conversion in muonic gold*, Eur. Phys. J. C **47**, 337 (2006), doi:10.1140/epjc/s2006-02582-x.

[5] A. Crivellin, S. Davidson, G. M. Pruna and A. Signer, *Renormalisation-group improved analysis of $\mu \rightarrow e$ processes in a systematic effective-field-theory approach*, J. High Energ. Phys. **05**, 117 (2017), doi:10.1007/JHEP05(2017)117.

[6] K. Arndt et al., *Technical design of the phase I Mu3e experiment* (2020), arXiv:2009.11690.

[7] I. Perić, *A novel monolithic pixelated particle detector implemented in high-voltage CMOS technology*, Nucl. Instrum. Meth. A **582**, 876 (2007), doi:10.1016/j.nima.2007.07.115.

[8] H. Augustin et al., *Performance of the large scale HV-CMOS pixel sensor MuPix8*, J. Inst. **14**, C10011 (2019), doi:10.1088/1748-0221/14/10/C10011.

[9] H. Augustin et al., *The MuPix system-on-chip for the Mu3e experiment*, Nucl. Instrum. Meth. A **845**, 194 (2017), doi:10.1016/j.nima.2016.06.095.

[10] F. Meier Aeschbacher, M. Deflorin and L. Olivier Sebastian Noehte, *Mechanics, readout and cooling systems of the Mu3e experiment* (2020), arXiv:2003.11077.

[11] A. Bravar, K. Briggl, S. Corrodi, A. Damyanova, L. Gerritzen, C. Grab, M. Hildebrandt, A. Papa and G. Rutar, *The Mu3e scintillating fiber timing detector*, Nucl. Instrum. Meth. A **958**, 162564 (2020), doi:10.1016/j.nima.2019.162564.

[12] H. Chen, K. Briggl, P. Eckert, T. Harion, Y. Munwes, W. Shen, V. Stankova and H. C. Schultz-Coulon, *MuTRiG: a mixed signal Silicon Photomultiplier readout ASIC with high timing resolution and gigabit data link*, J. Inst. **12**, C01043 (2017), doi:10.1088/1748-0221/12/01/C01043.

[13] P. Durante, N. Neufeld, R. Schwemmer, U. Marconi, G. Balbi and I. Lax, *100 Gbps PCI-express readout for the LHCb upgrade*, IEEE Trans. Nucl. Sci. **62**, 1752 (2015), doi:10.1109/TNS.2015.2441633.

[14] A. Kozlinskiy, A. Schöning, M. Kiehn, N. Berger and S. Schenk, *A new track reconstruction algorithm for the Mu3e experiment based on a fast multiple scattering fit*, J. Inst. **9**, C12012 (2014), doi:10.1088/1748-0221/9/12/C12012.

[15] H. Augustin et al., *The Mu3e data acquisition* (2020), arXiv:2010.15648.

[16] A.-K. Perrevoort, *The rare and forbidden: Testing physics beyond the standard model with Mu3e*, SciPost Phys. Proc. **1**, 052 (2019), doi:10.21468/SciPostPhysProc.1.052.

[17] R. Iwai et al., *Development of next generation muon beams at the Paul Scherrer Institute*, Proc. Sci. **369**, 125 (2020), doi:10.22323/1.369.0125.

Laser spectroscopy of light muonic atoms and the nuclear charge radii

Aldo Antognini[1,2*], Franz Kottmann[1,2] and Randolf Pohl[3]

1 Institute for Particle Physics and Astrophysics, ETH Zurich, 8093 Zurich, Switzerland
2 Paul Scherrer Institute, 5232 Villigen–PSI, Switzerland
3 QUANTUM, Institut für Physik & Exzellenzcluster PRISMA+, Johannes Gutenberg-Universität Mainz, 55099 Mainz, Germany

★ aldo@phys.ethz.ch

Abstract

The energy levels of hydrogen-like atomic systems are shifted slightly by the complex structure of the nucleus, in particular by the finite size of the nucleus. These energy shifts are vastly magnified in muonic atoms and ions, *i.e.* the hydrogen-like systems formed by a negative muon and a nucleus. By measuring the 2S-2P energy splitting in muonic hydrogen, muonic deuterium and muonic helium, we have been able to deduce the p, d, ^{3}He and ^{4}He nuclear charge radii to an unprecedented accuracy. These radii provide benchmarks for hadron and nuclear theories, lead to precision tests of bound-state QED in regular atoms and to a better determination of the Rydberg constant.

21.1 Introduction

Some energy levels of light, hydrogen-like muonic atoms are extremely sensitive to the influence of nuclear properties, such as the nuclear charge and magnetization distributions, and the nuclear polarizability. This makes laser spectroscopy of these states a unique tool for precision determination of these nuclear properties.

Of particular significance is the first excited 2S state in these H-like atoms. First, the 2S state has a large overlap of the muon wave function with the nucleus. Because of the large muon mass, $m_\mu \approx 200\,m_e$, the wave function overlap is about $200^3 \approx$ a few million times larger for muonic atoms, compared to the corresponding electronic atom. This results in a million-fold enhanced shift of the 2S state due to nuclear size effects. Second, in these light muonic atoms, the energy splitting to the neighboring 2P state is only on the order of 1 eV making the Lamb shift(2S-2P energy splitting) accessible to pulsed infrared lasers. And third, the 2S state is metastable.

The various contributions to the Lamb shift $(2S - 2P_{1/2})$ energy differences in μp, μd, and μ^4He$^+$ are [1–3]:

$$\Delta E(\mu\mathrm{p}) = \ 206.0336(15) + 0.0332(20) - 5.2275(10) \times r_{\mathrm{p}}^2 \qquad (21.1)$$

$$\Delta E(\mu\mathrm{d}) = \ 228.7767(10) + 1.7449(200) - 6.1103(3) \times r_{\mathrm{d}}^2 \qquad (21.2)$$

$$\Delta E(\mu^4\mathrm{He}) = 1668.489(14) + 9.201(291) - 106.220(8) \times r_{\alpha}^2 \, , \qquad (21.3)$$

in units of meV when the charge radii r_{X} are measured in fm, with the μd equation corrected for nuclear effects calculated only recently [4,5]. Here, the first term is the sum of the "pure" QED effects, the last term is the finite nuclear charge radius effect, and the second term is the remaining nuclear structure effects (elastic and inelastic two- and three-photon exchange, 2PE and 3PE, respectively) [6–12].

21.2 The principle of the experiment

The measurement of the 2S-2P transition in these light muonic atoms is based on pulsed laser spectroscopy. Low-energy muons (μ^-) with a kinetic energy of about 1 keV are stopped in a (H$_2$, D$_2$, He) gas target at low pressure (1-2 mbar) and room temperature, forming the corresponding muonic atoms (μp, μd, μHe$^+$) in highly excited states with a principal quantum number around $n \approx \sqrt{m_\mu/m_e} \approx 14$. At this low gas pressure, about 99% of the muons then cascade to the 1S ground state within about 100 ns, while the remaining 1% ends up in the metastable 2S state [13, 14]. The 2S state is metastable, because further fast radiative E1 deexcitation is not possible and two-photon deexcitation is slow for these light nuclei. Thus, for low enough gas pressures of $\sim$ 1 mbar, only collisional processes with surrounding gas atoms/molecules limit the 2S lifetime to $\tau_{2S} \approx 1\,\mu$s [14, 15]. This lifetime is suitable for pulsed resonant laser excitation to the neighboring 2P state, which quickly de-excites to the 1S ground-state via emission of a Lyman-α X-ray. The detection of this X-ray in time coincidence with the laser light is used to signal a successful laser transition. The resonance is observed by plotting the number of X-rays versus laser frequency.

The experimental setup is based on five main building blocks: a muon beam line delivering negative muons with keV kinetic energy, a detector for these muons based on a set of ultra-thin carbon foils providing a trigger signal for the laser, a laser system capable of delivering high-energy pulses within a short time upon a trigger, a multi-pass optical cavity enhancing the laser fluence at the position of the muonic atoms, and a detection system for the muonic Lyman-α X-rays of a few keV with good energy and time resolutions.

The design of the experiment is dominated by the stochastic arrival time of the muon, the short lifetime of the 2S state, the required very low target gas pressure, and the large laser fluence needed to drive the muonic atom transitions. Muons with energies of few keV stop in a 20 cm long gas target. The low-energy beam line delivers about 500/s detected low-energy muons, each of them triggering the laser system that provides pulses to excite the 2S-2P transition with delay of about 1 μs.

Due to the 200-times smaller size than regular atoms, muonic atoms have small matrix elements for optical excitation. In conjunction with the short lifetime of the 2S state, the large muon stopping volume (elongated target with size of $7 \times 20 \times 200$ mm^3) and the peculiar wavelength of the transition (e.g. 6.0 μm for μp), this sets severe requirements for the laser system and the enhancement cavity.

21.3 The low-energy beamline

A schematic diagram of the experimental setup is given in Figure 21.1. The low-energy muon beam line was realized at the πE5 secondary beamline tuned to a momentum of 102 MeV/c
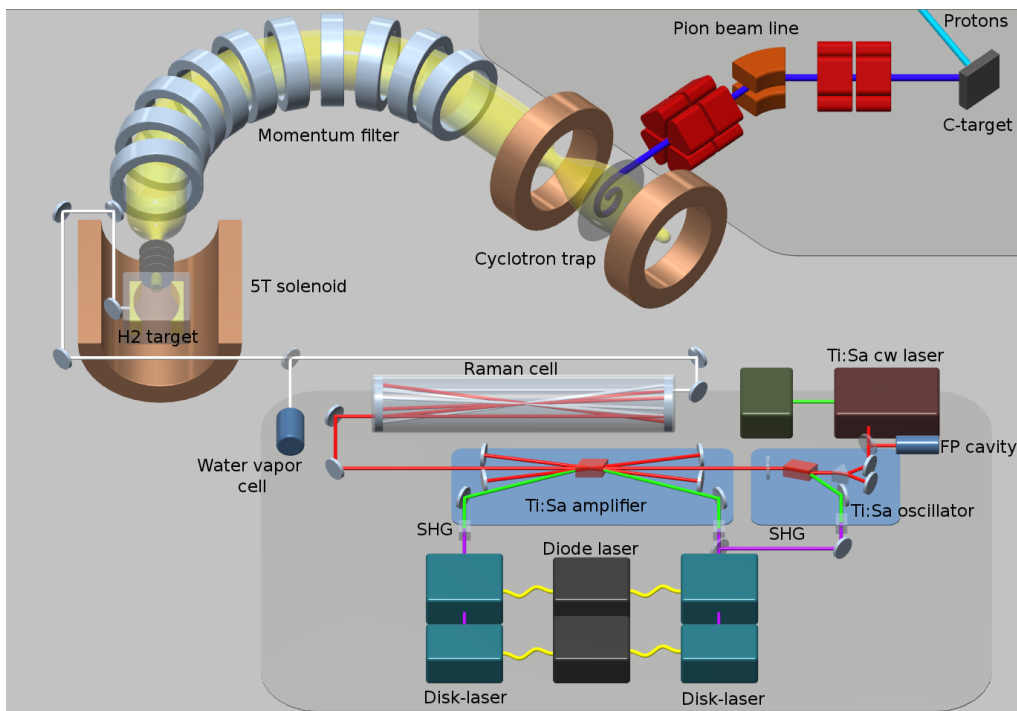
Figure 21.1: Experimental setup used to measure the 2S-2P transitions in μp.

of the HIPA accelerator at the Paul Scherrer Institute. The negative pions transported by the secondary beam line were injected at a rate of $10^8\,\mathrm{s^{-1}}$ into a cyclotron trap (CT) [16, 17] made of two superconducting 4 T coils. Muons from backwards-decaying pions with energies of a few MeV are confined in the magnetic bottle formed by the two coils. While confined in the trap, the muons slow down by repeatedly passing a 160 nm thick Formvar foil coated with Ni installed in the trap mid-plane. For sufficiently low kinetic energy (around 20 keV), the longitudinal momentum imparted by the –20 kV applied at the foil brings the muon momentum into the loss cone of the trap.

The muons escaping axially from the CT are transported into a region of lower background using a system of 17 coils forming a 0.15 T toroidal magnetic field. This toroidal field also acts as a momentum filter separating the charged particles in the vertical direction according to their momentum. After passing a collimator, which selects muons with the adequate momentum, the muon beam is focused into a 5T solenoid where the gas target is located. The focusing effect caused by the fringe field of the solenoid results in a beam of about 20 mm diameter with kinetic energy of about 20 keV. Before the muons enter the target with a rate of about $500\,\mathrm{s^{-1}}$, and a transverse size of $20 \times 7\mathrm{mm}^2$ (after collimation), they cross several 4 μg/cm^2 carbon foils that are held at high voltage as shown in Figure 21.2. The energy loss occurring in these foils reduces the kinetic energy of the muons to a few keV and frictional cooling [18] reduces their energy spread. The muons crossing the foils also release electrons, which are accelerated by the high voltage applied to the foils, separated from the muon using an $E \times B$-filter and detected in a thin plastic scintillator. This electron signal is used to signal the entering muon providing the trigger for the laser and the DAQ systems.

After crossing the target entrance window of 4 μg/cm^2 thickness, the muons slow down and efficiently (about 80% for 2 mbar pressure) stop in the 20 cm long gas target and form muonic atoms.
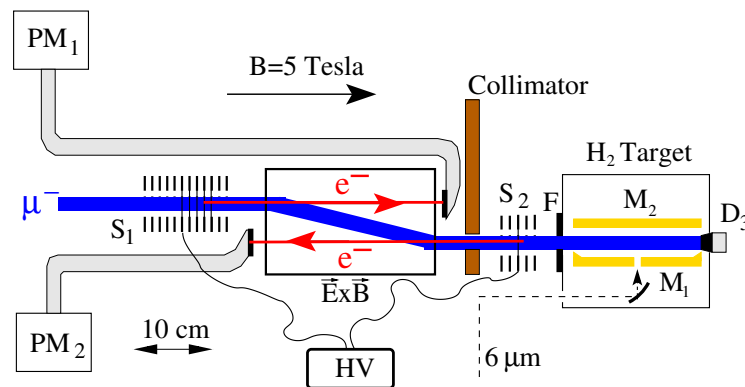
Figure 21.2: Muons are detected by electron emission from two "stacks" of ultra-thin carbon foils before they stop in the gas target. An $\vec{E} \times \vec{B}$ drift region separates the muons from the ejected electrons.

21.4 The laser system and the cavity

The laser system for the 2S-2P measurements has to deliver pulses of 0.15 mJ energy tunable from a wavelength of 5.5 to 6.0 μm for μp and μd [19], and of 10 mJ tunable from 800 to 970 nm for μ^3He$^+$ and μ^4He$^+$. Moreover the laser system has to respond to a stochastic trigger and have a short latency time ($\lesssim 1 \mu s$), i.e., a short delay between trigger and pulse delivery. Each detected muon that enters the target triggers the laser system, which has to provide the pulses before the 2S state has decayed.

To achieve the needed short latency time and large pulse energy, the laser system starts with two thin-disk lasers (TDL) [20] where the energy is continuously stored in the active medium through continuous wave (cw) pumping with commercial diodes of kW optical power at 940 nm. Each TDL consists of a Q-switched oscillator followed by a multi-pass amplifier. To further reduce the delay time, the oscillator operates in pre-seeding mode prior to the trigger, i.e. in cw-mode at low power close to threshold. The laser cavity is closed when triggered, so that a rapid pulse buildup can start from the circulating laser photons. Cavity dumping is used to extract the pulses which are subsequently sent to the multi-pass amplifier.

The frequency-doubled pulses of the TDL are used to pump a Ti:Sapphire oscillator-amplifier system. The Ti:Sapphire (Ti:Sa) oscillator is injection-locked by a single-frequency master cw Ti:Sapphire laser that is tunable in frequency. For μHe, the pulses of the Ti:Sa laser were used directly to drive the 2S-2P transitions, while for the μp and μd measurements the Ti:Sa pulses needed to be frequency-shifted to the 6 μm region using three Stokes shifts in a Raman cell filled with 15 bar of H$_2$ gas.

To enhance the laser fluence at the muonic atom position that are distributed over a volume of about $7 \times 20 \times 200$ mm^2, the laser light is coupled into a multipass cavity through a 0.6 mm diameter hole. The multipass cavity consists of two long mirrors as shown in Fig. 21.3. It is capable of illuminating a large volume extended in longitudinal direction from a transverse direction [21]. The cylindrical mirror confines the injected light in the vertical direction, while the other mirror, formed by a flat central substrate with two cylindrical end-pieces, confines the light in horizontal (longitudinal) direction. The injected light confined within these two mirrors reflects many times (from 500 to 1000 depending on the laser wavelength) between the two optical surfaces homogeneously illuminating the muon stop volume and enhancing the laser intensity.
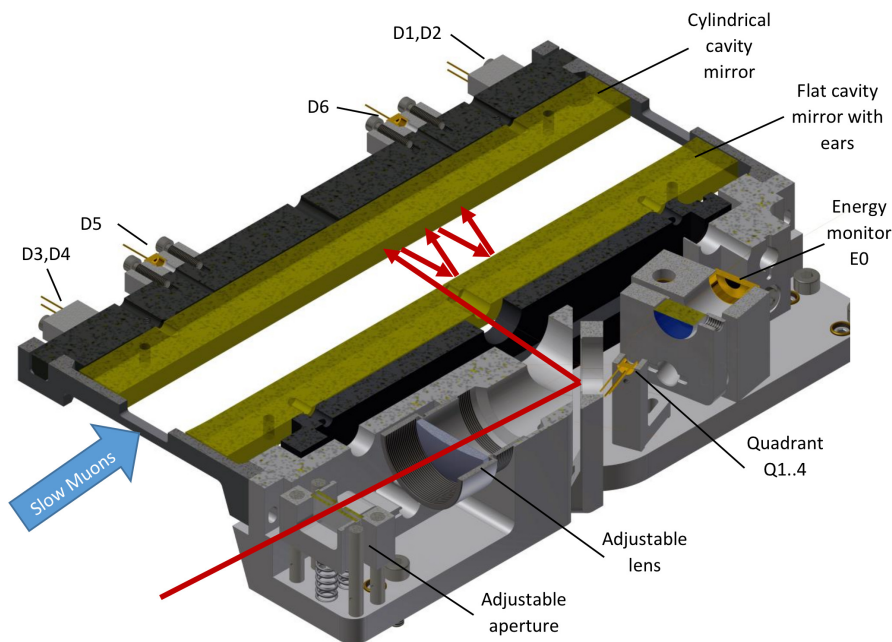
Figure 21.3: The multipass laser cavity used for efficient illumination of the large muon stop volume. The laser beam (red) enters through a hole with a diameter of only 0.6 mm, and bounces between the 2 elongated mirrors to fill the whole cavity volume. One long cylindrical mirror ensures vertical confinement of the light, while the other flat mirror has cylindrical "ears" attached at the ends that result in horizontal confinement [21].

21.5 The detectors

The X-ray detection system consists of two linear arrays, each with 10 large area avalanche photodiodes (LAAPDs) of 14×14 mm^2 active area read out with charge sensitive pre-amplifiers. The two detector–pre-amplifier arrays are mounted in the 5T magnetic field above and below the muon stopping volume, resulting in about 25% geometrical acceptance. The energy resolutions at $-30 \pm 0.1°$C are 27% and 16% FWHM for K$_\alpha$ photons at 1.9 keV (μp) and 8.2 keV (μHe), respectively. The LAAPDs also detect the Michel electrons from muon decays. To improve the electron detection efficiency four plastic scintillators are placed around the target.

The LAAPDs signals were recorded during data taking with waveform digitizers, allowing to reject pile-up events, to disentangle events where the X-ray is followed by the electron from muon decay, and to reject noisy events. Waveform analysis could distinguish between X-rays and electrons from muon decay [22], and improved the energy and time resolutions.

21.6 Measurements and results

In total, ten transition frequencies in μp [23,24], μd [25], μ^4He [26] and μ^3He were measured (manuscript on μ^3He is in preparation). A low background rate of 1 event/h was observed in all these measurements as due to the use of a continuous muon beam. With only a single muon at a time in the apparatus, the data analysis rejected events with multiple signals. The single-muon event analysis also allowed the detection of the muon-decay electron following a Lyman-α X-ray resulting in a strong suppression of background events. The detection of this decay-electron and related background suppression favors cw over pulsed muon beams. However, this comes at a price: the laser has to cope with large repetition rates, with a stochastic

trigger and has to have a small latency time between muon trigger and pulse delivery. The development of the adequate laser technologies was one of the main challenges of these experiments.

As a result of the successful background suppression, signal to background ratios (at resonance) of about 5 have been obtained. Signal rates of 6 events/h were observed on resonance, so that the measurement of each transition required about one week of data taking. The centroid positions were deduced for the measured resonances with accuracies between $\Gamma/10$ and $\Gamma/20$, where Γ is the FWHM linewidth of the resonances ($\Gamma \approx 20$ GHz for μp, $\Gamma \approx 320$ GHz for μHe$^+$). The 'pure"(free from hyperfine splitting effects) Lamb shifts [23–26], obtained from several measurements, are:

$$\Delta E(\mu p) = 202.3706\,(19)_{stat}\,(12)_{syst} \text{ meV} = 202.3706\,(23)_{total} \text{ meV} \tag{21.4}$$

$$\Delta E(\mu d) = 202.8785\,(31)_{stat}\,(14)_{syst} \text{ meV} = 202.8785\,(34)_{total} \text{ meV} \tag{21.5}$$

$$\Delta E(\mu^4He^+) = 1378.521\,(46)_{stat}\,(12)_{syst} \text{ meV} = 1378.521\,(48)_{total} \text{ meV} . \tag{21.6}$$

The experimental accuracies are all limited by statistical uncertainties. The experiment has small sensitivity to typical atomic physics systematic errors, such as Doppler, Stark and even the Zeeman shifts in the 5T field, and laser frequency calibration.

By comparing these measurements to the corresponding theoretical predictions (21.1)–(21.3), we obtain the following nuclear charge radii

$$r_p = 0.84087\,(26)_{exp}\,(29)_{theo} \text{ fm} \tag{21.7}$$

$$r_d = 2.12718\,(13)_{exp}\,(89)_{theo} \text{ fm} \tag{21.8}$$

$$r_\alpha = 1.67824\,(13)_{exp}\,(82)_{theo} \text{ fm} . \tag{21.9}$$

With the exception of μp, where the theoretical and experimental uncertainties are similar, the theoretical uncertainty of the calculated nuclear 2PE and 3PE contributions presently limit the extraction of the nuclear charge radii from these measurements.

21.7 Impact

The proton radius extracted from μp [23, 24] is an order of magnitude more precise than previous determinations. There is a large, unexpected discrepancy with the values from both electron scattering [38] and H spectroscopy: this is the "proton radius puzzle" [39, 40]. This has triggered various theoretical efforts including refinement of bound-state QED calculations for the atomic energy levels [41–46], refinement of techniques to extract the proton charge radius from scattering data [27, 47–53], investigations on the proton structure [8–12], investigation of beyond standard model physics [54–57], and refinements of laser spectroscopy systematic effects such as quantum interference [58, 59]. These investigations have considerably advanced our understanding but have been unable to explain the observed discrepancy. At the same time various experimental activities were initiated ranging from spectroscopy of hydrogen atoms, hydrogen molecules, electron and muon scattering, laser spectroscopy of Muonium and Rydberg atoms. Recently, several of these experimental efforts produced new results: all of them but one in excellent agreement with the proton radius value as extracted from muonic hydrogen and in some tension with previous hydrogen and electron-scattering results [29–33].

By assuming the correctness of the proton radius as extracted from muonic hydrogen, the Rydberg constant R_∞ has to be revised. Using the precise value of the proton radius from muonic hydrogen its relative uncertainty is decreased to 8×10^{-13}, which is the most precise value for a fundamental constant.
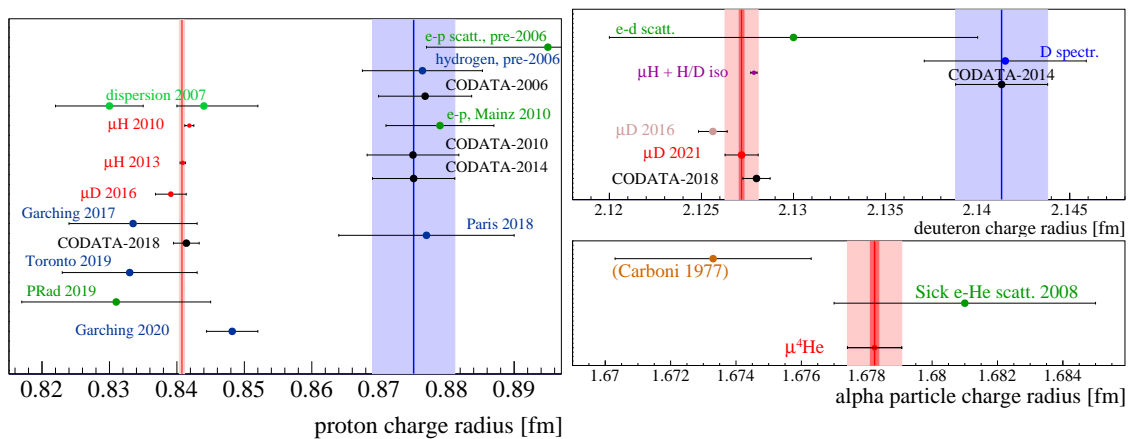
Figure 21.4: The charge radii from muonic atoms and other methods. For the radii from muonic atoms we separate the experimental uncertainties (dark red bands) from the theory uncertainties arising mainly from the 2PE contribution (lighter red band). For the proton (left), historical values and the 2010 Mainz A1 result [27] agree on a value around 0.88 fm, except for dispersion fits [28]. Muonic hydrogen [23, 24] and muonic deuterium [25] require a smaller radius around 0.84 fm. Whereas a new result from hydrogen 1S-3S (Paris 2018 [29]) seems to favor the larger radius, more recent measurements from hydrogen spectroscopy H(2S-4P) (Garching 2017 [30]), H(2S-2P) (Toronto 2019 [31]), and H(1S-3S) (Garching 2020 [32]) as well as a low-Q^2 e-p scattering experiment by the PRad Collaboration [33] favor the smaller radius. CODATA has now accepted the smaller radius.
For the deuteron (right top), older laser spectroscopy in atomic D favor the larger radius around 2.14 fm, but the smaller *proton* radius from muonic hydrogen, together with the isotope shift of the 1S-2S transition in regular H and D from Garching [34] yield a smaller radius of 2.12 fm. The value from muonic deuterium [25] has recently been brought into agreement with the latter more precise value by improved nuclear theory [4,5,35]. Elastic electron-deuteron scattering [36] cannot resolve the difference.
For the alpha particle, no value from regular atoms exists. Elastic e-He scattering [37] is five times less accurate than the muonic value. The historical μHe value from Carboni is wrong.

The r_α value extracted from μ^4He$^+$ [26] is in excellent agreement with the world average value from elastic electron scattering [37] but almost 5 times more precise. Hence it serves as a benchmark for few-nucleon theories [6, 60], for lattice QCD calculations and for elastic electron-He scattering. It serves also as an anchor point for isotopic shift measurements opening the way to improved values of the ^{3}He, ^{6}He and ^{8}He nuclei, and can be used to test higher-order bound-state QED contributions to an unprecedented sensitivity when combined with measurements in regular He$^+$ and He atoms.

21.8 Outlook

As a next step, the CREMA collaboration is addressing the hyperfine splitting of the ground state in muonic hydrogen. The goal is to measure this transition with 1-2 ppm precision from which the 2PE contribution can be obtained with 10^{-4} relative accuracy. The extracted 2PE contribution can be then compared to predictions from chiral perturbation theory (chPT) or from data-driven (proton structure functions and form factors) dispersion relations [11,61,62].

In this experimental effort, an improvement in laser technology is underway. The improved technology will also open the way for an improved measurement of the 2S-2P transitions: a factor of 5 improvement seems to be possible for all four muonic atoms.

References

[1] A. Antognini, F. Kottmann, F. Biraben, P. Indelicato, F. Nez and R. Pohl, *Theory of the 2S-2P Lamb shift and 2S hyperfine splitting in muonic hydrogen*, Ann. Phys. **331**, 127 (2013), doi:10.1016/j.aop.2012.12.003.

[2] J. Krauth, M. Diepold, B. Franke, A. Antognini, F. Kottmann and R. Pohl, *Theory of the n=2 levels in muonic deuterium*, Ann. Phys. **366**, 168 (2016), doi:10.1016/j.aop.2015.12.006.

[3] M. Diepold, B. Franke, J. Krauth, A. Antognini, F. Kottmann and R. Pohl, *Theory of the Lamb shift and fine structure in muonic ^{4}He ions and the muonic ^{3}He-^{4}He isotope shift*, Ann. Phys. **396**, 220 (2018), doi:10.1016/j.aop.2018.07.015.

[4] K. Pachucki, V. Patkos and V. Yerokhin, *Three-photon exchange nuclear structure correction in hydrogenic systems*, Phys. Rev. A **97**, 062511 (2018), doi:10.1103/PhysRevA.97.062511.

[5] M. Kalinowski, *Deuteron charge radius from the Lamb-shift measurement in muonic deuterium*, Phys. Rev. A **99**, 030501 (2019), doi:10.1103/PhysRevA.99.030501.

[6] C. Ji, S. Bacca, N. Barnea, O. Hernandez and N. N. Dinur, *Ab initio calculation of nuclear-structure corrections in muonic atoms*, J. Phys. G **45**, 093002 (2018), doi:10.1088/1361-6471/aad3eb.

[7] B. Acharya, V. Lensky, S. Bacca, M. Gorchtein and M. Vanderhaeghen, *Dispersive evaluation of the Lamb shift in muonic deuterium from chiral effective field theory*, Phys. Rev. C **103**, 024001 (2021), doi:10.1103/PhysRevC.103.024001.

[8] M. Birse and J. McGovern, *Proton polarisability contribution to the Lamb shift in muonic hydrogen at fourth order in chiral perturbation theory*, Eur. Phys. J. A **48**, 120 (2012), doi:10.1140/epja/i2012-12120-8.

[9] G. Miller, *Proton polarizability contribution: Muonic hydrogen Lamb shift and elastic scattering*, Phys. Lett. B **718**, 1078 (2012), doi:10.1016/j.physletb.2012.11.016.

[10] C. Carlson, M. Gorchtein and M. Vanderhaeghen, *Nuclear-structure contribution to the Lamb shift in muonic deuterium*, Phys. Rev. A **89**, 022504 (2014), doi:10.1103/PhysRevA.89.022504.

[11] F. Hagelstein, R. Miskimen and V. Pascalutsa, *Nucleon polarizabilities: From compton scattering to hydrogen atom*, Prog. Part. Nucl. Phys. **88**, 29 (2016), doi:10.1016/j.ppnp.2015.12.001.

[12] F. Hagelstein and V. Pascalutsa, *The subtraction contribution to muonic-hydrogen Lamb shift: a point for lattice qcd calculation of polarizability effect* (2020), arXiv:2010.11898.

[13] H. Anderhub et al., *Search for the metastable 2s state in muonic hydrogen*, Phys. Lett. B **71**, 443 (1977), doi:10.1016/0370-2693(77)90263-5.

[14] H. von Arb, F. Dittus, H. Heeb, H. Hofer, F. Kottmann, S. Niggli, R. Schaeren, D. Taqqu, J. Unternährer and P. Egelhof, *Measurement of the lifetime and quenching rate of metastable 2S muonic helium ions*, Phys. Lett. B **136**, 232 (1984), doi:10.1016/0370-2693(84)91152-3.

[15] R. Pohl, H. Daniel, F. Hartmann, P. Hauser, F. Kottmann, V. Markushin, M. Muhlbauer, C. Petitjean, W. Schott, D. Taqqu and P. Wojciechowski-Grosshauser, *Observation of long-lived muonic hydrogen in the 2S state*, Phys. Rev. Lett. **97**, 193402 (2006), doi:10.1103/PhysRevLett.97.193402.

[16] L. Simons, *Recent results on antiprotonic atoms using a cyclotron trap at LEAR*, Physica Scripta **T22**, 90 (1988), doi:10.1088/0031-8949/1988/t22/013.

[17] P. DeCecco, P. Hauser, D. Horvath, F. Kottmann, L. Simons and D. Taqqu, *A new method to produce a negative muon beam of keV energies*, Nucl. Inst. Meth. A **394**, 287 (1997), doi:10.1016/S0168-9002(97)00675-X.

[18] M. Mühlbauer, H. Daniel, F. Hartmann, P. Hauser, F. Kottmann, C. Petitjean, W. Schott, D. Taqqu and P. Wojciechowski, *Frictional cooling: Experimental results*, Hyp. Interact. **119**, 305 (1999), doi:10.1023/A:1012624501134.

[19] A. Antognini et al., *Powerful fast triggerable 6 μm laser for the muonic hydrogen 2S-Lamb shift experiment*, Opt. Comm. **253**, 362 (2005), doi:10.1016/j.optcom.2005.04.079.

[20] A. Antognini et al., *Thin-disk Yb:YAG oscillator-amplifier laser, ASE, and effective Yb:YAG lifetime*, IEEE J. Quant. Electr. **45**, 993 (2009), doi:10.1109/JQE.2009.2014881.

[21] J. Vogelsang et al., *Multipass laser cavity for efficient transverse illumination of an elongated volume*, Opt. Expr. **22**, 13050 (2014), doi:10.1364/OE.22.013050.

[22] M. Diepold et al., *Improved X-ray detection and particle identification with avalanche photodiodes*, Rev. Sci. Instrum. **86**, 053102 (2015), doi:10.1063/1.4921195.

[23] R. Pohl et al., *The size of the proton*, Nature **466**, 213 (2010), doi:10.1038/nature09250.

[24] A. Antognini et al., *Proton structure from the measurement of 2S-2P transition frequencies of muonic hydrogen*, Science **339**, 417 (2013), doi:10.1126/science.1230016.

[25] R. Pohl et al., *Laser spectroscopy of muonic deuterium*, Science **353**, 669 (2016), doi:10.1126/science.aaf2468.

[26] J. J. Krauth et al., *Measuring the α-particle charge radius with muonic helium-4 ions*, Nature **589**, 527 (2021), doi:10.1038/s41586-021-03183-1.

[27] J. Bernauer et al., *Electric and magnetic form factors of the proton*, Phys. Rev. C **90**, 015206 (2014), doi:10.1103/PhysRevC.90.015206.

[28] M. Belushkin, H. Hammer and U. Meissner, *Dispersion analysis of the nucleon form factors including meson continua*, Phys. Rev. C **75**, 035202 (2007), doi:10.1103/PhysRevC.75.035202.

[29] H. Fleurbaey, S. Galtier, S. Thomas, M. Bonnaud, L. Julien, F. Biraben, F. Nez, M. Abgrall and J. Guena, *New measurement of the 1S-3S transition frequency of hydrogen: Contribution to the proton charge radius puzzle*, Phys. Rev. Lett. **120**, 183001 (2018), doi:10.1103/PhysRevLett.120.183001.

[30] A. Beyer, L. Maisenbacher, A. Matveev, R. Pohl, K. Khabarova, A. Grinin, T. Lamour, D. Yost, T. Hänsch, N. Kolachevsky and T. Udem, *The Rydberg constant and proton size from atomic hydrogen*, Science **358**, 79 (2017), doi:10.1126/science.aah6677.

[31] N. Bezginov, T. Valdez, M. Horbatsch, A. Marsman, A. Vutha and E. Hessels, *A measurement of the atomic hydrogen Lamb shift and the proton charge radius*, Science **365**, 1007 (2019), doi:10.1126/science.aau7807.

[32] A. Grinin, A. Matveev, D. Yost, L. Maisenbacher, V. Wirthl, R. Pohl, T. Hänsch and T. Udem, *Two-photon frequency comb spectroscopy of atomic hydrogen*, Science **370**, 1061 (2020), doi:10.1126/science.abc7776.

[33] W. Xiong et al., *A small proton charge radius from an electron-proton scattering experiment*, Nature **575**, 147 (2019), doi:10.1038/s41586-019-1721-2.

[34] C. G. Parthey, A. Matveev, J. Alnis, R. Pohl, T. Udem, U. D. Jentschura, N. Kolachevsky and T. W. Hänsch, *Precision measurement of the hydrogen-deuterium 1S − 2S isotope shift*, Phys. Rev. Lett. **104**, 233001 (2010), doi:10.1103/PhysRevLett.104.233001.

[35] O. J. Hernandez, C. Ji, S. Bacca, N. Nevo Dinur and N. Barnea, *Improved estimates of the nuclear structure corrections in μD*, Phys. Lett. B **736**, 344 (2014), doi:10.1016/j.physletb.2014.07.039.

[36] I. Sick and D. Trautmann, *On the rms radius of the deuteron*, Nucl. Phys. A **637**, 559 (1998), doi:10.1016/S0375-9474(98)00334-0.

[37] I. Sick, *Precise root-mean-square radius of ^{4}He*, Phys. Rev. C **77**, 041302 (2008), doi:10.1103/PhysRevC.77.041302.

[38] I. Sick, *On the RMS radius of the proton*, Phys. Lett. B **576**, 62 (2003), doi:10.1016/j.physletb.2003.09.092.

[39] R. Pohl, R. Gilman, G. Miller and K. Pachucki, *Muonic hydrogen and the proton radius puzzle*, Ann. Rev. Nucl. Part. Sci. **63**, 175 (2013), doi:10.1146/annurev-nucl-102212-170627.

[40] H. Gao and M. Vanderhaeghen, *The proton charge radius* (2021), arXiv:2105.00571.

[41] U. Jentschura, *Lamb shift in muonic hydrogen – I. verification and update of theoretical predictions*, Ann. Phys. **326**, 500 (2011), doi:10.1016/j.aop.2010.11.012.

[42] M. Eides, *Weak interaction contributions to hyperfine splitting and Lamb shift in light muonic atoms*, Phys. Rev. A **85**, 034503 (2012), doi:10.1103/PhysRevA.85.034503.

[43] E. Borie, *Lamb shift in light muonic atoms – Revisited*, Ann. Phys. **327**, 733 (2012), doi:10.1016/j.aop.2011.11.017.

[44] S. Karshenboim, E. Korzinin, V. Shelyuto and V. Ivanov, *Theory of Lamb shift in muonic hydrogen*, J. Phys. Chem. Ref. Data **44**, 031202 (2015), doi:10.1063/1.4921197.

[45] A. Krutov and A. Martynenko, *Lamb shift in the muonic deuterium atom*, Phys. Rev. A **84**, 052514 (2011), doi:10.1103/PhysRevA.84.052514.

[46] C. Peset and A. Pineda, *The Lamb shift in muonic hydrogen and the proton radius from effective field theories*, Eur. Phys. J. A **51**, 1 (2015), doi:10.1140/epja/i2015-15156-2.

[47] I. Sick and D. Trautmann, *Proton root-mean-square radiii and electron scattering*, Phys. Rev. C **89**, 012201 (2014), doi:10.1103/PhysRevC.89.012201.

[48] G. Lee, J. Arrington and R. Hill, *Extraction of the proton radius from electron-proton scattering data*, Phys. Rev. D **92**, 013013 (2015), doi:10.1103/PhysRevD.92.013013.

[49] I. Lorenz, U. Meissner, H. Hammer and Y. Dong, *Theoretical constraints and systematic effects in the determination of the proton form factors*, Phys. Rev. D **91**, 014023 (2015), doi:10.1103/PhysRevD.91.014023.

[50] R. Hill and G. Paz, *Model-independent extraction of the proton charge radius from electron scattering*, Phys. Rev. D **82**, 113005 (2010), doi:10.1103/PhysRevD.82.113005.

[51] M. Horbatsch, E. Hessels and A. Pineda, *Proton radius from electron-proton scattering and chiral perturbation theory*, Phys. Rev. C **95**, 035203 (2017), doi:10.1103/PhysRevC.95.035203.

[52] D. Higinbotham, A. Kabir, V. Lin, D. Meekins, B. Norum and B. Sawatzky, *Proton radius from electron scattering data*, Phys. Rev. C **93**, 055207 (2016), doi:10.1103/PhysRevC.93.055207.

[53] J. Alarcón, D. Higinbotham and C. Weiss, *Precise determination of the proton magnetic radius from electron scattering data*, Phys. Rev. C **102**, 035203 (2020), doi:10.1103/PhysRevC.102.035203.

[54] C. Carlson, *The proton radius puzzle*, Prog. Part. Nucl. Phys. **82**, 59 (2015), doi:10.1016/j.ppnp.2015.01.002.

[55] B. Zhu and X. Liu, *Probing light dark matter with scalar mediator: muon $(g-2)$ deviation, the proton radius puzzle* (2021), arXiv:2104.03238.

[56] Y. Liu, I. Cloet and G. Miller, *Eta decay and muonic puzzles*, Nucl. Phys. B **944**, 114638 (2019), doi:10.1016/j.nuclphysb.2019.114638.

[57] S. Karshenboim, D. McKeen and M. Pospelov, *Constraints on muon-specific dark forces*, Phys. Rev. D **90**, 073004 (2014), doi:10.1103/PhysRevD.90.073004.

[58] M. Horbatsch and E. Hessels, *Shifts due to distant neighboring resonances*, Phys. Rev. A **82**, 052519 (2010), doi:10.1103/PhysRevA.82.052519

[59] M. Horbatsch and E. Hessels, *Shifts due to distant neighboring resonances for a four-level atom*, Phys. Rev. A **84**, 032508 (2011), doi:10.1103/PhysRevA.84.032508.

[60] C. Carlson, M. Gorchtein and M. Vanderhaeghen, *Two-photon exchange correction to 2S-2P splitting in muonic ^3He ions*, Phys. Rev. A **95**, 012506 (2017), doi:10.1103/PhysRevA.95.012506.

[61] C. Peset and A. Pineda, *Model-independent determination of the two-photon exchange contribution to hyperfine splitting in muonic hydrogen*, J. High Energy Phys. **04**, 60 (2017), doi:10.1007/JHEP04(2017)060.

[62] O. Tomalak, *Two-photon exchange correction to the hyperfine splitting in muonic hydrogen*, Eur. Phys. J. C **77**, 1 (2017), doi:10.1140/epjc/s10052-017-5435-z.

The *muX* project

F. Wauters[1][*] and A. Knecht[2] on behalf of the *muX* collaboration[1]

1 PRISMA+ Cluster of Excellence and Institute of Nuclear Physics,
Johannes Gutenberg Universität Mainz, Germany
2 Paul Scherrer Institut, Villigen, Switzerland

[*] fwauters@uni-mainz.de

Abstract

The *muX* project is conducting a series of muonic X-ray measurements in medium- and high-Z nuclei at PSI, utilizing a high-purity germanium detector array, in-beam muon detectors, and a modern digital data-acquisition system. A novel hydrogen target for muon transfer was developed, enabling measurements with as little as a few micrograms of target material. First measurements with radioactive Cm and Ra targets were conducted, aimed at determining their nuclear charge radii. These serve as important input for upcoming atomic parity violation experiments. The apparatus is also used to perform a feasibility study of an atomic parity violation experiment with the $2s - 1s$ muonic X-ray transition. In addition, the setup has been made available for a wider range of nuclear, particle, and solid-state physics measurements.

Check for updates

22.1 Introduction

Muonic atoms are exotic atoms that form when negative muons are stopped in a target and are subsequently captured by a nearby atom in a highly excited atomic orbital of $n \geqslant 14$. The muons quickly cascade down to the $1s$ orbital, initially predominantly via Auger transitions: at lower n radiative transitions take over. As the muon mass is about 207 times larger than the electron mass, the muonic X-rays range in energy from a few tens of keV for low-Z nuclei to several MeV for heavier nuclei. The capture and cascade processes occur on (sub)nanosecond timescales. The emitted radiation therefore appears prompt relative to a muon stopping in the target. Once in the $1s$ orbit, the muon either decays in orbit, or is captured by the nucleus. The latter is the dominant decay channel for Z=12 and above [1].

Muonic atoms have proven to be a valuable tool to measure nuclear properties and probe short-range interactions between the muon and the nucleus. With the Bohr radius of the muon

---

[1]https://www.psi.ch/en/ltp/mux

compared to the electron scaling as m_e/m_μ, there is substantial overlap between the muon and nuclear wave functions. Finite size effects are thus highly amplified. In the past, the absolute nuclear charge radii $<r^2>^{1/2}$ of almost all stable nuclei have been determined with a typical accuracy of 10^{-4} - 10^{-3} by measuring the $2p-1s$ transition energy [2]. More recently, the radii of the lightest nuclei were measured by the CREMA collaboration (Section 21 [3]) using laser spectroscopy on muonic atoms [4–7].

Formerly, this approach was limited to stable isotopes, as a sufficient amount of target material is needed to stop a μ^- beam with a momentum of typically 30 MeV/c. This excludes many interesting nuclei, such as the highly-deformed radium isotopes. Radium is a prime candidate for an Atomic Parity Violation (APV) experiment, using laser spectroscopy on a trapped ion [8,9], where the Parity Non-Conserving (PNC) $E1_{PNC}$ atomic $S-D$ transition is proportional to $K_r Z^2 Q_W$, with Q_W the weak nuclear charge, and K_r a relativistic enhancement factor which depends on the nuclear charge radius [10]. The *muX* collaboration aims to determine this radius by measuring the $2p-1s$ transition energy of ^{226}Ra ($T_{1/2}$=1600 y.). For this we have developed a novel technique, stopping muons in a high-pressure H_2/D_2 target, using a sequence of transfer reactions to efficiently stop muons in a few micrograms of target material. This technique was first established with gold targets, then applied to ^{226}Ra and ^{248}Cm (see Section 22.3).

With fundamental interactions being our primary physics motivation, the collaboration is also investigating the possibility of measuring APV directly in muonic atoms. A neutral parity-violating interaction mixes the $2s_{1/2}$ and $2p_{1/2}$ atomic levels, resulting in an E1 admixture in the otherwise pure M1 $2s_{1/2}-1s_{1/2}$ transition. Measuring such a parity-odd observable was first reviewed by Feinberg & Chen [11] and Missimer & Simons [12]. More recently, the possibility of searching for interactions between the muon and the nucleus beyond the Standard Model led to revived interest [13,14]. While the PNC effect is largest for low-Z atoms, separating the radiative M1/E1 transition from other transitions in the cascade severely complicates the design of such an experiment [15]. We focus on Z≃30 nuclei, where the single-photon $2s-1s$ transition becomes the dominant path depopulating the $2s$ level. The current goal of the collaboration is to isolate the transition in the cascade, and to significantly improve the signal-to-background ratio in the region-of-interest (ROI) in the X-ray spectrum (see Section 22.4.1).

Since 2015 we have been developing an advanced muonic X-ray experimental setup, combining a high-purity germanium (HPGe) detector array and a modern data-acquisition system (DAQ) with various target configurations. The setup is currently also being used for non-destructive elemental analysis, muon-capture studies probing matrix elements of interest for neutrinoless double β decay, and further nuclear-charge radius measurements of various radioactive elements and rare isotopes.

22.2 Experimental setup.

The *muX* apparatus (Figure 22.1 and Figure 22.2) is located at the πE1 beam-line of PSI, where a typically 30-40 MeV/c μ^- beam with a momentum width $\Delta p/p$ of 3 % passes through an electron separator before reaching the experiment. A custom beam snout houses an in-vacuum set of beam counters, thin plastic scintillator slabs read out by SiPMs, a lead target mounted away from the beam axis for calibration purposes, and a port for directly mounting various targets, thereby minimizing scattering of the low-energy muons.

The target itself is surrounded by 5 mm thick plastic scintillators, efficiently detecting outgoing decay electrons, thus enabling various cuts on the data such as suppressing Bremsstrahlung background in the HPGe detectors.

The *muX* HPGe detector array is constructed from various detectors provided by the collaborating institutions. Early campaigns, such as the $^{185/187}$Re measurement aimed at deter-

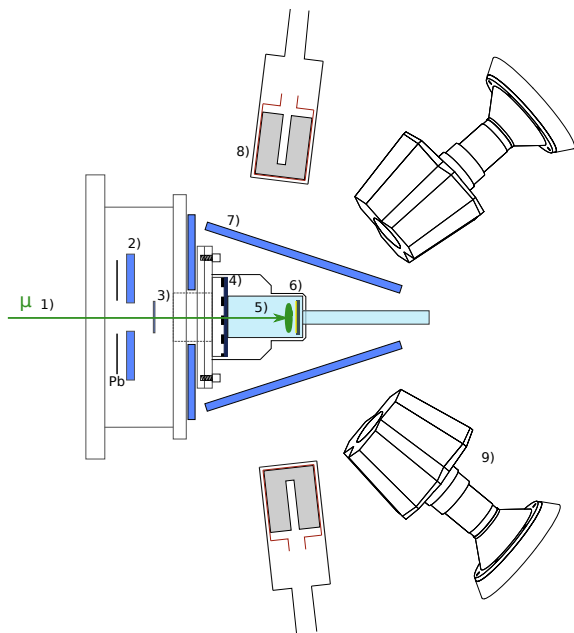Figure 22.1: The *muX* setup, with 1) the μ^- beam passing through 2) a veto detector with a 18 mm aperture, and 3) a 200 μm thick muon detector. The cell 4) with a 600 μm carbon fibre window supported by a Ti grid holds 5) 100 bar of hydrogen gas, with the 6) target mounted in the back. 7) Electron veto detectors. 8) Standard and 9) MiniBall cluster HPGe detectors.
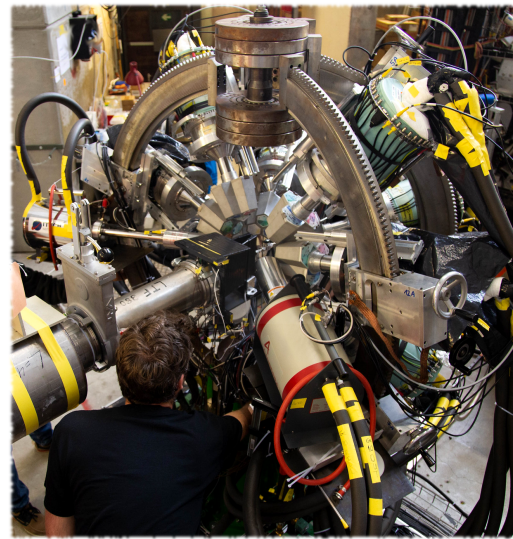

Figure 22.2: The MiniBall array with eight cluster detectors complemented by a 70 % coaxial detector and a low-energy planar detector installed at the πE1 beamline for the 2019 experimental run, with the *muX* beam snout. The target cell is covered by the black electron detectors.

mining the charge radii and quadruple moments [16], were conducted with just a few coaxial HPGe detectors. For the 2017 and 2018 campaigns, 7 compact coaxial detectors from the French/UK loan pool[2] with relative efficiencies of around 60% and one Miniball cluster detector were added. In the summer of 2019, the full MiniBall detector array [17] was installed at the πE1 beamline (Figure 22.2), operating for a 7 week measurement campaign. The *muX* automatic liquid-nitrogen filling system enables extended continuous operation of the HPGe detectors.

The MIDAS-based DAQ uses SIS3316 250 MSPS digitizers[3] which record all detector hits above threshold. Physics events are reconstructed offline by the analysis software. A digital filter running on the digitizer module FPGA integrates the detector signals, in addition, a section of the raw waveform is saved for offline analysis, where a time resolution of better than 10 ns (FWHM) for the HPGe detector hits is achieved.

22.3 Radioactive target measurements

One of the principal goals of the *muX* project [4] is to measure the $2p-1s$ transition energies for ^{226}Ra, a radioactive isotope for which the maximum allowed quantity in the experimental area is 5 μg. As the stopping power of such a low-mass target is insufficient by orders of

---

[2]https://gepool.in2p3.fr/

[3]https://www.struck.de/sis3316.html

[4]Proposal R-16-01

magnitude, the *muX* collaboration has developed a novel method, stopping muons in a small 100 bar H_2 target with a small admixture of D_2. Through a series of transfer reactions the muon is transported to the target material mounted at the back of the cell (Figure 22.3), hereby exploiting the Ramsauer-Townsend effect [18–21], which causes H_2 gas to become almost fully transparent for a μd atom.

After a first optimization of the target geometry and conditions with Monte-Carlo simulations, the transfer method was established by mounting a thin gold target at the back of the cylindrical gas cell. The beam momentum and deuterium concentration were optimized for the number of gold X-rays per muon, after which a small 3 nm thick gold target was installed. A total stopping efficiency per beam muon of 1.2 % was achieved for this 5 μg target (see Figure 22.4).

In order to have an efficient transfer target, it is imperative that the (radioactive) material is deposited as a uniform surface layer. Due to the low kinetic energy of the μd atom, an organic surface layer of >100 nm acts as a barrier and significantly reduces the transfer efficiency, rendering traditional molecular plating techniques inadequate. Several ^{248}Cm and ^{226}Ra targets were produced at the Institute of Nuclear Chemistry of the Johannes Gutenberg University Mainz, combining a custom electro-deposition technique combined with a novel *drop-on-demand* method where micro-drops of activity in solution are deposited on glassy carbon disks, the low-Z backing material of the target [22].

Figure 22.5 shows the muonic X-rays from ^{248}Cm measured during the 2019 campaign with a 15 μg curium target. After subtracting several background contributions, the $2p - 1s$ transitions are clearly visible. Despite having nuclear ground state of spin 0, the energy scale of high-Z muonic atoms is such that the muon spin couples to excited nuclear states with a non-zero spin [23, 24]. This leads to a complicated dynamic hyperfine structure in the observed transition energies, which needs to be understood to extract the nuclear charge radius from the data. The largest uncertainty in the calculations of the transition energies is caused by the two-photon exchange nuclear polarization [25, 26].

In addition to the ^{248}Cm target, two ^{226}Ra targets were used. The data obtained are currently under analysis to determine whether the X-ray yield is sufficient to achieve the necessary accuracy on the nuclear charge radius.
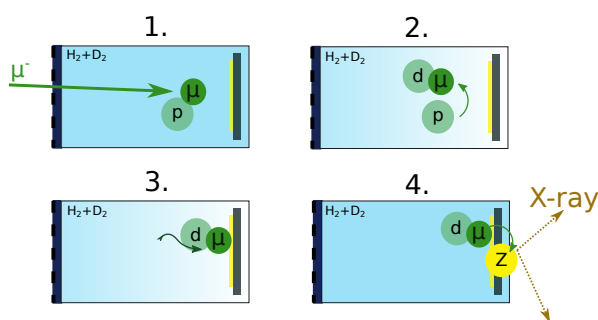

Figure 22.3: 1. After slowing down a μp atom is formed. 2. In $\mathcal{O}(100)$ ns, the muon transfers to deuterium, gaining 45 eV in kinetic energy. 3. After scattering down in energy to around 4 eV, the μd-H_2 scattering cross section becomes negligibly small, and the μd atom travels straight until it hits a wall or our target, where 4. the μ^- transfers to a high-Z atom.
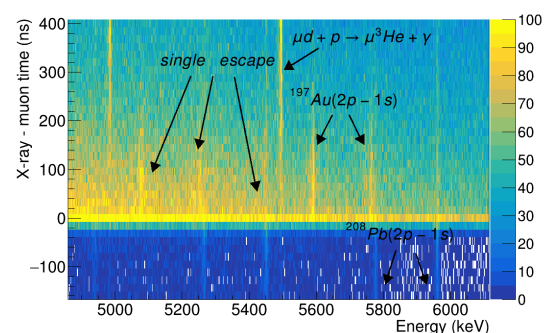

Figure 22.4: Muonic X-ray energies versus their time relative to an incoming muon. X-rays from direct stops appear at 0 ns. The Au X-rays appear over $\mathcal{O}(100)$ ns, the typical timescale for the transfer processes. The background mainly consists of decay electrons, and neutrons emitted after nuclear muon capture.
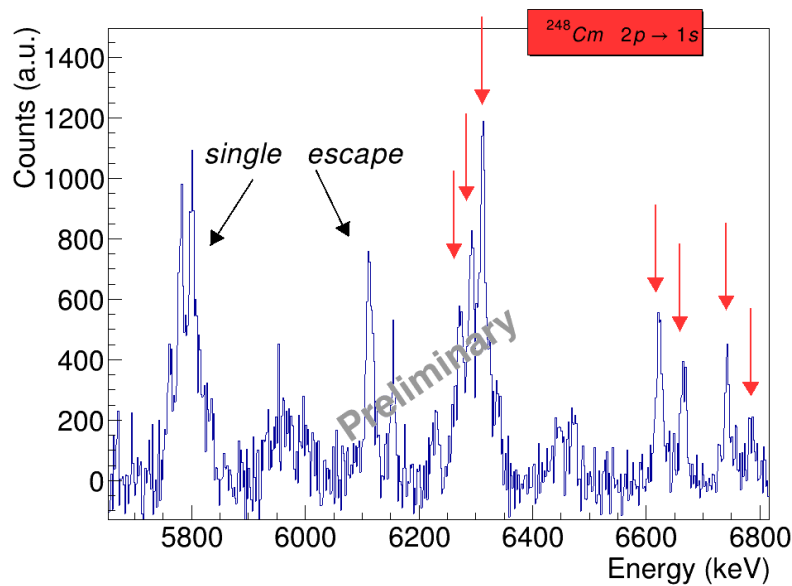
Figure 22.5: The ^{248}Cm muonic X-ray spectrum from the hydrogen transfer cell after subtracting the lead calibration lines and the γ background from muon capture on ^{16}O.

22.4 Extended experimental program

22.4.1 2s-1s measurements

With an expected branching ratio of $\mathcal{O}(10^{-4})$ for the single-photon $2s-1s$ muonic X-ray transition in the cascade of Z≃30 atoms, a possible APV experiment with a PNC observable using this transition is severely hampered by an overwhelming background in the energy region of interest (ROI) from scattered $(n \geqslant 3)p - 1s$ X-rays, Bremsstrahlung from decay electrons, and neutrons from muon capture. For this reason this transition has never been observed. The goal of the *muX* project is to observe this transition, significantly improve the signal-to-background in the ROI, and determine the reach of a possible APV experiment.

The initial average orbital quantum number l after $\mu H \rightarrow \mu Z$ transfer is lower than the initial l for direct atomic capture [27]. We have observed that as a consequence, the $2s$ population in the cascade of Ar, Kr, and Xe is increased by a factor of 3-4, thus increasing the branching ratio of the $2s-1s$ transition. A 7 day measurement with a 100 bar H$_2$ target and an 0.1 % Kr addition was performed. After subtracting the nuclear capture background from muon stops in the surrounding materials, the $2s-1s$ full energy peak is clearly visible, achieving a signal to background of about 1/10 (Figure 22.6).

To further reduce the background in the ROI, the transitions feeding the $2s$ level were used to tag events of interest. While sacrificing efficiency, this approach significantly reduces the background: the continuous Compton background from e.g. $3p - 1s$ photons is fully eliminated, and the accidental background from neutrons and decay electrons is at the same level as the signal yield, which can be further reduced by improving the time resolution. The only remaining challenging background is the satellite peaks introduced in the spectra by Compton scattered photons with energy depositions in the region of the $2s$ feeding transitions. This background needs to be controlled by optimizing the detector geometry. During the 2019 campaign, one week of data was taken with such an optimized geometry, collecting over 10^{11} muon stops on an isotopically pure ^{64}Zn target.
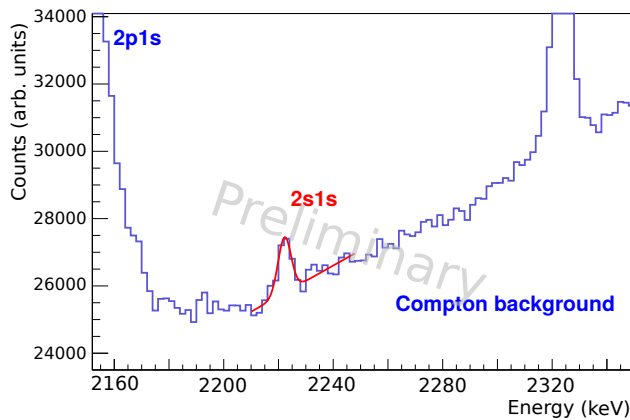
Figure 22.6: The $2s - 1s$ full energy peak of muonic Kr clearly visible at 2.22 MeV above the Compton background of $(n > 2)p - 1s$ transitions after subtracting background γ's from nuclear muon capture processes.
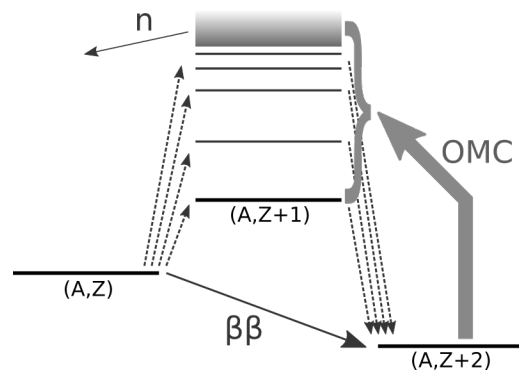

Figure 22.7: Partial muon capture rates of selected isotopes provide access to the transition strengths via virtual states in double β-decays.

22.4.2 Other measurements

To fully benefit from the availability of the MiniBall detector array, the *muX* experimental program was expanded in 2019. The partial ordinary muon capture rates on enriched ^{130}Xe, ^{82}Kr, and ^{24}Mg to specific excited states in the daughter nucleus were measured. Such measurements provide valuable information to determine the nuclear matrix elements in neutrinoless double β-decay [28,29], as these states act as intermediate virtual states in the double β-decay (Figure 22.7) of isotopes such as ^{130}Te [30,31] and ^{82}Se [32].

In addition, the *muX* apparatus was made available to perform elemental analysis on a series of cultural heritage samples, 17th century Japanese coins and an ancient Chinese mirror, significantly improving the sensitivity of previous J-PARC measurements [33], and a number of coins and recently found artifacts from the Roman Augusta Raurica site, nearby PSI. The intense muon beam and efficient detector setup permitted a narrowly collimated beam, probing different areas of a sample. Muonic X-ray spectroscopy provides information about the bulk material compared to the surface sensitivity of traditional fluorescence X-ray analysis. Furthermore, for high Z-elements such as lead the isotopic composition can be extracted.

22.5 Conclusions and Outlook

The *muX* efforts have resulted in a revived muonic X-ray program at the Paul Scherrer Institut. A new versatile experimental setup allows us to efficiently take data for extended periods of time.

The new hydrogen transfer target we have developed enables muonic X-ray measurements with a very small amount of target material. First measurements were performed with a Cm and Ra targets, with the purpose of extracting the nuclear charge radius, providing valuable input for upcoming APV experiments. The radioactive program will be extended to other elements, aiming to measure the third of three isotopes of odd Z-elements needed to calibrate the vast amount of isotope shift data available from laser spectroscopy on radioactive elements [34].

The single photon $2s - 1s$ transition in the muonic X-ray cascade was observed for the first time, and significant progress was made in reducing the backgrounds. This opens up the possibility for an APV experiment with a sensitivity of $\mathcal{O}(1)$ of the Standard Model amplitude,

i.e., such a measurement would act as a new physics search.

The two additional measurements of the 2019 campaign, the OMC capture measurements and the elemental analysis, will continue as separate projects with the support of the *muX* collaboration.

References

[1] T. Suzuki, D. F. Measday and J. P. Roalsvig, *Total nuclear capture rates for negative muons*, Phys. Rev. C **35**, 2212 (1987), doi:10.1103/PhysRevC.35.2212.

[2] G. Fricke, C. Bernhardt, K. Heilig, L. Schaller, L. Schellenberg, E. Shera and C. Dejager, *Nuclear ground state charge radii from electromagnetic interactions*, Atom. Data Nucl. Data Tables **60**, 177 (1995), doi:10.1006/adnd.1995.1007.

[3] A. Antognini, F. Kottmann and R. Pohl, *Laser spectroscopy of light muonic atoms and the nuclear charge radii*, SciPost Phys. Proc. **5**, 021 (2021), doi:10.21468/SciPostPhysProc.5.021.

[4] R. Pohl et al., *Laser spectroscopy of muonic deuterium*, Science **353**, 669 (2016), doi:10.1126/science.aaf2468.

[5] A. Antognini et al., *Proton structure from the measurement of $2S-2P$ transition frequencies of muonic hydrogen*, Science **339**, 417 (2013), doi:10.1126/science.1230016.

[6] R. Pohl et al., *Laser spectroscopy of muonic atoms and ions*, JPS Conf. Proc. **18**, 011021 (2017), doi:10.7566/JPSCP.18.011021, arXiv:1609.03440.

[7] J. J. Krauth et al., *Measuring the α-particle charge radius with muonic helium-4 ions*, Nature **589**, 527 (2020), doi:10.1038/s41586-021-03183-1.

[8] M. Nuñez Portela et al., *Towards a precise measurement of atomic parity violation in a single Ra^+ ion*, Hyperfine Interact. **214**, 157 (2013), doi:10.1007/s10751-013-0774-0.

[9] M. Fan, C. Holliman, A. Wang and A. Jayich, *Laser cooling of radium ions*, Phys. Rev. Lett. **122**, 223001 (2019), doi:10.1103/PhysRevLett.122.223001, arXiv:1901.09882.

[10] L. W. Wansbeek, B. K. Sahoo, R. G. E. Timmermans, K. Jungmann, B. P. Das and D. Mukherjee, *Atomic parity nonconservation in Ra^+*, Phys. Rev. A **78**, 050501 (2008), doi:10.1103/PhysRevA.78.050501.

[11] G. Feinberg and M. Chen, *The $2S_{(1/2)} \rightarrow 1S_{(1/2)}$ + 1 photon decay of muonic atoms and parity violating neutral current interactions*, Phys. Rev. D **10**, 190 (1974), doi:10.1103/PhysRevD.10.190.

[12] J. H. Missimer and L. M. Simons, *The neutral weak current of the muon*, Phys. Rept. **118**, 179 (1985), doi:10.1016/0370-1573(85)90013-4.

[13] B. Batell, D. McKeen and M. Pospelov, *New parity-violating muonic forces and the proton charge radius*, Phys. Rev. Lett. **107**, 011803 (2011), doi:10.1103/PhysRevLett.107.011803.

[14] D. McKeen and M. Pospelov, *Testing parity with atomic radiative capture of μ^-*, Phys. Rev. Lett. **108**, 263401 (2012), doi:10.1103/PhysRevLett.108.263401.

[15] K. Kirch, D. Abbott, B. Bach, P. DeCecco, P. Hauser, D. Horváth, F. Kottmann, J. Missimer, R. T. Siegel, L. M. Simons and D. Viel, *Metastability of the muonic boron 2S state*, Phys. Rev. Lett. **78**, 4363 (1997), doi:10.1103/PhysRevLett.78.4363.

[16] A. Antognini et al., *Measurement of the quadrupole moment of ^{185}Re and ^{187}Re from the hyperfine structure of muonic X rays*, Phys. Rev. C **101**, 054313 (2020), doi:10.1103/PhysRevC.101.054313.

[17] N. Warr et al., *The Miniball spectrometer*, Eur. Phys. J. A **49**, 40 (2013), doi:10.1140/epja/i2013-13040-9.

[18] F. Mulhauser et al., *Ramsauer-townsend effect in muonic atom scattering*, Phys. Rev. A **73**, 034501 (2006), doi:10.1103/PhysRevA.73.034501.

[19] A. Adamczak and J. Gronowski, *Diffusion radius of muonic hydrogen atoms in H-D gas*, Eur. Phys. J. D **41**, 493 (2007), doi:10.1140/epjd/e2006-00252-6, arXiv:physics/0609146.

[20] A. Adamczak, *Differential cross sections for muonic atom scattering from hydrogenic molecules*, Phys. Rev. A **74**, 042718 (2006), doi:10.1103/PhysRevA.74.042718, arXiv:physics/0608243.

[21] P. Strasser, A. Taniguchi, T. Matsuzaki, K. Ishida, Y. Matsuda, S. Ohya, M. Iwasaki and K. Nagamine, *Muon spectroscopy with trace alkaline-earth and rare-earth isotopes implanted in solid D2*, Hyperfine Interact. **193**, 121 (2009), doi:10.1007/s10751-009-0055-0.

[22] R. Haas, S. Lohse, C. Düllmann, K. Eberhardt, C. Mokry and J. Runke, *Development and characterization of a drop-on-demand inkjet printing system for nuclear target fabrication*, Nucl. Instr. Meth. Phys. Res. Sec. A**874**, 43 (2017), doi:10.1016/j.nima.2017.08.027.

[23] D. Hitlin, S. Bernow, S. Devons, I. Duerdoth, J. W. Kast, E. R. Macagno, J. Rainwater, C. S. Wu and R. C. Barrett, *Muonic atoms. i. dynamic hyperfine structure in the spectra of deformed nuclei*, Phys. Rev. C **1**, 1184 (1970), doi:10.1103/PhysRevC.1.1184.

[24] N. Michel and N. S. Oreshkina, *Higher-order corrections to the dynamic hyperfine structure of muonic atoms*, Phys. Rev. A **99**, 042501 (2019), doi:10.1103/PhysRevA.99.042501.

[25] P. Bergem, G. Piller, A. Rueetschi, L. Schaller, L. Schellenberg and H. Schneuwly, *Nuclear polarization and charge moments of Pb-208 from muonic x rays*, Phys. Rev. C **37**, 2821 (1988), doi:10.1103/PhysRevC.37.2821.

[26] A. Haga, Y. Horikawa and Y. Tanaka, *Nuclear polarization in muonic Pb-208*, Phys. Rev. A **66**, 034501 (2002), doi:10.1103/PhysRevA.66.034501.

[27] P. Haff, E. Rodrigo and T. Tombrello, *Muon transfer in gas targets*, Ann. Phys. **104**, 363 (1977), doi:10.1016/0003-4916(77)90336-0.

[28] D. Zinatulina, V. Brudanin, V. Egorov, C. Petitjean, M. Shirchenko, J. Suhonen and I. Yutlandov, *Ordinary muon capture studies for the matrix elements in ββ decay*, Phys. Rev. C **99**, 024327 (2019), doi:10.1103/PhysRevC.99.024327.

[29] L. Jokiniemi and J. Suhonen, *Comparative analysis of muon-capture and 0νββ -decay matrix elements*, Phys. Rev. C **102**, 024303 (2020), doi:10.1103/PhysRevC.102.024303.

[30] D. Q. Adams et al., *Improved limit on neutrinoless double-beta decay in* ^{130}Te *with cuore*, Phys. Rev. Lett. **124**, 122501 (2020), doi:10.1103/PhysRevLett.124.122501.

[31] S. Andringa et al., *Current status and future prospects of the SNO+ experiment*, Adv. High Energy Phys. 6194250 (2016), doi:10.1155/2016/6194250, arXiv:1508.05759.

[32] R. Arnold et al., *Probing new physics models of neutrinoless double beta decay with SuperNEMO*, Eur. Phys. J. C **70**, 927 (2010), doi:10.1140/epjc/s10052-010-1481-5, arXiv:1005.1241.

[33] K. Ninomiya et al., *Elemental analysis of bronze artifacts by muonic X-ray spectroscopy*, JPS Conf. Proc. **8**, 033005 (2015), doi:10.7566/JPSCP.8.033005.

[34] B. Cheal, T. Cocolios and S. Fritzsche, *Laser spectroscopy of radioactive isotopes: Role and limitations of accurate isotope-shift calculations*, Phys. Rev. A **86** (2012), doi:10.1103/PhysRevA.86.042501.

MUSE: The MUon Scattering Experiment

E. Cline[1], J. Bernauer[1,2], E. J. Downie[3] and R. Gilman[4*]

1 Stony Brook University, Stony Brook, NY
2 Riken BNL Research Center, Upton, NY
3 The George Washington University, Washington, DC USA
4 Rutgers, The State University of New Jersey, Piscataway, NJ

* rgilman@physics.rutgers.edu

Abstract

MUSE is a high-precision muon scattering experiment aiming to determine the proton radius. Muon, electron, and pion scattering will be measured at the same time. Two-photon exchange corrections will be determined with data using both beam polarities.

23.1 Introduction

The charge radius is a fundamental property of the proton. It is of interest to hadronic physicists as a test of calculations of proton structure. It is of interest to atomic physicists as it affects the determination of the Rydberg constant, and so is important in precision tests of quantum electrodynamics.

The charge radius can be determined using electromagnetic interactions in two ways. In atomic physics, the proton size changes the energies of S states by

$$\Delta E = \langle \Psi_S | \delta V | \Psi_S \rangle = \frac{2}{3}\pi\alpha |\Psi_S(0)|^2 r_p^2, \qquad (23.1)$$

thus allowing the radius and Rydberg constant to be determined simultaneously by measuring pairs of transition energies. In electron-proton scattering, the differential cross section depends on the square of the form factor, which is the momentum-space charge distribution. The charge radius is extracted from the slope of the electric form factor G_E at $Q^2 = 0$:

$$r_p^2 = -6\frac{dG_E}{dQ^2}|_{Q^2=0}. \qquad (23.2)$$

As the scattering data do not extend to $Q^2 = 0$, the radius is extracted from fits to measured cross sections.

In 2010 the proton charge radius was determined to be 0.84184 ± 0.00067 fm from a measurement of muonic hydrogen by the PSI CREMA collaboration [1]. This was quite puzzling as it was about 5σ smaller than the nearly order-of-magnitude less precise electronic measurements [2], which used both hydrogen spectroscopy and electron-proton scattering. This proton radius puzzle was quickly confirmed with reports from two new electron scattering measurements yielding $r_p = 0.879 \pm 0.008$ fm [3] and 0.875 ± 0.010 fm [4], and a second measurement of muonic hydrogen [5] that found $r_p = 0.84087 \pm 0.00039$ fm. New data are needed to resolve the proton radius puzzle, and a number of new experiments were developed [6–9]. Most aim to improve existing results, with new measurements of atomic hydrogen or electron-proton scattering. A new set of muonic atom measurements were also undertaken with other light nuclei.
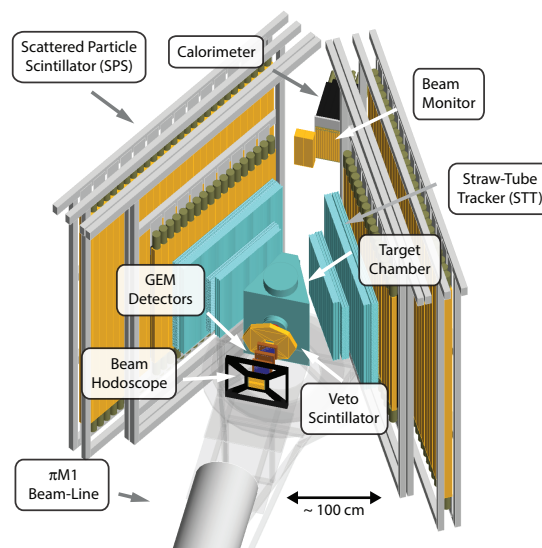
23.2   The MUSE experiment

Figure 23.1: The MUSE experimental system. See text for details.

The MUon Scattering Experiment (MUSE) addresses the radius puzzle in a unique way. The intent is to extract the first precise proton radius measurement from muon-proton scattering. The experiment uses the PSI HIPA PiM1 channel [10, 11], which provides a secondary beam of pions, muons, and electrons. This enables simultaneous measurements of both electron and muon scattering, so that the extracted proton radii and the cross sections for the two reactions can be directly compared. The PiM1 channel can produce beams with similar beam properties for both polarities. A difference between the scattering probability for the two beam polarities would result from two-photon exchange, a higher-order correction to the interaction. This correction is expected to be small, $O(0.1 – 1\%)$, depending on kinematics, but it is difficult to calculate accurately. It might affect the determination of the radius.

Figure 23.1 shows the experimental apparatus, taken from the MUSE Geant4 simulation. Beam particles exiting the channel first pass through a beam hodoscope, which measures particle times. In conjunction with the accelerator RF signal, these times can be used to determine particle species. The beam next passes through GEM chambers, which measure the

beam-particle trajectories. A veto scintillator is used to suppress background events such as upstream beam particle decays in flight or scattering from the detectors, leading to particles passing through the vacuum chamber wall. The target system inside the vacuum chamber includes a liquid hydrogen cell, an empty cell, solid targets, and a beam focus monitor. The unscattered beam exits through a thin window, and reaches the downstream beam monitor and a calorimeter, which are used to study radiative corrections. Scattered particles exit through thin side windows, are tracked by the straw tube tracker, and their times measured with the scattered particle scintillators.

The PiM1 channel has been used previously for precise pion scattering measurements. This is feasible as pions are often the dominant species in the beam, and hadronic scattering cross sections can be orders-of-magnitude larger than electromagnetic cross sections. A primary challenge of MUSE is to measure precise cross sections for the smaller muonic component of the beam. The first aspect of the challenge is that previous determinations of beam properties concentrated on the pionic component of the beam, so the properties of the muonic and electronic components are not as well known. The second aspect is that the experimental system has to largely prescale away pion scattering to be able to efficiently measuring muon and electron scattering.

To address the challenge of beam properties, MUSE has undertaken a program of simulations and measurements. The first step is to simulate the particle production mechanisms at the M target. Charged pions are produced at the M target through $pC \rightarrow \pi^{\pm}X$ reactions. From the perspective of the PiM1 channel, the proton beam crosses the M target generating pions with an effective millimeter-sized source. Muons are produced by the decays in flight of those pions. Simulations show that the majority of the muons that will pass through the PiM1 channel are generated by pions that decay in the first few centimeters of flight, at an angle of nearly 90° in the pion rest frame. The effective muon source size is larger than the pion source size, but still only a few millimeters. Electrons and positrons are produced mainly by a sequence of reactions, with $pC \rightarrow \pi^0 X$ producing neutral pions, followed by the decay $\pi^0 \rightarrow \gamma\gamma$, and subsequently pair production in the M target via $\gamma C \rightarrow e^{\pm}X$. Geant4 simulations show that higher momentum electrons and positrons are only produced when all these processes are in the direction of the PiM1 channel. As a result, the effective source size remains very close to that for pions.

The source simulations generate charged particles that are input to the TURTLE [12] and G4 beamline [13] magnetic transport codes. These codes include the channel quadrupoles and dipoles, as well as apertures from beam pipes and jaws. The simulation describes well several measured properties of the beam, including the beam distributions in position and angle at the channel intermediate focal plane and at the scattering target position, and the variation of particle times at the scattering target with respect to accelerator RF as a function of momentum: the pion time distribution is wider than that for electrons or muons due to the interplay of faster speed vs longer flight path for higher-momentum particles within the channel. While the measured time distributions of all particles are quite similar, the muon distribution is predicted to be somewhat larger than the pion and electron distributions, indicating that extreme rays are more constrained in reality than in the simulation.

In addition to the particle trajectories, it is important to know the beam momentum at the 0.2% (0.3%) level for muons (electrons). The channel momentum resolution is better than this. The absolute momentum of the beam selected by the PiM1 channel is determined in 3 ways. First, dedicated time-of-flight measurements with changes of the beam hodoscope and beam monitor positions determine the pion and muon momenta to the 0.2 – 0.3% level. Second, the timing of particles in the beam hodoscope relative to the accelerator RF provides an independent momentum measurement at the same level.[1] Third, the dispersion of the

---

[1]This timing measurement also checks the beam momentum stability at the $\approx 0.1\% - 0.2\%$ level.

channel at the intermediate focal point, of 7 cm/%, combined with the dispersion of the beam from the intermediate focus to the scattering target of $\approx$ 9.5 cm/%, provides a check of any momentum difference between the different particle species at the $\approx$0.1% level, through the similarity of the measured beam spot positions.

The challenge of suppressing pion scattering while efficiently measuring muon and electron scattering is addressed by the MUSE trigger system. A first-level trigger FPGA identifies all particle species in the 3.5-MHz beam using the time difference between the beam-hodoscope signal and the accelerator RF signal. Other first-level triggers identify scattered particles and hits in the veto detector. The combination of these first-level triggers allows muon and electron scattering to be read out efficiently while suppressing pion scattering.

One important feature of MUSE will be the implementation of a blinded analysis in the cross section measurement. A Monte Carlo simulation is needed to determine precise cross sections, and from them the proton radius. The blinding will be accomplished primarily through modifying the simulation-derived weight factor, while encrypting the actual weights. Additionally, some small fraction of the tracks for different particle species will be thrown away as a function of angle, to prevent accidental unblinding by direct comparison of charge and / or particle species. This will be programmed to be reversed by the application of two encryption keys. Once the analysis is complete, the actual weights can be extracted and the physics analysis rerun.

A more detailed description of the MUSE system is available in [14]. Detailed publications are also available for the target [15] and the SiPM detectors [16].
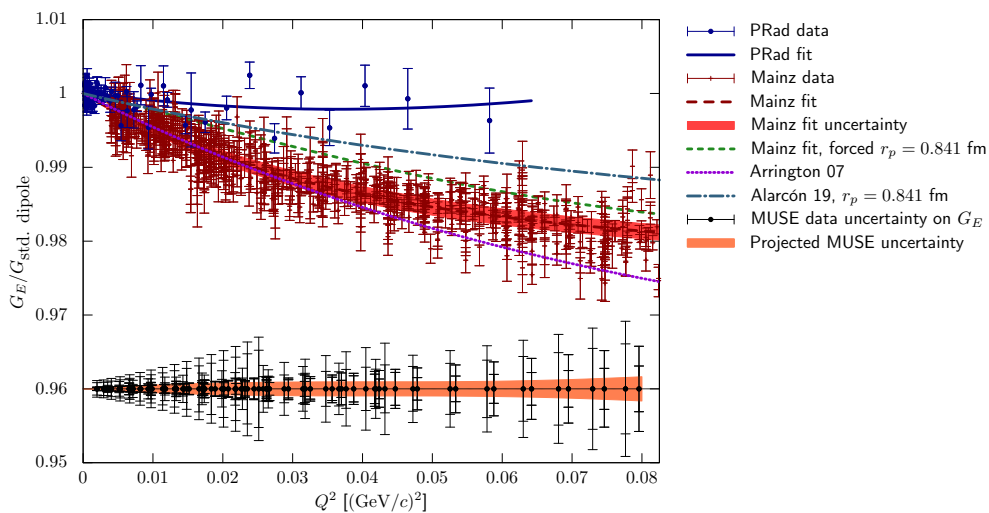
23.3 Anticipated results

Figure 23.2: Anticipated data for G_E from MUSE, arbitrarily placed at 0.96, compared to recent electron scattering experiments, and fits to these data, and to two world data fits. The MUSE data include both electron and muon points. The doubled uncertainty bars represent the uncertainties for + (inner bar) and - (outer bar) beam polarity. The muon and electron points are slightly offset due to the mass difference of muons and electrons. See text for further details.

With the planned 12 months of beam time, 4×10^7 μ^+ (2×10^7 μ^-) scattering events are expected for MUSE. This should give better than 1% statistical precision for the cross section in almost all of the 16 planned angle bins at each of 3 beam momenta and two beam polarities.

Figure 23.2 shows the expected uncertainties for the determination of the electric form factor, G_E, from MUSE, together with the results from Mainz [3] and from PRad [17], along with two selected fits [18,19]. The Arrington07 fit [18] is to older world data that are not shown, and has a large radius. The Alarcon19 curve [19] is a dispersively improved effective field theory calculation which has one free parameter, the radius, which can be fit, but here is chosen to be the muonic spectroscopy value. The green dashed "Mainz-fit" line is a fit to the Mainz data, but with the radius term set to the muonic spectroscopy value.

The experiments each measure in different kinematic regions, with MUSE at the lowest beam momentum and largest angles, and PRad at the highest beam momentum and smallest angles. The experiments also use different techniques. The more recent PRad measurement used a forward angle calorimeter to measure cross sections for 1.1 and 2.2 GeV beam energies at angles up to $\approx 7.5°$. The earlier Mainz measurements used magnetic spectrometers at larger scattering angles, with beam energies from 180 – 855 MeV. The Mainz and PRad data can be seen to diverge from each other, which probably indicates problems either with the experiments or with the radiative corrections. While the Mainz data are in good agreement with the Arrington fit to earlier data, neither the PRad nor the Mainz data agree with the prediction by Alarcon using the muonic radius. The expected MUSE uncertainties are competitive with those of the existing experiments. Muon scattering has much smaller single-photon radiative corrections, due to the larger muon mass, so any differences between muons and electrons might point to issues of radiative corrections or new physics.

The comparison of the cross sections for + and − polarities will yield a measurement of the two-photon exchange contribution, expected to be of similar size to the experimental uncertainties shown in Figure 23.2. The proton radius should be determined with an uncertainty of 0.006 – 0.010 fm, based on a sample of fits. The electron scattering data will have superior statistical precision, but larger systematic uncertainties due to radiative corrections. This should result in slightly better measurements for both the radius and the two-photon exchange contribution.

In addition to the electromagnetic scattering, pion cross sections need to be measured during MUSE to sufficiently characterize experimental backgrounds. The pion cross sections are interesting by themselves as a test of the application of chiral perturbation theory, to improve the existing πN scattering database, and as a constraint on occasional speculations about undiscovered resonances in the πN system. Because MUSE operates with a mixed beam, pion scattering will be measured in all MUSE kinematics at the same time as the electron and muon scattering. The experimental trigger includes beam particle information, which allows the pion scattering events to be pre-scaled to become a small fraction of the data set, while still recording on the order of 10^7 events.

23.4 Outlook

A test of the full MUSE system in December 2019 led to several planned upgrades to make the system more robust. Due to the ongoing international public health crisis and its resulting impact on international travel, we were only able to partially complete the upgrades during 2020. We plan to complete the upgrades and start MUSE production data taking in 2021. With 12 months of data taking and analysis to be performed, we anticipate publication of first results in 2023/24. MUSE will be the first experiment to measure elastic muon-proton scattering in an appropriate kinematic region, with a precision sufficient to address the proton radius puzzle. The corresponding results for the simultaneously-measured electron scattering, will put a strong constraint on potential systematic uncertainties, and may help settle the discrepancies between the Mainz and PRad results. MUSE will be the only experiment that can directly measure with its own data the difference between electron and muon extractions of the radius, making it highly compelling.

Acknowledgement

References

[1] R. Pohl et al., *The size of the proton*, Nature **466**, 213 (2010), doi:10.1038/nature09250.

[2] P. J. Mohr, B. N. Taylor and D. B. Newell, *CODATA recommended values of the fundamental physical constants: 2010*, Rev. Mod. Phys. **84**, 1527 (2012), doi:10.1103/RevModPhys.84.1527.

[3] J. Bernauer et al., *High-precision determination of the electric and magnetic form factors of the proton*, Phys. Rev. Lett. **105**, 242001 (2010), doi:10.1103/PhysRevLett.105.242001.

[4] X. Zhan et al., *High-precision measurement of the proton elastic form factor ratio $\mu_p G_E/G_M$ at low Q^2*, Phys. Lett. B **705**, 59 (2011), doi:10.1016/j.physletb.2011.10.002.

[5] A. Antognini et al., *Proton structure from the measurement of $2S-2P$ transition frequencies of muonic hydrogen*, Science **339**, 417 (2013), doi:10.1126/science.1230016.

[6] R. Pohl, R. Gilman, G. A. Miller and K. Pachucki, *Muonic hydrogen and the proton radius puzzle*, Ann. Rev. Nucl. Part. Sci. **63**, 175 (2013), doi:10.1146/annurev-nucl-102212-170627, 1301.0905.

[7] R. Pohl, R. Gilman and G. A. Miller, *Workshop on the proton radius puzzle at the trento european center for theory in nuclear physics and related areas* (2012).

[8] C. Carlson, R. Hill, S. Karshenboim and M. Vanderhaeghen, *Workshop on the proton radius puzzle at the mainz institute for theoretical physics* (2014).

[9] R. Pohl, R. Gilman and G. A. Miller, *Workshop on the proton radius puzzle at the trento european center for theory in nuclear physics and related areas* (2016).

[10] R. Balsiger, B. Berkes, D. Brombach, D. George, M. Ianovici, E. Pedroni, O. Szavits, M. Werner, J. Zichy, E. Boschitz, J.-P. Egger and C. Wiedner, *Technical aspects of the sin pion channel and spectrometer*, Nucl. Instr. Meth. **157**, 247 (1978), doi:10.1016/0029-554X(78)90298-7.

[11] J. P. Albanese et al., *The SIN high resolution pion channel and spectrometer*, Nucl. Instr. Meth. **158**, 363 (1979), doi:10.1016/S0029-554X(79)93570-5.

[12] K. L. Brown and C. Iselin, DECAY TURTLE, CERN Report 74-2 (1974).

[13] T. Roberts, *G4beamline* (2018).

[14] R. Gilman et al., *Technical design report for the Paul Scherrer Institute Experiment R-12-01.1: Studying the proton "radius" puzzle with µp elastic scattering* (2017), arXiv:1709.09753.

[15] P. Roy et al., *A liquid hydrogen target for the MUSE experiment at PSI*, Nucl. Instrum. Meth. A **949**, 162874 (2020), doi:10.1016/j.nima.2019.162874.

[16] T. Rostomyan et al., *Timing detectors with SiPM read-out for the MUSE experiment at PSI*, Nucl. Instrum. Meth. A **986**, 164801 (2021), doi:10.1016/j.nima.2020.164801.

[17] W. Xiong et al., *A small proton charge radius from an electron–proton scattering experiment*, Nature **575**, 147 (2019), doi:10.1038/s41586-019-1721-2.

[18] J. Arrington, W. Melnitchouk and J. Tjon, *Global analysis of proton elastic form factor data with two-photon exchange corrections*, Phys. Rev. C **76**, 035205 (2007), doi:10.1103/PhysRevC.76.035205.

[19] J. Alarcón, D. Higinbotham, C. Weiss and Z. Ye, *Proton charge radius extraction from electron scattering data using dispersively improved chiral effective field theory*, Phys. Rev. C **99**, 044303 (2019), doi:10.1103/PhysRevC.99.044303.

The pion beta and radiative electronic decays

Dinko Počanić⋆, for the PiBeta Collaboration

University of Virginia, Charlottesville, VA 22904-4714, USA

⋆ pocanic@virginia.edu

Abstract

As the lightest meson, pion offers unique opportunities for measuring parameters and testing limits of the Standard Model (SM). The PiBeta experiment, carried out at PSI, focused on SM tests accessible through the pion beta, $\pi^+ \to \pi^0 e^+ \nu_e(\gamma)$, and electronic radiative, $\pi^+ \to e^+ \nu_e \gamma$, decay channels. We review the PiBeta experiment, and update the pion beta decay branching ratio $B_{\pi\beta}^{\exp} = 1.038(6)_{\text{tot}} \times 10^{-8}$, along with the corresponding derived value of the Cabibbo-Kobayashi-Maskawa matrix element $V_{ud} = 0.9738(28)$.

24.1 Motivation

The unitary Cabibbo-Kobayashi-Maskawa (CKM) quark mixing matrix embodies some of the central parameters of the three-generation Standard Model. Departure from CKM matrix unitarity would signal the existence of "beyond Standard Model" (BSM) physics, i.e., processes and particles not included in the SM. The most sensitive test of the CKM matrix unitarity is via $|V_{\rm u}|^2$, the squared norm of the first row, which, given the smallness of $|V_{\rm ub}|^2 \simeq 10^{-5}$, simplifies as:

$$|V_{\rm u}|^2 \equiv |V_{\rm ud}|^2 + |V_{\rm us}|^2 + |V_{\rm ub}|^2 \simeq |V_{\rm ud}|^2 + |V_{\rm us}|^2, \quad \text{with} \quad |V_{\rm u}|^2 = 1 + \Delta_{\rm CKM}. \quad (24.1)$$

Since $|V_{\rm ud}|^2 \approx 0.95$ dominates $|V_{\rm u}|^2$, the uncertainty $\Delta V_{\rm ud}$ is critically important in evaluating $\Delta_{\rm CKM}$. In spite of notable improvements in measurement and theoretical precision since the 1980s, a shortfall of $\Delta_{\rm CKM} \sim -3\sigma$ has persisted for much of the past three decades. The discovery potential inherent in precision tests of CKM unitarity has motivated a worldwide effort. A summary of the present status of CKM unitarity tests is given in [1]. The most precise evaluations of $V_{\rm ud}$ have relied on the $0^+ \to 0^+$ superallowed Fermi (SAF) nuclear beta decays (for the most recent compilation see [2]). Despite the impressive experimental precision achieved in determining SAF ft values, uncertainties related to the complex structure of participating

nuclei remain, motivating the quest for V_{ud} evaluation in beta decays of simpler systems: neutrons and pions. Of the two, the pion beta semileptonic decay $\pi^+ \to \pi^0 e^+ \nu_e(\gamma)$[1], or $\pi_{e3(\gamma)}$, is the theoretically cleanest [3]. Given the small accessible phase space, π_{e3} decay is very rare: $B_{\pi\beta} \simeq 10^{-8}$. Neutron beta decay is not suppressed, but requires two measurements for an independent determination of V_{ud}: the lifetime, τ_n, and the axial-vector coupling, $g_A = G_A/G_V$, (for further details and current status see [1, 4–6]).

The international PiBeta collaboration [7], led by the University of Virginia group, was formed in the 1990s with the goal of measuring the pion beta decay branching ratio to a precision of 0.5 % at the Paul Scherrer Institute. Achieving this goal also requires accurate identification and detection of background and normalization decays: pion radiative electronic $\pi^+ \to e^+ \nu_e \gamma$, or $\pi_{e2\gamma}$, pion electronic $\pi^+ \to e^+ \nu_e$, or π_{e2}, radiative muon $\mu^+ \to e^+ \nu_e \bar{\nu}_\mu \gamma$, and ordinary muon $\mu^+ \to e^+ \nu_e \bar{\nu}_\mu$ decay. Each of these processes illuminates interesting aspects of SM/BSM physics. Muon decays will not be discussed here, while the electronic, π_{e2} decay is discussed in more detail in [8].

Unlike its muonic equivalent $\pi_{\mu2\gamma}$, the radiative electronic decay, $\pi_{e2\gamma}$, is not completely dominated by purely electromagnetic (QED) "inner" bremsstrahlung (IB). It also receives strong "structure-dependent" (SD) QCD contributions, parameterized in terms of F_V and F_A, the vector and the axial-vector form factors, respectively. Direct determination of $F_{A,V}$ is possible through a precise measurement of the differential branching ratio, or decay rate $d^2\Gamma_{\pi e2\gamma}/dE_e \, dE_\gamma$, over a suitably large portion of the decay phase space [9, 10]. Precise values of F_A and F_V provide information on nonperturbative QCD, such as the pion polarizabilities, and generally enter certain low energy (chiral) constants, LECs (for more details see, e.g., [11, 12]). On the other hand, a kinematically broad sample of $\pi_{e2\gamma}$ decays makes it possible to set limits on values of form factors other than $F_{A,V}$, that, if nonzero, would indicate presence of BSM particles or processes. PiBeta has pursued both of these research paths, as discussed below.

24.2 The PiBeta apparatus

The PiBeta apparatus, schematically shown in Figure 24.1, detected π^+ decays at rest in a solid cylindrical active target (AT), placed at the center of a pure CsI, 240-element spherical electromagnetic shower calorimeter. Prior to stopping, pions passed through a pair of scintillation detectors (BC and AD) separated by a ∼3.5 m flight path. The segmented target was surrounded by two MWPC tracking detectors, and a fast 20-element hodoscope, shown schematically in Figure 24.2. The apparatus acquired data during a "π-stop" gate spanning $t \simeq -50$ to 200 ns relative to a pion stop time ($t = 0$) in the target, with a break of ∼10 ns at $t = 0$ because of high rates of hadronic reactions by beam pions in AD and AT. The calorimeter modules were sized such that, on average, a crystal impacted centrally by a 70 MeV e^+ or γ would contain over 90% of the resulting shower energy. The location and energy of each distinct shower in an event were extracted for trigger purposes from continuous analog signal sums of overlapping clusters of 7–9 modules. A dozen trigger configurations, combining calorimeter and beam detector hit patterns of interest, were used to acquire the studied and normalization decay events, as well as all relevant background processes. Further details of the design and performance of the apparatus are given in [13]. For a discussion of the PiBeta technique in a broader context, see [14].

---

[1]A γ in parentheses denotes an undetected, usually soft photon. For brevity, in further text the (γ) will be dropped and implied; a detected photon in radiative processes will be explicitly denoted with a γ.
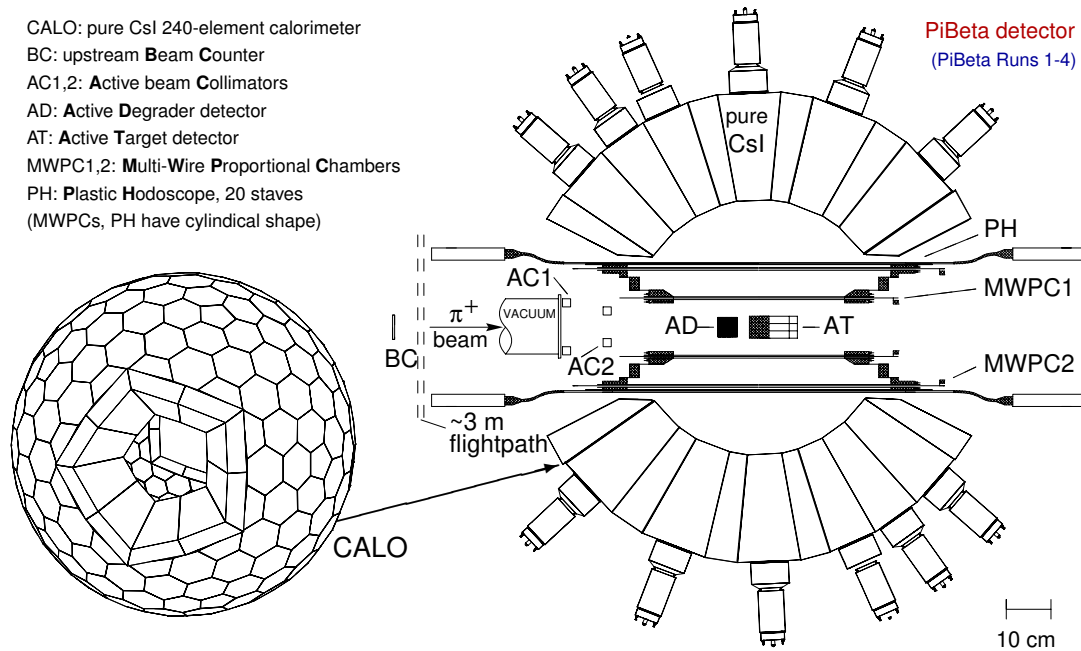
CALO: pure CsI 240-element calorimeter
BC: upstream **B**eam **C**ounter
AC1,2: **A**ctive beam **C**ollimators
AD: **A**ctive **D**egrader detector
AT: **A**ctive **T**arget detector
MWPC1,2: **M**ulti-**W**ire **P**roportional **C**hambers
PH: **P**lastic **H**odoscope, 20 staves
(MWPCs, PH have cylindical shape)

PiBeta detector
(PiBeta Runs 1-4)

pure
CsI

PH

MWPC1

AC1

VACUUM

π^+
beam

AD — ■ ▦⊞ — AT

MWPC2

BC

AC2

~3 m
flightpath

CALO

10 cm

Figure 24.1: Schematic cross section of the PiBeta apparatus, with its main components labeled. For details concerning the detector performance see [13].

C-fiber
shield

AT

(Active TGT)

MWPC1

PH
array

MWPC2

10 cm
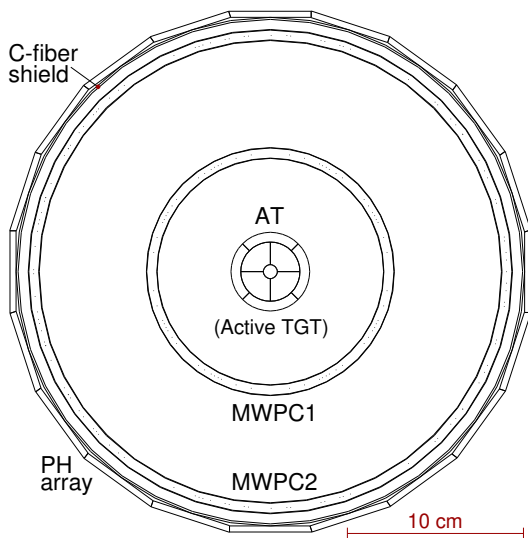
Figure 24.2: Axial (beam) view of the central detector region used in PiBeta Runs 1–3, and first half of Run 4. Outward from center: (i) the 9-element segmented active target AT, (ii) cylindrical MWPC1 and MWPC2 trackers, (iii) thin cylindrical carbon-fiber shield around MWPC2, and (iv) the 20-element plastic hodoscope (PH) array with approximate outer diameter of ∅**30** cm. Pion stopping rates in the inner five (fiducial) target elements were roughly matched; AT outer ring elements served for decay particle tracking. The BC, AD, AT and PH detectors were made of fast plastic scintillator.

24.3 The pion beta decay: $\pi^+ \to \pi^0 e^+ \nu_e(\gamma)$

PiBeta measurements were carried out in four run periods, using $114 \, \text{MeV}/c$ beam in the πE1 beamline at PSI. Over $\mathbf{6.4 \times 10^4}$ π_{e3} events were acquired in high-rate Runs 1-3 (1999-2001), with $\sim \mathbf{10^6}$ π_{stop}^+/s in the target. Run 4 (2004), with $\mathbf{10^4 - 10^5}$ π_{stop}^+/s in the target, focused on the radiative decay $\pi_{e2\gamma}$. The π_{e3} decay signal, two energetic, nearly back to back neutral showers in the calorimeter, initiated by the two photons from $\pi^0 \to \gamma\gamma$ decay, is robust and required minimal background subtractions. Figure 24.3 illustrates the quality of the PiBeta π_{e3} event sample. The $\theta_{\gamma1\gamma2}$ distribution, uniquely shaped by the decay kinematics and the shower response of the calorimeter, is not reproduced in other processes. The decay time distribution is purely exponential, and agrees well with the known pion lifetime of 26.033(5) ns [1]. The
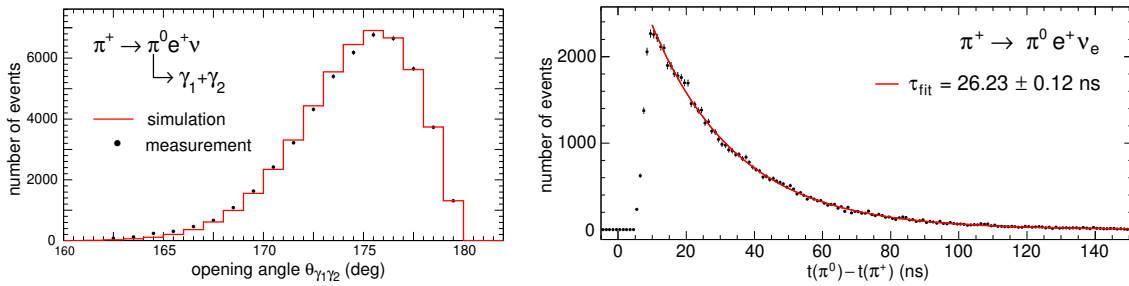
Figure 24.3: Left: measured photon-photon opening angle in $\pi^0 \to \gamma\gamma$, compared to a realistic Monte Carlo simulation. Right: decay time distribution for π_{e3} events. Events within ~ 10 ns of the π^+ stop in AT were not recorded due to high prompt hadronic background.

$\pi^+ \to e^+ \nu_e(\gamma)$ electronic decay events were used for branching ratio normalization. While the two decays shared many of the same systematics, such as the spatial and temporal distributions of the parent pions, and very similar acceptances, the π_{e2} signal had a significant background from the "Michel" $\mu^+ \to e^+ \nu\bar{\nu}(\gamma)$ decays. Details of the analysis and results for the π_{e3} branching ratio are discussed in [15]. Two values of $B_{\pi\beta} = \Gamma(\pi^+ \to \pi^0 e^+ \nu(\gamma))/\Gamma(\pi^+ \to \mu^+ \nu(\gamma))$ were evaluated and reported: one normalized to the accepted 2004 experimental average of $R_{e/\mu}^{\pi\text{-exp}} = \Gamma(\pi \to e\bar{\nu}(\gamma))/\Gamma(\pi \to \mu\bar{\nu}(\gamma)) = 1.230(4) \times 10^{-4}$ ("exp-norm"), and the second to the established theoretical value $R_{e/\mu}^{\pi\text{-th}} = 1.2352(5) \times 10^{-4}$ ("theo-norm"):

$$B_{\pi\beta}^{\text{exp-norm}} = 1.036(4)_{\text{stat}}(4)_{\text{syst}}(3)_{\pi_{e2}} \times 10^{-8}, \tag{24.2}$$

$$B_{\pi\beta}^{\text{theo-norm}} = 1.040(4)_{\text{stat}}(4)_{\text{syst}} \times 10^{-8}, \tag{24.3}$$

where the statistical (stat), systematic (syst) and π_{e2} normalization uncertainties are separated out. Since 2004, the π_{e2} branching ratio has become better known, $R_{e/\mu}^{\pi\text{-exp}} = 1.2327(23) \times 10^{-4}$ [1,16]. This leads to an update of the PiBeta π_{e3} branching ratio result

$$B_{\pi\beta}^{\text{exp-norm}} = 1.038(4)_{\text{stat}}(4)_{\text{syst}}(2)_{\pi_{e2}} \times 10^{-8} = 1.038(6)_{\text{tot}} \times 10^{-8}. \tag{24.4}$$

We note that the extraordinary sensitivity of pion beta decay afforded by the SM, with relative uncertainty (excluding the free parameter V_{ud}) of $\sim 2 \times 10^{-4}$ dominated by the radiative corrections [17], cannot be tested experimentally at the current precision of $\Delta B_{\pi\beta}/B_{\pi\beta} \simeq 0.006$. The same observation applies to the derived value of V_{ud}, now updated to

$$V_{ud}^{\pi\beta} = 0.9738(28), \tag{24.5}$$

which, while in excellent agreement with the PDG average $V_{ud} = 0.97370(14)$ [1], is 20 times less precise.

24.4 Pion radiative electronic decay: $\pi^+ \to e^+ \nu_e \gamma$

In addition to the fundamental physics motivations introduced in Section 24.1 (weak pionic form factors, inputs to LECs, limits on BSM contributions), pion radiative electronic decay generates background events for the pion beta (π_{e3}) signal, in large enough numbers to require a correction (the reverse also holds). For all these reasons, the PiBeta collaboration has extensively studied the $\pi_{e2\gamma}$ decay.

Prior to the early 2000s, data on the $\pi_{e2\gamma}$ decay were scarce, and contained significant ambiguities. The doubly differential decay rate $d^2\Gamma_{\pi e2\gamma}/dE_e\, dE_\gamma$ is separated into structure
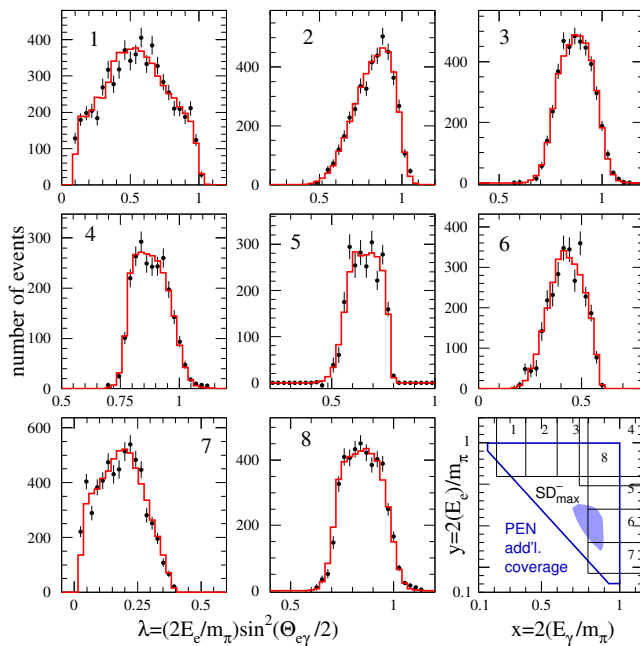
Figure 24.4: Measured (points) and simulated (histogram) values of $\pi_{e2\gamma}$ variable λ for eight (x, y) regions, mapped in the lower right panel. Triangle: added coverage by PEN [8]. Shaded contour: region of peak relative SD^- contribution.
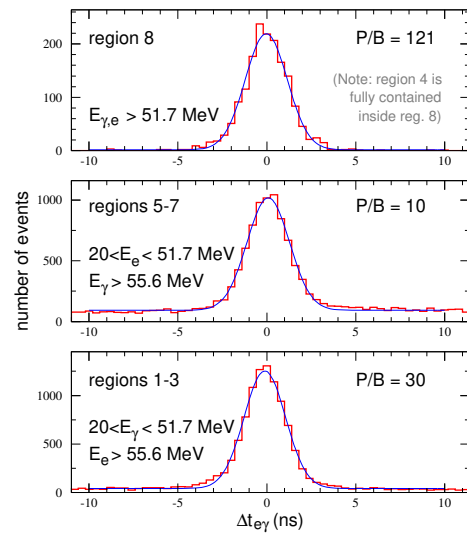

Figure 24.5: Plots of $\Delta t_{e\gamma}$, for three phase space regions in $\pi_{e2\gamma}$ decay, defined in Figure 24.4. Accidental background was low for all regions, reflected in the peak to background (P/B) values. Region 4/8 was dominated by Run 1–3 data; Run 4 data dominated the rest.

dependent terms: $SD^+ \propto (F_A + F_V)^2$, $SD^- \propto (F_A - F_V)^2$, the purely-QED IB, and several interference terms of the linear amplitudes, of which the most important are S_{int}^+ and S_{int}^-, the $IB \cdot (F_A + F_V)$ and $IB \cdot (F_A - F_V)$ terms, respectively. For simplicity in the analysis, dimensionless energy variables are routinely used and are limited to unity: $x, y = 2E_{\gamma,e}/m_\pi \in (0, 1)$. Since $(F_A + F_V)^2/(F_A - F_V)^2 \simeq 8$, SD^+ is the dominant QCD term in the decay. Further, its study is made more accessible by the fact that SD^+ peaks for $y \in (0.9, 1)$, and large x, where the IB term nearly vanishes. SD^-, on the other hand, peaks near the diagonal, $x + y = 1$, where IB is greatest, and dwarfs SD^- by several orders of magnitude. Consequently, pre-2000 studies used the conserved vector current (CVC) theoretical value for F_V (derived from the π^0 meson lifetime), and reported the ratio $\gamma \equiv F_A/F_V$ extracted from measurements. Early measurements, along with the inconsistencies and hints of BSM phenomena through a nonzero value for F_T, the tensor form factor, are discussed in detail in [14].

Against this backdrop, the PiBeta collaboration collected and analyzed over 4×10^4 $\pi_{e2\gamma}$ events in Runs 1–3, and published the results in [13]. The precision in γ was improved by a factor of four over prior world average, but a significant deficit of events was observed in a region of high x and low y. The high beam rate, and trigger configuration during Runs 1–3, challenged the $\pi_{e2\gamma}$ decay systematics in this kinematic regime.

Given the above, in 2004 the PiBeta collaboration carried out Run 4 at much lower beam rate ($\sim 10^5$ π_{stop}/s), focused on low-threshold $\pi_{e2\gamma}$ events. This made possible a precise calibration of subtle calorimeter gain differences in the low- and high-threshold triggers, the key to resolving previously observed inconsistencies. Results of the combined Run 1–4 data set analysis, with over 6.5×10^4 $\pi_{e2\gamma}$ events, were published in [18]. Kinematic coverage is shown in Figure 24.4, while Figure 24.5 illustrates the low level of accidental background present in the e^+-γ time difference data. Data in Figure 24.4 are presented in terms of $\lambda = y \sin^2(\theta_{e\gamma}/2)$,
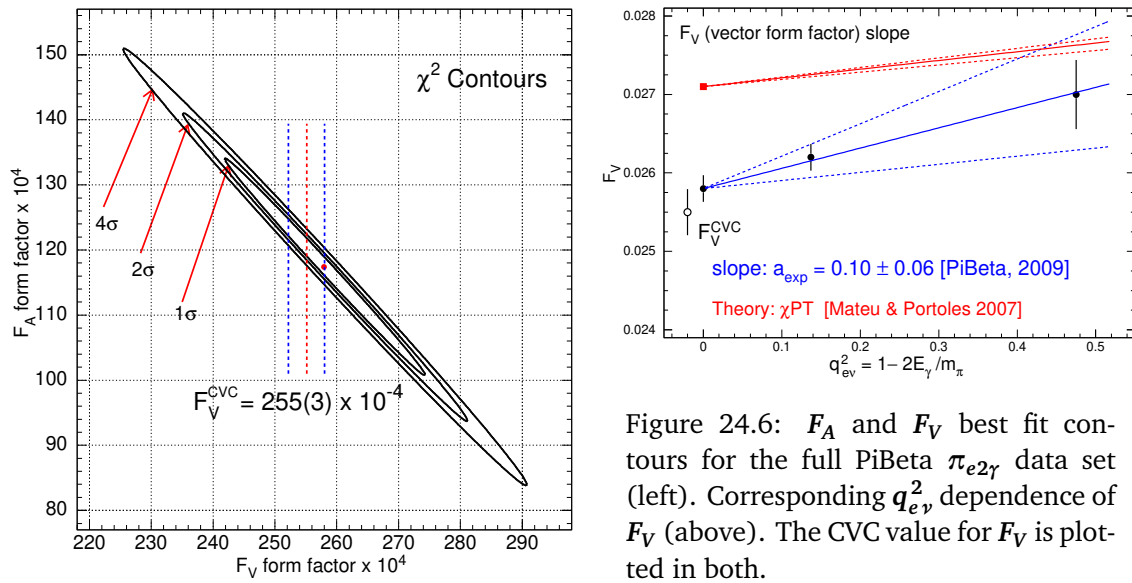
Figure 24.6: F_A and F_V best fit contours for the full PiBeta $\pi_{e2\gamma}$ data set (left). Corresponding $q_{e\nu}^2$ dependence of F_V (above). The CVC value for F_V is plotted in both.

where $\theta_{e\gamma}$ is the reconstructed e^+-γ opening angle. (Unlike y, λ retains the constant 0–1 value range regardless of x.) Agreement with the simulation based on best-fit values for F_A and F_V is excellent in all regions.

Contours of the best-fit values for F_A and F_V are shown in Figure 24.6. The thin shape of the resulting ellipse reflects the ~ 1% precision of the measurement of $F_A + F_V$ (SD^+ term), and the much lower sensitivity to $F_A - F_V$, i.e., SD^-. The narrow linear dependence of F_A on F_V reported in [18] enables future updates of the best-fit value of F_A based on improved evaluations of F_V^{CVC}.

Figure 24.6 also plots a, the slope parameter of F_V with respect to the momentum transfer to the lepton pair $q_{e\nu}^2$, a first such result, made possible by the broad combined kinematic coverage of PiBeta Runs 1–4. The slope is in qualitative agreement with the χPT calculation of Mateu and Portoles [19].

Analysis of the integral $\pi_{e2\gamma}$ decay rate yielded the primary result: branching ratio for the kinematic region $E_\gamma > 10$ MeV and $\theta_{e\gamma} > 40°$ of $B^{\mathrm{exp}} = 73.86(54) \times 10^{-8}$. At < 1%, this result marked a $\sim$20-fold precision improvement over previous measurements [1]. The excellent fit of the $\pi_{e2\gamma}$ differential decay rates has led to the arguably most important result of this work, the limit on a possible admixture of the tensor interaction $-5.2 \times 10^{-4} < F_T < 4.0 \times 10^{-4}$ with **90%** confidence [18]. To date, this limit provides the strongest constraint on a possible BSM tensor coupling [20].

24.5 Conclusions and path forward

The PiBeta research program has produced an order of magnitude improvement in the precision of the π_{e3} and $\pi_{e2\gamma}$ branching ratios, and related SM observables, low energy QCD parameters (LECs), and a leading limit on BSM tensor coupling.

PEN, the successor experiment to PiBeta, has focused on π_{e2} decay [8], and expanded the $\pi_{e2\gamma}$ kinematic coverage (Figure 24.4), fully enclosing the region of peak SD^-/total relative yield[2]. This is a modest improvement. A new, dedicated experiment would be needed to achieve greater sensitivity.

The scientific case is mounting for a new generation of experiment to fully exploit the

---

[2]Even at its peak relative to other terms, SD^- locally contributes only $\sim$8% of the decays.

precision of the SM description of pion decays, and realize the potential to settle the decades-old question of CKM unitarity in a process free from complex nuclear structure corrections.

Acknowledgments

References

[1] P. Zyla et al., *Review of particle physics*, Progr. Theor. Exper. Phys. 083C01 (2020), doi:10.1093/ptep/ptaa104.

[2] J. C. Hardy and I. S. Towner, *Superallowed $0^+ \rightarrow 0^+$ nuclear β decays: 2020 critical survey, with implications for V_{ud} and CKM unitarity*, Phys. Rev. C **102**, 045501 (2020), doi:10.1103/PhysRevC.102.045501.

[3] A. Czarnecki, W. J. Marciano and A. Sirlin, *Pion beta decay and Cabibbo-Kobayashi-Maskawa unitarity*, Phys. Rev. D **101**, 091301 (2020), doi:10.1103/PhysRevD.101.091301.

[4] B. Märkisch et al., *Measurement of the weak axial-vector coupling constant in the decay of free neutrons using a pulsed cold neutron beam*, Phys. Rev. Lett. **122**, 242501 (2019), doi:10.1103/PhysRevLett.122.242501.

[5] A. Czarnecki, W. J. Marciano and A. Sirlin, *Neutron lifetime and axial coupling connection*, Phys. Rev. Lett. **120**, 202002 (2018), doi:10.1103/PhysRevLett.120.202002.

[6] S. Baeßler, J. D. Bowman, S. Penttilä and D. Počanić, *New precision measurements of free neutron beta decay with cold neutrons*, J. Phys. G: Nucl. Part. Phys. **41**, 114003 (2014), doi:10.1088/0954-3899/41/11/114003.

[7] *Pibeta experiment home page*, http://pibeta.phys.virginia.edu.

[8] D. Počanić, *Pion electronic decay and lepton universality*, SciPost Phys. Proc. **5**, 025 (2021), doi:10.21468/SciPostPhysProc.5.025.

[9] P. De Baenst and J. Pestieau, *Extension of Cabibbo's theory to radiative leptonic decays of pseudoscalar mesons*, Nuov. Cim. A **53**, 407 (1968), doi:10.1007/BF02800120.

[10] D. A. Bryman, P. Depommier and C. Leroy, *$\pi \rightarrow e\nu$, $\pi \rightarrow e\nu\gamma$ decays and related processes*, Phys. Rep. **88**, 151 (1982), doi:10.1016/0370-1573(82)90162-4.

[11] J. F. Donoghue, E. Golowich and B. R. Holstein, *Dynamics of the standard model*, Cambridge University Press, ISBN 9780521362887 (1992), doi:10.1017/CBO9780511524370.

[12] J. Bijnens and G. Ecker, *Mesonic low-energy constants*, Annu. Rev. Nucl. Part. Sci. **64**, 149 (2014), doi:10.1146/annurev-nucl-102313-025528.

[13] E. Frlež et al., *Design, commissioning and performance of the PIBETA detector at PSI*, Nucl. Instrum. Meth. A **526**, 300 (2004), doi:10.1016/j.nima.2004.03.137.

[14] D. Počanić, E. Frlež and A. van der Schaaf, *Experimental study of rare charged pion decays*, J. Phys. G: Nucl. Part. Phys. **41**, 114002 (2014), doi:10.1088/0954-3899/41/11/114002.

[15] D. Počanić et al., *Precise measurement of the $\pi^+ \to \pi^0 e^+ \nu$ branching ratio*, Phys. Rev. Lett. **93**, 181803 (2004), doi:10.1103/PhysRevLett.93.181803.

[16] A. Aguilar-Arevalo et al., *Improved measurement of the $\pi \to e\nu$ branching ratio*, Phys. Rev. Lett. **115**, 071801 (2015), doi:10.1103/PhysRevLett.115.071801.

[17] A. Czarnecki, W. J. Marciano and A. Sirlin, *Radiative corrections to neutron and nuclear beta decays revisited*, Phys. Rev. D **100**, 073008 (2019), doi:10.1103/PhysRevD.100.073008.

[18] M. Bychkov et al., *New precise measurement of the pion weak form factors in $\pi^+ \to e^+ \nu\gamma$ decay*, Phys. Rev. Lett. **103**, 051802 (2009), doi:10.1103/PhysRevLett.103.051802.

[19] V. Mateu and J. Portolés, *Form factors in the radiative pion decay*, Eur. Phys. J. C **52**, 325 (2007), doi:10.1140/epjc/s10052-007-0393-5.

[20] T. Bhattacharya, V. Cirigliano, S. D. Cohen, A. Filipuzzi, M. González-Alonso, M. L. Graesser, R. Gupta and H.-W. Lin, *Probing novel scalar and tensor interactions from (ultra)cold neutrons to the LHC*, Phys. Rev. D **85**, 054512 (2012), doi:10.1103/PhysRevD.85.054512.

Pion electronic decay and lepton universality

Dinko Počanić[*], for the PEN Collaboration

University of Virginia, Charlottesville, VA 22904-4714, USA

[*] pocanic@virginia.edu

Abstract

In common with a number of simple processes involving elementary particles, charged pion decays are profoundly shaped by applicable Standard Model (SM) symmetries and properties. Given the highly precise SM theoretical description, pion decays are used as selective probes of SM parameters, and of possible SM extensions. The PEN experiment at PSI is studying the $\pi^+ \to e^+ \nu_e(\gamma)$, or $\pi_{e2(\gamma)}$ decay. The primary goal is to reach the relative precision of 5×10^{-4} in $R^\pi_{e/\mu}$, the branching ratio for $\pi_{e2(\gamma)}$ decay. We review the PEN research program, its present status, and prospects.

25.1 Motivation

Immediately following the discovery of the charged pion, its decays presented a puzzle: absence of the direct pion decay to an electron that persisted for over a decade. The solution to the puzzle became prominent among the early arguments for the $V{-}A$ form of the "universal" weak interaction [1]. The $V{-}A$ helicity suppression of the right-handed state of the electron led to the accurate prediction [2] of the tree level $\pi \to e\bar{\nu}(\gamma)$, or $\pi_{e2(\gamma)}$[1] branching fraction, $R^\pi_{e/\mu,0}$, even before the decay itself was discovered [3]:

$$R^\pi_{e/\mu,0} \equiv \frac{\Gamma(\pi \to e\bar{\nu})}{\Gamma(\pi \to \mu\bar{\nu})} = \frac{m_e^2}{m_\mu^2} \cdot \frac{(m_\pi^2 - m_e^2)^2}{(m_\pi^2 - m_\mu^2)^2} \simeq 1.283 \times 10^{-4}. \tag{25.1}$$

In the years that followed, π_{e2} decay served as an important theory testing ground, providing rapid experimental confirmations [4, 5] for predicted radiative corrections [6, 7]. This close interplay with theory, at the edge of experimentally accessible precision, remains the driving force behind π_{e2} measurements today.

---

[1] A γ in parentheses denotes an undetected, usually soft photon. For brevity, in further text the (γ) will be dropped and implied; a detected photon in radiative processes will be explicitly denoted with a γ.

In terms of its underlying physics, the π_{e2} decay stands out. By comparison, the much rarer $\mathcal{O}(10^{-8})$ pion beta, $\pi^+ \to \pi^0 e^+ \nu$, or π_{e3}, decay is fully allowed in the SM. It is suppressed only by the small available final-state phase space: a major hindrance to experimental study of an otherwise ultra clean SM process. On the other hand, the strong helicity suppression of the π_{e2} decay (squared lepton mass ratio in Eq. (25.1)) makes this decay uniquely sensitive to a class of pseudoscalar[2] (P), or P-loop-coupled, non-($V-A$) contributions, arising from new, "beyond Standard Model" (BSM) physics, undetectable in analogous, helicity-unsuppressed leptonic decays, such as the $\pi \to \mu\bar{\nu}$, or $\pi_{\mu2}$.

A more complete treatment of π_{e2} includes $\delta R^\pi_{e/\mu}$, the radiative and loop corrections, and the possibility of lepton universality (LU) violation, i.e., that g_e and g_μ, the electron and muon W couplings, may not be equal:

$$R^\pi_{e/\mu} \equiv \frac{\Gamma(\pi \to e\,\bar{\nu}(\gamma))}{\Gamma(\pi \to \mu\bar{\nu}(\gamma))} = \frac{g_e^2}{g_\mu^2}\frac{m_e^2}{m_\mu^2}\frac{(m_\pi^2 - m_e^2)^2}{(m_\pi^2 - m_\mu^2)^2}\left(1 + \delta R^\pi_{e/\mu}\right). \tag{25.2}$$

Steady improvements of the SM description of the π_{e2} decay have reached the precision level of 8 parts in 10^5: $R^{\pi,\,\mathrm{SM}}_{e/\mu} = 1.2352(1) \times 10^{-4}$ [8–10], which indicates that the radiative and loop corrections amount to ~4% of $R^\pi_{e/\mu}$. The best current experimental result, $R^{\pi,\,\mathrm{exp}}_{e/\mu} = 1.2327(23) \times 10^{-4}$, dominated by measurements at TRIUMF and PSI [11–14], is 23 times less precise than the theoretical one.

The primary motivation for the PEN [15] experiment is the unique sensitivity of the π_{e2} decay to BSM processes is. The international PEN collaboration, led by the University of Virginia (UVa) group, set out to measure $R^\pi_{e/\mu}$ at PSI, with a relative precision of $\Delta R^\pi_{e/\mu}/R^\pi_{e/\mu} \le 5 \times 10^{-4}$. At $\Delta R/R = 10^{-3}$, π_{e2} probes the pseudoscalar and axial vector mass scales up to 1,000 TeV and 20 TeV, respectively [16, 17]. For comparison, unitarity tests of the Cabibbo-Kobayashi-Maskawa matrix and precise measurements of superallowed nuclear beta decays constrain the non-SM vector contributions to > 20 TeV, and scalar ones to > 10 TeV [14]. Although scalar interactions do not directly contribute to $R^\pi_{e/\mu}$, they can do so through loop diagrams, resulting in a sensitivity to new scalar interactions up to 60 TeV [16, 17]. The subject was recently reviewed in Refs. [18, 19]. In addition, $R^{\pi,\,\mathrm{exp}}_{e/\mu}$ provides limits on the masses of certain SUSY partners [20], and on anomalies in the neutrino sector [21]. Mounting indications [22] of LU violation in B-meson decays make the subject additionally interesting (for a review see, e.g., [23]).

Additional goals of PEN include measurements of the radiative $\pi_{e2\gamma}$, and $\mu^+ \to e^+ \nu\bar{\nu}\gamma$ decays, as well as of τ_{π^+}, the pion mean life. The physics motivation for the study of $\pi_{e2\gamma}$ decay is discussed in [24], in the context of the PiBeta experiment, predecessor to PEN. Muon decays, sensitive to non-($V-A$) contributions, are not discussed here; neither is τ_{π^+}.

25.2 The PEN apparatus

As the successor to the PiBeta experiment, PEN took over the major components of this apparatus [24, 25], with enhancements and upgrades. PEN detected and analyzed decays of pions and muons at rest in this detector. The 240-element pure CsI crystal calorimeter and the two multiwire proportional chambers (MWPC1,2) were serviced but otherwise unmodified. The 3.2 mm thick plastic hodoscope (PH) array, exhibiting surface crazing, was rebuilt with new fast 4 mm thick plastic scintillator staves. The central beam detectors were reconfigured, as seen in Figure 25.1.

---

[2]The $\pi^- \to \ell\,\bar{\nu}_\ell$ decay connects the pion pseudoscalar 0^- state to the 0^+ vacuum.
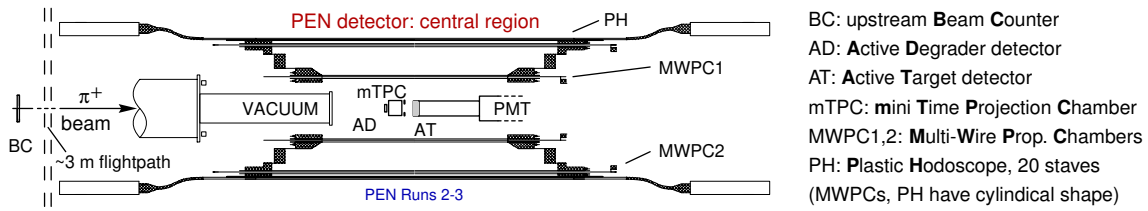
Figure 25.1: Schematic drawing of the central detector region in the PEN Runs 2–3 configuration, including the mTPC for beam tracking (see text for further details).

The upstream beam counter (BC) was rebuilt, the beam vacuum pipe was extended closer to the redesigned active degrader (AD) and the new one-piece active target (AT); all were optimized for the lower beam momentum $p_\pi \simeq 75\,\text{MeV}/c^2$, compared to $\simeq 114\,\text{MeV}/c^2$ in PiBeta running. The addition of PEN beam tracking detectors, discussed below, was also important. Three data-acquisition runs were completed from 2008 through 2010 in the PSI πE1 beam area. Over $\sim$25 weeks of beam, PEN accumulated $N_{\pi \to e\nu} \simeq 2.3\times10^7$, and $N_{\pi \to \mu \to e} > 1.5\times10^8$ events, along with significant numbers of pion and muon radiative decays.

During PEN Run 1, a plastic scintillator degrader made of four slanted wedges, was used for beam tracking. The wedge tracker was replaced in Runs 2 and 3 with low-mass mini time projection chambers, mTPCs, which improved the spatial resolution. The mTPCs, their design, performance, and the key input they provide in the analysis, are described in [26]. Signals from the beam detectors were sent to waveform digitizers, running at 2 GS/s for BC, AD, and AT, and at 250 MS/s for the mTPC. Given the critical role of the mTPCs in controlling the $R^\pi_{e/\mu}$ systematics, the analysis reported here excludes Run 1, or $\sim$20% of the full PEN data set.

25.3 Pion electronic decay: $\pi^+ \to e^+ \nu_e(\gamma)$

A long list of physical processes challenge any precise measurement of $R^\pi_{e/\mu}$ at rest, each complicating the prime objective to accurately identify, sort, count, and normalize the recorded π_{e2} and $\pi_{\mu2}$ decay events. It is a particular challenge to accurately separate and count the
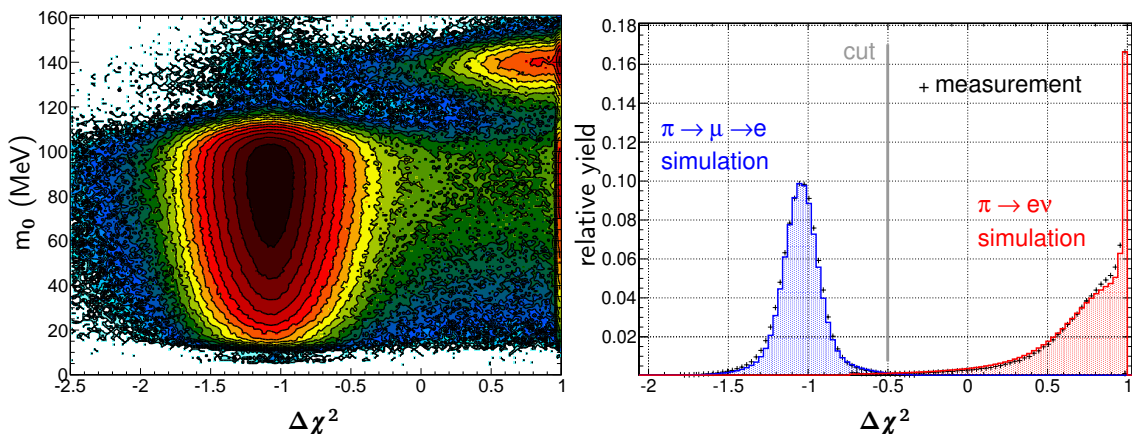

Figure 25.2: Separation of π_{e2} and $\pi_{\mu2}$ events through use of the $\Delta\chi^2$ observable. Left: event invariant mass, $m_0^{e\nu/e\nu\gamma} = \sum E_i + |\sum \vec{p}_i|$, where i denotes distinct tracks/showers and $c \equiv 1$, vs. $\Delta\chi^2$, for a set of Run 2 data recorded with a dedicated $\pi_{\mu2}$-suppressed trigger. Right: $\Delta\chi^2$ distribution for a set of standard-trigger Run 2 events. Gray line: typical choice for the cut separating the two decay types.
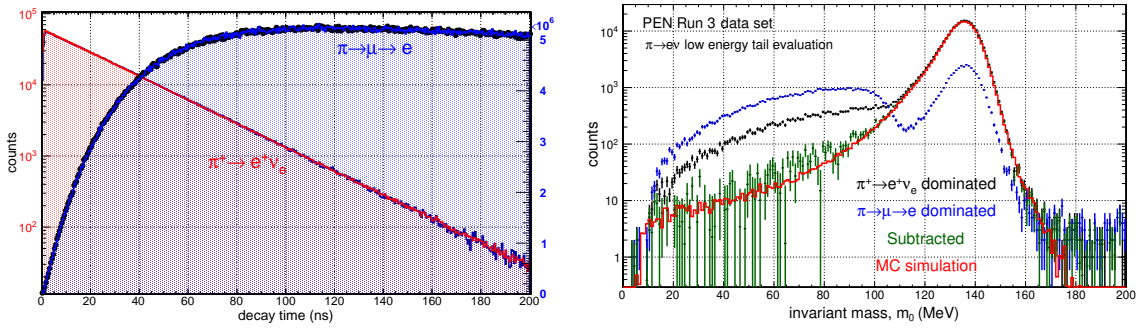
Figure 25.3: Left: decay time spectra for a subset of PEN Run 3 data (black crosses) with applied $\Delta\chi^2$ cuts shown in Figure 25.2. Geant4 simulation results are overlaid in red, for π_{e2}, and blue, for $\pi_{\mu2}$ decays. Right: low energy tail of the π_{e2} invariant mass, m_0, response before and after background subtraction for a subset of Run 3 data.

π_{e2} events that fall in the "tail" of the calorimeter energy response, under the vastly more numerous $\pi \to \mu \to e$ events. A number of observables are used to discriminate to some degree between the π_{e2} and $\pi_{\mu2}$ decay events in the data. The most effective is "$\Delta\chi^2$" which tests a filtered AT waveform [19] for agreement with 2-peak (π_{e2}), and 3-peak ($\pi_{\mu2}$) hypotheses based on predicted π^+ and e^+ signals (Figure 25.2).

Key to the effectiveness of the $\Delta\chi^2$ test are the (a) precise prediction of the decay vertex, based on the beam π^+ and decay e^+ tracking information, plus BC-AD time of flight, and (b) accurate calibration of the AT waveform [19, 26].

The effectiveness of the $\Delta\chi^2$ discriminator is highlighted in Figure 25.3, which shows the separation of the π_{e2}, and $\pi_{\mu2}$ decays in the data. After subtraction of backgrounds, the best experimental determination of the low-E response "tail" for π_{e2} events falls short of the required precision, leaving the determination of the final factor of 5 in precision (Table 25.1) to Monte Carlo simulations. This goal was recently made possible with the inclusion of corrected photoneutron cross sections (γ, n) and $(\gamma, 2n)$ on ^{133}Cs and ^{127}I [26, 27] into Geant4.

The experimental branching ratio $R_{e/\mu}^{\pi,\exp}$ is determined as

$$R_{e/\mu}^{\pi,\exp} = \frac{N_{\pi\to e\nu}^{\text{peak}}(1 + \epsilon_{\text{tail}})}{N_{\pi\to\mu\nu}} \cdot \frac{f_{\pi\to\mu\to e}(T_e)}{f_{\pi\to e\nu}(T_e)} \cdot \frac{\epsilon(E_{\mu\to e\nu\bar{\nu}})_{\text{MWPC}}}{\epsilon(E_{\pi\to e\nu})_{\text{MWPC}}} \cdot \frac{A_{\pi\to\mu\to e}}{A_{\pi\to e\nu}} \cdot \frac{\epsilon_{\text{pileup}}}{\epsilon_{\delta\chi^2}} \qquad (25.3)$$

$$= \frac{N_{\pi\to e\nu}^{\text{peak}}}{N_{\pi\to\mu\nu}} \cdot (1 + \epsilon_{\text{tail}}) \cdot r_f \cdot r_{\text{PC}} \cdot r_A \cdot r_{\text{cut}}, \qquad (25.4)$$

where ϵ_{tail} is the low energy tail fraction of the π_{e2} response, r_f is the ratio of the decay fractions for the two processes within the observed decay time gates, r_{PC} is the ratio of the MWPC efficiencies for the two processes, and r_A is the ratio of the geometrical acceptances for the two processes, evaluated from simulation. The quantities needed to determine $R_{e/\mu}^{\pi}$, given in (25.4), along with their uncertainties, are summarized in Table 25.1. As of this writing, a final critical pass through the calibration and analysis parameters is underway, so that some of the entries in the table may be improved.

25.4 Pion radiative electronic decay: $\pi^+ \to e^+ \nu_e \gamma$

The motivation for the measurement of the pion radiative electronic decay, $\pi_{e2\gamma}$, and results obtained for this channel by the PiBeta collaboration are discussed in detail in [19, 24, 28].

Thanks to a more open trigger, new PEN data greatly extend the phase space coverage of the $\pi_{e2\gamma}$ decay compared to PiBeta, of interst for determining the poorly known [28] amplitude $SD^- \propto (F_A - F_V)^2$. The region of peak sensitivity to SD^-, shown in Figure 25.4, is fully covered in PEN for the first time. The other two panels in Figure 25.4 compare the measured data and simulation using the best $F_{A,V}$ values of [28], updated in [19]. Expectations for a major breakthrough in SD^- precision are tempered, however, by the low peak SD^- contribution (<10%) to the differential decay rate.

25.5 Conclusions

The PEN collaboration is on course to improve the experimental precision of the pion electronic decay $\pi^+ \to e^+ \nu_e(\gamma)$ to a relative precision of $\sim 5 \times 10^{-4}$. In parallel with the current, final round of analysis parameter tuning, the collaboration is preparing for publication a series of technical papers describing the analysis, the first of which is [26]. Once the analysis is frozen, the collaboration will unblind the main result for $R_{e/\mu}^\pi$. Integral to this program are the studies of radiative pion ($\pi_{e2\gamma}$) and muon decays, as well as a new determination of τ_{π^+}, the charged pion mean life.

Acknowledgments

Table 25.1: Projected uncertainty budget for the determination of $R_{e/\mu}^\pi$ in PEN, focusing on the dominant sources. Label "DIF" denotes decay in flight of the particle so marked.

Type	Observable	Value	$\Delta R_{e/\mu}^\pi / R_{e/\mu}^\pi$
Systematic:	$\Delta \epsilon_{\text{tail}}$: low-$E$ "tail" fraction*	$\simeq 0.038$	$\begin{cases} \simeq 0.001^{\text{exp}} \\ 2 \times 10^{-4}\vert_{\text{goal}}^{\text{MC}} \end{cases}$
	r_f: observed decay fractions	0.0441	$< 10^{-4}$
	r_{PC}: ratio of MWPC efficiencies	$\simeq .99$	$< 10^{-4}$
	r_A: acceptance ratio (blinded)	$\simeq 1$	$\leq 10^{-4}$
	r_{cut}: cut efficiency ratio	$\simeq 1.0153$	$\leq 4 \times 10^{-4}$
	$N_{\pi_{\text{DIF}} \to e\nu}/N_{\pi \to e\nu}$	$< 2 \times 10^{-3}$	$10^{-6} - 10^{-5}$
	$N_{\pi_{\text{DIF}} \to \mu\nu}/N_{\pi \to \mu\nu}$	2.3×10^{-3}	$10^{-6} - 10^{-5}$
	$N_{\mu_{\text{DIF}} \to e\nu\bar{\nu}}/N_{\mu \to \nu\bar{\nu}}$	1.4×10^{-4}	$< 10^{-5}$
Statistical:	$\Delta N_{\pi \to e\nu}/N_{\pi \to e\nu}$		$\simeq 3 \times 10^{-4}$
Overall	goal		5×10^{-4}

* Depends on the chosen invariant mass cutoff, here $m_0 = 117.5$ MeV, which minimizes overall uncertainty.
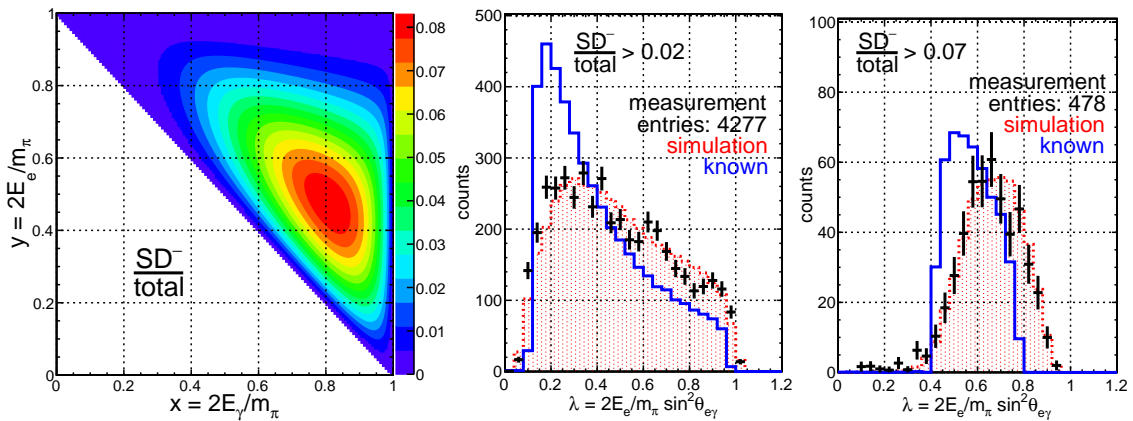
Figure 25.4: Left: phase space contours of constant fraction of the SD^- term in the overall $\pi_{e2\gamma}$ differential decay rate, calculated using $F_{A,V}$ values after [28]. Center and right: measured distributions (black) in λ for SD^-/total > 0.02 and 0.07, respectively, compared with Geant4 "known" values at decay event creation (blue), and results of realistic Geant4 simulation including the full effects of detector response resolution (red).

References

[1] M. Ruderman and R. Finkelstein, *Note on the decay of the π-meson*, Phys. Rev. **76**, 1458 (1949), doi:10.1103/PhysRev.76.1458.

[2] R. P. Feynman and M. Gell-Mann, *Theory of the Fermi interaction*, Phys. Rev. **109**, 193 (1958), doi:10.1103/PhysRev.109.193.

[3] T. Fazzini, G. Fidecaro, A. W. Merrison, H. Paul and A. V. Tollestrup, *Electron decay of the pion*, Phys. Rev. Lett. **1**, 247 (1958), doi:10.1103/PhysRevLett.1.247.

[4] H. L. Anderson, T. Fujii, R. H. Miller and L. Tau, *Branching ratio of the electronic mode of positive pion decay*, Phys. Rev. **119**, 2050 (1960), doi:10.1103/PhysRev.119.2050.

[5] E. Di Capua, R. Garland, L. Pondrom and A. Strelzoff, *Study of the decay $\pi \to e\nu$*, Phys. Rev. **133**, B1333 (1964), doi:10.1103/PhysRev.133.B1333.

[6] S. M. Berman, *Radiative corrections to pion beta decay*, Phys. Rev. Lett. **1**, 468 (1958), doi:10.1103/PhysRevLett.1.468.

[7] T. Kinoshita, *Radiative corrections to π-e decay*, Phys. Rev. Lett. **2**, 477 (1959), doi:10.1103/PhysRevLett.2.477.

[8] W. J. Marciano and A. Sirlin, *Radiative corrections to π_{l2} decays*, Phys. Rev. Lett. **71**, 3629 (1993), doi:10.1103/PhysRevLett.71.3629.

[9] M. Finkemeier, *Radiative corrections to π_{l2} and K_{l2} decays*, Phys. Lett. B **387**, 391 (1996), doi:10.1016/0370-2693(96)01030-1.

[10] V. Cirigliano and I. Rosell, *Two-loop effective theory analysis of $\pi(K) \to e\bar{\nu}_e(\gamma)$ branching ratios*, Phys. Rev. Lett. **99**, 231801 (2007), doi:10.1103/PhysRevLett.99.231801.

[11] D. I. Britton et al., *Measurement of the pi+ —> e+ neutrino branching ratio*, Phys. Rev. Lett. **68**, 3000 (1992), doi:10.1103/PhysRevLett.68.3000.

[12] G. Czapek et al., *Branching ratio for the rare pion decay into positron and neutrino*, Phys. Rev. Lett. **70**, 17 (1993), doi:10.1103/PhysRevLett.70.17.

[13] A. Aguilar-Arevalo et al., *Improved measurement of the $\pi \to e\nu$ branching ratio*, Phys. Rev. Lett. **115**, 071801 (2015), doi:10.1103/PhysRevLett.115.071801.

[14] P. Zyla et al., *Review of particle physics*, Progr. Theor. Exper. Phys. 083C01 (2020), doi:10.1093/ptep/ptaa104.

[15] *Pen experiment home page*, http://pen.phys.virginia.edu.

[16] B. A. Campbell and D. W. Maybury, *Constraints on scalar couplings from*, Nucl. Phys. B **709**, 419 (2005), doi:10.1016/j.nuclphysb.2004.12.015.

[17] B. A. Campbell and A. Ismail, *Leptonic pion decay and physics beyond the electroweak Standard Model* (2008), arXiv:0810.4918.

[18] D. A. Bryman, P. Depommier and C. Leroy, *$\pi \to e\nu$, $\pi \to e\nu\gamma$ decays and related processes*, Phys. Rep. **88**, 151 (1982), doi:10.1016/0370-1573(82)90162-4.

[19] D. Počanić, E. Frlež and A. van der Schaaf, *Experimental study of rare charged pion decays*, J. Phys. G: Nucl. Part. Phys. **41**, 114002 (2014), doi:10.1088/0954-3899/41/11/114002.

[20] M. J. Ramsey-Musolf, S. Su and S. Tulin, *Pion leptonic decays and supersymmetry*, Phys. Rev. D **76**, 095017 (2007), doi:10.1103/PhysRevD.76.095017.

[21] W. Loinaz, N. Okamura, S. Rayyan, T. Takeuchi and L. C. R. Wijewardhana, *NuTeV anomaly, lepton universality, and nonuniversal neutrino-gauge couplings*, Phys. Rev. D **70**, 113004 (2004), doi:10.1103/PhysRevD.70.113004.

[22] L. C. R. Aaij et al., *Test of lepton universality in beauty-quark decays* (2021), arXiv:2103.11769.

[23] G. Ciezarek, M. Franco Sevilla, B. Hamilton, R. Kowalewski, T. Kuhr, V. Lüth and Y. Sato, *A challenge to lepton universality in B-meson decays*, Nature **546**, 227 (2017), doi:10.1038/nature22346.

[24] D. Počanić, *The pion beta and radiative electronic decays*, SciPost Phys. Proc. **5**, 024 (2021), doi:10.21468/SciPostPhysProc.5.024.

[25] E. Frlež et al., *Design, commissioning and performance of the PIBETA detector at PSI*, Nucl. Instrum. Meth. A**526**, 300 (2004), doi:10.1016/j.nima.2004.03.137.

[26] C. J. Glaser, D. Pocanic, A. van der Schaaf, V. A. Baranov, N. V. Khomutov, N. P. Kravchuk and N. A. Kuchinsky, *Beam particle tracking with a low-mass mini time projection chamber in the PEN experiment* (2020), arXiv:2012.12266.

[27] C. Glaser, D. Počanić and V. Baranov, *Monte Carlo simulation of the (γ, n) and $(\gamma, 2n)$ reactions on cesium and iodine below 100 MeV*, in preparation (2021).

[28] M. Bychkov et al., *New precise measurement of the pion weak form factors in $\pi^+ \to e^+\nu\gamma$ decay*, Phys. Rev. Lett. **103**, 051802 (2009), doi:10.1103/PhysRevLett.103.051802.

Recent results of laser spectroscopy experiments of pionic helium atoms at PSI

Masaki Hori[1*], H. Aghai-Khozani[1†], A. Sótér[1‡], A. Dax[2] and D. Barna[3§]

1 Max-Planck-Institut für Quantenoptik,
Hans-Kopfermann-Strasse 1, D-85748 Garching, Germany
2 Paul Scherrer Institut, CH-5232 Villigen, Switzerland
3 CERN CH-1211, Geneva, Switzerland

* Masaki.Hori@mpq.mpg.de
† Current address: McKinsey and Company, Munich, Germany
‡ Current address: ETH Zürich, IPA, Zurich, Switzerland
§ Current address: Institute for Particle and Nuclear Physics,
Wigner Research Centre for Physics, Budapest, Hungary

Abstract

A review of a recent experiment carried out at PSI involving laser spectroscopy of metastable pionic helium ($\pi^4\text{He}^+ \equiv \pi^- + {}^4\text{He}^{2+} + e^-$) atoms is presented. An infrared transition $(n,\ell) = (17,16) \rightarrow (17,15)$ at a resonance frequency of $\nu \approx 183760$ GHz was detected.

26.1 Introduction

Metastable pionic helium is a neutral exotic atom [1–8] that contains a helium nucleus with an electron in the ground state, and a negatively-charged pion (π^-) occupying a state having high principal and orbital angular momentum quantum numbers of around $n \sim \ell + 1 \sim 16$. These states have nanosecond-scale lifetimes against the competing cascade processes of π^- nuclear absorption and $\pi^- \rightarrow \mu^- + \overline{\nu}_\mu$ decay. This longevity arises because the π^- orbitals have very small overlap with the nucleus and so the rates of electromagnetic cascade processes involving the rapid deexcitation of the π^-, such as Auger and radiative decays, are significantly reduced. This characteristic recently enabled laser spectroscopy [5,9] of $\pi^4\text{He}^+$ which constituted the first such measurement of an exotic atom that contained a meson, and showed the existence of this long-lived three-body atom. By comparing the atomic frequencies measured by laser spectroscopy with the results of quantum electrodynamics (QED) calculations, the π^- mass [10–12] can, in principle, be determined with a high precision. This can help set upper limits on constraints on the muon antineutrino mass by laboratory experiments [13]. Some upper limits may also be set on any exotic force [14–18] that involves the π^-, as has been done in the case of antiprotonic helium ($\overline{p}\text{He}^+ \equiv \overline{p} + \text{He}^{2+} + e^-$) atoms [19–30]. Unlike the $\overline{p}\text{He}^+$ case,
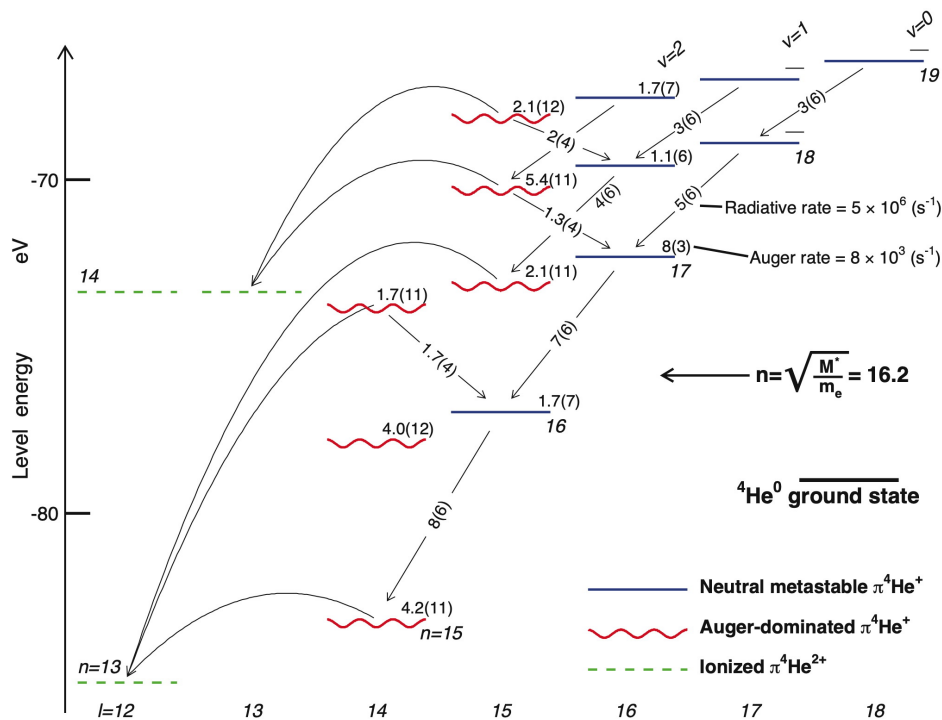
Figure 26.1: An energy level diagram of the exotic atom $\pi^4\text{He}^+$. The theoretical absolute energy of the states (n, ℓ) are plotted relative to the three-body-breakup threshold. The wavy lines indicate Auger-dominated states that have picosecond-scale lifetimes, and the solid lines show metastable levels with lifetimes of > 10 ns. The Auger decay rates are indicated in s^{-1}. The dashed lines show the $\pi^4\text{He}^{2+}$ ionic states which are formed after Auger electron emission. The curved arrows indicate the Auger transitions that have minimum $|\Delta \ell_A|$. The radiative transitions $(n, \ell) \to (n-1, \ell-1)$ and $(n, \ell) \to (n-1, \ell+1)$ are shown using straight arrows, with the corresponding decay rates indicated in s^{-1}. From [5].

the atomic structure of $\pi^4\text{He}^+$ contains no hyperfine structure that arises from the spin-spin interaction between the spin-0 π^- and ^4He nucleus [31, 32].

The existence of πHe^+ atoms had been inferred in an indirect way from four experiments [33–37] that were initially carried out using early synchrocyclotron facilities [38,39] and liquid helium bubble chambers [40]. All these experiments observed that some π^- coming to rest in helium targets have an anomalously long lifetime. Comparisons of the data with the theoretical calculations have been difficult, however, as some sets of calculated decay rates of $\pi^4\text{He}^+$ states have differed from each other by 1–2 orders of magnitude [2, 4, 5]. The transitions between short-lived states with a small principal quantum number n_i for singly charged, two-body pionic helium ($\pi^4\text{He}^{2+} \equiv \pi^- + {}^4\text{He}^{2+}$) ions have been measured by X-ray fluorescence spectroscopy with a relative precision of approximately 2×10^{-4} [41–44]. The atomic lines of $\pi^4\text{He}^+$ were not detected until very recently [9].

26.2 Experimental method

In the recent PSI experiment, laser pulses excited a transition from a pionic state of the neutral atom that had a nanosecond-scale lifetime, to a state with a picosecond-scale lifetime against Auger decay [5] (Figure 26.1). A $\pi^4\text{He}^{2+}$ ion was formed after Auger emission of the 1s
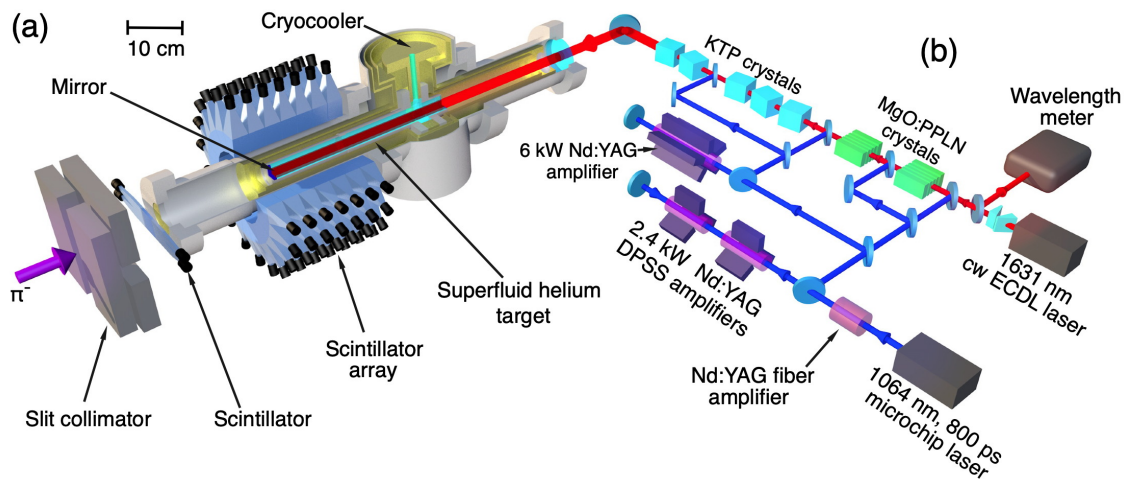
Figure 26.2: (a): Schematic showing the layout of the target used in the experiment. The π^- beam passed through a scintillation counter and then came to rest in the cryogenic helium target. The resulting atoms are irradiated with $\Delta t = 800$ ps long laser pulses with wavelength $\lambda \approx 1631$ nm. (b): Schematic layout of the laser system, see text. From [9].

electron. Collisions with other helium atoms caused Stark mixing between the Rydberg and low ℓ orbitals of the ion [43, 45] as well as other possible effects [46]. This Stark mixing led to the absorption of the π^- by the nucleus. The resonance condition between the laser beam and the $\pi^4\mathrm{He}^+$ atom was detected as a peak in the rates of neutrons, protons, and deuterons. This peak was superimposed on a background containing other $\pi^4\mathrm{He}^+$ atoms that decayed spontaneously with a lifetime of around ≈ 7 ns [5,37].

This experiment used the πE5 beamline [47] that provided a π^- beam that had a momentum between 83 and 87 MeV/c, and an average intensity of $N_\pi = (2-3) \times 10^7$ s^{-1}. A Wien filter was placed upstream of the target. This filter diverted most of the contaminant e^- that arrived at a rate $> 3 \times 10^9$ s^{-1} into the blades of a slit collimator made of steel. The purified π^- beam was focused into an elliptical beam spot that had a full-width-at-half-maximum (FWHM) horizontal size of 23 mm and vertical size of 15 mm. For this a pair of quadrupole magnets provided by the CERN magnet group was used. The π^- beam passed through a plastic scintillator plate that had a thickness $t_d = 4.7$ mm. The plate was segmented into four sections with each section having a size of 20×20 mm^2. The beam then entered the experimental target.

The correlations between the arrival times t_a and energy depositions ΔE of hits that occurred in the scintillator plates at the entrance of the target are shown in the contour plot of Figure 26.3 (a). The π^- arrived in bursts spaced by regular intervals $\Delta t = 19.75$ ns. This arose from the $f_a = 50.63$ MHz radiofrequency of the 590 MeV cyclotron, with each RF cycle containing on average $N_\pi/f_a \approx 0.4 - 0.6 \; \pi^-$. The π^- arrival events which are located in the rectangular area indicated by broken lines were distinguished from μ^- and e^- in the beam by the time-of-flight methods and the estimated ΔE value of 2.6 MeV for π^- in the scintillator plate.

Based on past experiments [37] we assumed that a 2.3% fraction of the π^- that were able to come to rest in the superfluid helium target (Figure 26.2 (a)) with a length of 150 mm, diameter of 42 mm, and a temperature of $T = 1.7$ K formed the metastable variant of the atoms. A laser beam that had a diameter of $d = 25$ mm, a pulse length of $\Delta t = 800$ ps, pulse energy $E = 10$ mJ, repetition rate $f_r = 80.1$ Hz and wavelength $\lambda \approx 1631$ nm entered the target. The beam irradiated $> 60\%$ of the $\pi^4\mathrm{He}^+$ produced in the target. The implied

production rate of the pionic atoms of $> 3 \times 10^5$ s^{-1} ensured that we retained a probability of coincidence of around 10^{-3} for a laser pulse to irradiate a π^4He$^+$ atom.

The nuclear fragments that emerged from the absorption of π^- tended to follow tranjectories that were anticollinear [5,48,49] with a typical kinetic energy of a few tens of MeV. The arrival times t_a and the energy depositions ΔE of the fragments were measured (Figure 26.3 (b)) by an array containing 140 plastic scintillation counters with size $40 \times 35 \times 34$ mm^3. These counters covered a solid angle of $\approx 2\pi$ steradians seen from the target. The size of the scintillation counters was chosen so that the detection efficiency for $E \geq 25$ MeV neutrons was significant ($< 10\%$) [5] while simultaneously achieving the discrimination condition which rejected most of the background e^- from either μ^- decay or the particle beam. The background e^- deposited an average energy $\Delta E = 6 - 8$ MeV. Monte Carlo simulations indicated that most of these events could be removed by rejecting those events an energy deposition of $\Delta E < 20 - 25$ MeV. The waveform [50–52] of the signal from the counters were recorded during each laser pulse arrival by using waveform digitizers that had sampling rates of $f = 3.06$ Gs·s^{-1}. We did this by developing a custom readout system, which used the DRS4 chip which is an application-specific integrated circuit (ASIC) that was based on switched capacitor arrays [53,54]. An earlier version of the electronics based on the DRS4 ASIC was used in an experiment to determine upper limits on the annihilation cross sections of antiprotons of kinetic energy $E \approx 125$ keV on thin target foils [51,55,56], the results of which were compared with the cross sections measured at higher energies $E = 5.3$ MeV [57,58].

Figure 26.3 (b) shows a $t_a - \Delta E$ contour plot of hits on the scintillator array surrounding the target. We selected those events that were within the area indicated by the broken lines. This removed most of the background e^- as well as fission products with low velocities. The blue time spectrum of Figure 26.3 (c) shows the distribution of scintillator hits that were measured without any laser beam irradiating the atoms. The consecutive π^- arrivals at $t = 0$ and at $t = 19.75$ ns produced a pair of peaks in the spectrum that contained the $> 97\%$ majority of π^- that underwent nuclear absorption immediately after arriving in the target. The fraction $(2.1\pm0.7)\%$ that remained constituted a spectrum with a decay lifetime of $\tau = (7\pm2)$ ns in the intervals between the arrivals of π^-. This approximately agreed with the results of a Monte Carlo simulation [5] of the expected signal, and with an experiment carried out previously [37] using a target filled with liquid helium.

The laser pulses that reached the experimental target at a time $t = 9$ ns after the arrival of π^- had a timing jitter of typically $\Delta t \leq 1$ ns. These laser pulses were produced by an injection-seeded, optical parameteric generator (indicated as OPG in Figure 26.2(b)) and amplifier (OPA) laser system. We constructed a diode-pumped solid state (DPSS) neodymium-doped yttrium aluminium garnet (Nd:YAG) laser that was of single pass design. The laser was precisely fired in synchronization with the RF of the cyclotron to pump the OPG-OPA laser. We based the OPG-OPA laser system on a continuous-wave (cw) external-cavity diode laser (ECDL) with a wavelength $\lambda \approx 1631$ nm. This seed beam was amplified using magnesium oxide doped periodically-polled lithium niobate (MgO:PPLN) crystals. This produced laser pulses of energy $E = 70$ uJ. OPA to $E = 10$ mJ was carried out in five potassium titanyl phosphate (KTP) crystals. The linewidth of the portion of the laser beam having a narrow spectral component was of order 10 GHz. These OPG and OPA processes introduced a 3 GHz uncertainty in the determination of the optical frequency of the laser pulses.

26.3 Experimental results

The experiments began by searching for the $(n, l) = (16, 15) \rightarrow (17, 14)$ transition by scanning a laser based on dye and Ti:Sapphire [59] pulse amplification over a 200 GHz wide region around the transition frequency $\nu_{\text{th}} = 781052.6(2.0)$ GHz which was calculated by theory [5]. The 2.0 GHz uncertainty is caused in large part by the experimental uncertainty on the mass
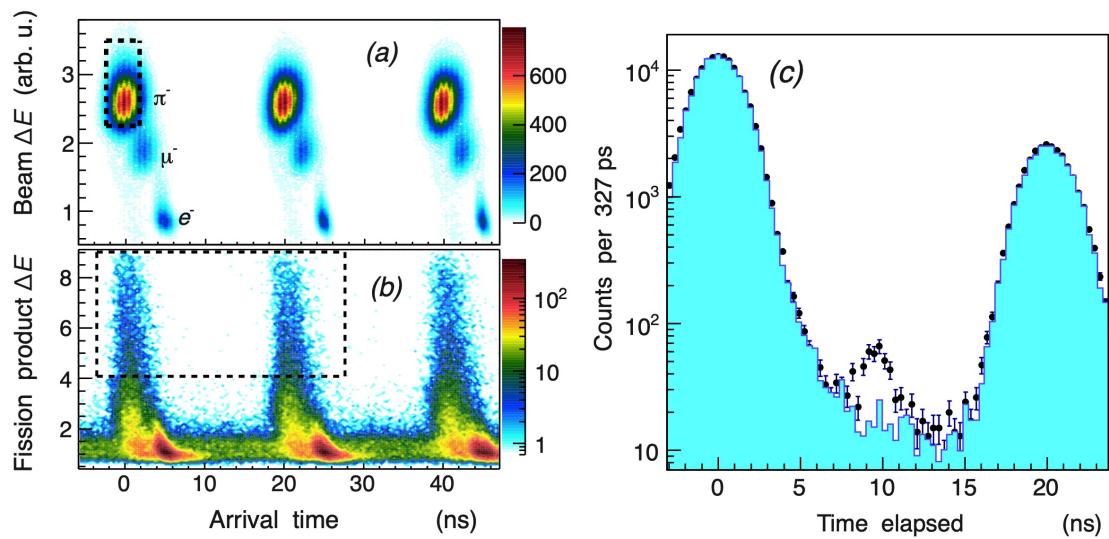
Figure 26.3: (a): A contour plot which shows the correlation between the arrival times t_a and the energy depositions ΔE of particles that were measured by a scintillation counter placed at the entrance of the helium target. The type of particle was identified. The π^- events in the rectangular region shown using broken lines were selected. (b): The $t_a - \Delta E$ plot of showing fission fragments that strike the scintillator array following π^- absorption by the helium nuclei. Background e^- with an energy deposition of $\Delta E < 20 - 25$ MeV were removed by accepting only the events in the region indicated by the rectangle. (c): The time spectra of nuclear fragments measured with (indicated by filled circles with error bars) and without (blue filled histogram) the laser irradiation at $t = 9$ ns. The peak in the former spectrum at $t = 9$ ns here corresponds to the laser resonance signal of $(17, 16) \rightarrow (17, 15)$. From [9].

of π^-. No significant signal was observed. The coupling of the resonance daughter state $(n, \ell) = (17, 14)$ to an electronically excited state of $\pi^4\mathrm{He}^+$ is theoretically expected to cause large scalar and tensor polarizabilities of amplitudes 4×10^4 and 70 atomic units, respectively [6], and this is believed to destabilize the daughter state against atomic collisions [60, 61].

We next searched for the $(16, 15) \rightarrow (16, 14)$ resonance at a theoretical transition wavelength $\lambda = 1515.3$ nm. The 250 fs lifetime [5] of the daughter state $(16, 14)$ should give rise to a large resonance width $\Gamma_A = 640$ GHz. Experimental data that corresponded to $> 6 \times 10^7$ detected π^- arrivals showed no signal that was statistically significant. The reason why the resonance was not observed is not understood. One possibility is that collisions with other helium atoms may destroy the π^- population that occupies the parent state $(n, \ell) = (16, 15)$. Similar effects have been observed in several states of $\overline{p}\mathrm{He}^+$ atoms [62–65]. Alternatively, it may be that only a negligible fraction of π^- are captured into state $(n, \ell) = (16, 15)$, as has been observed for some states of lower n in the $\overline{p}\mathrm{He}^+$ case [66–69].

We searched for the transition $(17, 16) \rightarrow (17, 15)$. The time spectrum indicated by filled circles in Figure 26.3 (c) was measured by accumulating data from 2.5×10^7 π^- arrivals with the laser wavelength tuned to $\lambda \approx 1631.4$ nm. A peak was observed at $t \approx 9$ ns which contained some 300 events. The signal-to-noise ratio was 4 and the statistical significance > 7 standard deviations. Its width $\Delta t = 2$ ns was compatible with the expected dispersion of the time-of-flights of the fission fragments that arrive at the scintillator array. We found that the rate of 3 h^{-1} of detected resonant $\pi^4\mathrm{He}^+$ events is roughly compatible with the production rate of $> 3 \times 10^5$ s^{-1} of the atoms and with Monte Carlo simulations [5] that were carried out by assuming that most of the metastable population are captured into the parent state
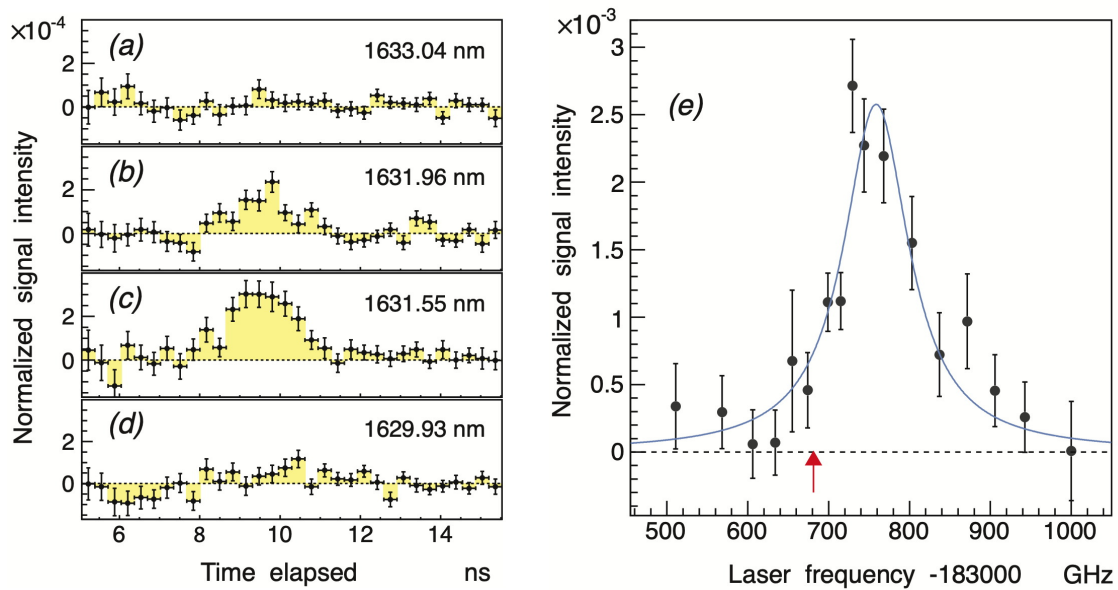
Figure 26.4: (a)–(d): The normalized time spectra of the resonance signal of the $\pi^4\mathrm{He}^+$ transition $(n,l) = (17,16) \rightarrow (17,15)$ which was measured at four laser wavelengths. The spectra were obtained by taking the difference between the timing distributions of π^- absorption that were measured with and without the laser irradiation. (e): The profile of the resonance measured by scanning the laser frequency over a 500 GHz wide region. The red arrow indicates the position of the spin-averaged transition frequency obtained by a three-body QED calculation [5]. From [9].

$(n,\ell) = (17,16)$. When the laser was detuned off the resonance frequency (Figure 26.4 (a)-(d)), the signal proceeded to decrease and disappear.

The resonance signal intensity (Figure 26.4(a)–(d)) was obtained by taking the difference between the normalized time spectra that were measured with and without laser irradiation. The number of detected events under the induced peak around $t = 9$ ns was then counted. The resonance profile of Figure 26.4(e) was obtained by scanning the laser frequency. Each data point shown here contains data that were collected over a 20–30 h period of the experiment. The statistical uncertainty that arises from the finite number of $\pi^4\mathrm{He}^+$ events is indicated by vertical error bars. The measured width of ≈ 100 GHz of this resonance agrees with a convolution of the expected 33 GHz Auger width [5] of the daughter state $(n,\ell) = (17,15)$ calculated by theory, collisional and power broadening [7] which are estimated to cause a contribution of ≈ 50 GHz, and the ≈ 10 GHz linewidth of the narrowband spectral component of the laser pulses. Some further broadening of this resonance may be caused by atomic collisions that shorten [6, 62] the lifetime of the resonance daughter state $(n,\ell) = (17,15)$. The spacing of 3.0 GHz [5, 70] between the fine structure sublines that is expected from the interaction between the electron spin and the orbital angular momentum of π^- cannot be resolved in our experiment since it is much smaller than the 33 GHz natural width of the resonance itself. The best fit (see blue curve) of two overlapping Lorentzian functions which take these sublines into account was shown to have a reduced χ^2 value of 1.0. The resonance centroid is $\nu_{\mathrm{exp}} = 183760(6)(6)$ GHz. The statistical uncertainty of 6 GHz is due to the finite number of detected $\pi^4\mathrm{He}^+$. The systematic uncertainty of 6 GHz contains the contribution of 5 GHz that is related to the selection of this fit function as well as other contributions related to the laser.

This ν_{exp} value determined in the experiment is larger by $\Delta\nu = (78 \pm 8)$ GHz compared to the theoretical value [5] $\nu_{\text{th}} = (183681.8 \pm 0.5)$ GHz. This shift in the resonance frequency is believed to be caused by collisions with other helium atoms [7]. Some similar effects have been previously observed [62,71] for some $\overline{p}\text{He}^+$ resonances. The gradient of this shift that is expected at a target temperature $T = 4$ K was calculated to be $d\nu/d\rho = (4.4 - 6.5) \times 10^{-21}$ GHz·cm^3 using the impact approximation of the binary collision theory of spectral lineshapes [7]. At the density of the superfluid target used in these experiments, the blueshift expected from theory corresponds to between $\Delta\nu = 96$ and 142 GHz. This theoretical result roughly agrees with the result of the experiment. This collisional shift must be experimentally measured before the π^- mass can be determined.

In future experiments, we are planning to search for other transitions such as $(n, l) = (17, 16) \rightarrow (16, 15)$ that should be narrower by a factor of at least 10^{-3} compared to the recently-detected transition using helium gas targets where the collisional shifts are small. Laser spectroscopic techniques that enable higher precision are available [22–24, 59]. The precision of the calculated transition frequencies ν_{th} is now limited by the experimental uncertainty of the π^- mass, but the precision of the calculations themselves [5] can be improved to a fractional precision of less than 10^{-8} for some transitions as in the HD$^+$ [72, 73] and $\overline{p}\text{He}^+$ [19, 20] cases. These pionic experiments at PSI will also complement the measurements on $\overline{p}\text{He}^+$ that will be carried out at the ELENA facility [74–76].

References

[1] G. T. Condo, *On the absorption of negative pions by liquid helium*, Phys. Lett. **9**, 65 (1964), doi:10.1016/0031-9163(64)90216-1.

[2] J. E. Russell, *Metastable states of $\alpha\pi^-e^-$, αK^-e^-, and $\alpha\overline{p}e^-$ atoms*, Phys. Rev. Lett. **23**, 63 (1969), doi:10.1103/PhysRevLett.23.63.

[3] J. E. Russell, *Structure of neutral mesonic atoms formed in liquid helium*, Phys. Rev. A **1**, 721 (1970), doi:10.1103/PhysRevA.1.721.

[4] J. E. Russell, *Auger rates for circular orbits of $\alpha\pi^-e^-$, αK^-e^-, and $\alpha\overline{p}e^-$ atoms*, Phys. Rev. A **1**, 742 (1970), doi:10.1103/PhysRevA.1.742.

[5] M. Hori, A. Sótér and V. I. Korobov, *Proposed method for laser spectroscopy of pionic helium atoms to determine the charged-pion mass*, Phys. Rev. A **89**, 042515 (2014), doi:10.1103/PhysRevA.89.042515.

[6] V. I. Korobov, A. K. Bekbaev, D. T. Aznabayev and S. A. Zhaugasheva, *Polarizability of the pionic helium atom*, J. Phys. B **48**, 245006 (2015), doi:10.1088/0953-4075/48/24/245006.

[7] B. Obreshkov and D. Bakalov, *Collisional shift and broadening of the transition lines in pionic helium*, Phys. Rev. A **93**, 062505 (2016), doi:10.1103/PhysRevA.93.062505.

[8] D. Baye and J. Dohet-Eraly, *Three-body Coulomb description of pionic helium*, Phys. Rev. A **103**, 022823 (2021), doi:10.1103/PhysRevA.103.022823.

[9] M. Hori, H. Aghai-Khozani, A. Sótér, A. Dax and D. Barna, *Laser spectroscopy of pionic helium atoms*, Nature **581**, 37 (2020), doi:10.1038/s41586-020-2240-x.

[10] S. Lenz et al., *A new determination of the mass of the charged pion*, Phys. Lett. B **416**, 50 (1998), doi:10.1016/S0370-2693(97)01337-3.

[11] M. Trassinelli et al., *Measurement of the charged pion mass using X-ray spectroscopy of exotic atoms*, Phys. Lett. B **759**, 583 (2016), doi:10.1016/j.physletb.2016.06.025.

[12] M. Daum, R. Frosch and P.-R. Kettle, *The charged and neutral pion masses revisited*, Phys. Lett. B **796**, 11 (2019), doi:10.1016/j.physletb.2019.07.027.

[13] K. Assamagan et al., *Upper limit of the muon-neutrino mass and charged-pion mass from momentum analysis of a surface muon beam*, Phys. Rev. D **53**, 6065 (1996), doi:10.1103/PhysRevD.53.6065.

[14] E. Salumbides, W. Ubachs and V. I. Korobov, *Bounds on fifth forces at the sub-Å length scale*, J. Mol. Spectrosc. **300**, 65 (2014), doi:10.1016/j.jms.2014.04.003.

[15] J. Murata and S. Tanaka, *A review of short-range gravity experiments in the LHC era*, Class. Quantum Gravity **32**, 033001 (2015), doi:10.1088/0264-9381/32/3/033001.

[16] F. Ficek et al., *Constraints on exotic spin-dependent interactions between matter and antimatter from antiprotonic helium spectroscopy*, Phys. Rev. Lett. **120**, 183002 (2018), doi:10.1103/PhysRevLett.120.183002.

[17] A. S. Lemos, G. C. Luna, E. Maciel and F. Dahia, *Spectroscopic tests for short-range modifications of Newtonian and post-Newtonian potentials*, Class. Quantum Gravity **36**, 245021 (2019), doi:10.1088/1361-6382/ab561f.

[18] J. Ding et al., *Constraints on the velocity and spin dependent exotic interaction at the micrometer range*, Phys. Rev. Lett. **124**, 161801 (2020), doi:10.1103/PhysRevLett.124.161801.

[19] V. I. Korobov, L. Hilico and J.-P. Karr, *$m\alpha^7$-order corrections in the hydrogen molecular ions and antiprotonic helium*, Phys. Rev. Lett. **112**, 103003 (2014), doi:10.1103/PhysRevLett.112.103003.

[20] V. Korobov, L. Hilico and J.-P. Karr, *Theoretical transition frequencies beyond 0.1 ppb accuracy in H_2^+, HD^+, and antiprotonic helium*, Phys. Rev. A **89**, 032511 (2014), doi:10.1103/PhysRevA.89.032511.

[21] V. I. Korobov, *Bethe logarithm for resonant states: Antiprotonic helium*, Phys. Rev. A **89**, 014501 (2014), doi:10.1103/PhysRevA.89.014501.

[22] M. Hori et al., *Determination of the antiproton-to-electron mass ratio by precision laser spectroscopy of $\overline{p}He^+$*, Phys. Rev. Lett. **96**, 243401 (2006), doi:10.1103/PhysRevLett.96.243401.

[23] M. Hori et al., *Two-photon laser spectroscopy of antiprotonic helium and the antiproton-to-electron mass ratio*, Nature **475**, 484 (2011), doi:10.1038/nature10260.

[24] M. Hori et al., *Buffer-gas cooling of antiprotonic helium to 1.5 to 1.7 K, and antiproton-to–electron mass ratio*, Science **354**, 610 (2016), doi:10.1126/science.aaf6702.

[25] A. Adamczak and D. Bakalov, *Shift and broadening of resonance lines of antiprotonic helium atoms in liquid ^4He*, Phys. Rev. A **88**, 042505 (2013), doi:10.1103/PhysRevA.88.042505.

[26] M.-H. Hu, S.-M. Yao, Y. Wang, W. Li, Y.-Y. Gu and Z.-X. Zhong, *Variational calculation of energy levels for metastable states of antiprotonic helium*, Chem. Phys. Lett. **654**, 114 (2016), doi:10.1016/j.cplett.2016.05.017.

[27] D. T. Aznabaev, A. K. Bekbaev and V. I. Korobov, *Nonrelativistic energy levels of helium atoms*, Phys. Rev. A **98**, 012510 (2018), doi:10.1103/PhysRevA.98.012510.

[28] D. Baye, J. Dohet-Eraly and P. Schoofs, *Structure changes along the lowest rotational band of the antiprotonic helium atom*, Phys. Rev. A **99**, 022508 (2019), doi:10.1103/PhysRevA.99.022508.

[29] Z.-D. Bai, Z.-X. Zhong, Z.-C. Yan and T.-Y. Shi, *Complex coordinate rotation method based on gradient optimization*, Chin. Phys. B **30**, 023101 (2021), doi:10.1088/1674-1056/abc156.

[30] T. P. Grozdanov and E. A. Solov'ev, *Hidden-crossing explanation of frozen-planet resonances in antiprotonic helium; their positions and widths*, Eur. Phys. J. D **74**, 50 (2020), doi:10.1140/epjd/e2020-100565-0.

[31] J. Koch and F. Scheck, *Quadrupole interactions in pionic and kaonic atoms*, Nucl. Phys. A **340**, 221 (1980), doi:10.1016/0375-9474(80)90272-9.

[32] M. Trassinelli and P. Indelicato, *Relativistic calculations of pionic and kaonic atoms' hyperfine structure*, Phys. Rev. A **76**, 012510 (2007), doi:10.1103/PhysRevA.76.012510.

[33] J. G. Fetkovich and E. G. Pewitt, *Experimental study of the cascade time of negative mesons in a liquid helium bubble chamber*, Phys. Rev. Lett. **11**, 290 (1963), doi:10.1103/PhysRevLett.11.290.

[34] M. M. Block et al., *Moderation time for nuclear capture of negative pions in liquid He^4*, Phys. Rev. Lett. **11**, 301 (1963), doi:10.1103/PhysRevLett.11.301.

[35] M. M. Block, J. B. Kopelman and C. R. Sun, *Moderation and cascade times of negative pions and negative kaons in liquid helium*, Phys. Rev. **140**, B143 (1965), doi:10.1103/PhysRev.140.B143.

[36] O. A. Zaimidoroga, R. M. Sulyaev and V. M. Tsupko-Sitnikov, *Measurement of the π^--meson cascade transition time in gaseous He^3*, Sov. Phys. JETP **25**, 63 (1967).

[37] S. N. Nakamura et al., *Negative-pion trapping by a metastable state in liquid helium*, Phys. Rev. A **45**, 6202 (1992), doi:10.1103/PhysRevA.45.6202.

[38] H. L. Anderson, J. Marshall, L. Kornblith Jr, L. Schwarcz and R. Miller, *Synchrocyclotron for 450-MeV protons*, Rev. Sci. Instrum. **23**, 707 (1952), doi:10.1063/1.1746144.

[39] J. Ashkin, J. P. Blaser, F. Feiner, J. G. Gorman and M. O. Stern, *Total cross sections for negative and positive pions in hydrogen and deuterium*, Phys. Rev. **96**, 1104 (1954), doi:10.1103/PhysRev.96.1104.

[40] R. J. Walker et al., *The Northwestern University 50 cm liquid helium bubble chamber*, Rev. Sci. Instrum. **39**, 1407 (1968), doi:10.1063/1.1683121.

[41] G. Backenstoss et al., *Pionic and muonic X-ray transitions in liquid helium*, Nucl. Phys. A **232**, 519 (1974), doi:10.1016/0375-9474(74)90637-X.

[42] S. Baird et al., *Measurements on exotic atoms of helium*, Nucl. Phys. A **392**, 297 (1983), doi:10.1016/0375-9474(83)90127-6.

[43] R. Landua and E. Klempt, *Atomic cascade of muonic and pionic helium atoms*, Phys. Rev. Lett. **48**, 1722 (1982), doi:10.1103/PhysRevLett.48.1722.

[44] D. Gotta, *Precision spectroscopy of light exotic atoms*, Prog. Part. Nucl. Phys. **52**, 133 (2004), doi:10.1016/j.ppnp.2003.09.003.

[45] M. Hori et al., *Observation of cold, long-lived antiprotonic helium ions*, Phys. Rev. Lett. **94**, 063401 (2005), doi:10.1103/PhysRevLett.94.063401.

[46] G. Y. Korenman and S. N. Yudin, *Neutralization of excited antiprotonic helium ion in collisions with helium atoms*, Eur. Phys. J. D **75**, 64 (2021), doi:10.1140/epjd/s10053-021-00046-2.

[47] R. Abela, F. Foroughi and D. Renker, *Muon beams at PSI*, Z. Phys. C **56**, S240 (1992), doi:10.1007/BF02426803.

[48] E. Daum et al., *Pion absorption at rest in ^{4}He*, Nucl. Phys. A **589**, 553 (1995), doi:10.1016/0375-9474(95)00068-C.

[49] C. Cernigoi et al., *Energy spectra of single neutrons and charged particles emitted following the absorption of stopped negative pions in ^{4}He*, Nucl. Phys. A **352**, 343 (1981), doi:10.1016/0375-9474(81)90414-0.

[50] A. Sótér et al., *Segmented scintillation detectors with silicon photomultiplier readout for measuring antiproton annihilations*, Rev. Sci. Instrum. **85**, 023302 (2014), doi:10.1063/1.4863648.

[51] K. Todoroki et al., *Instrumentation for measurement of in-flight annihilations of 130 keV antiprotons on thin target foils*, Nucl. Instr. and Meth. A **835**, 110 (2016), doi:10.1016/j.nima.2016.08.026.

[52] Y. Murakami, H. Aghai-Khozani and M. Hori, *Lead fluoride Cherenkov detector read out by avalanche photodiodes for measuring the intensities of pulsed antiproton beams*, Nucl. Instrum. and Meth. A **933**, 75 (2019), doi:10.1016/j.nima.2019.04.076.

[53] S. Ritt, R. Dinapoli and U. Hartmann, *Application of the DRS chip for fast waveform digitizing*, Nucl. Instrum. and Meth. A **623**, 486 (2010), doi:10.1016/j.nima.2010.03.045.

[54] H. Friederich et al., *A scalable DAQ system based on the DRS4 waveform digitizing chip*, IEEE Trans. Nucl. Sci. **58**, 1652 (2011), doi:10.1109/RTC.2010.5750359.

[55] H. Aghai-Khozani et al., *First experimental detection of antiproton in-flight annihilation on nuclei at $\sim$ 130 keV*, Eur. Phys. J. Plus **127**, 125 (2012), doi:10.1140/epjp/i2012-12125-8.

[56] H. Aghai-Khozani et al., *Limits on antiproton-nuclei annihilation cross sections at $\sim$ 125 keV*, Nucl. Phys. A **1009**, 122170 (2021), doi:10.1016/j.nuclphysa.2021.122170.

[57] A. Bianconi et al., *Measurement of the antiproton–nucleus annihilation cross section at 5.3 MeV*, Phys. Lett. B **704**, 461 (2011), doi:10.1016/j.physletb.2011.09.069.

[58] H. Aghai-Khozani et al., *Measurement of the antiproton–nucleus annihilation cross-section at low energy*, Nucl. Phys. A **970**, 366 (2018), doi:10.1016/j.nuclphysa.2018.01.001.

[59] M. Hori and A. Dax, *Chirp-corrected, nanosecond Ti:sapphire laser with 6 MHz linewidth for spectroscopy of antiprotonic helium*, Opt. Lett. **34**, 1273 (2009), doi:10.1364/ol.34.001273.

[60] O. I. Kartavtsev, D. E. Monakhov and S. I. Fedotov, *Auger decay rates of antiprotonic helium*, Phys. Rev. A **61**, 062507 (2000), doi:10.1103/PhysRevA.61.062507.

[61] H. Yamaguchi et al., *Anomalies in the decay rates of antiprotonic helium-atom states*, Phys. Rev. A **66**, 022504 (2002), doi:10.1103/PhysRevA.66.022504.

[62] M. Hori et al., *Sub-ppm laser spectroscopy of antiprotonic helium and a CPT-violation limit on the antiprotonic charge and mass*, Phys. Rev. Lett. **87**, 093401 (2001), doi:10.1103/PhysRevLett.87.093401.

[63] M. Hori et al., *Direct measurement of transition frequencies in isolated $\overline{p}He^+$ atoms, and new CPT-violation limits on the antiproton charge and mass*, Phys. Rev. Lett. **91**, 123401 (2003), doi:10.1103/PhysRevLett.91.123401.

[64] T. Kobayashi et al., *Observation of the 1154.9 nm transition of antiprotonic helium*, J. Phys. B **46**, 245004 (2013), doi:10.1088/0953-4075/46/24/245004.

[65] V. I. Korobov, Z.-X. Zhong and Q.-L. Tian, *Leading term of the He-$\overline{p}He^+$ long-range interaction*, Phys. Rev. A **92**, 052517 (2015), doi:10.1103/PhysRevA.92.052517.

[66] M. Hori et al., *Primary populations of metastable antiprotonic ^4He and ^3He atoms*, Phys. Rev. Lett. **89**, 093401 (2002), doi:10.1103/PhysRevLett.89.093401.

[67] M. Hori et al., *Populations and lifetimes in the $v = n - \ell - 1 = 2$ and 3 metastable cascades of $\overline{p}He^+$ measured by pulsed and continuous antiproton beams*, Phys. Rev. A **70**, 012504 (2004), doi:10.1103/PhysRevA.70.012504.

[68] J. S. Cohen, *Capture of negative exotic particles by atoms, ions and molecules*, Rep. Prog. Phys. **67**, 1769 (2004), doi:10.1088/0034-4885/67/10/R02.

[69] K. Sakimoto, *Formation of antiprotonic helium $\overline{p}He^+$ and ionization in low-energy collisions of $\overline{p}$ with He in the ground $1\,^1S$ and metastable $2\,^3S$ and $2\,^1S$ states*, Phys. Rev. A **91**, 042502 (2015), doi:10.1103/PhysRevA.91.042502.

[70] S. Friedreich et al., *Microwave spectroscopic study of the hyperfine structure of antiprotonic ^3He*, J. Phys. B **46**, 125003 (2013), doi:10.1088/0953-4075/46/12/125003.

[71] D. Bakalov, B. Jeziorski, T. Korona, K. Szalewicz and E. Tchoukova, *Density shift and broadening of transition lines in antiprotonic helium*, Phys. Rev. Lett. **84**, 2350 (2000), doi:10.1103/PhysRevLett.84.2350.

[72] S. Alighanbari, G. S. Giri, F. L. Constantin, V. I. Korobov and S. Schiller, *Precise test of quantum electrodynamics and determination of fundamental constants with HD^+ ions*, Nature **581**, 152 (2020),doi:10.1038/s41586-020-2261-5.

[73] S. Patra et al., *Proton-electron mass ratio from laser spectroscopy of HD^+ at the part-per-trillion level*, Science **369**, 1238 (2020), doi:10.1126/science.aba0453.

[74] V. Chohan et al., *Extra low energy antiproton (ELENA) ring and its transfer lines: Design report*, CERN-2014-002, Geneva, Switzerland (2014), doi:10.5170/CERN-2014-002.

[75] M. Hori and J. Walz, *Physics at CERN's Antiproton Decelerator*, Prog. Part. Nucl. Phys. **72**, 206 (2013), doi:10.1016/j.ppnp.2013.02.004.

[76] M. Hori and V. I. Korobov, *Calculation of transition probabilities and ac Stark shifts in two-photon laser transitions of antiprotonic helium*, Phys. Rev. A **81**, 062508 (2010), doi:10.1103/PhysRevA.81.062508.

The search for the neutron electric dipole moment at PSI

G. Pignol[1] and P. Schmidt-Wellenburg[2⋆] on behalf of the nEDM collaboration

1 Université Grenoble Alpes, Centre National de la Recherche Scientifique,
Grenoble INP, LPSC-IN2P3, Grenoble, France
2 Paul Scherrer Institute, 5232 Villigen, Switzerland

⋆ philipp.schmidt-wellenburg@psi.ch

Abstract

The existence of a nonzero permanent electric dipole moment (EDM) of the neutron would reveal a new source of CP violation and shed light on the origin of the matter–antimatter asymmetry of the Universe. The sensitivity of current experiments using stored ultracold neutrons (UCN) probe new physics beyond the TeV scale. Using the UCN source at the Paul Scherrer Institut, the nEDM collaboration has performed the most sensitive measurement of the neutron EDM to date, still compatible with zero ($|d_n| < 1.8 \times 10^{-26}\,e$cm, C.L. 90%). A new experiment designed to improve the sensitivity by an order of magnitude, n2EDM, is currently under construction.

27.1 Introduction

The permanent electric dipole moment (EDM) d of a simple quantum system of spin $1/2$ represents the coupling between the particle spin and an externally applied electric field $\vec{E}$, in the same way that the magnetic dipole moment μ quantifies the coupling between the spin and an applied magnetic field $\vec{B}$. The spin dynamics is entirely described by the Hamiltonian

$$\hat{H} = -\mu\, \hat{\vec{\sigma}} \cdot \vec{B} - d\, \hat{\vec{\sigma}} \cdot \vec{E}, \tag{27.1}$$

where $\vec{\sigma}$ are the Pauli matrices. Because $\hat{\vec{\sigma}} \cdot \vec{E}$ is odd with respect to time reversal, the CPT theorem implies that a non-zero EDM would result in a violation of CP symmetry. The search for a nonzero EDM was initiated in the 1950's [1], applying the newly invented resonance method with separated oscillating fields [2] on a thermal neutron beam. The quest for an EDM was then extended to many other systems, as shown in Figure 27.1, (see [3] for a review on EDM searches). All experiments to date have reported results compatible with zero, despite the million-fold improvement of the sensitivity of modern experiments. As discussed in the theory chapter of this volume, the present limits on EDMs provide stringent constraints on theories
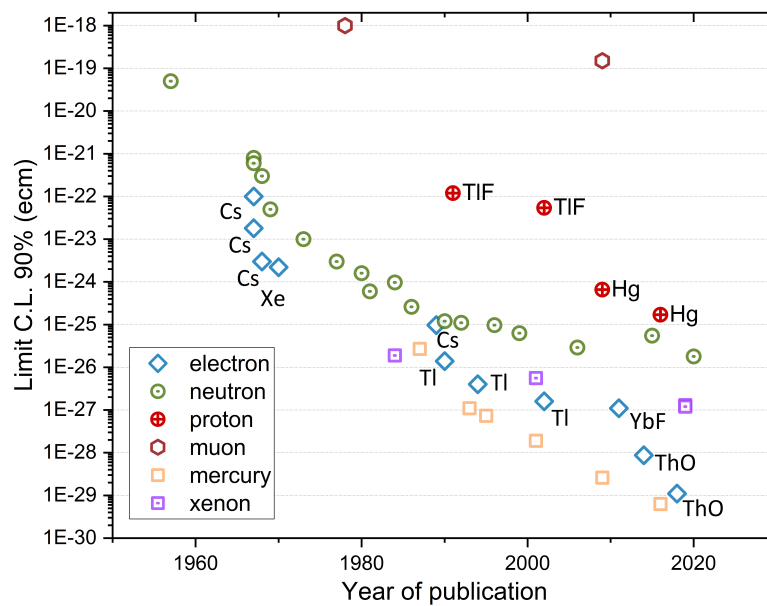
Figure 27.1: History of upper limits (90 % C.L.) for the EDM of various systems. Image first published in [4].

beyond the Standard Model of particle physics, which generally predict new sources of CP violation and therefore non-zero EDMs. The next generation of experiments with improved sensitivity are motivated by the exciting possibility of discovering a non-zero EDM induced by new physics at the multi-TeV scale.

An international collaboration of 15 laboratories (*the nEDM collaboration*) is conducting a long-term program at PSI to search for the neutron EDM. In 2009, the RAL/Sussex/ILL instrument [5], which was previously used at the Institut Laue Langevin in Grenoble for a long series of nEDM measurements [6–9], was connected to the newly built high-intensity source of ultracold neutrons [10, 11]. After a phase of hardware upgrades and commissioning of the instrument, data was collected during 2015 and 2016. This resulted in the currently most precise measurement of the neutron EDM, $d_\mathrm{n} = (0.0 \pm 1.1_\mathrm{stat} \pm 0.2_\mathrm{sys}) \times 10^{-26}\,e \cdot \mathrm{cm}$ [12]. This measurement, with the *single chamber instrument*, will be described in Section 27.3. The construction of the new *double chamber instrument* (called n2EDM: the new neutron EDM apparatus) started in 2018. It will be described in Section 27.4. In the next section we elaborate on the main challenges to neutron EDM searches.

27.2 The three challenges for searches for the neutron EDM

The coupling in (27.1) leads to a precession of the neutron spin around the fields at an angular frequency given by $\omega = 2\left(\mu B + dE\right)/\hbar$ in parallel electric and magnetic fields. In principle the EDM term can be separated from the magnetic term by taking the difference of the frequency measured in parallel and anti-parallel field configurations. However, the electric term that is to be measured is extremely small. For $d = 10^{-26}\,e\mathrm{cm}$ and $E = 15\,\mathrm{kV/cm}$, the spin would complete just about two full turns per year, due to the electric term. For the detection of such a minuscule coupling, one needs (i) a long interaction time with a large electric field, (ii) a high flux of neutrons, and (iii) precise control of the magnetic field. These requirements constitute the three main challenges for the measurement.

In many experiments, the neutron precession frequency is measured using Ramsey's resonance method: neutrons with spins parallel to the magnetic field are selected, then a first oscillating transverse magnetic-field pulse is applied with a strength and duration adjusted
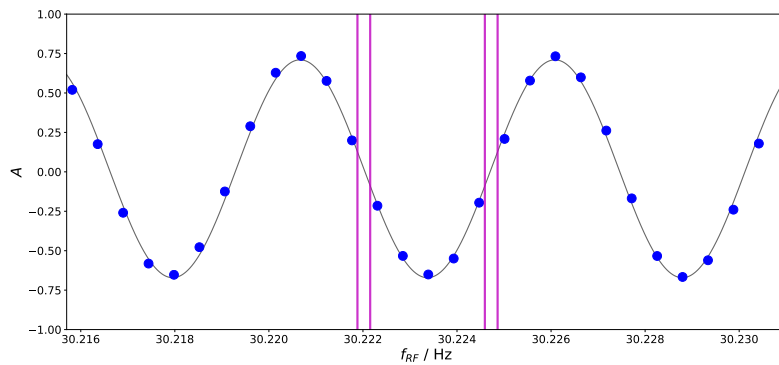
Figure 27.2: Measurement of the asymmetry $A = (N_\uparrow - N_\downarrow)/(N_\uparrow + N_\downarrow)$ as a function of the applied frequency f_{RF} of the pulses. Each point is a measurement cycle with a precession time of $T = 180\,$s performed with the single chamber apparatus in 2017. The vertical bars show the position of the four "working points" used in the nEDM data-taking to maximize the sensitivity. The line is a fit of (27.3) to the data.

to tilt the spin into the plane transverse to the magnetic field. The spins then process freely during a precession time T, after which a second pulse, identical to and in phase with the first one, is applied. At the end of the process the neutron spins are analyzed in order to extract the asymmetry A of neutrons counted with spin up and down. The asymmetry is a function of the applied pulse frequency and of the precession frequency to be measured, as shown in Figure 27.2. By measuring the asymmetry, the neutron precession frequency f_n is extracted. After combining several measurements, aka cycles, of f_n with different polarities of the electric field the neutron EDM is measured with a statistical sensitivity per cycle of

$$\sigma(d_n) = \frac{\hbar}{2ET\alpha\sqrt{N}}, \tag{27.2}$$

where N is the total number of neutron counts and α is the visibility of the resonance, corresponding to the product of the neutron polarization at the end of the precession period and the analyzing power of the spin analyzer. It is apparent from (27.2) that the combination ET enters linearly in the statistical sensitivity and must be maximized (first challenge) along with the statistical factor $\sqrt{N}$ (second challenge).

The first neutron EDM experiments used beams of neutrons interacting with the fields for only a few milliseconds. The turning point for higher sensitivities was the advent of ultracold neutron (UCN) sources which permitted neutrons to be stored in a precession chamber for a duration approaching the neutron half-life of 10 minutes. Care must be taken in the choice of materials constituting the precession chamber in order to minimize neutron losses.

In the single chamber apparatus at PSI, the precession chamber was a cylinder of radius 23.5 cm and height 12 cm, assembled from two aluminum electrodes coated with diamond-like-carbon [13–16] and a polystyrene ring coated with deuterated polystyrene [17]. In average $N = 15000$ neutrons per cycle were exposed to an electric field of 11 kV/cm during $T = 180$ s.

Based on experience and demonstrated developments, a double chamber apparatus was designed. Two vertically stacked chambers, with larger radii of 40 cm will sustain a larger electric field of opposite polarity and store more neutrons.
Table 27.1 shows the main parameters determining the statistical sensitivity.

The high statistical sensitivity must be combined with precise control of the magnetic field: the third challenge. This is accomplished with a combination of magnetic shielding, the generation of a stable and uniform magnetic field inside the shield, and measurements of the

Table 27.1: Comparison between (i) the achieved performance of the single chamber apparatus during the datataking at PSI in 2016, (ii) nominal parameters for the design of n2EDM.

	single chamber (2016)	double chamber (projection)
N (per cycle)	15'000	121'000
T	180 s	180 s
E	11 kV/cm	15 kV/cm
α	0.75	0.8
$\sigma(d_n)$ per day	11×10^{-26} $e \cdot$cm	2.6×10^{-26} $e \cdot$cm

magnetic field with atomic magnetometry. In the single chamber experiment, the change of the magnetic field between reversals of the electric polarity, needed to be controlled at a level better than the statistical sensitivity.

For this purpose, the co-magnetometer technique [18,19] was used. Polarized ^{199}Hg atoms were injected in the chamber and the precession frequency of the atoms was measured optically, providing the magnetic-field average over the same time and almost the same volume as the neutrons.

The mercury co-magnetometer is essential to control the residual time variations of the magnetic field (both correlated and uncorrelated with the electric polarity). However, this comes at the price of inducing a false EDM due to the combined effect of the relativistic motional field $v \times E/c^2$ seen by the mercury atoms and the magnetic field non-uniformities [20–23]. Due to this important systematic effect, the control of the uniformity of the magnetic field is of utmost importance. In particular, ferromagnetic impurities close to the precession chamber(s) must be avoided, and the residual large-scale magnetic gradients must be minimized and measured with a combination of online and offline methods.

27.3   Measurement and result

The principal characteristic of the instrument operated between 2009 to 2017 at PSI was a single-chamber precession volume for UCN, which at the same time contained spin-polarized ^{199}Hg atoms as reference or cohabiting magnetometer [18,19].

Figure 27.3 shows a technical sketch of the instrument. Ultracold neutrons from the PSI UCN source [11, 24] were polarized upon the passage through the 5 T solenoid and entered the precession chamber from the bottom. The spin-manipulation and free precession of UCN and ^{199}Hg took part here, 125 cm above the horizontal beam line, inside a 4-layer mu-metal shield. The top electrode made contact to the tip of a high voltage (HV) feed-through tested in operation up to 200 kV. An electric field of $E = \pm 11$ kV/cm was used for data-taking. The magnetic field, $B \approx 1$ µT, was generated by a current of about 17 mA in a $\cos\theta$-coil wound directly onto the cylindrical vacuum tank. In addition to the $\cos\theta$-coil there were a total of 35 saddle and cylindrical coils, aka trim coils, wound on the tank to adjust magnetic-field gradients. Two of these saddle coils, on the top and bottom of the vacuum tank, were used to set a small vertical magnetic-field gradient $\partial B_z / \partial z$, for each sequence. The ^{199}Hg-comagnetometer measured the time and volume averaged magnetic field within the precession chamber and was subject to the above-described motional systematic effect. At the same time an array of 15 optically-pumped Cs vapor magnetometers (CsM) [25], mounted above and below the chamber, was used to monitor the magnetic-field uniformity with a sampling rate of 1 Hz. Another three coils, two of them in a Helmholtz-like geometry and one a saddle coil, wound
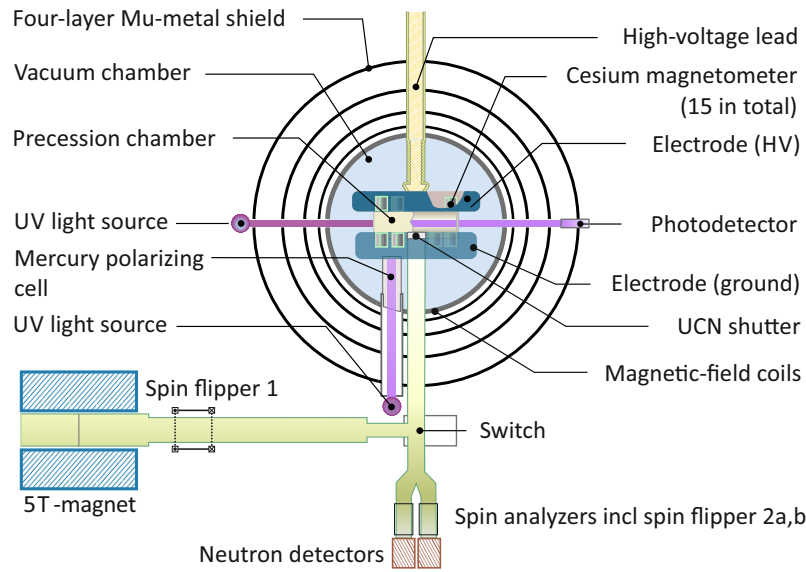
Figure 27.3: Scheme of the single chamber experiment operated during 2009-2017 at PSI. Image first published in [12].

onto the outside of the vacuum tank were used to generate the spin-manipulation pulses, once the UCN and ^{199}Hg-atoms were inside the chamber, with frequencies close to the resonance Larmor frequency of ^{199}Hg (~ 7.8 Hz) and neutron (~ 30.2 Hz).

After the second $t = 2$ s long spin-flip pulse of the Ramsey sequence the neutrons were counted in a spin-sensitive detection system [26,27]. For each cycle, from the recorded number of neutrons with spin up N_u and down N_d the asymmetry $A_i = \left(N_{u,i} - N_{d,i} \right) / \left(N_{u,i} + N_{d,i} \right)$ was computed. During data taking, the files containing the detector data were blinded by injection of an artificial unknown EDM signal [28], different for two distinct analysis groups.

During the nEDM data acquisition period from July 2015 until December 2016 a total of 54 068 cycles each with an average of about 11400 neutrons were recorded. The data were taken with different magnetic-field configurations, e.g. B up or downwards pointing with -25 pT/cm $\geq \partial B_z / \partial z \leq 25$ pT/cm. Each of these sequences contained several hundred cycles and multiple electric-field changes as can be seen in Figure 27.4. A total of 99 sequences were analyzed. In a first step, each sequence was divided into sub-sequences including at least two changes of the electric field polarity. The data of a sub-sequence, typically 114 cycles, was fit to

$$A_i = A_{\text{off}} \mp \alpha \cos \left(\frac{\pi f'_{\text{rf}}}{\nu} + \phi \right), \tag{27.3}$$

where f'_{rf} is the neutron spin flip frequency corrected for magnetic-field drift using the measured f_{Hg} and $\nu = 1/(T + 4t/\pi)$ is the width (FWHM) of the central fringe (see Figure 27.2). To extract the neutron resonance frequency, $f_{n,i}$, the fit parameters A_{off}, α were fixed for each cycle and (27.3) was solved for $\phi = \pi f_{n,i}/\nu$. Figure 27.4 bottom shows the ratio $\mathcal{R}_i = f_{n,i}/f_{\text{Hg},i}$ for a full measurement sequence. An optimized analysis strategy was implemented, accounting for all known effects [12] which affect the $\mathcal{R}$ ratio:

$$\mathcal{R} = \left| \frac{\gamma_n}{\gamma_{\text{Hg}}} \right| \left(1 + \delta_{\text{EDM}} + \delta_{\text{EDM}}^{\text{false}} + \delta_{\text{quad}} + \delta_{\text{grav}} + \delta_{\text{T}} + \delta_{\text{Earth}} + \delta_{\text{light}} + \delta_{\text{inc}} + \delta_{\text{other}} \right), \tag{27.4}$$
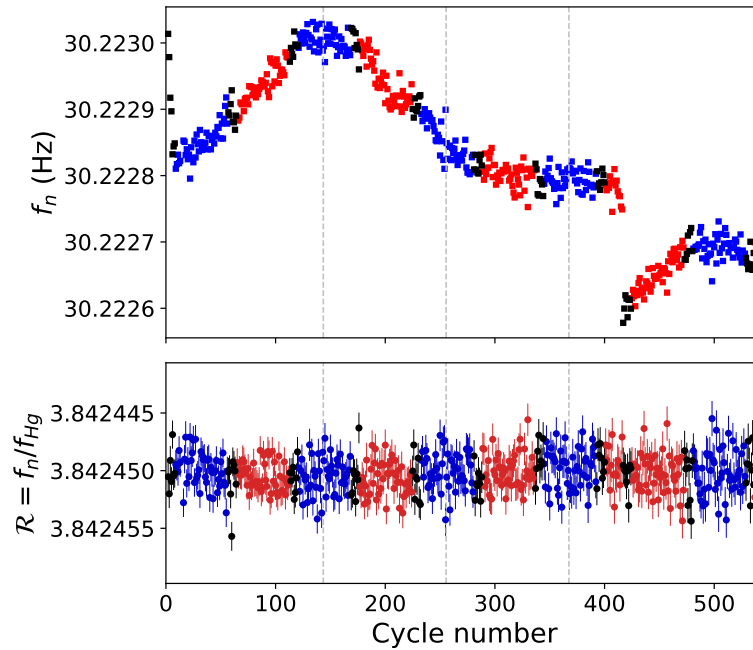
Figure 27.4: Plot of neutron frequency (top), f_n, and frequency ratio (bottom), $\mathcal{R}$, for a full sequence of nEDM data. Red data points indicate a positive voltage, while negative are marked blue. Black is used for cycles without electric field. A single EDM value is extracted for each sub-sequence, indicated by vertical dashed lines, before a weighted EDM average is calculated for the entire sequence. Figure reused from [12].

in particular the EDM term $\delta_{\mathrm{EDM}} = 2E/(\hbar\gamma_n B)d_n$. In fact, the dominating effect is the gravitational shift $\delta_{\mathrm{grav}} = G_{\mathrm{grav}}\langle z \rangle/B$, which is due to the relative center-of-mass offset $\langle z \rangle = -0.39(3)\,\mathrm{cm}$ between UCN and ^{199}Hg. This is both a source of drifts (a nuisance) and also an excellent measure of the effective vertical magnetic-field gradient G_{grav}. In each subsequence, the EDM signal d_n^{meas} and $\langle \mathcal{R} \rangle$ are determined by fitting the $\mathcal{R}_i$ values, compensated for the relative gradient drift, as a function of time and electric field by allowing, also, for a linear time drift, as shown in Figure 27.5. The measured d_n^{meas} for a given field configuration is shifted by the term $\delta_{\mathrm{EDM}}^{\mathrm{false}} = 2E/(\hbar\gamma_n B)d^{\mathrm{false}}$ corresponding to the motional false effect of ^{199}Hg mentioned previous section. This effect depends on the magnetic field gradients and can be expressed as [25]:

$$d^{\mathrm{false}} = \frac{\hbar}{8c^2}\left|\gamma_n\gamma_{\mathrm{Hg}}\right|R^2\left(G_{\mathrm{grav}} + \hat{G}\right), \qquad (27.5)$$

where $\hat{G}$ is the contribution from higher-order gradients and does not produce a gravitational shift. After correction of $\langle \mathcal{R} \rangle$ and d_n^{meas} for δ_{T} and δ_{Earth}, the contribution from $\hat{G}$, and minor systematic shifts, the remaining shift is linear in G_{grav} and was removed by a crossing point fit as shown in Figure 4 of [12]. The results of the crossing-point fit after unblinding of the two analysis teams were $d_{\times,1} = (-0.09 \pm 1.03) \times 10^{-26}\,e\cdot\mathrm{cm}$, $\mathcal{R}_{\times,1} = 3.8424546(34)$ with $\chi^2/\mathrm{dof} = 106/97$ and $d_{\times,2} = (0.15 \pm 1.07) \times 10^{-26}\,e\cdot\mathrm{cm}$, $\mathcal{R}_{\times,2} = 3.8424538(35)$ with $\chi^2/\mathrm{dof} = 105/97$. The excellent agreement of both $\mathcal{R}_{\times}$ values with each other and with the literature value $\gamma_n/\gamma_{\mathrm{Hg}} = 3.8424574(30)$ [23], demonstrates the excellent control and understanding of all magnetic-field-related shifts [25].
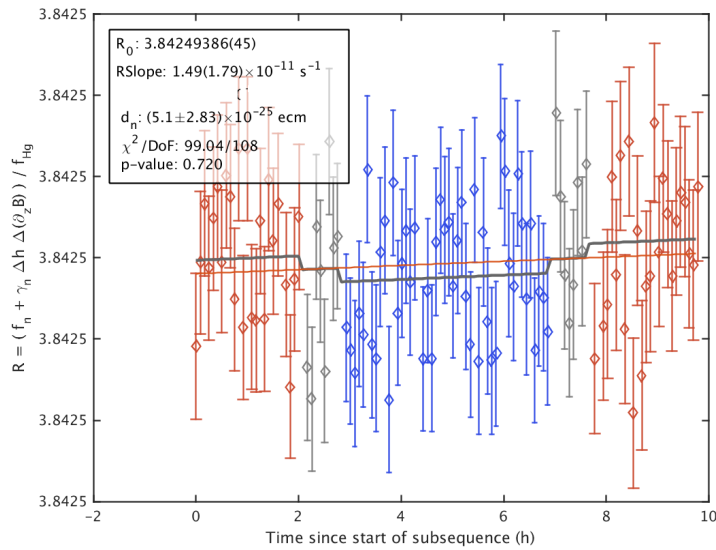
Figure 27.5: Subsequence with two polarity changes and a linear fit in time and $d_n E$ offsets. Note, that $E = -U/d$ hence positive electric fields (red) result from a negative charged electrode in Figure 27.4.

27.4 n2EDM: The double chamber apparatus

The concept and design of the new double chamber instrument, n2EDM [29], was based on maximizing the statistical sensitivity of a single measurement, see Table 27.1, while at the same time further reducing systematic effects.

As can be seen in Figure 27.6, the new apparatus has two cylindrical storage chambers of diameter $\varnothing 80$ cm, made from proven materials, stacked one above the other, separated only by a common high voltage electrode in the center. The UCN transport and storage layout was optimized for a maximum number of neutrons per cycle using the established and bench marked Monte Carlo code of the collaboration [30]. This resulted in ultracold-neutron guides with constant effective cross section and sub-nanometer roughness along the path up to the two precession chambers which in turn are placed at the optimal height relative to the beam line.

Both chambers are centered inside the same uniform magnetic field generated by a main magnetic-field coil and an advanced trim-coil system within a 6-layer magnetic and one-layer Eddy current shield. First measurements of the quasi-static shielding factor in 2020 exceeded the specified value of 80 000 in all directions. This is supplemented by an active magnetic shield (AMS), similar to the active coil system used previously [31], with eight degrees of freedom devised to further improve the shielding factors at very low frequencies. Dedicated coils were designed [32] and mounted onto the inner wall surfaces of the wooden thermal enclosure to compensate gradient magnetic fields up to first order. Hence, neutrons and mercury inside the two precession chambers are exposed to the same extremely low noise, highly uniform magnetic field while the electric field points in opposite directions. We expect that an application of electric fields up to $|E| \geq 15$ kV/cm can be achieved without difficulties, as the HV electrode is entirely enclosed in a grounded Faraday cage.

All CsM are placed at ground potential and the previous limitation on the electric-field strength due to flashovers along optical fibers of the CsM can be ruled out. The sensors were designed for an operation in Bell-Bloom mode [33], recording free spin-precession waveforms for highest accuracy and with a sensitivity of better than $200\,\text{fT}/\sqrt{\text{Hz}}$. This is an essential
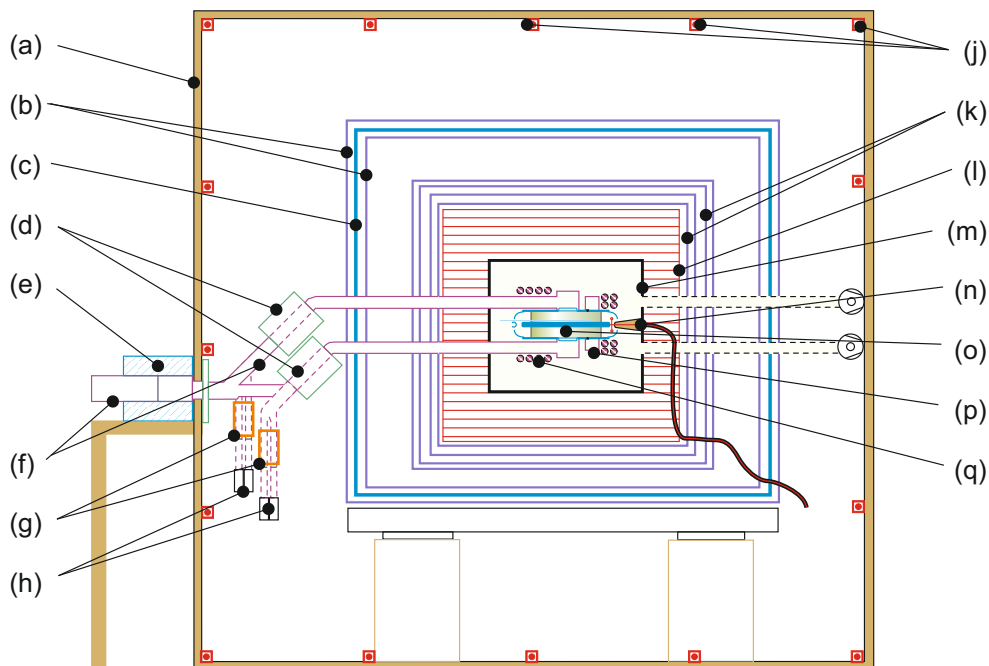
Figure 27.6: Sketch of the new double chamber instrument "n2EDM" at PSI from [29]. (a) Thermal shell, (b) outer MSR shell, (c) Eddy current shield, (d) UCN switches, (e) 5 T-solenoid, (f) UCN guides, (g) fast adiabatic spin flippers, (h) UCN detectors, (j) AMS, (k) inner MSR shells, (l) magnetic field coils, (m) vacuum chamber connected to turbo pumps, (n) high voltage feed through and cable, (o) double precession chamber with central electrode, (p) ^{199}Hgpolarization cell, (q) cesium magnetometers.

improvement for the accurate determination of higher order magnetic-field terms relevant for the correction of systematic effects.

Each precession chamber is connected via a UCN switch to a simultaneous spin detection device featuring each two UCN detectors. A gas mixture of CF4 and ^{3}He is used for neutron detection. The short scintillation pulse is registered by large surface photo-multipliers and enables high count rate with very low background counts from gamma rays or cosmic radiation.

In summary the new double chamber spectrometer, n2EDM, at PSI combines the newest concepts and technologies while relying on proven techniques and methods to improve the sensitivity frontier.

An attractive future option, which is described in great detail in [34], eliminates the motional false EDM by adjusting the magnetic-field strength so that the integral in equation (9) in [29] vanishes. This magic field configuration indicates a possible path to ultimate sensitivity using the n2EDM spectrometer at PSI.

27.5 Outlook and world-wide competition

With the publication of the latest, most stringent limit of $d_n < 1.8 \times 10^{-26}\,e\cdot$cm, PSI became the fourth member of the exclusive club of institutes that have hosted a successful nEDM search. It is now competing with a group of fierce and passionate competitors from all around the world [35–39] to break into the range of $1 \times 10^{-27}\,e\cdot$cm within the next decade. A discovery of an nEDM or a further improved limit would markedly and indelibly shape future models of particle physics beyond the current Standard Model.

We wish to thank all the members of the nEDM collaboration for their dedication to the experimental effort, and the Paul Scherrer Institute for the fantastic hosting conditions.

References

[1] J. H. Smith, E. M. Purcell and N. F. Ramsey, *Experimental limit to the electric dipole moment of the neutron*, Phys. Rev. **108**, 120 (1957), doi:10.1103/PhysRev.108.120.

[2] N. F. Ramsey, *A molecular beam resonance method with separated oscillating fields*, Phys. Rev. **78**, 695 (1950), doi:10.1103/PhysRev.78.695.

[3] T. E. Chupp, P. Fierlinger, M. J. Ramsey-Musolf and J. T. Singh, *Electric dipole moments of atoms, molecules, nuclei, and particles*, Rev. Mod. Phys. **91**, 015001 (2019), doi:10.1103/RevModPhys.91.015001.

[4] K. Kirch and P. Schmidt-Wellenburg, *Search for electric dipole moments*, EPJ Web Conf. **234**, 01007 (2020), doi:10.1051/epjconf/202023401007, arXiv:2003.00717.

[5] C. Baker et al., *Apparatus for measurement of the electric dipole moment of the neutron using a cohabiting atomic-mercury magnetometer*, Nucl. Instrum. Meth. A **736**, 184 (2014), doi:10.1016/j.nima.2013.10.005, arXiv:1305.7336.

[6] J. Pendlebury et al., *Search for a neutron electric dipole moment*, Phys. Lett. B **136**, 327 (1984), doi:10.1016/0370-2693(84)92013-6.

[7] K. F. Smith et al., *A search for the electric dipole moment of the neutron*, Phys. Lett. B **234**, 191 (1990), doi:10.1016/0370-2693(90)92027-G.

[8] P. Harris et al., *New experimental limit on the electric dipole moment of the neutron*, Phys. Rev. Lett. **82**, 904 (1999), doi:10.1103/PhysRevLett.82.904.

[9] C. Baker et al., *An Improved experimental limit on the electric dipole moment of the neutron*, Phys. Rev. Lett. **97**, 131801 (2006), doi:10.1103/PhysRevLett.97.131801, arXiv:hep-ex/0602020.

[10] A. Anghel et al., *The PSI ultra-cold neutron source*, Nucl. Instrum. Methods A **611**, 272 (2009), doi:10.1016/j.nima.2009.07.077.

[11] B. Lauss, *Ultracold neutron production at the second spallation target of the Paul Scherrer Institute*, Phys. Proc. **51**, 98 (2014), doi:10.1016/j.phpro.2013.12.022.

[12] C. Abel et al., *Measurement of the permanent electric dipole moment of the neutron*, Phys. Rev. Lett. **124**, 081803 (2020), doi:10.1103/PhysRevLett.124.081803, arXiv:2001.11966.

[13] F. Atchison et al., *First storage of ultracold neutrons using foils coated with diamond-like carbon*, Phys. Lett. B **625**, 19 (2005), doi:10.1016/j.physletb.2005.08.066.

[14] F. Atchison et al., *Diamondlike carbon can replace beryllium in physics with ultracold neutrons*, Phys. Lett. B **642**, 24 (2006), doi:10.1016/j.physletb.2006.09.024.

[15] F. Atchison et al., *Storage of ultracold neutrons in a volume coated with diamondlike carbon*, Phys. Rev. C **74**, 055501 (2006), doi:10.1103/PhysRevC.74.055501.

[16] F. Atchison et al., *Loss and spinflip probabilities for ultracold neutrons interacting with diamondlike carbon and beryllium surfaces*, Phys. Rev. C **76**, 044001 (2007), doi:10.1103/PhysRevC.76.044001.

[17] K. Bodek et al., *Storage of ultracold neutrons in high resistivity, non-magnetic materials with high Fermi potential*, Nucl. Instrum. Methods A **597**, 222 (2008), doi:10.1016/j.nima.2008.09.018.

[18] K. Green, P. G. Harris, P. Iaydjiev, D. J. R. May, J. M. Pendlebury, K. F. Smith, M. van der Grinten, P. Geltenbort and S. Ivanov, *Performance of an atomic mercury magnetometer in the neutron EDM experiment*, Nucl. Instrum. Methods A **404**, 381 (1998), doi:10.1016/S0168-9002(97)01121-2.

[19] G. Ban et al., *Demonstration of sensitivity increase in mercury free-spin-precession magnetometers due to laser-based readout for neutron electric dipole moment searches*, Nucl. Instrum. Methods A **896**, 129 (2018), doi:10.1016/j.nima.2018.04.025, arXiv:1804.05838.

[20] J. Pendlebury et al., *Geometric-phase-induced false electric dipole moment signals for particles in traps*, Phys. Rev. A **70**, 032102 (2004), doi:10.1103/PhysRevA.70.032102.

[21] S. K. Lamoreaux and R. Golub, *Detailed discussion of a linear electric field frequency shift induced in confined gases by a magnetic field gradient: Implications for neutron electric-dipole-moment experiments*, Phys. Rev. A **71**, 032104 (2005), doi:10.1103/PhysRevA.71.032104.

[22] G. Pignol and S. Roccia, *Electric-dipole-moment searches: Reexamination of frequency shifts for particles in traps*, Phys. Rev. A **85**, 042105 (2012), doi:10.1103/PhysRevA.85.042105.

[23] S. Afach et al., *Measurement of a false electric dipole moment signal from ^{199}Hg atoms exposed to an inhomogeneous magnetic field*, Eur. Phys. J. D **69**, 225 (2015), doi:10.1140/epjd/e2015-60207-4, arXiv:1503.08651.

[24] G. Bison, B. Blau, M. Daum, L. Göltl, R. Henneck, K. Kirch, B. Lauss, D. Ries, P. Schmidt-Wellenburg and G. Zsigmond, *Neutron optics of the PSI ultracold-neutron source: characterization and simulation*, Eur. Phys. J. A **56**, 33 (2020), doi:10.1140/epja/s10050-020-00027-w, arXiv:1907.05730.

[25] C. Abel et al., *Optically pumped Cs magnetometers enabling a high-sensitivity search for the neutron electric dipole moment*, Phys. Rev. A **101**, 053419 (2020), doi:10.1103/PhysRevA.101.053419, arXiv:1912.04631.

[26] S. Afach et al., *A device for simultaneous spin analysis of ultracold neutrons*, Eur. Phys. J. A **51**, 143 (2015), doi:10.1140/epja/i2015-15143-7, arXiv:1502.06876.

[27] G. Ban et al., *Ultracold neutron detection with ^6Li-doped glass scintillators*, Eur. Phys. J. A **52**, 326 (2016), doi:10.1140/epja/i2016-16326-4.

[28] N. Ayres et al., *Data blinding for the nEDM experiment at PSI* (2019), arXiv:1912.09244.

[29] C. Abel et al., *The n2EDM experiment at the Paul Scherrer Institute*, EPJ Web Conf. **219**, 02002 (2019), doi:10.1051/epjconf/201921902002, arXiv:1811.02340.

[30] G. Zsigmond, *The MCUCN simulation code for ultracold neutron physics*, Nucl. Instr. Methods A **881**, 16 (2018), doi:10.1016/j.nima.2017.10.065.

[31] S. Afach et al., *Dynamic stabilization of the magnetic field surrounding the neutron electric dipole moment spectrometer at the Paul Scherrer Institute*, J. Appl. Phys. **116**, 084510 (2014), doi:10.1063/1.4894158, arXiv:1408.6752.

[32] M. Rawlik, A. Eggenberger, J. Krempel, C. Crawford, K. Kirch, F. M. Piegsa and G. Quéméner, *A simple method of coil design*, Am. J. Phys. **86**, 602 (2018), doi:10.1119/1.5042244.

[33] Z. D. Grujić, P. A. Koss, G. Bison and A. Weis, *A sensitive and accurate atomic magnetometer based on free spin precession*, Eur. Phys. J. D **69**, 135 (2015), doi:10.1140/epjd/e2015-50875-3.

[34] G. Pignol, *A magic magnetic field to measure the neutron electric dipole moment*, Phys. Lett. B **793**, 440 (2019), doi:10.1016/j.physletb.2019.05.014, arXiv:1812.01420.

[35] F. Piegsa, *New concept for a neutron electric dipole moment search using a pulsed beam*, Phys. Rev. C **88**, 045502 (2013), doi:10.1103/PhysRevC.88.045502, arXiv:1309.1959.

[36] R. Picker, *How the minuscule can contribute to the big picture: The neutron electric dipole moment project at TRIUMF*, In Proceedings of the 14th International Conference on Meson-Nucleon Physics and the Structure of the Nucleon (MENU2016), 010005 (2017), doi:10.7566/JPSCP.13.010005, arXiv:1612.00875.

[37] T. Ito et al., *Performance of the upgraded ultracold neutron source at Los Alamos National Laboratory and its implication for a possible neutron electric dipole moment experiment*, Phys. Rev. C **97**, 012501 (2018), doi:10.1103/PhysRevC.97.012501, arXiv:1710.05182.

[38] M. Ahmed et al., *A new cryogenic apparatus to search for the neutron electric dipole moment*, J. Inst. **14**, P11017 (2019), doi:10.1088/1748-0221/14/11/P11017, arXiv:1908.09937.

[39] D. Wurm et al., *The PanEDM neutron electric dipole moment experiment at the ILL*, EPJ Web Conf. **219**, 02006 (2019), doi:10.1051/epjconf/201921902006.

Indirect searches for dark matter with the nEDM spectrometer

S. Roccia[1,2] and G. Zsigmond[3*] on behalf of the nEDM collaboration at PSI

1 Laboratoire de Physique Subatomique et de Cosmologie, Université Grenoble Alpes, CNRS/IN2P3, Grenoble, France
2 Institut Laue-Langevin, CS 20156 F-38042 Grenoble Cedex 9, France
3 Paul Scherrer Institut, 5232 Villigen PSI, Switzerland

★ geza.zsigmond@psi.ch

Abstract

The nEDM apparatus at PSI has been used to search for different dark matter signatures utilizing its high sensitivity to shifts in the neutron precession frequency and its well-controlled low magnetic field at the μT level. Such a shift could be interpreted as a consequence of a short-range spin-dependent interaction that could possibly be mediated by axions or axion-like particles, or as an axion-induced oscillating electric dipole moment of the neutron. Another search, based on so-called UCN disappearance measurements, targeted previously reported signals of neutron to mirror-neutron oscillations. These dark matter searches confirmed and improved previous results, as detailed in this review.

Check for
updates

28.1 Introduction

Apart from searching for the electric dipole moment of the neutron, the nEDM apparatus at PSI (Section 27 [1]) is also an excellent tool to search for signatures of dark matter particles. The first potential signature studied was a high precision measurement of the shift in the ratio of the spin-precession frequencies of ultracold neutrons (UCN) and ^{199}Hg atoms. This shift can be interpreted as originated from a possible short-range spin-dependent neutron–nucleon interaction [2]. A second search focused on ultra-low-mass axionlike dark matter. The aforementioned ratio was measured and analyzed as an axion-induced oscillating electric dipole moment of the neutron and an axion-wind spin-precession effect [3]. UCN disappearance experiments were conducted with this apparatus [4] to search for dark matter signatures. It has been proposed starting from the fifties that there could be a mirror copy of the Standard Model (SM) particles, restoring parity conservation in the weak interaction on the global level. Oscillations between a neutral SM particle, such as the neutron, and its mirror counterpart could

help explain various issues in physics, including dark matter. The neutron electric dipole moment collaboration at PSI conducted an experiment to search for anomalous signals reported before.

Below we summarize the results of our experiments aiming at identifying dark matter signatures with the nEDM apparatus at PSI. A comparison to previous constraints on model parameters will be given.

28.2 Search for axion-like particles

The most elegant solution to the strong CP problem is to introduce a global chiral U(1) symmetry, usually named $U(1)_{PQ}$ after the two physicists who first proposed it, R. D. Peccei and H. R. Quinn [5] in 1977. $U(1)_{PQ}$ is spontaneously broken at some energy scale f_a producing a pseudo-Nambu-Goldstone boson of the global $U(1)_{PQ}$ symmetry: the axion, as proposed by S. Weinberg and F. Wilczek [6].

One defining feature of the axion is the inverse proportionality of the mass m_a to the $U(1)_{PQ}$ symmetry breaking scale f_a. Therefore, one needs only one parameter to describe the axion's properties. In reference [7], the proportionality factor is computed from first principles and using lattice calculations giving

$$m_a = 5.70(6)(4)\ \mu\text{eV}\left(\frac{10^{12}\ \text{GeV}}{f_a}\right) \tag{28.1}$$

The axion is a well-motivated dark matter candidate, as it would solve the strong CP problem and possibly explain the observed abundance (or a fraction) of dark matter. However, observing the axion in the mass range where it would explain the dark matter abundance, requires probing a very weak coupling.

Experimentally, searching for an "axion" outside the window defined by (28.1) is referred to as searching for axionlike particles.

An important feature of the nEDM spectrometer [1] is the mercury co-magnetometer. The search for the neutron electric dipole moment employs the ratio $\mathcal{R}$ of the neutron precession frequency (f_n) to the mercury one (f_Hg) using the fact that this ratio is, to first order, free from magnetic field fluctuations. Similarly, this ratio can be used to search for exotic couplings forming a class of experiments called clock comparison. In the following, we focus on how to search for axion-like particles with advanced clock comparison experiments using the ratio $\mathcal{R}$ according to equation:

$$\mathcal{R} \equiv \frac{f_\text{n}}{f_\text{Hg}} = \frac{\gamma_\text{n}}{\gamma_\text{Hg}}\left(1 + \frac{\vec{b}.\vec{B}}{B^2} \pm \left(d_\text{n} - \frac{\gamma_\text{n}}{\gamma_\text{Hg}}d_\text{Hg}\right)\frac{2E}{hf_\text{Hg}}\right) \tag{28.2}$$

In this expression $\vec{B}$ ($\vec{E}$) is the applied magnetic (electric) field. These fields are parallel to each other. This ratio is sensitive to an EDM-like coupling (for the neutrons (d_n) or for the mercury atoms (d_Hg)) and to any coupling generating a pseudo-magnetic field acting differently on neutrons and mercury atoms so that its effective strength $\vec{b}$ is not null.

Some models predict that low mass axions ($m_a \leq 0.1\ \text{eV}/c^2$) [8] could have been produced in the early universe and would form now a coherently oscillating classical field of amplitude a depending only on the axion's mass m_a [9]

$$a(t) = a_0 \cos(\frac{m_a c^2}{\hbar}t) \tag{28.3}$$

The same models predict an oscillation of the ratio $\mathcal{R}$ induced by the coupling [3]

$$\mathcal{L} = \frac{C_G}{f_a} \frac{\alpha_S}{8\pi} G_{b\mu\nu} \widetilde{G}^{b\mu\nu} - \frac{C_N}{2f_a} \partial_\mu a \bar{N} \gamma^\mu \gamma^5 N \tag{28.4}$$

where b is the color index while C_G, the axion-gluon coupling, and C_N, the axion-nucleon coupling, are model dependent dimensionless parameters. The first term is the axion-gluon coupling. It induces an oscillation of the neutron EDM through the same mechanism as the QCD theta term. The second term is the axion-nucleon coupling. It induces an E-independent frequency modulation of the ratio $\mathcal{R}$. In both cases, the frequency of the oscillation depends on the (unknown) mass of the axion, see (28.3). The limits obtained at PSI on the couplings C_G and C_N for different axion masses are shown in Figure 28.1a and Figure 28.1b respectively.

A limit on a completely different mass range can be obtained searching for a scalar-pseudo-scalar coupling between the polarized neutrons and the unpolarized nuclei in the electrodes of the storage chamber. Due to gravity, the neutron density is higher close to the bottom electrode so globally the effective field $\vec{b}$ in (28.2) due to the two electrodes does not cancel out for neutrons (it does for mercury atoms whose density is homogeneous). We searched for the effective field $\vec{b}$ as a shift in the $\mathcal{R}$ ratio correlated with the direction of the applied magnetic field. The obtained limit is shown in Figure 28.1c and compared with other limits established using atoms.

28.3 Search for mirror neutrons

Lee and Yang suggested [12] that parity symmetry in the weak interaction could be restored by the existence of a parity conjugated copy of the same set of weakly interacting particles. It was shown later [13] that SM particles would not interact with their *mirror* counterparts (SM′) via SM forces, and SM′ would have its own interactions. However there may exist interactions beyond the SM, between neutral SM and SM′ particles. The idea that by the introduction of mirror matter, parity and time reversal symmetries could be restored in the weak interactions, and thus in a global sense as well, was detailed further in [14, 15]. Berezhiani and others proved that the interaction of SM and SM′ particles could answer several open questions in physics: (i) mirror matter could be a viable dark matter candidate [16–21], (ii) it would provide a mechanism to help solve sterile neutrino anomalies [22–24], (iii) SM neutrinos could be endowed with mass [23, 25], (iv) it could open up additional channels of CP and baryon number violation, helping to explain baryogenesis and the baryon asymmetry of the universe [26, 27], (v) it could provide a mechanism to relax the Greisen-Zatsepin-Kuzmin (GZK) limit on cosmic rays [28, 29]. A comprehensive review can be found in [16, 30–32].

In [33] Berezhiani et al. showed that as long as neutrons and their mirror counterparts have the same mass, decay width and gravitational potential, application of a magnetic field, B, equal to a mirror magnetic field, B', in the same place can induce a degeneracy between the SM and SM′ states, and an $n - n'$ oscillation would be possible. The time constant for the coupling, $\tau_{nn'}$, could be as low as several seconds. By inducing or destroying the degeneracy, this oscillation could be made visible by means of scanning the applied magnetic field in the experiments.

Pokotilovski proposed [34] that if ultracold neutrons (UCN) would be stored, and they would oscillate into the mirror state, then by such disappearance experiments a signature to mirror states could be probed. First experiments with UCN [35–37] obtained a limit under the assumption of a mirror magnetic field $B' = 0$ of $\tau_{nn'} > 448$ s (90% C.L.) [37]. Reference [38] relaxed the conditions to $B' \neq 0$ and set a constraint of $\tau_{nn'} > 12$ s for $0.4\,\mu\text{T} < B' < 12.5\,\mu\text{T}$ (95% C.L.). In [39], Berezhiani *et al.* further analysed the above experiments and reported signal-like anomalies for $n - n'$ oscillation when $B' \neq 0$. Reference [40] again identifies statisti-
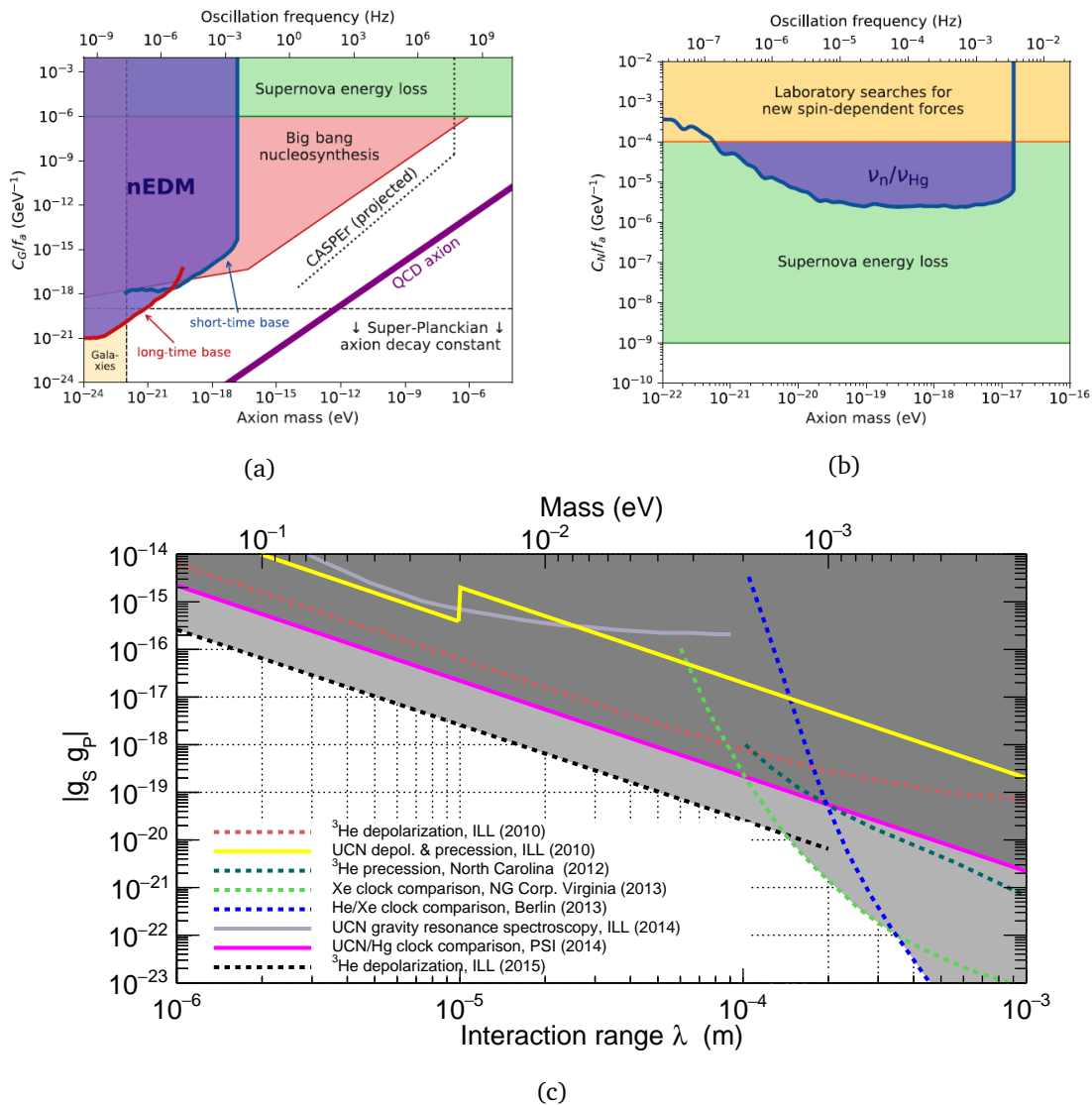
(a)

(b)

(c)

Figure 28.1: (a) first laboratory-based limit on the axion-gluon coupling C_G taken from [3]. (b) limit on the axion-nucleon coupling C_N. (c) shows the limit established in [10] for the scalar-pseudoscalar coupling for axion or axion-like particle (pink solid line). In this plot, reproduced from [11] (courtesy M. Guigue), the solid lines are constraints established with free neutrons (dark grey excluded zone) while dot-dashed lines are constraints established on bound nucleons (light grey excluded zone).

cally significant signals: a 3σ signal from the data in [35], a 5.2σ signal from data in [36,37], and a 2.5σ signal in [40].

The potential signals of [39] motivated a new measurement at PSI by the neutron electric dipole moment (nEDM) collaboration [4]. The nEDM apparatus was re-purposed for these storage measurements using unpolarized neutrons in order to increase statistics. The B magnetic field was alternately switched off and on using both polarities, thus modifying the degeneracy between the SM and the assumed SM' energy levels. We did not observe any statistically significant changes in the stored UCN counts from different magnetic field settings, and set constraints on the parameters of $n - n'$ oscillation.

The parameter space of the mirror magnetic field, B' and $(\tau_{nn'}/\sqrt{\cos\beta})$, constrained by different experiments is shown in Figure 28.2 [4]. The angle between the assumed B' and the applied magnetic field B is denoted by β. We also plotted the results from previous searches, including the signal-like anomalies detailed in the caption.
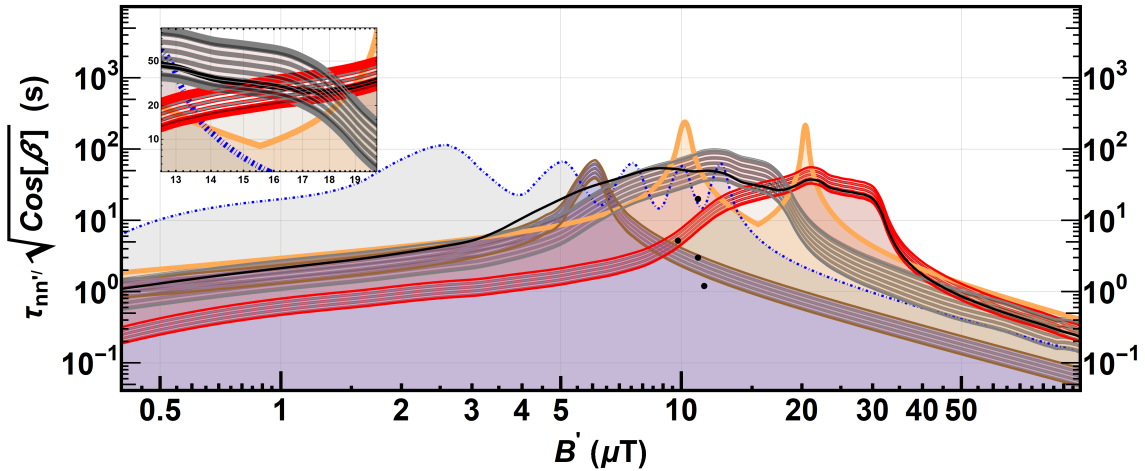

Figure 28.2: Lower limits [4] on the $n-n'$ oscillation time, $\tau_{nn'}$ at 95% C.L. while assuming $B' \neq 0$. From the asymmetry analysis, the solid orange curve represents the lower limit on $(\tau_{nn'}^{B'\neq 0}/\sqrt{\cos\beta})$. The black curve is the global constraint calculated in [40]. The dot-dashed blue curve represents the lower limit imposed using data in [38] by [40]. The three striped regions are the signals (95% C.L.): (i) the red striped region, is the signal region calculated in [39, 40] from the 5.2σ anomaly in [37]; (ii) the brown striped region is the signal calculated in [39, 40] from the 3σ anomaly in [35]; and (iii) the gray striped region is the signal from the 2.5σ anomaly observed in [40]. The black dots indicate the the solution consistent with the statistically significant signals as reported in [39].

As in [33], we considered that the mirror magnetic field B' and β are constant at the experiment site. The constraints in [33,35–40] were measured at the Institute Laue-Langevin (ILL) in Grenoble. The experiment in [4] was performed at PSI. We worked with the natural assumption that a mirror magnetic field created within the Earth [33] displays approximate rotational symmetry around the Earth's rotation axis, similar to the Earth's magnetic field. Then its components would only change on a level of 5% between ILL and PSI, and similarly in time, causing a negligible offset on the B' axis of Figure 28.2.

The solid orange curve in Figure 28.2 excludes all signal spots (see black dots) reported in [39], for which the experiment at PSI was optimized in 2017. The three signal bands in [37, 39, 40] exclude each other since they don't overlap at the same mirror magnetic field, B'. Our analysis excludes three of the five areas where at least two of the signal bands overlap.

28.4 Outlook

Competitive searches for dark matter have been conducted using the nEDM spectrometer over the last decade. More ideas are still being explored to extend the limits on axion-like particles: a limit on the oscillating EDM signal at higher frequency (axion mass range up to 10^{-15} eV) is under study and dedicated data to push the limit of reference [10] are being analyzed.

Additionally, similar searches of axion-like particles are planned with the next generation n2EDM apparatus making use of the much improved sensitivity in the frequency measurements and of the better control over systematic effects. The not yet excluded regions of the signal bands of [40] for mirror neutrons will be a focus of future efforts.

References

[1] G. Pignol and P. Schmidt-Wellenburg, *The search for the neutron electric dipole moment at PSI*, SciPost Phys. Proc. **5**, 027 (2021), doi:10.21468/SciPostPhysProc.5.027.

[2] J. Moody and F. Wilczek, *New macroscopic forces?*, Phys. Rev. D **30**, 130 (1984), doi:10.1103/PhysRevD.30.130.

[3] C. Abel et al., *Search for axionlike dark matter through nuclear spin precession in electric and magnetic fields*, Phys. Rev. X **7**, 041034 (2017), doi:10.1103/PhysRevX.7.041034.

[4] C. Abel et al., *A search for neutron to mirror-neutron oscillations using the nEDM apparatus at PSI*, Phys. Lett. B **812**, 135993 (2021), doi:10.1016/j.physletb.2020.135993.

[5] R. Peccei and H. R. Quinn, *Constraints imposed by CP conservation in the presence of pseudoparticles*, Phys. Rev. D **16**, 1791 (1977), doi:10.1103/PhysRevD.16.1791.

[6] F. Wilczek and A. Zee, *Instantons and spin forces between massive quarks*, Phys. Rev. Lett. **40**, 83 (1978), doi:10.1103/PhysRevLett.40.83.

[7] G. Grilli di Cortona, E. Hardy, J. Pardo Vega and G. Villadoro, *The QCD axion, precisely*, J. High Energy Phys. **01**, 034 (2016), doi:10.1007/JHEP01(2016)034.

[8] D. A. Dicus, E. W. Kolb, V. L. Teplitz and R. V. Wagoner, *Astrophysical bounds on very low mass axions*, Phys. Rev. D **22**, 839 (1980), doi:10.1103/PhysRevD.22.839.

[9] J. Preskill, M. B. Wise and F. Wilczek, *Cosmology of the invisible axion*, Phys. Lett. B **120**, 127 (1983), doi:10.1016/0370-2693(83)90637-8.

[10] S. Afach et al., *Constraining interactions mediated by axion-like particles with ultracold neutrons*, Phys. Lett. B **745**, 58 (2015), doi:10.1016/j.physletb.2015.04.024.

[11] M. Guigue, D. Jullien, A. Petukhov and G. Pignol, *Constraining short-range spin-dependent forces with polarized ^3He*, Phys. Rev. D **92**, 114001 (2015), doi:10.1103/PhysRevD.92.114001.

[12] T. Lee and C.-N. Yang, *Question of parity conservation in weak interactions*, Phys. Rev. **104**, 254 (1956), doi:10.1103/PhysRev.104.254.

[13] I. Kobzarev, L. Okun and I. Pomeranchuk, *On the possibility of experimental observation of mirror particles*, Sov. J. Nucl. Phys. **3**, 837 (1966).

[14] R. Foot, H. Lew and R. Volkas, *Possible consequences of parity conservation*, Mod. Phys. Lett. A **7**, 2567 (1992), doi:10.1142/S0217732392004031.

[15] R. Foot, H. Lew and R. Volkas, *A model with fundamental improper space-time symmetries*, Phys. Lett. B **272**, 67 (1991), doi:10.1016/0370-2693(91)91013-L.

[16] Z. Berezhiani, *Mirror world and its cosmological consequences*, Int. J. Mod. Phys. A **19**, 3775 (2004), doi:10.1142/S0217751X04020075.

[17] H. Hodges, *Mirror baryons as the dark matter*, Phys. Rev. D **47**, 456 (1993), doi:10.1103/PhysRevD.47.456.

[18] Z. Berezhiani, *Unified picture of ordinary and dark matter genesis*, Eur. Phys. J. ST **163**, 271 (2008), doi:10.1140/epjst/e2008-00824-6.

[19] R. Foot, *Mirror dark matter interpretations of the DAMA, CoGeNT and CRESST-II data*, Phys. Rev. D **86**, 023524 (2012), doi:10.1103/PhysRevD.86.023524.

[20] R. Foot, *Mirror dark matter: Cosmology, galaxy structure and direct detection*, Int. J. Mod. Phys. A **29**, 1430013 (2014), doi:10.1142/S0217751X14300130.

[21] R. Foot, *Experimental implications of mirror matter - type dark matter*, Int. J. Mod. Phys. A **19**, 3807 (2004), doi:10.1142/S0217751X04020087.

[22] V. Berezinsky, M. Narayan and F. Vissani, *Mirror model for sterile neutrinos*, Nucl. Phys. B **658**, 254 (2003), doi:10.1016/S0550-3213(03)00191-3.

[23] E. K. Akhmedov, Z. G. Berezhiani and G. Senjanovic, *Planck scale physics and neutrino masses*, Phys. Rev. Lett. **69**, 3013 (1992), doi:10.1103/PhysRevLett.69.3013.

[24] Z. G. Berezhiani and R. N. Mohapatra, *Reconciling present neutrino puzzles: Sterile neutrinos as mirror neutrinos*, Phys. Rev. D **52**, 6607 (1995), doi:10.1103/PhysRevD.52.6607.

[25] Z. Silagadze, *Neutrino mass and the mirror universe*, Phys. Atom. Nucl. **60**, 272 (1997), arXiv:hep-ph/9503481.

[26] L. Bento and Z. Berezhiani, *Leptogenesis via collisions: The Lepton number leaking to the hidden sector*, Phys. Rev. Lett. **87**, 231304 (2001), doi:10.1103/PhysRevLett.87.231304.

[27] Z. Berezhiani, *Neutron–antineutron oscillation and baryonic majoron: low scale spontaneous baryon violation*, Eur. Phys. J. C **76**, 705 (2016), doi:10.1140/epjc/s10052-016-4564-0.

[28] Z. Berezhiani and A. Gazizov, *Neutron oscillations to parallel world: Earlier end to the cosmic ray spectrum?*, Eur. Phys. J. C **72**, 2111 (2012), doi:10.1140/epjc/s10052-012-2111-1.

[29] Z. Berezhiani and L. Bento, *Fast neutron: Mirror neutron oscillation and ultra high energy cosmic rays*, Phys. Lett. B **635**, 253 (2006), doi:10.1016/j.physletb.2006.03.008.

[30] Z. Berezhiani, D. Comelli and F. L. Villante, *The Early mirror universe: Inflation, baryogenesis, nucleosynthesis and dark matter*, Phys. Lett. B **503**, 362 (2001), doi:10.1016/S0370-2693(01)00217-9.

[31] Z. Berezhiani, *Through the looking-glass: Alice's adventures in mirror world*, In From Fields to Strings: Circumnavigating Theoretical Physics: A Conference in Tribute to Ian Kogan, 2147, doi:10.1142/9789812775344_0055 (2005).

[32] L. Okun, *Mirror particles and mirror matter: 50 years of speculations and search*, Phys. Usp. **50**, 380 (2007), doi:10.1070/PU2007v050n04ABEH006227.

[33] Z. Berezhiani, *More about neutron - mirror neutron oscillation*, Eur. Phys. J. C **64**, 421 (2009), doi:10.1140/epjc/s10052-009-1165-1.

[34] Y. Pokotilovski, *On the experimental search for neutron —> mirror neutron oscillations*, Phys. Lett. B **639**, 214 (2006), doi:10.1016/j.physletb.2006.06.005.

[35] G. Ban et al., *Direct experimental limit on neutron–mirror-neutron oscillations*, Phys. Rev. Lett. **99**, 161603 (2007), doi:10.1103/PhysRevLett.99.161603.

[36] A. Serebrov et al., *Experimental search for neutron–mirror neutron oscillations using storage of ultracold neutrons*, Phys. Lett. B **663**, 181 (2008), doi:10.1016/j.physletb.2008.04.014.

[37] A. Serebrov et al., *Preparation of UCN facilities for fundamental research at PNPI*, Nucl. Instrum. Meth. A **611**, 276 (2009), doi:10.1016/j.nima.2009.07.078.

[38] I. Altarev et al., *Neutron to mirror-neutron oscillations in the presence of mirror magnetic fields*, Phys. Rev. D **80**, 032003 (2009), doi:10.1103/PhysRevD.80.032003, 0905.4208.

[39] Z. Berezhiani and F. Nesti, *Magnetic anomaly in UCN trapping: signal for neutron oscillations to parallel world?*, Eur. Phys. J. C **72**, 1974 (2012), doi:10.1140/epjc/s10052-012-1974-5.

[40] Z. Berezhiani, R. Biondi, P. Geltenbort, I. Krasnoshchekova, V. Varlamov, A. Vassiljev and O. Zherebtsov, *New experimental limits on neutron - mirror neutron oscillations in the presence of mirror magnetic field*, Eur. Phys. J. C **78**, 717 (2018), doi:10.1140/epjc/s10052-018-6189-y.

Current status and prospects of muonium spectroscopy at PSI

Ben Ohayon, Zakary Burkley and Paolo Crivelli⋆

ETH Zurich, Institute of Particle Physics and Astrophysics, 8093 Zurich, Switzerland

⋆ paolo.crivelli@cern.ch

Abstract

Recent and ongoing developments of low energy muon beamlines are heralding a new era of precision Muonium spectroscopy. While past spectroscopic measurements of Muonium were performed at pulsed muon facilities and were statistically limited, the advent of continuous low energy muon beams, such as at the LEM beamline at PSI, paired with the development of efficient muon-muonium converters and laser advancements, will overcome these limitations. Current experiments presently underway at the LEM facility and in the near future at the muCool beamline, which is under development at PSI, aim to improve the precision of both the 1S-2S transition determination and Lamb shift by several orders of magnitude. In this Chapter we give an overview of the current status and future prospects of these activities at PSI, highlighting how their projected significance fits into a broader context of other ongoing efforts worldwide.

29.1 Introduction

The usefulness of precision spectroscopy for atomic systems with a hadronic nucleus is limited by our knowledge of quantum chromodynamics (QCD), which is not yet tractable at low energies. As an example, the hyperfine structure of the ground state of hydrogen was measured to better than the part-per-trillion (ppt) precision half a century ago but theoretical calculations are limited by proton structure and other hadronic effects to the level of parts-per-million (ppm) [1]. Pure leptonic systems, such as positronium (Ps) and Muonium (M), are hydrogenic atoms composed of point-like particles. As such, they are devoid of finite-size effects and largely free of other hadronic contributions, making them ideal for determining fundamental constants, testing bound-state QED, and searching for new physics. Specific scenarios include the search for dark-sector particles and new muonic forces [2], as well as testing Lorentz and CPT symmetry [3].

Ps spectroscopy is an active field with current efforts focused on measuring optical and microwave transitions from its ground [4] and first-excited states [5,6]. The recent measurement of the Ps $n = 2$ fine-structure is 4.5 standard deviations from its calculated value [6],

which motivates further investigations of this system. The linewidth of low-lying transitions in Ps is inherently limited by the triplet annihilation lifetime of 142 ns in the ground-state and 1136 ns in the 2S state. Its light mass, and corresponding high velocity, poses great challenges to determining first and second-order Doppler effects.

With a longer lifetime of 2196.9803(22) ns [7], limited by the muon decay, and a larger mass, M is a more suitable candidate for precision spectroscopy experiments. Past M spectroscopy experiments were conducted between $1980 - 2000$ at TRIUMF, RAL and LAMPF (see [8] for a recent review). As a result of the difficulty in obtaining a high flux of μ^+, and the necessity to slow down the muons so that M can be formed efficiently, all past M spectroscopy experiments were essentially limited by statistics, or statistics-related systematic effects [8]. With its intense μ^+ beam, PSI harbours tremendous opportunities for improving M spectroscopy experiments. Higher statistics makes it possible to implement experimental techniques which are systematically more robust and precise. In this respect the Low-Energy-Muon (LEM) beamline at PSI plays a crucial role.

The development of the LEM beamline was motivated by the desire to apply the Muon Spin Rotation (μSR) technique to surface and thin film physics [9]. A high intensity surface ($E = 4.1$ MeV) muon beam from the μE4 beamline [10] is moderated to $\sim$15 eV by injecting it into a solid noble gas layer [9]. The beam is then re-accelerated to energies tunable in the range $1-30$ keV. The availability of an intense 10^4/s μ^+ beam in this energy range opens new possibilities for high precision M spectroscopy.

In this Chapter we review the ongoing measurements of the 1S-2S transition and the Lamb shift (LS) of muonium in the context of the MuoniuM lAser SpectroScopy (Mu-MASS) experiment at PSI. A future measurement of the muonium Fine Structure (FS) is also currently under consideration. A schematic overview of these efforts is given in Figure 29.1. The Muonium Spectroscopy Experiment Using Microwave (MuSEUM) is ongoing at J-PARC [11] aiming to improve the muonium HyperFine Splitting (HFS).
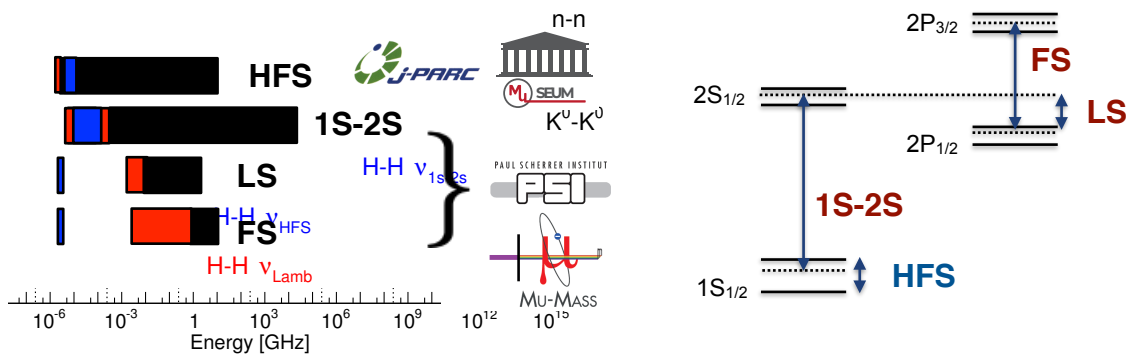
Figure 29.1: Left: M spectroscopy precision goals. Edges from right to left are: Transition frequency, highest precision literature value (black), precision goal of ongoing experiments (red), present or near-future magnitude of uncalculated QED terms (blue). Right: Schematic energy levels of M with planned and ongoing experiments at PSI (red) and J-PARC (blue).

29.2 Background

Strictly speaking, the fundamental constants that are prominent in the muonic sector at low energy are the muon mass and lifetime [12]. However, a general way of searching for physics beyond the standard model (SM) is to compare constants determined with different systems [13]. The relevant constants are the Rydberg constant R_∞, the muon magnetic moment μ_μ,

the fine structure constant α, and the muon mass m_μ.

Assuming the validity of high-order bound-state QED corrections, m_μ is [14]

$$\frac{m_\mu}{m_e} = 206.768281(2)(3), \tag{29.1}$$

where the first uncertainty is from the experimental M ground-state hyperfine splittings measurement $\Delta\nu_{\text{HFS}}$ [15], and the second is due to uncalculated QED terms [14], resulting in a combined relative uncertainty at a level 19 ppb. There is a strong motivation to 'free up' $\Delta\nu_{\text{HFS}}$ from having to determine m_μ. Currently, a 100 ppm test of bound-state QED corrections is achieved by comparing the experimental and theoretical ground-state, zero-field M hyperfine splitting [14]

$$\Delta\nu_{\text{HFS}}^{\text{th}} - \Delta\nu_{\text{HFS}}^{\text{ex}} = 96(51_{\text{ex}})(511_{\text{mass}})(70_{\text{QED}})\text{Hz}. \tag{29.2}$$

Here, one has to use the second-best determination of m_μ, at the level of 120 ppb, which comes from a high-field determination of the magnetic moment μ_μ through the Breit-Rabi technique [15], and does not depend strongly on QED corrections. It is apparent that our lack of an independent, accurate determination of m_μ is limiting the ability to test QED. This is especially true considering ongoing efforts to improve both experimental and theoretical errors on the M hyperfine splitting below 10 Hz [14, 16].

The Mu-MASS experiment is the measurement of the 1S-2S transition in M to the few ppt level. The reduced mass contributes to this transition at the 0.5% level and so, adopting the current value of R_∞, m_μ may be deduced from this experiment to the level of 1 ppb. This accuracy is a 20-fold improvement over the currently best known value given in eq. (29.1). From eq. (29.2) one can see that combining the results of Mu-MASS, MuSEUM, and the continued improvement in theoretical calculations will culminate in a 2 ppb comparison between experiment and theory.

Assuming the validity of QED corrections, the combination of Mu-MASS and MuSEUM will determine other fundamental constants. The fine structure constant α can be determined to 1 ppb. Even though this is not competitive to the current best determination [17, 18], it is an interesting byproduct measurement.

The current value of R_∞ is known to 2 ppt [19], and reflects a partial resolution of the proton radius puzzle [20]. The precision goal of ongoing M experiments will result in a determination of R_∞, independent of proton structure, with a comparable accuracy of 4 ppt. Adopting this value and obtaining the proton charge radius from the M-H isotope shift may further drive the proton radius puzzle to its resolution. The M R_∞ could also be interpreted as a ppt level test of the absolute charge equality between e^- and μ^+, improving the previous limits by three orders of magnitudes [21]. Such a test is interesting in the context of possible lepton universality violation encountered in [22]. The 4σ departure from unitarity in the first row of the CKM matrix may also be interpreted as a hint for lepton flavour universality violation [23].

The anomalous magnetic moment of the muon $a_\mu = (g_\mu - 2)/2$ was calculated with an accuracy of 0.37 ppm recently in a massive effort [24]. It can be compared to the anomalous frequency ω_a, through the relation

$$a_\mu = \frac{\omega_a/\omega_p}{\mu_\mu/\mu_p - \omega_a/\omega_p}, \tag{29.3}$$

where ω_p is a free proton NMR frequency in the same magnetic field, and μ_μ is the magnetic moment of the muon derived from the Breit-Rabi measurement [15]. The combination of the recent measurement at Fermilab [25] with the previous one at BNL [26], results in a discrepancy of 4.2σ with the theoretical value extracted from dispersion relations [24]. However, it

should be noted that the discrepancy is reduced if one considers the latest lattice QCD calculations [27]. This motivates further improvements to both experiments and theory. The ongoing efforts at FNAL aim for an improvement of the current determination by a factor of four. At this level, more accurate values of either μ_μ or m_μ are needed as an input to the theory. The relationship between various quantities discussed in this section is portrayed in Figure 29.2.

In contrast to the hyperfine and gross-structure, the lamb shift in M is a pure bound-state QED correction, and so the desired precision to make a measurement interesting is less stringent. This is especially true for high order recoil and radiative-recoil corrections, which due to the lower mass of M are much larger than in H. The theoretical value for the LS is at the 2 ppm level [2], limited by uncalculated recoil contributions, and is four orders of magnitude more precise than the experimental determination. An improvement by factor of 100 or more on the current experimental accuracy of 1% will test QED corrections on the level of which they are currently tested by the HFS.
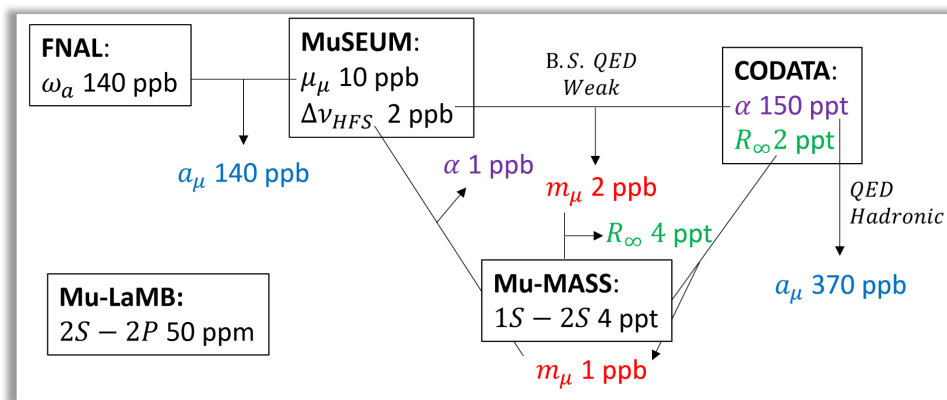

Figure 29.2: Relationship of experimental quantities measured in ongoing and planned M spectroscopy and storage ring experiments. Comparison of constants determined by different methods tests the validity of the theoretical calculations.

29.3 Ongoing Mu-MASS experiment at PSI

29.3.1 1S-2S transition

The best experimental determination of the value of the 1S-2S line in M is 2455528941.0(9.8) MHz [21], in good agreement with the predictions of bound-state QED which is 2455528935.4(1.4) MHz [28, 29]. The uncertainty of the theoretical value is dominated by our current knowledge of the muon mass (to 120 ppb) extracted with the Rabi-method [15]. The QED calculations are known with an accuracy of 20 kHz (8 ppt) [28–30], with prospects to improve by at least a factor of two in the near future [31].

The experiment was performed using the pulsed muon source at RAL. M atoms were formed in a SiO_2 powder and emerged into vacuum with a thermal Maxwell-Boltzmann velocity distribution at 296(10) K and a conversion efficiency per impinging muon of 2.2%. A fraction of them would then interact with a 244 nm counter-propagating pulsed laser beam inducing the 1S-2S transition detected via photoionization of the 2S M state in the same laser field. The combined excitation and detection efficiency on resonance was around 3×10^{-5} and a total of 99 events were collected for 3×10^6 laser shots.

The use of a pulsed laser for such a measurement imposes several limitations [8]. The rapid optical phase changes, due to the high intensity in the pulsed optical amplifiers, result in frequency variations within the laser pulse which can reach several tens of MHz. This so
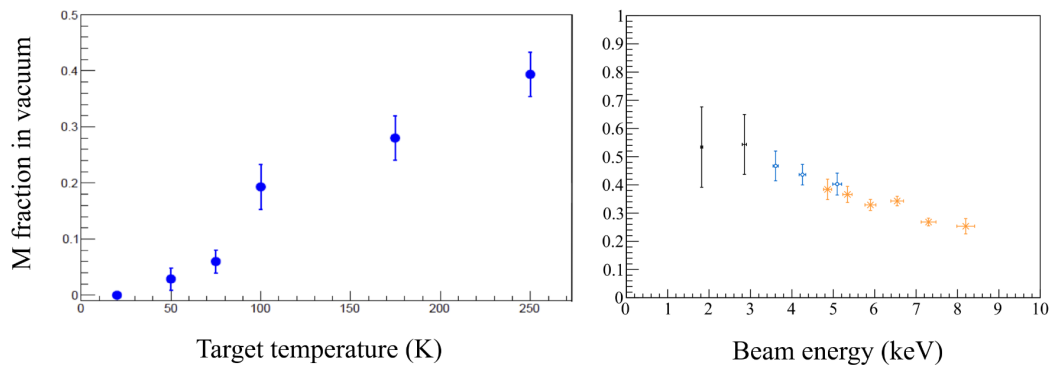
Figure 29.3: Efficient M production at the LEM beamline. Left: Fraction of muonium emitted into vacuum per incoming muon at 5 keV from porous silica thin films as a function of temperature. Reproduced with permission from [32]. Right: Fraction of muonium emerging from a thin carbon foil as a function of the exit energy. Reproduced with permission from [33]. The fraction of M formed in the 2*S* state is of the order of 10%.

called chirping effect, even if measured on a pulse-by-pulse basis, introduces a systematic error at the MHz level. In addition, the limited interaction time of the laser pulse with the atoms and the high instantaneous power results in a broadening of the experimental linewidth to 20 MHz. These issues can be completely resolved using a continuous wave (CW) laser for which the expected linewidth will be well below 1 MHz, limited by time-of-flight broadening. A crucial step in performing CW laser spectroscopy is the development at LEM of M converters emitting 20(40)% of the incident low-energy muons as M back into vacuum (see Figure 29.3) with a thermal Maxwell Boltzmann velocity distribution at 100(250) K and a cosine angular distribution [32,34]. The increased atom–laser interaction time will compensate for the lower available power compared to a pulsed laser. These new converters combined with the recent demonstration of high-power CW lasers at 243/244 nm [35,36] that can be cavity enhanced to more than 33 W of intracavity power [37] will enable an improved measurement of the 1S-2S transition frequency by three orders of magnitude which is the aim of the ongoing Mu-MASS experiment.

A schematic representation of Mu-MASS is given in Figure 29.4. A collimated beam of monoenergetic 5 keV μ^+ is focused using a segmented conical lens to a 6×20 mm target coated with a thin film of mesoporous silica where M atoms are formed. When muons hit the target, secondary electrons are emitted and guided to a nearby Micro-channel plate (MCP) detector. These electrons give a start signal to the data acquisition system. The M atoms emitted into vacuum travel through the waist of a cavity-enhanced laser beam, which on resonance excites them to the 2S state with an efficiency of few 10^{-6}. A pulsed electric field is used to mix the 2S and 2P states so that the radiative lifetime is reduced to a few ns. The Lyman-Alpha photon emitted in this quenching process is detected efficiently with a pair of CsI coated MCP detectors, giving a stop signal to the system which allows for a narrow (roughly 10 ns) detection window. To suppress the background to the required level, scintillation counters surround the system to detect the emitted positron from μ^+ decay in coincidence with the electron which was bound in the M system detected in the same MCP used for the secondary electrons, following the Ly-α detection. The estimated event rate is of order of few per hour and allows the 1 MHz transit-time-broadened linewidth to be resolved to below 100 kHz within 10 days. Further improvements in the detection and laser systems would further push the uncertainty limit to the final goal of 10 kHz.
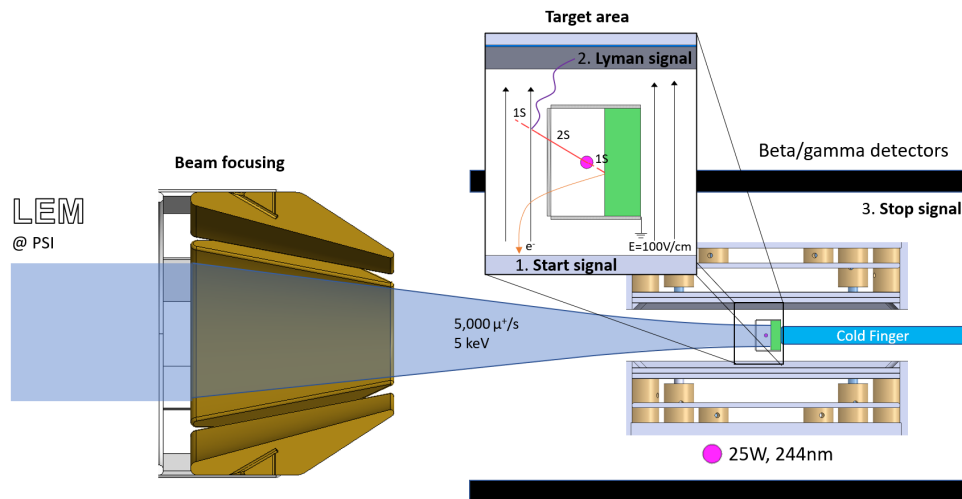
Figure 29.4: Schematic diagram of the Mu-MASS laser experiment.

29.3.2 n=2 Lamb Shift

The classical Lamb Shift of hydrogenic atoms $2S_{1/2}-2P_{1/2}$ is in the microwave (MW) range. In contrast with narrow two-photon transitions, allowed MW transitions are well-suited for measurements with a fast beam. In hydrogen, the most precise LS measurement was accomplished recently using charge exchange of a proton beam with velocity of $c/100$ with H_2 gas [38]. The linewidth of a single-pass resonance experiment is limited to 100 MHz by the radiative lifetime of the $2P$ state. To resolve this linewidth to a level of roughly 50 kHz, where systematic effects are expected to dominate [39], millions of $2S-2P$ detected transition events are needed. Clearly, M excitation from the ground state by either pulsed or CW laser is not suited for this task because of the low excitation probability.

On the other hand, it was demonstrated that M(2S) can be efficiently produced by using the so called beam-foil technique [40]. In this scheme, muons passing through a thin foil capture an electron to produce muonium with population in the levels with principal quantum number n scaling roughly as $1/n^3$. Based on hydrogen data and calculations, it is estimated that the 2S fraction is roughly $5-10\%$ [40], which agrees with experimental data [33]. After exiting the foil, np states decay rapidly, leaving a beam composed mainly of ground-state and M(2S) suitable for spectroscopy experiments.

Using the beam-foil technique, M in vacuum was first observed at LAMPF in 1981 with 4.0 MeV surface μ^+ at a rate of 3×10^6/s traveling through different foil materials [41]. A similar campaign was conducted at the same time in TRIUMF [42]. Having measured M(2S) in vacuum, both groups determined the LS, with the TRIUMF results achieving higher precision, and the value of $\nu_{LS} = 1070^{+12}_{-15}$ MHz [43], limited by statistics. Both groups used high-energy (> 2 MeV) μ^+ beams which had to be degraded to form M in the foil, creating a small signal above a large muon-related background. It is apparent that it is not only the accelerator intensity which was the limiting factor, but also the lack of a well-collimated μ^+ beam below 20 keV.

Recently at the PSI LEM beamline, it was demonstrated [33] that an intense/collimated M(2S) beam can be produced paving the way to an improved measurement of the LS in M which is ongoing. As shown Figure 29.5, monoenergetic μ^+ at 10 keV traverse an ultrathin (10 nm) carbon foil, creating M(2S) atoms with 2% efficiency while emitting secondary electrons. These electrons are guided to an MCP detector by an electrostatic field too weak to significantly quench the 2S beam. The 2S beam then traverses a hyperfine selection transmission line which quenches $2S_{F=1}$ states, followed by another transmission line tuned around the

$2S_{F=0} - 2P_{1/2,F=1}$ resonance around 600 MHz. On resonance the atoms reach the detection stage, which consist of a strong electrostatic quenching field and two CsI-coated MCP detectors detecting Ly-α photons. To reduce the background, an MCP detector in the back is used in coincidence. A Monte-Carlo simulation of the experiment predicts that the linewidth can be resolved below 1 MHz within a few days of beamtime, constituting an improvement over the state-of-the-art by more than one order of magnitude.
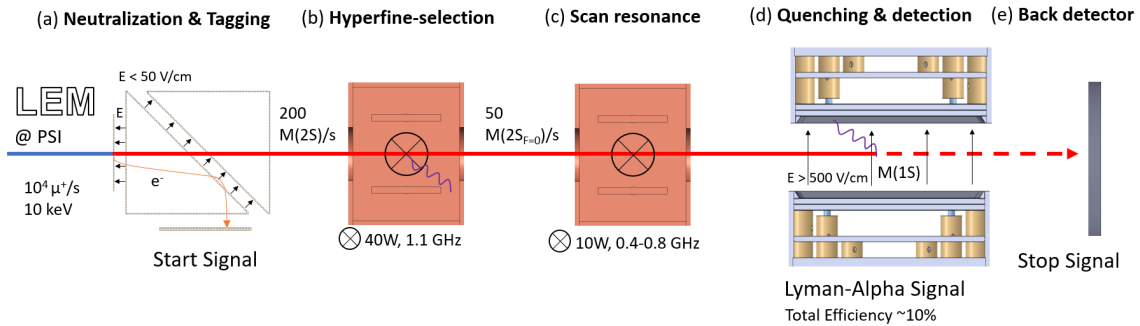

Figure 29.5: Overview of the scheme for the Lamb shift measurement.

29.4 Summary and Outlook

All previous M spectroscopic measurements were performed at pulsed muon facilities and were statistically limited. The demonstration at PSI of the production of ground state M atoms emitted into vacuum at cryogenic temperatures [32] and a high intensity metastable M 2S beam [33] will allow past limitations to be overcome. The Mu-MASS final goal is to measure the 1S-2S energy to 10 kHz which is an improvement by a factor of 1000 compared to the current results. The current projected accuracy for the Lamb shift measurement at LEM is at a level of 1 MHz. Paired with ongoing work on the HFS at J-PARC, those measurements will result in a stringent test of bound-state QED, the determination of fundamental constants, and tests of new physics.

The development of muCool [16] and the high intensity Muon Beam (HiMB) [44] will further increase the available statistics by orders of magnitude. This will help to implement more systematically robust measurement schemes, such as the employment of an enhancement cavity with a larger laser beam to reduce AC-stark shift in the 1S-2S measurement and the use of variations of Ramsey-spectroscopy to measure the Lamb shift.

References

[1] S. G. Karshenboim, *Nuclear structure-dependent radiative corrections to the hydrogen hyperfine splitting*, Phys. Lett. A **225**, 97 (1997), doi:10.1016/S0375-9601(96)00861-4.

[2] C. Frugiuele, J. Pérez-Ríos and C. Peset, *Current and future perspectives of positronium and muonium spectroscopy as dark sectors probe*, Phys. Rev. D **100**, 015010 (2019), doi:10.1103/PhysRevD.100.015010.

[3] A. H. Gomes, V. Alan Kostelecký and A. J. Vargas, *Laboratory tests of Lorentz and CPT symmetry with muons*, Phys. Rev. D **90**, 076009 (2014), doi:10.1103/PhysRevD.90.076009.

[4] A. Ishida, T. Namba, S. Asai, T. Kobayashi, H. Saito, M. Yoshida, K. Tanaka and A. Yamamoto, *New precision measurement of hyperfine splitting of positronium*, Phys. Lett. B **734**, 338 (2014), doi:10.1016/j.physletb.2014.05.083.

[5] M. W. Heiss, G. Wichmann, A. Rubbia and P. Crivelli, *The positronium hyperfine structure: Progress towards a direct measurement of the 23S1 → 21S0 transition in vacuum*, J. Phys.: Conf. Ser. **1138**, 012007 (2018), doi:10.1088/1742-6596/1138/1/012007.

[6] L. Gurung, T. J. Babij, S. D. Hogan and D. B. Cassidy, *Precision microwave spectroscopy of the positronium n=2 fine structure*, Phys. Rev. Lett. **125**, 073002 (2020), doi:10.1103/PhysRevLett.125.073002.

[7] D. M. Webber et al., *Measurement of the positive muon lifetime and determination of the Fermi constant to part-per-million precision*, Phys. Rev. Lett. **106**, 041803 (2011), doi:10.1103/PhysRevLett.106.041803.

[8] K. P. Jungmann, *Precision muonium spectroscopy*, J. Phys. Soc. Jpn. **85**, 091004 (2016), doi:10.7566/JPSJ.85.091004.

[9] E. Morenzoni, F. Kottmann, D. Maden, B. Matthias, M. Meyberg, Th. Prokscha, Th. Wutzke and U. Zimmermann, *Generation of very slow polarized positive muons*, Phys. Rev. Lett. **72**, 2793 (1994), doi:10.1103/PhysRevLett.72.2793.

[10] T. Prokscha, E. Morenzoni, K. Deiters, F. Foroughi, D. George, R. Kobler, A. Suter and V. Vrankovic, *The new beam at PSI: A hybrid-type large acceptance channel for the generation of a high intensity surface-muon beam*, Nucl. Instr. Meth. Phys. Res. Sec. A **595**, 317 (2008), doi:10.1016/j.nima.2008.07.081.

[11] S. Kanda et al., *New precise spectroscopy of the hyperfine structure in muonium with a high-intensity pulsed muon beam*, Phys. Lett. B **815**, 136154 (2021), doi:10.1016/j.physletb.2021.136154.

[12] M. Tanabashi, K. Hagiwara, K. Hikasa, K. Nakamura, Y. Sumino, F. Takahashi, J. Tanaka, K. Agashe, G. Aielli, C. Amsler, M. Antonelli and Asner, *Review of particle physics*, Phys. Rev. D **98**, 030001 (2018), doi:10.1103/PhysRevD.98.030001.

[13] R. H. Parker, C. Yu, W. Zhong, B. Estey and H. Müller, *Measurement of the fine-structure constant as a test of the Standard Model*, Science **360**, 191 (2018), doi:10.1126/science.aap7706.

[14] M. I. Eides, *Hyperfine splitting in muonium: Accuracy of the theoretical prediction*, Phys. Lett. B **795**, 113 (2019), doi:10.1016/j.physletb.2019.06.011.

[15] W. Liu et al., *High precision measurements of the ground state hyperfine structure interval of muonium and of the muon magnetic moment*, Phys. Rev. Lett. **82**, 711 (1999), doi:10.1103/PhysRevLett.82.711.

[16] A. Antognini et al., *Demonstration of muon-beam transverse phase-space compression*, Phys. Rev. Lett. **125**, 164802 (2020), doi:10.1103/PhysRevLett.125.164802.

[17] R. H. Parker, C. Yu, W. Zhong, B. Estey and H. Müller, *Measurement of the fine-structure constant as a test of the Standard Model*, Science **360**, 191 (2018), doi:10.1126/science.aap7706.

[18] L. Morel, Z. Yao, P. Cladé and S. Guellati-Khélifa, *Determination of the fine-structure constant with an accuracy of 81 parts per trillion*, Nature **588**, 61 (2020), doi:10.1038/s41586-020-2964-7.

[19] E. Tiesinga, P. J. Mohr, D. B. Newell and B. N. Taylor, *The 2018 codata recommended values of the fundamental physical constants*, Codata.org **8** (2019).

[20] J.-P. Karr and D. Marchand, *Progress on the proton-radius puzzle*, Nature **575**, 61 (2019), doi:10.1038/d41586-019-03364-z.

[21] V. Meyer et al., *Measurement of the 1s − 2s energy interval in muonium*, Phys. Rev. Lett. **84**, 1136 (2000), doi:10.1103/PhysRevLett.84.1136.

[22] R. Aaij et al., *Measurement of CP-averaged observables in the $B^0 \rightarrow K^{*0}\mu^+\mu^-$ decay*, Phys. Rev. Lett. **125**, 011802 (2020), doi:10.1103/PhysRevLett.125.011802.

[23] A. Crivellin and M. Hoferichter, *β decays as sensitive probes of lepton flavor universality*, Phys. Rev. Lett. **125**, 111801 (2020), doi:10.1103/PhysRevLett.125.111801.

[24] T. Aoyama et al., *The anomalous magnetic moment of the muon in the Standard Model*, Phys. Rep. **887**, 1 (2020), doi:10.1016/j.physrep.2020.07.006.

[25] B. Abi, *Measurement of the positive muon anomalous magnetic moment to 0.46 ppm*, Phys. Rev. Lett. **126**, 141801 (2021), doi:10.1103/PhysRevLett.126.141801.

[26] G. W. Bennett et al., *Final report of the E821 muon anomalous magnetic moment measurement at BNL*, Phys. Rev. D **73**, 072003 (2006), doi:10.1103/PhysRevD.73.072003.

[27] Sz. Borsanyi et al., *Leading hadronic contribution to the muon magnetic moment from lattice QCD*, Nature **593**, 51 (2021), doi:10.1038/s41586-021-03418-1.

[28] K. Pachucki, D. Leibfried, M. Weitz, A. Huber, W. König and T. W. Hänsch, *Theory of the energy levels and precise two-photon spectroscopy of atomic hydrogen and deuterium*, J. Phys. B: At. Mol. Opt. Phys. **29**, 177 (1996), doi:10.1088/0953-4075/29/2/008.

[29] S. G. Karshenboim, *The Lamb shift of excited s-levels in hydrogen and deuterium atoms*, Zeitschrift für Physik D Atoms, Molecules and Clusters **39**, 109 (1997), doi:10.1007/s004600050116.

[30] M. I. Eides, H. Grotch and V. A. Shelyuto, *Theory of light hydrogenlike atoms*, Phys. Rep. **342**, 63 (2001), doi:10.1016/S0370-1573(00)00077-6.

[31] S. G. Karshenboim, Private Communication (2020).

[32] A. Antognini et al., *Muonium emission into vacuum from mesoporous thin films at cryogenic temperatures*, Phys. Rev. Lett. **108**, 143401 (2012), doi:10.1103/PhysRevLett.108.143401.

[33] G. Janka et al., *Intense beam of metastable Muonium*, Eur. Phys. J. C **80**, 804 (2020), doi:10.1140/epjc/s10052-020-8400-1.

[34] K. S. Khaw, A. Antognini, T. Prokscha, K. Kirch, L. Liszkay, Z. Salman and P. Crivelli, *Spatial confinement of muonium atoms*, Phys. Rev. A **94**, 022716 (2016), doi:10.1103/PhysRevA.94.022716.

[35] Z. Burkley, A. D. Brandt, C. Rasor, S. F. Cooper and D. C. Yost, *Highly coherent, watt-level deep-UV radiation via a frequency-quadrupled Yb-fiber laser system*, Appl. Opt. **58**, 1657 (2019), doi:10.1364/AO.58.001657.

[36] Z. Burkley, L. de Sousa Borges, B. Ohayon, A. Golovozin, J. Zhang and P. Crivelli, *Stable high power deep-UV enhancement cavity in ultra high vacuum with fluoride coatings* (2021), arXiv:2105.14977.

[37] S. Cooper, Z. Burkley, A. Brandt, C. Rasor and D. Yost, *Cavity-enhanced deep ultraviolet laser for two-photon cooling of atomic hydrogen*, Optics Lett. **43**, 1375 (2018).

[38] N. Bezginov, T. Valdez, M. Horbatsch, A. Marsman, A. C. Vutha and E. A. Hessels, *A measurement of the atomic hydrogen Lamb shift and the proton charge radius*, Science **365**, 1007 (2019), doi:10.1126/science.aau7807.

[39] D. A. Andrews and G. Newton, *Radio-frequency atomic beam measurement of the* $(2^2s_{\frac{1}{2}}, f = 0)$-$(2^2p_{\frac{1}{2}}, f = 1)$ *Lamb-shift interval in hydrogen*, Phys. Rev. Lett. **37**, 1254 (1976), doi:10.1103/PhysRevLett.37.1254.

[40] C. Fry, J. Warren, R. Kiefl, C. Oram, G. Ludgate, P. Schmor, A. Olin, G. Marshall, B. Erickson and G. Morris, *Observation of epithermal 2s muonium*, Hyperfine Inter. **18**, 691 (1984).

[41] P. R. Bolton et al., *Observation of muonium in vacuum*, Phys. Rev. Lett. **47**, 1441 (1981), doi:10.1103/PhysRevLett.47.1441.

[42] C. J. Oram, C. A. Fry, J. B. Warren, R. F. Kiefl and J. H. Brewer, *Observation of the 2S state of muonium in a vacuum*, J. Phys. B: At. Mol. Phys. **14**, L789 (1981), doi:10.1088/0022-3700/14/23/007.

[43] C. J. Oram, J. M. Bailey, P. W. Schmor, C. A. Fry, R. F. Kiefl, J. B. Warren, G. M. Marshall and A. Olin, *Measurement of the Lamb shift in muonium*, Phys. Rev. Lett. **52**, 910 (1984), doi:10.1103/PhysRevLett.52.910.

[44] K. Kirch, *Slow muons and muonium*, In Proceedings of the Seventh Meeting on CPT and Lorentz Symmetry, pp. 53, World Scientific (2017).

muCool: muon cooling for high-brightness μ^+ beams

Aldo Antognini[1,2⋆] and David Taqqu[1,2]

1 Institute for Particle Physics and Astrophysics, ETH Zurich, 8093 Zurich, Switzerland
2 Paul Scherrer Institute, 5232 Villigen–PSI, Switzerland

⋆ aldo@phys.ethz.ch

Abstract

A number of experiments with muons are limited by the poor phase space quality of the muon beams currently available. The muCool project aims at developing a phase-space cooling method to transform a surface μ^+ beam with 4 MeV energy and 1 cm size into a slow muon beam with eV energy and 1 mm size. In this process the phase space is reduced by a factor of $10^9 - 10^{10}$ with efficiencies of $2 \cdot 10^{-5} - 2 \cdot 10^{-4}$. The beam is then re-accelerated to keV-MeV energies. Such a beam opens up new avenues for research in fundamental particle physics with muons and muonium atoms as well as in the field of μSR spectroscopy.

30.1 Introduction

Precision experiments with muons [1] require muon beams with large rates and low energy. Thus experiments often make use of secondary beam lines with large acceptance tuned to transport surface muons with momentum $p = 29$ MeV/c (equivalent to 4 MeV kinetic energy). These μ^+ are copiously created by π^+ stopping close to the surface of the pion production target. Muons of lower momenta, from π^+ decaying below the surface of the target, can also be extracted from the production target. However, because of the momentum straggling in the target, the intensity of these sub-surface muon beams decreases rapidly with momentum ($p^{3.5}$-dependence [2]).

The large area of the production target, the scattering in the target, and the large acceptance of the secondary beamline result in muon beams with poor phase space quality ($\sigma_{x,y} \approx 10$ mm, $\theta_{x,y} \approx 100$ mrad) [3–5]. The muCool project aims to improve the phase-space quality of these secondary μ^+ beams by a factor of $10^9 - 10^{10}$ while reducing the efficiency by only $2 \cdot 10^{-5} - 2 \cdot 10^{-4}$, transforming a standard secondary μ^+ beam into a sub-mm keV beam.

30.2 The muCool compression scheme

In the proposed muCool scheme [6], a surface muon beam propagating in the $-z$-direction is slowed down in a He gas target featuring a strong electric (E) field inside a strong magnetic (B) field as shown in Figure 30.1. In the slowing-down process, the muon energy is rapidly reduced to the eV range where the E-field becomes important. The E-field, in conjunction with the B-field and gas density gradients, leads to drifting of the slowed-down muons drastically reducing their initially large spatial extent. In this drift process in the gas, the muons are guided into a sub-mm spot.
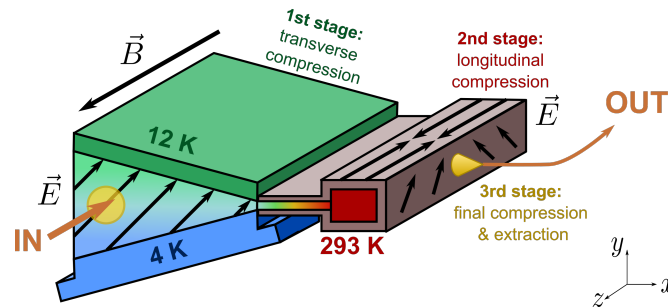

Figure 30.1: Schematic diagram of the muCool device. A surface muon beam is stopped in a cryogenic He gas target with a vertical temperature gradient inside a 5 T field. The extent of the stopped muons is reduced first in the transverse (y), then in the longitudinal (z) direction using a complex arrangement of E-field and gas density gradient. The compressed muon beam is then extracted through an orifice into vacuum and re-accelerated along the z-axis.

The drift velocity of the μ^+ in a gas with E- and B-fields is given by [7]

$$\vec{v}_D = \frac{\mu|\vec{E}|}{1 + \omega^2/\nu^2}\left[\hat{E} + \frac{\omega}{\nu}\hat{E} \times \hat{B} + \frac{\omega^2}{\nu^2}\left(\hat{E} \cdot \hat{B}\right)\hat{B}\right]. \tag{30.1}$$

In this equation μ is the muon mobility, $\omega = eB/m$ the cyclotron frequency of the muon, ν the average μ^+–He collision rate, and $\hat{E}$ and $\hat{B}$ the unit vectors of the electric and magnetic fields, respectively.

The spatial extent of the muon stop distribution decreases by making $\vec{v}_D$ position-dependent, so that μ^+ stopped at different locations in the target drift in different directions, and converge to a small spot. This can be achieved by applying a complex E-field pointing in different directions at different positions, and by making the collision frequency ν position-dependent through a height-dependent gas density.

The muCool setup is conceived as a sequence of stages having various density and electric field conditions. In the first stage, which is at cryogenic temperatures, the muon beam is stopped and compressed in y-direction (transverse compression). In the second stage, which is at room temperature, the muon beam is compressed in z-direction (longitudinal direction). In the third stage, the muons are extracted from the gas target into vacuum, re-accelerated in $-z$-direction, and extracted from the B-field.

The 4-MeV μ^+ beam with $\sigma_{x,y} \approx 10$ mm is degraded in a moderator and then stopped in the first stage of the muCool target containing the He gas at cryogenic temperatures and 10 mbar pressure. In this first stage, the third term in (30.1) is zero because $\vec{E} = (E_x, E_y, 0)$, with $E_x = E_y \approx 1$ kV/cm, is perpendicular to the B-field $\vec{B} = (0, 0, -|B|)$ and at 45° with respect to the x-axis. The peculiarity of this stage is the presence of a strong temperature gradient

in vertical direction from about 4 K to 12 K as shown in Figure 30.1. At lower densities (top part of the target) the collision frequency $\nu \approx 3$ GHz is smaller than the cyclotron frequency $\omega \approx 4$ GHz and therefore $\vec{v}_D$ is dominated by the $\hat{E} \times \hat{B}$ term in (30.1). Hence, the muons that are stopped in the top part of the target move downwards (in $-y$-direction) while drifting in $+x$-direction. By contrast, at larger densities (bottom part of the target) the collision frequency $\nu \approx 55$ GHz is larger than the cyclotron frequency ω. Therefore, $\vec{v}_D$ in this region is dominated by the first term in (30.1), resulting in a drift velocity approximately in the $\hat{E}$ direction, so that muons stopped in the lower part of the target move upwards (in $+y$-direction) while drifting in $+x$-direction. Combining these considerations, we see that the first stage is used to stop the muons and to compress the vertical extension of the large stopping distribution.

The μ^+ drifting in x-direction then enter into the second stage, which is at room temperature and has a field $\vec{E} = (0, E_y, \pm E_z)$, with $E_y = 2E_z = 0.1$ kV/cm, with a strong z-component pointing towards $z = 0$. Because ν is small at room temperature, the μ^+ motion in this stage is dominated by the third term of (30.1) resulting in a fast reduction of the longitudinal extent. During this fast compression, the E_y-component (see $\hat{E} \times \hat{B}$ term in (30.1)) drifts the μ^+ in x-direction towards the extraction stage. From there, the compressed beam can be extracted though a small orifice into vacuum, and moved quickly into a region of low gas pressure where re-acceleration can occur. Finally the beam needs to be extracted from the solenoid through an iron grid that terminates the magnetic field lines.

30.3 Demonstration of transverse and longitudinal compression

To demonstrate transverse compression, a cryogenic target as sketched in Figure 30.2 (left) was constructed, capable of sustaining the needed temperature gradient in vertical direction [8]. The target walls were lined with conducting tracks held at high voltage to define a homogeneous electric field at 45° angle w.r.t. the x-axis. A 13 MeV/c sub-surface muon beam was injected into the target and the slowed down muons drifted in the x-direction towards the tip of the target, while being compressed in y-direction by the combined action of the E- and B-fields, as well as the density gradient. A simulation of the μ^+ trajectories is shown in Figure 30.2 (middle). To study the μ^+ motion, a system of plastic scintillators detecting the positrons from muon decay was placed around the target. The recorded time spectra (see Figure 30.2 (right)) of these detectors were compared to simulations and good agreement was found [8,9].

To test the longitudinal compression, a room temperature target as sketched in Figure 30.3 (left) has been constructed with a wall-lining defining E-field with components in z- and y-direction [10, 11]. A 10 MeV/c muon beam was injected and slowed down in the elongated target. Muons drifted towards the target mid-plane at $z = 0$ using the z-components of the E-field while the y-component drifted the μ^+ in the x-direction. Such behavior is demonstrated by the simulated trajectories in Figure 30.3 (middle). A scintillator telescope (T1&T2), visible in Figure 30.3 (left) is used to measure the μ^+ accumulating around $z = 0$. The measured time spectrum given in red in Figure 30.3 (right) shows that muons can be attracted in a short time to the $z = 0$ plane. Also in this case, good agreement between simulated and measured time spectra has been observed [11].

Summarizing, both transverse and longitudinal compression have been tested independently [9]. The observed time spectra for various experimental conditions behave as expected from simulations, validating the simulations, in particular the assumed cross sections obtained from scaling of proton data [9].
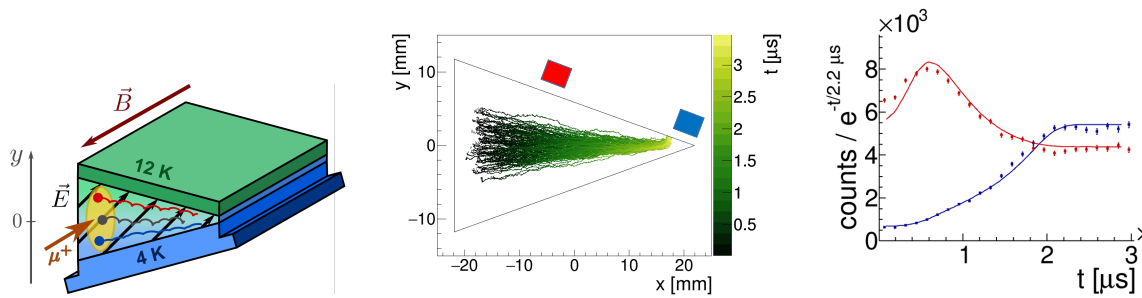
Figure 30.2: (Left) Sketch of the target used to test the transverse compression. (Middle) GEANT4 simulation of muon trajectories starting at $x \approx -15$ mm and drifting with time in $+x$-direction while compressing in the y-direction. The approximate positions of two plastic scintillators (red, blue) used to measure decay positrons are indicated. (Right) Measured and simulated time spectra for the two plastic scintillators indicated in the middle panel. The time zero is given by a counter detecting the muon entering the target. The counts are lifetime compensated, i.e., divided by $e^{-t/2.2\,\mu s}$.

30.4 Shortcut: the mixed transverse-longitudinal compression

According to the scheme of Figure 30.1 the next step would be to develop a target where the transverse compression stage is followed by a longitudinal compression stage. For this purpose, a connection between the cryogenic and the room temperature parts must be realized, with a short μ^+ transit time. To avoid this challenge, a cryogenic target has been developed, in which both transverse and longitudinal compression occur simultaneously [9]. Such a mixed transverse-longitudinal compression target can be realized by adding a longitudinal component to the E-field of the transverse target (see Figure 30.4 (left)). The resulting μ^+ motion in this target is sketched in Figure 30.4 (right).

Targets based on this concept have been simulated, developed and commissioned. The measured performance confirms the validity of this approach and of the simulations. They show that in the target a muon stop distribution with volume $\Delta x \times \Delta y \times \Delta z = 10 \times 10 \times 50$ mm^3 can be transformed within about $5\,\mu s$ into a beam drifting in x-direction in the He gas with 10 eV kinetic energy and capable of passing an aperture of $\Delta y \times \Delta z = 1 \times 1$ mm^2 size with efficiency larger that 50% (excluding muon decay losses).

The simplicity of this target and the shortening of the total (transverse + longitudinal) compression time is a major advantage of this configuration compared to the original proposal [6]. Its major downside is the shorter active region in $z-$direction which is limited by the time needed for the longitudinal compression at the much higher gas density compared to the scheme in the original proposal with longitudinal compression at room temperature.

30.5 Vacuum extraction and re-acceleration

The mixed-compression target can be modified to allow μ^+ extraction from the gas target into "vacuum" through an orifice of about 1 mm diameter. To compensate for the He atoms leaving the target through the same orifice, new He gas has to be continuously injected into the system. We plan to inject the He gas right at the orifice, perpendicular to the μ^+ motion (see Figure 30.5 (left)), so that the injected gas acts as a barrier for the target gas. The injected gas needs to be efficiently evacuated through a system of differentially pumped regions, so that the μ^+ leaving the target experience a rapid decrease of the collision rates with the He atoms,
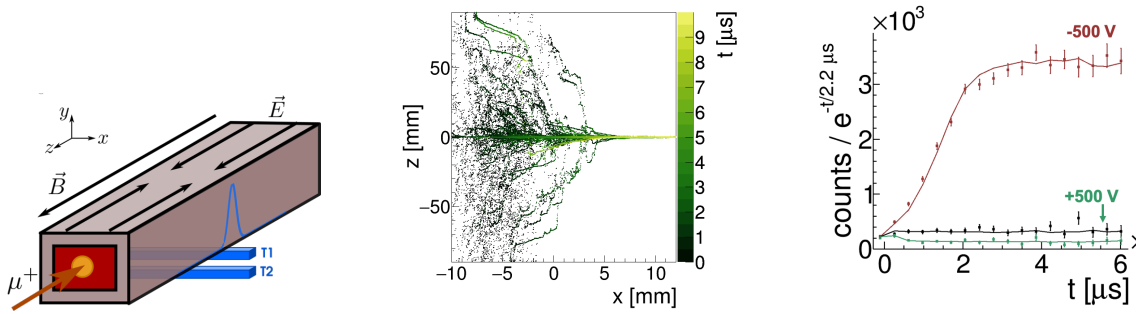
Figure 30.3: (Left) Sketch of the setup used to test the longitudinal compression. The scintillators T1 and T2 in coincidence constrain the μ^+ accumulating to $z \approx 0$. The blue curve indicates the region of acceptance for coincident events. (Middle) Simulated μ^+ trajectories. (Right) Measured and simulated time spectra for negative HV (red), positive HV (green) and no HV (black) at the target mid plane. The counts are lifetime compensated.
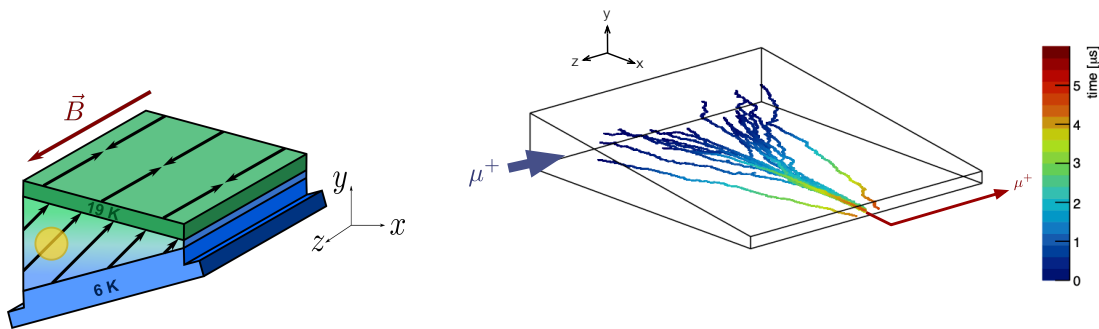

Figure 30.4: (Left) Sketch of the mixed transverse-longitudinal compression target with a vertical density gradient, E_x and E_y components as in the transverse compression target, and an E_z component pointing to the target mid-plane at $z = 0$. (Right) Sketch of the muon trajectories in the mixed-compression target.

which is necessary to maintain a good beam quality.

We plan to define the electric field for the μ^+ transport out of the target by adding six electrodes at the tip of the target as shown in Figure 30.5. The two electrodes at $z = 0$, connected to the high-voltages HV2 and HV5, define an E-field pointing in y-direction to drift the muons in $+x$-direction from the gas target to the re-acceleration region. The other two pairs of electrodes connected to the high-voltages HV3,6 and HV1,4 are kept at a slightly larger potential compared to HV2 and HV5 to define a V-shaped potential in z-direction with minimum at $z = 0$. This V-shaped potential confines the μ^+ around $z \approx 0$ while they drift in $+x$-direction from the target to the re-acceleration region. A small electrode could be located in the re-acceleration region acting as a pulsed gate: for a short time it cancels one side of the V-shape potential barrier so that μ^+ in the gate region can escape the confinement and be re-accelerated in $-z$-direction to a kinetic energy given by HV2 $\simeq$ HV5 $\approx$ 10 kV. Switching of this gate-electrode with high repetition rates up to about 1 MHz is needed to minimize losses in the accumulation and re-acceleration processes. Alternatively, the muon could be re-accelerated in $-z$-direction in a continuous way (without any pulsed gate) simply by modifying the six electrodes so that at a position along the x-axis (with sufficiently good vacuum conditions)

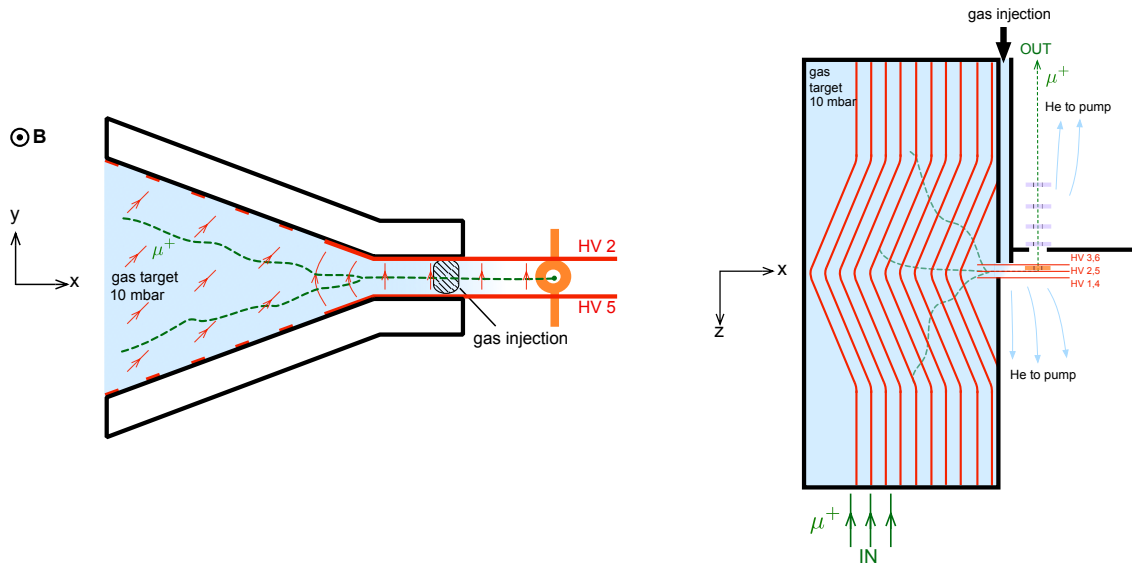one side of the V-shaped confinement (in $-z$-direction) is absent.

Figure 30.5: Schematic diagram (not to scale) of the baseline setup performing mixed longitudinal-transverse compression followed by vacuum extraction and re-acceleration. The electrodes are in red, the He gas flow is indicated by blue arrows, and muon trajectories are sketched in green. (Left) In the xy-plane the compression in vertical direction and the drift in x-direction is visible. In the orifice region, an E-field in y-direction, defined by the electrodes HV2 and HV5, is used to extract the muons from the gas target and to guide them in $+x$-direction due to the $\vec{E} \times \vec{B}$ drift. The electrode shown in orange is used as a pulsed gate to accelerate the muons. (Right) Similar to left panel, but for the xz-plane where the longitudinal compression and the re-acceleration in $-z$ direction are well visible.

30.6 The new beam

The muCool target transforms an input beam of 4 MeV energy beam, 1 cm diameter, 100 mrad divergence and 500 keV energy spread into a beam moving in He gas with 10 eV energy and about 1 mm diameter. Using the already-commissioned mixed-compression target, this transformation occurs within $5\,\mu$s with efficiencies of 90%, for a target with an active region of 50 mm length. This observed performance can be used to estimate the total conversion efficiency from muons entering the He gas target at 4 MeV energy to muons exiting the B-field of the solenoid with a kinetic energy of about 10 keV. Several other losses occurring prior or after the muon compression in the gas target have to be included as summarized in Table 30.1. As can be seen from this table, the total baseline (that assumes the commissioned gas target as a reference point) compression efficiency is estimated to be $7.5 \cdot 10^{-5}$. Note that this efficiency does not include possible losses at the incoupling of the solenoid and also does not account for the transverse (geometrical) acceptance of the gas target.

A muCool setup with this baseline efficiency applied to the $\pi E5$ beamline delivering surface μ^+ at a rate of $2.1 \cdot 10^8\,\text{s}^{-1}$ (for the "slanted" target and 2.0 mA proton current), can yield a keV-energy beam with a rate of $2 \cdot 10^4\,\text{s}^{-1}$ and small phase space (40 mm mrad at 10 keV). Here, we assumed 25% incoupling losses due to reflections at the solenoid and transverse acceptance of the muCool target. Applied to the envisioned High Intensity Muon Beam HiMB, delivering μ^+ with a rate of $1 \cdot 10^{10}\,\text{s}^{-1}$, a muCool output rate of $3 \cdot 10^5\,\text{s}^{-1}$ could be reached, provided

Table 30.1: Estimate of the muCool baseline efficiency using the commissioned mixed-compression target as a reference point for the compression towards the orifice. We thus assume here a target having an active region of 50 mm length operated at 10 mbar pressure with a 6-20 K temperature gradient. The stopping probability of 0.6% has been simulated assuming a surface muon beam with 10% (FWHM) momentum bite. A 3% (FWHM) momentum bite would increase the stopping probability to 1.6%. All the other entries have only been estimated and depend strongly on the upcoming R&D results.

Efficiency	
$6 \cdot 10^{-3}$	Stopping probability in He gas within the active region of the target
$1 \cdot 10^{-1}$	Compression towards the orifice including muon decay losses (within 5 μs)
$6 \cdot 10^{-1}$	Extraction from the orifice
$4 \cdot 10^{-1}$	Drift from orifice to re-acceleration region (in about 2 μs)
$8 \cdot 10^{-1}$	Muon decay from re-acceleration region to iron grid
$7 \cdot 10^{-1}$	Transmission through iron grid terminating the B-field
$7.5 \cdot 10^{-5}$	Total baseline compression efficiency

the operational stability of the target is not disrupted by the higher degree of ionization of the high intensity muon beam (we assume 60% in-coupling losses).

The above-described baseline compression efficiency can be improved by extending the active region in z-direction, by increasing the longitudinal E-field strength, and by decreasing the gas temperature. At the cost of additional complexity, the stopping probability can be greatly increased by using a target with multiple active regions in z-direction, each having its own extraction orifice. In this case, the various beams exiting the target at different z-positions but same x- and y-positions, can be merged in the re-acceleration process into a single beam. The original scheme of Figure 30.1 can also be used to significantly extend the active region in z-direction. A moderate increase by a factor of 2 of the baseline efficiency would result in competitive beam rates of $4 \cdot 10^4$ s^{-1} and $5 \cdot 10^5$ s^{-1} when applying the muCool setup to the $\pi E5$ and the HiMB, respectively.

30.7 Selected possible applications

This new beam opens the way for next generation experiments with muons where the reduced phase-space is of great advantage.

The search for a muon EDM represents a well motivated channel for physics beyond the Standard Model [12]. While muon EDM searches with a sensitivity of 10^{-21} e cm are ongoing at Fermilab and J-PARC as a "by-product" of their efforts to measure the muon g-2 [13], a muon EDM experiment has been proposed at PSI based on a frozen-spin technique applied to a compact muon storage ring [14]. Preliminary studies show that a sensitivity of $6 \cdot 10^{-23}$ e cm could be reached in the PSI experiment using the μE1 beam at 125 MeV/c delivering $2 \cdot 10^8$ μ^+/s. Because of the small phase space acceptance of the storage ring, the coupling efficiency for the μE1 beam is only $2.5 \cdot 10^{-4}$ so that only $5 \cdot 10^4$ μ^+/s are stored in orbit. The muCool beam with a rate $5 \cdot 10^5$ s^{-1} accelerated to 125 MeV/c or 200 MeV/c would result in a larger rate of stored muons as it avoids the coupling losses into the storage ring due to its small phase space.

The muCool beam can also greatly improve μSR investigations of sub-mm samples. Because the pile-up effects in the typically 10 μs-long observation time window become increas-

ingly unsustainable for rates exceeding $5 \cdot 10^4$ s^{-1}, the full HiMB-muCool potential could be exploited by switching the keV-energy sub-mm beam between several μSR instruments operating simultaneously.

Muon to vacuum-muonium conversion is very efficient for keV-energy muons [15]. Hence, the sub-mm muCool beam at keV-energy could be converted into a high-brightness muonium source. This novel muonium source could be exploited to improve on the precision of muonium spectroscopy by orders of magnitude (e.g. the 1S-2S with a relative accuracy of 10^{-12} [16]), and could be used to study the influence of gravity on the muonium to investigate the gravitational interaction of antimatter and second generation leptons in the earth's gravitational field [17].

References

[1] T. P. Gorringe and D. W. Hertzog, *Precision muon physics*, Prog. Part. Nucl. Phys. **84**, 73 (2015), doi:10.1016/j.ppnp.2015.06.001.

[2] A. E. Pifer, T. Bowen and K. R. Kendall, *A high stopping density μ+ beam*, Nucl. Instr. Meth. **135**, 39 (1976), doi:10.1016/0029-554X(76)90823-5.

[3] T. Prokscha, E. Morenzoni, K. Deiters, F. Foroughi, D. George, R. Kobler, A. Suter and V. Vrankovic, *The new μ E 4 beam at PSI: A hybrid-type large acceptance channel for the generation of a high intensity surface-muon beam*, Nucl. Instr. Meth. Phys. Research A **595**, 317 (2008), doi:10.1016/j.nima.2008.07.081.

[4] J. Adam et al., *The MEG detector for $\mu^+ \rightarrow e + \gamma$ decay search*, Eur. Phys. J. C **73**, 2365 (2013), doi:10.1140/epjc/s10052-013-2365-2.

[5] F. Berg, L. Desorgher, A. Fuchs, W. Hajdas, Z. Hodge, P.-R. Kettle, A. Knecht, R. Lüscher, A. Papa, G. Rutar and M. Wohlmuther, *Target studies for surface muon production*, Phys. Rev. Accel. Beams **19**, 024701 (2016), doi:10.1103/PhysRevAccelBeams.19.024701.

[6] D. Taqqu, *Compression and extraction of stopped muons*, Phys. Rev. Lett. **97**, 194801 (2006), doi:10.1103/PhysRevLett.97.194801.

[7] W. Blum, W. Riegler and L. Rolandi, *The drift of electrons and ions in gases*, In Particle Detection with Drift Chambers pp. 1–48 (2008), doi:10.1007/978-3-540-76684-1_2.

[8] A. Antognini et al., *Demonstration of muon-beam transverse phase-space compression*, Phys. Rev. Lett. **125**, 164802 (2020), doi:10.1103/PhysRevLett.125.164802.

[9] I. Belosevic, *Simulation and experimental verification of transverse and longitudinal compression of positive muon beams: Towards a novel high-brightness low-energy muon beamline*, Thesis: PhD Zurich (2020), doi:10.3929/ETHZ-B-000402802.

[10] Y. Bao et al., *Muon cooling: Longitudinal compression*, Phys. Rev. Lett. **112**, 224801 (2014), doi:10.1103/PhysRevLett.112.224801.

[11] I. Belosevic et al., *muCool: a next step towards efficient muon beam compression*, Eur. Phys. J. C **79**, 430 (2019), doi:10.1140/epjc/s10052-019-6932-z.

[12] A. Crivellin, M. Hoferichter and P. Schmidt-Wellenburg, *Combined explanations of (g-2)μ,e and implications for a large muon EDM*, Phys. Rev. D **98**, 113002 (2018), doi:10.1103/PhysRevD.98.113002.

[13] R. Chislett, *The muon EDM in the g-2 experiment at Fermilab*, EPJ Web of Conferences **118**, 01005 (2016), doi:10.1051/epjconf/201611801005.

[14] A. Adelmann et al., *Search for a muon edm using the frozen-spin technique* (2021), arXiv:2102.08838.

[15] A. Antognini, P. Crivelli, T. Prokscha, K.-S. Khaw, B. Barbiellini, L. Liszkay, K. Kirch, K. Kwuida, E. Morenzoni, F. Piegsa, Z. Salman and A. Suter, *Muonium emission into vacuum from mesoporous thin films at cryogenic temperatures*, Phys. Rev. Lett. **108**, 143401 (2012), doi:10.1103/PhysRevLett.108.143401.

[16] P. Crivelli, *The Mu-MASS (muonium laser spectroscopy) experiment*, Hyperfine Inter. **239**, 49 (2018), doi:10.1007/s10751-018-1525-z.

[17] A. Antognini, D. Kaplan, K. Kirch, A. Knecht, D. Mancini, J. Phillips, T. Phillips, R. Reasenberg, T. Roberts and A. Soter, *Studying Antimatter Gravity with Muonium*, Atoms **6**, 17 (2018), doi:10.3390/atoms6020017.

Development of a cold atomic muonium beam
for next generation atomic physics and gravity experiments

Anna Sótér[1⋆] and Andreas Knecht[2]

1 ETH Zürich, John-von-Neumann-Weg 9, 8093 Zürich, Switzerland
2 Paul Scherrer Institut, CH-5232 Villigen, Switzerland

⋆ anna.soter@psi.ch

Abstract

A high-intensity, low-emittance atomic muonium (M $= \mu^+ + e^-$) beam is being developed, which would enable improving the precision of M spectroscopy measurements, and may allow a direct observation of the M gravitational interaction. Measuring the free fall of M atoms would be the first test of the weak equivalence principle using elementary antimatter (μ^+) and a purely leptonic system. Such an experiment relies on the high intensity, continuous muon beams available at the Paul Scherrer Institute (PSI, Switzerland), and a proposed novel M source. In this paper, the theoretical motivation and principles of this experiment are described.

31.1 Introduction

Muonium (M) is a two-body exotic atom consisting of a positive anti-muon (μ^+) and an electron (e^-). This purely leptonic system can be a unique precision probe to test bound-state QED without the influence of nuclear- and finite size effects. Laser spectroscopy of the M 1S-2S transition [1, 2], and microwave spectroscopy of the M ground state hyperfine structure [3] provided precision measurements of fundamental constants (muon mass, magnetic moment), while searches for muonium-antimuonium conversion put limits on the strength of charged lepton number violation [4]. Improvements in these measurements especially 1S-2S spectroscopy is strongly motivated by recent experiments measuring the anomalous muon $g-2$ [5]. A high intensity, cold atomic beam could significantly improve statistical limitations and systematic effects originating from the (residual) Doppler shift.

Another unique and so far unexplored facet of M is that its mass is dominated by the μ^+, which is not only an elementary antiparticle, but also a second-generation lepton. Direct measurement of the gravitational interaction, thereby tests the weak equivalence principle of such particles, has not yet been attempted [6, 7]. Besides muonium, only antihydrogen

($\bar{H} = \bar{p} + e^+$) [8–10] and positronium (Ps = $e^- + e^+$) [11–13] have been proposed as laboratory candidates for antimatter gravity experiments, and M is the only viable candidate for testing gravity with purely leptonic, second generation matter.

31.1.1 The weak equivalence principle

The Standard Model (SM), as any local, Lorentz-invariant quantum field theory, incorporates CPT symmetry - the simultaneous transformations of charge conjugation (C) parity transformation (P) and time reversal (T) - as an exact symmetry [14]. An important consequence of this is the equivalence of various measurable properties of matter and antimatter, such as the mass, the magnitude of the charge, and the strength of certain interactions. Comparative measurements between matter and antimatter put stringent limits on CPT violation by different experiments using mesons ($K_0 - \bar{K}_0$) [15] leptons ($e^+ - e^-$, $\mu^+ - \mu^-$) [16,17] and baryons ($p - \bar{p}$) [18–21].

With the lack of a unified theory of General Relativity (GR) and the SM, the considerations above however do not imply anything about the gravitational interaction of matter and antimatter. Our expectations originate from the assumed equivalency of the inertial and gravitational masses of particles, which is incorporated in GR as part of the equivalence principle [22,23]. The exact formulation of this principle varies in the literature, and frequently cited as a collective of some these statements below:

1. Weak equivalence principle (WEP) or *universality of free-fall*: all particles (and antiparticles) fall with the same acceleration in a gravitational field.

2. Local position invariance (LPI): The outcome of any local non-gravitational experiment is independent of its location in space or time. Experimental consequences:

   (a) the *universality of clocks* (WEP-c), meaning all systems regardless of their composition (e.g. matter or antimatter) experience the same local time.

   (b) the lack of *variation of fundamental constants* (WEP-v) in time.

3. Local Lorentz invariance (LLI): The outcome of any local non-gravitational experiment in a free-falling laboratory is independent of its velocity.

4. Strong equivalence principle (SEP): states LLI and LPI combined and extended to the gravitational measurements as well (e.g. test bodies with significant contributions from their own gravitational field.)

The combination of the above weak statements (LLI with LPI, sometimes WEP included) is frequently referred to as Einstein's equivalence principle. Most importantly, violation of one of these principles would not necessarily mean the violation of all, and depending on the underlying new physics, it would effect GR and the SM on different levels [23, 24]. Hence, testing the above equivalence principles independently in different experiments using different SM particles is essential [22, 23, 25].

For example, in Earth-based or satellite-borne laboratories, gravitational redshift experiments (WEP-c) and direct free-fall experiments (WEP) using different types of matter may be considered. WEP-c was tested to relatively high accuracy ($\Delta g/g < 10^{-6}$) using matter and antimatter clocks, H and $\bar{H}$ [18, 24] as well as by measuring cyclotron frequencies of trapped p and $\bar{p}$ [19]. Such experiments arguably also constrain direct WEP-violation originating from certain SM extensions [24,26]. However, direct gravitational free-fall experiments (tests of the WEP) have never been carried out using anything other than normal matter, more precisely macroscopic objects of different material composition, neutral atoms or neutrons.

31.2 Experiments for testing the WEP

The most rigorous tests of the WEP utilize Earth-based and satellite-borne experiments that either use the modern versions of the Eötvös torsion pendulum, or other sensitive accelerometers. These experiments compare gravitational accelerations of two macroscopic test masses (g_1, g_2) in terms of the Eötvös parameter

$$\eta(1,2) = 2\frac{|g_1 - g_2|}{|g_1 + g_2|}. \tag{31.1}$$

The highest precision comes from the satellite-borne MICROSCOPE experiment [27] for titanium and platinum, giving $\eta(\text{Ti}, \text{Pt}) = [1 \pm 9(\text{stat}) \pm 9(\text{syst})] \times 10^{-15}$, which is about an order or magnitude better than the best torsion pendulum results from the Eöt-Wash group [28]. On the largest mass scales, the Lunar Ranging Test is the most notable, constraining differences between the Earth and Moon gravitational and inertial mass ratios to levels below $\sim 10^{-13}$ [29].

The WEP has been tested on the atomic scales as well. The latest atom interferometry results comparing two isotopes of rubidium in free-falling cold atom clouds confirmed a null measurement with $\eta(^{85}\text{Rb}, ^{87}\text{Rb}) = [1.6 \pm 1.8(\text{stat}) \pm 3.4(\text{syst})] \times 10^{-12}$ [30].

Gravitational acceleration has only been observed with one subatomic particle, the neutron. The most precise experiments were carried out using neutron refractometers [31], neutron spin-echo technique [32] and also the gravitational quantum states of ultracold neutrons [33, 34]: they have reached an overall precision of ~0.3 %. New experiments plan to improve this by at least an order of magnitude [35].

In summary, WEP tests have limited the Eötvös parameter to $\eta < 1.3 \times 10^{-14}$ for different (macroscopic) elements. Future satellite-borne experiments may improve the precision by two orders of magnitude [23, 36].

31.2.1 Possibilities for new physics violating WEP in exotic atoms

Conservative extensions of the SM and GR that would differentiate matter and antimatter in a free fall experiment were discussed with the specific case of antihydrogen [24]. The possibilities discussed include extensions of the existing theories like Kostelecký's extension of the SM [37] containing Lorentz- and CPT violating terms, or minimal modifications of GR that would maintain core principles (like local Lorentz invariance, causality, description as a Riemannian manifold) but modify the dynamics described by the action by adding extra terms that modify the energy-momentum tensor. Several possibilities of 'fifth force' scenarios have also been discussed in the literature, most recently in e.g. Refs. [38, 39]. In Ref. [24] it is pointed out how such new vector bosons could have different couplings to the oppositely charged matter and antimatter, and how this would impact WEP measurements.

The resulting theoretical possibilities are narrow, especially in light of existing WEP measurements on ordinary matter that arguably constrain effects of antimatter gravity via the core principles above and the potential and kinetic energies incorporated in the rest mass [26], and WEP-c measurements that already set constraints on GR extensions [24]. The overall conclusion from theory is that while possible violations of WEP in antihydrogen free-fall experiments may be envisaged, present viable models that do not break the principles of the GR or SM suggest that they are small, and almost certainly already constrained with WEP-c experiments at the $\Delta g/g < 10^{-6}$ level [24]. This consideration also applies to the proposed positronium experiments [11–13] that would probe the antimatter counterpart of the electron.

The same considerations however do not necessarily apply to muonium, which contains an elementary antiparticle from the second generation (μ^+). Direct gravitational tests have never been carried out before neither with μ^+ nor μ^-. Hence, we may not need to envision long-range vector bosons (fifth forces) that differentiate matter and antimatter to explain an

unexpected result, but could explore other new physics that couples differently to muons than electrons. In the light of recent precision experiments that show intriguing discrepancies in the charged lepton sector like the muon g-2 anomaly [5] or the B anomalies [40], such exotic BSM physics may not be so far fetched.

As to WEP-c tests, next generation experiments of the 1S-2S transition frequency of M have the capability of reaching ~ 0.1 ppm fractional precision, and of being sensitive to the effects of gravitational redshift change while the laboratory travels in the solar system (annual modulations of the gravitational potential in perihelion-aphelion) [41]. The interpretation of the muon g-2 result as a clock measurement [5, 41] may also bring some intriguing hints in the same direction.

We also note that there has been an ambiguity in interpreting what experiments with composite objects like neutrons or neutral atoms already tell us about the connection of gravity to the SM particles and interactions [26, 41]. About 99 % of the rest mass of protons and neutrons comes from the strong interaction that confines the constituent quarks. Nuclear binding- and kinetic energies further shift the mass up to ~ 9 MeV/c^2 per nucleon, while electrostatic interactions with another few eV/c^2. In this sense, direct gravity experiments have so far tested mainly binding energies from the strong interaction.

However, the mass of the muonium is dominated by the elementary muon mass, which is a fundamental parameter in the SM. Hence measuring muonium gravity may provide cleaner access to understanding the connection of gravity to elementary particles in the absence of an overwhelming strong interaction.

31.3 Prospects for a gravity experiment with a novel M beam

A direct gravity experiment using muonium is inherently challenging due to the short lifetime ($\tau \sim 2.2 \ \mu s$) of the μ^+ and the fact that M atoms must be created in matter, while experiments must be carried out *in vacuo*. These imply that we need to envision experiments using propagating atomic beams. A straightforward method is to use atom interferometry, which is known to be a sensitive method to observe inertial forces [30]. However, this requires ultracold atomic clouds, or well-collimated atomic beams with small transverse momentum.

Present vacuum muonium sources are room temperature, porous materials that allow combination of the muon with an electron from the bulk, and a following quick diffusion inside the nanoscopic pores (See Figure 31.1 A). Laser ablated silica aerogel is one of the best room temperature converters; the microscopic holes created by the laser enhance the emission of the M atoms into vacuum. Such sources provide $\sim 3\%$ muon-to-vacuum M conversion using surface μ^+ beams of 28 MeV/c momentum [42]. However, such converters produce a M beam with broad (thermal) energy and angular ($\sim\cos\theta$) distributions.

Mesoporous materials have been shown to convert μ^+ to vacuum M with efficiencies of 40% at room temperature when using a highly moderated, keV energy μ^+ beam; this has an intensity four orders-of-magnitude lower than a surface muon beam. These low-energy muons penetrate only a few μm into the surface, but are emitted with wide energy- and angular distributions [43]. Improving the source quality by cooling these samples results in lower emission rates, with no observable emission below ~ 50 K due to the decreased diffusion constant, and the sticking of M to the pore walls that occurs unavoidably with any conventional M converter [43, 44].

31.3.1 Vacuum muonium from superfluid helium

Superfluid helium (SFHe) may overcome the above mentioned difficulties due to its inert nature that rejects impurities from its bulk even at the lowest temperatures. This can be qualitatively explained by the unusually small mean distance (~ 0.3 nm) of the condensed He atoms:

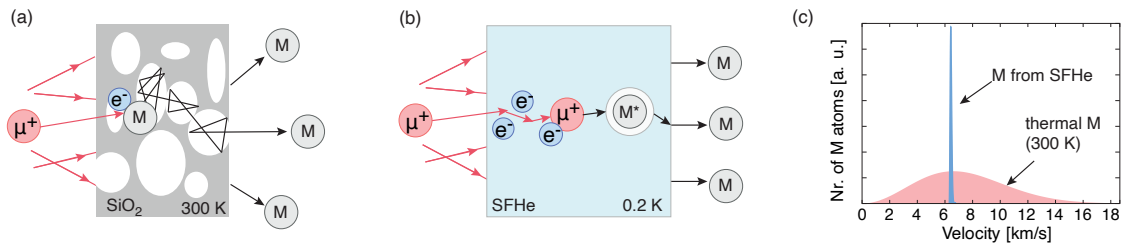Figure 31.1: (a) Principle of a conventional μ^+-to-vacuum-M converter based on porous materials. (b) Principle of a SFHe-based converter. (c) Comparison of the expected M velocity distribution from SFHe (blue) and a mesoporous (red) converters.

when implanting large impurity atoms or negative ions, nearby He atoms will be repelled by the Pauli core repulsion [45], resulting in a spherical cavity (bubble) around the impurity. This exercises an inward pressure that results in a positive chemical potential of M, that results in the ejection of the impurity from the bulk when they reach the surface.

The principle of the proposed M source relying on this mechanism [6,46] is summarized in Figure 31.1 (b). The μ^+ are stopped in the bulk of SFHe, where they capture an electron from the ionization trails. The M atom formed in the bubble state (M*) diffuses to the surface where it will be emitted perpendicularly, with kinetic energy defined by the chemical potential, only slightly broadened by thermal energies (Figure 31.1 (c)).

The chemical potentials for ^{4}He, ^{3}He, H, D and T in SFHe have been calculated [47,48], and these predictions have been experimentally verified for ^{4}He, ^{3}He and D [49]. Modelling M atoms as a light hydrogen isotope gives an approximate chemical potential of $E/k_B \approx 270$ K [50], implying that the M atom will leave the SFHe surface with a well defined longitudinal velocity of $v_M \sim 6300$ m/s. The velocity spread and the transverse velocities are given in first approximation by the thermal motion of the M* bubble in the liquid. Predicting this is difficult without a microscopic theory of the quantum liquid.

Based on [47], the M* acquires an effective mass of $m^*_M \approx 2.5\ m_{He}$ due to hydrodynamic back-flow effects in SFHe, similar to all hydrogen isotopes [50]. In a simplified model, the M* loses energy in a 200 mK isotopically-pure superfluid ^{4}He solely by creating rotons and phonons (no scattering on ^{3}He), until its kinetic energy falls below the roton gap [51] ($\Delta_{rot}/k_B = 8.6$ K), resulting in thermal velocities distributed below $v_t \approx 110$ m/s. Thermally available phonons are sparse at this temperature, hence scattering on phonons is unlikely on the relevant μs timescales [52]. The small effective mass of the M* suggests we can neglect other hydrodynamic effects like vortex nucleation as well [53], and assume that M* moves afterwards ballistically in the SFHe medium, with average velocities of $\bar{v}_t \approx v_t/2$. This allows a large fraction of the atoms to escape from $\sim 100\ \mu$m thick SFHe layers, a thickness that can efficiently stop μ^+ beams of 10-12 MeV/c momentum.

In summary, with the assumptions above and neglecting further surface effects, we expect efficient muon-to-vacuum-M ($\sim 10-30\%$) conversion with a mean atomic velocity of $v_M \approx 6.3$ mm/μs in the longitudinal direction (originating from the chemical potential), and a spread given approximately as $v_t \approx 0.11$ mm/μs from the thermal velocities above. This yields to a momentum bite of $< 0.01\%$, and $\alpha \approx v_t/v_M \approx 17$ mrad angular distribution. Moreover, the cold temperature of the SFHe (~ 200 mK) leads to a to a small saturated vapor density (equivalent to UHV conditions at room temperature) which is needed to reduce the collision of the vacuum M with the He gas that would degrade the quality of the M beam.

We have constructed a 200 mK cryogenic target cooled by a dilution refrigerator for the first proof-of-principle experiments to test the above theoretical assumptions, and presently carrying out the first measurements at PSI [54].
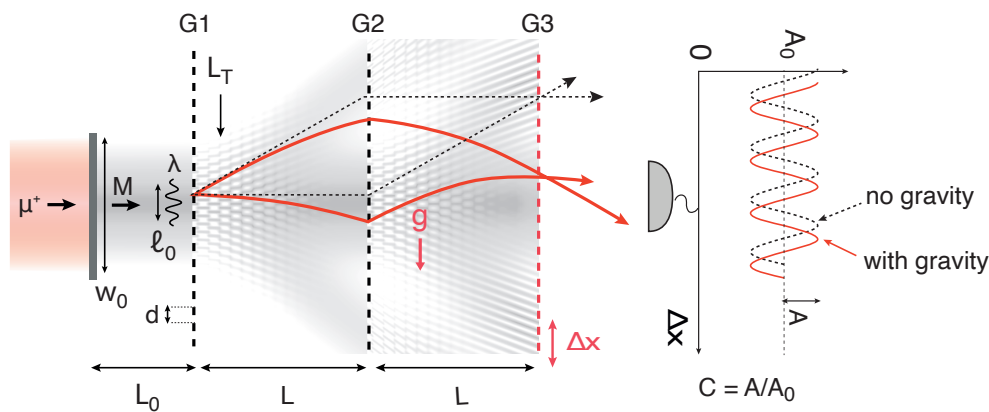
Figure 31.2: A three-grating interferometer used to measure the gravitational interaction of M atoms. The quantum diffraction pattern caused by the gratings G1 and G2 with a fully coherent beam is given in grey. Classical trajectories (red and dashed lines) are shown to illustrate the effect of gravity on the measured interference pattern appearing at G3. The vertical shift of the interference pattern caused by the gravitational acceleration g is detected by measuring the transmitted M rate while scanning G3 in vertical direction. See details in text.

31.3.2   Free fall experiment using M-atom interferometry

If the M atoms are initially at rest in the vertical direction and obey the weak equivalence principle, they fall a mere $\Delta x = \frac{1}{2}gt^2 = 600$ pm in a time of $t = 5\tau$. The measurement of this tiny gravitational fall needs precise knowledge of the initial momentum of the atoms, and requires strict momentum selection. Two periodic gratings (G1 and G2) with horizontal slits of pitch d and spaced by a distance L could be used to achieve this momentum selection as shown in Figure 31.2.

The classical and quantum regime of this device is characterized by de Broglie wavelength of the atoms, $\lambda = h/p$, and grating pitch d in terms of the Talbot length, $L_T = d^2/\lambda$, which is approximately 18 microns for thermal M atoms with $\lambda_M \approx 0.56$ nm. If the grating distances are much smaller than the Talbot length ($L \ll L_T$, the diffraction of the atoms can be neglected during propagation in the device, and this classical device is called a Moiré deflectometer. With the choice of much smaller grating pitch or larger distances $L \gg L_T$ diffraction and in general the wave nature of the atoms become significant, and we work on an interferometer.

With both classical and quantum cases, trajectory selection at G1 and G2 will result in an intensity pattern with the same periodicity d at a distance L after G2. Gravitational acceleration and deflection of the atoms causes a phase shift $\delta\phi$ of this pattern in the vertical direction as $\delta\phi = 2\pi g T^2/d$, where $T = L/v_M$ is the M time of flight between each pair of gratings.

Direct observation of this sub-micron patters and sub-nanometer shifts needed for measuring M gravity would be extremely hard. It is possible however to carry out an indirect measurement using a third grating (G3) of the same pitch d, placed at distance L from G2. By counting the total rate of M atoms transmitted through G3 as a function of the G3 vertical position Δx the phase shift can be measured.

The contrast of the intensity pattern C is defined by the ratio of the amplitude and the average yield $C = A/A_0$ as shown in Figure 31.2. When the three gratings work as an interferometer, this contrast strongly depends on the transverse coherence length of the beam, ℓ_0, that determines how many slits of G1 are illuminated with a coherent wavefront. This coherence length in relation to the beam width w_0 and the interferometer parameters (the grating

periodicity d and distances L) together with the de Broglie wavelength (λ) of the atoms is sufficient to estimate to describe the interferometer performance in the first approximation. In analogy to statistical optics (Van Cittert-Zernike theorem [55]), we can relate the transverse coherence length of the M beam to the transverse momentum distribution of the atoms: $\ell_0 = \frac{1}{2}\frac{\lambda}{\alpha} \approx 16$ nm, where α is the above mentioned angular spread of the M source. This initial transverse coherence is naturally increasing as the atoms experience diffraction on the first grating. In simplified terms, diffraction results in a new coherent wavefront, that expands along the angle of diffraction. Regardless whether the 3-grating device works in the classical regime or as an interferometer, the sensitivity in measuring the gravitational acceleration g is given by [56]

$$\Delta g = \frac{1}{2\pi T^2} \frac{d}{C\sqrt{N}} , \tag{31.2}$$

where N is the number of M atoms transmitted through G3 and measured by the detector given by

$$N = N_0\, \varepsilon_0\, e^{-(t_0 + 2T)/\tau}\, (T_G)^3\, \varepsilon_{\det}, \tag{31.3}$$

with N_0 being the number of M atoms produced at the M source, and ε_0 the M transport efficiency from the source to G1. The M decay is accounted for by the third term $e^{-(t_0+2T)/\tau}$, where t_0 is the time of flight from the source to G1. The number of detected M atoms is further reduced by the M detection efficiency $\varepsilon_{\det}$, and by the limited transmission T_G of a single grating. The short lifetime of the muon necessitates a gain in sensitivity by using a small grating pitch d. Maximal sensitivity, as a tradeoff between phase shift $\delta\phi$ and statistics N, is obtained for $T \approx 6 - 8\ \mu$s corresponding to an interferometer length of 40-50 mm.

A calculation of the interferometer parameters to extract the contrast C, uses an approximation of the M source with a Gaussian Schell-model beam [57], and adapted mutual intensity functions that are widely used to describe the propagation of partially coherent light [55]. Using realistic parameters on the initial beam size and quality expected from the superfluid source above, the fringe contrast of $C \approx 0.3$ at the exact position of G3 can be achieved. The contrast in this three-grating setup is less sensitive to the beam quality, but the sensitivity of the high contrast region along the propagation axis is, and shrinks to few μm. Such a measurement thus requires precise G3 positioning with μm-accuracy in the optical axis, and below-nm-accuracy in the vertical direction.

From (31.2) we see that determining the sign of g (more precisely to reach $\Delta g/g = 1$) in about one day, requires the detection of 3.2 M/s, assuming a contrast $C = 0.3$. Following (31.3), and taking pessimistic estimates from Monte Carlo simulations and initial detector and grating studies studies by using $T_G = 0.3$, $\varepsilon_0 = 0.75$ and $\varepsilon_{\det} = 0.3$, at the source we need $N_0 \approx 1.4 \times 10^4$ M/s. As a comparison the πE5 beam line at PSI can presently deliver $3.6 \times 10^6\ \mu^+$/s at a momentum of 10 MeV/c within a transverse area of about 400 mm². At this muon momentum we can expect a muon-to-vacuum-M conversion efficiency of about 0.1-0.3 based on the above discussion. This will result in M rates of up to $\sim 1.1 \times 10^6$ M/s. These high rates may allow a further collimation of the M beam to a 5×1 mm area, which would put less strain on grating production and alignment and would cut the number of useful M atoms conservatively by a factor 5 mm²/400 mm² = 0.013. Using these parameters where there is room for contingency, we expect to produce the necessary rate of $\sim 5 \times 10^4$ M/s in an small area of $\sim 5 \times 1$ mm², and reach the goal sensitivity of $\Delta g = \frac{9.8 \text{ m/s}^2}{\sqrt{\# \text{ days}}}$ with present μ^+ sources. An increase by two orders of magnitude in μ^+ rates expected by the proposed HIMB (High Intensity Muon Beam [58]) project at PSI will further improve the sensitivity of to g.

31.4 Summary and outlook

With the development of a novel, cold atomic M beam with high yields of $10^4 - 10^5$ M/s and angular divergence of $\alpha \sim 10 - 20$ mrad, direct measurement of the gravitational acceleration of M seems feasible on a $\Delta g/g = 10^{-2}$ level of precision. While this precision is not comparable to present tests of the equivalence principle using normal matter ($\Delta g/g < 10^{-15}$), this experiment would be the first direct free fall demonstration using second generation (anti)matter. Moreover, the purely leptonic content of the atom would make it possible to study gravity for the first time in the absence of large binding energies from the strong interaction.

We are presently carrying out feasibility studies, and developing the first prototype of the cryogenic atomic source and the accompanying detector system needed for this experiment at PSI. We are also investigating further theoretical aspects using realistic M beams, and working on production methods for the 100-nm-pitch M interferometer and stabilization methods needed for this precision.

References

[1] S. Chu, A. P. Mills, A. G. Yodh, K. Nagamine, Y. Miyake and T. Kuga, *Laser excitation of the muonium 1S-2S transition*, Phys. Rev. Lett. **60**, 101 (1988), doi:10.1103/PhysRevLett.60.101.

[2] V. Meyer et al., *Measurement of the1S-2S energy interval in muonium*, Phys. Rev. Lett. **84**, 1136 (2000), doi:10.1103/PhysRevLett.84.1136.

[3] W. Liu et al., *High precision measurements of the ground state hyperfine structure interval of muonium and of the muon magnetic moment*, Phys. Rev. Lett. **82**, 711 (1999), doi:10.1103/PhysRevLett.82.711.

[4] L. Willmann et al., *New bounds from a search for muonium to antimuonium conversion*, Phys. Rev. Lett. **82**, 49 (1999), doi:10.1103/PhysRevLett.82.49.

[5] B. Abi et al., *Measurement of the positive muon anomalous magnetic moment to 0.46 ppm*, Phys. Rev. Lett. **126**, 141801 (2021), doi:10.1103/PhysRevLett.126.141801.

[6] K. Kirch and K. Siang Khaw, *Testing antimatter gravity with muonium*, Int. J. Mod. Phys. Conf. Ser. **30**, 1460258 (2014), doi:10.1142/S2010194514602580.

[7] K. Kirch, *Testing gravity with muonium* (2007), arXiv:physics/0702143.

[8] A. Charman et al., *Description and first application of a new technique to measure the gravitational mass of antihydrogen*, Nat. Commun. **4**, 1785 (2013), doi:10.1038/ncomms2787.

[9] P. Scampoli and J. Storey, *The AEgIS experiment at CERN for the measurement of antihydrogen gravity acceleration*, Mod. Phys. Lett. A **29**, 1430017 (2014), doi:10.1142/S0217732314300171.

[10] P. Perez and Y. Sacquin, *The GBAR experiment: gravitational behaviour of antihydrogen at rest*, Class. Quantum Grav. **29**, 184008 (2012), doi:10.1088/0264-9381/29/18/184008.

[11] A. C. L. Jones et al., *Focusing of a Rydberg positronium beam with an ellipsoidal electrostatic mirror*, Phys. Rev. Lett. **119**, 053201 (2017), doi:10.1103/PhysRevLett.119.053201.

[12] D. B. Cassidy and S. D. Hogan, *Atom control and gravity measurements using Rydberg positronium*, Int. J. Mod. Phys. Conf. Ser. **30**, 1460259 (2014), doi:10.1142/S2010194514602592.

[13] P. Crivelli, D. A. Cooke and S. Friedreich, *Experimental considerations for testing antimatter antigravity using positronium 1S-2S spectroscopy*, Int. J. Mod. Phys. Conf. Ser. **30**, 1460257 (2014), doi:10.1142/S2010194514602579.

[14] S. Weinberg, *The quantum theory of fields*, vol. 2, Cambridge University Press (1995).

[15] J. Ellis and N. E. Mavromatos, *Comments on CP, T and CPT violation in neutral kaon decays*, Phys. Rep. **320**, 341 (1999), doi:10.1016/S0370-1573(99)00058-7.

[16] H. Dehmelt, R. Mittleman, R. S. Van Dyck and P. Schwinberg, *Past electron-positron g-2 experiments yielded sharpest bound on CPT violation for point particles*, Phys. Rev. Lett. **83**, 4694 (1999), doi:10.1103/PhysRevLett.83.4694.

[17] G. W. Bennett et al., *Search for Lorentz and CPT violation effects in muon spin precession*, Phys. Rev. Lett. **100**, 091602 (2008), doi:10.1103/PhysRevLett.100.091602.

[18] M. Ahmadi et al., *Characterization of the 1S–2S transition in antihydrogen*, Nature **557**, 71 (2018), doi:10.1038/s41586-018-0017-2.

[19] S. Ulmer et al., *High-precision comparison of the antiproton-to-proton charge-to-mass ratio*, Nature **524**, 196 (2015), doi:10.1038/nature14861.

[20] C. Smorra et al., *Direct limits on the interaction of antiprotons with axion-like dark matter*, Nature **575**, 310 (2019), doi:10.1038/s41586-019-1727-9.

[21] M. Hori et al., *Buffer-gas cooling of antiprotonic helium to 1.5 to 1.7 K, and antiproton-to-electron mass ratio*, Science **354**, 610 (2016), doi:10.1126/science.aaf6702.

[22] T. Damour, *Theoretical aspects of the equivalence principle*, Class. Quantum Grav. **29**, 184001 (2012), doi:10.1088/0264-9381/29/18/184001.

[23] A. M. Nobili and A. Anselmi, *Relevance of the weak equivalence principle and experiments to test it: Lessons from the past and improvements expected in space*, Phys. Lett. A **382**, 2205 (2018), doi:10.1016/j.physleta.2017.09.027.

[24] M. Charlton, S. Eriksson and G. M. Shore, *Testing fundamental physics in antihydrogen experiments* (2020), arXiv:2002.09348.

[25] M. Martin Nieto and T. Goldman, *The arguments against "antigravity" and the gravitational acceleration of antimatter*, Phys. Rep. **205**, 221 (1991), doi:10.1016/0370-1573(91)90138-C.

[26] M. A. Hohensee, H. Müller and R. B. Wiringa, *Equivalence principle and bound kinetic energy*, Phys. Rev. Lett. **111**, 151102 (2013), doi:10.1103/PhysRevLett.111.151102.

[27] P. Touboul et al., *MICROSCOPE mission: First results of a space test of the equivalence principle*, Phys. Rev. Lett. **119**, 231101 (2017), doi:10.1103/PhysRevLett.119.231101.

[28] S. Schlamminger, K.-Y. Choi, T. A. Wagner, J. H. Gundlach and E. G. Adelberger, *Test of the equivalence principle using a rotating torsion balance*, Phys. Rev. Lett. **100**, 041101 (2008), doi:10.1103/PhysRevLett.100.041101.

[29] J. G. Williams, S. G. Turyshev and D. H. Boggs, *Lunar laser ranging tests of the equivalence principle*, Class. Quantum Grav. **29**, 184004 (2012), doi:10.1088/0264-9381/29/18/184004.

[30] P. Asenbaum, C. Overstreet, M. Kim, J. Curti and M. A. Kasevich, *Atom-interferometric test of the equivalence principle at the 10-12 level*, Phys. Rev. Lett. **125**, 191101 (2020), doi:10.1103/PhysRevLett.125.191101.

[31] J. Schmiedmayer, *The equivalence of the gravitational and inertial mass of the neutron*, Nucl. Instr Meth. Phys. Res. Sec. A **284**, 59 (1989), doi:10.1016/0168-9002(89)90248-9.

[32] V.-O. de Haan, J. Plomp, A. A. van Well, M. Theo Rekveldt, Y. H. Hasegawa, R. M. Dalgliesh and N.-J. Steinke, *Measurement of gravitation-induced quantum interference for neutrons in a spin-echo spectrometer*, Phys. Rev. A **89**, 063611 (2014), doi:10.1103/PhysRevA.89.063611.

[33] V. V. Nesvizhevsky et al., *Quantum states of neutrons in the earth's gravitational field*, Nature **415**(6869), 297 (2002), doi:10.1038/415297a.

[34] V. V. Nesvizhevsky et al., *Study of the neutron quantum states in the gravity field*, Eur. Phys. J. C **40**, 479 (2005), doi:10.1140/epjc/s2005-02135-y.

[35] G. V. Kulin, A. I. Frank, S. V. Goryunov, D. V. Kustov, P. Geltenbort, M. Jentschel, A. N. Strepetov and V. A. Bushuev, *Spectrometer for new gravitational experiment with UCN*, Nucl. Instr Meth. Phys. Res. Sec. A **792**, 38 (2015), doi:10.1016/j.nima.2015.04.009.

[36] A. M. Nobili et al., *'Galileo Galilei' (GG): space test of the weak equivalence principle to 10-17 and laboratory demonstrations*, Class. Quantum Grav. **29**, 184011 (2012), doi:10.1088/0264-9381/29/18/184011.

[37] V. Alan Kostelecký and J. D. Tasson, *Prospects for large relativity violations in matter-gravity couplings*, Phys. Rev. Lett. **102**, 010402 (2009), doi:10.1103/PhysRevLett.102.010402.

[38] L. Basso, A. Belyaev, S. Moretti and C. H. Shepherd-Themistocleous, *Phenomenology of the minimal B-L extension of the standard model: Z' and neutrinos*, Phys. Rev. D **80**, 055030 (2009), doi:10.1103/PhysRevD.80.055030.

[39] J. Heeck, *Unbroken B − L symmetry*, Phys. Lett. B **739**, 256 (2014), doi:10.1016/j.physletb.2014.10.067.

[40] R. Aaij et al., *Test of lepton universality in beauty-quark decays* (2021), arXiv:2103.11769.

[41] S. G. Karshenboim, *A constraint on antigravity of antimatter from precision spectroscopy of simple atoms*, Astron. Lett. **35**, 663 (2009), doi:10.1134/S1063773709100028.

[42] G. A. Beer et al., *Enhancement of muonium emission rate from silica aerogel with a laser-ablated surface*, Progr. Theor. Exper. Phys. **2014**, 91C01 (2014), doi:10.1093/ptep/ptu116.

[43] A. Antognini et al., *Muonium emission into vacuum from mesoporous thin films at cryogenic temperatures*, Phys. Rev. Lett. **108**, 143401 (2012), doi:10.1103/PhysRevLett.108.143401.

[44] K. S. Khaw, *Towards next generation fundamental precision measurements with muons*, Ph.D. thesis, ETH Zürich Research Collection (2015), doi:https://www.research-collection.ethz.ch/handle/20.500.11850/102926.

[45] J. Peter Toennies and A. F. Vilesov, *pectroscopy of atoms and molecules in liquid helium*, Annu. Rev. Phys. Chem. **49**, 1 (1998), doi:10.1146/annurev.physchem.49.1.1.

[46] D. Taqqu, *Ultraslow muonium for a muon beam of ultra high quality*, Physics Procedia **17**, 216 (2011), doi:10.1016/j.phpro.2011.06.039.

[47] M. Saarela and E. Krotscheck, *Hydrogen isotope and ^3He impurities in liquid ^4He*, J Low Temp Phys **90-90**, 415 (1993), doi:10.1007/BF00681890.

[48] J. M. Marín, J. Boronat and J. Casulleras, *Atomic and molecular hydrogen impurities in liquid ^4He*, J. Low Temp. Phys. **110**, 205 (1998), doi:10.1023/A:1022599725388.

[49] M. E. Hayden and W. N. Hardy, *Atomic hydrogen-deuterium mixtures at 1 kelvin: Recombination rates, spin-exchange cross sections, and solvation energies*, J Low Temp Phys **99**, 787 (1995), doi:10.1007/BF00753562.

[50] E. Krotscheck, *Private communication* (2020).

[51] D. R. Tilley and J. Tilley, *Superfluidity and superconductivity*, CRC Press (1990).

[52] S. K. Lamoreaux et al., *Measurement of the ^3He mass diffusion coefficient in superfluid ^4He over the 0.45–0.95 K temperature range*, Europhys. Lett. **58**, 718 (2002), doi:10.1209/epl/i2002-00408-4.

[53] P. McClintock and D. Zmeev, *Private communication* (2021).

[54] *BVR meeting, PSI*, https://indico.psi.ch/event/6381/.

[55] J. W. Goodman, *Statistical optics*, John Wiley & Sons (2015).

[56] M. K. Oberthaler, S. Bernet, E. M. Rasel, J. Schmiedmayer and A. Zeilinger, *Inertial sensing with classical atomic beams*, Phys. Rev. A **54**, 3165 (1996), doi:10.1103/PhysRevA.54.3165.

[57] B. McMorran and A. D. Cronin, *Model for partial coherence and wavefront curvature in grating interferometers*, Phys. Rev. A **78**, 013601 (2008), doi:10.1103/PhysRevA.78.013601.

[58] *The HIMB project, PSI*, https://www.psi.ch/en/ltp-muon-physics/the-high-intensity-muon-beam-himb-project.